Aix*Marseille université
Socialement engagée

NNT : 0000AIXM0000

THÈSE DE DOCTORAT

Soutenue à Aix-Marseille Université
le 04 avril 2024 par

Romain AVELLAN

Inhibiteurs sélectifs pour décrypter le métabolisme des lipides chez les mycobactéries pathogènes

Discipline : Sciences chimiques

École doctorale 250 :
Sciences Chimiques

Laboratoire d'ingénierie des systèmes macromoléculaires UMR7255

Centre National de la Recherche Scientifique

Devant le jury :

Yann GUERARDEL Rapporteur
UMR8576, UGSF, CNRS, Université de Lille

Dominique GUIANVARC'H Rapportrice
UMR8182, ICMMO, CNRS, Université Paris-Saclay

Mickaël BLAISE Examinateur
UMR9004, IRIM, CNRS, Université de Montpellier

Odile SCHILTZ Examinatrice
UMR5089, IPBS, CNRS, Université de Toulouse

Stéphane GASTALDI Président du jury
UMR7273, IRC, CNRS, Aix-Marseille Université

Jean-François CAVALIER Directeur de thèse
UMR7255, LISM, CNRS

cnrs LISM anr Institut de Microbiologie de la Méditerranée imm

Affidavit

Je soussigné, Romain Avellan, déclare par la présente que le travail présenté dans ce manuscrit est mon propre travail, réalisé sous la direction scientifique de Jean-François Cavalier, dans le respect des principes d'honnêteté, d'intégrité et de responsabilité inhérents à la mission de recherche. Les travaux de recherche et la rédaction de ce manuscrit ont été réalisés dans le respect à la fois de la charte nationale de déontologie des métiers de la recherche et de la charte d'Aix-Marseille Université relative à la lutte contre le plagiat.

Ce travail n'a pas été précédemment soumis en France ou à l'étranger dans une version identique ou similaire à un organisme examinateur.

Fait à Marseille, le 9 janvier 2024



Cette œuvre est mise à disposition selon les termes de la Licence Creative Commons Attribution - Pas d'Utilisation Commerciale - Pas de Modification 4.0 International.

Liste de publications et/ou brevets et participation aux conférences

1) Liste des publications et/ou brevet réalisées dans le cadre du projet de thèse :

1. **R. Avellan***, M. Sarrazin*, C.D. Spilling, C. Crauste, S. Canaan, J.-F. Cavalier, "*Chapter 11 - Deciphering the physiological role of serine enzymes involved in mycobacterial lipid metabolism using activity-based protein profiling"*, in: Z. Fatima, S. Canaan (Eds.) Biology of Mycobacterial Lipids, Academic Press, 2022, pp. 235-251. https://doi.org/10.1016/B978-0-323-91948-7.00001-4 (* contribution égale)
2. M. Sarrazin*, B.P. Martin*, **R. Avellan***, G.R. Gnawali*, I. Poncin, H. Le Guenno, C.D. Spilling, J.-F. Cavalier, S. Canaan, "*Synthesis and Biological Characterization of Fluorescent Cyclipostins and Cyclophostin Analogues: New Insights for the Diagnosis of Mycobacterial-Related Diseases*" ACS Infect Dis 2022, 8(12), 2564-2578. https://doi.org/10.1021/acsinfecdis.2c00448 (* contribution égale).
3. S. Barelier, **R. Avellan**, G.R. Gnawali, P. Fourquet, V. Roig-Zamboni, I. Poncin, V. Point, Y. Bourne, S. Audebert, L. Camoin, C.D. Spilling, S. Canaan, J.-F. Cavalier, G. Sulzenbacher, "*Direct capture, inhibition and crystal structure of HsaD (Rv3569c) from M. tuberculosis*" Febs J. 2023, 290, 1563-1582. https://doi.org/10.1111/febs.16645.
4. **R. Avellan***, J. Lehoux*, T. Dargham*, T. Francis, L. Celik, A. Guy, I. Poncin, V. Point, L. Kremer, T. Durand, S. Audebert, L. Camoin, C.D. Spilling, P. Santucci, C. Crauste, S. Canaan, J.-F. Cavalier, "*Mapping of mycobacterial lipolytic enzymes involved in triacylglycerol accumulation as intrabacterial lipid inclusions using multi-target inhibitor-like affinity-based probes*" Manuscrit en preparation (* contribution égale).
5. T. Dargham*, J. Aguilera-Correa*, **R. Avellan***, I. Mallick, L. Celik, G. Brasseur, I. Poncin, V. Point, S. Audebert, L. Camoin, W. Daher, J.-F. Cavalier, L. Kremer & S. Canaan, "*A proteomic and functional view of intrabacterial lipid inclusion biogenesis in mycobacteria*" Manuscrit en soumission (* contribution égale).

2) Participation aux conférences et écoles d'été au cours de la période de thèse :

1. Présentation Poster : "*Synthesis and antimycobacterial activity of Fluorescent Labeled Affinity Probes Based on Monocylic Phosphonate and Phosphate Analogs of the Cyclipostins and Cyclophostin*" **R. Avellan**, M. Sarrazin, B.P. Martin, G.R. Gnawali, H. Le Guenno, C. Crauste, T. Durand, S. Audebert, L. Camoin, C.D. Spilling, S. Canaan, J.-F. Cavalier. Mycodays 2022, Lyon les 20-22 Juin 2022.
2. Présentation Poster : "*New selective inhibitors for deciphering lipid metabolism in pathogenic mycobacteria*" **R. Avellan**, C.D Spilling, C. Crauste, L. Camoin, G.

Sulzenbacher, S. Canaan, J.-F. Cavalier. JSM3 Conference 6ème edition, Marseille les 4-6 Juin 2022.

3. Présentation Orale : "*New selective inhibitors for deciphering lipid metabolism in pathogenic mycobacteria*" **R. Avellan**. JSM3 Conference 6ème edition, Marseille les 4-6 Juin 2022.

Résumé

Une des principales caractéristiques des mycobactéries, est leur capacité à importer et à retraiter les acides gras libres dérivés de l'hôte, stockés sous forme de triacylglycérols (TAG) sous la forme d'Inclusions Lipidiques Intrabactériennes (ILI). Ces ILI servent de source de carbone et d'énergie pour la survie de la bactérie, impliquant donc la présence d'enzymes mycobactériennes responsables de leur synthèse et de leur hydrolyse ; enzymes dont la plupart possèdent une sérine ou une cystéine catalytique dans leur site actif : *i.e.*, (Ser/Cys)-enzymes.

Dans ce contexte, nous avons utilisé deux familles d'inhibiteurs, les **CyCs** et les **OXs**, comme outils pour le diagnostic des infections mycobactériennes et comme sondes pour décrypter le métabolisme des lipides chez *M. abscessus* (*M. abs*) et *M. tuberculosis* (*M. tb*). En utilisant des approches de chemobiologie, nous avons réalisé la capture directe des enzymes inhibées par nos **CyCs** et **OXs** à partir d'une culture de *M. tb*. Parmi la variété d'enzymes identifiées, majoritairement impliquées dans le métabolisme des lipides ou des stérols, nous avons caractérisé biochimiquement et structurellement HsaD (Rv3569c), protéine impliquée dans le métabolisme du cholestérol et annotée comme essentielle pour la survie de *M. tb* dans les macrophages. Cette approche de CC-ABPP a ensuite été appliquée sur des cultures de *M. abs* dans des conditions mimant l'accumulation des ILI. Les données de protéomique obtenues ont été soumises à une analyse statistique conduisant à une liste de 65 enzymes potentiellement impliquées dans le métabolisme des lipides ou des acides gras chez *M. abs*. La construction de mutant de délétion, complémentation et de surexpression, nous a permis de valider que MAB_1978c (FadD15), une acyl-CoA ligase, était directement impliquée dans la biogénèse de ces ILI chez *M. abs*.

Mot clefs : *Mycobacterium tuberculosis, Mycobacterium abscessus*, Oxadiazolone, Cyclophostine/Cyclipostins, Métabolisme des lipides, Chemobiologie, Chimie click, Inclusions lipidiques Intrabactériennes

Abstract

One of the main characteristics of mycobacteria is their ability to import and process host-derived free fatty acids, which are then stored as triacylglycerols (TAGs) in their own cytoplasm in the form of Intrabacterial Lipid Inclusions (ILI), which serve as a source of carbon and energy for the bacterium's survival. This property underscores the essential role of lipid metabolism in the survival and long-term persistence of mycobacteria and, consequently, of the mycobacterial enzymes responsible for the synthesis and hydrolysis of these mycobacterial lipids. Most of these enzymes have a catalytic serine or cysteine in their catalytic sites: *i.e.*, (Ser/Cys) enzymes.

In this context, we used two families of inhibitors, the **CyCs** and the **OXs**, as tools for the diagnosis of mycobacterial infections and as probes for deciphering lipid metabolism in *M. abscessus* (*M. abs*) and *M. tuberculosis* (*M. tb*). Using chemobiological approaches (click-chemistry activity-based protein profiling, CC-ABPP), we were able to directly capture enzymes inhibited by our **CyCs** and **OXs** from a *M. tb* culture. Among the enzymes identified, mostly involved in lipid or sterol metabolism, we biochemically and structurally characterized HsaD (Rv3569c), a protein involved in cholesterol metabolism and annotated as essential for *M. tb* survival in macrophages. This CC-ABPP approach was further applied to *M. abs* cultures under conditions mimicking ILI accumulation. The proteomic data obtained were subjected to statistical analysis, resulting in a setlist of 65 enzymes potentially involved in lipid or fatty acid metabolism in *M. abs*. The construction of deletion, complementation and overexpression mutants allowed us to validate that MAB_1978c (FadD15), a long-chain-fatty-acid--CoA ligase, is directly involved in the biogenesis of these ILI in *M. abs*.

Keywords: *Mycobacterium tuberculosis, Mycobacterium abscessus*, Oxadiazolone, Cyclophostin/Cyclipostins, Lipid metabolism, Chemobiology, Click-chemistry, Intrabacterial Lipid Inclusions.

Remerciements

Pour commencer je tiens à remercier chaleureusement le Dr Jean François CAVALIER, mon directeur de thèse, qui est à l'origine de ce projet et sans qui il n'aurait pas vu le jour. Je voudrais lui exprimer ma gratitude pour tout le temps qu'il m'a consacré, l'ensemble de ses conseils et méthodologies techniques ainsi que les discussions scientifiques que nous avons partagé et qui m'ont énormément appris au cours de ces trois ans. Il a toujours été d'une aide précieuse dans la conception et la réalisation de mes travaux ainsi que dans l'écriture des différents articles et rapports, et de ce manuscrit. Je tiens également à le remercier de la confiance qu'il m'a accordé en me confiant les sujets de recherche développés dans ce manuscrit.

Je voudrais également remercier mes rapporteurs, la Professeure Dominique GUIANVARC'H et le Docteur Yann GUERARDEL d'avoir accepté d'évaluer ce travail de thèse. Je remercie également le Docteur Odile SCHILTZ et le Docteur Mickaël BLAISE d'avoir accepté d'examiner mon travail et de participer à mon jury de thèse, ainsi que le Docteur Stéphane GASTALDI qui préside ce jury.

Ce travail n'aurait pas été possible sans l'accueil chaleureux et le soutien de l'équipe *Lipolyse et Pathogénie Bactérienne* au sein de laquelle j'ai évolué durant mes travaux. J'ai énormément appris à leur côté, et leurs conseils précieux se sont révélés indispensables à la conduite des études menées durant ce projet. Je souhaite remercier particulièrement le Docteur Pierre SANTUCCI pour ces innombrables conseils en design expérimental, ses retours bibliographiques profonds et inestimables ainsi que pour sa bonne humeur. Je voudrais également remercier le docteur Stéphane CANAAN, qui dirige cette équipe, pour le temps qu'il a pu m'accorder et ces retours expérimentaux et théoriques, ainsi que pour la motivation qu'il impulse à l'équipe. Je veux également remercier Vanessa POINT et Isabelle PONCIN pour leurs innombrables conseils pratiques et formations techniques, ainsi que pour leur bonne humeur constante et vivifiante. J'adresse également ici un grand merci à l'ensemble des doctorants de l'équipe, notamment Tonia DARGHAM et Morgane SARRAZIN pour les collaborations effectuées, ayant résulté à la publication de belles études, ainsi qu'à Thomas FRANCIS, mon ami depuis dix ans maintenant, et dont la collaboration sur mes travaux a été conséquente et précieuse. Collaborer avec lui et travailler à ses coté a été un plaisir et je lui

souhaite de réussir une belle thèse. Je veux également adresser un énorme merci à Emma FOREST, que j'aime de tout mon cœur. Sa présence à mes côtés lors de la réalisation de mes expériences et surtout lors de la rédaction de ce manuscrit a été un soutien et une aide précieuse et indispensable. Je la remercie pour les heures passées à corriger, reformuler et collaborer à l'écriture de ce manuscrit, pour sa présence et son soutien pendant les longues heures d'écriture sans lesquelles la qualité de ce manuscrit n'aurait pas été la même.

Je voudrais également remercier les docteurs Gilles IACAZIO, Michel FONS, Eric DURAND, Jean-Emmanuel HUGONNET et Gilles LABESSE pour leur participation à mon comité de suivi de thèse. Leurs analyses et retours sur mes travaux ont été d'une aide précieuse, et leurs conseils utiles ont contribué à l'élaboration de ce travail.

Je voudrais remercier l'ensemble des collaborateurs qui ont contribué à la réalisation des études présentées dans ce manuscrit, l'équipe du Prof. SPILLING pour la synthèse des composés CyC, celle du Dr Céline CRAUSTE pour la synthèse des composés OX, l'équipe du Dr Luc CAMOIN pour la réalisation des analyses de spectrométrie de masse ainsi que Sarah BARELIER et l'équipe du Dr Gerlind SULZENBACHER pour l'obtention et l'analyse des structures cristallines des complexes HSAD/inhibiteurs.

Je remercie également l'ensemble de l'institut IMM et du LISM dans lequel j'ai évolué durant ces trois années. Ce fut un cadre stimulant et j'ai pu y rencontrer de nombreuses personnes intéressantes lors des différent congrès et séminaires et y développer ma curiosité scientifique ainsi que mes connaissances théoriques.

Enfin je voudrais remercier ma famille et mes amis pour leur soutien durant la réalisation de ces travaux, et pour avoir toujours cru en moi durant ces trois années. Ils ont fait de moi la personne que je suis aujourd'hui et la réussite de ce projet est également la leur.

Ce manuscrit est le fruit d'un travail collégial, et je sais qu'il est difficile de remercier toutes les personnes y ayant contribué. Je remercie énormément toutes les personnes qui m'ont entourées et qui ont collaboré pendant la réalisation et la rédaction de ces travaux, et je leur dédie ce manuscrit.

Sommaire

Abréviations

Introduction bibliographique 1

I. Généralités sur les mycobactéries 2

a) Classification et phylogénie des mycobactéries 4

b) L'enveloppe mycobactérienne 5

II. *M. tuberculosis* 9

a) Epidémiologie, incidence 9

b) Physiopathologie et cycle de vie de l'infection 10

c) Granulome, niches bactériennes, macrophages spumeux, ILI et dormance 12

d) Le diagnostic de *M. tb* 14

e) Antibiothérapie contre *M. tb* 15

f) Nouvelles molécules en développement 20

III. *Mycobacterium abscessus* 26

a) Généralités 26

b) Physiopathologie des infections pulmonaires 27

c) Mucoviscidose et *M. abs* 32

d) Le diagnostic de *M. abs* 35

e) Antibiothérapie contre *M. abs* 36

f) Nouvelles molécules en développement 38

IV Les enzymes lipolytiques mycobactériennes et leur étude par « *Activity-Based Protein Profiling* » (ABPP) 42

V. Métabolisme des ILI et modèles pour leur étude 42

a) Synthèse des TAG 43

b) Le système FAS et la synthèse *de novo* des acides gras 44

c) Import d'acides gras exogènes 47

d) Les ILI, source de carbone et résistance au stress 48

e) ILI et pathogénie 49
f) ILI et résistance aux antibiotiques 51
g) Induction expérimentale de la synthèse d'ILI 51
VI. Nouveaux inhibiteurs sélectifs : les **OX** et les **CyC** 54
a) Les Oxadiazolones (**OX**) 54
b) Cyclophostines et Cyclipostins (**CyC**) 59
c) Inhibiteurs de croissance mycobactérienne multi-cibles 64
d) Inhibiteurs multi-cibles et ABPP avec les **CyC** et les **OX** 69
Objectifs 74
Résultats 78
Article I 79
Deciphering the physiological role of serine enzymes involved in mycobacterial lipid metabolism using activity-based protein profiling
Article II 100
Synthesis and Biological Characterization of Fluorescent Cyclipostins and Cyclophostin Analogues: New Insights for the Diagnosis of Mycobacterial-Related Diseases
Article III 156
Direct capture, inhibition and crystal structure of HsaD (Rv3965c) from *M. tuberculosis*
Article IV 195
Mapping of mycobacterial lipolytic enzymes involved in triacylglycerol accumulation as intrabacterial lipid inclusions using multi-target inhibitor-like affinity-based probes
Article V 269
A proteomic and functional view of intrabacterial lipid inclusion biogenesis in mycobacteria
Conclusion et perspectives 320
Références bibliographiques 329

Abréviations

ABC : « *ATP Binding Cassette* »

ABPP : « *Activity-Based Protein Profiling* »

ABP : « *Activity-Based Probe* »

ACC : Acyl-CoA Carboxylase

AG : Arabinogalactane

Ag85 : Antigène 85

ARN : Acides RiboNucléiques

ATP : Adénine Tri-Phosphate

ATS : « *American Thoracic Society* »

BAAR : Bacille Acido-Alcoolo Résistant

CC_{50} : Concentration de composé causant 50% de mortalité cellulaire

CC-ABPP : « *Click Chemistry Activity-Based Protein Profiling* »

CFTR : « *Cystic Fibrosis Transmembrane Conductance Regulator* »

CMI : Concentration Minimale Inhibitrice

CMI_{50} : Concentration minimale de composé inhibant 50% de la croissance bactérienne

CoA : Coenzyme A

CyC : Analogues de Cyclophostines et Cyclipostins

DAG : Diacylglycérol

DMSO : Dimethyl Sulfoxide

EMB : Ethambutol

EPTB : « *Extrapulmonary Tuberculosis* »

FAS : « *Fatty Acid Synthase* »

FATP : « *Fatty Acid Transport Proteins* »

FFA : « *Free Fatty Acids* »

FM : « *Foamy Macrophage* »

FP : Fluorophosphonate

GlcNAC : *N*-acétylglucosamine

GPL : Glycopeptidolipide

hMGL : Monoacylglycérol lipase humaine

HSL : Lipase Hormono-Sensible

IDSA : « *Infectious Diseases Society of America* »

ILI : Inclusions Lipidiques Intrabactériennes

INH : Isoniazide

KAN : Kanamycine

LAM : Lipoarabinomannane

LB : « *Lipid Body* »

LD : « *Lipid Droplets* »

LTBI : « *Latent Tuberculosis Infection* »

MABc : *Mycobacterium abscessus* complex

M. abs : *Mycobacterium abscessus*

MCL : Mycobactérie à Croissance Lente

MCR : Mycobactérie à Croissance Rapide

MDR-TB : « *Multi-Drug Resistant Tuberculosis* »

MM : Mycomembrane

MNT : Mycobactéries Non Tuberculeuses

MP : Membrane Plasmique

MrNAc : *N*-acétylmuramique

M. smeg : *Mycobacterium smegmatis*

MSM-NL : « *Minimal Salt Media – Nitrogen Limited* »

M. tb : *Mycobacterium tuberculosis*

MTBC : *Mycobacterium tuberculosis* complex

NBD : « *Nucleotid Binding Domain* »

NK : « *Natural Killer* »

OMS : Organisation Mondiale de la Santé

OX : Oxadiazolone

PBP : Penicillin-Binding Protein

PDIM : Phthiocerol Dimycocerosates

PG : Peptidoglycane

PGL : Phenolic Glycolipids

PIM : Phosphatidylinositol Mannoside

POA : Acide Pyrazinoïque

PZA : Pyrazinamide

R : « *Rough* »

RIF : Rifampicine

ROS : « *Reactive Oxygen Species* »

S : « *Smooth* »

SDS-PAGE : « *Sodium Dodecyl Sulfate PolyAcrylamide Gel Electrophoresis* »

STR : Streptomycine

TAG : Triacylglycérol

TB : Tuberculose

TDM : Tréhalose Dimycolate

TDR-TB : « *Total Drug Resistant Tuberculosis* »

TGS : Triglycéride Synthase

TMM : Tréhalose Monomycolate

VIH : Virus de l'Immunodéficience Humaine

WE : « *Wax Esters* »

XDR-TB : « *Extensively-Drug Resistant Tuberculosis*

Introduction bibliographique

I. Généralités sur les mycobactéries

Les mycobactéries sont un genre bactérien très diversifié, pour lequel la communauté scientifique présente un fort intérêt en raison de nombreuses bactéries pathogènes représentant un problème majeur de santé publique telles que *Mycobacterium tuberculosis (M. tb)* ou encore *Mycobacterium leprae (M. leprae)*. Il comprend également des pathogènes opportunistes tels que *Mycobacterium abscessus* (*M. abs*) et un grand nombre de bactéries environnementales. De plus les mycobactéries pathogènes présentent un nombre important et grandissant de résistances naturelles ou acquises aux antibiotiques contribuant à l'ampleur du défi de santé publique qu'elles représentent.

Les premières mycobactéries décrites furent *M. leprae* en 1880 [1] (initialement appelé *Bacillus leprosy*) et *M. tb* en 1883 [2] (initialement appelée *Bacterium tuberculosis*). Cependant, ce n'est qu'en 1896 que Lehmann et Neumann [3] regroupent ces organismes sous le genre *Mycobacterium* et les renomment sous leur nom actuel. Bien que seulement 41 espèces [4] aient initialement été incluses dans cette clade, elle est aujourd'hui très diversifiée et compte plus de 190 espèces identifiées.

Le genre Mycobacterium appartient à la famille des *Mycobacteriaceae*, l'ordre des *Actinomycetales* dans la classe des Actinomycètes (**Figure 1**). Ce genre se caractérise par trois caractères particuliers :

- Un génome très riche en guanine et cytosine (jusqu'à 70% pour certaines souches)
- Une importante résistance à l'acide et à l'alcool (on parle de Bacilles Acido-Alcoolo Résistants ou BAAR) ne permettant pas leur caractérisation grâce à la coloration de Gram. Il est donc nécessaire d'utiliser une coloration spécifique : la coloration de Ziehl-Neelsen [5].
- La présence dans leur membrane d'un type particulier d'acides gras α-ramifiés et β-hydroxylés appelés acides mycoliques possédant entre 60 et 90 atomes de carbone [6].

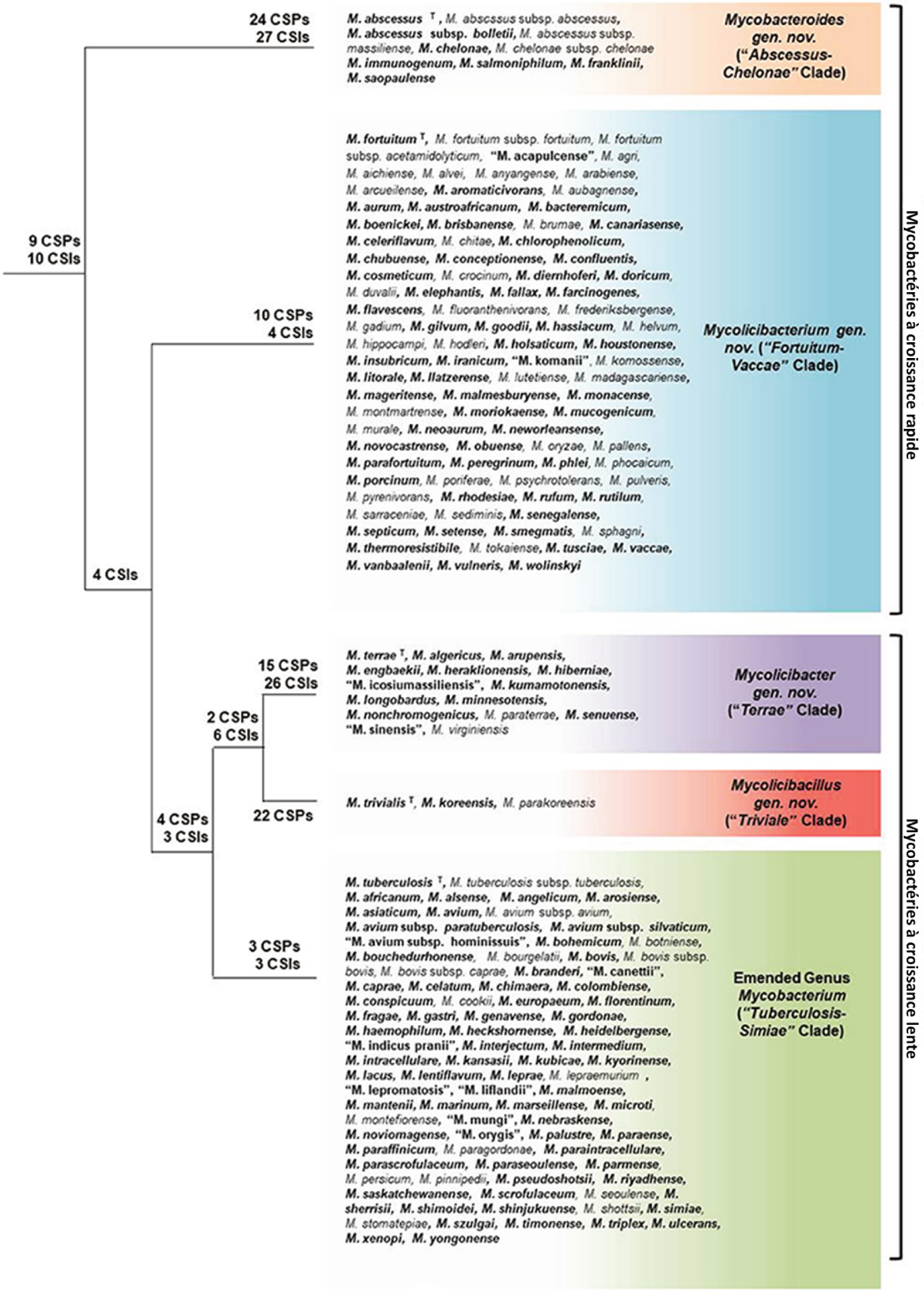

Figure 1 : Arbre phylogénétique du genre mycobactérien montrant les relations des différents membres de ce clade selon une comparaison génétique récente [7] réalisée sur 150 espèces de mycobactéries, sur la base de 1941 protéines centrales de ce clade. Le nombre de CSIs (*conserved signature indels*) et de CSPs (*conserved signature proteins*) spécifiques à chaque clade est indiqué sur les nœuds de l'arbre. Ce travail a conduit en la distinction 5 clades de mycobactéries que sont : *Mycolicibacterium*, *Mycolicibacter*, *Mycolicibacterium*, *Mycobacteroides* et *Mycoavidus*. Elles ont également été classées selon un critère phénotypique de croissance qui se superpose à cette classification génétique où on distingue les mycobactéries à croissance rapide (*Mycolicibacterium* et *Mycolicibacter*) des mycobactéries à croissance lente (*Mycolicibacterium*, *Mycobacteroides* et *Mycoavidus*). Adapté de [7].

a) Classification et phylogénie des mycobactéries

Les bactéries du genre *Mycobacterium* peuvent être classifiées de différentes façons en fonction de leurs caractéristiques phénotypiques et génétiques, ou encore en fonction de leur pathogénicité.

On distingue d'une part les mycobactéries à croissance rapide (MCR) qui poussent sur gélose en moins de 7 jours, et les mycobactéries à croissance lente (MCL) qui peuvent prendre plusieurs semaines à pousser en milieu liquide [8] (**Figure 1**). Bien que la phylogénie de ce groupe fût initialement principalement basée sur leur caractère phénotypique, elle est aujourd'hui établie sur la base d'analyse de génétique comparative et de phylogénique. Ainsi, on peut voir en **Figure 1** l'arbre phylogénétique résultant d'une étude récente [7] d'analyse génomique comparative réalisée sur 150 espèces de mycobactéries, en comparant les séquences de 1941 protéines centrales de ce clade. Cette étude a conduit à affiner la classification des mycobactéries en cinq clades différents (**Figure 1**). On distingue un clade Mycobacterium restreint comprenant *M. tb*, *M. bovis* ou encore *M. avium*, ainsi que quatre nouveaux clades introduits suite à cette étude : *Mycolicibacterium*, *Mycolicibacter*, *Mycobacteroides*, et *Mycoavidus*. Les auteurs justifient également cette classification génétique par différents caractères phénotypiques concernant la composition membranaire et le métabolisme :

- *Mycobacterium* : Ce clade comprend l'espèce type *M. tb* ainsi que plusieurs autres espèces étroitement apparentées appartenant au complexe *Mycobacterium tuberculosis* comme *M. africanum*, *M. bovis M. microti*, *M. canettii*, *M. caprae* ou encore *M. pinnipedii*. Ces bactéries possèdent une paroi cellulaire complexe contenant des acides mycoliques et sont connues pour causer la tuberculose et d'autres maladies chez les humains et les animaux.
- *Mycolicibacterium* : Ce clade comprend plusieurs espèces précédemment classées comme membres du complexe *Mycobacterium fortuitum*. Ces bactéries ont une structure de paroi cellulaire similaire à celle du clade *Mycobacterium*, mais sont génétiquement distinctes et présentent certaines différences au niveau de leurs voies métaboliques. Elles se retrouvent dans l'environnements, y compris le sol et l'eau, et certains membres peuvent causer des infections opportunistes chez les humains.

- *Mycolicibacter* : Ce clade comprend plusieurs espèces précédemment classées comme membres du groupe *Mycobacterium smegmatis*. Ces bactéries ont une structure de paroi cellulaire plus simple que les clades *Mycobacterium* et *Mycolicibacterium*, et se trouvent dans un large éventail d'environnements, y compris le sol, l'eau et les animaux. Elles sont généralement non pathogènes mais peuvent causer des infections chez les personnes immunodéprimées.
- *Mycobacteroides* : Ce clade comprend plusieurs espèces précédemment classées comme membres du complexe *Mycobacterium abscessus*. Ces bactéries ont une structure de paroi cellulaire complexe similaire à celle du clade *Mycobacterium*, mais sont génétiquement distinctes et présentent certaines différences au niveau des voies métaboliques. Elles se trouvent dans le sol et l'eau et peuvent causer des infections opportunistes chez les humains, en particulier chez les personnes atteintes de mucoviscidose.
- *Mycoavidus* : Ce clade comprend une seule espèce, *Mycoavidus cysteinexigens*, précédemment classée comme membre du genre *Corynebacterium*. Cette bactérie a une structure de paroi cellulaire simple et se retrouve dans le sol. Elle est connue pour former une relation symbiotique avec un champignon et peut fixer l'azote de l'atmosphère.

b) L'enveloppe mycobactérienne

Une des caractéristiques principales des mycobactéries repose sur la nature de leur enveloppe qui contient beaucoup de lipides complexes (**Figure 2**). En effet, les lipides sont une composante essentielle de l'enveloppe mycobactérienne et représentent jusqu'à 60% de sa composition totale, là où ils ne représentent que 20% chez les bactéries à Gram négatif riches en lipides [9]. De plus, les lipides représentent jusqu'à 40% du poids sec total chez certaines mycobactéries comme *M. tb* [10].

L'enveloppe mycobactérienne protège les mycobactéries des milieux hostiles et joue de ce fait un rôle fondamental dans la capacité des mycobactéries pathogènes à survivre à la phagocytose des macrophages de l'hôte, l'éviction de l'immunité et la résistance aux antibiotiques. Elle joue aussi un rôle d'interface avec le milieu extérieur à travers les mécanismes de transport de nutriments, de sécrétion ainsi que dans la formation de biofilm.

Cette enveloppe est constituée d'une membrane plasmique, d'un espace périplasmique, d'une couche de peptidoglycane (PG) formant des liaisons covalentes avec une couche d'arabinogalactane (AG), puis d'une mycomembrane comprenant les acides mycoliques et de nombreux lipides complexes, ainsi que des matériaux de capsule qui ne sont pas présents chez toute les souches mycobactériennes [10].

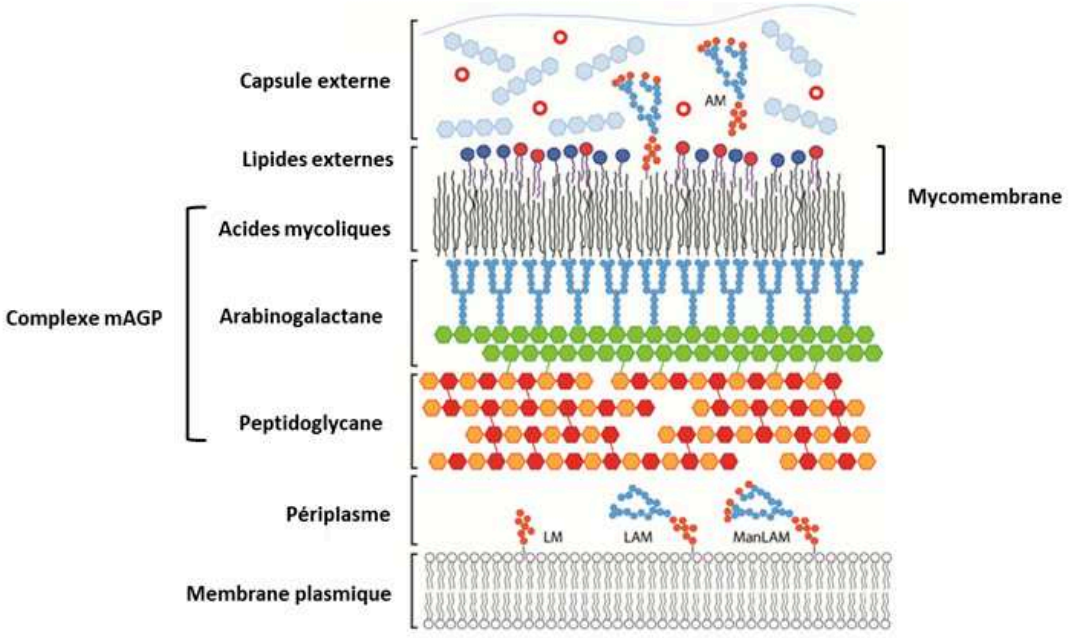

Figure 2 : Structure de la mycomembrane adaptée de [11]. La structure de la mycomembrane est complexe et comporte, de l'intérieur vers l'extérieur, une membrane plasmique, un espace périplasmique, une couche de peptidoglycane (PG) formant des liaisons covalentes avec une couche d'arabinogalactane (AG), puis d'une mycomembrane comprenant les acides mycoliques et de nombreux lipides complexes, ainsi que des matériaux de capsule.

La structure de la mycomembrane est bien conservée entre les différentes souches mycobactériennes pour lesquelles elle a été élucidée [12], et son organisation, de la couche la plus interne à la couche la plus externe, est structurée de la façon suivante :

- **La membrane plasmique (MP)**. Elle sépare le cytoplasme de l'espace périplasmique. Cette membrane est composée d'une bicouche de phospholipides et de protéines similaires à celles des autres procaryotes. Quelques différences existent, telle que la présence du phosphatidylinositol mannoside (PIM) (**Figure 3**) chez les *actinomycètes*. Aucune différence notable n'a été observée dans la composition de la MP entre les MCR et MCL [12]. Son rôle dans la pathogénicité des mycobactéries est d'ailleurs considéré comme mineur [13].

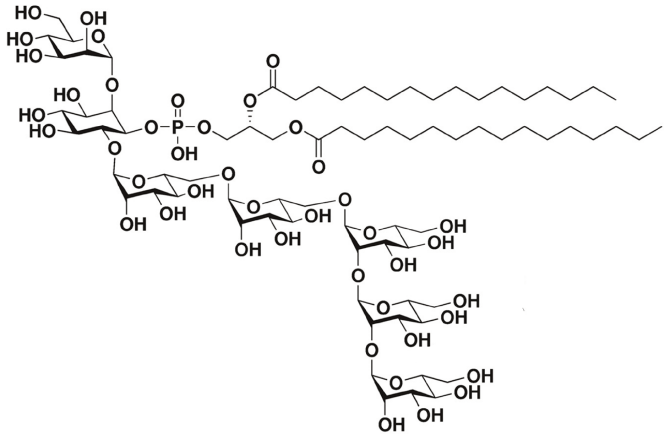

Figure 3 : Structure du phosphatidylinositol mannoside (PIM). Adaptée de [14].

- **Le complexe peptidoglycane-arabinogalactane (PG-AG)**. Il maintient la morphologie cellulaire et permet aux cellules de résister aux pressions osmotiques. Le PG est constitué de chaînes polysaccharidiques de N-acétylglucosamine (GlcNAc) et d'acide N-acétylmuramique (MurNAc) (**Figure 4**) reliées par des liaisons de type β(1-4). Ces chaînes sont liées entre elles par des ponts tétra-peptidiques. L'arabinogalactane est un hétéropolysaccharide formé de chaînes de galactose et d'arabinose qui est lié de manière covalente au PG. Il sert de point d'ancrage pour les acides mycoliques de la mycomembrane, formant ainsi une structure rigide autour des cellules [12].

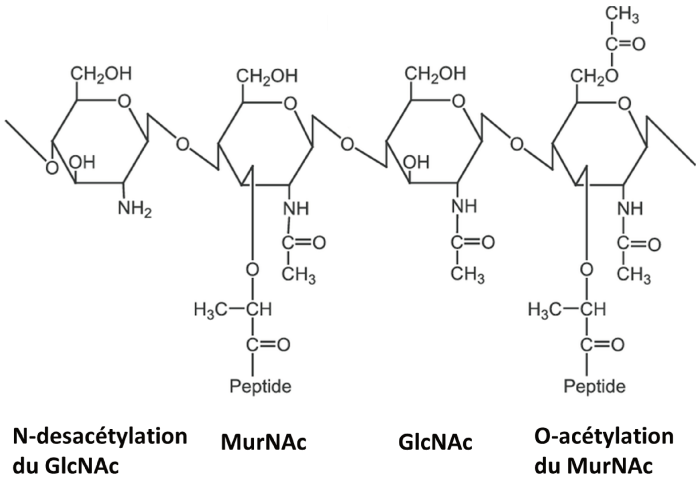

Figure 4 : Structure du peptidoglycane. Le PG est constitué de chaînes polysaccharidiques de N-acétylglucosamine (GlcNAc) et d'acide N-acétylmuramique (MurNAc). Adaptée de [15].

- **La mycomembrane (MM)**. Il s'agit d'une structure analogue à la membrane externe des bactéries à Gram négatif, constituée d'une bicouche lipidique non conventionnelle de 7 à 8 nm d'épaisseur. La couche externe de la MM contient des glycolipides extractibles, comme le tréhalose dimycolate (TDM), le tréhalose monomycolate (TMM), ou chez certaine souches mycobactériennes, des glycopeptidolipides (GPL) (**Figure 5**). Ces derniers sont dits libres car ils ne sont pas liés de façon covalente à la MM. Ils ont été montrés comme jouant un rôle important dans la pathogénie et la formation de biofilms chez *M. tb* et notamment dans les phénomènes de latence et de réactivation pour ces infections [10]. Des protéines sont également présentes dans la mycomembrane, comme celles du complexe Antigène 85 (Ag85) qui par son activité mycolyltransferase, catalyse la formation de TDM et des TMM à partir d'acides mycoliques [9].

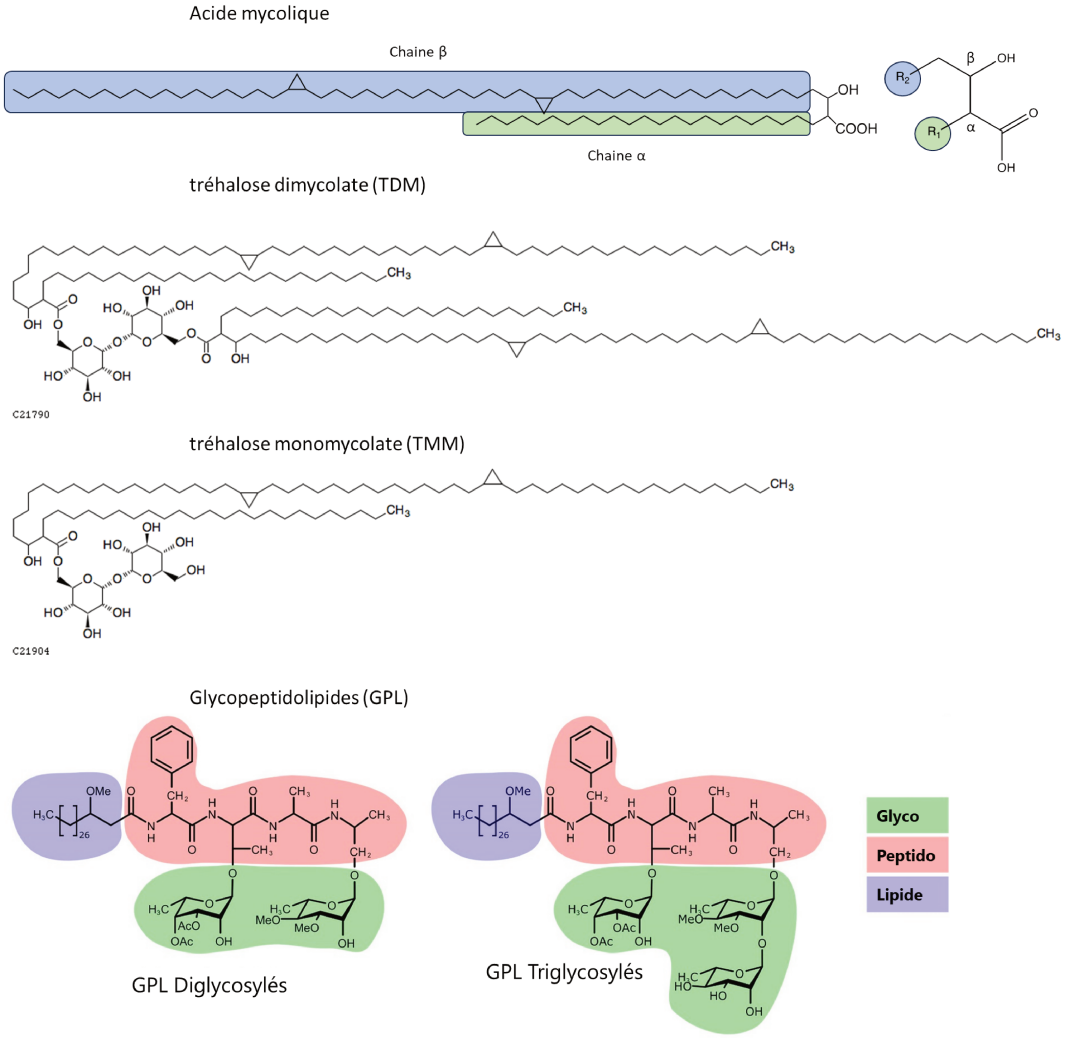

Figure 5 : Structure des acides mycoliques, des tréhaloses dimycolates (TDM), des tréhaloses monomycolates (TMM) et des glycopeptidolipides (GPL) [16].

- **La capsule**. La capsule est la dernière couche à la surface des mycobactéries et son existence a longtemps fait l'objet de débats avant qu'elle ne soit confirmée par microscopie électronique à haute résolution en 2010 [17]. La capsule est constituée majoritairement de protéines et de polysaccharides (de 70 à 95%) ainsi que d'une faible proportion de lipides (2 à 5%). La proportion de protéines est bien plus importante chez les mycobactéries non pathogènes comme *M. smegmatis* [9]. Chez les mycobactéries pathogènes, la capsule joue également un rôle important dans l'éviction de la réponse immunitaire, la cytotoxicité et la résistance aux antibiotiques [12, 13, 18].

II. *M. tuberculosis*

a) Epidémiologie, incidence

Avec près de 10.6 millions de nouveaux cas et 1.3 millions de morts dans le monde en 2022 [19] (**Figure 6**), la tuberculose est la maladie infectieuse la plus mortelle à ce jours. Cette maladie est causée par *M. tb* et reste un problème majeur de santé publique principalement en Afrique Subsaharienne, en Russie, en Europe de l'Est et en Asie du Sud-Est [20] notamment à cause des nombreuse formes poly-résistantes ou totalement résistantes aux antibiotiques [21].

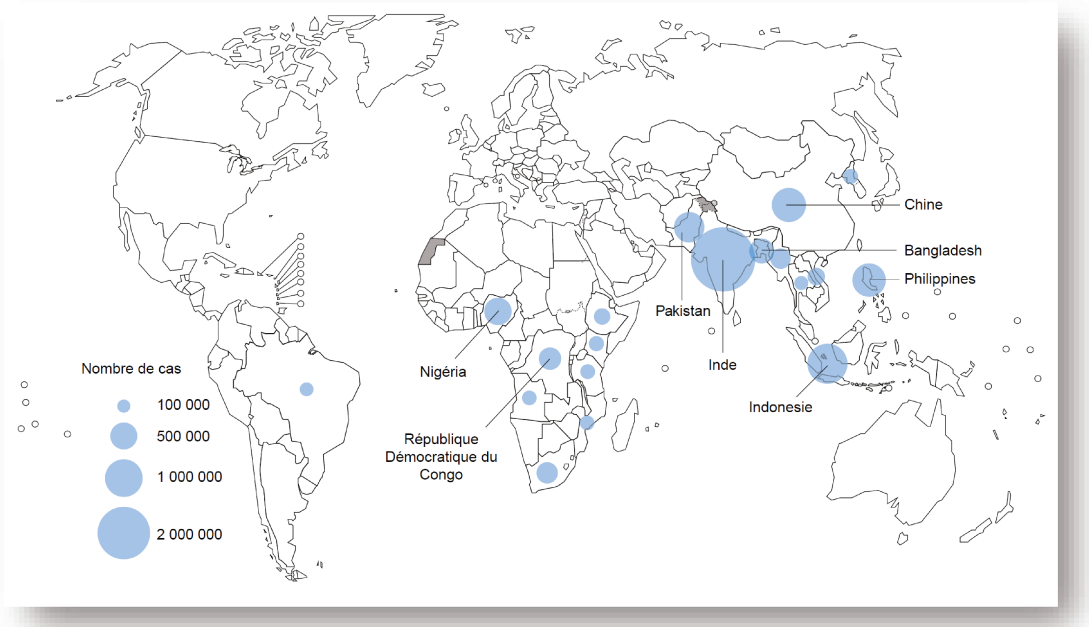

Figure 6 : Carte de l'incidence des infections à *M. tb* en 2023 réalisée par l'OMS. Adaptée de [22].

Cette maladie principalement causée par le pathogène *M. tb* peut occasionnellement être due à d'autres bactéries du complexe *Mycobacterium tuberculosis* (MTBC) comme *M. africanum*, *M. orygis*, *M. bovis*, *M. microti*, *M. canettii* ou *M. caprae*.

C'est une maladie typiquement pulmonaire mais qui peut également présenter des formes extra-pulmonaires (EPTB) infectant d'autres tissus tels que la plèvre pulmonaire, les ganglions, l'abdomen, l'appareil génito-urinaire, la peau et les articulations [23, 24] .

On estime qu'environ un tiers de la population globale serait infectée par *M. tb* mais la plupart des cas d'infection présentent une forme latente d'infection (« *latent tuberculosis infection* » ou LTBI) [25]. Les patients atteints de LTBI n'ont aucun symptôme apparent mais présentent des structures spécifiques dans les poumons appelées granulomes qui contiennent localement l'infection [26].

Environ 5 à 15% de ces infections latentes peuvent devenir actives [27]. Toutefois ce taux d'infection active est significativement plus élevé chez des personnes présentant des co-infections pulmonaires, des patient immunodéprimés ou encore les gros fumeurs.

L'antibiothérapie standard recommandée par l'OMS est effective contre les souches susceptibles de *M. tb* dans 85% des cas, et consiste en un traitement lourd de 6 à 12 mois avec un cocktail de quatre antibiotiques. En revanche, l'émergence de nombreuses souches multirésistantes (« *multi-drug resistant* » TB ou MDR-TB), extensivement résistante (« *extensively drug resistant* » TB ou XDR-TB) ou totalement résistante aux antibiotiques (« *totally drug resistant* » ou TDR-TB) devient extrêmement problématique [21, 28, 29]. On estime environ 500000 cas de tuberculose MDR en 2023 [20], pour un taux de survie de seulement 56% en 2023. Il y a donc un besoin constant de trouver de nouvelles cibles thérapeutiques mycobactériennes ainsi que de nouvelles molécules pour traiter ces infections résistantes aux antibiotiques pour lesquelles les traitements actuels sont peu voire pas efficaces.

b) Physiopathologie et cycle de vie de l'infection

La transmission de *M. tb* se fait par voie aérienne lorsqu'une personne respire des aérosols émis par la toux d'une autre personne en phase d'infection active à *M. tb*. Le cycle de vie de cette infection peut être globalement divisé en quatre phases : la transmission, la réponse immunitaire, la latence et la réactivation [30, 31] (**Figure 7**).

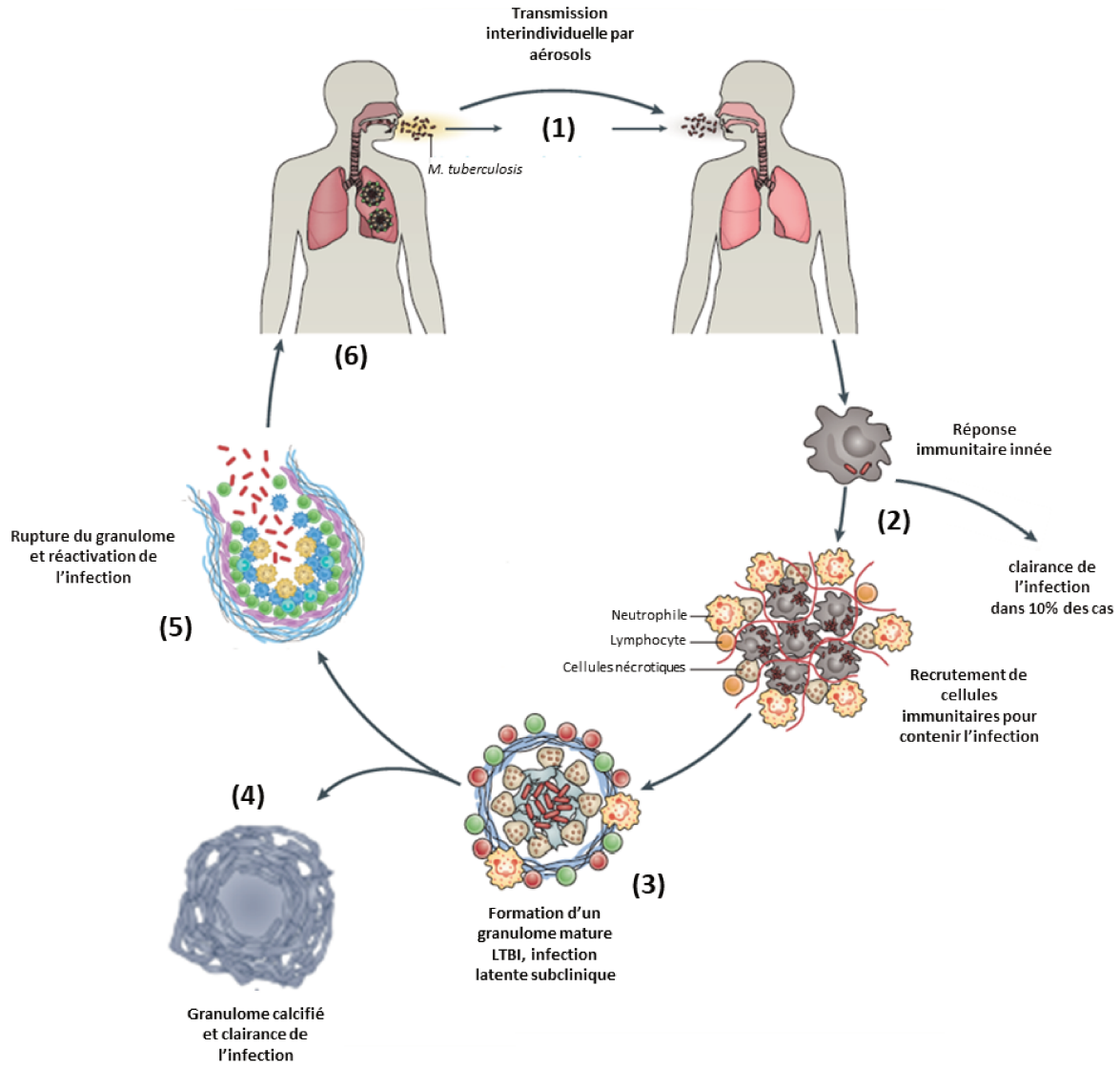

Figure 7 : Cycle infectieux de la tuberculose pulmonaire. Adapté de [30].

Lors d'une infection active à *M. tb*, les symptômes sont typiquement une toux chronique et du sang dans l'expectorât, de la fièvre et des sueurs nocturnes ainsi qu'une perte de poids. En l'absence de traitement, la tuberculose est mortelle dans environ 70% des cas.

Ainsi, la toux d'une personne atteinte de tuberculose active va donc la conduire à émettre des aérosols contenant *M. tb*. Parmi ces aérosols, les plus petits (1 à 5 µm) sont capables de pénétrer les voies respiratoires inférieures et de survivre plusieurs heures à l'air libre grâce à l'imperméabilité de la membrane mycobactérienne [32] (**Figure 7-(1)**).

Une fois dans les voies respiratoires, les bacilles vont être phagocytés par les macrophages alvéolaires et les cellules dendritiques, qui sont la 1ère ligne de défense du système immunitaire [30] (**Figure 7-(2)**). A ce stade, dans 10% des cas les cellules phagocytaires vont

être capables d'aboutir à une clairance totale de l'infection. Cependant, *M. tb* a acquis au cours de l'évolution un nombre important de mécanismes d'adaptation lui permettant d'échapper au système immunitaire de l'hôte. Plus particulièrement, la capacité d'inhiber la fusion phagolysosomale ou la résistance au stress acide que lui confère sa membrane [30, 33] lui permettent de survivre à la phagocytose des macrophages et même de se reproduire au sein de ces derniers (**Figure 7-(3)**). Ainsi, en l'absence de clairance (**Figure 7-(4)**), deux formes d'infection distinctes peuvent se présenter :

Le premier cas correspond à une phase d'infection appelée tuberculose primaire progressive, qui se présente typiquement chez l'enfant mais peut parfois être présente chez l'adulte [34, 35]. Cette phase comprend des bactéries intracellulaires et des bactéries libres, qui sont libérées après lyse des macrophages et qui peuvent se disséminer par le sang et le système lymphatique dans les autres organes, déclenchant alors des tuberculoses extra-pulmonaires.

Dans le deuxième cas, le système immunitaire est capable de contenir la progression de l'infection et le bacille devient dormant (**Figure 7-(3)**) ; on parle alors de tuberculose latente (ou LTBI) et le patient est asymptomatique et non contagieux [36]. Chez les patients atteints de LTBI, le bacille est capable de surmonter les défenses immunitaires dans 5 à 10% des cas et de reprendre sa croissance ; on parle alors de phase de réactivation (**Figure 7-(5)**). La réactivation peut se produire rapidement après l'infection primaire ou après plusieurs années. Cette réactivation intervient souvent à l'occasion d'une co-infection, d'un changement des conditions immunitaires de l'hôte ou chez les gros fumeurs [37]. De plus, les patients atteints de VIH présentent une probabilité de réactivation de 10% chaque année une fois une infection latente installée, en raison de leur état immunitaire ce qui fait de *M. tb* la première cause de mortalité chez les patients VIH en 2023 [22, 38].

c) Granulome, niches bactériennes, macrophages spumeux, ILI et dormance

L'une des caractéristiques des infections à *M. tb* est la forme que va prendre la réponse immunitaire suite à l'infection. En effet, lors du déroulement d'une infection à *M. tb*, le bacille est phagocyté par les macrophages alvéolaires. Dans 10% des cas, cette première réponse est insuffisante pour éliminer l'infection et *M. tb* établit une infection durable. Il y a ensuite

recrutement de cellules immunitaires avec la formation d'un granulome, structure histologique qui va contenir l'infection localement [26] (**Figure 8**) .

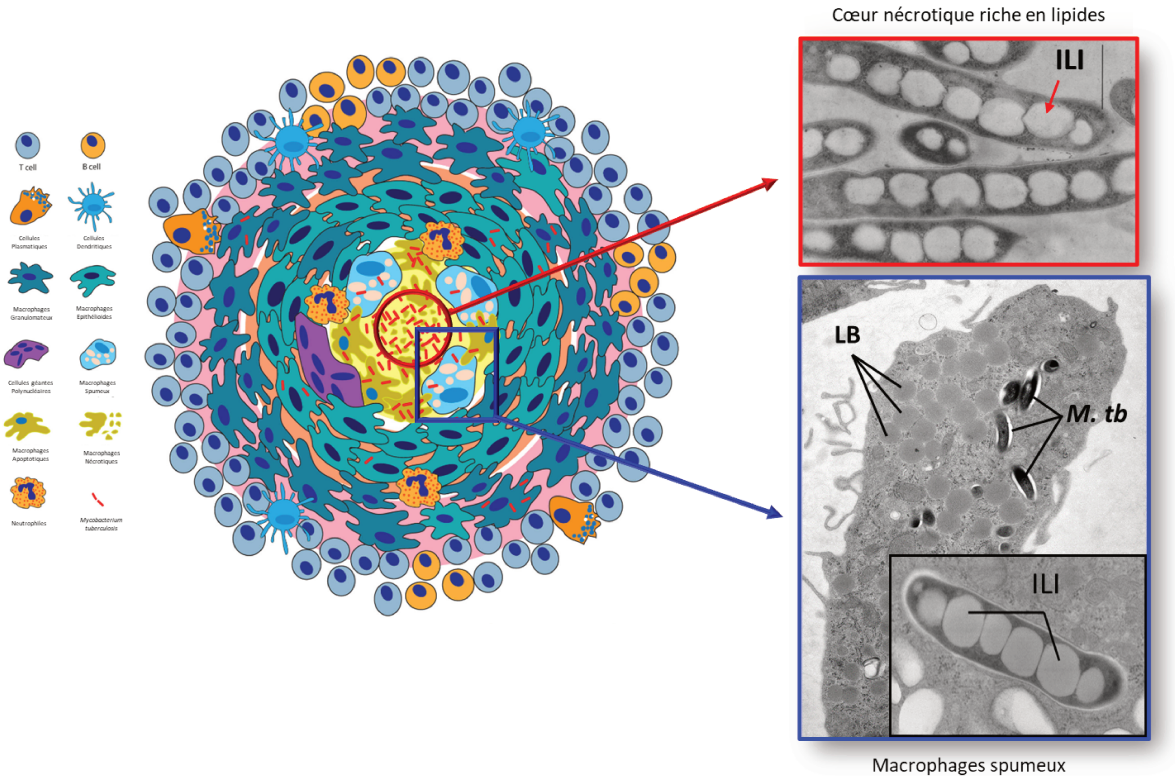

Figure 8 : Schéma du granulome. Le granulome est une réponse histologique permettant de contenir localement l'infection à *M. tb* par recrutement de cellules immunitaires. Au centre se trouve un cœur nécrotique riche en lipides au sein duquel *M. tb* peut resynthétiser des triacylglycérols à partir d'acides gras libres et les accumuler sous la forme d'inclusions lipidiques intrabactériennes (ILI). A la périphérie du cœur, certains macrophages infectés se différentient en macrophages « *foamy* » gorgés de gouttelettes lipidiques (LB) au sein desquels *M. tb* accumule des ILI en dégradant les vésicules lipidiques (LB) de l'hôte. Images de microscopie extraites de [39].

La formation du granulome est médiée à la fois par l'immunité innée et adaptative [30]. Une diversité importante de cellules immunitaires vient encapsuler la zone nécrotique de l'infection contenant les bactéries et les cellules immunitaires lysées suite à leur infection par *M. tb* (**Figure 8**). On y trouve des cellules géantes présentant plusieurs noyaux, des cellules dendritiques, des neutrophiles, de cellules NK (« *natural killer* »), des cellules épithélioïdes, mais également des macrophages présentant un phénotype spumeux ou « *foamy* » (FM) suite à l'accumulation de corps lipidique appelés « *lipid body* » (LB) [31] au sein de leur cytoplasme. Le granulome est également entouré par une couche dense de lymphocytes qui constitue une barrière empêchant la propagation de l'infection en dehors de la structure [33].

Ainsi, *M. tb* peut persister dans le granulome au sein du cœur nécrotique, mais également au sein des macrophages (**Figure 8**). Une des principales caractéristiques de *M. tb* est sa capacité à détourner à son propre profit les lipides de l'hôte au sein du granulome, soit en utilisant les

acides gras libres présents dans le cœur nécrotique, soit en dégradant les lipides contenus dans les LB des FM. Les chaînes acyles ainsi formées vont être internalisées puis stockées à leur tour sous forme de triacylglycérols (TAG) au sein d'Inclusions Lipidiques Intrabactériennes (ILI) [40] (**Figure 8**). L'accumulation de ces ILI permet à *M. tb* de rentrer dans un état de dormance caractérisé par l'absence de réplication et une résistance accrue aux antibiotiques. Cette accumulation de lipides est l'une des caractéristiques de la tuberculose latente : le patient n'est pas contagieux et ne présente aucun symptôme. On estime qu'environ ¼ de la population mondiale serait porteuse de tuberculose latente. Lors d'une co-infection ou d'un changement du statut immunitaire de l'hôte, les lipides contenus dans ces ILI vont servir de source de carbone à la bactérie pour se réactiver, provoquant la rupture du granulome et déclenchant une infection active. Le patient est alors contagieux et présente les symptômes de la tuberculose [31].

d) Le diagnostic de *M. tb*

Un diagnostic efficace et rapide de la tuberculose est de première importance dans la lutte contre cette pathologie de façon à commencer le plus rapidement possible l'antibiothérapie et limiter la transmission par les personnes infectées. Bien que les symptômes cliniques soient bien caractérisés, ils restent communs avec d'autres infections pulmonaires et il est donc nécessaire d'employer diverses approches pour établir un diagnostic définitif [41].

Une approche bactériologique peut être employée : elle consiste en la mise en culture d'échantillons biologiques en milieu solide ou liquide spécifique, suivi d'analyses de microscopie associées à la coloration spécifique de Ziehl-Neelsen. Cependant, cette méthode peut s'avérer trop longue en raison du temps de croissance lent de *M. tb* qui présente un temps de doublement de 24h.

D'autre part, une approche radiologique est souvent réalisée en complément : une analyse de radio des poumons peut permettre de mettre en évidence des lésions granulomateuses typiques des infections à *M. tb*. Cette méthode a été grandement améliorée par l'évolution rapide des techniques d'acquisition et de traitement de l'image [42].

Enfin, une approche génétique est également utilisée, faisant intervenir une amplification ou un séquençage de gènes mycobactériens spécifiques, qui a donné lieu à des tests modernes comme le Gene-Xpert® MTB/RIF assay ou le FluoroType® MTBDR. L'avantage de cette

approche est qu'elle permet d'obtenir des informations concernant le génome de la souche présente chez le patient. Ces informations permettent en effet de prédire de potentielles résistances aux antibiotiques de première ligne comme la résistance à l'isoniazide ou à la rifampicine, qui sont dues à des mutations dans les gènes *inhA*, *katG* ou *rpoB* [43-45]. La prédiction de résistance est une information cruciale qui peut permettre de gagner un temps précieux sur le traitement de la maladie, d'où l'importance de cette approche.

e) Antibiothérapie contre *M. tb*

A ce jour, seules 23 molécules sont recommandées par l'OMS dans la lutte contre *M. tb.* Le grand nombre de molécules découvertes durant le 20ème siècle, telles que la streptomycine (STR), l'isoniazide (INH), la kanamycine (KAN) ou encore la pyrazinamide (PZA), ont radicalement changé nos capacités de traitement de la tuberculose [46]. L'antibiothérapie recommandée actuellement est très lourde et consiste en 6 mois de traitement faisant intervenir quatre antibiotiques de première ligne que sont l'INH, la RIF, l'éthambutol (EMB) et la PZA (

Figure 9).

Le traitement se découpe en deux phases : une première phase où les quatre antibiotiques de première ligne sont pris simultanément pendant deux mois, suivie d'une seconde phase où seul l'INH et la RIF sont conservés.

Ce traitement fonctionne dans 85% des cas pour les souches de *M. tb* susceptibles mais de nombreuses souches de *M. tb* échappent complétement à ces antibiotiques pourtant les plus efficaces contre cette bactérie.

A

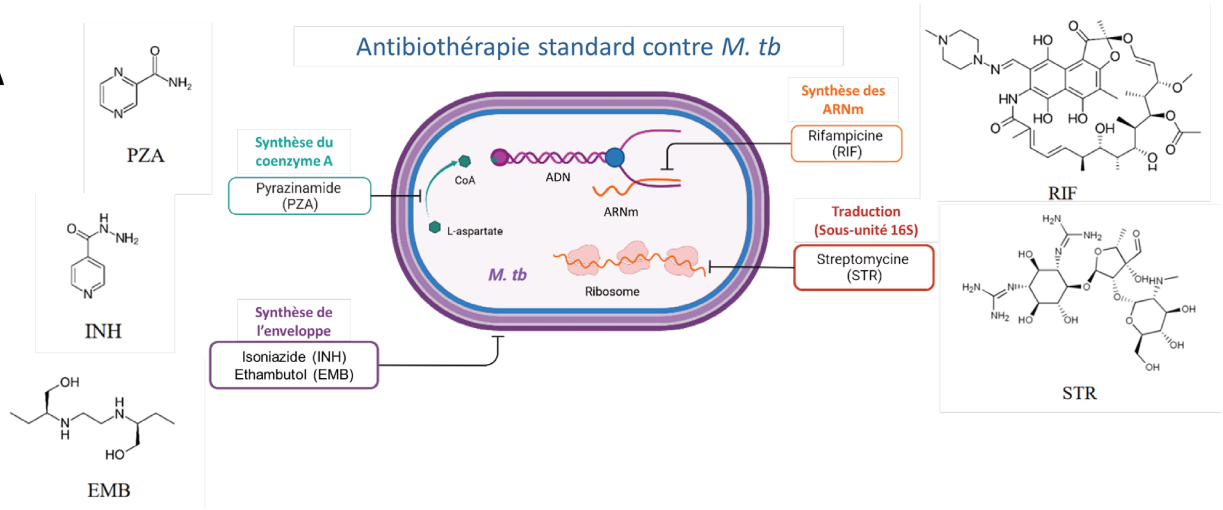

B

Nom	Cible	Mécanisme d'action	Gène impliqué dans la résistance
Isoniazide (INH)	InhA : Enoyl acyl carrier protein reductase	Inhibe la synthèse des acides mycoliques	*katG :* catalase peroxydase *inhA :* Enoyl acyl carrier protein reductase
Rifampicine (RIF)	Sous-unité β de l'ARN polymérase	Inhibe la synthèse de l'ARN	*rpoB* : sous-unité β de l'ARN polymérase
Ethambutol (EMB)	EmbABC : arabinosyl transférase	Inhibe la synthèse de l'arabinogalactane et des lipoarabinomannanes	*embABC* : arabinosyl transférase
Pyrazinamide (PZA)	PanD : aspartate décarboxylase	Inhibe la voie de synthèse du CoA et/ou disrupte le pH cytoplasmique	*pncA* : pyrazinamidase *panD* : aspartate décarboxylase
Streptomycine (STR)	ARN ribosomal 16s Protéine ribosomale S12	Inhibe la synthèse des protéines	*rrs* : ARN ribosomal 16s *rpsL* : protéine ribosomale S12

Figure 9 : **(A)** Structure des antibiotiques de l'antibiothérapie standard contre *M. tb.* **(B)** Antibiotiques de première ligne avec leur mécanisme d'action et leurs cibles.

Isoniazide (INH).

L'INH est l'une des molécules les plus efficaces dans la lutte contre *M. tb* depuis 1952 [47]. Bien qu'inefficace sur les formes latentes d'infection, l'INH a toujours fait partie des antibiotiques de première ligne depuis son introduction dans l'antibiothérapie standard contre *M. tb* [48, 49]. L'INH est une pro-drogue qui doit être activée par la catalase peroxydase KatG, ce qui en fait un antibiotique à l'usage spécifique contre *M. tb*. L'action de KatG va créer un intermédiaire radicalaire isonicotinolyl qui va ensuite réagir avec le NAD+ pour former la forme active (**Figure 10**). Ce produit ainsi activé va être capable d'inhiber une enzyme essentielle de *M. tb* appelée l'InhA qui est une enoyl acyl carrier protein reductase. L'inactivation de InhA va venir perturber la voie de synthèse des acides mycoliques, et ainsi la

synthèse de l'enveloppe mycobactérienne, conduisant à un effet bactéricide de cette molécule [50].

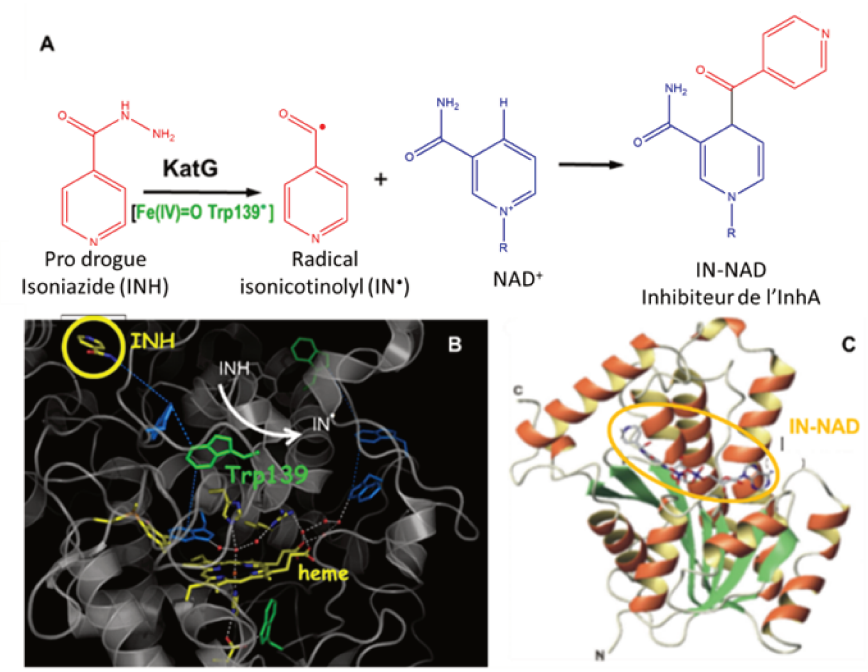

Figure 10 : **(A)** Schéma de l'activation de l'INH par KatG. **(B)** Structure de KatG de *B. pseudomallei* en complexe avec l'INH [51] **(C)** Structure de l'InhA de *M. tb* en complexe avec l'IN-NAD+ [52].

La Rifampicine (RIF).

La rifampicine a été introduite dans l'antibiothérapie contre *M. tb* en 1972 [53]. Cette molécule présente une très bonne activité bactéricide et est utilisée pour traiter un large spectre d'infections. La rifampicine agit sur la sous-unité beta de l'ARN polymérase en se complexant à cette dernière (**Figure 11**). La molécule occupe alors la poche catalytique de la polymérase, la rendant ainsi inopérante [54] et sur *M. tb*, son utilisation en combinaison avec les autres antibiotiques de première ligne réduit de moitié le temps de l'antibiothérapie standard [55].

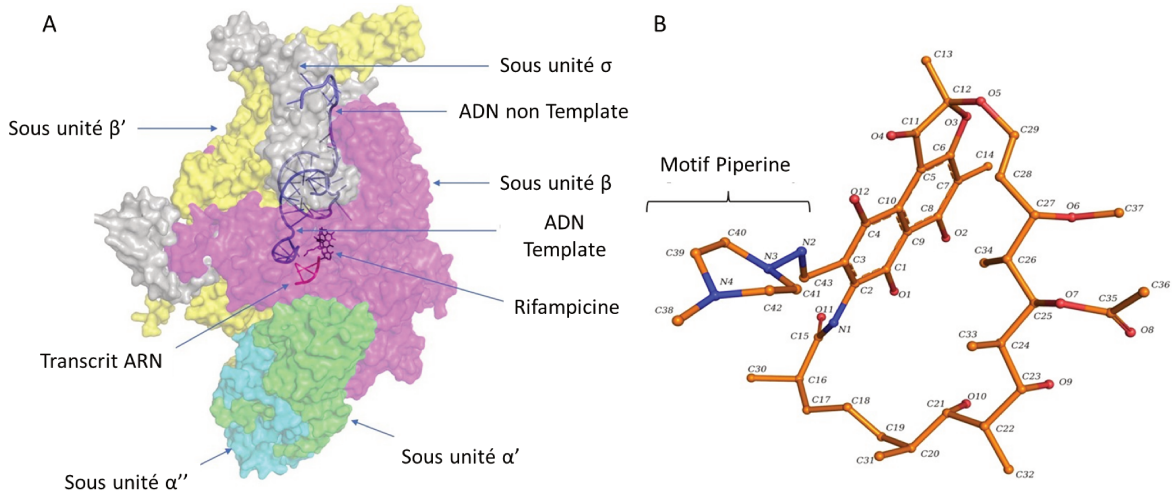

Figure 11 : **(A)** ARN polymérase de *M. leprae* en complexe avec un squelette d'ADN et d'ARN synthétique et la Rifampicine. **(B)** Structure hétérocyclique de la rifampicine au sein du complexe. Adaptée de [56].

L'éthambutol (EMB).

L'éthambutol inhibe la synthèse de l'arabinogalactane et des lipoarabinomannanes (LAM), les arabinosyl transférases EmbABC (**Figure 12**), et inhibe également le transfert de acides mycoliques vers l'enveloppe [57]. Ainsi, l'EMB est utilisé spécifiquement contre les mycobactéries et fait partie de l'antibiothérapie standard depuis 1960 [53].

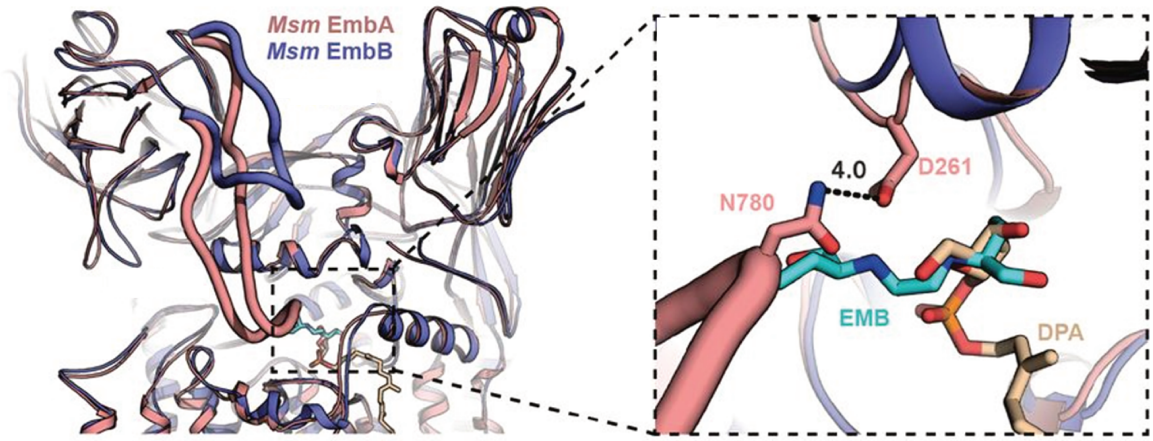

Figure 12 : Superposition des structures du domaine périplasmique de EmbA (rose) et EmbB (bleu) de *M. tb* en complexe avec l'EMB. Adapté de [58].

L'effet de l'EMB met en cause l'intégrité du complexe mycolyl-arabinogalactan-peptidoglycane et augmente ainsi la perméabilité membranaire chez les mycobactéries [59] ce qui lui permet de potentialiser l'action de nombreuses autres molécules sur les mycobactéries telles que les aminoglycosides, la rifampicine et les quinolones [60]. Ainsi, l'EMB est particulièrement intéressant pour la lutte contre les formes MDR et XDR de *M. tb*.

La pyrazinamide (PZA).

La PZA a été synthétisée en 1950 et, bien qu'inactive sur les tuberculoses latentes, elle fait aujourd'hui partie de l'antibiothérapie standard contre *M. tb* car son introduction a permis de réduire de 9 à 6 mois la durée du traitement [61]. La découverte du mécanisme d'action de la PZA est assez récente [62] et fait encore l'objet de débat. La PZA est converti au sein de la cellule par la pyrazinamidase PncA en acide pyrazinoïque (POA) et deux hypothèses non concurrentes sur son mode d'action coexistent (**Figure 13 D**).

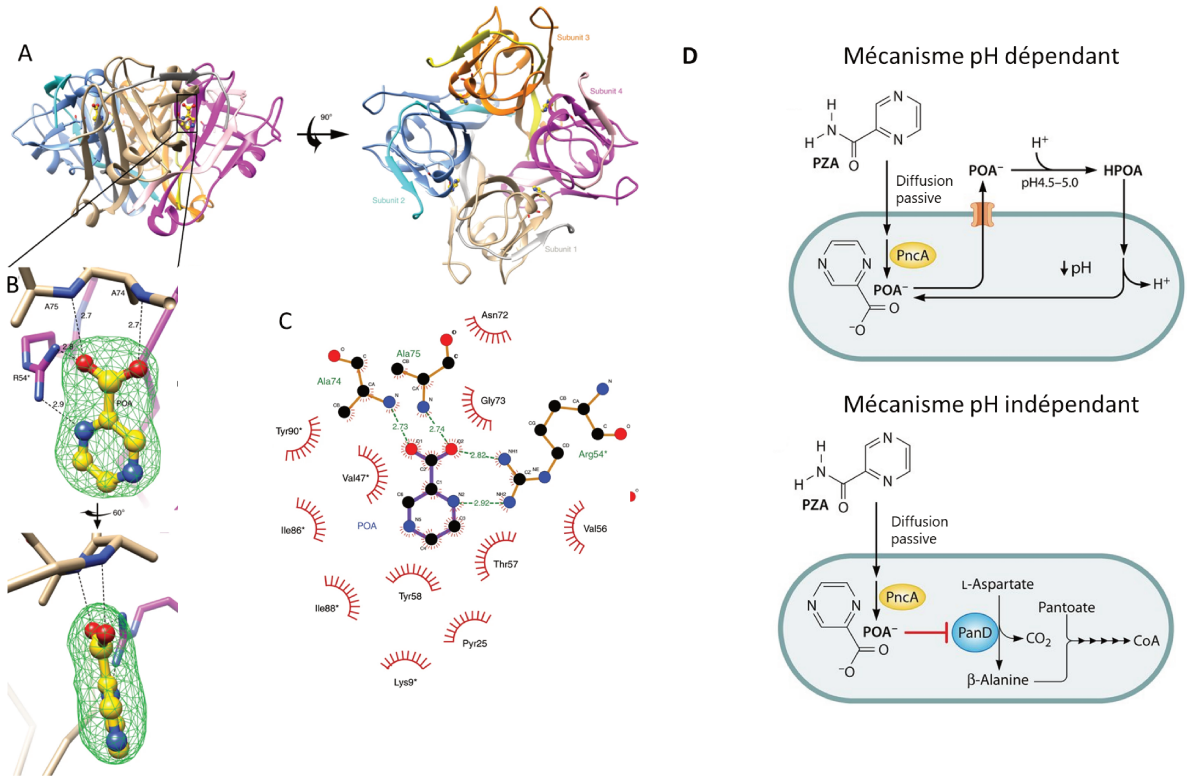

Figure 13 : **(A)** structure d'un tétramère de Pan D de *M. tb* en complexe avec le POA. **(B)** zoom sur le site de liaison du POA avec la carte de densité électronique a 3,5σ (en vert). **(C)** Diagramme Ligplot+ des interactions stabilisant le POA dans le site catalytique de PanD. Adapté de [63]. **(D)** Schéma du fonctionnement des deux mécanismes d'action possibles du PZA. Adapté de [64].

- Une hypothèse dite pH dépendante : Le POA sous sa forme pyrazinoate serait actif à pH acide. Le POA serait exporté de la cellule par des porines puis converti en HPOA, qui pénètrerait dans la cellule et disrupterait le pH intra bactérien de *M. tb* en relarguant des ions H^+. Dès lors, ce mécanisme est fortement dépendant du microenvironnement intracellulaire dans lequel évolue *M. tb* [65, 66].
- Une hypothèse dite pH indépendante : Le POA inhiberait de manière compétitive l'aspartate décarboxylase (PanD) (**Figure 13**) qui intervient dans la voie de synthèse du coenzyme A (CoA) et qui est une protéine essentielle chez *M. tb* [63].

La streptomycine (STR).

La streptomycine est le dernier antibiotique en date à avoir été ajouté à l'antibiothérapie standard contre *M. tb*. Cette molécule découverte en 1943 s'utilise contre un large spectre d'infections et agit en ciblant l'ARN ribosomal 16s (**Figure 14**) ainsi que la protéine ribosomale S12. Elle se lie au squelette phosphoré de l'ARN 16s, qui est une composante de la sous-unité 30S du ribosome bactérien, et interrompt ainsi la synthèse des protéines [67, 68].

La streptomycine présente une bonne activité bactéricide, équivalente à celle de l'EMB, ce qui a conduit à son utilisation en substitut de l'EMB dans l'antibiothérapie standard contre *M. tb*. Cependant son utilisation en tant qu'antibiotique unique contre *M. tb* dans les années 40 a conduit à l'émergence de nombreuses formes résistantes [69]. Bien que très active contre *M. tb* en phase de réplication active *in vitro*, la streptomycine ne présente pas d'activité contre les formes latentes et intracellulaires de *M. tb*.

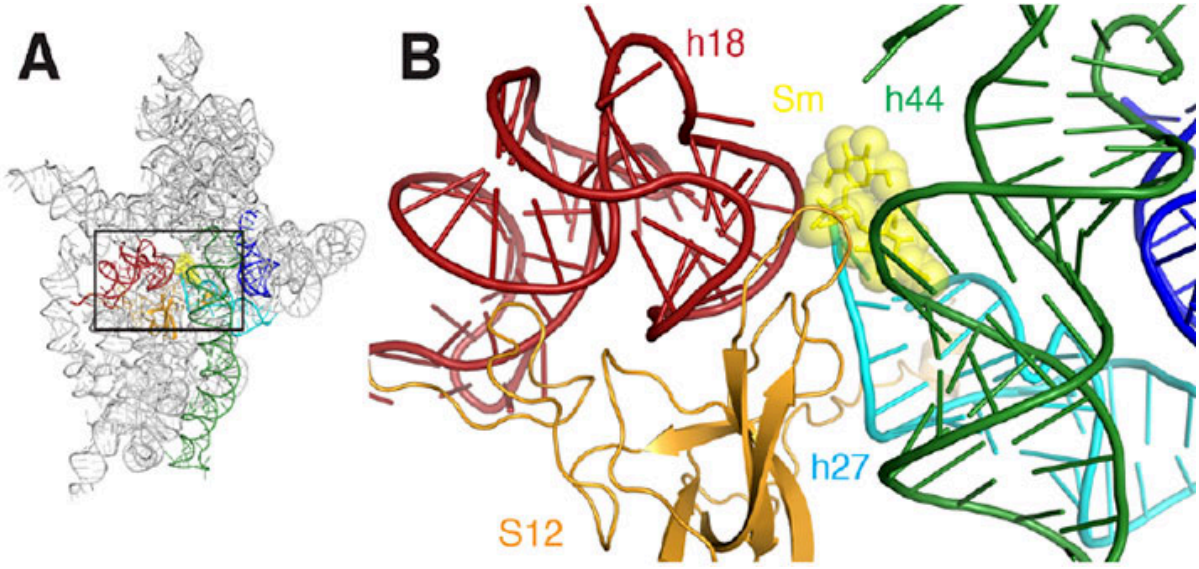

Figure 14 : **(A)** Structure de la sous unité 16s du ribosome bactérien en complexe avec la streptomycine. **(B)** Zoom sur le site de liaison de la streptomycine (représenté en jaune). Adapté de [70].

f) Nouvelles molécules en développement

L'apparition de souches de *M. tb* résistantes aux antibiotiques (MDR ou XDR) est un problème d'ampleur, avec environ 500 000 cas recensés en 2023 (**Figure 15**) [21, 22, 28, 29]. Ces souches, peu ou pas sensibles à l'antibiothérapie standard, sont alors traitées par des traitements particulièrement longs et complexes (6 à 12 mois, antibiothérapie combinée), ce

qui augmente à nouveau la probabilité d'induction de nouvelles résistances dans des souches déjà résistantes.

Il n'existe pas de traitement unifié contre ces souches, et le taux de survie des patients est seulement de 56%. Ainsi, il y a un fort besoin de développer des nouvelles molécules antituberculeuses à la fois pour traiter les infections MDR et XDR et pour réduire et simplifier le traitement pour toutes les souches de *M. tb*.

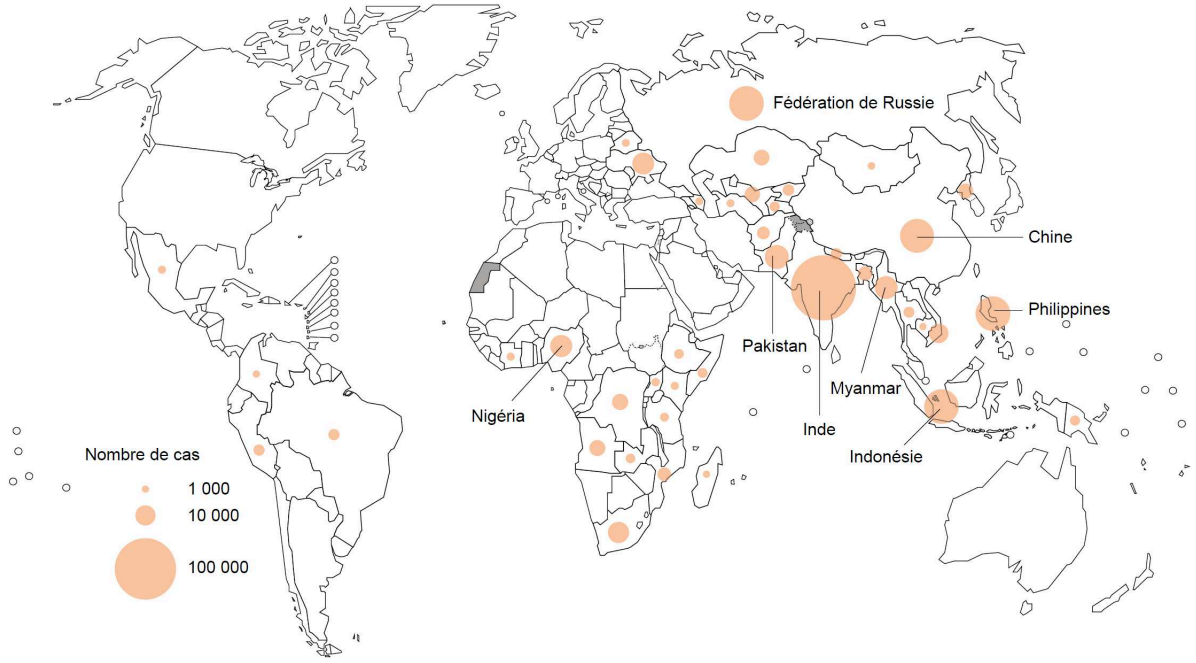

Figure 15 : Carte de l'incidence de tuberculose MDR ou RR-TB en 2023 réalisée par l'OMS. Adaptée de [22].

Dans cette optique, il est nécessaire d'étendre les mécanismes d'actions de nouvelles molécules afin de contourner les résistances déjà mises en place dans les souches ciblées. Il faut également chercher à minimiser les interactions négatives avec les molécules existantes, et prendre en compte la dimension économique du développement de nouveaux traitements.

La plupart des antibiotiques de première et seconde ligne contre *M. tb* ont été découverts dans les années 1940 et 1970. Or, la forte augmentation des formes XDR de tuberculose dans les années 2000 a poussé à l'augmentation des efforts de recherche pour de nouveaux traitements dans les dernières décennies. Le financement de cette recherche par des organismes internationaux (https://www.theglobalfund.org/fr/tuberculosis/) a permis de développer de nouveaux antituberculeux prometteurs, dont plusieurs sont entrés en phase

d'essai clinique. Les essais cliniques se divisent en trois phases de tests, et une quatrième de surveillance (**Figure 16**).

- La phase I sert à évaluer la toxicité du traitement, la tolérance de l'organisme, et la dose d'administration recommandée. Elle est effectuée sur un petit nombre de patients sains.
- La phase II a pour but de préciser les effets pharmacologiques et/ou cliniques du traitement. Elle implique un plus grand nombre de patients (40 à 80 en moyenne).
- La phase III est un essai comparatif : le nouveau traitement est testé en parallèle d'un traitement dit « de référence » et d'un placebo, afin d'évaluer son impact. Cette phase est réalisée sur un grand nombre de patients malades afin d'obtenir des données représentatives.

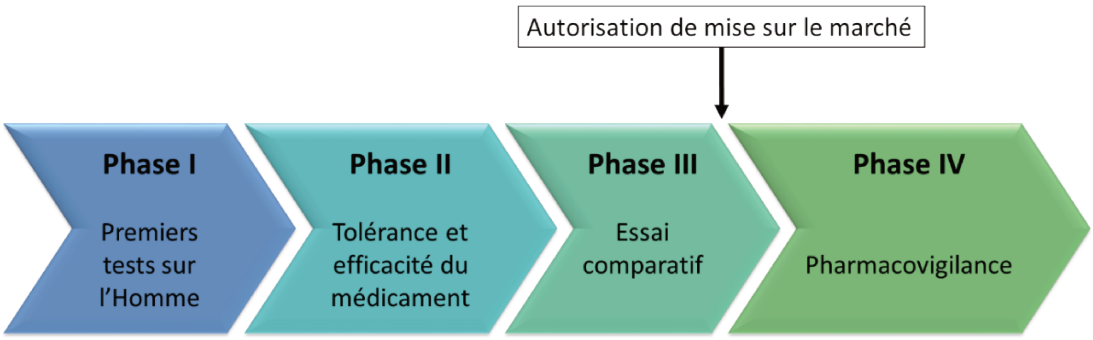

Figure 16 : Schéma des étapes d'essai clinique nécessaires à la commercialisation d'un traitement.

Ainsi, trois nouvelles molécules ont récemment été approuvées pour le traitement des infections à *M. tb* et sont actuellement en essai clinique de phase 3 : la bédaquiline, la delamanide et le prétomanide. Plus de 100 nouvelles molécules sont actuellement en développements [71] parmi lesquelles 16 sont en phase clinique de développement (**Tableau 1**). La bédaquiline et la delamanide ont été approuvées comme suppléments dans le traitement des forme XDR de tuberculose alors que le prétomanide a été approuvé dans le contexte d'un nouveau régime de 3 molécules (bédaquiline, linézolide et moxifloxacine) contre toutes les souches de *M. tb* [72].

Tableau 1 : tableau des antibiotiques en développement clinique précoce contre *M. tb.*

Molécule	Famille	Analogue licencié	Mécanisme	Phase clinique
Sutezolide	Oxazolidinone	Linézolide	Inhibe la synthèse des protéines	2
Delpazolide	Oxazolidinone	Linézolide	Inhibe la synthèse des protéines	2
TBI 230	Oxazolidinone	Linézolide	Inhibe la synthèse des protéines	1
GSK 3,036,656	Oxaborole		Inhibition de la synthèse des leucyl-tARN	1
TBA-7371	Azaindole		Inhibition de la synthèse de l'enveloppe (inhibition de DprE1)	2
BTZ-043	Benzothiazone		Inhibition de la synthèse de l'enveloppe (inhibition de DprE1)	2
Macozinone	Benzothiazone		Inhibition de la synthèse de l'enveloppe (inhibition de DprE1)	1
OPC-167832	Corbostyril		Inhibition de la synthèse de l'enveloppe (inhibition de DprE1)	2
SQ109	1,2 éthylène diamine		Inhibition de Mmpl3	2
TBAJ-876	Diarylquinoline	Bédaquiline	Inhibe l'ATP synthase	1
TBAJ-587	Diarylquinoline	Bédaquiline	Inhibe l'ATP synthase	1
Telacebec	Imidazopyridine amide		Inhibe le cytochrome bbc	2
TBI-166	Riminophenazine	Clofazimine	Inhibe la chaine de transport des électrons et produit des espèces réactives à l'oxygène	1
SPR720	Benzimidazole		Inhibe la synthèse de l'ADN (GyrB)	1
GSK2556286			Inhibe le catabolisme du cholestérol	1
BVL-GSK098			Inhibe le régulateur transcriptionnel EthR	1

La Bédaquiline.

La bédaquiline est le premier antibiotique de la classe des diarylquinolines [73]. La bédaquiline a une activité bactéricide sur *M. tb* en réplication active et en dormance. Elle présente des synergies avec les antibiotiques de première ligne, et présente une activité stérilisante en modèle murin où elle permet une réduction du temps de traitement [74, 75]. Elle agit en inhibant l'ATP synthase mycobactérienne. En effet, des mutations ponctuelles du gène *atpE* qui code pour l'ATP synthase mycobactérienne après exposition à la bédaquiline ont conduit à une augmentation de sa CMI d'un facteur 8 à 133 [76, 77].

L'apparition de ces résistances a conduit à des échecs cliniques lors des essais ce qui a mené par la suite au développement de nouvelles diarylquinolines ayant pour but de surmonter ces

résistances (**Tableau 1**) qui ont montré une activité contre un mutant *atpE* résistant à la bédaquiline en modèle souris [78].

La Délamanide.

La délamanide est une prodrogue du nitroimidazole qui nécessite une bio-réduction de son groupe nitro aromatique par la nitroréductase mycobactérienne Ddn dont l'activité est dépendante de la coenzyme mycobactérienne 8-hydroxy-5-deazaflavin (coenzyme F_{420}) [79]. Une fois activée, la délamanide va par la suite produire un radical libre venant inhiber la synthèse des acides mycoliques. Cette molécule est bactéricide sur *M. tb* en réplication active et en dormance et a montré une activité stérilisante en modèle murin supérieur au régime d'antibiothérapie standard [80, 81].

Diverses mutations spontanées ont été observées après exposition à cette molécule, notamment sur l'enzyme de conversion Ddn qui est non-essentielle chez *M.tb* [82, 83], ou encore dans la voie de synthèse de la coenzyme F_{420} qui lui est associée [83].

Le Prétomanide.

Le prétonamide est aussi une prodrogue du nitroimidazole dont le mécanisme d'action est strictement identique à celui de la délamanide. Cependant, sa structure chimique distincte lui confère des propriétés pharmacologiques et pharmacocinétiques spécifiques, avec notamment une plus faible affinité pour les protéines et une meilleure pénétration dans les tissus [71].

Cette molécule présente une activité bactéricide et a été approuvée pour un usage dans un régime antibiotique alternatif à l'antibiothérapie standard comprenant la bédaquiline, le linézolide ou la moxifloxacine et le PZA. Ce régime d'antibiotique a montré des meilleures performances bactéricides et stérilisantes en modèle animal comparé au régime d'antibiothérapie standard [84, 85] et parait réduire significativement le temps de traitement. Les résistances spontanées observées chez *M. tb* après exposition au prétomanide sont les mêmes que celle observées pour la délamanide, ce qui s'explique par un mode d'action identique [83].

Autres molécules en essai clinique.

Des approches génétiques ont permis de mettre en évidence les gènes essentiels de *M. tb* et ainsi d'identifier de nouvelles cibles thérapeutiques. Ces approches ont également permis de

déchiffrer le mécanisme d'action des molécules identifiées de manière empirique (**Tableau 1**) [86].

Parmi la centaine de molécules antituberculeuses actuellement en développement, 16 sont en cours d'essai clinique de phase 1 ou 2 (**Tableau 1**). Beaucoup de ces nouvelles molécules ciblent un mécanisme d'action déjà identifié et validé comme efficace, et cherchent à améliorer les performances d'une classe d'antibiotique déjà connue en sélectionnant des molécules plus active et/ou moins toxique parmi ces familles.

Les oxazolidinones sont un bon exemple de cette démarche d'optimisation. En effet, le linézolide est le premier antibiotique de la famille des oxazolidinones à être utilisé en clinique. Cet antibiotique inhibe la synthèse protéique en empêchant la formation du complexe d'initiation. Il est utilisé contre les staphylocoques, les streptocoques, les entérocoques, les corynébactéries et contre certaine souches XDR de *M. tb* [87]. Bien que le sutezolide (PNU-10048) ait été découvert en même temps que le linézolide, il n'avait pas encore donné lieu à un développement clinique.

Ce composé montre une forte activité contre *M. tb* en intracellulaire, et son principal métabolite, qui se retrouve à des fortes concentrations dans le plasma, présente une activité contre les bacilles extracellulaires [88]. De plus, il a été montré sur un modèle murin que le sutezolide démontre de meilleures performances stérilisantes que le linézolide et montre un potentiel de réduction de la durée du traitement standard lorsque utilisé en combinaison avec la bédaquiline et le prétomanide [89-92].

De plus, le Delpazolide (LCB01-0371) et le TBI-223, sont deux nouveaux oxadiazolones qui présentent une bonne activité antimycobactérienne et une plus faible inhibition de la synthèse protéique mitochondriale que le linézolide, ainsi qu'une demie vie plus courte [93, 94].

Les essais cliniques concernant ces oxazolidinones vont ainsi pouvoir conduire au développement de nouveaux antibiotiques, mais également pousser notre compréhension du mode d'action de cette famille de molécules et ainsi conduire au développement de nouveaux oxazolidinones plus performants et plus surs.

L'une des perspectives les plus importantes se trouve dans l'identification de nouvelles cibles thérapeutiques qui guide le développement de nouvelles molécules. Ainsi, l'identification de

la protéine DprE2 comme essentielle pour la synthèse de l'enveloppe mycobactérienne a l'aide d'une plateforme de criblage intracellulaire à haut débit [95] a permis la découverte de plusieurs pharmacophores ciblant cette protéine [95, 96] et par la suite le développement de nouveaux anti tuberculeux pour optimiser les performance de ces pharmacophores comme le BTZ-043 ou la macozinone (**Tableau 1**) [97, 98].

III. *Mycobacterium abscessus*

a) Généralités

M. abs a pour la première fois été isolé depuis un abcès sous-cutané et nommé en 1953 [99]. Il s'agit d'une mycobactérie environnementale, qui fait partie du groupe des mycobactéries non tuberculeuses (MNT) à croissance rapide. Elle est considérée comme la principale mycobactérie à croissance rapide pathogène pour l'homme, capable de provoquer un grand nombre d'infections pulmonaires, cutanéomuqueuses, voire même osseuses. Ce pathogène opportuniste peut causer des infections pulmonaires particulièrement sévères chez les personnes immunodéprimées ou atteintes de mucoviscidose [100, 101].

Suite à l'isolement de deux nouvelles espèces mycobactériennes [102-104] qui ont été déterminées comme étant des sous espèces de *M. abs* grâce au séquençage des gènes *rpoB* et *hsp65*, on parle désormais de complexe *M. abscessus* (MABc) [104]. Ce complexe comprend *M. abs*, *M. massiliense* qui a été isolée en 2004 depuis des échantillons cliniques d'expectorât [102], et *M. bolletii*, isolée en 2006 depuis des échantillons de voies respiratoires [103].

Toutes les sous-espèces du MABc se présentent sous deux morphotypes distincts : un morphotype rugueux R (« *rough* ») et un morphotype lisse S (« *smooth* ») [105, 106] (**Figure 17**). Ces deux morphotypes se différencient par l'incapacité du morphotype R à synthétiser ou à exporter les glycopeptidolipides (GPL) à la surface de son enveloppe [107]. Le morphotype S présente des colonies lisses, la capacité de former des biofilms, ainsi qu'une motilité ; alors que le morphotype R ne forme pas de biofilm, n'est pas motile et forme des cordes [16, 108]. Le morphotype R est associé à des infections pulmonaires sévères et à la capacité de persister pendant plusieurs années chez un hôte infecté [109, 110].

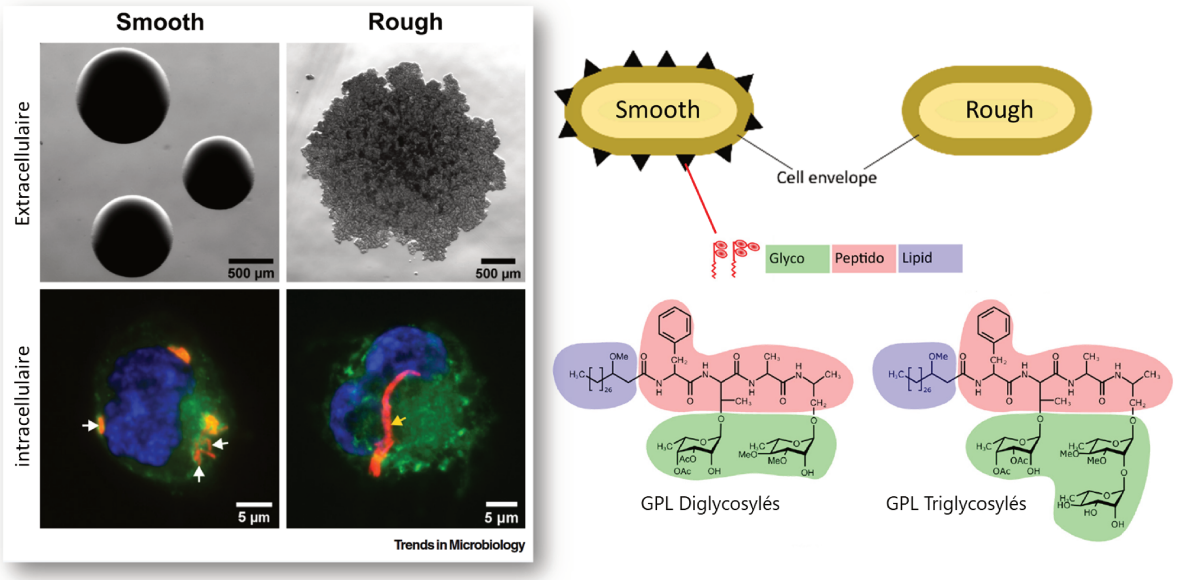

Figure 17 : Différences entre les morphotypes S (« *smooth* ») et R (« *rough* ») de *M. abs*. Le morphotype S se caractérise par une production abondante de glycopeptidolipides (GPL) qui donnent un aspect lisse à la mycobactérie et lui permettent d'être phagocytée par les macrophages alvéolaires. Le morphotype R a un aspect rugueux en raison d'une mutation du gène codant pour la synthèse ou l'exportation des GPL. Le caractère très hydrophobe des formes rugueuses stimule la formation d'agrégats bactériens aboutissant à la formation de cordes, très difficiles à dissocier et résistantes à la phagocytose. D'après [16].

M. abs représente aujourd'hui l'espèce de MNT la plus problématique en raison de sa capacité à infecter des individus sains, mais également du fait de sa poly-résistance naturelle aux antibiotiques classiques. Cette poly-résistance rend les infections à *M. abs* extrêmement difficiles à traiter, ce qui a valu à cette bactérie le surnom de « cauchemar pour les antibiotiques » [111, 112].

C'est également la principale MCR responsable d'infections pulmonaires chez l'homme [113, 114]. En effet, 90% des infections à *M. abs* sont pulmonaires, bien que cette bactérie puisse aussi occasionnellement infecter les ganglions lymphatiques, la peau, les tissus mous et présente un très large spectre d'infection [101, 115].

b) Physiopathologie des infections pulmonaires

Les infections pulmonaires représentent la principale forme d'infection à *M. abs* (90%). Ces dernières sévissent principalement chez des patients déjà atteints d'une pathologie pulmonaire telle que la mucoviscidose, la fibrose pulmonaire ou encore la bronchiectasie [111, 116]. Cependant, près d'un tiers des infections touche des individus sains : ces derniers sont souvent âgés, ce qui peut se traduire par un système immunitaire plus faible [101]. On note que ces infections sont souvent associées à la présence de *M. avium* [101], mais il existe assez

peu d'informations sur la physiopathologie des infections à *M. abs* provenant de données cliniques.

En revanche, l'usage de modèles expérimentaux tels que l'infection de macrophages murins, d'embryons de poissons zèbres ou encore d'organoïdes pulmonaires [117] avec *M. abs* ont permis d'investiguer la pathogénie de cette bactérie [118]. Ainsi, de nombreux points communs avec les infections pulmonaires à *M. tb* ont pu être mis en évidence [114, 119, 120].

La contamination par *M. abs* serait environnementale car on retrouve cette bactérie dans l'eau et le sol, où elle se présente majoritairement sous le morphotype S [121]. Le développement de l'infection peut être très lent : une progression de plus de 13 ans a été observée chez des patients atteints de mucoviscidose avant de passer à un stade d'infection sévère [122]. Ce genre d'infection peut présenter une palette variée de symptômes, comme de la fièvre, des douleurs thoraciques et de la perte de poids, de l'asthénie, de la dyspnée ou de l'hémoptysie [101]. Cette diversité de symptômes, couplée avec le fait que la plupart des infections à *M. abs* s'accompagnent d'une pathologie sous-jacente, rend particulièrement compliqué l'établissement d'un diagnostic sur des bases cliniques [101, 114, 123].

On peut cependant identifier des lésions causées par l'infection sur une radio des poumons (**Figure 18**). On distingue alors deux types distincts de lésions :

- Des lésions nodulaires, ou bronchiectasiques, (**Figure 18A**) qui sont généralement caractéristiques d'une infection moins agressive et moins douloureuse, à l'évolution plus lente mais pouvant conduire à terme à la mort du patient [101, 114, 124].
- Des lésions fibrocavitaires qui se manifestent par la formation de cavités fibreuses dans les lobes supérieurs des poumons (**Figure 18B**). Ces lésions sont présentes dans des infections évoluant plus rapidement, et touchent principalement les hommes et les personnes abusants du tabac et de l'alcool [101, 114, 124].

Les lésions nodulaires contiennent généralement les deux morphotypes de *M. abs*, bien que la forme S y soit majoritaire, alors que les lésions fibrocavitaires ne présentent que le morphotype R [124] confirmant son rôle dans les infections plus sévères [83-85].

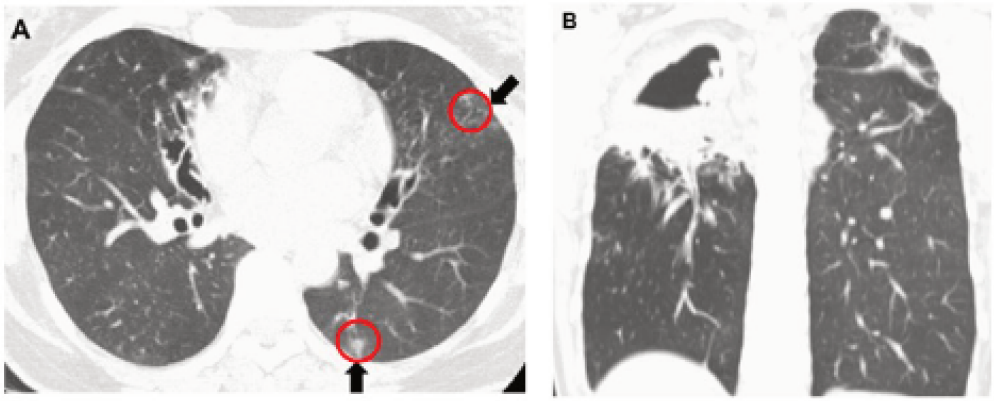

Figure 18 : Scanner thoracique montrant les deux types de lésions pulmonaire typiques lors d'une infection à *M. abscessus* : **(A)** lésions nodulaire entourées en rouge et bronchiectasies, **(B)** cavités fibreuses des lobes supérieurs. D'après [124].

Les infections à *M. abs* suivent généralement un cycle infectieux bien défini (**Figure 19**) [105]. Après la contamination des voies respiratoires du patient (généralement depuis des réservoirs environnementaux) les bacilles vont être phagocytés par les macrophages alvéolaires, résister à la phagocytose et se reproduire en intracellulaire et installer une population extracellulaire. Ce stade d'infection commence généralement par une infection par le morphotype S, qui va former un biofilm dans les poumons. A ce stade, les GPL à la surface de ce morphotype jouent un rôle important dans l'éviction de l'immunité innée [125].

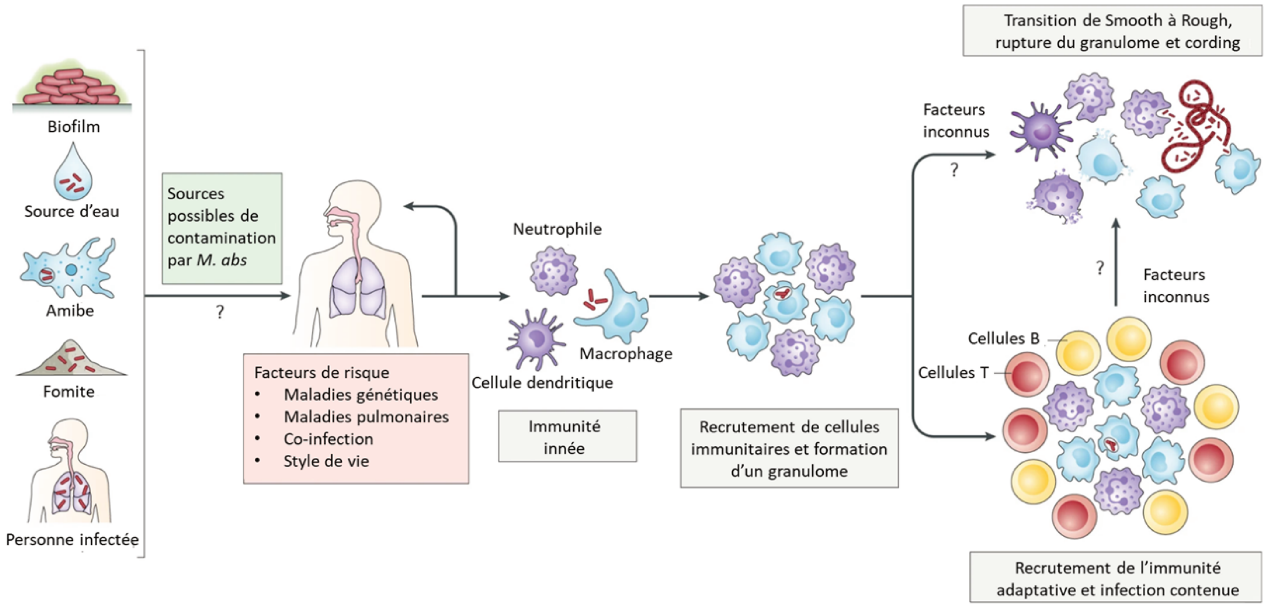

Figure 19 : Schéma du développement des infections à *M. abs*. Adapté de [105]

Cette première infection va conduire au recrutement de cellules immunitaires et à la formation d'un granulome qui va contenir localement l'infection. Dans cet état, *M. abs* peut persister dans les poumons de façon non-symptomatique, ce qui est assez semblable à ce qui se passe lors des infections latentes à *M. tb*. Le patient présente alors des lésions nodulaires des poumon comme décrit précédemment [101, 112, 122].

On observe ensuite une phase de maturation du granulome où la réponse immunitaire adaptative est activée et des lymphocytes B et T sont recrutés et entourent le granulome. L'infection peut rester contenue dans cet état pour de très longues périodes. Cependant, pour des raisons qu'il reste encore à éclaircir, le variant S de *M. abs* peut évoluer de façon irréversible vers la forme R, qui va former des cordes et provoquer la rupture du granulome et les tissus environnants, passant ainsi à un mode plus virulent d'infection [105].

L'analyse de la transition S/R chez *M. abs* est particulièrement importante étant donnée la virulence accrue du morphotype R. Dans ce contexte, un travail de génomique comparative séminal a été effectué en analysant de nombreuses SNPs observées dans le cluster génétique des GPL (**Figure 20**) entre les variants S et R, soulignant la nature génétique de cette transition et expliquant ainsi son irréversibilité [110].

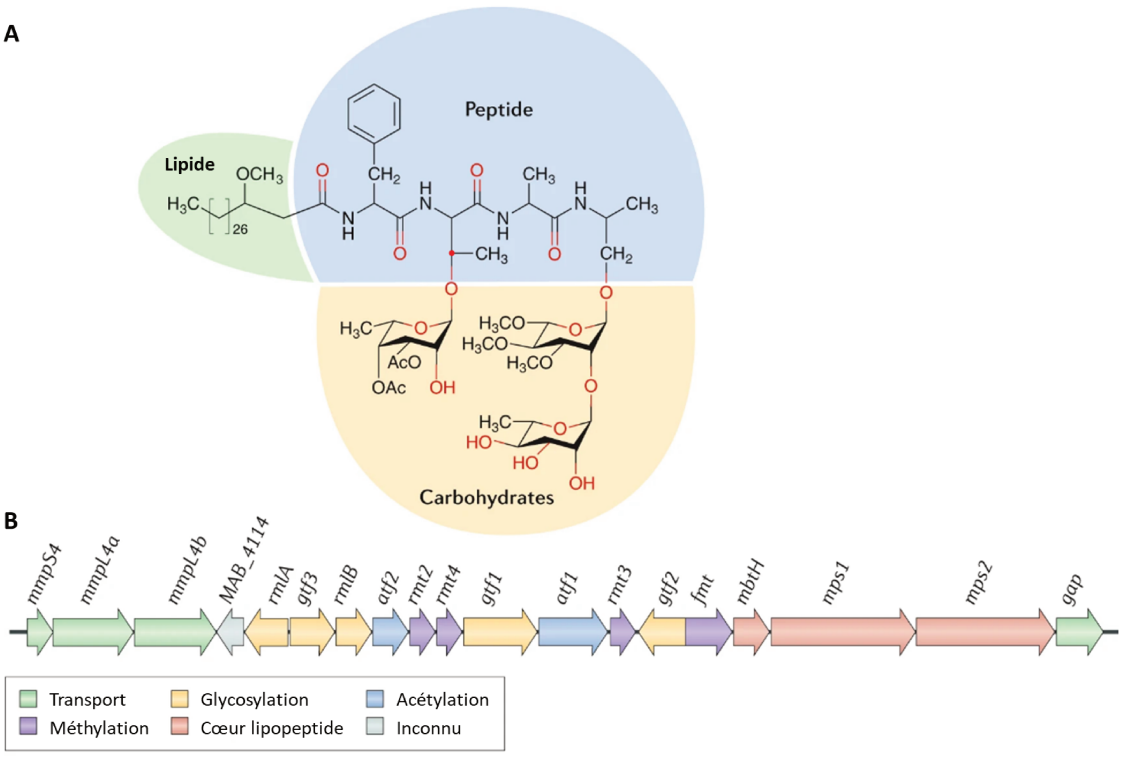

Figure 20 : **(A)** Structure des GPL de *M. abs.* **(B)** Locus *gpl* codant pour la production, la modification et le transport des GPL [105]

Parmi les mutations identifiées, on observe des délétions du gène *mmpL4* qui code pour un transporteur transmembranaire responsable de l'export des GPL, ainsi que des gènes *mps1* et *mps2,* qui sont directement impliqués dans la synthèse des GPL [110]. Une autre étude a montré que des mutations dans les gènes *mmpL4a* et *mmpS4*, également responsables de l'export des GPL, étaient associés à la transition S/R [126]. Ainsi, ces études montrent qu'une disruption de la voie de synthèse ou de la voie d'export des GPL conduit à une transition du morphotype S vers le morphotype R.

La transition S/R peut s'observer spontanément *in vitro* au bout d'un certain nombre de cultures successives, et s'observe également dans des modèles *in vivo* de souris où elle se produit dans environ 20% des infections [127]. Cette transition de morphotype va provoquer une invasion plus agressive des tissus pulmonaires en raison de la virulence accrue de la forme R. En effet, l'absence de GPL chez *M. abs* R expose d'autre composants de la membrane, notamment les phosphatidyl-myo-inositol mannosides qui stimulent la réponse inflammatoire [125], et les tréhaloses dimycolates (TDM). Ces derniers, aussi appelés « *cord factor* », jouent un rôle dans le phénomène de cordes ou « *cording* » (**Figure 21**), et sont également un facteur de virulence [128]. De plus, il a été récemment montré par microscopie à force atomique avec une pointe hydrophobe que les motifs à la surface des deux morphotypes de *M. abs* sont très distincts [129]. En effet, les GPL définissent des nano-domaines d'hydrophobicité variables qui sont complètement absents chez le morphotype R, qui présente une surface d'hydrophobicité homogène. Cette différence de surface joue ainsi un rôle important dans l'adhésion bactérienne, l'agrégation et le cording, ainsi que dans la virulence et la pathogénie [129].

La formation de cordes est un paramètre central de la virulence du morphotype R, car elle induit une lyse accrue des macrophages lorsque *M. abs* R a déjà été phagocyté (**Figure 21**). La taille de ces cordes peut également permettre d'éviter complètement la phagocytose (**Figure 21**) [106, 130]. La transition vers la forme R de *M. abs* entraînant une colonisation rapide du tissu pulmonaire et une dégradation de ce dernier, cette phase d'infection est alors symptomatique et présente un taux plus élevé de mortalité [106, 128, 131].

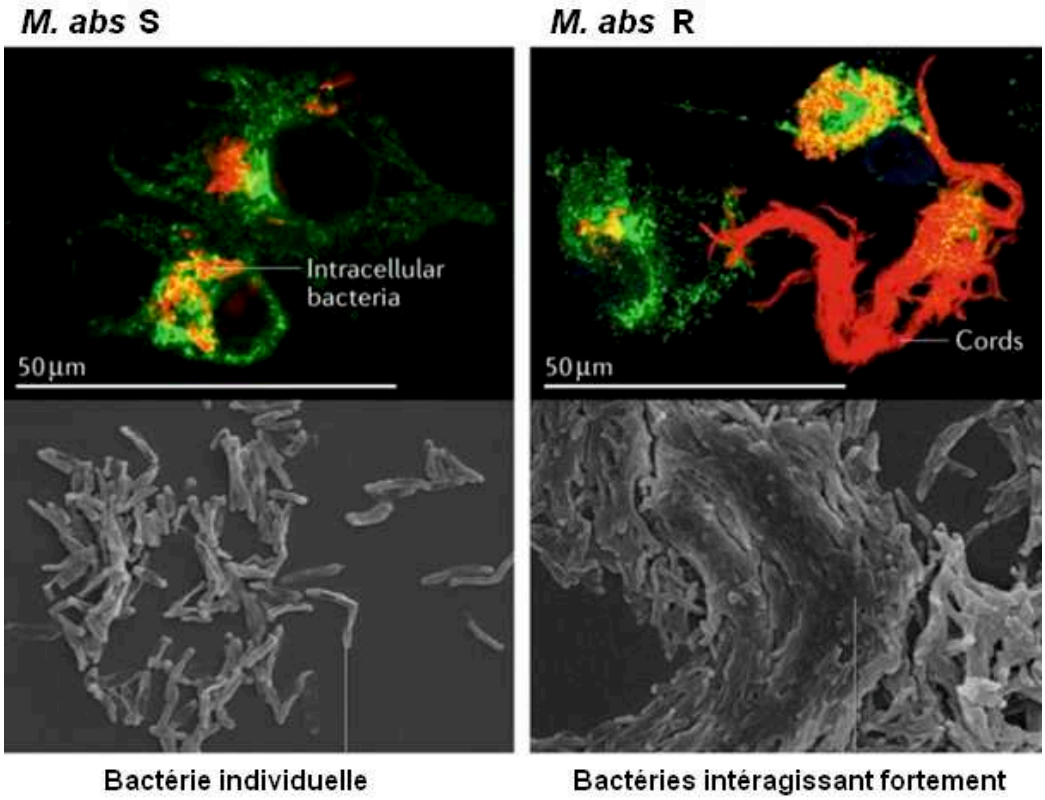

Figure 21 : Différences d'interaction des deux morphotypes de *M. abs* avec des monocytes humains. Extrait de [105].

c) Mucoviscidose et *M. abs*

La mucoviscidose est une maladie génétique induisant des symptômes pulmonaires importants, avec notamment l'accumulation de mucus dans les voies respiratoires ainsi que des symptômes gastro-intestinaux et reproducteurs.

Aujourd'hui, près de 7000 personnes sont atteintes de mucoviscidose en France, et environ un enfant sur 2500 nait chaque année avec la mucoviscidose en Europe et en Amérique du nord, en faisant la maladie génétique la plus répandue dans la population caucasienne.

La cause de cette maladie vient d'une mutation du gène *CFTR* (« *Cystic Fibrosis Transmembrane Conductance Regulator* »), qui code pour un transporteur transmembranaire de type ABC [132].

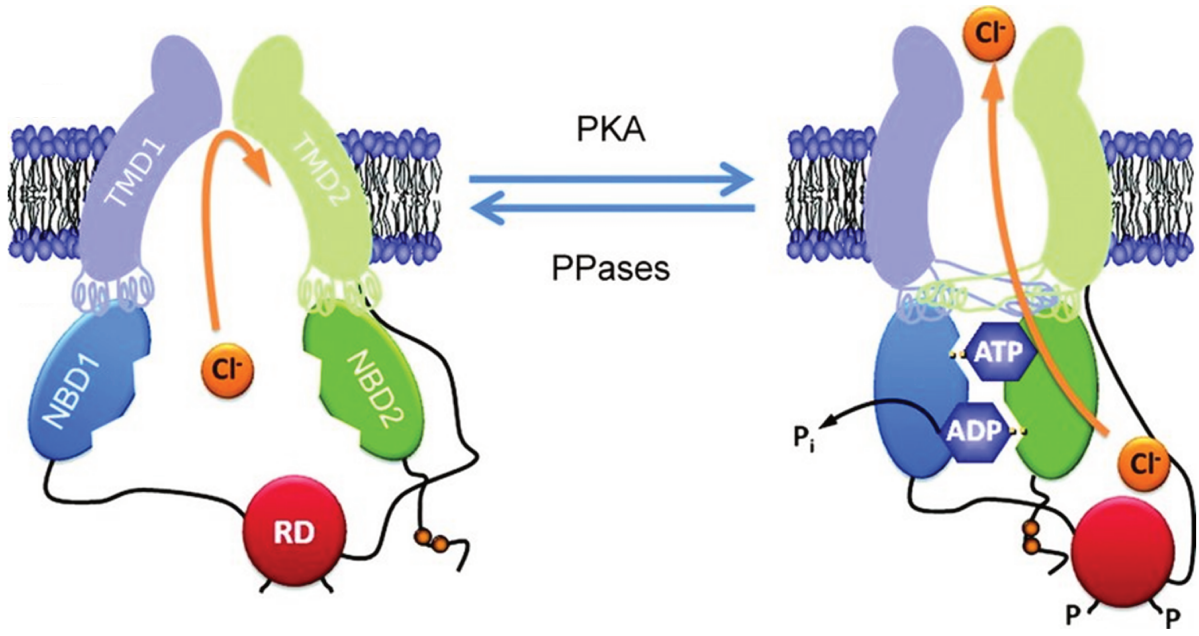

Figure 22 : Modèle du fonctionnement du canal CFTR. Le canal est representé sur la gauche dans son état de repos et sur la droite dans son état activé. La lettre P indique la phosphorylation du domaine de régulation noté RD. D'après [93].

La protéine CFTR se retrouve à la surface des cellules épithéliales des voie respiratoires, mais également du tractus intestinal, des canaux pancréatiques, des testicules et des glandes sudoripares [133]. Cette protéine est constituée de deux domaines transmembranaires ou TMDs, deux domaines cytoplasmiques appelés NBDs (*Nucleotide Binding Domain*) et un domaine de liaison des deux parties de la protéine (**Figure 22**) [134].

La protéine CFTR est un canal transmembranaire, dont l'ouverture est contrôlée par les domaine NBD1 et NBD2, et qui joue un rôle fondamental dans le maintien de l'équilibre hydro-électrostatique, notamment à travers le contrôle du passage transmembranaire des ions chlorure et bicarbonate [135]. Elle joue également un rôle dans le trafic intracellulaire des vésicules [136].

La plupart des patients atteints de mucoviscidose présentent une mutation du résidu phénylalanine Phe508 dans le domaine NBD1, qui empêche sa maturation et conduit à sa dégradation, mais on retrouve également d'autres mutations qui entraînent une baisse ou une suppression totale de sa fonction.

Au niveau pulmonaire, l'effet principal de ces mutations est l'épaississement du mucus, dû à la déshydratation, qui constitue alors un milieu riche et propice au développement d'infections bactériennes (**Figure 23**) [133].

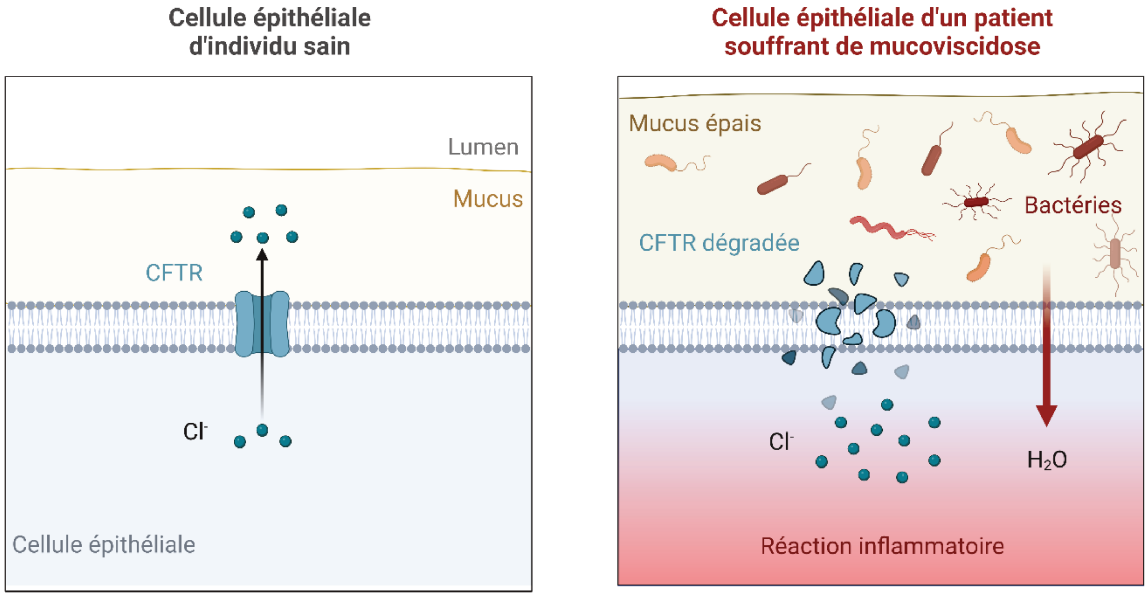

Figure 23 : Différences phénotypiques des voies respiratoires d'un individu sain par rapport à un patient mucoviscidose.

Parmi les infections bactériennes les plus communes chez les patients atteints de mucoviscidose, on retrouve principalement des infections à *Pseudomonas aeruginosa*, *Staphylococcus aureus* et *Burkholderia cenocepacia*. De manière générale, *S. aureus* est le premier pathogène à coloniser les voies respiratoires des patients, mais il est supplanté à l'adolescence par *P. aeruginosa*, responsable d'infections chroniques de plus longue durée [137]. Ces infections peuvent causer des atteintes respiratoires, qui représentent la principale cause de mortalité chez les patients (de 80 à 95% des décès) [132, 138].

On retrouve dans une moindre mesure des infections pulmonaires dues à des MNT comme *M. abs*. Cette dernière représente néanmoins un problème majeur en raison de sa forte résistance aux antibiotiques, qui peut conduire à des impasses thérapeutiques et à la mort du patient. Ces infections conduisent, comme celles causées par d'autres bactéries, à une inflammation importante des voies respiratoires et à une perte de fonction pulmonaire, qui cause à terme la mort des patients [139]. De plus, une infection à *M. abs* est une contre-indication à toute greffe de poumon, qui est souvent la seule chance de survie chez ces patients atteint de mucoviscidose [140].

La prévalence des MNT associées à la mucoviscidose est aujourd'hui en constante augmentation [113, 120]. En effet, 5 à 20 % des patients atteints de mucoviscidose sont

infectés par des MNT [141] parmi lesquelles on retrouve dans 48% des cas une espèce du complexe MABc.

Cependant la prévalence des infections aux MNT chez ces patients peut varier fortement en fonction de la région géographique [142] mais également en terme d'espèces isolées. Ainsi, si les espèces du MABc sont majoritaires en France, on retrouve plus fréquemment des espèces du complexe *M. avium* aux Etats-Unis [113, 141].

d) Le diagnostic de *M. abs*

Le diagnostic des infections pulmonaires à *M. abs* est extrêmement important, afin d'adapter le traitement au plus tôt et d'éviter les impasses thérapeutiques, fréquentes pour ce type d'infections.

Le diagnostic actuel, assez complexe, a été établi par l'*American Thoracic Society* (ATS) et l'*Infectious Diseases Society of America* (IDSA) [101], ainsi que par les associations européennes et américain de la mucoviscidose [139], et est constitué d'un ensemble de critères cliniques et microbiologiques.

Les critères microbiologiques de diagnostic recommandent d'avoir au moins l'une des conditions suivantes :

- Une culture positive de deux échantillons différents d'expectorâts
- Une culture positive d'un échantillon de lavage bronchoalvéolaire
- Une biopsie montrant des caractéristiques histopathologiques mycobactériennes comme un granulome, associée à un lavage bronchoalvéolaire

Les critères cliniques, outre les symptômes de perte de fonction pulmonaire qui sont partagés par de nombreuses autres infections, recommandent la réalisation d'une radio des poumons montrant des lésions typiques des MNT, comme des nodules ou des cavités opaques, ou un scanner montrant une bronchiectasie associée à des nodules.

L'établissement d'un diagnostic d'infection pulmonaire à *M. abs* est un processus complexe, nécessitant souvent l'intervention d'un expert du domaine, et la procédure peut s'avérer assez longue. Ainsi, il est recommandé d'effectuer le suivi d'un patient suspecté de ce type d'infection tout au long du processus d'établissement d'un diagnostic.

e) Antibiothérapie contre *M. abs*

M. abs et l'ensemble des bactéries du complexe MABc présentent toutes de fortes résistances à la plupart des antibiotique de première intention en clinique, comme les β-lactamines, les tétracyclines, les aminoglycosides et les macrolides ; mais également contre les antituberculeux de première ligne comme la rifampicine et l'isoniazide, ce qui a conduit à qualifier *M. abs* de cauchemar pour les antibiotiques [111]. De ce fait, l'antibiothérapie contre ces infections est longue et coûteuse et présente un grand nombre d'effets secondaires [143].

A

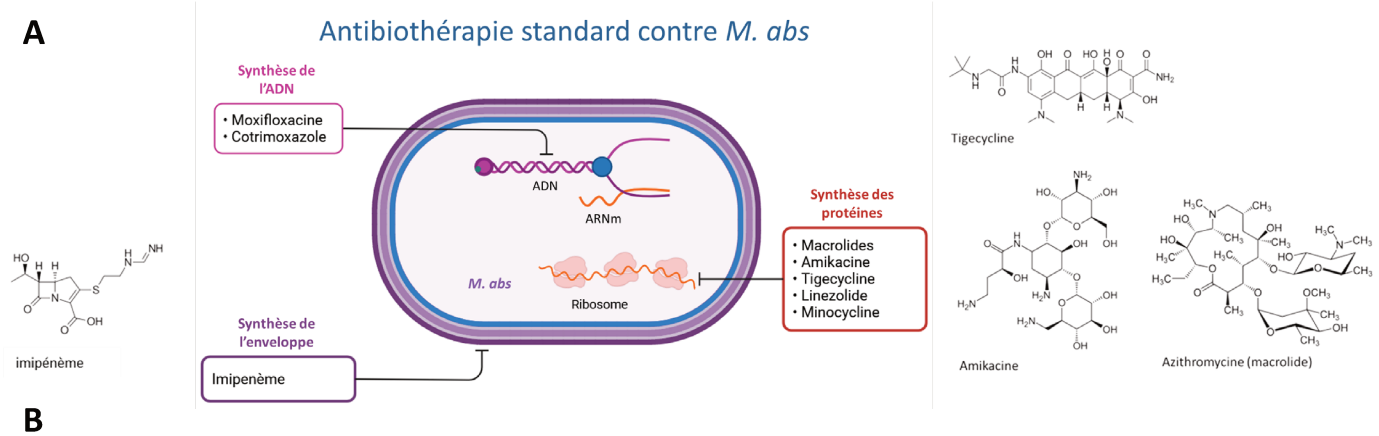

B

Nom	Phase du traitement	Cible	Mécanisme d'action	Gene impliqué dans la résistance
Imipénème	Première phase	Penicillin-binding proteins	Inhibe la synthèse du peptidoglycane	*pknG, fbpA, mtrAB, bla$_{MAB}$*
Tigecycline		Région hélicale H34 de la sous-unité 30S du ribosome	Inhibe la synthèse des protéines	*tetV, tap*
Amikacine		ARN 16S	Inhibe la synthèse des protéines	*rrs, eis2*
Azithromycine		ARN 23S et 16S	Inhibe la synthèse des protéines	*rrs, erm41*
Linézolide	Deuxième phase	Sous-unité 50S du ribosome	Inhibe la synthèse des protéines	*rrs*
Minocycline		Sous-unité 30S du ribosome	Inhibe la synthèse des protéines	*tetV, tap*
Cotrimoxazole (Trim éthoprime / sulfaméthoxazole)		Dihydrofolate réductase / Dihydroptéroate synthase	Inhibe la synthèse d'ADN bactérien (inhibition de la synthèse de l'acide folique)	*dhfrI, dhfrII, dhps, folP*
Moxifloxacine		ADN gyrase	Inhibe la réplication cellulaire	*gyrA, gyrB, lfrA, efpA, pstB*

Figure 24 : **(A)** Structure des antibiotiques de l'antibiothérapie standard contre *M. abs*. **(B)** Tableau de leur mode d'action, cibles et gènes impliqué dans la résistance chez *M. abs* [143-145].

L'antibiothérapie standard recommandée par la British Thoracic Society contre les infections pulmonaires au MABc se découpe en deux phases distinctes :

- La première phase, de 1 mois, fait intervenir un cocktail d'antibiotiques comprenant l'amikacine, la tigecycline et l'imipenème en intraveineuse, et peut également contenir un macrolide si l'isolat clinique est déterminé comme sensible aux macrolides (**Figure 24**) [146].
- Intervient ensuite une phase de continuité du traitement durant à minima 12 mois, qui consiste en la prise d'amikacine nébulisée couplée à la prise d'un à trois des antibiotiques suivants : linezolide, clofazimine, minocycline, cotrimoxazole et moxifloxacine [146].

Imipénème (IMP).

L'imipenème est le premier antibiotique de la famille des carbapénèmes à avoir été utilisé en clinique [147].

Les carbapénèmes possèdent un noyau β-lactame, et leur mécanisme d'action est identique aux autres β-lactamines. L'imipenème se lie aux penicillin-binding proteins (PBP), qui sont des peptidases bactériennes responsables de l'élongation et du crosslinking du peptidoglycane. Ainsi, en inactivant ces enzymes, l'imipénème vient perturber la synthèse du peptidoglycane et de l'enveloppe mycobactérienne, ce qui conduit à une inhibition de la croissance et à la mort cellulaire [148].

Amikacine (AMK).

L'amikacine est un analogue synthétique de la kanamycine qui appartient à la famille des aminoglycosides.

Cette famille de molécules cible l'ARN 16S, qui est une composante de la sous unité 30S du ribosome bactérien, ce qui interfère fortement avec la traduction des protéines [149]. En effet, plusieurs études ont établi que des mutations de l'ARN 16S chez *M. abs* étaient responsables d'une résistance aux aminoglycosides [111, 150].

Tigecycline.

La tigecycline est un antibiotique bactériostatique de la famille des glycylcyclines qui présente une structure similaire à la tétracycline (**Figure 24**) [151-153].

Comme les autres cyclines, la tigecycline est un inhibiteur de la traduction des protéines. En effet, elle est capable de se lier de manière réversible à la région hélicale H34 de la sous-unité 30S du ribosome bactérien, et d'inhiber ainsi l'élongation des protéines en empêchant l'ajout d'acides aminés [151-153].

La tigecycline a été développé spécifiquement pour éviter les résistances principales à la tétracycline comme les pompes à efflux spécifiques (*tet*A) et les protections ribosomales (*tetM*) [154] par l'addition d'un glycyclamide en position 9 de la minocycline.

Les macrolides : azithromycine ou clarithromycine.

Les macrolides sont également une famille d'antibiotiques bactériostatiques au mode d'action similaire, qui vont inhiber la synthèse des protéines en se liant au l'ARN 23S et 16S et ainsi perturber le fonctionnement du ribosome bactérien.

Beaucoup de souches de *M. abs* présentent une résistance induite aux macrolides en raison de la protéine Erm41 qui est capable, en présence de macrolides, de méthyler le site de fixation de ces molécules sur l'ARN 23S et ainsi d'empêcher son inhibition. En revanche, ce gène n'est pas présent chez la sous-espèce *M. massiliense*. La susceptibilité de la souche clinique à traiter doit être vérifiée avant d'utiliser des macrolides dans une antibiothérapie contre une espèce du complexe MABc [111, 155].

Le traitement contre *M. abs* est lourd et coûteux mais ne présente qu'un faible taux de guérison de 30 à 50% [143]. Ainsi, bien que ce pathogène soit peu fréquent, les impasses thérapeutiques, le taux de morbidité et le taux de mortalité lors des infections par le complexe MABc en font un problème majeur de santé publique, particulièrement dans le cadre de la mucoviscidose. Il y a donc une nécessité à identifier de nouvelles molécules et cibles thérapeutiques dans la lutte contre les infections mycobactériennes.

f) Nouvelles molécules en développement

Le traitement des infections à *M. abs* est extrêmement complexe en raison des nombreuses résistances innées et induites que présente cette bactérie, ce qui limite l'usage des antibiotiques les plus couramment utilisés en clinique. De plus, l'antibiothérapie standard présentée précédemment est peu efficace et comporte de nombreux effets secondaires en raison de sa toxicité, ce qui souligne l'importance de développer des nouvelles molécules plus efficaces et moins toxique pour lutter contre *M. abs* [156, 157].

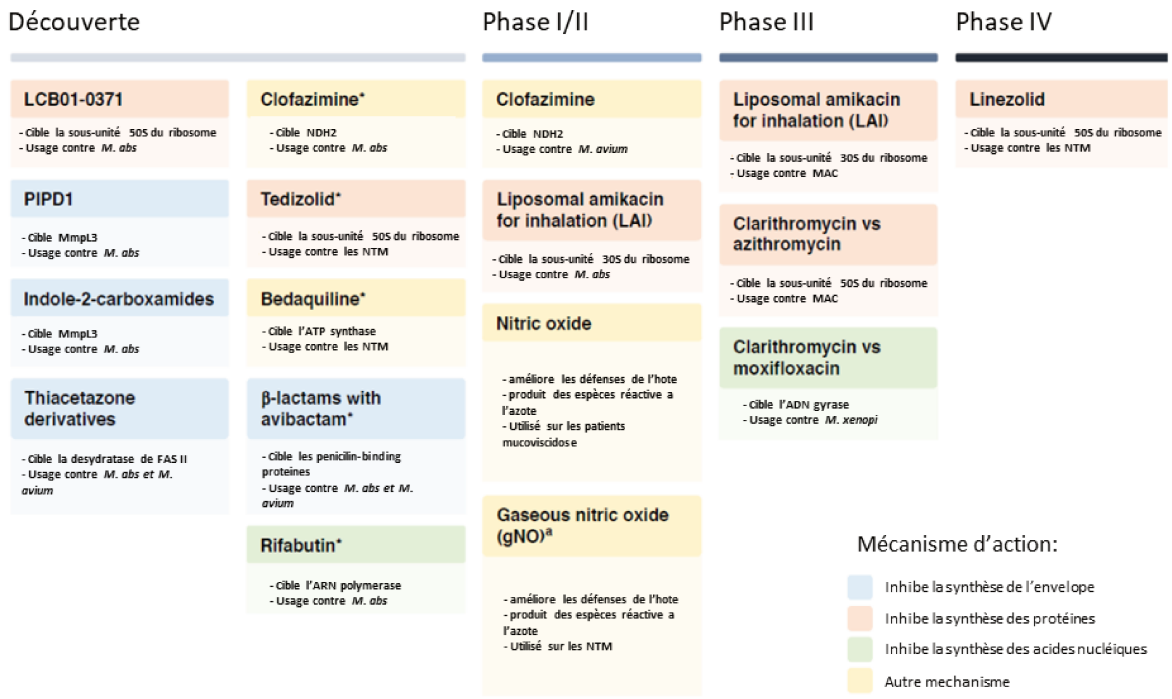

Figure 25 : Antibiotiques actuellement en développement pour lutter contre les MNT [157].

L'état d'avancement du développement de nouvelles molécules contre *M. abs* est très différent de celui des antituberculeux. En effet, sur les 17 nouveaux traitements actuellement en développement, seul 8 sont en cours d'essai clinique (**Figure 25**) [157]. Ainsi, un manque de développement couplé à l'émergence de nombreuses souches résistantes au traitement actuel pourrait augmenter le taux de fatalité de ces infections [156, 158].

Les principaux antibiotiques en cours de développement contre les infections à *M. abs* sont représentés ci-dessous en **Figure 26**.

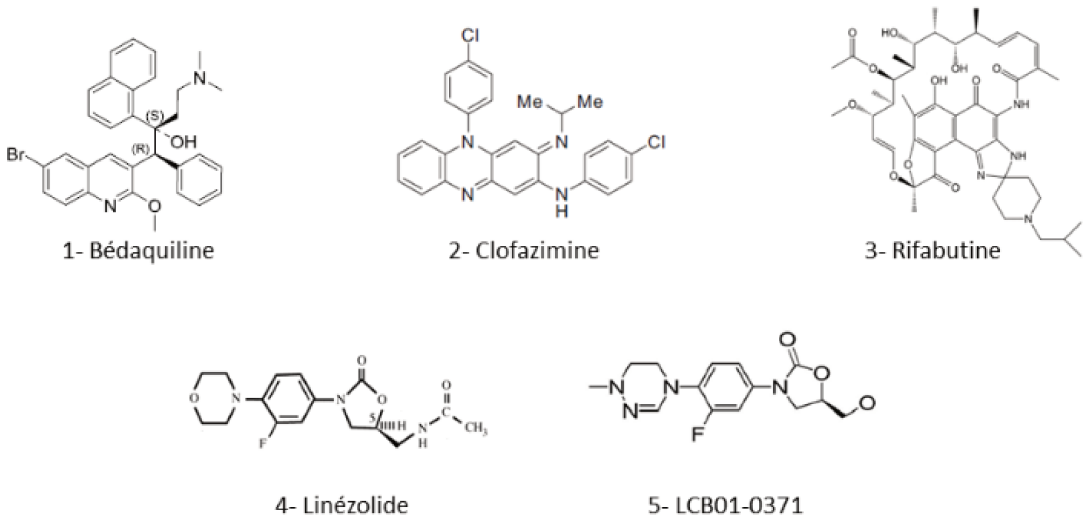

Figure 26 : Structure des principaux antibiotiques contre *M. abs* en cours de développement [159-161].

La Bédaquiline.

Le mode d'action de la bédaquiline a déjà été discutée en **Partie III.f** de ce manuscrit ; c'est un inhibiteur de l'ATP synthase qui est également en développement pour un usage dans l'antibiothérapie contre *M. tb*.

Cette molécule a été par la suite investiguée pour le traitement contre *M. abs* [158] et s'est avérée avoir une activité bactériostatique contre *M. abs in vitro* et en modèle d'infection de macrophages [162] et d'embryons du poisson zèbre [163]. De plus, elle a été investiguée pour traiter une ostéomyélite causée par *M. abs* en combinaison avec la clofazimine [164], et la rifabutine contre des infections actives et dormantes à *M. abs* en raison de la synergie entre ces deux antibiotiques [165]. D'autre part, des synergies ont été observées *in vitro* entre la bédaquiline et d'autre antibiotiques en développement comme les oxazolidinones [166] et la clofazimine [167].

La Clofazimine.

La clofazimine est un antibiotique de la famille des phénazines, qui est une nouvelle classe d'antibiotiques initialement utilisée pour traiter les cas de tuberculose poly-résistante [168-170]. Elle été d'abord utilisée dans la phase de prolongation du traitement contre *M. abs* [139, 171] car elle présente une très bonne activité *in vitro* contre de nombreux isolats cliniques de *M. abs* [172].

Par la suite, cet antibiotique a montré de bons résultats sur des cas cliniques d'ostéomyélite de la mâchoire [173] et de péritonite dus à *M. abs* [174]. Enfin, l'ajout de clofazimine à l'antibiothérapie standard a permis une nette amélioration des performances thérapeutiques de ce régime contre des infections pulmonaires à *M. abs* [175].

Le mode d'action de cette molécule est peu décrit chez *M. abs*, mais des études menées chez *M. tb* et *M. smeg* montrent qu'il s'agirait d'une prodrogue qui serai réduite par NDH2 qui est une NADH quinone oxydoréductase appartenant à la chaine respiratoire bactérienne [176].

Une oxydation spontanée de la clofazimine réduite conduirait ensuite à la formation d'espèces réactives à l'oxygène (ou ROS) qui présentent une toxicité pour la bactérie [176, 177].

Les Oxazolidinones.

Les oxazolidinones sont une classe d'antibiotiques connue depuis les années 70 qui comprend notamment le linézolide. Cet antibiotique est le premier oxazolidinone à avoir été utilisée en clinique [178] et a été brièvement décrit au **Chapitre II.f** de ce manuscrit.

Il a été initialement montré comme ayant une activité contre *M. tb* [179] et présente des propriétés pharmacocinétiques intéressantes avec une bonne absorption par voie orale. Cet antibiotique agit en se liant à proximité du site catalytique de la sous-unité 50S du ribosome bactérien, perturbant ainsi la synthèse des protéines [180-183].

Le linézolide présente une bonne activité antibactérienne contre *M. abs in vitro* [184] et s'est avéré efficace dans plusieurs cas cliniques [185, 186]. De plus, il présente des activités synergiques avec l'amikacine, la tigecycline [187] et la clarithromycine [188] mais il présente cependant de nombreux effets indésirables.

La Rifabutine.

La rifabutine est un analogue structurel de la rifampicine qui a été identifié comme ayant une activité sur plusieurs espèces du complexe MABc [161]. Elle est active contre de nombreux isolats cliniques de *M. abs in vitro* [189] et également dans des modèles d'infection de macrophages humains et murins [190, 191]. La rifabutine montre également des activités synergiques avec l'imipénème [191, 192] , la tigecycline et la clarithromycine [193].

Comme la RIF, la rifabutine inhibe la transcription en se fixant à la sous-unité beta de l'ARN polymérase, et des mutations du gène *rpoB* qui code pour cette sous-unité peuvent conduire à une résistance [194, 195].

Dans ce contexte, notre équipe s'intéresse particulièrement à une classe d'enzymes mycobactériennes : les enzymes à sérine ou cystéine catalytique. En effet, ces enzymes sont fondamentales dans la pathologie et le cycle de vie des mycobactéries ce qui en fait des candidats de choix dans la recherche de nouvelles cibles thérapeutiques.

IV Les enzymes lipolytiques mycobactériennes et leur étude par « *Activity-Based Protein Profiling* » (ABPP)

Il est aujourd'hui bien établi que le métabolisme des lipides joue un rôle central dans la physiologie et la pathologie des mycobactéries. A titre d'exemple, une analyse du génome complet de *M. tb* a mis en évidence 250 enzymes dédiées au métabolisme des lipides, soit 6% de son génome contre 50 enzymes chez *E. coli* [196].

Ces enzymes, dites lipolytiques, ont été longuement étudiées au cours des dernières années par notre groupe en raison de leurs rôles multiples dans la pathologie et les interactions hôte-pathogène [197], et dans la physiopathologie des infections mycobactériennes [198].

En effet, ces enzymes interviennent dans de nombreux processus liés à la croissance mycobactérienne [199-201], aux mécanismes de dormance [202, 203], de réactivation, de propagation et de virulence [204-207], à la synthèse de l'enveloppe mycobactérienne [198, 200], et aux mécanismes de stockage et de dégradation des lipides [199, 202, 208, 209].

Il a été montré qu'une majorité de ces enzymes possède une sérine ou une cystéine catalytique, ce qui a conduit à l'exploitation de cette spécificité chimique pour les étudier. Ainsi, j'ai rédigé une revue bibliographique détaillée sur la nature et la fonction de ces enzymes, ainsi que sur les outils moléculaires de chimioprotéomique dédiés à leur étude qui se trouve au premier chapitre de la partie **Résultats** - **Article 1** de ce manuscrit.

V. Métabolisme des ILI et modèles pour leur étude

Les gouttelettes lipidiques ou « *lipid droplets* » (LD), également appelées corps lipidiques ou « *lipid bodies* » (LB), sont des organelles synthétisées par de nombreux organismes eucaryotes comme les mammifères et les plantes [210-212]. On retrouve également ces structures chez les procaryotes, où elles sont appelées inclusions lipidiques intracytoplasmique (ILI) [40, 213-215].

Les ILI sont composés de lipides neutres (principalement des triacylglycérols ou TAG) qui sont entourés d'une monocouche amphiphile de phospholipides au sein de laquelle des protéines de surface interagissent de façon dynamique [215, 216].

La présence d'ILI a été décrite chez un grand nombre de mycobactéries non pathogènes et pathogènes comme *M. smegmatis* (*M. smeg*) [199, 217-219], *M. abs* [218, 220], *M. avium* [39], *M. marinum* [221], *M. ulcerans* [222], *M. leprae* [223] et plusieurs membres du complexe *M. tuberculosis* (**Figure 27**) [205, 209, 224-226].

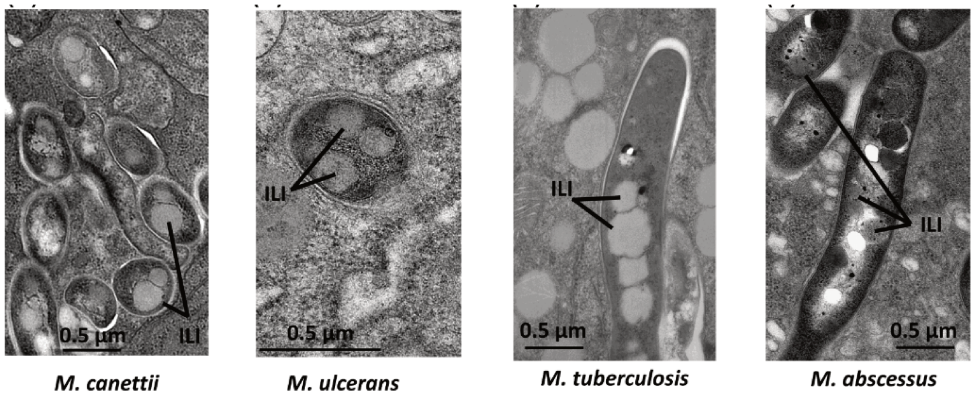

Figure 27 : Images de microscopie électronique à transmission montrant l'accumulation d'ILI chez plusieurs souches mycobactériennes. Adapté de [40].

a) Synthèse des TAG

La synthèse des TAG et des gouttelettes lipidiques suit une voie de synthèse bien définie et conservée chez les bactéries et les eucaryotes, appelée voie Kennedy (**Figure 28 A**).

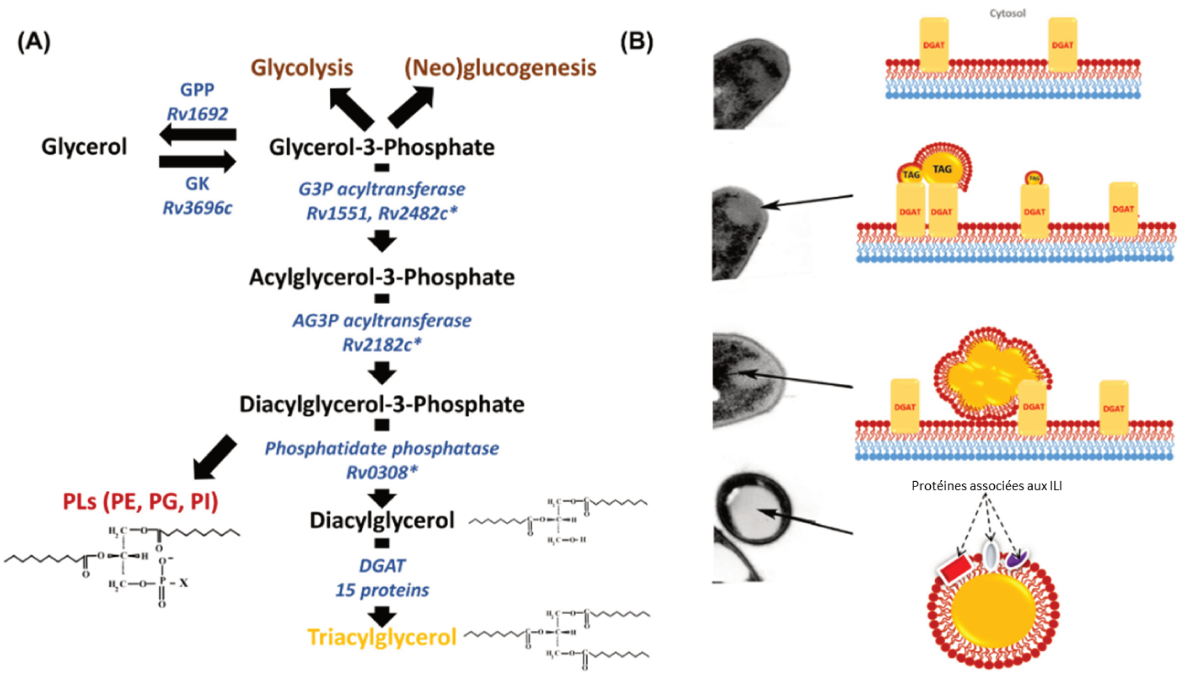

Figure 28 : Schéma de la synthèse des TAG chez les actinobactéries. **(A)** Représentation de la voie Kennedy chez *M. tb.* **(B)** Représentation schématique de la formation des ILI, basée sur des images de microscopie électronique chez *R. opacus*. Adaptée de [40].

L'étape limitante de cette voie est médiée par la protéine DGAT aussi connue sous le nom de TGS (triglycéride synthase) qui catalyse la production des TAG à partir des diacylglycérols (DAG). Elle a été initialement identifiée chez *Acinetobacter calcoaceticus* ADP1 (appelé AtfA) [227]. De nombreux homologues de cette enzyme ont été identifiés, particulièrement chez les *Actinomycetes* tels que les mycobactéries, les *streptomyces* et les *rhodococcus* où elle est liée à l'accumulation des TAG et des esters cireux ou « *wax esters* » (WE) [213, 215]. *M. tb* H37Rv présente 15 homologues de TGS [227, 228] parmi lesquelles 11 possèdent le motif HHxxDG correspondant à une activité acyltransférase impliquée dans la synthèse des TAG, et quatre présentaient un site actif modifié. Après production et purification de ces quatre enzymes, il a été établi qu'elles présentaient une activité de triglycérides synthase *in vitro* et ont alors été renommées Tgs1-4 [228]. De plus, il a été démontré par de nombreuses études que Tgs1 était le contributeur principal de la synthèse des TAG chez les mycobactéries et que sa délétion abolit intégralement la synthèse des TAG [202, 228, 229]. Chez *M. abs*, 7 gènes de protéines codant pour des Tgs ont été trouvés ; parmi lesquels Tgs1. Cette enzyme a été identifiée comme nécessaire pour la synthèse des TAG [220]. Il a été montré que chez *M. abs,* Tgs1 peut utiliser une large gamme d'acyl-CoA pour la synthèse des TAG mais est plus active en présence de palmitoyl-CoA [220].

Il a également été montré que la mycolytransférase Ag85A de *M. tb* surexprimée chez *M. smeg* conduit à une altération de la morphologie cellulaire, de la division et de la biosynthèse des ILI [230]. Dans des conditions de culture pauvres en lipides, les enzymes associées à la synthèses des ILI se retrouvent localisées sur la membrane [220, 230, 231] ce qui va dans le sens de l'hypothèse selon laquelle la synthèse des ILI démarre dans le feuillet interne de la membrane cytoplasmique avant d'être relâchés dans le cytosol [232]. En effet, l'analyse de la synthèse des ILI chez *R. opacus* PD630 commence par la formation de petites inclusions lipidiques associées à la membrane interne qui vont ensuite s'agglomérer entre elles pour former des pré-ILI, avant d'être relâchées dans le cytoplasme sous forme d'ILI matures qui vont continuer à grossir, emportant avec elles un grand nombre de protéines associées (**Figure 28 B**) [232].

b) Le système FAS et la synthèse *de novo* des acides gras

La biosynthèse *de novo* des acides gras et des acide mycoliques fait intervenir un système enzymatique appelé le système FAS (**Figure 29**) qui se divise en deux parties : FAS I et FAS II.

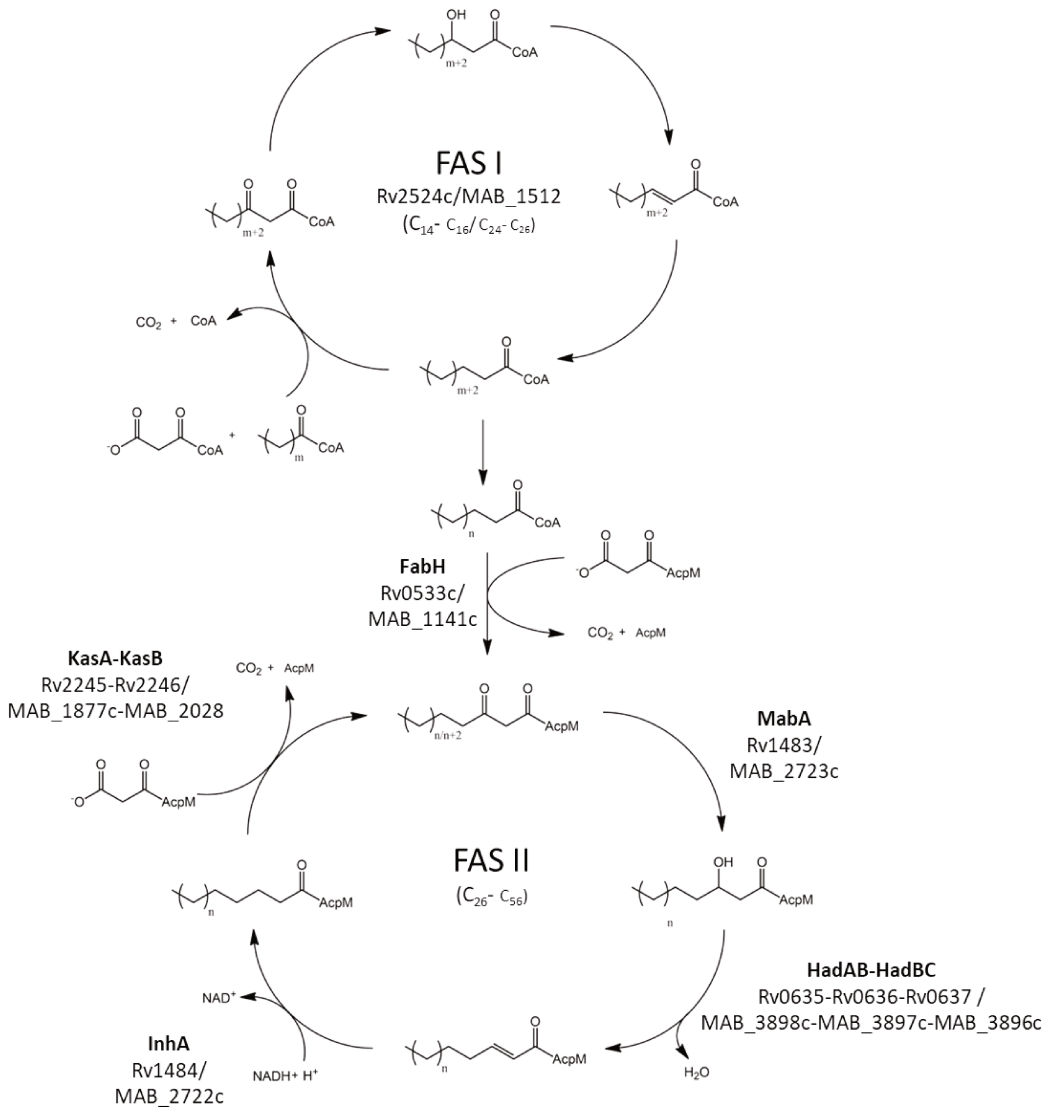

Figure 29 : Schéma des systèmes FAS I et FAS II chez les mycobactéries. Adapté de [233, 234].

FAS I.

Le système FAS I est présent chez les eucaryotes et les procaryotes et notamment chez les *Actinomycetes* et les mycobactéries [235, 236]. FAS I est responsable de la synthèse *de novo* des FFA à partir du malonyl-CoA et a été montré comme essentiel chez *M. smeg* [237] et chez *M. tb* [238]. FAS I est une enzyme multi-domaine et multifonctionnelle (Rv2524c chez *M. tb*, MAB_1512 chez *M. abs*) présentant une structure complexe en sept domaines [239, 240]. Les sept domaines sont organisés séquentiellement selon l'ordre des sept étapes du cycles FAS I. Ansi, la même enzymes présente plusieurs activités (**Figure 29**) [240] :

- Activités acyltransférase, 2-trans-énoyl réductase,

- Activités déshydratase, malonyl/palmitoyl transférase, « *acyl carrier protein* » (ACP) ou protéine porteuse d'acyl,
- Activité ß-ketoacyl réductase,
- Activité ß-ketoacyl synthase.

Durant le déroulement du cycle, chaque intermédiaire reste lié à l'enzyme et est déplacé de domaine en domaine par *trans*-acylation [241]. Ce cycle permet la synthèse de deux types d'acyl-CoA distincts [235, 237]: les acyl-CoA C16-C18, qui représentent la majorité des acyl-CoA synthétisés par FAS I, et les produits d'élongation acyl-CoA C24-26 qui peuvent être synthétisés par FAS I après leur carboxylation par un complexe Acyl-CoA Carboxylase (ACC) [242, 243].

FAS II.

Le système FAS II est quant à lui spécifique des mycobactéries et est incapable de synthétiser les acides gras *de novo*. Il est responsable de l'élongation des acyl-CoA C16-C18 produit par FAS I en acyl-CoA C40-C60. Il est composée de plusieurs enzymes multifonctionnelles qui agissent sur un substrat malonyl porté par une protéine ACP appelée AcpM (Rv2244 chez *M. tb,* MAB_1878c chez *M. abs*) [244] qui transfère les intermédiaires à toutes les enzymes du système FAS II [245].

Le transfert entre le système FAS I et II commence par une réaction de condensation de Claisen entre les acyl-CoAs C16-18 et le malonyl-ACP qui est catalysée par FabH qui est une ß-ketoacyl ACP synthase de type III qui vas former des ß-ketoacyl-ACPs qui sont pris en charge par FAS II [246].

Le cycle FAS II se décompose en quatre étapes, et chaque cycle conduit à l'élongation de la chaine acyl de deux carbones (**Figure 29**).

La première étape est une réduction du ß-ketoacyl-ACP en ß-hydroxyacyl-ACP par la ß-ketoacyl-ACP réductase NADPH-dépendante MabA (Rv1483 chez *M. tb,* MAB_2723c chez *M. abs*) [246]. Cette enzyme s'organise en tétramère et présente une spécificité pour les substrats à chaine longue (C8-C20) [247, 248].

L'étape suivante est effectuée par les enzymes HadAB/HadBC qui sont des hétérodimères de ß-hydroxyacyl-ACP déshydratases, codées par le cluster de gènes essentiels Rv0635-Rv0636-

Rv0637 chez *M. tb*. Ces enzymes vont catalyser la déshydratation des ß-hydroxyacyl-ACP en 2-trans-énoyl ACP [249].

La troisième étape de ce cycle fait intervenir l'InhA (Rv1484 chez *M. tb*) qui est la cible de l'isoniazide (**Chapitre III.e**). Cette enzyme va catalyser la réduction des 2-trans-énoyl ACP en acyl-ACP en présence de NADH [249, 250].

Enfin, la dernière étape du cycle FAS II fait intervenir deux enzymes : KasA et KasB. Ces enzymes catalysent la condensation entre les acyl-ACP produits à l'étape précédente avec le malonyl-ACP pour produire les ß-ketoacyl ACP qui peuvent alors être les substrats d'un nouveau cycle d'élongation [251, 252]. Ces deux enzymes remplissent le même rôle mais montrent des spécificités de substrat différentes. En effet, KasA va prendre en charge des substrats monoinsaturés allant jusqu'à C40, alors que KasB prend en charge des substrats polyinsaturés allant jusqu'à C54 [251, 253].

c) Import d'acides gras exogènes

Il est aujourd'hui bien établi que *M. tb* possède la capacité d'acquérir des acide gras dérivés de l'hôte qui lui fournissent une source de carbone critique dans la persistance et la réactivation des tuberculoses latentes (**Figure 30**) [254]. L'hypothèse initiale concernant l'import des acides gras de l'hôte fait intervenir des protéines transmembranaires impliquées dans l'acquisition de lipides chez les mammifères appelées « *fatty acid transport proteins* » (FATPs) car ces dernières sont largement conservées chez un large panel d'organismes incluant *Caenorhabditis elegans*, *Drosophila melanogaster*, *Saccharomyces cerevisiae* et *M. tb* [255]. D'autres études indépendantes ont montré que ces enzymes présentaient une activité d'acyl-CoA synthétase et que leur expression hétérologue chez *E. coli* induisaient un import accru d'acides gras [256]. Il a également été montré dans cette étude que la disruption génétique de FACL6 (Rv1206) chez *M. tb* permet de perturber l'import des acides gras exogènes de l'hôte et donc l'accumulation d'ILI dans un système intracellulaire.

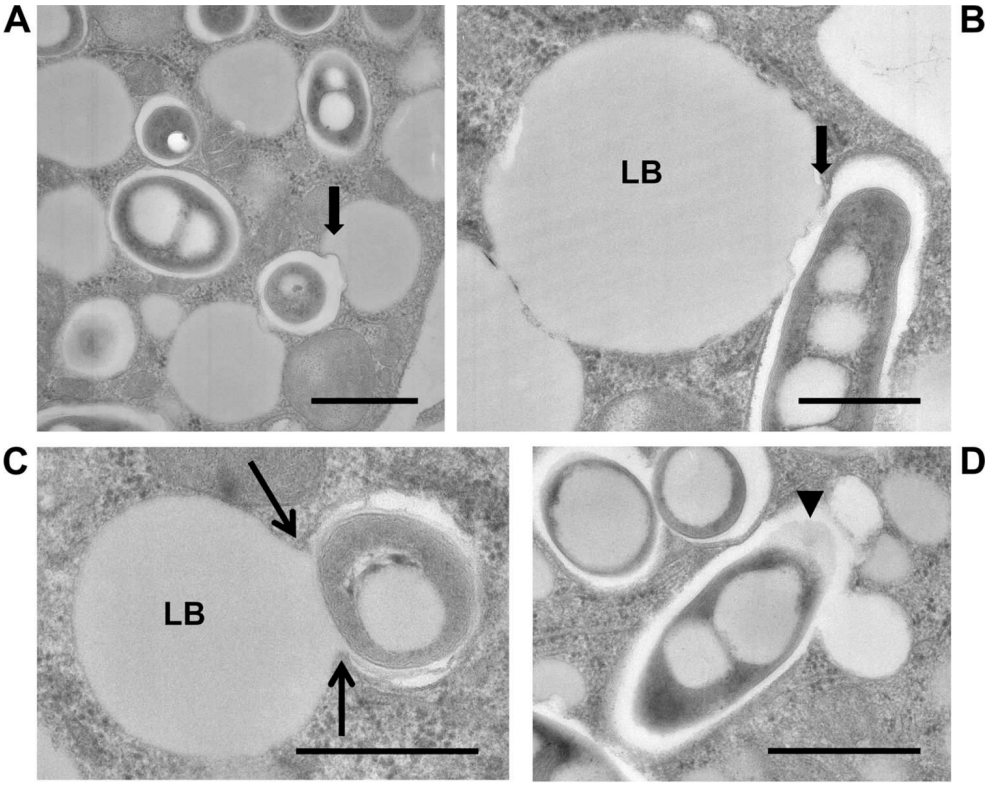

Figure 30 : Accumulation d'ILI par *M. avium* depuis les LB de l'hôte dans un modèle d'infection de macrophage murin dérivé de moelle osseuse. **(A)** Phagosome contenant *M. avium* en contact avec un LB. Une flèche indique la déformation de la membrane du phagosome. **(B)** Les lipides s'infiltre dans le phagosome. **(C)** Fusion de LB de l'hôte avec un phagosome contenant *M. avium.* D) Décharge des lipides de l'hôte dans le phagosome contenant *M. avium.* Adapté de [39].

Il a également été démontré que l'import de cholestérol chez *M. tb* est médié par le système Mce [257]. En effet, on retrouve chez *M. tb* quatre loci (mce1-4) qui comportent également un grand nombre de protéines de fonctions inconnues mais dont les similarités importantes laissent supposer qu'elles jouent toutes un rôle dans l'import de molécules hydrophobes [257-259].

Plus récemment, Mce1 a été confirmée comme la machinerie principale impliquée dans l'import des acide gras *in vitro* et *in cellulo* [260]. Cette étude a également montré que LucA/Rv3723 joue un rôle central dans cet import en stabilisant les protéines des transporteurs Mce1 et Mce4, et une délétion de LucA a conduit à un défaut de croissance au sein des macrophages ainsi qu'à une diminution de l'inflammation dans un modèle de souris, ce qui met en avant l'importance de l'import des lipides de l'hôte dans la pathogénie de *M. tb*.

d) Les ILI, source de carbone et résistance au stress

Les ILI étaient initialement considérés comme de simples organelles de stockage des lipides, mais il est aujourd'hui bien établi que ces structures remplissent un grand nombre de

fonctions complexes allant bien au-delà [261-263]. Les ILI représentent une source de carbone majeure pour les mycobactéries latentes et pour la reprise de leur croissance lors du passage à une infection active [202, 217, 224, 264]. En effet, en l'absence de source exogène de FFA ou de capacité à les synthétiser, la dégradation des TAG contenus dans les ILI par la voie de beta-oxydation permet d'une part de soutenir la production d'ATP, mais fournit également une source alternative d'acétyl-CoA et permet de plus le maintien de l'intégrité membranaire [261-263].

Les ILI semblent également jouer un rôle important dans la résistance au stress réducteur et à la lipotoxicité due à un excès de FFA endogènes [265]. De plus, la synthèse de TAG et de phthiocérol dimycocérosates permettent de réduire le stress métabolique au cours des infections à *M. tb* [266]. Cette fonction de résistance au stress lipotoxique de la synthèse des TAG a également été observée sur des fibroblastes et des levures [267-270].

D'autre part, le stockage de lipides résistants à l'évaporation a été proposé comme mécanisme de résistance à la déshydratation chez les bactéries car la dégradation des lipides permet une production alternative de molécules d'eau [271].

Il a également été récemment démontré que les ILI chez *R. jostii* RHA1 sont capables de se lier à l'ADN [272] grâce à une protéine (Ro02105) associée aux ILI qui est un homologue de HBHA (*heparin-binding haemagglutinin*), dont le rôle dans la formation des ILI et la localisation sur les ILI a été démontré [273]. Il a ainsi été montré que Ro02105 est présente sur les ILI, et qu'elle est capable de fixer et stabiliser l'ADN et d'augmenter ainsi la survie suite à un stress mutagène comme l'exposition aux UV [272].

e) ILI et pathogénie

Le rôle des ILI dans la pathogénie est aujourd'hui bien établi par de nombreuses études indépendantes [260, 266, 274-277].

Ainsi, pour investiguer le rôle des ILI dans la pathogénie, des embryons de poisson-zèbre ont été infectés par du *M. abs* riche ou pauvre en ILI [218] (**Figure 31**).

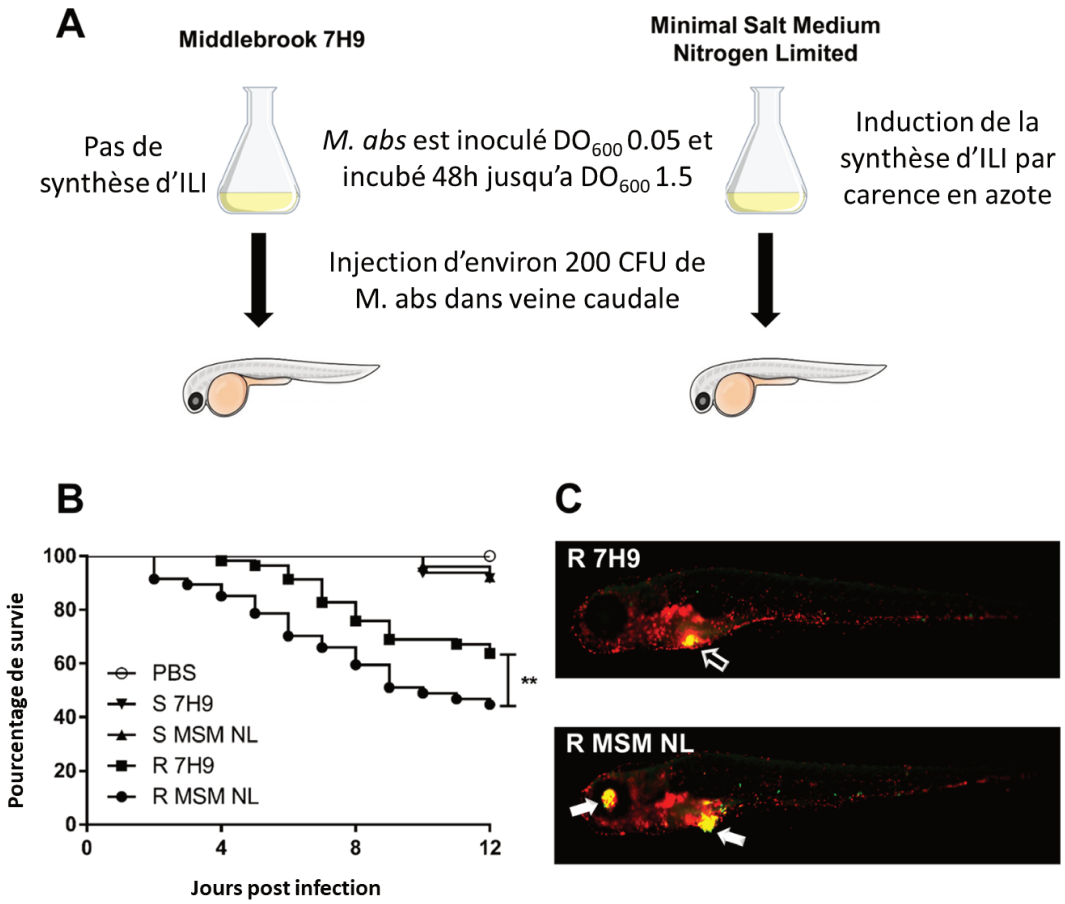

Figure 31 : Hyper virulence de *M. abs* après induction de la synthèse d'ILI par carence d'azote. **(A)** Schéma simplifié de l'induction *in vitro* de la synthèse d'ILI par carence en azote et de l'infection du poisson-zèbre. **(B)** La présence d'ILI chez *M. abs* lors de l'infection entraine une mortalité accrue. **(C)** Image Montrant une infection plus importante par une souche de *M. abs* ayant accumulé des ILI par rapport à une souche cultivée dans son milieu standard 7H9. Adapté de [218].

Les bacilles de *M. abs* riches en ILI ont montré une réplication et un nombre de lésions granulomateuses supérieur, ce qui valide l'intérêt des ILI dans la virulence de ces souches. De plus l'observation de bacilles riches en lipides dans l'expectorât de patients atteints de souches plus virulentes de tuberculose a initialement conduit à poser l'hypothèse que ces structures jouaient un rôle dans la pathogénie et dans la capacité de *M. tb* à résister au stress induit par l'hôte [217, 224, 278, 279]. Des études similaires avec *M. tb* chez la souris ont également démontré une virulence accrue des mycobactéries chargées en ILI [218, 280, 281].

De plus, il a été montré que le métabolisme des TAG, à la fois de l'hôte et de la bactérie, joue un rôle important dans les infections aux mycobactéries [224, 282, 283]. En effet, un mutant Δtgs1 de *M. tb* incapable de synthétiser des TAG présentaient des défauts importants de croissance et de survie *in cellulo* et *in vivo* [202, 260]. Il a également été récemment proposé [284] que des formes acétylées de lipides directement liées au métabolisme des TAG [266,

285] joueraient un rôle immunorégulateur en inhibant la réponse de l'hôte pour établir une infection chronique [284].

D'autre part, les mécanismes de résistance aux stress acide et oxydatif médiés par les ILI décrits précédemment, font de ces structures un des acteurs importants dans la résistance à la phagocytose par les macrophages en aidant les bactéries à survivre au stress induit par le phagolysosome, et jouant donc un rôle important dans la virulence.

f) ILI et résistance aux antibiotiques

La présence d'ILI dans les mycobactéries impacte drastiquement la susceptibilité de ces dernières aux antibiotiques, ce qui joue un rôle crucial dans le cas d'infections latentes où les bactéries présentent à la fois une absence de réplication, une activité métabolique réduite, un phénotype riche en ILI et une résistance accrue aux antibiotiques [218, 261, 286-288]. En induisant la dormance par un modèle multi-stress, une résistance induite par la présence d'ILI à la rifampicine et à l'isoniazide a été mise en évidence [261]. D'autre part, il a été montré que la stimulation de la synthèse des TAG et les conditions de culture en stress nutritif induisaient également une résistance accrue aux antibiotiques [286]. Plus récemment, il a également été confirmé que la présence d'ILI chez diverses bactéries du complexe *tuberculosis* comme *M. bovis* (BCG) et d'autres MNT comme *M. marinum* et *M. fortuitum* induisaient une baisse de susceptibilité aux antibiotiques pour ces souches [288].

g) Induction expérimentale de la synthèse d'ILI

Les processus physiologiques liés à la synthèse et à la dégradation des ILI sont donc essentiels au cycle de vie des mycobactéries et au cycle infectieux des mycobactéries pathogènes [40].

Dans ce contexte, divers modèles expérimentaux ont été développés afin d'induire expérimentalement l'accumulation et/ou la dégradation de ces ILI, et donc de mimer les phases de dormance et de réactivation chez les mycobactéries. De nos jours, un nombre assez restreint de conditions expérimentales sont connues pour promouvoir expérimentalement la synthèse des TAG.

Le premier modèle consiste en des conditions hypoxiques de culture chez *M. tb* qui font rentrer la bactérie dans un état non réplicatif de dormance induisant la formation d'ILI [228, 289]. Dans ce modèle appelé modèle de Wayne, il a été montré que la régulation positive de

la synthèse des TAG et d'enzymes associées telle que Tgs1 étaient sous le contrôle du régulon *dosR* [228, 229, 289]. Suite à ces découvertes, des systèmes d'induction de sa synthèse des TAG par divers stress extérieurs combinés tels que des combinaisons d'hypoxie, de stress acide et d'exposition à des oxydes nitriques ont été développés [261].

De plus, il a également été reporté que la complémentation de milieux de culture avec des acides gras à longue chaîne induisaient également la synthèse d'ILI en réponse à un stress lipotoxique [217, 265, 290, 291]. L'ensemble de ces études a permis de montrer une signature transcriptionnelle commune entre toutes ces formes d'induction de la synthèse de TAG médiées par le régulon *dosR* [265].

Des modèles d'induction de la synthèse des TAG par stress nutritif ont également été développés. Un modèle de carence en fer couplée à un stress oxydatif a permis de montrer que le métabolisme du fer joue un rôle dans la survie et la virulence de *M. tb* [292]. En effet, la séquestration du fer par l'hôte constitue un mécanisme de défense classique ayant pour but de carencer un potentiel pathogène *in vivo.* Or il a été observé que des concentrations basses conduisent à l'expression de gènes de virulence et de gènes impliqués dans la synthèse des lipides [293]. De plus, des conditions de culture pauvres en azote chez *M. tb* H37Rv ont permis de mettre en évidence une synthèse accrue de TAG mais également de nouveaux WE non identifiés [292, 294]. Un autre modèle similaire basé sur le même principe consiste à carencer *M. tb* en fer par l'ajout de sel de defroxamine mésylate, qui est un chélateur puissant du fer qui va alors le séquestrer dans le milieu. Dans ces conditions, il a également été mis en évidence une forte production d'ILI sur des souches cliniques de *M. tb* [295].

Le dernier modèle majeur d'induction de la synthèse des ILI dans une culture *in vitro* par stress nutritif consiste en une carence en azote dans le milieu de culture. Ce modèle expérimental fournit une méthode rapide et efficace d'induction de la production d'ILI qui constitue le modèle principal exploité au cours de cette thèse pour étudier le métabolisme des ILI *in vitro* [218]. En effet, la carence en azote a été largement documentée comme une des causes majeures déclenchants la synthèse de TAG et la formation d'ILI, notamment chez *Streptomyces sp*, *Rhodococcus opacus* et plus récemment chez *M. smeg* et *M. abs* [217, 218, 296, 297].

Dans le contexte des mycobactéries, il a initialement été montré qu'une accumulation de TAG était induite chez *M. smeg* au bout de plusieurs jours de croissance dans des conditions limitantes en azote [217]. De plus, une analyse de chromatographie en phase gazeuse couplée à de la spectrométrie de masse des lipides issu de ce modèle ont montré la présence d'acides gras libres en quantités bien supérieures à celles déjà synthétisées en l'absence de stress nutritif résultant d'une synthèse *de novo* de ces derniers [217].

Plus récemment, notre équipe a mis au point un milieu minimal en sel présentant une carence en azote (« *minimal salt media nitrogen limited* » ou MSM-NL) capable d'induire facilement l'accumulation d'ILI *in vitro* chez *M. smeg* et *M. abs* (**Figure 32**) [218].

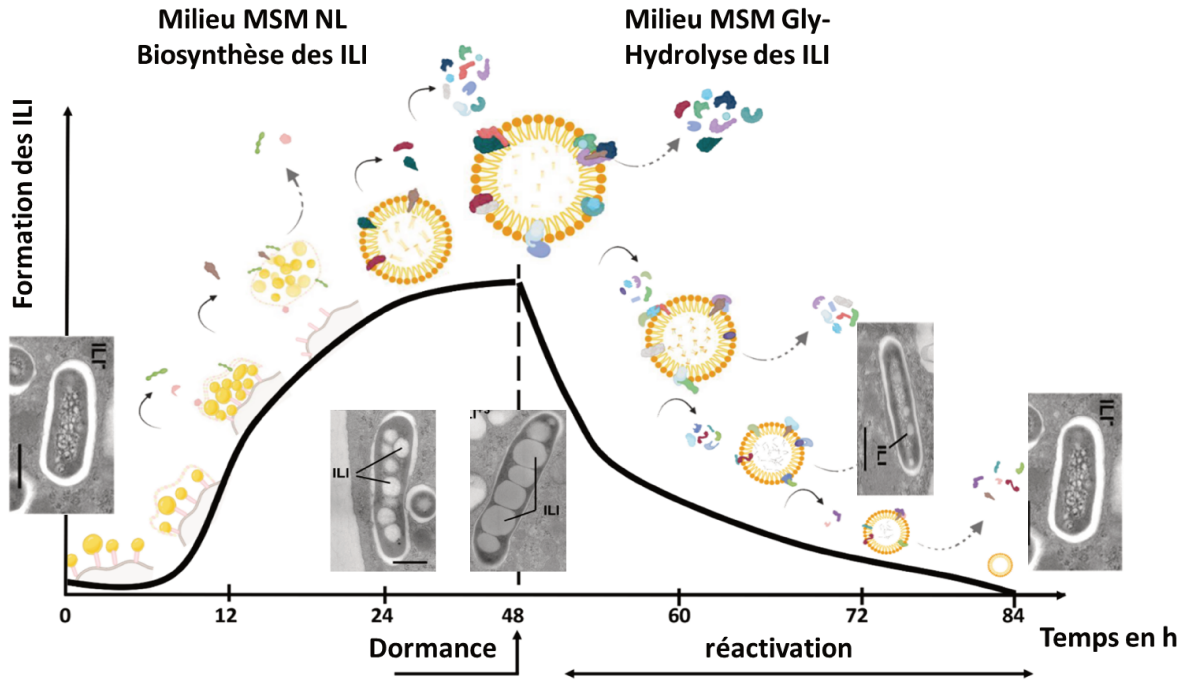

Figure 32 : Schéma du modèle d'induction *in vitro* de la biosynthèse et de l'hydrolyse des ILI. La synthèse est induite par la carence en azote du milieu MSM NL et l'hydrolyse est induite par le transfert de la culture dans un milieu sans glycérol qui est exempt de toute source de carbone. D'après [298].

Il a donc été proposé que la réponse à ce type de stress nutritif était conservée chez les mycobactéries.

En effet, les différentes adaptations conservées chez les actinomycètes dans la réponse à la carence en azote ont déjà été longuement étudiées au cours de la dernière décennie [299-302].

Ainsi, on retrouve le gène *nlpR* qui code pour un régulateur de la lipogenèse dans le cadre d'une carence azotée chez *Rhodococcus jostii* RHA1 [303]. Ce gène est conservé chez les

mycobactéries et est présent chez *M. tb* (Rv0260) et chez *M. smeg* (MSMEG_0432) et joue un rôle central dans le processus d'assimilation de l'azote [301, 304] mais son lien avec la synthèse des TAG n'est aujourd'hui pas encore établi.

D'autre part, on retrouve le système PrrAB qui a été identifié comme un régulateur directement lié à la synthèse des TAG et à la carence en azote [305]. En effet, la délétion de ce gène a conduit à une surexpression significative de la voie Kennedy, qui est la voie de synthèse principale des TAG et des phospholipides chez les mammifères (**Figure 28**).

Le lien entre la synthèse des ILI et la carence en azote est donc bien établi et partagé chez les actinomycètes. Ainsi, le modèle *in vitro* d'accumulation des ILI développé par notre équipe dans un milieu limitant en azote (MSM-NL) et contenant un excès de glycérolé comme seule source de carbone [218] offre un outil maitrisé, bien caractérisé et simple à mettre en œuvre pour étudier le métabolisme de synthèse des ILI. L'utilisation de ce milieu MSM-NL entraine la formation d'ILI au sein de la mycobactérie, permettant de mimer son entrée en persistance/dormance. Le transfert de cette culture ILI^+ dans un milieu dépourvu de nutriments entraîne l'hydrolyse des lipides contenus dans les ILI par la bactérie, mimant alors la phase de réactivation. Ce modèle constitue donc un analogue des phénomènes physiologiques au sein du cœur nécrotique du granulome lors d'une infection mycobactérienne, et sera donc utilisé au cours des études présentées dans ce travail.

Étant donné que la présence d'ILI est associée à un phénotype persistant, résistant aux antibiotiques et hyper-virulent, l'étude du métabolisme associé aux ILI représente une source centrale de potentielles cibles thérapeutiques et de stratégies d'anti-virulence dans le contexte des infections aux mycobactéries. Des modèles expérimentaux développés à cette fin représentent donc des outils centraux dans la lutte contre les infections mycobactériennes.

VI. Nouveaux inhibiteurs sélectifs : les OX et les CyC

a) Les Oxadiazolones (OX)

Parmi les inhibiteurs d'enzymes lipolytiques, les dérivés de la famille des Oxadiazolones (**OX**) présentent des propriétés inhibitrices intéressantes qui dépendent de la nature de leurs substituants.

Ainsi, il a tout d'abord été montré que les composés **1** [306] et **2** [307] (**Figure 33**) , initialement développés come pesticides, étaient capables d'inhiber l'acétylcholinestérase AChE de *D. melanogaster*. Dans les années 2000, Aventis Pharma a utilisé des plateformes de criblage à haut débit pour identifier des inhibiteurs de la lipase hormono-sensible humaine (HSL) [308]. Cette étude a conduit à identifier des dérivés de 3-phelyl oxadiazolone comme le **M*m*PPOX** ou le CAY10499 (**Figure 33**) à partir de leur activité sur la HSL de rat partiellement purifiée depuis des tissus adipeux [309].

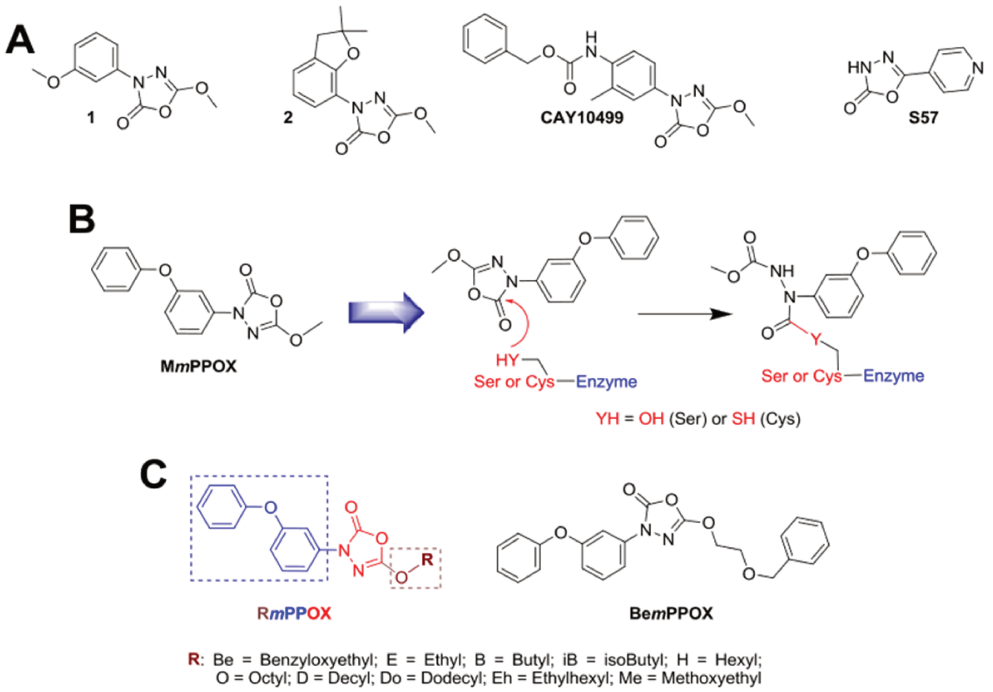

Figure 33 : **(A,C)** Structures chimiques et **(B)** mécanisme réactionnel des Oxadiazolones. Adapté de [310-312].

Il a ensuite été établi que le mécanisme d'inhibition de la HSL par les Oxadiazolones implique une attaque nucléophile du groupe hydroxyle de la sérine catalytique de ces enzymes sur le carbonyle du cycle oxadiazolone, ce qui conduit à l'ouverture de ce cycle et à la formation d'un lien covalent entre le site catalytique de l'enzyme et l'inhibiteur [313] (**Figure 33 B**). Ces composés ont également été identifiés comme capables d'inhiber des enzymes d'hydrolyse des endocanabinoïdes comme la « *fatty acid amide hydrolase* » FAAH et la monoacylglycérol lipase humaine (hMGL), qui sont toutes deux impliquées dans le processus inflammatoire [314-316].

Plus récemment, le **M*m*PPOX** et une dizaine de dérivés (**Figure 33 B-C**) ont été synthétisées et testés pour leur capacité à inhiber les lipases digestives de mammifères [311, 312]. Ces composés ont montré une forte sélectivité pour les lipases gastriques par rapport aux lipases

pancréatiques. Parmi les composés testés, le **Be*m*PPOX** (**Figure 33 C**) a présenté la meilleure activité d'inhibition sur la lipase gastrique. Des études complémentaires *in vivo* sur un modèle de canal lymphatique de rat canulé ont montré que le **Be*m*PPOX** était capable de réduire de 55% l'absorption intestinale des acides gras. Ainsi, l'ensemble de ces données montre que le **Be*m*PPOX** est capable de réguler la lipolyse gastro-intestinale, ce qui en ferait donc un bon candidat dans la lutte contre l'obésité.

Par la suite, plusieurs études se sont centrées sur le potentiel antimycobactérien de ces inhibiteurs. Ainsi, le composé S57 (**Figure 33 A**) [317, 318] ayant été décrit pour avoir une forte activité contre *M. tb* [319-321], une nouvelle série d'analogues a été synthétisée [322, 323] et testée sur la croissance de *M. tb* H37Rv. Des intéressantes CMI variant de 1.25 à 2.5 µg/mL ont été obtenues, ce qui est de l'ordre de grandeur des antibiotiques de première ligne (par exemple, CMI_{INH} = 0.5 µg/mL).

De plus, des études de modélisation moléculaire ont pu montrer une bonne stabilisation par interactions hydrophobes et liaisons hydrogènes de ces composés dans la poche catalytique de la 14a-stérol déméthylase dépendante du cytochrome P450 (P45014DM) [324, 325]. L'ensemble de ces études a donc fortement suggéré l'usage des dérivés d'oxadiazolones comme alternative thérapeutique contre *M. tb.*

Au sein de notre laboratoire, nous avons également démontré la capacité du **M*m*PPOX** à inhiber la croissance de *M. tb* en milieu solide avec des valeurs de CMI allant de 50 à 90 µg/mL [326].

De plus, notre équipe a montré que le **M*m*PPOX** était capable d'inhiber les enzymes de la famille de la HSL (Lip-HSL) de *M. tb* purifiées *in vitro* [326], dont LipY (Rv3097c). LipY est une lipase impliquée dans l'acquisition des lipides de l'hôte et la dégradation des ILI chez *M. tb* [201, 204, 209, 218]. De plus, le **M*m*PPOX** s'est révélé capable de bloquer la dégradation des ILI dans un modèle d'infection de macrophages murins dérivés de moelle osseuse infectée par *M. bovis* BCG [39, 208, 209]. Dans ce modèle, après infection par *M. bovis* BCG, les macrophages sont incubés avec des VLDL (« *Very Low-Density Lipoproteins* ») ce qui induit leur différentiation en macrophages spumeux. Les bactéries sont alors capables d'accumuler des ILI à partir des lipides de l'hôte (**Figure 34 A,C**). Le retrait du VLDL du milieu permet d'induire

l'hydrolyse des ILI par les mycobactéries (**Figure 34 F**) et ainsi mimer la phase de réactivation de l'infection.

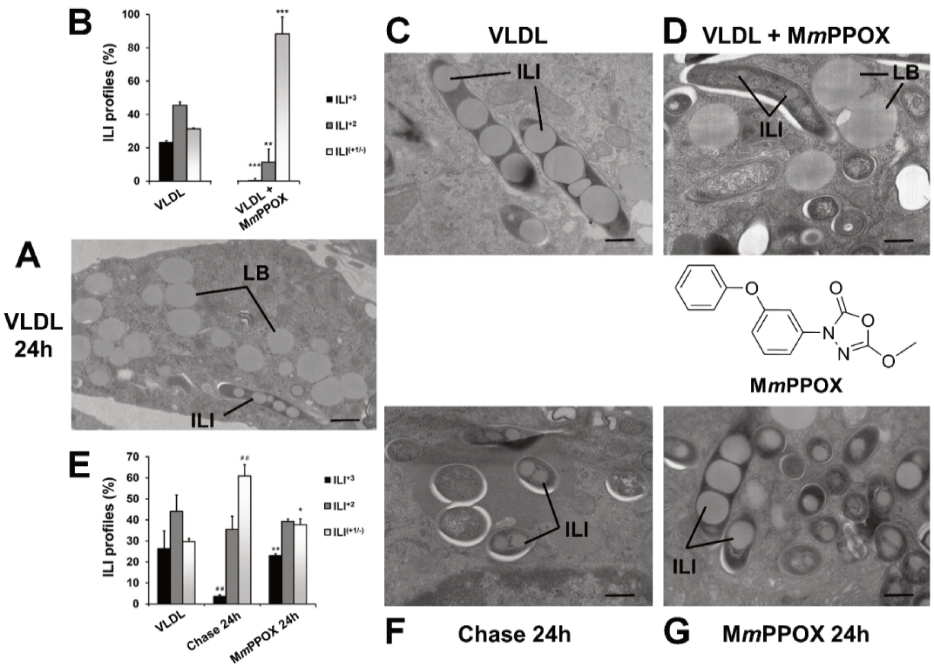

Figure 34: **(A)** macrophages spumeux après 24h d'exposition au VLDL présentant un nombre important de LB et *M. bovis* BCG contenant des ILI. **(B-D)** effet du **M*m*PPOX** pendant l'exposition au VLDL sur l'accumulation des LB chez l'hôte et des ILI chez *M. bovis* BCG. Les mBMDM ont été exposée 24h à des VLDL en présence **(C)** et en absence **(D)** de **M*m*PPOX** 6 jours après leur infection par *M. bovis* BCG. **(E-G)** effet du **M*m*PPOX** pendant la consommation des TAG contenus dans les ILI. 6 jours après leur infection par *M. bovis* BCG, les mBMDM ont été exposée 24h à du VLDL,.puis réincubés dans une culture sans VLDL pour induire l'hydrolyse des ILI en absence **(F)** ou présence **(G)** du **M*m*PPOX**. Adapté de [39, 327].

Dans ce modèle, en présence de 50 µM de **M*m*PPOX**, si les macrophages ont conservé la capacité à développer un phénotype spumeux, l'accumulation des ILI chez *M. bovis* BCG a été quasi-totalement bloquée (**Figure 34 D**). De plus, en phase de réactivation, le **M*m*PPOX** inhibe la quasi-totalité de l'hydrolyse des ILI par *M. bovis* BCG avec près de 90% des ILI qui sont conservés après la phase d'hydrolyse (**Figure 34 E-G**) [209].

Cette inhibition de l'hydrolyse des ILI a également été confirmée sur le modèle *in vitro* d'induction de la synthèse et de la consommation des ILI par carence nutritive en azote développé dans notre laboratoire [218]. Dans ce modèle, le **M*m*PPOX** a été capable d'inhiber quasi intégralement la lipolyse des TAG chez *M. abs* et *M. smeg* [218].

Ces résultats ont conduit à la synthèse de 18 nouveaux dérivés **OX** en faisant varier la longueur de la chaine alkyle R ainsi que la présence ou absence du groupement phénoxy en position *meta* ou *para* du cycle aromatique (**Figure 35**) [312].

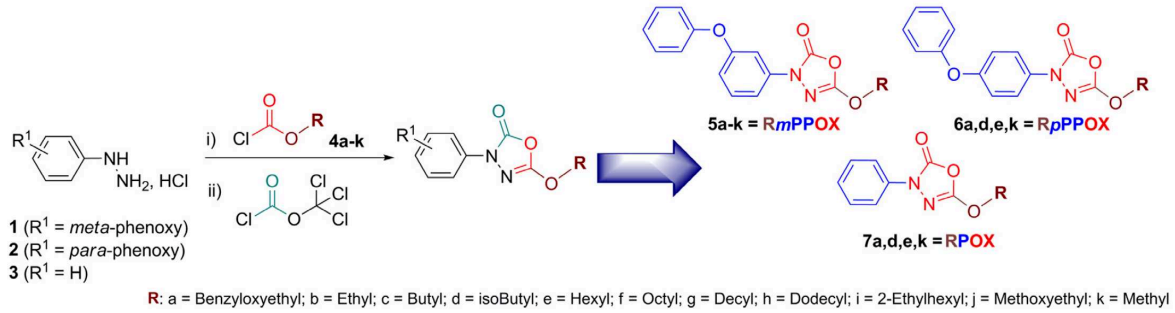

Figure 35 : Voie de synthèses des analogues d'Oxadiazolones. Conditions : i) chloroformiate d'alkyle 4a-k, Pyridine, 0 °C à RT ; ii) $ClCO_2CCl_3$, $CHCl_2$, Pyridine, 0 °C à RT, 38-50%.Adapté de [312]

Concernant leur voie de synthèse celle-ci se déroule en une seule étape (**Figure 35**). Les phénylhydrazines **1-3** sont tout d'abord ***i)*** couplées avec différents chloroformiates d'alkyle **(4a-k)** en présence de pyridine, puis ***ii)*** cyclisés avec du diphosgène. Les nouveaux composés ainsi synthétisés ont été obtenus avec des rendements globaux en produit pur variant de 38 à 50% en fonction de la chaîne alkyle R testée. Enfin, ces différents composés **OX** ont été nommés suivant une nomenclature spécifique (**Figure 35**), notés **R*m*(ou *p*)PPOX**. Ainsi, *m*(ou *p*)PP indique que le groupement **P**hénoxy est positionné en ***méta*** (ou ***para***) du cycle **P**hényle, et OX représente le noyau, **Ox**adiazolone. Enfin R correspond au groupement alkyle.

Chacun de ces composés a ensuite été testé pour sa capacité d'inhibition de LipY (**Tableau 2**). Il a ainsi été montré que la quasi-totalité de ces **OX** inhibaient LipY avec des ratios molaires d'inhibition allant de 0.59 à 0.93, soit une meilleure inhibition que le **M*m*PPOX** (x_{I50} = 2.4), mais également que l'Orlistat (x_{I50} = 7.1) utilisée comme inhibiteur de référence [328, 329].

Tableau 2 : Structures chimiques des nouveaux **OX** et Inhibition de la TAG-lipase LipY de *M. tb* après une période d'incubation de 30 minutes avec chaque composé **OX**.

Composés	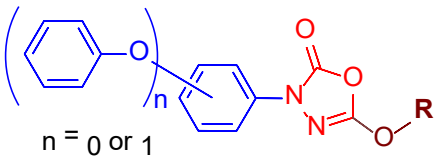 n = 0 or 1	LipY		
		%inhibition [a]		x_{I50} [b]
		x_I = 4	x_I = 20	
Orlistat		26.8±1.5	87.6±4.8	7.1
M*m*PPOX		63.6±4.6	85.9±4.9	2.4
M*p*PPOX		60.8±2.1	79.4±3.3	0.93
MPOX		34.4±2.4	81.8±3.3	10.9
E*m*PPOX		21.7±1.4	53.8±3.3	6.5
Me*m*PPOX	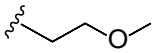	92.4±0.30	93.7±1.3	0.69
B*m*PPOX	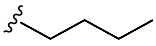	15.6±0.50	36.7±1.8	>40
iB*m*PPOX		37.4±2.4	49.4±1.5	3.9
iB*p*PPOX	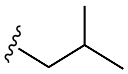	33.8±1.5	41.6±0.40	>40
iBPOX		31.6±1.0	47.9±2.1	9.2
H*m*PPOX		39.9±1.2	76.5±1.9	3.3
H*p*PPOX	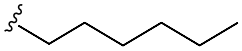	38.7±1.7	77.2±2.7	2.9
HPOX		35.0±0.27	38.8±0.11	>40
Be*m*PPOX		88.0±0.70	90.2±0.91	0.72
Be*p*PPOX	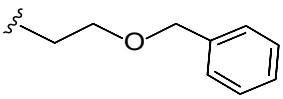	97.1±3.9	98.4±2.2	0.59
BePOX		89.0±1.9	92.2±0.20	0.61
O*m*PPOX	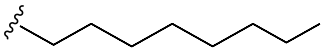	83.2±5.8	86.6±2.2	0.71
Eh*m*PPOX	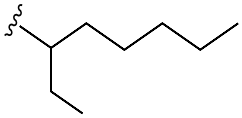	89.6±1.1	94.8±2.7	0.73
D*m*PPOX	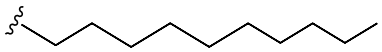	91.5±2.8	94.2±3.1	0.67
Do*m*PPOX	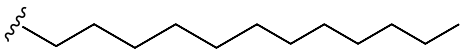	88.7±4.2	90.4±2.2	0.77

[a] Données d'inhibition (% de l'activité enzymatique initiale), à un excès molaire d'inhibiteur (x_I) de 4 ou 20 par rapport à 1 mole d'enzyme [329].

[b] x_{I50} : excès molaire d'inhibiteur conduisant à une inhibition de 50% de l'activité enzymatique de LipY. Adapté de [330].

b) Cyclophostines et Cyclipostins (CyC)

Les Cyclophostines sont des composés organophosphates bicycliques d'origine naturelle. Ces molécules (**Figure 36 A**) ont été isolées depuis une solution de fermentation de *Streptomyces*

lavendulae (NK901093) dans un effort de recherche d'insecticides naturels [331]. Ces molécules ont montré une bonne capacité d'inhibition de l'acétylcholine estérase de mouche AChE avec un IC_{50} de 0.76 nM. On retrouve également cette structure d'énol-phosphate bicyclique dans une autre famille de molécules naturelles proches, les Cyclipostins (**Figure 36 B**), isolées à partir de *Streptomyces sp.* DSM13381 [332, 333].

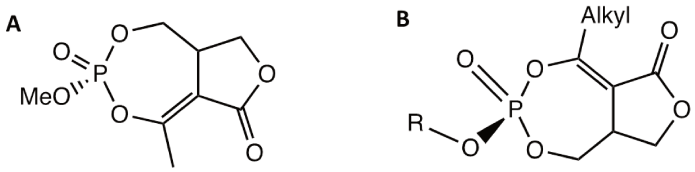

Composé	Formule brute	Masse molaire	Structure	Groupe Alkyle
Cyclipostine A	$C_{23}H_{41}O_7P$	460.55	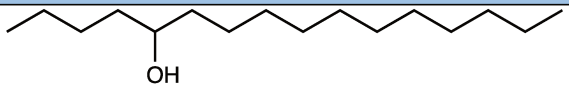	Méthyle
Cyclipostine F	$C_{23}H_{39}O_7P$	458.54	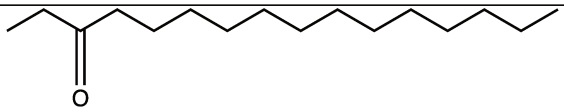	Méthyle
Cyclipostine N	$C_{21}H_{37}O_6P$	416.50	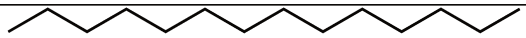	Méthyle
Cyclipostine P	$C_{23}H_{41}O_6P$	444.55	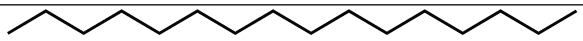	Méthyle
Cyclipostine P2	$C_{23}H_{41}O_6P$	444.55		Méthyle
Cyclipostine R	$C_{22}H_{39}O_6P$	430.53		Méthyle
Cyclipostine R2	$C_{22}H_{39}O_6P$	430.53	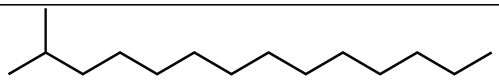	Méthyle
Cyclipostine S	$C_{24}H_{43}O_5P$	458.58	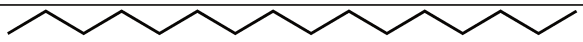	Éthyle
Cyclipostine T	$C_{25}H_{45}O_5P$	472.61	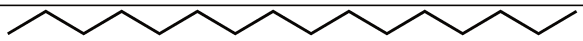	Propyle
Cyclipostine T2	$C_{25}H_{45}O_5P$	472.61	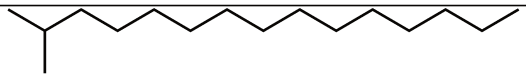	Propyle

Figure 36 : Structures chimiques des Cyclophostines et des Cyclipostins naturelles. Adapté de [331, 333].

Les Cyclipostins ont une structure très similaire aux Cyclophostines mais leur groupement phosphate est estérifié avec des chaines carbonées de longueur et de structure variables (**Figure 36 B**). Toutes les Cyclipostins identifiées sont de puissants inhibiteurs de la HSL [332] et sont également capable d'inhiber la croissance de plusieurs souches mycobactériennes dont *M. smeg*, *M. philei*, *Nocardia abcessus* et *Corynebacterium diphteriae* [334] avec des zones d'inhibition sur milieu solide comparable à celle d'antibiotiques bien connus comme la rifampicine ou la pénicilline.

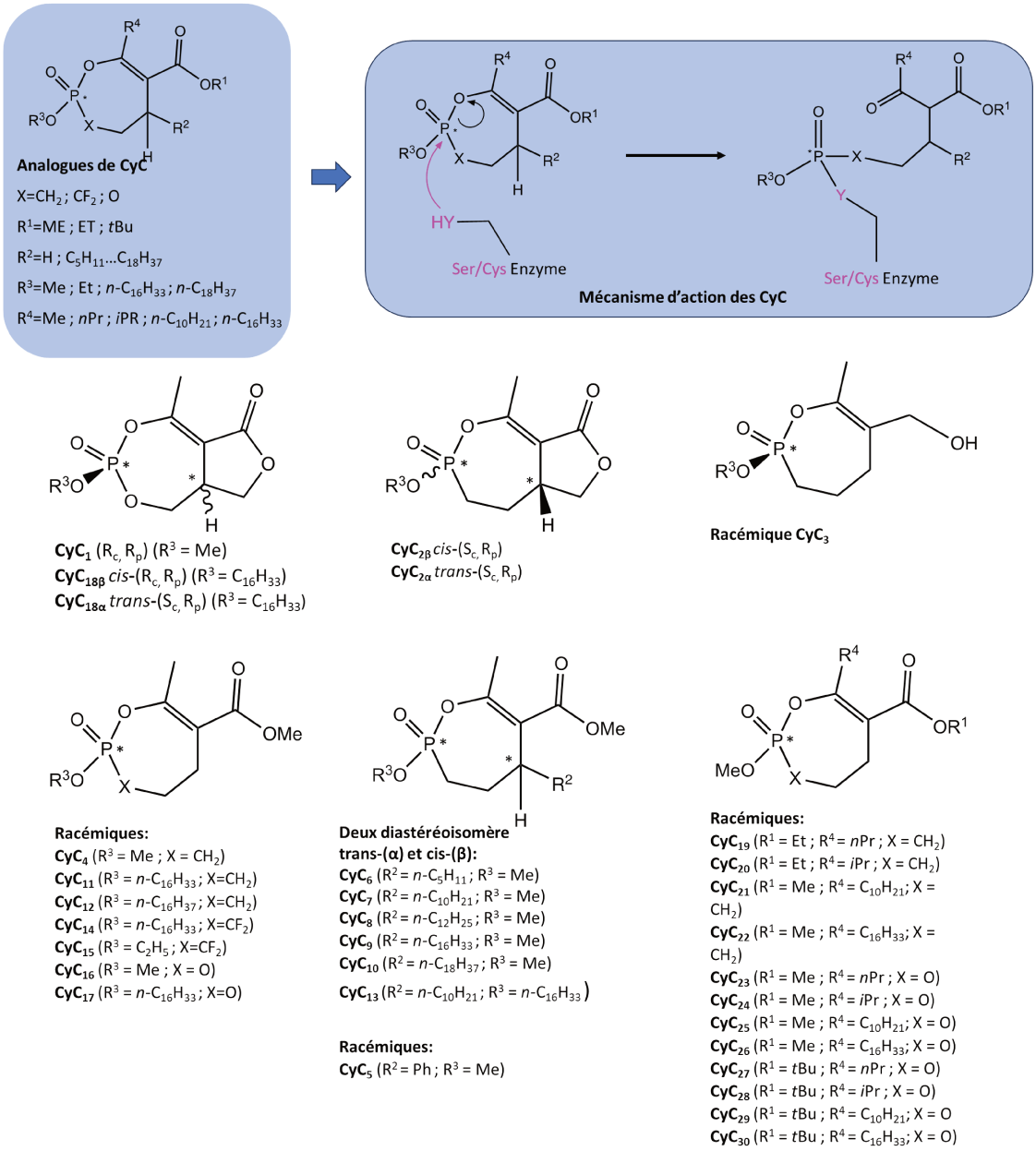

Figure 37 : Nouveaux analogues de Cyclophostines et de Cyclipostins (**CyC**) synthétisés et leur mode d'inhibition par formation d'un lien covalent sur les résidus sérine ou cystéine catalytiques dans le site actif de leurs enzymes cibles. Adapté de [311, 335, 336].

Par la suite, dans un effort pour augmenter la spécificité de ces composés pour les mycobactéries, une série d'analogues notés **CyC** (**Figure 37**) a été synthétisée par l'équipe du Prof. Christopher D. Spilling (Université du Missouri St Louis, USA) en faisant varier la nature du groupe alkyle sur le carbone C5 (R^2 sur la **Figure 37**), du substituant sur l'atome de phosphore (R^3 sur la **Figure 37**) et la nature phosphate (X=O) ou phosphonate ($X=CH_2$) du composé. La différence entre un composée phosphate et phosphonate est que ce dernier forme une liaison irréversible avec la serine ou cystéine de son enzyme cible, ce qui n'est pas le cas des phosphate qui peuvent potentiellement être hydrolysé par la suite [337].

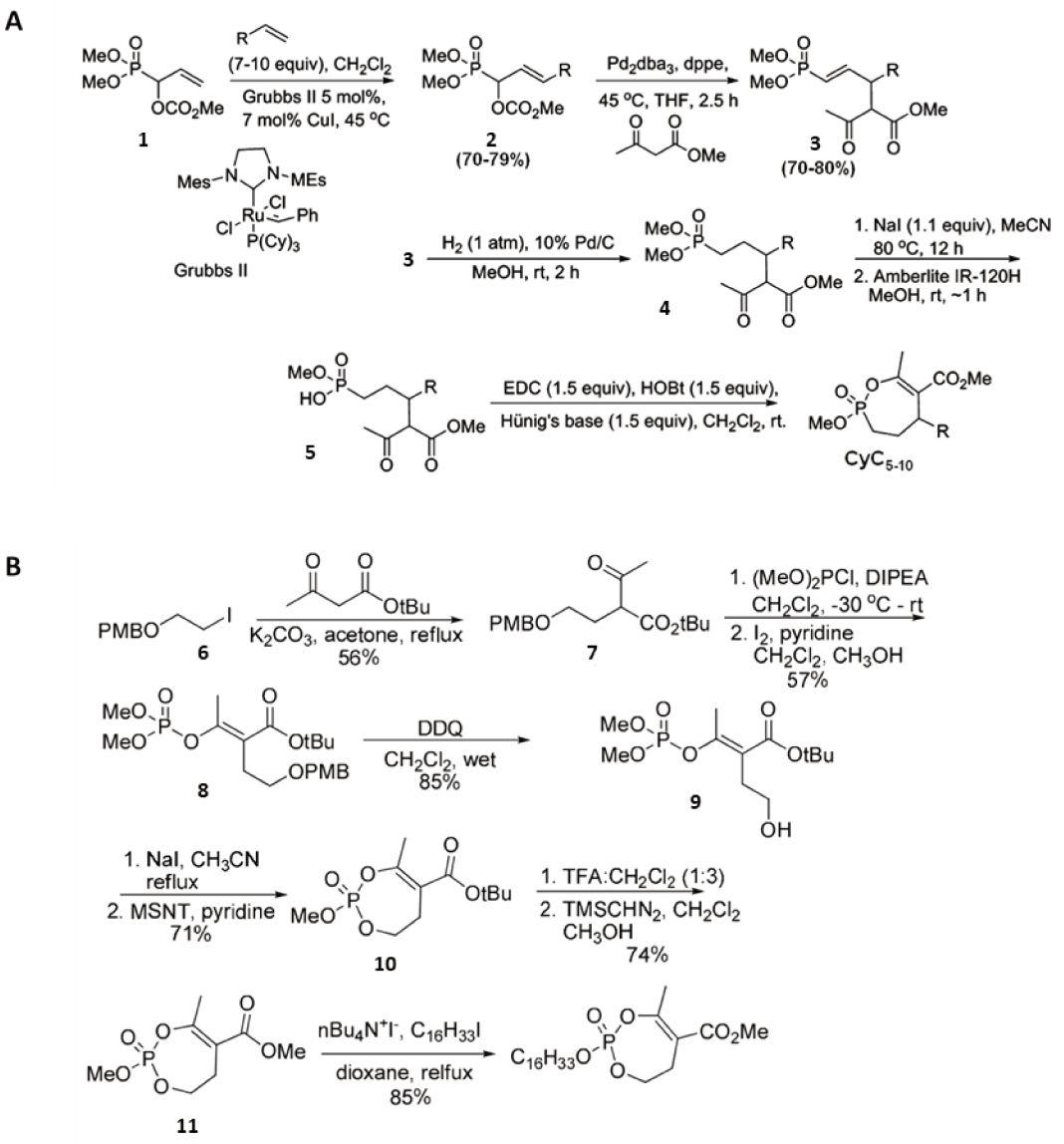

Figure 38 : voie de synthèse des analogues de cyclophostine et cyclipostin. **(A)** voie de synthèse des analogue phosphonate de **CyC**. **(B)** voie de synthèse des analogues phosphate de **CyC.** Adapté de [338].

Deux voies de synthèses ont donc été développées par l'équipe du professeur Spilling, une pour les analogues phosphonates et une pour les analogues phosphates.

La voie de synthèse des phosphonates (**Figure 38 A**) [311, 335, 339, 340] implique une réaction de métathèse en présence de catalyseur de Grubbs entre les carbonates phospho-allyliques **1** et les alkyl vinyle pour obtenir le composé **2**. Par la suite, une réaction de substitution catalysée au palladium avec l'acétoacétate de méthyle permet d'obtenir le phosphate vinylique **3**. Ce composé subit ensuite une hydrogénation sélective sur palladium sur charbon pour obtenir le phosphonate saturé **4**. Après déméthylation sélective et protonation du sel résultant, on obtient le composé **5** qui va pouvoir être cyclisé pour obtenir l'enolphosphonate final **CyC$_{5\text{-}10}$**.

La voie de synthèse des analogues phosphate (**Figure 38 B**) [341] part de l'acétoacétate de *ter*-butyle qui va être alkylé avec le 2-iodoéthanol protégé **6** pour donner un β-cétoester **7**. La réaction de ce composé **7** avec le chlorophosphite de diméthyle suivi de l'oxydation par de l'iode (I_2) dans le méthanol conduit à l'énolphosphate **8**. L'alcool porteur du groupement 4-méthoxybenzyl éther (PMB) a ensuite été déprotégé à l'aide de 2,3-dichloro-5,6-dicyano-1,4-benzoquinone (DDQ) pour obtenir l'alcool 9 qui est ensuite déméthylé et cyclisé par l'action du 1-mesitylène-sulfonyl-3-nitrotriazole (MSNT) pour obtenir l'ester de *ter*-butyle du phosphate monocyclique **10**. Le clivage de la partie *tert*-butyle avec l'acide trifluoroacétique (TFA) dans des conditions anhydres, suivi d'un traitement au triméthylsilyldiazométhane ($TMSCHN_2$) a conduit à la formation des esters méthyliques d'énolphosphate monocyclique **11** racémiques avec de bons rendements (79-100%). Enfin, la réaction de transestérification de l'ester méthylique du phosphate **11** est réalisée en une seule étape par traitement avec un excès d'iodure d'alkyle dans le dioxane à reflux en présence d'une quantité catalytique d'iodure de tétrabutylammonium (nBu_4NI - 5 mol%.) conduisant au phosphate d'alkyle monocyclique désiré.

Nos partenaires ont ainsi développé une synthèse totale de la Cyclophostine naturelle **CyC_1** et de son analogue phosphonate **$CyC_{2\alpha,\beta}$** [342, 343], ainsi que de plusieurs analogues enol-phosphonates **$CyC_{3\text{-}10,19\text{-}22}$** et -phosphates **$CyC_{23\text{-}30}$** [311, 339, 344]. Ils ont également développé la synthèse d'analogues de la Cyclipostins **$CyC_{18\beta}$** et son diastéréoisomère *trans*-(α) **$CyC_{18\alpha}$** [343] ainsi que les analogues énolphosphonates correspondant **$CyC_{11\text{-}13}$** [311, 344], les analogues di-fluorophosphonates **$CyC_{14\text{-}15}$** et phosphates **$CyC_{16\text{-}17}$** [340, 341].

Parmi ces composées, les énolphosphonates monocycliques **$CyC_{6\text{-}10}$** ont été criblés pour leur capacité à inhiber 6 enzymes à sérine : les lipases digestives des mammifères (HPL, DGL et GPLRP2) et trois lipases microbiennes (Cutinase, Rv0183 et LipY) [311]. Aucun des composés testés n'a montré d'activité contre la lipase gastrique de chien (DGL) et les lipases pancréatiques (HPL et GPLRP2) [345]. De même, ces analogues **CyC** se sont révélés inactifs vis-à-vis de l'acétylcholinesterase AchE et la HSL [341], deux enzymes initialement inhibées respectivement par les Cyclophostines et les Cyclipostins naturelles. Par contre, une inhibition totale des enzymes lipolytiques mycobactériennes Rv0183 et LipY [200, 346] ainsi que de la cutinase de *Fusarium solani* a été observée. De plus, il a été montré que la modulation de la lipophilie de ces composés, en faisant varier la longueur de la chaine alkyle des groupes R^2 et

R^3 (**Figure 37**), impactait fortement leur capacité d'inhibition [340, 345]. Il est donc possible de moduler l'activité inhibitrice des **CyC** en fonction de la nature de la chaine R^2 de façon à optimiser leur affinité pour une famille d'enzymes par rapport à une autre [335, 345, 347].

c) Inhibiteurs de croissance mycobactérienne multi-cibles

Le fait que les **OX** et les **CyC**, initialement développés pour inhiber des lipases de mammifères, se soient révélés être de puissants inhibiteurs de la croissance de mycobactéries, suggère le fait que les enzymes de la famille des α/β-hydrolases qui sont leurs cibles, jouent un rôle central dans la physiologie mycobactérienne, comme décrit aux **Chapitre IV** et **Chapitre V** de ce manuscrit.

Les α/β-hydrolases présentent de fortes similitudes structurales et comptent de nombreuses enzymes essentielles chez *M. tb*. De plus, l'importance de ces enzymes dans le métabolisme des lipides mycobactériens permet également d'insister sur la nécessité d'utiliser des inhibiteurs qui leur sont spécifiques, dans une optique de développer de nouveaux traitements.

Ainsi, 19 **OX** et 26 **CyC** développés par notre laboratoire ont été évalués pour leur activité contre *M. tb* en utilisant une souche H37Rv-GFP *via* un criblage à haut débit basé sur la fluorescence [336, 348]. La croissance de *M. tb* en présence de ces inhibiteurs a été mesurée sur 5 jours, à la fois *in vitro* et *ex vivo* dans un modèle de macrophages murins (Raw264.7) infectés. Les valeurs de CMI_{50}, concentration inhibant 50% de la croissance extracellulaire ou intracellulaire, ont pu être déterminées. La toxicité de chaque composé a également été évalué par détermination de la valeur de CC_{50}, concentration causant 50% de mortalité cellulaire sur les Raw264.7 [349, 350]. Parmi les molécules criblées, 14 ont montré des activités antituberculeuses prometteuses (**Tableau 3**) allant de 0.5 µM à 50 µM ; mais surtout, aucun composé n'a démontré de cytotoxicité pour les macrophages murins jusque 100 µM.

Tableau 3 : Activités des dérivés **OX** et des analogues **CyC** les plus actifs contre *M. tb*.

Composés	***M. tb* H37Rv-GFP**		
	Croissance extracellulaire	**Croissance intra cellulaire** (macrophages RAW 264.7)	
	CMI_{50} [µM] [a]	CMI_{50Raw} [µM] [b]	CC_{50} [µM] [c]

Isoniazid (INH)		1.2	1.2	>150
Rifampicin (RIF)		0.01	2.9	24
Analogues OX				
iB*p*PPOX	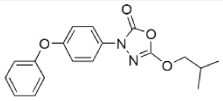	32.0 ±0.89	8.5 ±0.30	>100
iBPOX	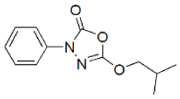	>50	17.1 ±1.10	>100
H*p*PPOX	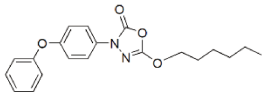	>50	9.5 ±0.49	>100
HPOX	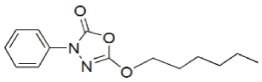	44.6 ±2.50	*Pas d'effet*	>100
Be*p*PPOX	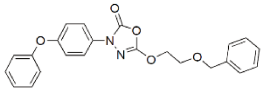	>50	3.5 ±0.28	>100
BePOX	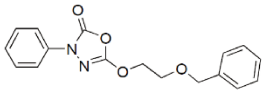	30.8 ±2.40	*Pas d'effet*	>100
Analogues CyC				
CyC$_{6\beta}$	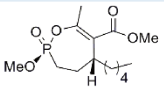	*NE*	12.6 ±0.90	>100
CyC$_{7\alpha}$	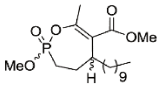	92.6 ±6.5	4.5 ±0.39	>100
CyC$_{7\beta}$		16.6 ±0.78	3.1 ±0.11	>100
CyC$_{8\alpha}$	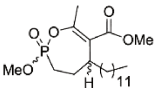	40.4 ±2.5	4.0 ±0.30	>100
CyC$_{8\beta}$		>100	11.7 ±0.26	>20
CyC$_{17}$	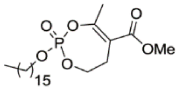	0.50 ±0.02	*Pas d'effet*	>100
CyC$_{18\alpha}$	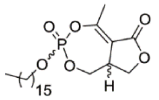	24.4 ±2.14	*Pas d'effet*	>100
CyC$_{18\beta}$		1.7 ±0.03	*Pas d'effet*	>100

[a] CMI_{50} : concentration de composé conduisant à 50% d'inhibition de la croissance bactérienne *in vitro*. [b] CMI_{50RAW} : concentration de composé conduisant à 50% d'inhibition de la croissance bactérienne dans des macrophages infectés (MOI 10). [c] CC_{50} : concentration de composé conduisant à 50% de mortalité cellulaire sur macrophages murins Raw264.7. Adaptée de [336, 348].

Les données issues de ces expériences permettent de distinguer deux groupes d'inhibiteurs parmi les 14 précités, en fonction de leur activité antibactérienne :

- Une premier groupe de 9 composés (**iB*p*PPOX**, **iBPOX**, **H*p*PPOX**, **Be*p*PPOX**, **CyC$_{6\beta}$**, **CyC$_{7\alpha,\beta}$** et **CyC$_{8\alpha,\beta}$**) présentant une activité intracellulaire intéressante et peu ou pas d'activité extracellulaire ;

- Un deuxième groupe de 5 composés (**HPOX**, **BePOX**, **CyC$_{17}$**, **CyC$_{18\alpha,\beta}$**) qui sont actifs sur la croissance extracellulaire contre *M. tb* mais présentent peu ou pas d'activité intracellulaire.

Les différences observées entre ces deux classes de composés pourraient être dues à des propriétés de pénétration différenciées dans les macrophages ou les bacilles, ou encore à des spectres de cibles différents d'un composé à l'autre.

Suite aux résultats obtenus chez *M. tb*, les 26 composés **CyC** disponibles ont été testés sur de nombreuses souches bactériennes incluant *P. aeruginosa*, *E. coli*, *B. subtilis*, *M. abs*, *M. marinum* et *M. bovis* BCG [351].

Cette étude a démontré que les **CyC** étaient capables d'inhiber uniquement la croissance de mycobactéries, sans aucune activité sur les souches à Gram-positif et Gram-négatif testées. Ces résultats indiquent une forte spécificité des **CyC** vis-à-vis des mycobactéries. De plus, le **CyC$_{17}$** s'est avéré être le meilleur inhibiteur de la croissance de *M. abs* avec une CMI$_{50}$ respectivement de 12.7 µM et 0.37 µM contre les morphotypes S et R, ce qui est 20 à 37 fois supérieur aux valeurs obtenues avec des antibiotiques de référence comme l'amikacine (7.4 µM), l'imipenème (12 µM) ou la cefoxitine (27 µM) [351].

Par la suite, 12 nouveaux analogues de **CyC** ont été synthétisés en faisant varier la taille de la chaine R^4 du cycle énolphosphonique [344]. Cette stratégie a été partiellement guidée par l'isolation d'un composé anti-malaria analogue des Cyclipostins, le Salinipostin, qui est une molécule naturelle produite par *Salinispora sp. bacterium*, avec des variations sur la chaine R^4 [352, 353].

Tableau 4 : Activités des dérivés **OX** et des analogues **CyC** les plus actifs contre *M. abs*.

Composés		*M. abs* CIP 104536^T		
		CMI_{50} [µM] [a]		CMI_{50Raw} [µM] [b]
		variant S	variant R	
Amikacin (AMK)		3.9 ±0.19	7.4 ±0.26	*Non déterminé*
Imipenem (IMP)		11.3 ±0.50	29.9 ±1.6	28.3 ±4.7
Analogues OX				
iB*p*PPOX	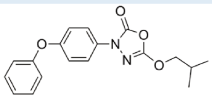	33.0 ±2.0	53.2 ±1.8	< 30µM
M*p*PPOX	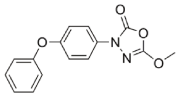	88.2 ±7.3	>200	75.2 ±5.1
MPOX	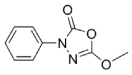	>200	>200	36.5 ±2.6
Analogues CyC				
$CyC_{7\alpha}$	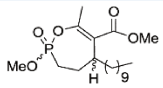	>100	>100	29.3 ±2.9
$CyC_{7\beta}$		>100	>100	65.3 ±6.2
$CyC_{8\alpha}$	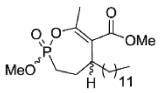	>100	>100	7.9 ±0.23
$CyC_{8\beta}$		>100	>100	2.0 ±0.91
CyC_{17}	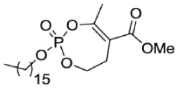	12.7 ±0.26	0.37 ±0.01	*Pas d'effet*
CyC_{25}	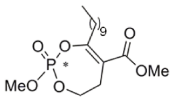	85.0 ±0.86	13.9 ±0.56	*Pas d'effet*
CyC_{26}	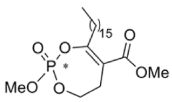	60.0 ±2.50	6.9 ±0.16	*Pas d'effet*

[a] CMI_{50} : concentration de composé conduisant à 50% d'inhibition de la croissance bactérienne *in vitro*. [b] CMI_{50RAW} : concentration de composé conduisant à 50% d'inhibition de la croissance bactérienne dans des macrophages infectés (MOI 10). Adaptée de [344, 354].

Parmi les 12 nouveaux **CyC** synthétisés, deux d'entre eux (**CyC_{25}** et **CyC_{26}**) présentent des activités antibactériennes intéressantes contre *M. abs* R (**Tableau 4**) [344]. De façon intéressante, il a été constaté que les **CyC** présentant la meilleure activité contre *M. abs* étaient tous des dérivés phosphates (**CyC_{17}**, **CyC_{25}**, **CyC_{26}**) porteurs d'une longue chaine alkyle en position R^3 ou R^4 (**Tableau 4**).

Concernant les **OX**, il a été démontré que *M. abs* R était 1.6× moins sensible aux composés testés que *M. abs* S, le meilleur inhibiteur testé pour les deux morphotypes étant l'**iB*p*PPOX** [107].

Etant donné que *M. abs* est capable de survivre à l'intérieur de macrophages [107, 355], les 38 **CyC** et 19 **OX** ont été testé pour leur capacité à inhiber la croissance intracellulaire de *M. abs* dans un modèle d'infection de macrophages murins Raw264.7. Suite à ces expériences, les **CyC$_{8\alpha}$** et **CyC$_{8\beta}$** ont montré une activité intracellulaire intéressante contre *M. abs* avec des activités respectivement de 7.9 et 2.0 µM, ce qui représente une augmentation de performance d'un facteur 3.6 et 14 comparé à l'imipenème (**Tableau 4**).Ces CMI sont du même ordre de grandeur que celles observées chez *M. tb* pour ces deux composés [348] (**Tableau 3**).

Seuls trois **OX** (**MPOX**, **M*p*PPOX** et **iB*p*PPOX**) se sont révélés capables d'inhiber la croissance intracellulaire de *M. abs* (**Tableau 4**), comme observé précédemment avec *M. tb* (**Tableau 3**).

Parmi ces **OX**, seul l'**iB*p*PPOX** bloque à la fois la croissance intra et extracellulaire de *M. abs* avec une efficacité similaire à celle de l'imipenème (**Tableau 4**).

Les résultats obtenus avec les **CyC** et les **OX** vont dans le sens de molécules multi-cibles agissant sur de nombreuses enzymes à sérines ou cystéines impliquées dans diverses voies métaboliques. Cette hypothèse est d'autant plus intéressante que la tendance actuelle est pour la recherche d'inhibiteurs multi-cibles dans les stratégies thérapeutiques [356, 357]. En effet, l'inconvénient majeur des inhibiteurs mono-cible est l'apparition « rapide » de résistances, notamment par mutation de la cible unique, conduisant à la nécessité d'utiliser des cocktails d'antibiotiques et d'appliquer des antibiothérapies courtes et lourdes.

Dans ce contexte, la nature multi-cible des **CyC** et des **OX** en fait de bons candidats dans la lutte contre les mycobactéries pathogènes. En effet ces deux familles de composés se sont révélées capables de bloquer très efficacement la croissance de *M. tb* [336, 348] et des deux morphotypes R et S de *M. abs* [344, 354] à la fois *in vitro* en milieu liquide, et *ex vivo* au sein de macrophages infectés, avec des concentrations minimales inhibitrices similaires à celles obtenues avec les antibiotiques de référence. Il a également été démontré que ces composés inhibaient spécifiquement la croissance de souches mycobactériennes et étaient sans effet sur des bactéries à Gram-positif et à Gram-négatif [336]. De plus, les **OX** et les **CyC** se sont révélés non toxiques sur des cellules de macrophages humains et murins mais également chez la souris [312].

Enfin, il a été démontré que ces deux familles d'inhibiteurs réagissent avec des enzymes dont le site catalytique comporte une sérine ou une cystéine nucléophile, parmi lesquelles on retrouve un grand nombre d'enzymes lipolytiques qui jouent un rôle central dans la physiologie et la pathogénie mycobactérienne, et notamment dans la synthèse et la dégradation des ILI. Ainsi, les **CyC** et les **OX** constituent des outils de choix pour étudier ces enzymes qui constituent de nouvelles cibles thérapeutiques potentielles dans la lutte contre les mycobactéries pathogènes [330].

d) Inhibiteurs multi-cibles et ABPP avec les CyC et les OX

Les **OX** & **CyC** réagissent spécifiquement avec des enzymes dont le site catalytique comporte une sérine ou une cystéine nucléophile avec formation d'une liaison covalente. Cette caractéristique a permis d'identifier les cibles impactées par les meilleurs **OX** et **CyC** chez *M. tb* et *M. abs* en suivant une approche d'« *activity-based protein profiling* » (ABPP) compétitive [358, 359].

Pour cela une culture de *M. tb* ou *M. abs* a été préalablement incubée soit avec *i)* du DMSO, soit avec *ii)* les composés **OX** ou **CyC**. Après lyse bactérienne, chaque lysat total est incubé avec une sonde capable de se fixer sur les protéines possédant des résidus sérine ou cystéine réactifs, la Desthiobiotine-FP [360, 361] (**Figure 39**). Pour cette approche la sonde Desthiobiotine FP a été utilisée en raison de son large spectre de cibles enzymatiques à sérine et cystéine qui en font un outil largement utilisé dans les démarches d'ABPP compétitive pour ce type d'enzyme [336, 348, 362, 363]. Les protéines ayant fixé la sonde ont été extraites du lysat après incubation avec des billes magnétiques de Streptavidine permettant leur capture et enrichissement à l'aide d'un aimant. L'identification finale des protéines cibles a été réalisée après digestion trypsique et analyse des peptides générés par chromatographie liquide couplée à la spectrométrie de masse (**Figure 39**).

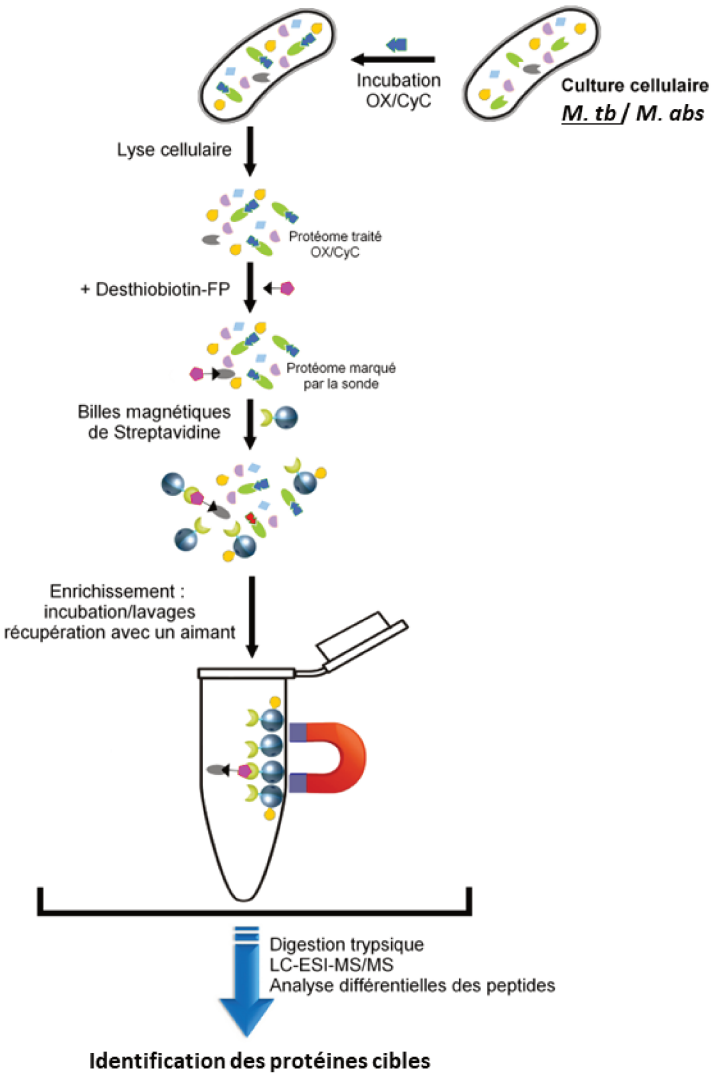

Figure 39 : Identification des molécules ciblées par les **OX/CyC**. Une culture cellulaire de *M. tb* ou *M. abs* a été prétraitée avec les OX/CyC avant lyse cellulaire, puis incubée avec la sonde Desthiobiotine-FP. Les échantillons ont ensuite été traités avec des billes magnétiques de Streptavidine pour la capture et l'enrichissement des protéines marquées. Enfin, après digestion trypsique suivie de l'analyse par spectrométrie de masse en tandem et d'une analyse différentielle des peptides obtenus permet d'identifier les protéines cibles potentielles impactées par les composés. D'après [330, 336, 348].

Ces expériences d'ABPP compétitive menées sur *M. tb* avec l'**HPOX** et le **CyC_{17}** ont conduit à l'identification respectivement de 18 et 23 cibles pour l'**HPOX** et le **CyC_{17}**, dont la majorité sont impliquées dans le métabolisme des lipides et la synthèse de l'enveloppe mycobactérienne [336, 348]. Parmi les cibles identifiées, plusieurs sont annotées comme essentielles pour la croissance *in vitro* et/ou la survie intracellulaire de *M. tb* [358, 359]. Ainsi, on retrouve le complexe antigène 85, avec Ag85A (Rv3804c), Ag85B (Rv1886c) et Ag85C (Rv0129c) [364], la thioestérase TesA (Rv2928) [365], la β-ketoacyl synthase KasA (Rv2245) [253], LipG qui est une enzyme bifonctionnelle thioestérase-phospholipase (Rv0646c) [366], et l'hydrolase HsaD (Rv3569c) [367, 368].

Suite à l'identification de ces cibles, des études biochimiques et structurales ont été effectuées afin de les valider.

Ainsi, une étude portant sur le complexe antigène 85 [369] a permis de valider, après production et purification des protéines de ce complexe avec diffèrent **CyC**, que ces protéines étaient bien des cibles effectives des **CyC_{17}**, **$CyC_{7\beta}$** et **$CyC_{8\beta}$**. De plus, il a été montré que les **CyC** bloquent la synthèse des tréhaloses dimycolates (TDM) ainsi que la mycolylation de l'arabinogalactane, avec pour conséquence la disruption de l'intégrité de l'enveloppe mycobactérienne [369].

TesA est une thioestérase impliquée dans la synthèse des phthiocerol dimycocerosates (PDIM) et des phenolic glycolipids (PGL). Ces lipides se lient de façon covalente à l'enveloppe mycobactérienne et représentent des facteurs de virulence importants chez *M. tb*. Il a ainsi été montré que le **CyC_{17}** [370] et l'**HPOX** [348] étaient capable d'inhiber l'activité de TesA *in vitro* avec des ratios molaires d'inhibition de x_{I50} = 12.4 et x_{I50} = 0.59 respectivement.

Grâce aux protéines TesA et Ag85C purifiées, les structure des complexes **$CyC_{8\beta}$**-Ag85C [369] et **CyC_{17}**-TesA [370] ont été obtenus et ont permis de déchiffrer le mécanisme moléculaire de leur inhibition respective (**Figure 40**).

L'obtention de ces cristaux et l'analyse Maldi-Tof du complexe enzyme-**CyC** a ainsi permis de valider la fixation de nos inhibiteurs sur les résidus catalytiques Ser^{104} pour TesA et Ser^{124} pour l'Ag85C.

Il a également été montré que, dans le cas du **CyC_{17}** qui est un analogue phosphate, après la phosphorylation du site catalytique de l'enzyme, ce composé subit un réarrangement de structure qui résulte par la perte de la partie β-ketoester de la molécule (**Figure 40**) [369, 370].

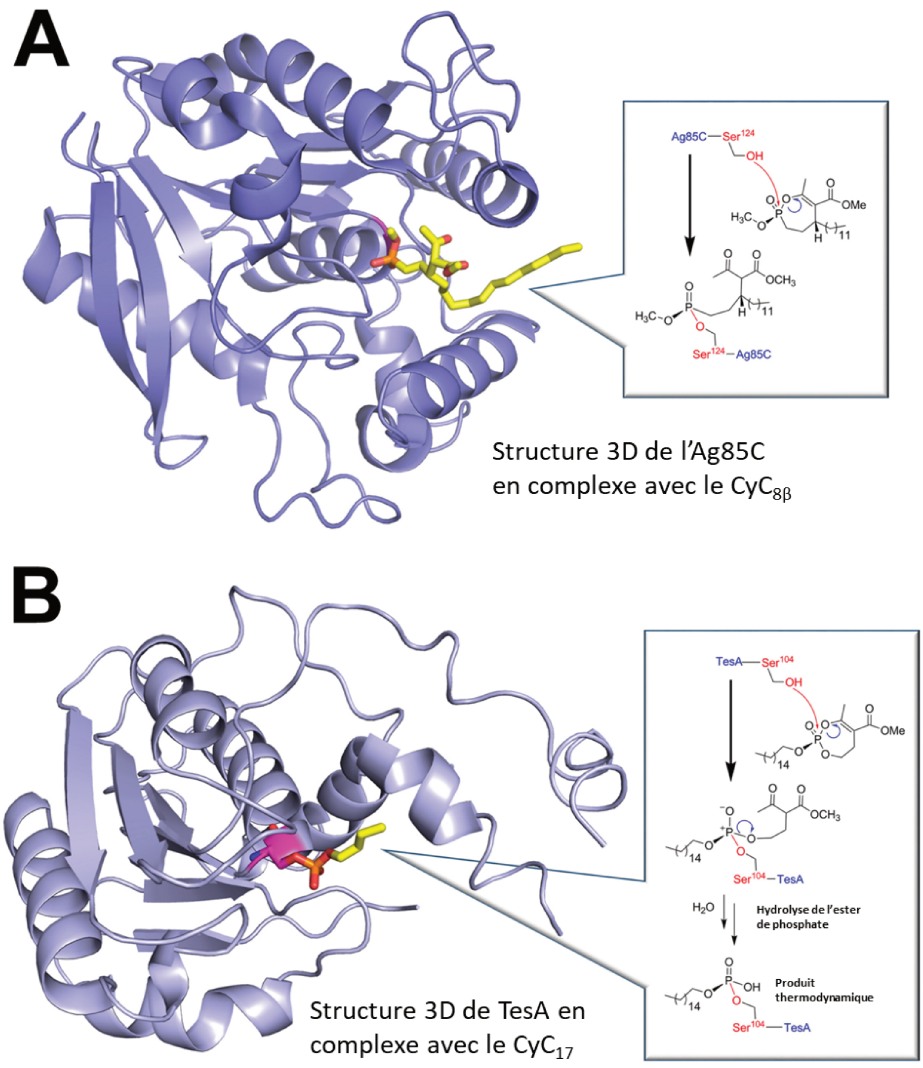

Figure 40 : **(A)** Structure de l'Ag85C en complexe avec le **CyC$_{8\beta}$** [369]. **(B)** Structure de TesA en complexe avec le **CyC$_{17}$** [370].

Enfin, la dernière cible de *M. tb* investiguée est LipG (Rv0646c) qui est une thioestérase-phospholipase essentielle pour la survie intracellulaire de *M. tb* [366]. Cette cible a été caractérisée biochimiquement par notre équipe [371]. Cette enzyme est impliquée dans la modification et le remodelage de l'enveloppe mycobactérienne et les cinétiques d'inhibition effectuées montrent qu'elle est capable de réagir avec le **CyC$_{7\alpha}$** (x_{I50} = 5.0) et le **CyC$_{17}$** (x_{I50} = 0.98), mais pas avec les **CyC$_{7\beta}$** et **CyC$_{8\alpha,\beta}$**.

Par la suite, la même approche d'ABPP compétitive a été effectuée sur *M. abs* ce qui a conduit à l'identification de 39 et 21 cibles potentielles respectivement pour le **CyC$_{17}$** et l'**iB*p*PPOX**. Parmi ces cibles, 11 sont annotées comme essentielles chez *M. tb* et la plupart sont également impliquées dans le métabolisme des lipides et la biosynthèse de l'enveloppe [344, 354].

Parmi ces cibles, on retrouve plusieurs enzymes de la famille des cutinases, des lip-HSL, et les membre du complexe Ag85 jouant un rôle dans la survie et la synthèse de l'enveloppe [372, 373].

Le fait que les protéines Ag85A/B/C soient identifiées comme cibles des **CyC** et des **OX** chez *M. tb* [348, 369] et chez *M. abs* [344, 354], mais également chez d'autres inhibiteurs d'enzymes à sérine et cystéine comme l'Orlistat et ses analogues [374-376], suggère qu'il s'agit d'une cible commune à toutes les espèces de mycobactéries. Ces protéines sont importantes dans le métabolisme des acides mycoliques et représentent des cibles thérapeutiques intéressantes pour le développement de nouvelles molécules [364, 369].

Cette approche a permis de démontrer que les cibles des **OX**/**CyC** étaient aussi bien membranaires que cytoplasmiques ; faisant donc de ces composés des inhibiteurs multi-cibles très prometteurs [336, 344, 348, 354].

Objectifs

Dans ce contexte, la première phase de mon projet de thèse fait intervenir des analogues des **OX** et **CyC** présentant les meilleures activités biologiques sur la croissance *in vitro* et *ex vivo* de *M. tb* et *M. abs* (**HPOX**, **H*p*PPOX**, **iBPOX**, **iB*p*PPOX**, **CyC$_{31}$** et **CyC$_{32}$** – **Figure 41 A**), dont la structure chimique a été modifiée de façon à inclure soit un fluorophore (Dansyl ou NBD) soit un groupement alcyne pour la mise en place de capture directe des cibles par réaction de chimie-click (**Figure 41 B**).

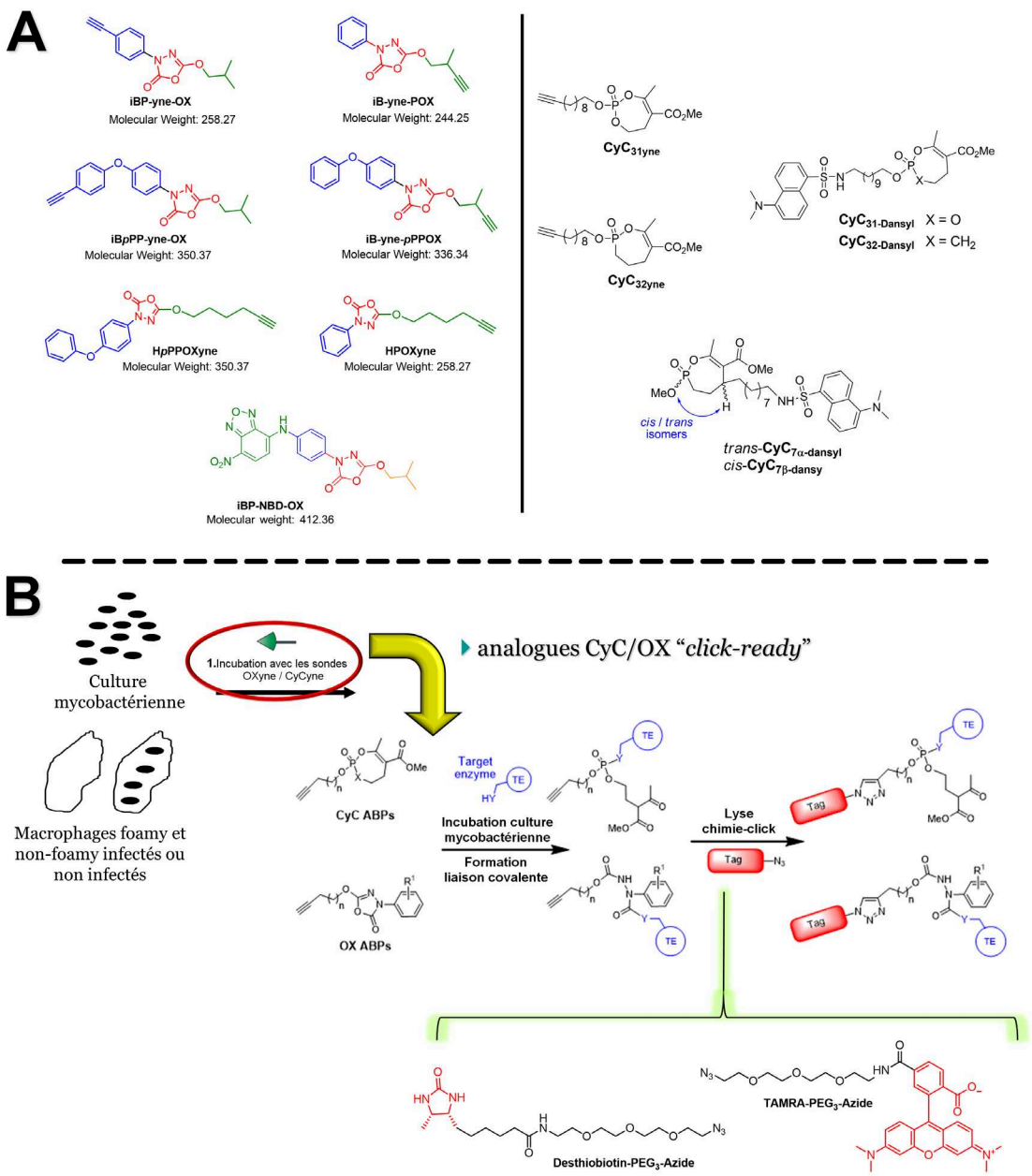

Figure 41 : **(A)** Structure des inhibiteurs **OX** & **CyC** « *click-ready* » porteurs d'un groupe alcyne en vue d'effectuer une réaction de chimie-click pour la capture directe des enzymes cibles. **(B)** Schéma de principe de la réaction d'ABPP. Les inhibiteurs porteurs d'un groupement alcyne sont incubés avec l'échantillon biologique et vont former une liaison covalente avec leurs enzymes cibles. Après lyse cellulaire, la réaction de chimie-click permet de coupler un tag aux inhibiteurs eux-mêmes liés aux enzymes cibles. Deux types d'étiquettes sont utilisés : une étiquette TAMRA pour révéler le profil des cibles sur gel SDS PAGE par imagerie de fluorescence ; et une étiquette Desthiobiotine pour enrichir les cibles sur billes de Streptavidine en vue d'une identification par spectrométrie de masse.

Dès lors, mon projet de thèse se décompose en quatre objectifs :

1°) Etudier la pénétration et la répartition des inhibiteurs dans la bactérie ainsi que dans les cellules hôtes. :

Les inhibiteurs fluorescents synthétisés par nos partenaires nous ont permis de suivre la pénétration et la répartition de ces deux familles d'inhibiteurs, à la fois dans les mycobactéries et dans diverses souches bactériennes, mais également dans les cellules hôte seules et en contexte d'infection. Nous avons ainsi pu établir un lien entre l'activité de nos composés, leur pénétration et leur localisation en contexte d'infection.

2°) Identifier les enzymes impactées lors des phases de réplication active et valider la démarche de capture directe des cibles par CC-ABPP

Les inhibiteurs modifiés avec une triple liaison terminale ont été utilisés comme sondes ABPP. Cette démarche de chimioprotéomique puissante permet d'identifier une sous-partie d'un protéome complexe en fonction de l'affinité des enzymes pour un groupe chimique spécifique, ici les **OX** & **CyC**. Dans cette démarche, de nouveaux inhibiteurs **OX** & **CyC** « *click-ready* » ont été incubés avec l'échantillon biologique à analyser ce qui leur permet de se fixer à leurs enzymes cibles. Une réaction de chimie-click a ensuite été effectuée sur le lysat bactérien afin de lier de façon covalente *via* la formation d'un cycle triazole un tag rapporteur sur les inhibiteurs qui sont eux même liés à leurs enzymes cibles. Nous avons ainsi utilisé les sondes **CyC** et **OX** « *click-ready* » afin d'établir le spectre de cibles enzymatiques de ces composés chez *M. tb in vitro* et ainsi décrypter leur mode d'action moléculaire et également identifier des nouvelles cibles thérapeutiques parmi les enzymes à sérine et cystéine de ces deux organismes.

Parmi les cibles identifiées durant les expériences d'ABPP, une cible (HsaD) a été choisie pour être validée comme cible effective de nos inhibiteurs. Après purification de la protéine sous forme recombinante, des mesures d'inhibition de son activité par les **CyC** et les **OX** ont été réalisées. De plus, cette protéine purifiée a été co-cristallisée en complexe avec différents **CyC** ce qui a permis d'établir la nature moléculaire de l'inhibition, le site de liaison et les interactions stabilisant les composés dans le site catalytique.

3°) Déterminer les enzymes cibles impliquées dans la synthèse des ILI dans le model MSM-NL et valider leur implication dans ce métabolisme.

Enfin, l'usage du modèle d'induction *in vitro* de la biosynthèse des ILI par carence en azote (milieu MSM-NL) en conjonction avec les sondes **CyC** et **OX** « *click-ready* » nous ont permis de déterminer l'ensemble des enzymes cibles de nos composés qui sont impliquées dans le métabolisme de biosynthèse des ILI. Dans ce modèle, *M. abs* est mis en culture dans un milieu minimal carencé en azote (MSM-NL) ce qui va induire un stress nutritif chez la bactérie, déclenchant la biosynthèse des ILI. Au cours de cette accumulation, des captures de cibles par ABPP avec les sondes **CyC** et **OX** « *click-ready* » ont été effectuées à 24h et 48h d'accumulation pour établir le spectre des cibles enzymatiques de ces composés au cours de l'accumulation. La comparaison des données protéomiques acquises au cours de ces expériences avec celles acquises sur *M. abs* dans un milieu MSM non carencé en azote (qui n'induit pas l'accumulation des ILI) nous a ainsi permis de déterminer les enzymes statistiquement plus abondantes en phase de biosynthèse des ILI et ainsi potentiellement identifier de nouvelles cibles thérapeutiques liées à ce métabolisme des ILI.

Enfin, concernant les cibles identifiées comme prenant potentiellement part à la biosynthèse des ILI, des mutants de délétion et de complémentation ont été construits chez *M. abs* afin d'évaluer leur capacité à accumuler des ILI dans le modèle *in vitro* carencé en azote, MSM-NL afin de valider leur implication dans ce métabolisme. Des mutants de fusion avec un rapporteur fluorescent ont également été construits chez *M. abs* pour étudier la localisation de ces enzymes durant le processus de biosynthèse des ILI.

Résultats

Article I

Deciphering the physiological role of serine enzymes involved in mycobacterial lipid metabolism using activity-based protein profiling

---

R. Avellan*, M. Sarrazin*, C.D. Spilling, C. Crauste, S. Canaan, J.-F. Cavalier

Biology of Mycobacterial Lipids, Academic Press, 2022, pp. 235-251.

https://doi.org/10.1016/B978-0-323-91948-7.00001-4

* Contribution égale

Le métabolisme des lipide est un acteur central dans le cycle de vie, les interactions hôte-pathogène [197] et la physiopathologie des infections mycobactériennes [198]. De plus, il est impliqué dans un large panel de fonctions, comme la croissance mycobactérienne [199-201], les mécanismes de dormance [202, 203], de réactivation, de propagation et de virulence [204-207], la synthèse de l'enveloppe mycobactérienne [198, 200] et les mécanismes de stockage et de dégradation des lipides [199, 202, 208, 209].

Ainsi, une caractéristique des infections mycobactériennes et tout particulièrement de *M. tb*, réside dans la capacité qu'ont ces bactéries d'exploiter les lipides de l'hôte et de les internaliser sous forme de TAG dans leur propre cytoplasme [217, 224, 278, 279]. Ces TAG dérivés de l'hôte ou synthétisés par la mycobactérie sont stockés dans des vésicules lipidiques intracellulaires appelés ILI, qui jouent un rôle central dans les mécanismes de dormance et de réactivation caractéristiques des infections mycobactériennes latentes [224, 282, 283].

Il a été ainsi établi que les enzymes lipolytiques jouaient un rôle essentiel dans tous ces processus et que parmi ces dernières, la plupart possèdent une sérine ou une cystéine catalytique [199, 202, 208, 209]. Ces enzymes catalysent un panel très large de réactions comme l'hydrolyse des esters ou leur transestérification, l'alcoolyse, l'acidolyse ou l'aminolyse, et interviennent dans l'ensemble des processus biologique précités, ce qui en fait des cibles de choix pour le développement de nouvelles chimiothérapies contre les infections mycobactériennes au premier rang desquelles on retrouve la tuberculose.

Dans le but d'étudier ces enzymes lipolytiques mycobactériennes à serine ou cystéine catalytique, une nouvelle approche de chimioprotéomique appelée ABPP a émergé dans la dernière décennie [377] Cette approche permet le profilage de ces enzymes en fonction de leur réactivité chimique et d'évaluer leur fonction dans un système biologique.

Cette stratégie repose sur l'utilisation de sondes moléculaires appelées ABP (« *activity based probe* »). Ces sondes sont composées d'une tête réactive qui va réagir de façon covalente avec les enzymes cibles, et qui est responsable de la spécificité de la sonde utilisée, un linker généralement lipide saturé et un tag de visualisation (*p. ex*. : TAMRA) ou d'affinité (exemple biotine) qui permet l'enrichissement des cibles depuis un lysat pour pouvoir ensuite les identifier par spectrométrie de masse [377-379].

De nombreuses sondes ont été développées à partir d'inhibiteurs d'enzyme à sérine ou cystéine et ont été utilisées avec succès pour étudier le métabolisme des lipides mycobactériens [336, 348, 362, 376, 378, 380-384].

L'ABPP se présente classiquement sous trois formes distinctes. Dans sa forme classique, le système biologique est incubé avec la sonde puis lysé, et les cibles sont directement enrichies et analysées par spectrométrie de masse.

Une autre approche d'ABPP compétitive permet d'identifier les cibles d'un inhibiteur sans développer de sonde spécifique à partir de ce dernier. Dans cette approche, une sonde ABP qui possède un spectre de cible similaire à celui de l'inhibiteur mais plus large est choisie. D'une part le spectre de cibles de cette sonde est alors établi selon une approche standard d'ABPP. D'autre part le spectre des cibles de cette sonde est établi en ayant au préalable incubé avec l'inhibiteur dont on veut connaitre les cibles. Ainsi, une baisse de signal dans le spectre pré-incubé avec l'inhibiteur signale une compétition de celui-ci avec la sonde et indique donc que la protéine concernée est ciblée par l'inhibiteur

Enfin, une dernière approche d'ABPP fait intervenir une réaction de chimie-click (CC-ABPP). Dans cette approche, l'inhibiteur d'intérêt a été modifié pour y ajouter un groupe compatible avec la chimie-click (alcyne ou azoture).

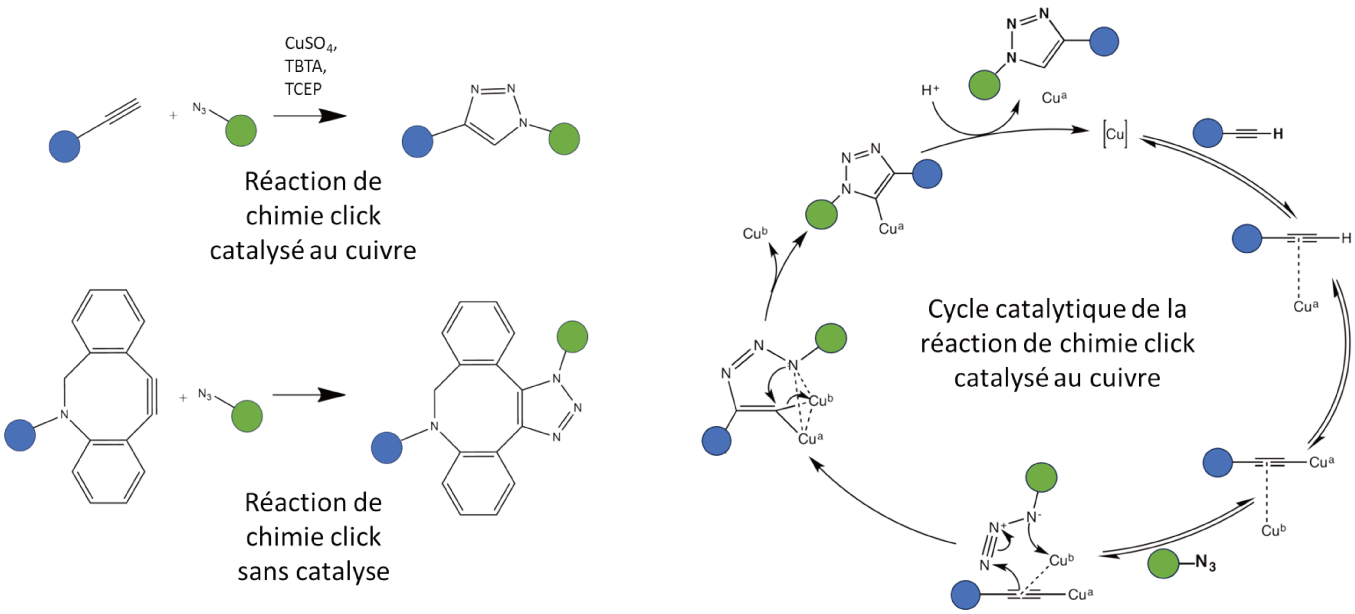

Figure 42 : schéma réactionnel de la réaction de chimie-click entre des alcynes et des dérivés azotures (N3) et cycle catalytique de la chimie-click catalysé au cuivre. Adapté de [385].

Deux types de réaction de chimie-click sont couramment utilisés lors des expériences d'ABPP, donnant lieu dans les deux cas à la formation d'un cycle triazole (**Figure 42**) :

- Une réaction catalysée au cuivre entre un azoture et un alcyne terminal dont le cycle catalytique est représenté en **Figure 42**. Cette réaction est rapide et présente un bon rendement. En revanche la toxicité du cuivre la rend difficile à utiliser sur des systèmes vivants. Dans ce contexte, l'inhibiteur est préalablement incubé avec le système biologique qui est ensuite lysé. La réaction de chimie-click est ensuite effectué sur le lysat afin de coupler de manière covalente un tag d'affinité aux inhibiteurs, eux-mêmes liées à leurs cibles, par la réaction de cycloaddition 1,3-dipolaire de Huisgen (ou chimie-click) conduisant à la formation d'un cycle triazole [386]. Un enrichissement des cibles et une analyse par protéomique est ensuite effectuée de façon similaire à la démarche normale d'ABPP.
- Une réaction non-catalysée au cuivre, qui permet l'usage en système biologique entier, entre un azoture et un dérivé du DBCO. Ce dernier composé possède un cycle à 8 carbones particulièrement tendu du fait du partage de deux doubles liaisons avec des noyaux aromatiques et d'une triple liaison en son sein. La tension de cycle va ainsi augmenter la réactivité de la triple liaison et permettre sa réaction avec l'azoture sans nécessité de catalyse au cuivre.

Toute ces démarches ont été appliquées à l'étude des enzymes à sérine et cystéine mycobactériennes en utilisant des sondes développées à partir d'un large panel d'inhibiteurs de ces enzymes tels que les fluorophosphonates, les β-lactones, les 1,2,3-triazole urées, les carbamates, les **CyC** ou les **OX** [336, 348, 362, 376, 378, 380-384].

Ce chapitre a pour but de présenter l'état de l'art et de la connaissance concernant les enzymes à sérine et cystéine mycobactériennes. Il cherche également à investiguer les différents outils d'étude de ces enzymes par ABPP en comparant la sélectivité chimique de diverses sondes ABP utilisées dans ce cadre pour lesdites enzymes.

CHAPTER

11

Deciphering the physiological role of serine enzymes involved in mycobacterial lipid metabolism using activity-based protein profiling

Romain Avellan[1,a], *Morgane Sarrazin*[1,a], *Christopher D. Spilling*[2], *Céline Crauste*[3], *Stéphane Canaan*[1] *and Jean-François Cavalier*[1]

[1]**Aix-Marseille University, CNRS, LISM, Institut de Microbiologie de la Méditerranée, Marseille, France;** [2]**Department of Chemistry and Biochemistry, University of Missouri—St. Louis, One University Boulevard, St. Louis, MO, United States;** [3]**IBMM, Université de Montpellier, CNRS, ENSCM, Montpellier, France**

Introduction

Tuberculosis (TB), caused by *Mycobacterium tuberculosis* (*M. tb*), is an ancient disease that is one of to the top-ten causes of death worldwide and still remains in 2021, the leading cause of death by a bacterial pathogen. Every year, TB claims the lives of nearly 1.4 million people, despite being curable with affordable and accessible antibiotics to treat the infection [1]. The increasing global health burden of TB is further aggravated by the alarming increase of multi- and extensively drug-resistant *M. tb* strains, which requires longer and more costly therapeutic regimens.

A hallmark of *M. tb*, as well as other pathogenic mycobacteria, is its ability to not only synthetize its own lipids, but also to metabolize host lipids. Indeed, upon infection, *M. tb* exploits metabolic pathways to import and process host-derived free fatty acids, subsequently stored

[a] Both authors should be considered as equal first authors, and are listed in alphabetical order.

Biology of Mycobacterial Lipids
https://doi.org/10.1016/B978-0-323-91948-7.00001-4

© 2022 Elsevier Inc. All rights reserved.

as TAG in its own cytoplasm in the form of intracytoplasmic lipid inclusions (ILI). Under nutrient-starvation, these ILI serve as carbon source and energy promoting bacterial survival. At this stage, lipid-loaded mycobacteria could stop their replication and enter in a persistent and nondividing state. During the reactivation phase, the bacilli hydrolyze the lipids contained inside the ILI and the fatty acids thus released are used to fuel the regrowth leading to its exit from the nonreplicating state [2]. These findings therefore emphasize the essential role of central lipid metabolism in long-term survival and persistence of the bacilli [3]; and consequently, that of mycobacterial lipid hydrolyzing and synthesizing enzymes, most of which possess a catalytic serine or cysteine residue in their catalytic site (i.e., (Ser/Cys)-based enzymes).

Accordingly, Serine enzymes (SEs) can catalyze a large variety of reactions: ester hydrolysis, trans- or interesterification, alcoholysis, acidolysis, or aminolysis; and have been shown to play critical roles in the physiopathology of the disease, being involved in various crucial processes, including lipid storage and degradation, in addition to cell wall biosynthesis and maintenance [4]. Accordingly, SEs represent a promising class of potential therapeutic enzyme targets in the fight against this pathogenic mycobacterium [5]. Therefore, finding ways to identify, inhibit, or control the activity of such mycobacterial SEs may open the way to new chemotherapeutic developments against pathogenic mycobacterial-related infections, especially against *M. tb*.

In this context, the use of small molecule inhibitors that covalently bind the active site of their protein targets has led to the development of a powerful chemoproteomic technique, termed activity-based protein profiling (ABPP), allowing the identification of bacterial SEs in complex proteome [6].

In this chapter, we will highlight the use of SE inhibitors as activity-based probes (ABP) for the identification and characterization of the functional state of mycobacterial SEs specifically involved in lipid synthesis or lipid degradation within *M. tb*.

Serine enzymes in M. *tb*—the fundamental of a new drug family development

Serine enzymes from M. *tb*

Genome sequencing of *M. tb* H37Rv strain, composed of 4.4 million base pairs and encoding about 4000 proteins, revealed that this bacterium possesses 250 enzymes involved in lipid metabolism, representing 6% of the full genome [7]. Among these enzymes, SEs play many roles in the assembly, the modification, and the maintenance of the waxy mycobacterial cell envelope.

SEs are characterized by a common α/β-hydrolase fold as secondary structure, and a conserved catalytic triad (Fig. 11.1). This fold is composed of 5−13 β-strands, usually eight, forming a parallel β-sheet and one antiparallel β-strand surrounded on both sides by α-helices (Fig. 11.1A) [8]. The catalytic triad is formed by a histidine, a nucleophilic serine, and an acidic residue (Asp or Glu). The nucleophilic serine is mainly present in the consensus pentapeptide motif Gly-Xaa-Ser-Xaa-Gly and located at the center of a structural moiety called nucleophilic elbow at the terminal end on an α-helix and the beginning of the following β-sheet. This unique α/β-hydrolase fold structure therefore brings the serine, glutamic/aspartic acid, and histidine in close proximity allowing the formation of the correct

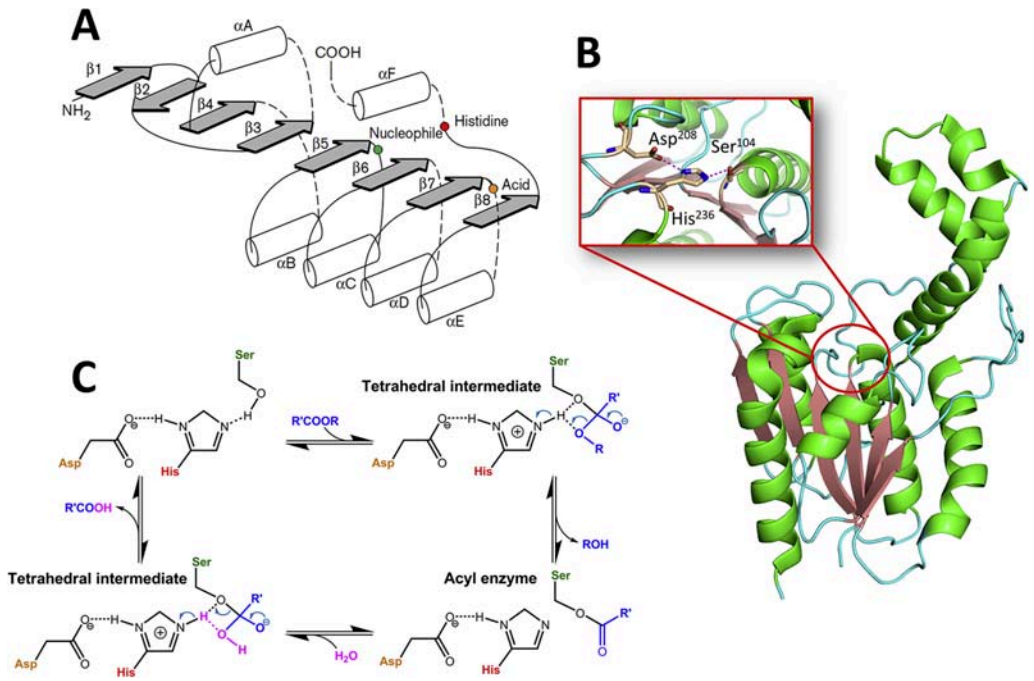

FIGURE 11.1 **(A) Secondary structure diagram of α/β-hydrolase**. α-helices and β-strands are represented by cylinders and arrows, respectively. Dashed lines indicate the location of possible insertions. The catalytic triad is composed of nucleophilic (green), acidic (orange), and histidine (red) residues. **(B) Ribbon view of overall structure of the *M. tb* thioesterase TesA (Rv2928)**. The α-helices are colored green and the β-strands salmon. The TesA catalytic triad Ser^{104}—His^{236}—Asp^{208} side chains are colored by atom type (N: blue, O: red, C: wheat) with black labels. The hydrogen bonds are colored magenta. **(C) Mechanism of action of serine enzymes**. *(A) Adapted from M. Nardini, B.W. Dijkstra, Alpha/beta hydrolase fold enzymes: the family keeps growing, Curr. Opin. Struct. Biol. 9 (1999) 732—737. (B) Adapted from PDB id: 6fw5 P.C. Nguyen, V.S. Nguyen, B.P. Martin, P. Fourquet, L. Camoin, C.D. Spilling, J.F. Cavalier, C. Cambillau, S. Canaan, Biochemical and structural characterization of TesA, a major thioesterase required for outer-envelope lipid biosynthesis in Mycobacterium tuberculosis, J. Mol. Biol. 430 (2018) 5120—5136. (C) Adapted from S. Raza, L. Fransson, K. Hult, Enantioselectivity in Candida Antarctica lipase B: a molecular dynamics study, Protein Sci. 10 (2001) 329—338.*

hydrogen-bond network to create the catalytic triad for catalysis (Fig. 11.1A—B) [9]. The spatial arrangement of these residues decreases the acid-ionization constant of the serine hydroxyl group, enabling the nucleophilic attack on the carbonyl group of the substrate, leading to a tetrahedral intermediate stabilized by coordination by the so-called oxyanion hole (Fig. 11.1C). The geometry of the nucleophile elbow also contributes to the formation of the oxyanion-binding site, which is needed to stabilize the negatively charged transition state that occurs during hydrolysis. Finally, a nucleophile (either a water molecule or an alcohol) further attacks this acyl-enzyme intermediate via hydrolysis or alcoholysis and releases the product, thus regenerating the enzyme (Fig. 11.1C) [10,11].

The active site is usually located inside a pocket surrounded by hydrophobic residues which interact with their hydrophobic substrates. The binding site of SEs differs, however, in their hydrophobic interaction area, shape, size, deepness of the catalytic pocket, and physicochemical characteristics of their amino acids. Such characteristics are indeed responsible

for their difference in substrate specificity, and therefore for their enzyme activity. Some subclasses like amidases and patatin-like proteins possess, however, a different catalytic mechanism involving either a triad formed by Ser-Ser-Lys or a Ser-Asp dyad, respectively [12,13].

In *M. tb* H37Rv genome, 105 proteins predicted to be α/β-hydrolases have been identified; among which, approximately 30 enzymes possess the consensus sequence Gly-Xaa-Ser-Xaa-Gly most of them belonging to the Lip family [4]. Globally, although α/β-hydrolase enzymes vary in their amino acid sequences as well as in their broad range of substrates, they, however, share a conserved fold architecture and display a similar mechanism of action between all members of this superfamily. This point can be considered as a key to design efficient inhibitors. SEs obviously represent a gold mine awaiting to be exploited as new therapeutic targets against TB.

The following paragraphs will depict some mycobacterial SEs based on the nature and the specificity of their corresponding lipidic substrates.

Physiological role

True lipases

Lipases are lipolytic enzymes capable of hydrolyzing long-chain fatty acids from natural water-insoluble carboxylic esters, mainly triacylglycerols (TAG). Among the 12 genes in the so-called *M. tb* Lip family (LipC to LipZ) [14] only the *rv3097c* gene, named LipY, exhibited a lipase activity on long-chain TAG allowing the release of fatty acids which can be further used as a source of energy [15]. Moreover, an *M. tb* lipY-deficient mutant failed to escape from dormancy in an in vitro granuloma model [16]. LipY possesses a Pro-Glu (PE) signature motif at its N-terminus and is found either as a full-length intracytosolic form or as a mature extracellular form lacking its N-terminal PE domain and associated with the mycobacterial cell surface. LipY is indeed exported to the cell wall via the type VII secretion system ESX-5 after recognition of the specific amino acid sequence YxxxD/E, contained in this N-terminal PE domain [17–19]. Biochemical characterization suggested that due to its dual location, LipY is a major contributor to the breakdown of host and bacterial TAG, thus playing an essential role in *M. tb* intracytosolic lipid catabolism and exit from dormancy state [2].

In addition to LipY, the monoacylglycerol (MAG) lipase annotated Rv0183 has been reported to display true lipase activity by catalyzing the hydrolysis of MAG into free glycerol and fatty acid, which can be further reprocess by the bacteria [20]. Immunolocalization studies revealed that this enzyme is present either in culture medium, or in bacterial cell wall. Drastic changes in colony morphology, together with important antibiotic susceptibility modifications, were observed with a disrupted mutant of its ortholog MSMEG_0220 in *M. smegmatis*, which were partly restored in the complemented mutant [21]. These results point out the critical structural role of Rv0183 in mycobacterial cell wall architecture, in addition to its contribution to the hydrolysis of host cell lipids.

(Thio)Esterase family

Esterases catalyze the hydrolysis of soluble ester substrates rather than water-insoluble substrates like long-chain TAG. Among *M. tb* proteome, around 20 esterases have been biochemically characterized, but their physiological roles are not yet clearly elucidated. The

thioesterases LipG (Rv0646c) and TesA (Rv2928) have been showed to be involved in the synthesis and remodeling of the membrane [22,23]. LipG has also been proposed to be involved in mycobacterial phospholipid metabolism and was found to induce a high production of proinflammatory cytokines such as IL-6, TNF-α, IL-1, and reactive oxygen species in THP-1 cells [24]. Since cytokines are important actors in the establishment of the immune response and macrophage activation to kill bacteria [25], LipG may thus participate in the regulation of the host's immune responses favoring bacterial survival.

Localized in the membrane fraction of the bacteria, TesA is non-essential for the in vitro growth of *M. tb*. However, a Δ*tesA* deletion mutant strain of *M. tb* was found more susceptible to antibiotics, due to the fact that this Δ*tesA* mutant was defective in phthiocerol dimycocerosate (PDIM) [26]. Moreover, TesA has also been shown to plays a crucial role in the production of phenolic glycolipids (PGL) [23]. These two lipids, PDIM and PGL, are noncovalently bound to the outer cell wall in pathogenic mycobacteria and are required for *M. tb* virulence and pathogenesis [27,28]. Consequently, TesA represents a major contributing partner in the synthesis of both PDIM and PGL and is believed to play an important role in vivo by increasing the virulence of pathogenic mycobacteria.

Another interesting SE is CaeA (Rv2224c) also named Hip1 (Hydrolase important for pathogenesis 1). This cell wall-associated carboxylesterase was initially reported as being involved in cell wall biosynthesis and/or integrity [29]. CaeA was also found to be important for survival and growth during infection and virulence by modulating cytokines balance to promote *M. tb* survival and growth within macrophages [30]. Accordingly, deletion of the *caeA* gene in *M. tb* resulted in a reduction of mycobacterial load in mouse's lung and spleen, and reduced mycobacterial virulence in infected mice [29]. Recent studies in *M. tb* revealed that this enzyme exhibited more a serine protease activity rather than a carboxylesterase one [31]. CaeA was indeed found to cleave GroEL2 protein both in vitro and in vivo, a proteolytic activity responsible for the immunomodulation of host inflammatory responses.

Lastly, among the 12 proteins belonging to the "Lip" family, LipC (Rv0220), LipH (Rv1399c) and LipI, −N, −R, −U, and −W were identified as esterases [14], while LipF (Rv3487c) displays an esterase [14] as well as a phospholipase C activity [32]. This latter enzyme would also be important for *M. tb* intracellular survival and growth during infection. Indeed, the *lipF* gene was upregulated by acidic stress [33], and a transposon insertion between the promoter and the *lipF* gene resulted in a decrease of bacterial growth in mouse's lung [34]. These results suggest that this protein might contribute to the survival of the tubercle bacilli under acidic environment of the phagosome.

Cutinase-like family proteins

Cutinases belong to a family of SEs able to degrade a large panel of substrates such as cutin, TAG and phospholipids. In the *M. tb* genome, seven proteins homologous to the *Fusarium solani pisi* cutinase have been identified and named cutinase-like proteins with the following correspondence: Cut1 (Rv1758 or Culp5), Cut2 (Rv2301 or Culp2), Cut3 (Rv3451 or Culp3), Cut4 (Rv3452 or Culp4), Cut5b (Rv3724B or Culp7), Cut6 (Rv3802 or Culp6), and Cfp21 (Rv1984c or Culp1) [7,35]. They all belong to the α/β-hydrolase fold family proteins and contain the conventional Ser-His-Asp catalytic triad, with Ser also located in a conserved Gly-Xaa-Ser-Xaa-Gly sequence. Enzymatically, Cut1, Cut2, Cut3, and Cut5b

displayed weak or no activity at all toward the various substrates tested, in contrast to Cfp21, Cut4, and Cut6 which exhibited various enzymatic activities [35,36].

In one hand, Cfp21 and Cut4 are two secreted proteins which showed distinct substrate specificities, despite their 50% amino acid sequences identity and their similar overall predicted structures. Cfp21 preferentially hydrolyzes medium-chain carboxylic esters and MAGs with a preference for C8 fatty acid chains, whereas Cut4 behaves like a phospholipase A2 and is able to induce macrophage lysis [36]. These later data suggest a role of these both enzymes in the host–pathogen interactions. On the other hand, Cut6 which is located in the cell wall fraction exhibits a phospholipase and thioesterase activity [37]. Moreover, the *cut6* gene which has been found to be essential for *M. tb* growth is located in a gene cluster involved in mycolic acid biosynthesis. These observations therefore support the fact that this enzyme would participate in mycolic acids biosynthesis by maintaining the integrity of the cell wall [37].

Overall, these features suggest that Cfp21, Cut4, and Cut6 might interact with the host membranes and participate in the virulence/infection process by degrading host lipids.

Mycolyltransferases

Mycolic acids are composed of very long chain fatty acids (C70–90) that are either covalently attached to the arabinan moiety of the arabinogalactan (AG) polymer forming the mycolylarabinogalactan (mAG), or form the lipophilic tails of extractable glycolipids, such as trehalose dimycolate (TDM), that are located predominantly in the mycomembrane outer leaflet.

The synthesis of TDM and mAG is catalyzed by the *M. tb* encoded antigen 85 (Ag85) complex, which includes three homologous secreted transferases named Ag85A (FbpA or Rv3804c), Ag85B (FbpB or Rv1886c), and Ag85C (FbpC2 or Rv0129c). These enzymes catalyze a transesterification reaction that transfers a mycolic acid from one molecule of trehalose monomycolate (TMM) to another thereby synthesizing TDM, as well as the covalent attachment of mycolic acids from TMM to the mAG [38].

These enzymes belong to the α/β-hydrolase superfamily and share a 68%–79% sequence identity. The resolution of their tridimensional structure shows that the three proteins possess the same catalytic triad, with the active site Ser124 within the Gly-Xaa-Ser-Xaa-Gly consensus sequence, and the same substrate specificity [39]. Whereas the hydrolytic mechanism of SEs usually uses a water molecule to hydrolyze the bond between the enzyme and the acyl chain, the transfer mechanism of the Ag85 enzymes likely uses a hydroxyl group of a terminal arabinose on the mycobacterial cell wall [39]. In addition, more recent work demonstrates that all three members of the Ag85 complex mediate the transesterification of diacylglycerol using long-chain acyl-CoA to produce TAG, with Ag85C exhibiting the most pronounced diacylglycerol acyltransferase activity. This suggests that Ag85C, as well as Ag85A and Ag85B, may also make an important contribution in TAG synthesis in *M. tb* [38].

Finally, members of Ag85 complex are conserved in mycobacterial species and play an essential role in the maintenance of the highly hydrophobic cell wall which is central to the survival of *M. tb* within its host environment. Accordingly, the Ag85 proteins therefore represent prime targets for the development of anti-TB drugs.

Overall, all the data collected from the last decades on *M. tb*'s SEs have clearly emphasized their major role in the life cycle of the bacilli [4,5]. Consequently, development of novel tools to investigate and modulate such mycobacterial SEs remains of great interest.

Activity-based protein profiling, a powerful versatile chemical proteomic platform applied to characterize the functional state of serine enzymes in mycobacteria

In the last decades, chemoproteomic strategy such as ABPP has emerged as a major approach to profile enzymes activities and evaluate their functions directly in native biological systems. Using ABPP, a subset of expressed proteins can be identified based on their specific activity for a chemical warhead used as a selective chemical probe called ABP (Fig. 11.2A). This strategy has been successfully used to identify and characterize mycobacterial SEs by the use of enzyme inhibitors as ABP. Those probes allow the identification and characterization of the functional state of mycobacterial SEs within mycobacteria [40] taking advantage of the existing inventory of predicted gene products of mycobacteria and their host, as well as development of mass spectroscopy, used to analyze complex biological samples. The core elements of such ABP remain constant and are composed of an electrophile "warhead" which covalently reacts with the catalytic serine residue in the active site of targeted SEs; an extended saturated lipid linker; and a tag for either visualization (e.g., TAMRA group) or affinity purification (e.g., biotin group) of targets (Fig. 11.2A) [6,40,41].

The work flow of a typical ABPP experiment is depicted in Fig. 11.2. In a classical experiment, the ABP-labeled proteome can be capture and enriched by affinity purification using an affinity tag and further digested, so that targets can be identified by LC-MS/MS (Fig. 11.2B). In contrast, competitive ABPP involves pretreating a biological system with a first small molecule inhibitor followed by labeling with an efficient ABP inhibitor (Fig. 11.2C) that will be enable to interact with the active site serine residue of the enzymes covalently linked to the first compound. Comparison of labeling patterns of the untreated proteome with the inhibitor-pretreated proteome allows identification of the targeted enzymes. Finally, a variant of ABPP known as click-chemistry ABPP (CC-ABPP) can be applied for covalent inhibitors (Fig. 11.2D). This strategy involves converting the inhibitor of interest into a "clickable" probe through incorporation of an alkyne (or an azide) group. After inhibitor probe labeling, an azide (or alkyne)-containing fluorophore or biotin can be added via copper-free or copper-catalyzed alkyne-azide cycloaddition (CuAAC), allowing the direct capture of the target enzymes [41].

A wide range of electrophilic warhead has been developed for ABP that allows for covalent binding with the catalytic nucleophilic site of SEs. These included fluorophosphonates (FP), β-lactones, 1,2,3-triazole ureas, carbamates, and oxadiazolones (Fig. 11.3). Since these compounds differ in their nucleophile and enzyme class specificity, the choice of an optimal warhead must be carefully considered. In this case, a balance must indeed be reached between a high reactivity leading to a large number of off-target results, and a low reactivity leading to potentially ineffective labeling.

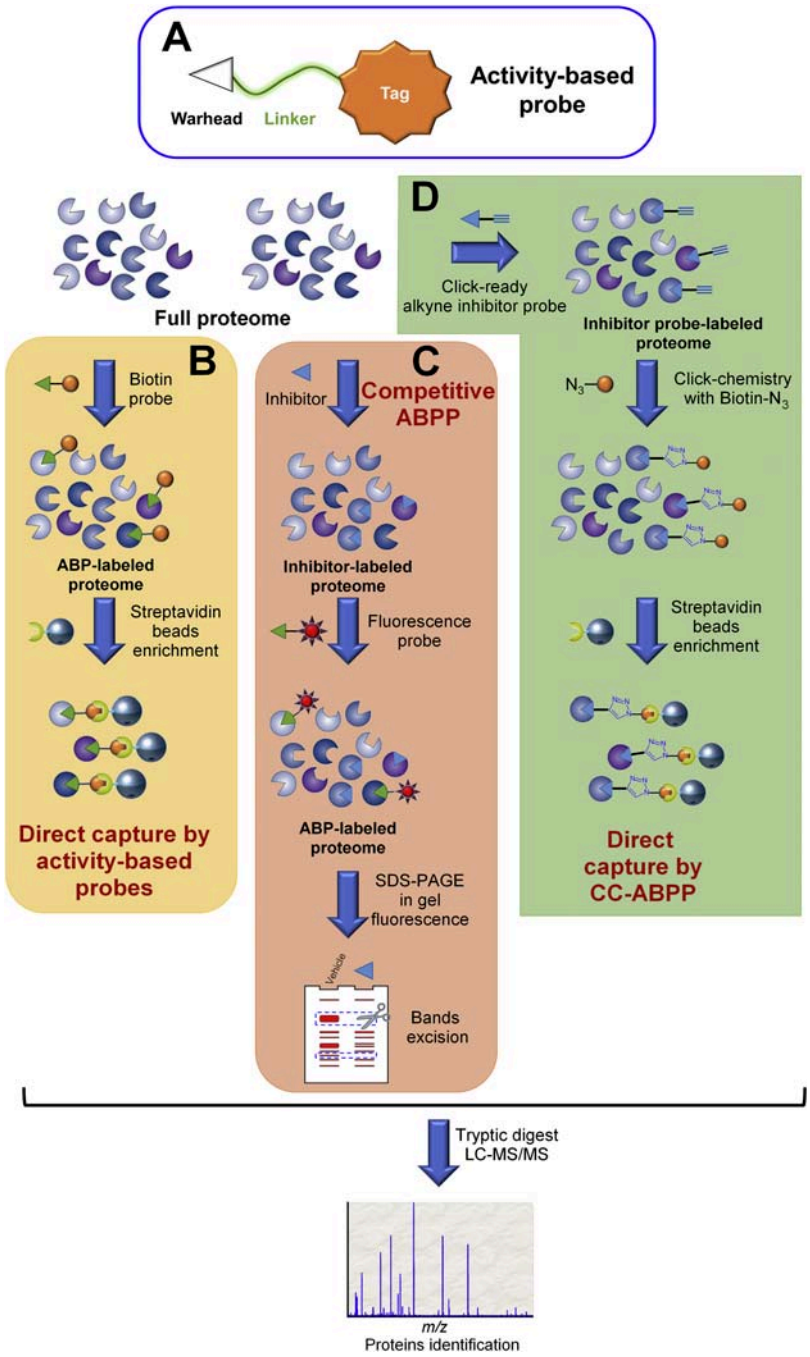

FIGURE 11.2 **(A) General design of an ABP**. Such probes are typically composed of a reactive warhead (triangle representation) responsible for the specificity of the probe for the desire subset of expressed proteins; a linker (in green) which can also add some specificity to the probe; and a tag (in orange) which allows for the identification of targeted proteins by mass spectrometry analysis. This tag can either be a fluorophore for direct visualization, an affinity group such as biotin to perform affinity purification of the targets, or an alkyne or an azide allowing coupling via click-chemistry with any desire tag. **(B–D) Work flow of a typical activity-based protein profiling (ABPP)**

This part will present some of the most significant ABPs that has been used to study mycobacterial SEs and their relative specificity.

Fluorophosphonates as classical ABPs for SEs

FP-ABP is the most widely used SE reactive warhead for ABPP. FP indeed shows a high inhibitory selectivity for nucleophilic serine while showing no reactivity for free hydroxyl groups. Initially developed to target fatty acid amide hydrolase, FP turned out to exhibit a wide spectrum of activity toward SEs, ranging from lipid esterase's to proteases by forming an irreversible covalent bond with the nucleophilic active site serine. Consequently, FP has thus become a classical benchmark for studying SEs.

This type of probe has been used to capture *M. tb*'s SEs in several culture conditions [42,43]. Accordingly, using the **alkyne-PEG-FP** probe and click chemistry ABPP in replicating and nonreplicating *M. tb*, Ortega et al. have identified 78 proteins annotated as hydrolase and hypothetical proteins; among which 34 SEs were found active in both conditions, 41 only active in aerated culture, and three only active in hypoxic culture [43]. Under hypoxia, the activities of the antigen 85 complex and the thioesterase TesA were reduced by around threefold to 10-fold, while the carboxylesterase CaeA retains active in both conditions. Together, these activity changes are consistent with reduced metabolism related to cell-wall biosynthesis during dormancy. In a similar study, Tallman et al. identified 52 SEs with **Desthiobiotin-FP** probe [42], with five esterases active in both normoxic and hypoxic states, including CaeA, suggesting that these enzymes may be promising targets to treat both active and latent TB (Table 11.1).

Competitive ABPP with selective SE inhibitors

Competitive ABPP is a way of performing target identification for a given small molecule inhibitor that is neither an ABP nor possesses any tag to visualize or enrich its targets, as depicted in Fig. 11.2C. The main drawback of this approach resides in the fact that it is mostly an indirect identification by measuring reductions in probe-labeling signals for assessing an inhibitor's target(s). Consequently, competitive ABPP requires additional formal validation to confirm the identified enzymes as effective targets of the tested inhibitor.

This strategy has been successfully applied by Nguyen et al. with two multitarget SE inhibitors: **CyC$_{17}$**, a Cyclipostins analog [44], and **HPOX**, an oxadiazolone-core derivative

experiment. **(B)** Cells or lysate is incubated with a biotin ABP for the **direct capture** of target enzymes through streptavidin affinity enrichment followed by Tryptic digestion and mass spectroscopy analysis. **(C)** When performing **competitive ABPP**, cells or lysate is first pretreated with a covalent inhibitor before incubation with a broad-spectrum fluorescent ABP. Protein targets are further visualized via in gel fluorescence. Bands exhibiting a lower or no fluorescence as compared to the vehicle control lane are excised and the proteins identified by mass spectroscopy. **(D)** Alternatively, **click chemistry ABPP (CC-ABPP)** provides a direct capture of probe-labeling enzymes, by incubating cells or lysate with the click-ready alkyne inhibitor probe prior to perform click-reaction with an azide reporter tag. *Adapted from M.J. Niphakis, B.F. Cravatt, Enzyme inhibitor discovery by activity-based protein profiling, Annu. Rev. Biochem. 83 (2014) 341–377.*

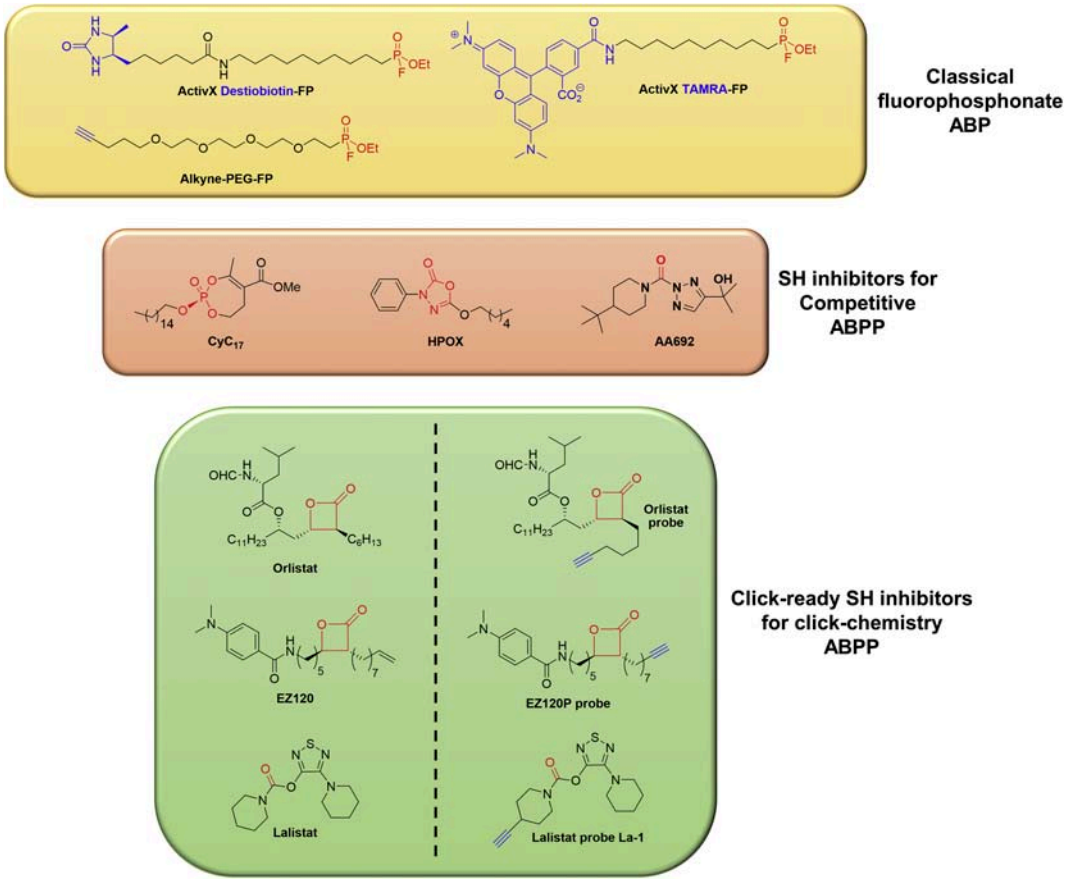

FIGURE 11.3 **Chemical structures of several compounds targeting SEs**. The warhead is colored red, and the reactive tag is colored blue. **TAMRA-FP** and **Desthiobiotin-FP** have been used in regular ABPP on *M. tb* [42]; **HPOX**, **CyC_{17}** and **AA692** have been used in competitive ABPP on *M. tb* [44,45,48]; **Alkyne-Peg-FP**, **Orlistat**, **EZ120**, and **Lalistat** probes have been used in click-chemistry ABPP on *M. tb* or *M. bovis* BCG [43,53,54,57].

[45] (Fig. 11.3) which selectively inhibit *M. tb* growth in culture broth medium with minimal inhibitory concentration (MIC) of 0.5 and 44.6 μM, respectively. Both compounds inhibit SE enzymatic activity by formation of a covalent bond with the catalytic serine residue in the enzyme active site [46]. The comparative proteomic analysis between the control sample and the **HPOX**- or **CyC_{17}**-pretreated sample prior to either **TAMRA-FP** or **Desthiobiotin-FP** labeling, resulted in mass spectrometry identification of a panel of 18 and 23 distinct proteins, respectively (Table 11.1). Remarkably, most of these identified proteins were involved in *M. tb* lipid metabolism and in cell wall biosynthesis. Among them, the bifunctional thioesterase-phospholipase enzyme LipG, the antigen 85 complex and TesA have been further validated as effective targets, and the respective crystal structures of the latter two enzymes in complex with **CyC_{17}** were also solved [46].

TABLE 11.1 Proteins targeted by at least three of the serine enzyme inhibitors as determine by ABPP.

Protein name	Rv number	Alkyne-PEG-FP[a]	Desthiobiotin-FP[b]	HPOX[c]	CyC_{17}[d]	AA692[e]	EZ120[f]	Orlistat[g]	Lalistat[h]
Cfp21	Rv1984c		■	■	■				■
Cut2	Rv2301	■	■	■		■			
LipD	Rv1923	■	■			■		■	
LipE	Rv3775		■		■	■			
LipG	Rv0646c		■		■	■		■	■
LipH	Rv1399c	■	■	■	■			■	■
LipI	Rv1400c	■	■					■	■
LipM	Rv2284	■	■		■	■	■	■	■
LipN	Rv2970c	■	■		■	■		■	■
LipO	Rv1426c		■					■	■
LipV	Rv3203	■	■	■	■			■	
LipW	Rv0217c		■			■		■	
Rv0045c		■	■		■				■
Rv0183		■	■	■	■				■
BpoC	Rv0554			■	■	■			
TesA	Rv2928			■	■	■	■	■	
Ag85A	Rv1886c			■	■	■	■		
Ag85B	Rv3804c			■		■	■		
Ag85C	Rv0129c			■	■	■	■	■	
LH57_07490	Rv1367c			■	■				■
AmiC	Rv2888c			■	■				■
CaeA	Rv2224c	■	■	■	■				
Total hits identified		17	22	18	23	18	5	14	20

Data from [a] [43]; [b] [42]; [c] [45]; [d] [44]; [e] [48]; [f] [57]; [g] [53]; [h] [54]

Compounds 1,2,3-triazole ureas also represent potent and selective inhibitors of SEs through covalent inhibition of their active site serine [47]. More recently and given its ability to restrict *M. tb* growth with a MIC of 12 μM, a competitive ABPP study was conducted with the 1,2,3-triazole urea SE inhibitor **AA692** (Fig. 11.3) [47,48]. By comparing compound- and vehicle-treated *M. tb* with **Desthiobiotin-FP** probe [48], 56 predicted SEs were identified of which 44 have been also detected in previous studies [42,43]. The difference in percent inhibition between **AA692** *versus* an inactive 1,2,3-triazole urea for each detected SE, narrowed the results to 11 prioritized targets (Table 11.1) including Ag85A and Ag85B, TesA and Rv3802, four enzymes involved in cell wall biosynthesis.

Overall, these studies strengthen the fact that such multitarget SE inhibitors preferentially inhibit several key SEs involved in lipid metabolism and in cell wall biosynthesis and thus mainly exert their antibacterial activity by disrupting the mycobacterial cell wall.

Direct capture of SEs *via* click-chemistry ABPP

One limitation of traditional ABPP is due to the size of the tag used, which is typically around 700−1000 Da. This can cause uptake and distribution limitation of the probe when performing target capture in whole cells. By changing the shape and affinity for the targeted proteins, a large tag can also modify the reactivity of the chemical warhead compared to its parent molecule.

To overcome these issues, a label free probe can be used through click-chemistry ABPP (CC-ABPP—Fig. 11.2D) strategy. CC-ABPP consists in using an ABP bearing a smaller clickable group such as an alkyne or an azide, allowing the formation of a stable triazole cycle

between the (enzyme-)probe and a chosen reporter (i.e., a fluorophore, a biotin or another enrichment group or directly with agarose beads) using the copper(I)-catalyzed Huisgen's 1,3-dipolar cycloaddition reaction [49]. Such bio-orthogonal reaction can be performed in aqueous solvent with no harmful byproduct, and all reagents can be purified through non-chromatographic methods like protein precipitation in acetone. CC-ABPP allows the direct capture of enzyme by labeling the same compound. Indeed, it is possible to "click" a biotin or an enrichment group to make affinity purification; or alternatively a fluorophore that allows for protein visualization on an SDS PAGE gel and for fluorescent microscopy to study target repartition and uptake of the probe in whole cell.

Since most of the SE inhibitors characterized in *M. tb* likely act by inhibiting the cell wall biosynthesis, several potent and covalent SEs inhibitors have been chemically modified and further used in CC-ABPP, not only to discover their corresponding targets in *M. tb* but also to delineate key pharmacologically targetable SEs and their associated pathways.

β-Lactones ABPs

Among the potent SE inhibitors, β-Lactones represent an important class of compounds bearing the strained 2-oxetanone 4-membered ring that presents potent inhibitory activity against SEs. The most representative member of this family of inhibitors is the FDA approved antiobesity drug **Orlistat** (Fig. 11.3). **Orlistat** is an active site-directed inhibitor that forms a stoichiometric long-lived acyl-enzyme complex with SE after the nucleophilic attack of the catalytic serine residue on the β-lactone group [50]. Functioning as a versatile SE inhibitor, **Orlistat** was indeed found to inhibit the Cut family including the mycobacterial phospholipase/thioesterase Cut6 [37], as well as the Lip family enzymes [14]. Consequently, when tested as a possible anti-mycobacterial agent, **Orlistat** was found to block *M. tb* growth with MIC ranging from 25 to 50 μM [14,51]. Other work confirmed the ability of **Orlistat** to destabilize the outer membrane of the cell envelope by reducing the amount of PDIM content in the mycobacterial cell wall, facilitating the action of Vancomycin; and thus, highlighted its synergetic antimycobacterial action in combination with Vancomycin to inhibit *M. bovis* BCG and *M. tb* growth [52]. Based on this result, a CC-ABPP approach on whole cell lysates of *M. bovis* BCG culture using an **Orlistat-probe** resulted in identifying 14 enzymes targeted, in which 10 were SEs. These included nine Lip-enzymes and TesA. Cellular overexpression of TesA further led to a decreased susceptibility of the *M. bovis* BCG to **Orlistat**, thus providing target validation [53].

In an attempt to improve the effect of **Orlistat** toward *M. tb* growth, a collection of β-lactones was examined for their antibacterial activity and compound **EZ120** (Fig. 11.3) has emerged as a potent effective and exclusive antibacterial inhibitor against *M. tb* H37Rv with MIC value of 1.6 μM and low cytotoxicity to mouse macrophages [54]. CC-ABPP approach with the alkyne-modified **EZ120P** probe allows identification of Ag85A and the C-terminal thioesterase domain of polyketide synthase 13 (TE-Pks13) as the two main targets of this inhibitor (Table 11.1). Since TE-Pks13 and Ag85 enzymes catalyze essential steps in mycolic acid biosynthesis, additional experiments demonstrated that **EZ120** was capable of decreasing the pool of mycolate α-chains. Moreover, and similar to **Orlistat**, the combined application of **EZ120** and Vancomycin led to a 100-fold and fourfold reduced MIC, respectively, compared to individual treatment. All together, these results support that **EZ120** inhibits mycolic acid biosynthesis.

Lalistat ABP

Similar to **Orlistat**, **Lalistat** (Fig. 11.3), a thiadiazole carbamate initially designed to inhibit the human lysosomal acid lipase [55], binds covalently to the active site serine of SEs and thereby inhibits their activity. Given the structural and electronic properties of **Lalistat**, it was anticipated that such inhibitor will react with diverse mycobacterial enzymes which may deviate from the Orlistat target spectrum. When tested on *M. tb* growth, **Lalistat** exhibited a MIC of 25−50 μM [54]. Interestingly, **Lalistat** displayed a strong synergetic effect in combination with Vancomycin resulting in a MIC dropt of around four- and 16-times for **Lalistat** and Vancomycin, respectively. Again, when tested on *M. tb* infected human macrophages, **Lalistat** was found to substantially reduce bacterial load by 55% compared to the untreated control suggesting that it could even address intracellular bacteria [54]. Target identification experiments via CC-ABPP using a **Lalistat** probe analog bearing a terminal alkyne tag (**La-1**, Fig. 11.3) on *M. tb* cells provided 20 target enzymes, including eight Lip-enzymes as well as the MAG lipase Rv0183, the Cutinase-like protein Cfp21 and the esterase Rv0045c (Table 11.1). Interestingly, comparison of these results with those previously reported with **Orlistat** proteome labeling studies in *M. bovis* BCG revealed LipM, −O, −N, −I and -G as shared targets [53], while LipR and -T were additionally captured by **Lalistat** [54].

Conclusion and prospects

M. tb produces more than 100 major lipid end products [28,56], most of them being involved in the architecture of the cell wall. The complexity of these mycobacterial lipids is reflected by the large number of *M. tb* genes encoding for proteins participating in these processes. Among these latter enzymes, mycobacterial SEs play a central role in lipid metabolism and represent thus essential key players in survival, persistence, and virulence of the bacilli [3,4].

To date, all reported SE inhibitors displaying antimycobacterial activity, target multiple enzymes, mainly involved in cell wall biosynthesis. Interestingly, the Ag85 A/B/C proteins have been captured and validated as effective targets of most of tested SE inhibitors in *M. tb* [38,45,48,57], but also in *M. abscessus* [58,59] an opportunistic pathogen responsible for chronic lung infection in patients with respiratory diseases such as cystic fibrosis [60]. Indeed, since the Ag85 A/B/C proteins are among the most abundantly secreted enzymes in *M. tb* [61], they may thus be easily accessible to the inhibitor probe, suggesting that these mycolyltransferases would be a common primary target of the SE inhibitors, regardless of the mycobacterial strain tested. Moreover, as highlighted in the case of **Lalistat** and β-lactone derivatives, their use in combination with known anti-TB drugs may offer a great opportunity to improve and shorten antibiotics therapy.

All these findings clearly state that SEs represent a broad, but biologically significant, enzyme superfamily with promising therapeutic applications against *M. tb*, but also toward all mycobacterial-related diseases.

More particularly, the use of selective click-ready SE inhibitor probes is a major asset for the in vivo identification of mycobacterial SEs together with their respective associated

physiological pathways, notably focusing on the accumulation and consumption of ILI at key stages of the bacterial infection [2] (for an extensive review on this topic, refer to the chapter entitled "***Intrabacterial Lipid Inclusions: overview of an amazing organelle***"). Indeed, to date, no ABPP experiments have been conducted on *M. tb* under conditions stimulating the import and process of host-derived free fatty acids which are subsequently resynthesized into TAG and stored in the form of ILI. Under such nutrient-limiting conditions, ILI constitutes an essential source of carbon and nutrients required for *M. tb* survival and persistence for extensive periods of time. A critical link between such lipid accumulation and the development of phenotypic drug-resistance in *M. tb* has also been established, therefore suggesting that lipid biosynthetic genes might be appropriate targets for novel drugs that could kill *M. tb* in latent phase [62].

Using ABPP approach, more than 80 SEs have been identified so far. Among these enzymes, a shift in the activity of over 30% was observed in relation to dormant growth conditions, including hypoxia and carbon starvation [42,43,53]. Accordingly, small molecule inhibitors represent interesting chemical tools that allow simultaneous and selective detection/inhibition of SEs in living mycobacteria.

In this context, the use of ABPP will provide a comprehensive map of the SEs involved in ILI formation (i.e., entry into dormancy) and degradation (i.e., reactivation step). Deciphering the physiological role of the mycobacterial SEs involved in these processes will generate results that are directly relevant for better understanding the pathogenesis of actively replicating and latent bacilli and will contribute to discover new chemotherapeutic targets in the fight against *M. tb*.

Acknowledgments

This work was supported by the Center National de la Recherche Scientifique (CNRS), Aix-Marseille University (AMU), the Association Grégory Lemarchal and Vaincre la Mucoviscidose (project N° RF20190502466), and the Agence Nationale de la Recherche (LipInTB project N°ANR-19-CE44-0011).

References

[1] WHO, Global Tuberculosis Report, 2021. https://www.who.int/teams/global-tuberculosis-programme/data.
[2] I. Mallick, P. Santucci, I. Poncin, V. Point, L. Kremer, J.F. Cavalier, S. Canaan, Intrabacterial lipid inclusions in mycobacteria: unexpected key players in survival and pathogenesis? FEMS Microbiol Rev (2021) fuab029. https://doi.org/10.1093/femsre/fuab029.
[3] G. Singh, G. Singh, D. Jadeja, J. Kaur, Lipid hydrolizing enzymes in virulence: *Mycobacterium tuberculosis* as a model system, Crit. Rev. Microbiol. 36 (2010) 259–269.
[4] G. Johnson, The alpha/beta hydrolase fold proteins of *Mycobacterium tuberculosis*, with reference to their contribution to virulence, Curr. Protein Pept. Sci. 18 (2017) 190–210.
[5] L. Dedieu, C. Serveau-Avesque, L. Kremer, S. Canaan, Mycobacterial lipolytic enzymes: a gold mine for tuberculosis research, Biochimie 95 (2013) 66–73.
[6] L.J. Keller, B.M. Babin, M. Lakemeyer, M. Bogyo, Activity-based protein profiling in bacteria: applications for identification of therapeutic targets and characterization of microbial communities, Curr. Opin. Chem. Biol. 54 (2020) 45–53.
[7] S.T. Cole, R. Brosch, J. Parkhill, T. Garnier, C. Churcher, D. Harris, S.V. Gordon, K. Eiglmeier, S. Gas, C.E. Barry 3rd, F. Tekaia, K. Badcock, D. Basham, D. Brown, T. Chillingworth, R. Connor, R. Davies, K. Devlin, T. Feltwell, S. Gentles, N. Hamlin, S. Holroyd, T. Hornsby, K. Jagels, A. Krogh, J. McLean, S. Moule, L. Murphy, K. Oliver, J. Osborne, M.A. Quail, M.A. Rajandream, J. Rogers, S. Rutter, K. Seeger,

J. Skelton, R. Squares, S. Squares, J.E. Sulston, K. Taylor, S. Whitehead, B.G. Barrell, Deciphering the biology of *Mycobacterium tuberculosis* from the complete genome sequence, Nature 393 (1998) 537–544.
[8] M. Nardini, B.W. Dijkstra, Alpha/beta hydrolase fold enzymes: the family keeps growing, Curr. Opin. Struct. Biol. 9 (1999) 732–737.
[9] J.D. Schrag, M. Cygler, Lipases and alpha/beta hydrolase fold, Methods Enzymol. 284 (1997) 85–107.
[10] M. Holmquist, Alpha/Beta-hydrolase fold enzymes: structures, functions and mechanisms, Curr. Protein Pept. Sci. 1 (2000) 209–235.
[11] S. Raza, L. Fransson, K. Hult, Enantioselectivity in Candida Antarctica lipase B: a molecular dynamics study, Protein Sci. 10 (2001) 329–338.
[12] S. Shin, T.H. Lee, N.C. Ha, H.M. Koo, S.Y. Kim, H.S. Lee, Y.S. Kim, B.H. Oh, Structure of malonamidase E2 reveals a novel Ser-cisSer-Lys catalytic triad in a new serine hydrolase fold that is prevalent in nature, EMBO J. 21 (2002) 2509–2516.
[13] A. Dessen, J. Tang, H. Schmidt, M. Stahl, J.D. Clark, J. Seehra, W.S. Somers, Crystal structure of human cytosolic phospholipase A2 reveals a novel topology and catalytic mechanism, Cell 97 (1999) 349–360.
[14] V. Delorme, S.V. Diomande, L. Dedieu, J.F. Cavalier, F. Carriere, L. Kremer, J. Leclaire, F. Fotiadu, S. Canaan, MmPPOX inhibits *Mycobacterium tuberculosis* lipolytic enzymes belonging to the hormone-sensitive lipase family and alters mycobacterial growth, PLoS One 7 (2012) e46493.
[15] C. Deb, J. Daniel, T.D. Sirakova, B. Abomoelak, V.S. Dubey, P.E. Kolattukudy, A novel lipase belonging to the hormone-sensitive lipase family induced under starvation to utilize stored triacylglycerol in *Mycobacterium tuberculosis*, J. Biol. Chem. 281 (2006) 3866–3875.
[16] N. Kapoor, S. Pawar, T.D. Sirakova, C. Deb, W.L. Warren, P.E. Kolattukudy, Human granuloma in vitro model, for TB dormancy and resuscitation, PLoS One 8 (2013) e53657.
[17] M.H. Daleke, A. Cascioferro, K. de Punder, R. Ummels, A.M. Abdallah, N. van der Wel, P.J. Peters, J. Luirink, R. Manganelli, W. Bitter, Conserved Pro-Glu (PE) and Pro-Pro-Glu (PPE) protein domains target LipY lipases of pathogenic mycobacteria to the cell surface via the ESX-5 pathway, J. Biol. Chem. 286 (2011) 19024–19034.
[18] P. Santucci, S. Diomande, I. Poncin, L. Alibaud, A. Viljoen, L. Kremer, C. de Chastellier, S. Canaan, Delineating the physiological roles of the PE and catalytic domains of LipY in lipid consumption in mycobacterium-infected foamy macrophages, Infect. Immun. 86 (2018).
[19] P. Santucci, N. Smichi, S. Diomande, I. Poncin, V. Point, H. Gaussier, J.F. Cavalier, L. Kremer, S. Canaan, Dissecting the membrane lipid binding properties and lipase activity of *Mycobacterium tuberculosis* LipY domains, FEBS J. 286 (2019) 3164–3181.
[20] K. Cotes, R. Dhouib, I. Douchet, H. Chahinian, A. de Caro, F. Carriere, S. Canaan, Characterization of an exported monoglyceride lipase from *Mycobacterium tuberculosis* possibly involved in the metabolism of host cell membrane lipids, Biochem. J. 408 (2007) 417–427.
[21] R. Dhouib, F. Laval, F. Carriere, M. Daffe, S. Canaan, A monoacylglycerol lipase from Mycobacterium smegmatis Involved in bacterial cell interaction, J. Bacteriol. 192 (2010) 4776–4785.
[22] P. Santucci, V. Point, I. Poncin, A. Guy, C. Crauste, C. Serveau-Avesque, J.M. Galano, C.D. Spilling, J.F. Cavalier, S. Canaan, LipG a bifunctional phospholipase/thioesterase involved in mycobacterial envelope remodeling, Biosci. Rep. 38 (2018).
[23] P.C. Nguyen, V.S. Nguyen, B.P. Martin, P. Fourquet, L. Camoin, C.D. Spilling, J.F. Cavalier, C. Cambillau, S. Canaan, Biochemical and structural characterization of TesA, a major thioesterase required for outer-envelope lipid biosynthesis in *Mycobacterium tuberculosis*, J. Mol. Biol. 430 (2018) 5120–5136.
[24] R. Rastogi, A. Kumar, J. Kaur, V. Saini, J. Kaur, A. Bhatnagar, Rv0646c, an esterase from *M. tuberculosis*, upregulates the host immune response in THP-1 macrophages cells, Mol. Cell. Biochem. 447 (2018) 189–202.
[25] Y.V. Cavalcanti, M.C. Brelaz, J.K. Neves, J.C. Ferraz, V.R. Pereira, Role of TNF-alpha, IFN-gamma, and IL-10 in the development of pulmonary tuberculosis, Pulm. Med. 2012 (2012) 745483.
[26] L. Alibaud, Y. Rombouts, X. Trivelli, A. Burguiere, S.L. Cirillo, J.D. Cirillo, J.F. Dubremetz, Y. Guerardel, G. Lutfalla, L. Kremer, A Mycobacterium marinum TesA mutant defective for major cell wall-associated lipids is highly attenuated in *Dictyostelium discoideum* and zebrafish embryos, Mol. Microbiol. 80 (2011) 919–934.
[27] J. Yu, V. Tran, M. Li, X. Huang, C. Niu, D. Wang, J. Zhu, J. Wang, Q. Gao, J. Liu, Both phthiocerol dimycocerosates and phenolic glycolipids are required for virulence of *Mycobacterium marinum*, Infect. Immun. 80 (2012) 1381–1389.
[28] M. Jackson, The mycobacterial cell envelope—lipids, Cold Spring Harbor Perspecti. Med. 4 (2014).

[29] S. Lun, W.R. Bishai, Characterization of a novel cell wall-anchored protein with carboxylesterase activity required for virulence in *Mycobacterium tuberculosis*, J. Biol. Chem. 282 (2007) 18348–18356.
[30] J. Rengarajan, E. Murphy, A. Park, C.L. Krone, E.C. Hett, B.R. Bloom, L.H. Glimcher, E.J. Rubin, *Mycobacterium tuberculosis* Rv2224c modulates innate immune responses, Proc. Natl. Acad. Sci. U. S. A. 105 (2008) 264–269.
[31] J.L. Naffin-Olivos, M. Georgieva, N. Goldfarb, R. Madan-Lala, L. Dong, E. Bizzell, E. Valinetz, G.S. Brandt, S. Yu, D.E. Shabashvili, D. Ringe, B.M. Dunn, G.A. Petsko, J. Rengarajan, *Mycobacterium tuberculosis* Hip1 modulates macrophage responses through proteolysis of GroEL2, PLoS Pathog. 10 (2014) e1004132.
[32] M. Srinivas, S. Rajakumari, Y. Narayana, B. Joshi, V.M. Katoch, R. Rajasekharan, K.N. Balaji, Functional characterization of the phospholipase C activity of Rv3487c and its localization on the cell wall of *Mycobacterium tuberculosis*, J. Biosci. 33 (2008) 221–230.
[33] L. Richter, B. Saviola, The lipF promoter of *Mycobacterium tuberculosis* is upregulated specifically by acidic pH but not by other stress conditions, Microbiol. Res. 164 (2009) 228–232.
[34] L.R. Camacho, D. Ensergueix, E. Perez, B. Gicquel, C. Guilhot, Identification of a virulence gene cluster of *Mycobacterium tuberculosis* by signature-tagged transposon mutagenesis, Mol. Microbiol. 34 (1999) 257–267.
[35] N.P. West, F.M. Chow, E.J. Randall, J. Wu, J. Chen, J.M. Ribeiro, W.J. Britton, Cutinase-like proteins of *Mycobacterium tuberculosis*: characterization of their variable enzymatic functions and active site identification, Faseb. J. 23 (2009) 1694–1704.
[36] M. Schue, D. Maurin, R. Dhouib, J.C. Bakala N'Goma, V. Delorme, G. Lambeau, F. Carriere, S. Canaan, Two cutinase-like proteins secreted by *Mycobacterium tuberculosis* show very different lipolytic activities reflecting their physiological function, Faseb. J. 24 (2010) 1893–1903.
[37] S.K. Parker, R.M. Barkley, J.G. Rino, M.L. Vasil, *Mycobacterium tuberculosis* Rv3802c encodes a phospholipase/thioesterase and is inhibited by the antimycobacterial agent tetrahydrolipstatin, PLoS One 4 (2009) e4281.
[38] A. Viljoen, M. Richard, P.C. Nguyen, P. Fourquet, L. Camoin, R.R. Paudal, G.R. Gnawali, C.D. Spilling, J.F. Cavalier, S. Canaan, M. Blaise, L. Kremer, Cyclipostins and cyclophostin analogs inhibit the antigen 85C from *Mycobacterium tuberculosis* both in vitro and in vivo, J. Biol. Chem. 293 (2018) 2755–2769.
[39] D.R. Ronning, V. Vissa, G.S. Besra, J.T. Belisle, J.C. Sacchettini, *Mycobacterium tuberculosis* antigen 85A and 85C structures confirm binding orientation and conserved substrate specificity, J. Biol. Chem. 279 (2004) 36771–36777.
[40] F. Faucher, J.M. Bennett, M. Bogyo, S. Lovell, Strategies for tuning the selectivity of chemical probes that target serine hydrolases, Cell Chem. Biol. 27 (2020) 937–952.
[41] M.J. Niphakis, B.F. Cravatt, Enzyme inhibitor discovery by activity-based protein profiling, Annu. Rev. Biochem. 83 (2014) 341–377.
[42] K.R. Tallman, S.R. Levine, K.E. Beatty, Small molecule probes reveal esterases with persistent activity in dormant and reactivating *Mycobacterium tuberculosis*, ACS Infect. Dis. 2 (2016) 936–944.
[43] C. Ortega, L.N. Anderson, A. Frando, N.C. Sadler, R.W. Brown, R.D. Smith, A.T. Wright, C. Grundner, Systematic survey of serine hydrolase activity in *Mycobacterium tuberculosis* defines changes associated with persistence, Cell Chem. Biol. 23 (2016) 290–298.
[44] P.C. Nguyen, V. Delorme, A. Bénarouche, B.P. Martin, R. Paudel, G.R. Gnawali, A. Madani, R. Puppo, V. Landry, L. Kremer, P. Brodin, C.D. Spilling, J.-F. Cavalier, S. Canaan, Cyclipostins and Cyclophostin analogs as promising compounds in the fight against tuberculosis, Sci. Rep. 7 (2017) 11751.
[45] P.C. Nguyen, V. Delorme, A. Bénarouche, A. Guy, V. Landry, S. Audebert, M. Pophillat, L. Camoin, C. Crauste, J.-M. Galano, T. Durand, P. Brodin, S. Canaan, J.-F. Cavalier, Oxadiazolone derivatives, new promising multitarget inhibitors against *M. tuberculosis*, Bioorg. Chem. 81 (2018) 414–424.
[46] J.F. Cavalier, C.D. Spilling, T. Durand, L. Camoin, S. Canaan, Lipolytic enzymes inhibitors: a new way for antibacterial drugs discovery, Eur. J. Med. Chem. 209 (2021) 112908.
[47] A. Adibekian, B.R. Martin, C. Wang, K.L. Hsu, D.A. Bachovchin, S. Niessen, H. Hoover, B.F. Cravatt, Click-generated triazole ureas as ultrapotent in vivo-active serine hydrolase inhibitors, Nat. Chem. Biol. 7 (2011) 469–478.
[48] M. Li, H.V. Patel, A.B. Cognetta, T.C. Smith, I. Mallick, J.-F. Cavalier, S. Canaan, B.B. Aldridge, B.F. Cravatt, J.C. Seeliger, A competitive activity-based protein profiling platform yields cell wall synthesis inhibitors active against replicating and non-replicating *Mycobacterium tuberculosis*, bioRxiv (2021), 2021.2004.2016.440156.
[49] S. Díez-González, Chapter three - Copper(I)–Acetylides: access, structure, and relevance in catalysis, in: P.J. Pérez (Ed.), Advances in Organometallic Chemistry, Academic Press, 2016, pp. 93–141.

[50] P. Hadváry, W. Sidler, W. Meister, W. Vetter, H. Wolfer, The lipase inhibitor tetrahydrolipstatin binds covalently to the putative active site serine of pancreatic lipase, J. Biol. Chem. 266 (1991) 2021–2027.
[51] P. Santucci, C. Dedaki, A. Athanasoulis, L. Gallorini, A. Munoz, S. Canaan, J.F. Cavalier, V. Magrioti, Synthesis of long-chain beta-lactones and their antibacterial activities against pathogenic mycobacteria, ChemMedChem 14 (2019) 349–358.
[52] C. Rens, F. Laval, M. Daffe, O. Denis, R. Frita, A. Baulard, R. Wattiez, P. Lefevre, V. Fontaine, Effects of lipid-lowering drugs on Vancomycin susceptibility of mycobacteria, Antimicrob. Agents Chemother. 60 (2016) 6193–6199.
[53] M.S. Ravindran, M.R. Wenk, Activity-based lipid esterase profiling of M. Bovis BCG at different metabolic states using tetrahydrolipstatin (THL) as bait, in: H.S. Overkleeft, B.I. Florea (Eds.), Activity-Based Proteomics: Methods and Protocols, Springer New York, New York, NY, 2017, pp. 75–85.
[54] J. Lehmann, J. Vomacka, K. Esser, M. Nodwell, K. Kolbe, P. Ramer, U. Protzer, N. Reiling, S.A. Sieber, Human lysosomal acid lipase inhibitor lalistat impairs *Mycobacterium tuberculosis* growth by targeting bacterial hydrolases, MedChemComm 7 (2016) 1797–1801.
[55] A.I. Rosenbaum, C.C. Cosner, C.J. Mariani, F.R. Maxfield, O. Wiest, P. Helquist, Thiadiazole carbamates: potent inhibitors of lysosomal acid lipase and potential Niemann-Pick type C disease therapeutics, J. Med. Chem. 53 (2010) 5281–5289.
[56] E. Layre, R. Al-Mubarak, J.T. Belisle, D. Branch Moody, Mycobacterial lipidomics, Microbiol. Spectr. 2 (2014), 2.3.03.
[57] J. Lehmann, T.Y. Cheng, A. Aggarwal, A.S. Park, E. Zeiler, R.M. Raju, T. Akopian, O. Kandror, J.C. Sacchettini, D.B. Moody, E.J. Rubin, S.A. Sieber, An antibacterial beta-lactone kills *Mycobacterium tuberculosis* by disrupting mycolic acid biosynthesis, Angew. Chem. Int. Ed. 57 (2018) 348–353.
[58] A. Madani, I. Mallick, A. Guy, C. Crauste, T. Durand, P. Fourquet, S. Audebert, L. Camoin, S. Canaan, J.F. Cavalier, Dissecting the antibacterial activity of oxadiazolone-core derivatives against *Mycobacterium abscessus*, PLoS One 15 (2020) e0238178.
[59] A. Madani, J.N. Ridenour, B.P. Martin, R.R. Paudel, A. Abdul Basir, V. Le Moigne, J.L. Herrmann, S. Audebert, L. Camoin, L. Kremer, C.D. Spilling, S. Canaan, J.F. Cavalier, Cyclipostins and cyclophostin analogues as multi-target inhibitors that impair growth of *Mycobacterium abscessus*, ACS Infect. Dis. 5 (2019) 1597–1608.
[60] M.D. Johansen, J.-L. Herrmann, L. Kremer, Non-tuberculous mycobacteria and the rise of *Mycobacterium abscessus*, Nat. Rev. Microbiol. 18 (2020) 392–407.
[61] G. Harth, B.Y. Lee, J. Wang, D.L. Clemens, M.A. Horwitz, Novel insights into the genetics, biochemistry, and immunocytochemistry of the 30-kilodalton major extracellular protein of *Mycobacterium tuberculosis*, Infect. Immun. 64 (1996) 3038–3047.
[62] C. Deb, C.M. Lee, V.S. Dubey, J. Daniel, B. Abomoelak, T.D. Sirakova, S. Pawar, L. Rogers, P.E. Kolattukudy, A novel in vitro multiple-stress dormancy model for *Mycobacterium tuberculosis* generates a lipid-loaded, drug-tolerant, dormant pathogen, PLoS One 4 (2009) e6077.

Article II

Synthesis and Biological Characterization of Fluorescent Cyclipostins and Cyclophostin Analogues: New Insights for the Diagnosis of Mycobacterial-Related Diseases

---

M. Sarrazin*, B.P. Martin*, **R. Avellan***, G.R. Gnawali*, I. Poncin, H. Le Guenno, C.D. Spilling, J.-F. Cavalier, S. Canaan

ACS Infect Dis 2022, 8 (12), 2564-2578.
https://doi.org/10.1021/acsinfecdis.2c00448

* Contribution égale

Les infections par des mycobactéries sont responsables de nombreuses morbidités et décès. En plus de la tuberculose causée par *M. tb* [22], les mycobactéries non-tuberculeuses (MNT) sont également responsables de nombreuses infections pulmonaires chez les patients présentant des défenses immunitaires réduites [185, 387], mais également cutanées (*M .abs*, *M. ulcerans* et *M. marinum*) [388]. Bien que l'on compte plus de 200 espèces de MNT [389], *M. avium* et les espèces du complexe MABc représentent 90% des infections pulmonaires dues aux MNT [390, 391].

M. abs est responsable d'infections pulmonaires pseudo-granulomateuses semblables à la tuberculose chez les patients immunodéficients [392] et chez les patients atteints de pathologies pulmonaires comme la mucoviscidose et la bronchiectasie [100, 141, 393]. Chez les patients atteints de mucoviscidose, les infections à *M. abs* représentent une contre-indication à la greffe de poumons en raison des risques d'infection post-chirurgie, alors que cette option est parfois la seule pour les patients [394]. Ces infections à *M. abs* sont d'autant plus problématiques que cette mycobactérie est connue pour sa poly-résistance naturelle à la plupart des antibiotiques utilisés en clinique, étant qualifiée de « cauchemar pour les antibiotiques » [111].

De plus, les patients atteints de mucoviscidose présentent généralement des infections pulmonaires poly-bactériennes [395, 396] incluant des bactéries à Gram-négatifs (*P. aeruginosa*, *Haemophilus influenzae*, et le complexe *Burkholderia cepacia*), et à Gram-positifs (*Staphylococcus aureus*), et des mycobactéries avec notamment *M. abs* qui représentent 68% des isolats d'infection aux MNT [141, 397, 398].

Il y a donc nécessité de rechercher de nouveaux antibiotiques pour lutter contre ces infections polymicrobiennes impliquant des mycobactéries, ainsi que de nouveaux outil de diagnostic pour rapidement les identifier et adapter les traitements en conséquence.

C'est donc dans ce contexte que les analogues de **CyC** ont été investigués dans cette étude, à la fois pour comprendre leur mécanisme d'action, mais également pour exploiter la sélectivité de ces composés pour les mycobactéries afin de développer un nouvel outil de diagnostic pour ces infections.

Une série de 38 analogues de **CyC** a présenté des activités d'inhibition de croissance à la fois *in vitro* et en contexte d'infection de macrophages chez *M. tb* et *M. abs* [336, 344]. De plus,

ces composés ont été testés pour leur activité antimicrobienne sur plusieurs souches de bactéries responsables d'infections nosocomiales comprenant 6 bactéries à Gram-négatif et 5 bactéries à Gram-positif [335]. Certains **CyC** ont montré une activité contre des mycobactéries à croissance rapide comme *M. abs*, *M. marinum* ou *M. bovis* BCG mais aucun composé n'a montré d'activité contre les souches non mycobactériennes testées [351].

En particulier, le **CyC$_{17}$** a montré une très bonne activité contre *M. abs* et *M. tb,* comparable aux activités de certains antibiotiques de référence [336, 351]. D'autre part les **CyC$_{7\alpha}$** et **CyC$_{7\beta}$** se sont montrés capables d'inhiber la croissance intracellulaire de *M. tb* [336] et *M. abs* [351] dans un modèle d'infection de macrophages murin Raw264.7 avec des activités supérieures aux antibiotiques de référence, rifampicine et imipenème.

Dans cette étude, nous reportons la synthèse de nouveaux analogues des **CyC$_{17}$**, **CyC$_{7\alpha}$** et **CyC$_{7\beta}$** porteurs d'un groupement fluorophore, le Dansyl, de façon à monitorer leur pénétration et leur répartition à la fois dans différentes souches bactériennes et dans des macrophages sains ou en contexte d'infection [399, 400].

Ces nouveaux **CyC** fluorescents nous ont ainsi permis de mieux comprendre l'absence d'activité des **CyC** sur les bactéries à Gram-négatif et à Gram-positif, mais également leur mode d'action intracellulaire contre *M. abs*. En effet, nous avons pu montrer que les **CyC** actifs sur la croissance intracellulaire s'accumulent dans des compartiments acides au sein des macrophages et que cette accumulation est essentielle pour leur activité intracellulaire à travers leur délivrance dans les phagosomes contenant *M. abs*. Nous avons également pu montrer que la disruption de l'acidification des lysosomes, en utilisant la Concanamycin A, un inhibiteur de la pompe à proton vacuolaire eucaryote, conduisait à une abolition de cette localisation subcellulaire de nos composés ainsi qu'à une perte de leur activité.

Enfin, nous avons montré que ces composés pénétraient de façon spécifique dans les mycobactéries, expliquant leur absence d'activité sur les bactéries à Gram-négatif et à Gram-positif dans lesquelles ils ne pénètrent pas. Ces résultats nous ont donc conduit à montrer que les **CyC** fluorescents pouvaient permettre de marquer de façon spécifique les mycobactéries dans un mélange bactérien contenant d'autres pathogènes comme *P. aeruginosa* et *S. aureus.* Ces résultats ouvrent la porte à l'utilisation de ces molécules en tant que puissants outils de diagnostic des infections mycobactériennes.

ACS Infectious Diseases

pubs.acs.org/journal/aidcbc

Article

Synthesis and Biological Characterization of Fluorescent Cyclipostins and Cyclophostin Analogues: New Insights for the Diagnosis of Mycobacterial-Related Diseases

Morgane Sarrazin, Benjamin P. Martin, Romain Avellan, Giri Raj Gnawali, Isabelle Poncin, Hugo Le Guenno, Christopher D. Spilling,* Jean-François Cavalier,* and Stéphane Canaan*

Cite This: *ACS Infect. Dis.* 2022, 8, 2564−2578

Read Online

ACCESS | Metrics & More | Article Recommendations | Supporting Information

ABSTRACT: Patients with cystic fibrosis (CF) have a significantly higher risk of acquiring nontuberculous mycobacteria infections, predominantly due to *Mycobacterium abscessus*, than the healthy population. Because *M. abscessus* infections are a major cause of clinical decline and morbidity in CF patients, improving treatment and the detection of this mycobacterium in the context of a polymicrobial culture represents a critical component to better manage patient care. We report here the synthesis of fluorescent Dansyl derivatives of four active cyclipostins and cyclophostin analogues (**CyCs**) and provide new insights regarding the **CyC**'s lack of activity against Gram-negative and Gram-positive bacteria, and above all into their mode of action against intramacrophagic *M. abscessus* cells. Our results pointed out that the intracellularly active **CyC** accumulate in acidic compartments within macrophage cells, that this accumulation appears to be essential for their delivery to mycobacteria-containing phagosomes, and consequently, for their antimicrobial effect against intracellular replicating *M. abscessus*, and that modification of such intracellular localization via disruption of endolysosomal pH strongly affects the **CyC** accumulation and efficacy. Moreover, we discovered that these fluorescent compounds could become efficient probes to specifically label mycobacterial species with high sensitivity, including *M. abscessus* in the presence several other pathogens like *Pseudomonas aeruginosa* and *Staphylococcus aureus*. Collectively, all present and previous data emphasized the therapeutic potential of unlabeled **CyCs** and the attractiveness of the fluorescent **CyC** as a potential new efficient diagnostic tool to be exploited in future diagnostic developments against mycobacterial-related infections, especially against *M. abscessus*.

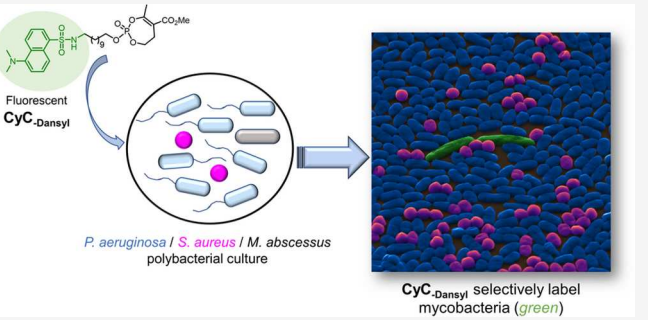

KEYWORDS: *drug susceptibility, fluorescence microscopy, M. abscessus, probes*

Downloaded via INIST-CNRS on December 16, 2022 at 13:48:18 (UTC).
See https://pubs.acs.org/sharingguidelines for options on how to legitimately share published articles.

Pulmonary diseases caused by mycobacterial species still continue to result in significant morbidity and mortality to human health. In addition to *Mycobacterium tuberculosis* the ethiologic agent of tuberculosis (TB),[1] nontuberculous mycobacteria (NTM) are opportunistic pathogens responsible for a wide spectrum of clinical syndromes, ranging from skin infections (i.e., *Mycobacterium ulcerans* and *Mycobacterium marinum*[2]) to pulmonary infections (*Mycobacterium avium* and *Mycobacterium abscessus* complexes) in humans with compromised natural defenses.[3,4] Although the NTM group comprises more than 200 different species,[5] *M. avium* and *M. abscessus* complexes are the most frequently encountered pathogenic species. They are associated with pulmonary diseases, accounting for >90% of all reported cases of NTM-pulmonary infection.[6,7] *M. abscessus* causes TB-like pulmonary diseases in immunocompromised[8] and vulnerable individuals, including cystic fibrosis (CF) and bronchiectasis patients.[9−11] *M. abscessus* exists as two distinct colony morphotypes, smooth (S) and rough (R), which may evolve differently in response to host immunity, resulting in different fates for the mycobacteria in its host.[12−14] The R variant is often associated with severe pulmonary infections[15,16] and is likely to persist for years, especially in infected CF patients.[17] Moreover, the lung infection of CF patients is usually polybacterial[18,19] including combinations of Gram-negative (i.e., *Pseudomonas aeruginosa*, *Haemophilus influenzae*, and *Burkholderia cepacia* complex) and Gram-positive bacteria (i.e., *Staphylococcus aureus*), as well as NTM species where *M. abscessus* represents up to 68% of all isolated NTM.[9,20,21] Furthermore, because this mycobacterium is one of the most drug-resistant mycobacterial species, often

Received: September 1, 2022
Published: November 15, 2022



© 2022 American Chemical Society

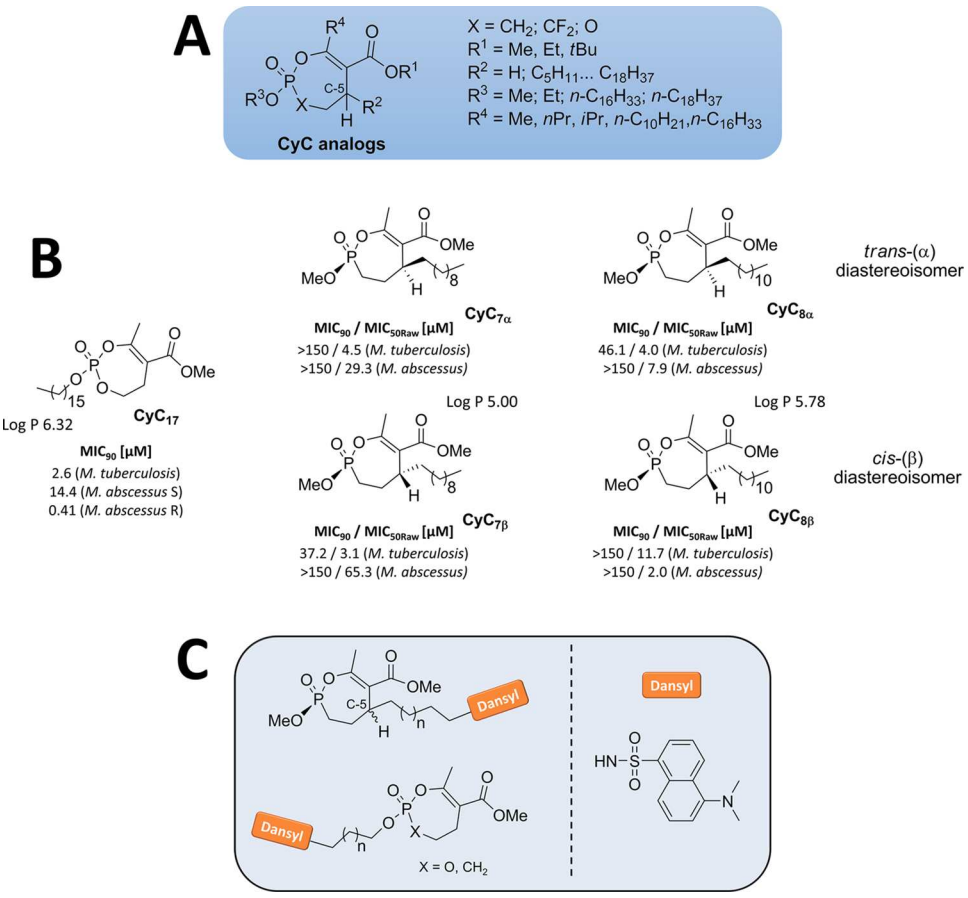

Figure 1. (A) Chemical structure of cyclipostins and cyclophostin analogues (**CyC**),[25,27] with (B) best **CyC** growth inhibitors. MIC_{90}, compound concentration leading to 90% bacterial growth inhibition in culture medium; MIC_{50Raw}, compound concentration leading to a 50% decrease in CFU count in infected Raw264.7 macrophages as compared to untreated cells. Log P-values were computed using the ALOGPS 2.1 applet (http://www.vcclab.org). (C) Chemical structure of fluorescent **CyC** affinity probes.

referred to as an "antibiotic nightmare",[22] its presence prior to lung transplantation is a major risk factor for developing a pulmonary infection or a disseminated disease postsurgery.[23] Therefore, there is an emergency to discover new efficient antibiotics, and in the context of polybacterial infections involving mycobacteria, it is of utmost importance to discriminate between the various species and in particular to quickly detect the presence of *M. abscessus* to rapidly determine a specific therapeutic course.

To reach this objective, the cyclipostins and cyclophostin analogues (namely the **CyCs** − Figure 1) are useful and powerful tools.[24] Indeed, a series of 38 monocyclic enol-phosphate (X = O, Figure 1A) and -phosphonate (X = CH_2, CF_2, Figure 1A) derivatives have been found to efficiently inhibit the growth of *M. tuberculosis* both in vitro and in infected macrophages with very low toxicity toward the host cells.[25] Furthermore, susceptibility testing conducted on various mycobacterial clinical isolates and bacteria responsible for nosocomial infections including six Gram-negative and five Gram-positive bacteria, 29 rapid-growing mycobacteria belonging to the *M. chelonae*−*abscessus* clade, and two slow-growing mycobacteria (*M. marinum*, *M. bovis* BCG) revealed that some **CyCs** exhibited very promising minimal inhibitory concentration (MIC) values, but also that their antibacterial activity was exclusively restricted to mycobacteria.[26] Notably, the enolphosphate $\mathbf{CyC}_{17}$ was found as the most potent extracellular inhibitor (Figure 1) with MICs comparable to those of most classical antibiotics used to treat either *M. tuberculosis* or *M. abscessus* infections.[25,26] Interestingly, its phosphonate analogue (i.e., $\mathbf{CyC}_{11}$) was inactive against the latter two mycobacteria with MIC > 100 μM.[25,27] Moreover, among all tested **CyC** analogues, only $\mathbf{CyC}_{7(\alpha,\beta)}$ and $\mathbf{CyC}_{8(\alpha,\beta)}$ (Figure 1) were able to impair intracellular replication of *M. tuberculosis*[25] and *M. abscessus*[27] inside Raw264.7 macrophages, with MIC_{50Raw} values better than those of the reference antibiotics rifampicin and imipenem, respectively.

Because these inhibitors act via the formation of a covalent bond between the enol-phosphorous atom and the catalytic Ser or Cys residue,[26,28−30] by using activity-based protein profiling, the target enzymes impacted by the **CyCs** were next identified, demonstrating that these compounds are multitarget inhibitors. Indeed, the **CyCs** impair various mycobacterial (Ser/Cys)-base enzymes mostly involved in the whole bacterial lipid metabolism or cell wall synthesis processes.[27]

Collectively, all these results emphasized the attractiveness of the **CyCs** that are nontoxic toward mammalian cells and specific to mycobacteria, to be exploited in future therapeutic developments against mycobacterial-related infections, especially against *M. abscessus*.[26]

In this context, the modification of the **CyC** core-structure by the direct introduction of a fluorescent moiety (Figure 1) could result in an activity-based probe (ABP), as a means to specifically label living mycobacterial species through the covalent binding to (Ser/Cys)-based enzymes. Such a fluorescent **CyC**-ABP

https://doi.org/10.1021/acsinfecdis.2c00448
ACS Infect. Dis. 2022, 8, 2564−2578

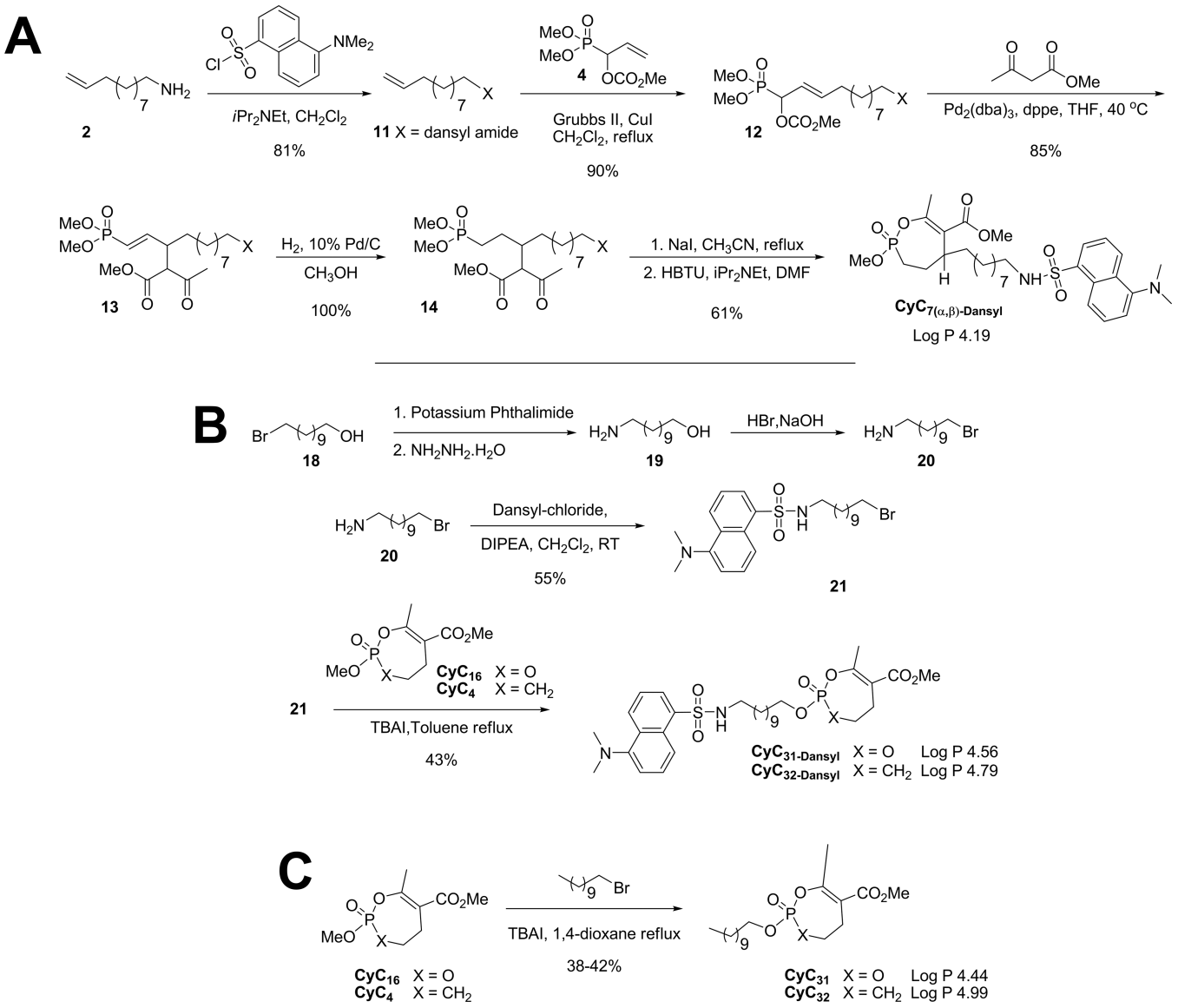

Figure 2. Synthesis of the Dansyl-labeled (A) enolphosphonate $\mathbf{CyC}_{7(\alpha,\beta)\text{-Dansyl}}$; (B) phosphate $\mathbf{CyC}_{31\text{-Dansyl}}$ and phosphonate $\mathbf{CyC}_{32\text{-Dansyl}}$ analogues of cyclipostins as well as (C) corresponding $\mathbf{CyC}_{31}$ and $\mathbf{CyC}_{32}$ unlabeled compounds. The 11-bromo-1-undecanamine **20** was prepared according to the literature procedure.[39] Log *P*-values were computed using the ALOGPS 2.1 applet (http://www.vcclab.org).

would also help monitoring and quantifying the **CyC** penetration inside the bacterial cells based on the fluorescent signal.[31,32]

By synthesizing several selected fluorescent **CyCs** that displayed potent antibacterial activity against either extracellular or intracellular replicating mycobacteria, we not only evaluated their penetration properties, but above all developed a new, powerful, and efficient diagnostic tool to specifically identify *M. abscessus* in a polybacterial mixture to help in the treatment of diseases related to mycobacterial infections.

RESULTS

Synthesis of New Fluorescent CyC Affinity Probes. The $\mathbf{CyC}_{7\alpha}$ and $\mathbf{CyC}_{7\beta}$ active against intramacrophagic mycobacteria and the $\mathbf{CyC}_{17}$ active against extracellular replicating mycobacteria as well as its inactive phosphonate counterpart $\mathbf{CyC}_{11}$ were chosen for incorporation of a fluorescent tag. Moreover, with regard to the mechanism of action of these three **CyCs** toward Ser-/Cys-based enzymes,[26,28−30] the fluorophore would be placed either on the terminal R^2 chain at the C-5 carbon atom for the *cis* and *trans* isomers of $\mathbf{CyC}_7$ (n = 6, Figure 1C) or on the phosph(*on*)ate ester moiety for the $\mathbf{CyC}_{17}$ and $\mathbf{CyC}_{11}$ (n = 13, Figure 1C) by adaption of the chemistry already developed for the synthesis of such derivatives.[25,27,33−35] Based upon its spectral properties such as a large Stokes shift, its wide usage in such areas as pharmacology, toxicology, organic synthesis, and biochemistry,[36,37] and because it is the smallest available fluorophore, the Dansyl group was chosen as a fluorescent probe.

Introduction of a Fluorescent Group at the C-5 Carbon Atom. The initial approach to introduce a label at C-5 employed late-stage installation of the fluorescent group via coupling to a primary amine, an approach biologically compatible with fluorescent Dansyl molecules. This chemical route (Figure S1) involved the application of the phthalimide protecting group at the terminal alkyl chain on the C-5 of the enolphosphonate **9**, which after removal would react with Dansyl-chloride, therefore giving the desired $\mathbf{CyC}_{7\text{-Dansyl}}$ derivative. However, despite all

https://doi.org/10.1021/acsinfecdis.2c00448
ACS Infect. Dis. 2022, 8, 2564−2578

Table 1. Antibacterial Activities of the Selected CyC Compounds against Various Bacterial Strains[a]

	MIC$_{90}$ (μM)								
					M. abscessus CIP 104536^T				
Cpds	*M. smegmatis* mc^{2}155	*M. marinum* ATCC BAA-535/M	*M. bovis* BCG	*M. tuberculosis* mc^2 6230	S variant	R variant	*E. coli* DH10B	*P. aeruginosa* PAO1	*S. aureus*
AMK		2.9 ± 0.17	0.82 ± 0.05	0.63 ± 0.03	5.8 ± 0.20	10.1 ± 0.45			
INH	29.8 ± 1.0	67.6 ± 3.5	1.7 ± 0.07	1.5 ± 0.07	>100	>100			
CyC$_{17}$[b]	1.6 ± 0.02	1.7 ± 0.05	0.80 ± 0.03	2.6 ± 0.13	14.4 ± 0.73	0.41 ± 0.01	|←	*No effect*	→|
CyC$_{31}$	35.1 ± 0.46	16.5 ± 2.3	0.87 ± 0.06	5.3 ± 0.15	1.2 ± 0.30	27.1 ± 1.6	|←	*No effect*	→|
CyC$_{31\text{-Dansyl}}$	32.1 ± 1.7	25.1 ± 1.3	5.8 ± 0.31	10.0 ± 0.59	6.1 ± 0.40	63.4 ± 2.9	|←	*No effect*	→|
CyC$_{32}$	55.5 ± 1.6	37.0 ± 0.56	1.1 ± 0.15	5.4 ± 0.70	168 ± 2.0	>200	|←	*No effect*	→|
CyC$_{32\text{-Dansyl}}$	55.7 ± 2.4	37.3 ± 0.90	7.4 ± 0.89	13.3 ± 0.57	>200	>200	|←	*No effect*	→|
CyC$_{7\alpha}$[b]	119 ± 7.2	31.5 ± 0.77	69.3 ± 2.5	>200	>200	154 ± 3.9	|←	*No effect*	→|
CyC$_{7\alpha\text{-Dansyl}}$	>200	44.4 ± 2.0	62.3 ± 1.8	>200	>200	>200	|←	*No effect*	→|
CyC$_{7\beta}$[b]	164 ± 3.4	6.0 ± 0.40	47.2 ± 2.0	37.2 ± 3.9	>200	142 ± 2.0	|←	*No effect*	→|
CyC$_{7\beta\text{-Dansyl}}$	>200	19.5 ± 1.2	32.0 ± 1.1	60.5 ± 3.0	>200	>200	|←	*No effect*	→|

[a]MIC$_{90}$, compound minimal concentration leading to 90% of bacterial growth inhibition as determined by the REMA assay. Values are mean ± SD of two independent assays performed in triplicate. [b]Data for **CyC$_{17}$** and **CyC$_{7(\alpha,\beta)}$** are from refs 25−27. AMK, amikacin; INH, isoniazid.

our efforts, the desired molecule was only obtained in very low overall 4% yields.

Given the difficulties experienced with the late-stage introduction of the fluorescent label, an alternative approach was devised in which the fluorescent tag is introduced earlier in the synthesis. The amine **2** was first reacted with Dansyl-chloride under stirring at room temperature in CH_2Cl_2, giving alkenyl sulfonamide **11** in 81% yields. Further coupling reaction with phosphonate **4** via cross-metathesis using Grubb's second-generation catalyst afforded carbonate **12** in 90% yields. Then the fluorescent monocyclic enolphosphonate **CyC$_{7(\alpha,\beta)\text{-Dansyl}}$** was obtained in racemic form following a classical route (Figure 2A): (i) palladium(0)-catalyzed reaction of carbonate **12** with methyl acetoacetate, (ii) reduction with hydrogen over palladium on carbon in methanol, and (iii) selective mono-demethylation with sodium iodide followed by cyclization with HBTU.

As previously demonstrated in the synthesis of racemic bicyclic phosphonate analogues,[28] the **CyC$_7$** compound was characterized by the relationship between the OMe on phosphorus and the H-substituent on the C-5 carbon atom as being either in a *trans* (α-isomer) or *cis* (β-isomer) relationship (Figure 1B). Accordingly, the two racemic diastereoisomers **CyC$_{7\alpha\text{-Dansyl}}$** and **CyC$_{7\beta\text{-Dansyl}}$** were further separated by careful silica gel column chromatography.

Introduction of a Fluorescent Label at Phosphorus. To introduce the Dansyl group on the alkyl chain at the phosphorus atom, we first examined the use of cross metathesis to build the required functionalized alkane chain with **CyC$_{11}$**, the phosphonate analogue of **CyC$_{17}$**. Two alternative routes were used (Figure S2). The first one involved metathesis of 6-bromohex-1-ene and Dansyl-amide alkene **11** using Grubb's second-generation catalyst, followed by the coupling reaction of resulting alkyl bromide **15** with **CyC$_4$**,[24,33] and finally, hydrogenation of the resulting phosphonate ester **16** (Figure S2A). Alternatively, the **CyC$_{11\text{-Dansyl}}$** was obtained by trans-esterification of **CyC$_4$** with 6-bromo-1-hexene, followed by a cross-metathesis reaction with the Dansyl-amide alkene **11** and subsequent hydrogenation (Figure S2B). In both cases, high-resolution mass spectrometry data and liquid chromatography−mass spectrometry spectra showed the presence of a mixture of compounds with various chain lengths (i.e., M-CH_2, M, and M + CH_2 − Figure S2C,D). Similar variation of the ring size from the ring closing metathesis reaction had previously been observed in the total synthesis of Dolabelide C.[38] These later byproducts were presumed to occur from double-bond isomerization followed by ring-closing metathesis, resulting in smaller macrocycles. Here, the chain length variation may also result from the isomerization of the terminal double bond during the cross metathesis (Figure S2C).

To overcome such product heterogeneity, two new Dansyl-labeled **CyCs** were synthesized starting from commercially available 11-bromo-1-undecanol **18** (Figure 2B). The enol-phosphonate **CyC$_{31}$** analogue of **CyC$_{17}$** and its phosphate derivative **CyC$_{32}$** analogue of **CyC$_{11}$** were then obtained with a shorter $C_{11}H_{23}$ alkyl chain on the phosphorus atom *versus* a $C_{16}H_{33}$ chain for the **CyC$_{17}$** and **CyC$_{11}$**. Briefly, following a published procedure,[39] compound **18** was first converted to the 11-amino-1-undecanol **19**[40] in a Gabriel synthesis employing the Ing-Mansk[41] variation. Treatment with boiling HBr[42] converted the alcohol group of **19** to the bromine **20**, which was reacted with Dansyl-chloride to give the Dansyl-labeled bromide compound **21** in 55% yields. The ester exchange reaction process with either the phosphate **CyC$_{16}$**[24,35] or the phosphonate **CyC$_4$** in the presence of an excess Dansyl-bromide **21** and TBAI in refluxing toluene yielded the corresponding fluorescent labeled alkyl phosphate **CyC$_{31\text{-Dansyl}}$** or phosphonate **CyC$_{32\text{-Dansyl}}$** derivative in 43% yields (Figure 2B). In parallel, the respective unlabeled analogues, that is, **CyC$_{31}$** and **CyC$_{32}$**, were also synthesized in 38−42% yields using the one-pot ester exchange process from **CyC$_{16}$** and **CyC$_4$**, respectively, and the commercial 1-bromoundecane (Figure 2C).

New CyC-Dansyl Affinity Probes Retain Antibacterial Activity Similar to That of Their Parent Molecules. The antimicrobial potency of the selected **CyCs** [**CyC$_{7(\alpha,\beta)\text{-Dansyl}}$**, **CyC$_{31\text{-Dansyl}}$**, and **CyC$_{32\text{-Dansyl}}$** as well as **CyC$_{31}$** and **CyC$_{32}$**] was next evaluated toward the nonpathogenic *M. smegmatis* strain, four pathogenic mycobacterial species (i.e., *M. marinum*, *M. bovis* BCG, *M. tuberculosis* mc^{2}6230, and both S/R variants of *M. abscessus*), two Gram-negative bacteria (i.e., *Escherichia coli* and *Pseudomonas aeruginosa*), and one Gram-positive (i.e., *Staphylococcus aureus*) bacteria. The corresponding **CyCs** minimal concentration leading to 90% bacterial growth inhibition (i.e., MIC$_{90}$), as determined by the resazurin microtiter assay (REMA),[25−27] is reported in Table 1.

https://doi.org/10.1021/acsinfecdis.2c00448
ACS Infect. Dis. 2022, 8, 2564−2578

Table 2. Antibacterial Activities of the New CyC Analogues against *M. abscessus* S Infected Macrophages

Cpds		CC_{50} (μM) [a]	MIC_{50Raw} (μM) [b]
IMP [c]		ND	28.3±4.7
$CyC_{7\alpha}$ [c]	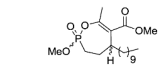	>100	29.3±2.9
$CyC_{7\beta}$ [c]		>70	65.3±6.2
$CyC_{7\alpha\text{-Dansyl}}$	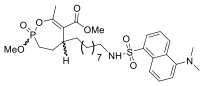	>100	39.9±6.2
$CyC_{7\beta\text{-Dansyl}}$		>100	80.6±7.1
CyC_{31} (X=O)	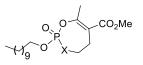	>100	*No effect*
CyC_{32} (X=CH_2)		>100	*No effect*
$CyC_{31\text{-Dansyl}}$ (X=O)	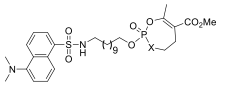	>100	*No effect*
$CyC_{32\text{-Dansyl}}$ (X=CH_2)		>100	*No effect*

[a]CC_{50}, compound concentration leading to 50% Raw264.7 macrophages toxicity. [b]MIC_{50Raw}, minimal compound concentration leading to a 50% decrease in CFU count as compared to untreated cells. Raw264.7 macrophages were infected by *M. abscessus* S-LuxAB at a MOI of 10, and further treated with each **CyC** or IMP for 24 h. The viable mycobacteria were quantified by measurement of luminescence which was further correlated to CFU. Untreated infected macrophages were used as the control representing 100% of bacterial viability. MIC_{50Raw} valyes were calculated from curve fitting of CFU% as a function of the inhibitor concentration and are expressed as mean values of three independent assays. [c]Data from ref 27. IMP, imipenem; ND, not determined.

As previously reported with the other **CyCs**[26,27] the in vitro growth of *E. coli*, *P. aeruginosa,* and *S. aureus* was not impacted. Satisfyingly, the *trans*-(α)- and *cis*-(β)-isomers of the **$CyC_{7\text{-Dansyl}}$** retained extracellular activity comparable to the parent unlabeled molecules, with a fold change in MIC_{90} ranging from 0.7−3.2 μM (Table 1). In addition, each respective labeled and unlabeled pair of the new phosphate and phosphonate esters bearing a medium lipophilic C11 alkyl chain at the R^3 position, that is, **CyC_{31}**/**$CyC_{31\text{-Dansyl}}$** and **CyC_{32}**/**$CyC_{32\text{-Dansyl}}$** (Figure 2B,C), displayed similar antibacterial activity against the five mycobacteria, respectively. Interestingly, **CyC_{31}** and **CyC_{32}** exhibited similar MIC_{90} values to **CyC_{17}** against *M. bovis* BCG (MIC_{90} = 0.87−1.1 vs 0.80 μM) and *M. tuberculosis* (MIC_{90} = 5.3 vs 2.6 μM). Surprisingly, in the case of *M. abscessus*, although the **CyC_{32}**/**$CyC_{32\text{-Dansyl}}$** phosphonate analogues were almost inactive, the **CyC_{31}** and **$CyC_{31\text{-Dansyl}}$** phosphate esters displayed very good (MIC_{90} = 1.2−6.1 μM) to moderate (MIC_{90} = 27.1−63.4 μM) antimycobacterial activity against the S and R variant, respectively (Table 1).

The cytotoxicity of the 6 new **CyCs** was also assessed using murine Raw264.7 macrophages.[43] As expected from previous toxicity results obtained with the **CyC_{1-30}**,[25,27] these new **CyCs** showed again a very low toxicity toward host mammalian cells with CC_{50} > 100 μM (Table 2), similarly to AMK ($CC_{50} \geq 150$ μM).[44] Given these results, the ability of the **CyC** analogues to inhibit *M. abscessus* intramacrophagic growth was investigated as reported previously.[27] Murine Raw264.7 macrophage cells were infected with *M. abscessus* S-LuxAB[45] at a multiplicity of infection (MOI) of 10 and then incubated for 24 h with various concentrations of each **$CyC_{\text{-Dansyl}}$**, or imipenem (IMP; 267 μM; 43 × MIC_{90}) used as the positive drug control. First, whatever the concentration used, the **$CyC_{31\text{-Dansyl}}$**, **$CyC_{32\text{-Dansyl}}$**, and the unlabeled **CyC_{31}** and **CyC_{32}** remained fully inactive toward infected macrophages (Table 2). Conversely, and in agreement with previous work,[27] both (α)- and (β)-isomers of **$CyC_{7\text{-Dansyl}}$**, inactive against extracellular bacilli, displayed a moderate activity against intracellular *M. abscessus* S with a calculated MIC_{50Raw} of 39.9 and 80.6 μM, respectively, similar to that of unlabeled **$CyC_{7\alpha}$** and **$CyC_{7\beta}$** (Table 2).

Overall, these results indicate that incorporation of a fluorescent Dansyl group either at the C5 carbon atom (i.e., **$CyC_{7\text{-Dansyl}}$**) or at the R^3 chain on the phosphorus (i.e., **$CyC_{31\text{-Dansyl}}$** & **$CyC_{32\text{-Dansyl}}$**) does not affect the extracellular or intracellular antibacterial activity of the resulting **$CyC_{\text{-Dansyl}}$** fluorescent affinity-based probes, as compared to the unlabeled parent molecules.

$CyC_{\text{-Dansyl}}$ Analogues Label Mycobacterial Strains Whatever Their Antibacterial Activity. To further investigate whether the fluorescent **CyCs** were able to penetrate into the above-mentioned bacteria, each strain was preincubated with the **$CyC_{\text{-Dansyl}}$**. The obtained **$CyC_{\text{-Dansyl}}$**-treated bacteria were visualized by fluorescence microscopy, and total fluorescence related to the Dansyl group was quantified using a Tecan Spark 10 M multimode microplate reader (Figures 3 & S3).

Surprisingly, each of the four **$CyC_{\text{-Dansyl}}$** was found to penetrate efficiently and label all mycobacterial species tested, regardless of their respective MIC values (Figure 3A). In particular, the **$CyC_{7\alpha\text{-Dansyl}}$** and **$CyC_{7\beta\text{-Dansyl}}$** almost exclusively active against intracellular bacterial growth are also able to efficiently tag mycobacteria in vitro. Quantification of total fluorescence intensity of the four **$CyC_{\text{-Dansyl}}$** incubated with the mycobacterial strains revealed a similar overall profile (Figure S3). However, significant variations in the fluorescence level were obtained between each **CyC** (Figure 3B). Indeed, the mean fluorescence values of the **$CyC_{7\beta\text{-Dansyl}}$**-treated *M. smegmatis* (23,000 ± 8756 au) and both the **$CyC_{7(\alpha,\beta)\text{-Dansyl}}$**-treated *M. abscessus* S (34,874 ± 5363 au) and *M. abscessus* R (18,066 ± 2279 au) were found significantly 1.2- to 2.8-fold higher (*p*-value <0.001, Figure 3B) than those of the respective **$CyC_{31\text{-Dansyl}}$** and **$CyC_{32\text{-Dansyl}}$**-treated mycobacteria. In contrast, no significant difference was observed with *M. marinum*, *M. bovis* BCG, or *M. tuberculosis* labeled strains whatever the **$CyC_{\text{-Dansyl}}$** used (Figure 3B). When **$CyC_{7\alpha\text{-Dansyl}}$**- (*data not shown*) or **$CyC_{31\text{-Dansyl}}$**-treated *M. abscessus* S cells were subjected to cellular fractionation followed by in-gel fluorescence scanning, the inhibitor was found within both the insoluble (i.e., cell wall/membrane) and soluble (i.e., cytoplasm) fractions (Figures 3C

https://doi.org/10.1021/acsinfecdis.2c00448
ACS Infect. Dis. 2022, 8, 2564−2578

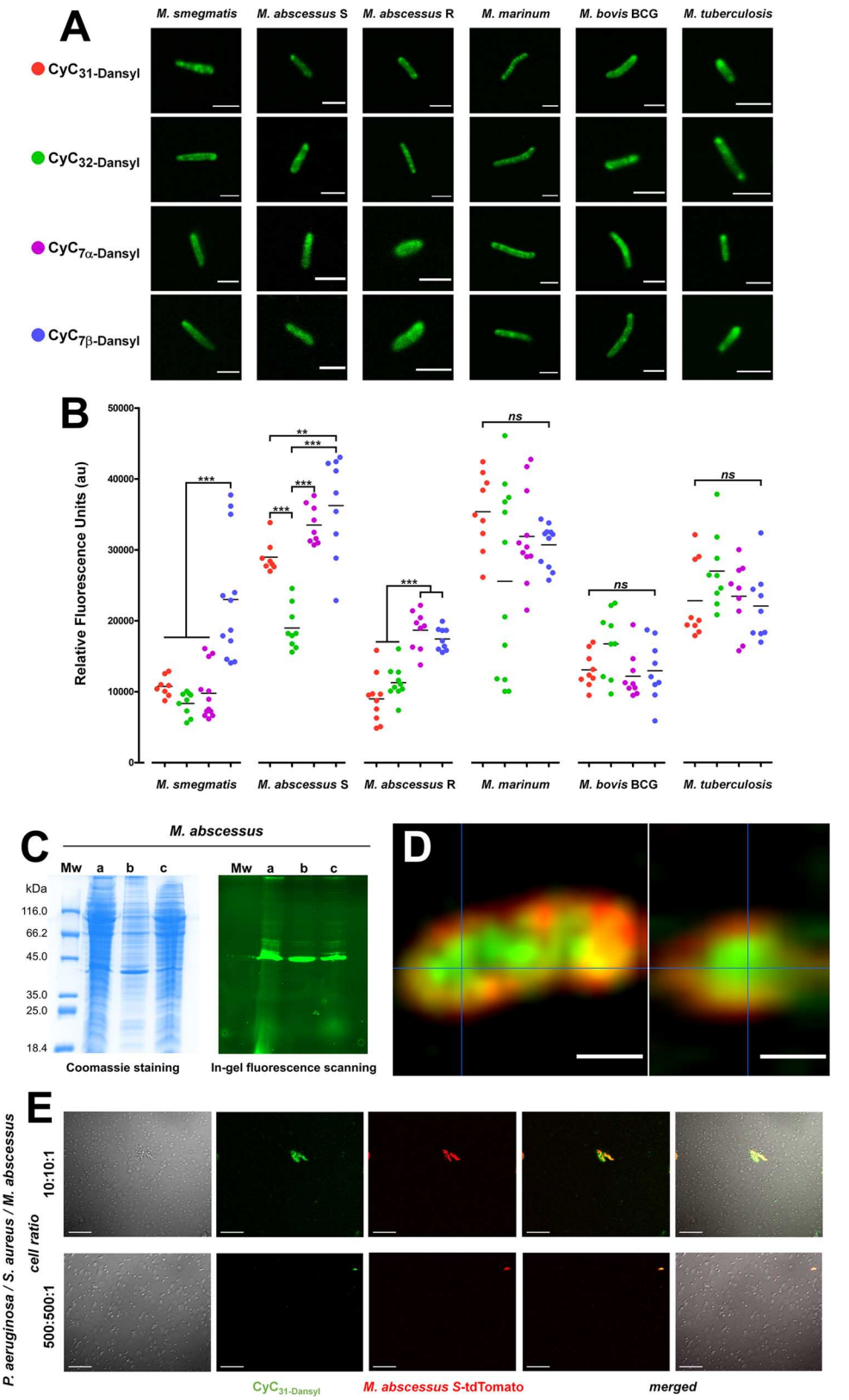

Figure 3. $CyC_{\text{-Dansyl}}$ probes are able to label all mycobacterial strains regardless of their antibacterial activity. (A) Representative fluorescence images of *M. smegmatis*, *M. abscessus* S and R, *M. marinum*, *M. bovis* BCG, and *M. tuberculosis* $mc^2$6230 strains in presence of fluorescent **CyC**. The mycobacteria were exposed to 200 μM **$CyC_{\text{-Dansyl}}$** for 3 h, washed and fixed with 4% paraformaldehyde. Fixed bacteria were imaged using an Olympus IX81 confocal microscope. Scale bars: 2 μm. (B) Total fluorescence intensity of each **$CyC_{\text{-Dansyl}}$**-treated mycobacteria expressed as arbitrary units (au) recorded at $\lambda_{ex}/\lambda_{em} = 400/535 \pm 10$ nm using a Tecan Spark 10 M multimode microplate reader (Tecan Group Ltd., France). Compound color code is indicated in panel (A). Statistical significance was assessed with one-way ANOVA followed by Tukey's post hoc test using Prism 4.0 (Graphpad, Inc): ** *p*-value <0.01; *** *p*-value <0.001; *ns*, not significant (*p*-value >0.05). Results are corresponding to $n = 3$ biologically independent experiments performed in triplicate. (C) Cellular localization of the $CyC_{31\text{-Dansyl}}$ in *M. abscessus* S. The bacteria were exposed to 200 μM **$CyC_{31\text{-Dansyl}}$** for 3 h, then washed, and

https://doi.org/10.1021/acsinfecdis.2c00448
ACS Infect. Dis. 2022, 8, 2564−2578

Figure 3. continued

lysed. Equal amounts of proteins (50 μg) from total lysate (**a**), insoluble (**b**), and soluble (**c**) fractions recovered after centrifugation were separated by 12% SDS-PAGE and visualized by Coomassie blue staining (*left*) or in-gel fluorescence (*right*). The **CyC$_{31\text{-Dansyl}}$**-labeled proteins were detected by fluorescent gel scanning using trans-UV illumination (λ_{ex} 302 nm) as excitation source, and as emission the 530/28 filter of a ChemiDoc MP Imager (Bio-Rad) before staining of the gels with Coomassie Brilliant Blue dye. (D) 3-D reconstruction of a stack of deconvoluted images of CyC$_{31\text{-Dansyl}}$-treated *M. abscessus* S cells from an epi-fluorescence microscope. XY (*left panel*) and YZ (*right panel*) orthogonal views. The bacterium was incubated with **CyC$_{31\text{-Dansyl}}$** (green fluorescence) and the bacterial membrane was further stained with Nile Red (red fluorescence). The orange color results from merge fluorescence between the Dansyl and the Nile Red (see also Movie S1). Scale bars: 0.5 μm. (E) The CyC$_{\text{-Dansyl}}$ probes specifically label *M. abscessus* cells in polybacterial cultures. Fluorescence micrographs of polybacterial cultures formed by *M. abscessus* -tdTomato, *P. aeruginosa*, and *S. aureus* stained by **CyC$_{31\text{-Dansyl}}$** after overnight culture in 7H9 media for mycobacterial enrichment. Scale bars: 20 μm.

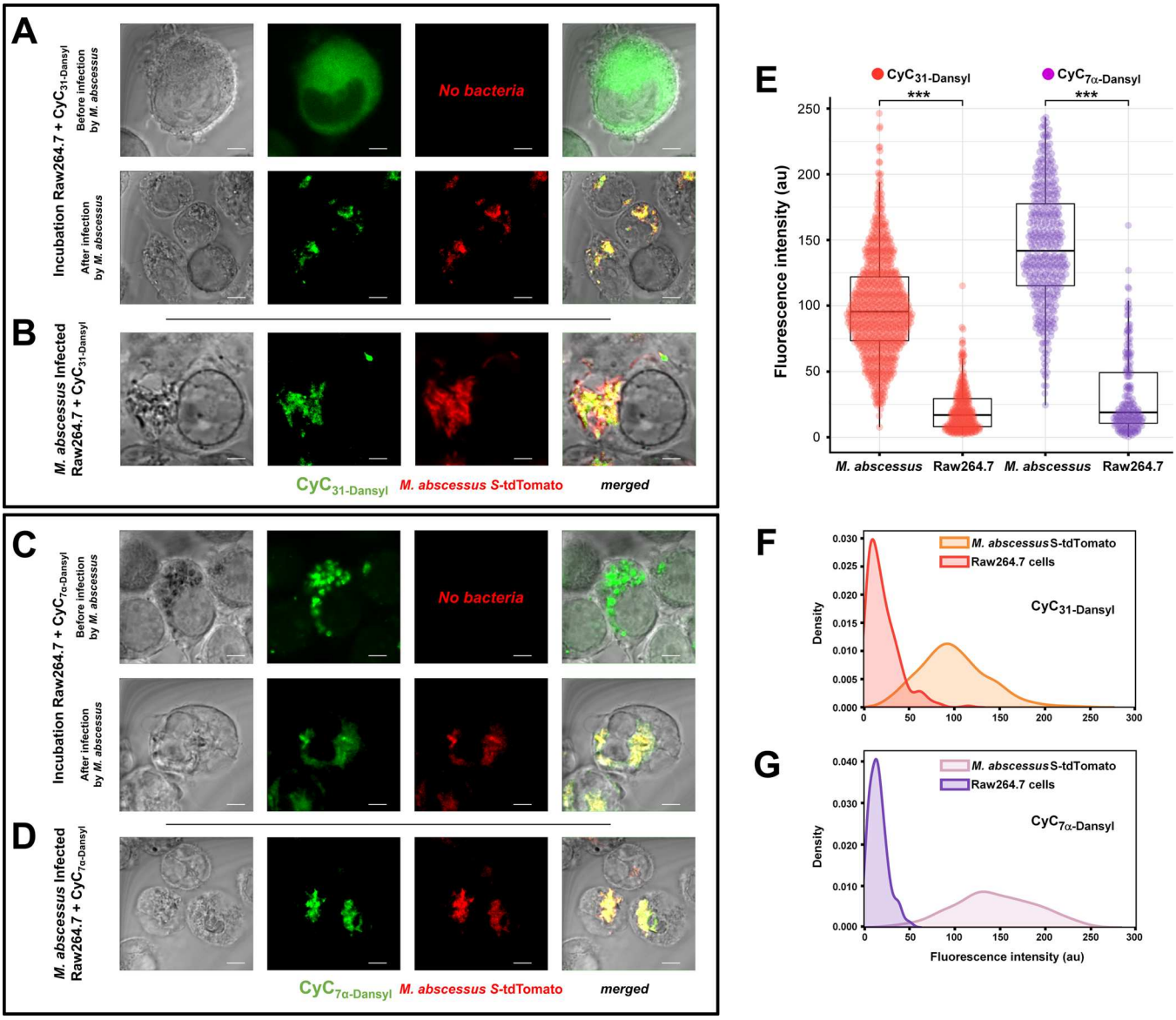

Figure 4. CyC$_{31\text{-Dansyl}}$ and CyC$_{7\alpha\text{-Dansyl}}$ specifically localized on *M. abscessus* S inside infected Raw264.7 macrophages. Representative images of the **CyC$_{31\text{-Dansyl}}$** and **CyC$_{7\alpha\text{-Dansyl}}$** distribution in intracellular *M. abscessus* S-dtTomato strains. (A, C) Raw264.7 macrophages were preincubated with 100 μM **CyC$_{31\text{-Dansyl}}$** (A) or **CyC$_{7\alpha\text{-Dansyl}}$** (C) for 24 h prior to be infected with *M. abscessus* S-tdTomato (MOI 10) for another 24 h. (B, D) Alternatively, *M. abscessus* S-dtTomato infected Raw264.7 were treated with each inhibitor for 24 h before chemical fixation and confocal fluorescence imaging. Scale bars: 5 μm. Micrographs are representative of two independent experiments. (E) Quantitative analysis of the Dansyl fluorescence signal per bacterium and Raw264.7 cell positive area shown as a sinaplot-boxplot and expressed as arbitrary units (au). Results are from two biologically independent experiments; 122 to 258 cells were observed resulting in 389 to 808 segmented intracellular *M. abscessus* S-dtTomato positive regions. The *p*-values were calculated by using a two-tailed *t*-statistic test with Prism 4.0 (Graphpad, Inc): *** *p*-value <0.001. (F, G) Density plot of the Dansyl fluorescent signal profile of *M. abscessus* S-tdTomato and Raw264.7 positive cells.

https://doi.org/10.1021/acsinfecdis.2c00448
ACS Infect. Dis. 2022, 8, 2564−2578

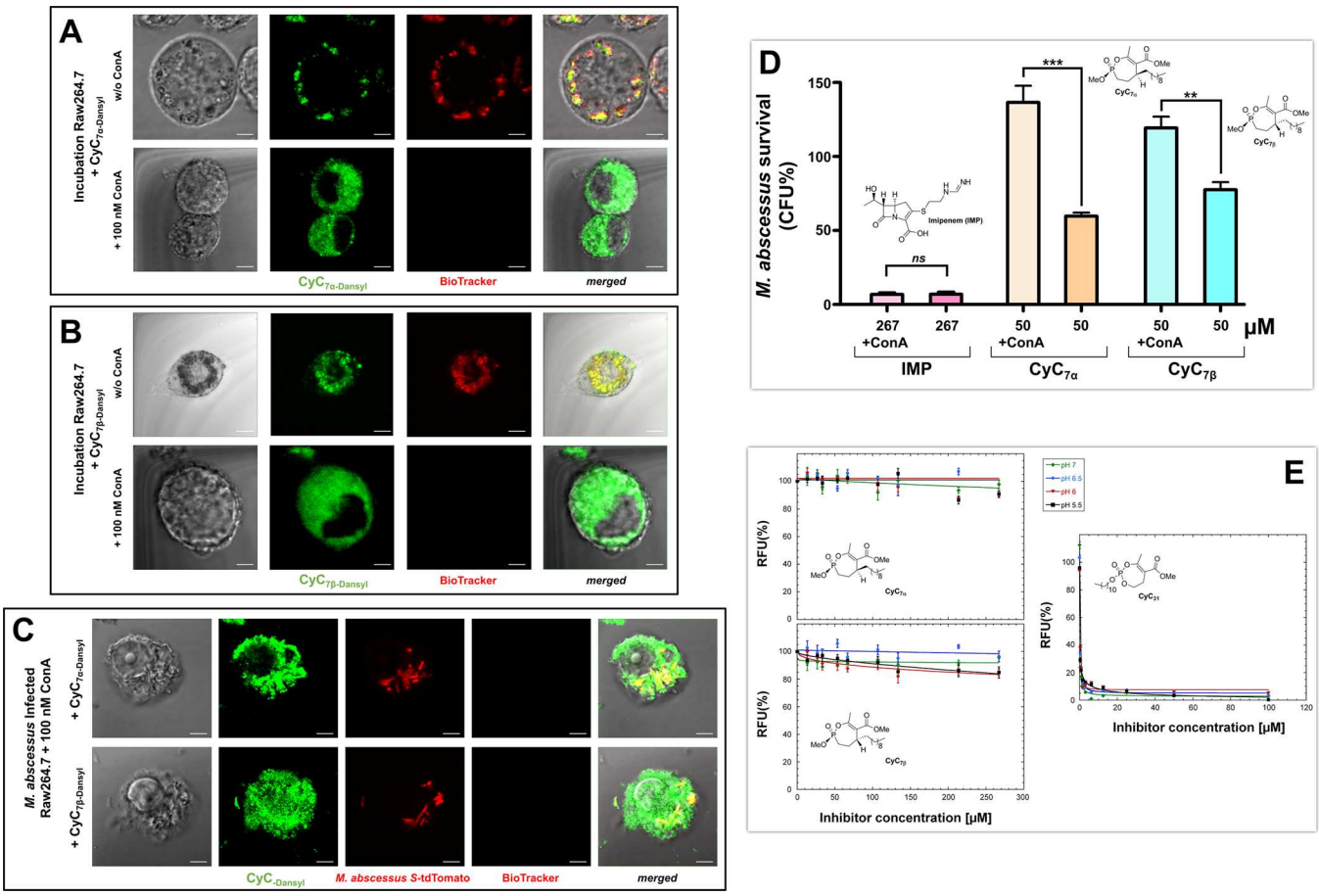

Figure 5. $\mathbf{CyC_{7(\alpha,\beta)\text{-Dansyl}}}$ accumulate in acidic compartments inside Raw264.7 macrophages. Raw264.7 macrophages were preincubated with 100 μM $\mathbf{CyC_{7\alpha\text{-Dansyl}}}$ (A) or $\mathbf{CyC_{7\beta\text{-Dansyl}}}$ (B) for 24 h in the presence or absence of 100 nM Concanamycin A (ConA) prior to be stained with 1× BioTracker NIR633 dye and processed for confocal fluorescence imaging. Micrographs are representative of 106 to 136 observed cells from two biologically independent experiments. Scale bars: 5 μm. (C) Disruption of endolysosomal acidification impairs $\mathrm{CyC_{\text{-Dansyl}}}$ colocalization with *M. abscessus* cells inside infected Raw264.7 macrophages. *M. abscessus* S-dtTomato infected Raw264.7 macrophages treated with 100 nM Concanamycin A (ConA) were preincubated with 100 μM $\mathbf{CyC_{7\alpha\text{-Dansyl}}}$ or $\mathbf{CyC_{7\beta\text{-Dansyl}}}$ for 24 h prior to be stained with 1× BioTracker NIR633 dye and processed for confocal fluorescence imaging. Micrographs are representative of around 120 observed cells from two biologically independent experiments. Scale bars: 5 μm (D) Addition of ConA suppresses the intracellular antibacterial activity of $\mathrm{CyC_{7\alpha}}$ and $\mathrm{CyC_{7\beta}}$ against *M. abscessus* in infected Raw264.7 murine macrophages. Cells were infected at an MOI of 10 with *M. abscessus* S-LuxAB and treated for 24 h with 50 μM $\mathbf{CyC_{7\alpha}}$/$\mathbf{CyC_{7\beta}}$, or 267 μM IMP as the positive drug control, in the presence or absence of 100 nM ConA. Surviving bacteria were next quantified from macrophage lysates by measurement of luminescence, which was further correlated to CFU. Untreated infected macrophages in presence (i.e., $0.97 \pm 0.21 \times 10^6$ CFU) or absence (i.e., $1.04 \pm 0.11 \times 10^6$ CFU) of ConA were used as control representing 100% of bacterial viability. Results are shown as mean ± standard error of the mean of three independent assays. The *p*-values were calculated by using a two-tailed *t*-statistic test with Prism 4.0 (Graphpad, Inc): ***, *p*-value <0.001. **, *p*-value <0.01. *ns*, not significant (*p*-value >0.05). (E) Antibacterial activity of the CyC against extracellular *M. abscessus* S growth is not pH-dependent. Activity of $\mathbf{CyC_{7\alpha}}$, $\mathbf{CyC_{7\beta}}$, and $\mathbf{CyC_{31}}$ against *M. abscessus* S replicating in broth medium, expressed as normalized relative fluorescence units (RFU%). *M. abscessus* S strains were grown until reaching mid-exponentially growing phase in 7H9-S medium, inoculated in fresh media adjusted at pH 7.0, 6.5, 6.0, or 5.5, and further used in susceptibility testing using the REMA assay toward the three **CyC** compounds. Each value is the mean ± SD of two independent assays.

& S4). Moreover, 3-D reconstruction of confocal laser scanning microscopy images of $\mathbf{CyC_{31\text{-Dansyl}}}$-treated *M. abscessus* S cells confirmed that the diffuse fluorescence (i.e., green and orange resulting colors) observed with the $\mathbf{CyC_{\text{-Dansyl}}}$-treated strains would result from a homogeneous distribution of these inhibitors in the cell wall and in the cytoplasm (Figure 3D and Movie S1). Such observations agree with our all previous studies, where identified protein targets of the **CyCs** in *M. abscessus* ($\mathbf{CyC_{17}}$ and $\mathbf{CyC_{26}}$) and *M. tuberculosis* ($\mathbf{CyC_{17}}$) originated from both cellular compartments.[25,27]

$\mathbf{CyC_{\text{-Dansyl}}}$ Analogues Are Unable to Label Gram-Positive and Gram-Negative Bacteria, but Can React with Their Respective Lysates. Conversely and in good agreement with MIC data and previously published work with the **CyC**,[26] no significant fluorescence signal was detected when treating *E. coli*, *P. aeruginosa* or *S. aureus* with the four $\mathbf{CyC_{\text{-Dansyl}}}$ probes (Figure S5), thus suggesting that the **CyCs** would not be able to cross the cell wall of these latter bacteria. To check if these inhibitors would however be able to react with bacterial enzymes, a lysate of each of the three above-mentioned bacteria was incubated with each $\mathbf{CyC_{\text{-Dansyl}}}$, and then equal amounts of the obtained labeled proteome were separated by 12% SDS-PAGE and visualized by Coomassie staining or in-gel fluorescence for Dansyl detection using a ChemiDoc MP Imager (Bio-Rad) (Figure S6). In each treated lysate, clear distinct fluorescent bands were detected corresponding to bacterial (Ser/Cys)-enzymes that presumably had reacted with the $\mathbf{CyC_{\text{-Dansyl}}}$ probes. Given together, these findings confirm

https://doi.org/10.1021/acsinfecdis.2c00448
ACS Infect. Dis. 2022, 8, 2564−2578

that the absence of antibacterial activity of the **CyCs** clearly results from their inability to cross the cell wall of Gram-positive and Gram-negative bacteria.

In the context of CF patients, the presence of numerous Gram-negative and Gram-positive bacteria from the microbiota represents a significant challenge for detecting mycobacteria in sputum.[46] Therefore, we examined the ability of the **CyC$_{\text{-Dansyl}}$** to specifically label *M. abscessus* in polymicrobial cultures. Exponential cultures of *P. aeruginosa*, *S. aureus* and *M. abscessus* S harboring a tdTomato fluorophore were mixed at a 10:10:1 cell ratio, incubated overnight in a 7H9-S medium for mycobacteria enrichment, and then stained with **CyC$_{31\text{-Dansyl}}$** probe. In line with our results, we observed the selective staining of *M. abscessus* in this mixed microbial culture (Figure 3E). To assess the sensitivity of the **CyC$_{31\text{-Dansyl}}$**, different ratios of the polymicrobial culture were tested. Imaging results showed that the **CyC$_{31\text{-Dansyl}}$** could detect a single mycobacterium in the presence of 1000 other bacteria (Figure 3E). Taken together, these results confirm that the **CyC$_{\text{-Dansyl}}$** are highly specific and selective for mycobacteria with high sensitivity.

CyC$_{\text{-Dansyl}}$ Affinity Probes Efficiently Label Intramacrophagic *M. abscessus*. In parallel, we investigated the ability of the **CyC$_{\text{-Dansyl}}$** analogues to interact with *M. abscessus* S-tdTomato within infected Raw264.7 macrophage cells. Raw264.7 macrophages were first incubated with each **CyC$_{\text{-Dansyl}}$** probe at a 100 μM final concentration for 24 h and then processed for fluorescent microscopy (Figures 4 & S7). At this stage, and despite a similar hydrophobicity between all **CyC$_{\text{-Dansyl}}$** (i.e., mean Log P = 4.51 ± 0.24), two different fluorescence profiles were observed depending on the compounds used (Figures 4A,C and S7A,C).

With the **CyC$_{31\text{-Dansyl}}$** (Figure 4A) and **CyC$_{32\text{-Dansyl}}$** (Figure S7A), a large and diffuse fluorescence was observed inside the macrophage. Remarkably, and despite the absence of intracellular antibacterial activity, infection of the latter **CyC$_{31/32\text{-Dansyl}}$**-treated cells with *M. abscessus* S-dtTomato resulted in a clear re-colocalization of the Dansyl inhibitors with the mycobacteria. Moreover, when the Raw264.7 were infected prior to incubation with **CyC$_{31/32\text{-Dansyl}}$**, the same final colocalization was also observed. A quantitative analysis of **CyC$_{31/32\text{-Dansyl}}$** accumulation in *M. abscessus* S-tdTomato-infected macrophages revealed a higher level of each **CyC$_{\text{-Dansyl}}$** associated with the mycobacteria than the Raw264.7 cells (average mean intensity [au] of 99.38 ± 1.32 vs 21.29 ± 1.10 and 156.9 ± 1.91 vs 25.41 ± 1.19 for **CyC$_{31\text{-Dansyl}}$** and **CyC$_{32\text{-Dansyl}}$** positive bacteria *vs* positive Raw264.7 cells, respectively; *p-value* <0.001) (Figures 4E & S7E). Analysis of the distribution of each **CyC$_{\text{-Dansyl}}$** mean intensity between intracellular *M. abscessus* S-tdTomato and Raw264.7 cells areas by the density plot confirms that *M. abscessus* bacteria displayed a higher **CyC$_{\text{-Dansyl}}$** signal enrichment than macrophage cells (Figures 4F & S7F). These findings are consistent with a dynamic relocation process of the **CyC** inside the macrophage and leading to a clear tropism of both **CyC$_{31/32\text{-Dansyl}}$** for intracellular *M. abscessus* S.

In contrast, when macrophages were treated with the **CyC$_{7(\alpha,\beta)\text{-Dansyl}}$**, which are active mainly in intracellular conditions, a totally different behavior from the other two **CyC$_{31/32\text{-Dansyl}}$** compounds was reached (Figures 4C & S7C). Indeed, their fluorescence was mainly localized into foci as if these two inhibitors accumulated in specific cell compartments. Interestingly, after infection both **CyC$_{7(\alpha,\beta)\text{-Dansyl}}$** colocalized with the intracellular mycobacteria (Figures 4C,D & S7C,D), as also observed with the **CyC$_{31/32\text{-Dansyl}}$** inhibitors. In addition, the quantitative analysis of **CyC$_{7(\alpha,\beta)\text{-Dansyl}}$** accumulation in *M. abscessus* S-tdTomato-infected macrophages revealed a higher level of each **CyC$_{7\text{-Dansyl}}$** associated with the mycobacteria than the Raw264.7 cells (average mean intensity [au] of 144.6 ± 2.25 vs 31.85 ± 2.34, and 137.2 ± 2.13 vs 48.78 ± 2.25 for **CyC$_{7\alpha\text{-Dansyl}}$** and **CyC$_{7\beta\text{-Dansyl}}$** positive bacteria vs positive Raw264.7 cells, respectively; *p-value* <0.001) (Figures 4E & S7E). Such tropism was further confirmed by analysis of the distribution of **CyC$_{7(\alpha,\beta)\text{-Dansyl}}$** fluorescence intensity between intracellular *M. abscessus* S-tdTomato and Raw264.7 cells by the density plot (Figures 4G & S7G).

CyC$_{7(\alpha,\beta)\text{-Dansyl}}$ Analogues Accumulate in Acidic Intracellular Compartments. Among the four **CyC$_{\text{-Dansyl}}$** analogues tested, the fact that only the **CyC$_{7(\alpha,\beta)\text{-Dansyl}}$** is active against intramacrophagic replicating bacteria (Table 2) prompted us to investigate further their particular localization as foci-like inside macrophages. More precisely, the fact that lysosomes are acidic and hydrolytic organelles responsible for the degradation of macro and small molecules inside macrophages,[47] we tested whether these two compounds accumulate in acidic compartments. Raw264.7 macrophages were then treated with 100 μM of each of the four **CyC$_{\text{-Dansyl}}$** compounds, and acidic compartments were labeled using BioTracker NIR633, a deep red fluorescent dye that labels acidic organelles in live cells. First, in agreement with our previous observation (Figures 4 and S7), the **CyC$_{31\text{-Dansyl}}$** and **CyC$_{32\text{-Dansyl}}$** exhibited a diffuse fluorescence and only few colocalization between the Dansyl and the BioTracker signals were observed inside Raw264.7 cells (Figure S8). Conversely, the **CyC$_{7(\alpha,\beta)\text{-Dansyl}}$** displayed a clear colocalization with BioTracker positive regions (Figure 5A,B). Quantitative analysis of the Dansyl fluorescence signal in these BioTracker positive regions showed a significant 1.5 to 1.8-fold change in the average mean intensity for **CyC$_{7\alpha\text{-Dansyl}}$** (85.5 ± 0.76 au) and **CyC$_{7\beta\text{-Dansyl}}$** (79.8 ± 0.89 au) vs **CyC$_{31\text{-Dansyl}}$** (48.2 ± 0.85 au) and **CyC$_{32\text{-Dansyl}}$** (51.8 ± 0.89 au) (Figure S9), therefore confirming the preferential colocalization of the **CyC$_{7(\alpha,\beta)\text{-Dansyl}}$** within acidic compartments.

From these findings, **CyC$_{7\text{-Dansyl}}$**-treated macrophages were next incubated in the presence of the vacuolar-type H^+-ATPase inhibitor Concanamycin A (ConA) (i.e., an inhibitor of endolysosomal acidification).[48] Indeed, ConA inhibited endolysosomal acidification resulting in the loss of BioTracker staining, but unexpectedly also impaired the **CyC$_{7\text{-Dansyl}}$** accumulation phenotype resulting in a diffuse Dansyl fluorescence all around the cell, similar to those reached with both **CyC$_{31/32\text{-Dansyl}}$** (Figures 5A,B and S8A,B). Furthermore, with infected macrophages the presence of ConA results mainly in the loss of the strict colocalization of the **CyC$_{\text{-Dansyl}}$** with the intracellular mycobacteria (Figures 5C & S8C), as observed above in Figures 4 and S7. Finally, intracellular antibiotic activity assays performed with 100 nM ConA led to a complete abrogation of the **CyC$_{7(\alpha,\beta)}$** inhibitory effects, without altering intramacrophage *M. abscessus* growth or intracellular efficacy of imipenem used as drug control (Figure 5D). Because the intracellular activity of the compounds appears to be correlated with acidic compartments, we investigated whether low pH was needed for activating the **CyC** in extracellular conditions. Then, we conducted susceptibility testing at various pH in the 5.5−7.0 range and showed that **CyC$_{7(\alpha,\beta)}$** or **CyC$_{31}$** MIC values against extracellular *M. abscessus* S growth were not modified, thus

https://doi.org/10.1021/acsinfecdis.2c00448
ACS Infect. Dis. 2022, 8, 2564−2578

suggesting that the antibacterial activity of these compounds is not pH-dependent (Figure 5E).

DISCUSSION

The continuous and rapid emergence of drug-resistant mycobacteria, associated with the lack of new antibiotics entering the market, has become a global public health concern that threatens the effective diagnosis and treatment of pulmonary infectious diseases. Infections caused by NTM have now become clinically relevant and are extremely difficult to treat due to the intrinsic resistance of such mycobacteria to many common antibiotics. Among NTM, *M. abscessus* is the most antibiotic-resistant mycobacterial species responsible for severe respiratory, skin and mucosal infections in humans, frequently found in immunocompromised patients or patients with CF or chronic obstructive pulmonary disease.[49,50] In the case of CF patients, *M. abscessus* infection may also be exacerbated by polybacterial lung infections with other microorganisms, such as *P. aeruginosa* and/or *S. aureus*.[46] In this context of coinfection, *M. abscessus* would be missed in the absence of effective microbiological surveillance, whereas it is of great importance to accurately detect its presence in patient's sputum in order to adapt the antimicrobial treatment.[22,49]

Toward the generation of new antibacterial leads, the **CyC** analogues are not only nontoxic for mammalian cells, but above all represent a novel class of selective and efficient multitarget inhibitors leading to the arrest of *M. abscessus* extracellular and/or intracellular growth through the inhibition of various mycobacterial enzymes involved in important physiological processes.[24] Herein, we report an optimized and efficient total synthesis of fluorescent Dansyl derivatives of four active **CyC** analogues and their use as efficient probes. We demonstrated that these fluorescent $\mathbf{CyC}_{\text{-Dansyl}}$ not only behave similarly to their parent molecules in terms of antibacterial activity and toxicity toward host cells, but also specifically label all mycobacterial species tested, including *M. abscessus* in the context of a polybacterial mixture with *P. aeruginosa* and *S. aureus*, with high sensitivity because a single mycobacterium in the presence of 10^3 other bacteria can be detected. Moreover, we provide compelling evidence that the absence of the antibacterial effect on Gram-positive and Gram-negative bacteria results from the inability of these **CyCs** to cross the bacterial membrane of the latter microorganisms. The most likely hypothesis is that the hydrophobic nature of the **CyCs** would favor their diffusion across the waxy and lipid-rich mycobacterial membrane, unlike that of Gram-positive and Gram-negative bacteria. Such property could be used for the rapid detection of *M. abscessus* in patient's sputum thus paving the way for new promising applications of the **CyCs** in diagnostics.

Another important issue resides in the fact that the penetration of the fluorescent **CyC** inside the mycobacteria was not correlated with their respective MIC values (Table 1 and Figure 3). Accordingly, $\mathbf{CyC}_{\text{32-Dansyl}}$ and $\mathbf{CyC}_{7(\alpha,\beta)\text{-Dansyl}}$ which are ineffective against *M. abscessus* extracellular growth behave similarly to $\mathbf{CyC}_{\text{31-Dansyl}}$ in terms of bacterial fluorescence labeling (Figure 3B). This unexpected feature implies that the antibacterial activity of the **CyC** against the extracellular growth of *M. abscessus* would result from the inhibition of mycobacterial target enzymes specific to each compound, as recently demonstrated in the case of *M. tuberculosis*,[51] independent of their penetration properties because they are all capable to enter the mycobacteria. In other words, the discrepancy in terms of extracellular activity between the four **CyC** might simply rely on relative chemical reactivity between the phosphate (i.e., potent $\mathbf{CyC}_{17}$ & $\mathbf{CyC}_{31}$) and phosphonate (i.e., inactive $\mathbf{CyC}_{7(\alpha,\beta)}$ & $\mathbf{CyC}_{32}$) chemical groups.

When tested against *M. abscessus* infected macrophages, each $\mathbf{CyC}_{\text{-Dansyl}}$ probe also perfectly colocalized with intracellular bacterial cells, regardless of their respective intracellular MIC_{Raw} values (Table 2). A distinct fluorescent profile inside Raw264.7 macrophages was however obtained, depending on the compounds. Following BioTracker labeling, our results clearly suggest that the $\mathbf{CyC}_{7(\alpha,\beta)\text{-Dansyl}}$, only active against intramacrophagic *M. abscessus* growth, would accumulate preferentially in acidic compartments contrary to $\mathbf{CyC}_{31/32\text{-Dansyl}}$ for which a predominantly diffuse fluorescence was observed within the cells (Figures 5 & S8). The inhibitor of the vacuolar-type H^+-ATPase Concanamycin A (ConA) disrupted the intracellular accumulation phenotype of $\mathbf{CyC}_{7(\alpha,\beta)\text{-Dansyl}}$, drastically abolished their colocalization with intracellular *M. abscessus* inside infected macrophages, and impaired their antibacterial efficacy as shown by intracellular antibiotic susceptibility assays (Figures 4 and 5). Conversely, the presence of ConA did not significantly alter $\mathbf{CyC}_{31/32\text{-Dansyl}}$ fluorescent profile inside Raw264.7 cells. These novel results support the idea that in conditions where acidification is suppressed, the ability of the $\mathbf{CyC}_{7(\alpha,\beta)}$ to accumulate in specific acidic compartments and restrict intramacrophagic *M. abscessus* replication would be limited.

Moreover, the fact that the extracellular antibacterial activity of the **CyC** is not pH-dependent (Figure 5E) also presumes that the partitioning and accumulation of $\mathbf{CyC}_{7(\alpha,\beta)}$ in acidic compartments represents the crucial step that drives their delivery to the mycobacterial containing phagosomes. In a similar way to bedaquiline which accumulates in host lipid bodies (LB) and is transferred to *M. tuberculosis* as LBs are consumed thus leading to enhanced antibacterial activity,[52] host-cell acidic compartments constitute a transferable reservoir responsible for the $\mathbf{CyC}_{7(\alpha,\beta)}$ antimicrobial efficacy against intracellularly replicating *M. abscessus*. Consequently, even though endolysosomal acidification appears to be an important determinant contributing to the $\mathbf{CyC}_{7(\alpha,\beta)}$ intracellular efficacy, their mode of action would differ drastically from that of pyrazinamide[53] or clofazimine[54] for which the pH is the critical issue for the activation of the drug against *M. tuberculosis*-infected macrophages. Given all these findings, it is also tempting to hypothesize that the mostly diffuse localization of $\mathbf{CyC}_{31/32}$ inside the cells may be responsible for the lack of intracellular activity.

CONCLUSIONS

Diseases caused by pathogenic mycobacterial species continue to cause significant morbidity and mortality to human health. In this context, the discovery few years ago of a very promising family of multitargeted inhibitors, called cyclipostins and cyclophostin analogues (**CyCs**), with potent antimycobacterial activities has opened the way to new therapeutic strategies in the fight against mycobacterial-related diseases. These include *M. tuberculosis* and *M. abscessus*, two major human pathogens responsible for severe lung infections. Moreover, these **CyCs** do not alter the growth of Gram-positive and Gram-negative bacteria and do not exhibit significant toxicity toward mammalian cells. In this work, using several selected fluorescent **CyCs**, we brought new insights into their mode of action against both extracellular and intracellular mycobacterial growth. All these studies have not only reinforced the great interest of the

https://doi.org/10.1021/acsinfecdis.2c00448
ACS Infect. Dis. 2022, 8, 2564−2578

CyC compounds, but above all our results provide a first set of explanations related to the antibacterial activity of the **CyC**, both in vitro and ex vivo, underlining the huge and combined effect of the host-cell environment with antibiotics during mycobacterial infection, and particularly here in the case of *M. abscessus* infections. Apart from the therapeutic potential of unlabeled **CyC** compounds, thanks to their multitargeted covalent mechanism of action, fluorescent **CyC** probes could be used to specifically label pathogenic mycobacteria in polybacterial mixtures thus leading to new efficient, selective, and sensitive diagnostic markers. This is of particular importance to patients with CF for whom identification of *M. abscessus* is crucial, especially for transplantation purposes.[23]

METHODS

Chemistry. Detailed procedures and the full chemical characterization (^{1}H, ^{13}C, and ^{31}P NMR spectra) of each new analogue (i.e., the four $\mathbf{CyC}_{\text{-Dansyl}}$ and $\mathbf{CyC}_{31/32}$) are reported in the Supporting Information.

Stock solutions (10 mM) in which the **CyC** compounds (purity of ≥95%) were found to be completely soluble in dimethyl sulfoxide (DMSO) were prepared and stored at 4 °C.

Bacterial Culture. *Escherichia coli* DH10B, *Pseudomonas aeruginosa* PAO1, and *Staphylococcus aureus* (clinical isolate) cells were grown in Luria−Bertani broth (Invitrogen, Carlsbad CA, USA) at 37 °C under shaking at 200 rpm. *M. smegmatis* was cultured in Middlebrook 7H9 liquid media (BD Difco) supplemented with 0.05% Tween 80 (Sigma-Aldrich, Saint-Quentin Fallavier, France) and 0.2% glycerol (Euromedex, France) (7H9-S). *M. abscessus* CIP104536^{T} with either a smooth (S) or a rough (R) morphotype, *M. marinum* ATCC BAA-535/M, *M. bovis* BCG Pasteur 1173P2, and *M. tuberculosis* mc^{2}6230 (H37Rv Δ*RD1* Δ*panCD*[55]) were cultured in 7H9-S supplemented with 10% oleic albumin dextrose catalase (OADC enrichment, BD Difco) (7H9-S^{OADC}). In the case of *M. tuberculosis* mc^{2}6230, 24 μg/mL D-pantothenate (Sigma-Aldrich) was also added in the 7H9-S^{OADC} medium. Recombinant *M. abscessus* S carrying pTEC27 (Addgene, plasmid 30182) expressing red fluorescent tdTomato protein was grown in 7H9-S^{OADC} with 500 μg/mL hygromycin B (Euromedex, France).[56] Recombinant *M. abscessus* S carrying the pSMT3-GFP-LuxAB plasmid allowing luminescence and fluorescence was grown in 7H9-S^{OADC} with 1000 μg/mL hygromycin B (Euromedex, France).[45] The latter *M. abscessus* S-LuxAB strain was a generous gift from Prof. Jean-Louis Herrmann (Université Versailles-Saint-Quentin-en-Yvelines, France) and was used for measurement of bacterial load inside infected macrophages. All cultures were incubated at 37 °C, except *M. marinum* which was cultured at 32 °C. *M. smegmatis* and *M. abscessus* were stirred at 200 rpm; *M. bovis* BCG, *M. tuberculosis* mc^{2}6230, and *M. marinum* at 50 rpm.

Determination of MICs. Susceptibility testing for mycobacteria was performed using the Middlebrook 7H9 broth microdilution method. MICs of the **CyCs** were determined in 96-well flat-bottom Nunclon Delta Surface microplates with lid (Thermo-Fisher Scientific, ref. 167008) using REMA as described previously.[26,27,57] Briefly, log-phase bacteria were diluted to a cell density of 5×10^{6} cells/mL in appropriate 7H9-S medium. Then, 100 μL of this bacterial suspension (5×10^{5} cells per well) was added to each well containing 100 μL of the appropriate 7H9-S medium, serial twofold dilutions of the selected **CyCs** or controls to a final volume of 200 μL. Plates were incubated at 37 °C (32 °C for *M. marinum*) for either 3−5 days (*M. smegmatis* and *M. abscessus*) or 7−14 days (*M. marinum*, *M. bovis* BCG and *M. tuberculosis* mc^{2}6230). Then, 20 μL of 0.025% (w/v) resazurin solution was added, and incubation was proceeded for color change (from blue to pink) in the control well (bacteria without antibiotic). Fluorescence of the resazurin metabolite resorufin ($\lambda_{ex}/\lambda_{em}$ = 530/590 ± 10 nm) was quantified using a Tecan Spark 10 M multimode microplate reader (Tecan Group Ltd., France). Relative fluorescence units were defined as: RFU% = (test well FU/mean FU of growth control wells) × 100. MIC values were determined by fitting the RFU% sigmoidal dose−response curves[25,58] in Kaleidagraph 4.2 software (Synergy Software). The lowest compound concentration leading to 90% bacterial growth inhibition was defined as the MIC_{90}.

In parallel, MICs of *E. coli*, *P. aeruginosa*, and *S. aureus* were assessed using the broth microdilution method.[59] Log-phase bacteria were diluted in Luria−Bertani medium to around 5×10^{5} cells/mL. Then 100 μL of this latter inoculum were added into each well containing serial dilution of the **CyCs**, and the plates were incubated at 37 °C for 18−24 h. After incubation, OD_{600nm} was recorded using a Tecan Spark 10 M multimode microplate reader (Tecan Group Ltd., France). The MIC was defined as the lowest concentration of **CyC** that inhibited visible growth of the bacteria.

Each assay for each strain was carried out at least in triplicate.

Determination of Cytotoxic Activity for New CyCs. The cytotoxicity of each new synthesized **CyC** against eukaryotic cells was measured based on the reduction of resazurin as a value of cellular viability by metabolic activity.[27,60] Murine (Raw264.7) macrophages (American Type Culture Collection TIB-71) were cultured from a freezer stock in Dulbecco's modified Eagle's medium (DMEM; Gibco) supplemented with 10% heat-inactivated fetal calf serum (FBS, Invitrogen) (DMEM^{FBS}). Cells were grown at 37 °C and 5% CO_2 to subconfluent concentrations. Then 5×10^{4} cells/well were seeded in 96-well flat-bottom Nunclon Delta Surface microplates with lid (ThermoFisher Scientific) in a final volume of 200 μL per well and incubated for additional 24 h. The medium was removed by aspiration, and 200 μL of serial twofold dilution of each compound ($\mathbf{CyC}_{7(\alpha,\beta)\text{-Dansyl}}$, $\mathbf{CyC}_{31\text{-Dansyl}}$, $\mathbf{CyC}_{32\text{-Dansyl}}$, as well as $\mathbf{CyC}_{31}$ and $\mathbf{CyC}_{32}$) in DMEM^{FBS} were then added to each well. After 24 h incubation, 20 μL of a 0.025% (w/v) resazurin solution was added to each well. Fluorescence was measured following a 4 h incubation at 37 °C and 5% CO_2 in the dark, by excitation at 530 nm and emission at 590 nm as described above, leading to relative metabolic activities. Addition of DMSO was used as 100% viability reference and addition of 0.2% Triton X-100 solution served as the negative standard (0% viability). All experiments were performed as two independent triplicates.

Intramacrophage Killing Assay. Raw264.7 macrophages were grown in DMEM^{FBS} medium at 37 °C and 5% CO_2 to subconfluent concentrations. Then 5×10^{4} cells/well were seeded in 96-well flat-bottom Nunclon Delta Surface microplates with lid in a final volume of 200 μL per well and cultured for additional 24 h. The cells were infected with *M. abscessus* S-LuxAB at a MOI of 1:10 and incubated at 37 °C in the presence of 5% CO_2 for 3 h. Cells were then washed three times with DMEM, then refed with DMEM^{FBS} supplemented with 200 μg/mL amikacin for 1 h at 37 °C and 5% CO_2 to kill any extracellular bacteria, and washed again three times with DMEM prior to the addition of 2-fold dilutions of the **CyC** compounds or IMP in DMEM^{FBS} supplemented with 50 μg/mL (i.e., 85.4 μM) amikacin (200 μL final volume). In each plate, negative controls

https://doi.org/10.1021/acsinfecdis.2c00448
ACS Infect. Dis. 2022, 8, 2564−2578

consisting of amikacin (50 μg/mL) and 1% DMSO (i.e., infected macrophages only) as well as positive controls containing amikacin (50 μg/mL) plus 80 μg/mL (i.e., 267 μM) IMP were also included.[27,61] Plates were incubated for 24 h at 37 °C, 5% CO_2.

Luminescence measurement was then used to check intracellular bacterial viability of *M. abscessus* S-LuxAB[45] following treatment with each **CyC** compound concentration. Infected macrophage cells were first washed three times with PBS and lysed by addition of 200 μL cold PBS-0.1% Triton X-100. A solution of 1% *n*-decanal (Sigma-Aldrich) in ethanol (20 μL) was added into each well after lysis of macrophages, and luminescence was read immediately using a Tecan Spark 10 M multimode microplate reader (Tecan Group Ltd., France). DMSO-treated infected macrophages corresponded as the control representing 100% of bacterial viability. The luminescence value obtained was next correlated to CFU using a calibration curve $Log_{10}(Lux) = f(Log_{10}(CFU))$ initially built by plating 10-fold serial dilutions of *M. abscessus* S-LuxAB on 7H9 agar medium, followed by colony enumeration after 4−5 days of incubation at 37 °C. Intracellular MIC_{Raw} values were further determined by fitting the CFU% sigmoidal dose−response curves in Kaleidagraph 4.2 software (Synergy Software). The lowest compound concentration inhibiting 50% of intracellular bacterial growth was defined as the MIC_{50Raw}. Each experiment was performed three times independently.

Mycobacteria and Infected/Noninfected Macrophages Labeling with the $CyC_{\text{-Dansyl}}$. Mid-log phase mycobacterial suspension in appropriate 7H9-S medium was harvested for 15 min at 3500 rpm and resuspended in PBS buffer (pH 7.4) containing 0.05% (v/v) Tween 20 (Euromedex, France) (PBS-T) at an OD_{600} corresponding to 1.5×10^{10} cells/mL. Then, the cells were incubated with 200 μM of each $\mathbf{CyC_{\text{-Dansyl}}}$ (i.e., $\mathbf{CyC_{31\text{-Dansyl}}}$, $\mathbf{CyC_{32\text{-Dansyl}}}$, $\mathbf{CyC_{7\alpha\text{-Dansyl}}}$, and $\mathbf{CyC_{7\beta\text{-Dansyl}}}$) or DMSO (negative control) for 3 h at 37 °C (32 °C for *M. marinum*) under shaking at 200 rpm. After incubation, bacteria were washed three times with PBS-T and resuspended in 100 μL PBS-T. For quantification of total fluorescence, 100 μL of each sample (i.e., 7.5×10^9 cells/mL) in PBS-T was dispensed in a 96-well Chimney black microplate (Greiner Bio-one, Germany). The fluorescence related to the Dansyl group was recorded at $\lambda_{ex}/\lambda_{em} = 400/535 \pm 10$ nm using a Tecan Spark 10 M multimode microplate reader (Tecan Group Ltd., France). For microscopy observation, the bacteria were fixed with 4% paraformaldehyde in PBS for 1 h at room temperature, washed three times with PBS-T, and resuspended in 100 μL PBS-T. Microscopy observations also performed in PBS buffer but in the absence of Tween 20 resulted in similar labeling results, thus excluding any interference of detergent in the labeling of mycobacteria (*data not shown*).

Raw264.7 macrophages were grown in $DMEM^{FBS}$ medium at 37 °C and 5% CO_2 to subconfluent concentration. Then 2.5×10^5 cells/well were seeded in eight-well Nunc Lab-Tek II Chamber Slide System, RS glass (ThermoFisher Scientific) in a final volume of 250 μL per well and cultured for additional 24 h. Cells were washed three times with DMEM, then refed with $DMEM^{FBS}$ supplemented with 100 μM fluorescent $\mathbf{CyC_{\text{-Dansyl}}}$ probes, and incubated for additional 24 h at 37 °C and 5% CO_2. Cells were then washed three times with DMEM and infected with the fluorescent *M. abscessus* S-tdTomato strain at a MOI of 10 and processed as described above (see Intramacrophage Killing Assay section). Alternatively, the cells were first infected with *M. abscessus* S-tdTomato strain prior to a 24 h incubation period with 100 μM $\mathbf{CyC_{\text{-Dansyl}}}$ probes. After incubation, the infected and noninfected macrophages were washed three times with sterile PBS, fixed using 4% paraformaldehyde for 15 min, then washed twice with PBS, and re-filled with 250 μL PBS.

Fluorescence Microscopy. Fixed samples (4 μL bacterial suspension, i.e., 3.0×10^7 cells, spotted between a microscope slide and coverslip; or macrophage cells in Lab-Tek II Chamber Slide System) were analyzed by snapshot fluorescence imaging at room temperature using an Olympus IX81 confocal microscope equipped with a UPlanSApo 100× 1.40 NA objective and operated with the FV1000 software. Acquisitions were taken using a two-line Kalman integration. Exposure time was 10 μs/pixel for both laser transmission and fluorescence images with conserved settings (X, Y, Z, HV, Gain and offset). The Dansyl was detected by excitation with a 405 nm laser with 39−50% intensity, and emission was collected using a semitransparent mirror collecting all wavelength under 560 nm. The tdTomato was detected by excitation with a 515 nm laser with 20−40% intensity, and emission was collected using a semitransparent mirror collecting all wavelength over 560 nm.

3D-fluorescence images were acquired on a DeltaVision OMX SR imaging system from GE Healthcare, with an Olympus PlanApo N 60× 1.42 NA and 2 cameras sCMOS. The Dansyl was detected by a 405 nm diode laser (61 mW) at 2%T during 50 ms and with a 435/31 nm emission filter and the Nile Red was detected by a 568 nm diode-pumped solid-state laser (61 mW) at 2%T during 100 ms and with a 609/37 nm emission filter. Eleven sections of images of 512 × 512 pixels (pixel size of 80 nm) were acquired with a section spacing of 0.125 μm and a sample thickness of 1.25 μm. Images were then deconvoluted with the microscope software "Softworks 7.0.0" and then analyzed with Fiji 1.53f51. With each $\mathbf{CyC_{\text{-Dansyl}}}$ probe, two biological replicates were made with infected and noninfected macrophages; and for each sample, eight different images were taken per frame in order to get more than 200 macrophage cells in total. Images were next converted to an 8-bit intensity color range. In all cases, the corresponding control images were taken/checked prior to any fluorescence imaging and quantification.

Analysis of Dansyl Mean Fluorescence Intensity (Adapted from ref 53). A background noise was first calculated by taking the mean fluorescence intensity of 20 different areas free of any cells for each channel (i.e., Dansyl and tdTomato frames, respectively) and was subtracted to each frame. Segmentation and analysis of the images recorded (126.98 × 126.98 μm; 512 × 512 pixels) were performed using the open-source program ImageJ/Fiji 1.53f51. Cell segmentation was performed by manually detouring the Raw264.7 cells on the laser transmission frame and transforming it into a mask. This Raw-mask was then used to determine the Dansyl mean fluorescence intensity of pixels associated to the macrophage region and corresponding to the inhibitor cellular uptake. For intracellular bacterial segmentation, a manual threshold was first applied to the tdTomato frame to create a binary mask, defining all bacterial regions of interest. This bacterial-mask was used to measure the Dansyl mean fluorescence intensity of pixels associated to the *M. abscessus* S-tdTomato region and corresponding to the inhibitor bacterial uptake.

Live Fluorescence Imaging and BioTracker Staining. For live-cell imaging, infected and noninfected Raw264.7 macrophages ±100 nM ConA and ±100 μM $\mathbf{CyC_{\text{-Dansyl}}}$ were washed with PBS buffer (pH 7.4) and stained for 30 min with $DMEM^{FBS}$ medium containing 1X BioTracker NIR633 Lysosome Dye (Sigma-Aldrich) at 37 °C and 5% CO_2 following

https://doi.org/10.1021/acsinfecdis.2c00448
ACS Infect. Dis. 2022, 8, 2564−2578

the manufacturer recommendations. Live-cell imaging was further performed by excitation with a 633 nm laser with 10% intensity, and emission was collected using a semitransparent mirror collecting all wavelength over 560 nm as described above. Segmentation and analysis were performed as described above. First, the background was removed from each **CyC$_{\text{-Dansyl}}$** and BioTracker frames as described previously. To segment the BioTracker positive area, a manual threshold was applied to the BioTracker frames in order to create a binary mask, thereby defining all regions of interest. This BioTracker-mask was further used to quantify the Dansyl mean intensity inside BioTracker positive areas which allowed to compare the uptake of each **CyC$_{\text{-Dansyl}}$** inhibitor in acidic compartments inside the macrophages.

Statistical Analyses. Statistical analyses were performed using Prism 4.0 (Graphpad, Inc) and are detailed in each figure legend. Density plot of the resulting fluorescence data was calculated using the distplot tool from the seaborn statistical data visualization python library,[62] and the sinaplot-boxplots were generated with the PlotOfData web tool.[63]

■ ASSOCIATED CONTENT

Supporting Information

The Supporting Information is available free of charge at https://pubs.acs.org/doi/10.1021/acsinfecdis.2c00448.

Detailed protocols, full chemical characterization, NMR spectra of the new fluorescent **CyC** compounds; Figures S1 and S2, synthesis of racemic **CyC$_{7\text{-Dansyl}}$** and **CyC$_{11\text{-Dansyl}}$**; Figure S3, fluorescence intensity profile of each **CyC$_{\text{-Dansyl}}$**-treated mycobacteria; Figure S4, in-gel fluorescence of DMSO-treated total lysate of *M. abscessus*; Figure S5, fluorescence intensity profile of **CyC$_{\text{-Dansyl}}$**-treated *E. coli*, *P. aeruginosa* or *S. aureus* bacteria; Figure S6, in-gel fluorescence of **CyC$_{\text{-Dansyl}}$**-treated total lysate of *E. coli*, *P. aeruginosa*, or *S. aureus*; Figures S7−S9, fluorescence imaging and quantification of the **CyC$_{\text{-Dansyl}}$** inside infected and noninfected macrophages (PDF)

Movie S1, 3-D reconstruction of a stack of deconvoluted images of **CyC$_{31\text{-Dansyl}}$**-treated *M. abscessus* S cells from an epi-fluorescence microscope (AVI)

■ AUTHOR INFORMATION

Corresponding Authors

Christopher D. Spilling − *Department of Chemistry & Biochemistry, University of Missouri St. Louis, St. Louis, Missouri 63121, United States*; Email: SpillingC@msx.umsl.edu

Jean-François Cavalier − *CNRS, LISM, IMM FR3479, Aix-Marseille Univ, Marseille 13009, France*; orcid.org/0000-0003-0864-8314; Email: jfcavalier@imm.cnrs.fr

Stéphane Canaan − *CNRS, LISM, IMM FR3479, Aix-Marseille Univ, Marseille 13009, France*; orcid.org/0000-0001-7478-300X; Email: canaan@imm.cnrs.fr

Authors

Morgane Sarrazin − *CNRS, LISM, IMM FR3479, Aix-Marseille Univ, Marseille 13009, France*

Benjamin P. Martin − *Department of Chemistry & Biochemistry, University of Missouri St. Louis, St. Louis, Missouri 63121, United States*

Romain Avellan − *CNRS, LISM, IMM FR3479, Aix-Marseille Univ, Marseille 13009, France*

Giri Raj Gnawali − *Department of Chemistry & Biochemistry, University of Missouri St. Louis, St. Louis, Missouri 63121, United States*

Isabelle Poncin − *CNRS, LISM, IMM FR3479, Aix-Marseille Univ, Marseille 13009, France*

Hugo Le Guenno − *Microscopy Core Facility, IMM FR3479, CNRS, Aix-Marseille Univ, Marseille 13009, France*

Complete contact information is available at: https://pubs.acs.org/10.1021/acsinfecdis.2c00448

Author Contributions

Conceptualization: C.D.S., S.C., and J.-F.C. Resources: B.P.M., G.R.G., and C.D.S. Investigations: M.S., R.A., I.P., and H.L.G. Formal analysis: M.S., R.A., H.L.G., S.C., and J.-F.C. Funding acquisition: S.C. and J.-F.C. Supervision: C.D.S., S.C., and J.-F.C. Writing-original draft: M.S., R.A., and J.-F.C. Writing-review & editing: M.S., R.A., H.L.G., C.D.S., S.C., and J.-F.C. M.S., B.P.M., R.A., and G.R.G. contributed equally and should be considered as first coauthors. All authors have given approval to the final version of the manuscript.

Notes

The authors declare no competing financial interest.

■ ACKNOWLEDGMENTS

This work was supported by the Centre National de la Recherche Scientifique (CNRS), Aix-Marseille University (AMU), the Association Grégory Lemarchal and Vaincre la Mucoviscidose (project N° RF20190502466), and the Agence Nationale de la Recherche (LipInTB project N°ANR-19-CE44-0011). M.S. was supported by a PhD fellowship from the Association Grégory Lemarchal and Vaincre la Mucoviscidose (project n°RF20190502466). R.A. was supported by a PhD fellowship from the Agence Nationale de la Recherche (LipInTB project N°ANR-19-CE44-0011). We thank Prof. Jean-Louis Herrmann (Université Versailles-Saint-Quentin-en-Yvelines, France) for sharing the *M. abscessus* S-LuxAB bacterial strain.

■ ABBREVIATIONS

ABP, activity-based probe; au, arbitrary unit; AMK, amikacin; CC_{50}, compound concentration leading to 50% of cell cytotoxicity; CF, cystic fibrosis; CFU, colony-forming units; ConA, Concanamycin A; CyC, cyclipostins and cyclophostin analogues; IMP, imipenem; INH, isoniazid; MIC_{50Raw}, minimal compound concentration leading to a 50% decrease in CFU count as compared to untreated cells; MIC_{90}, minimal inhibitory concentration leading to 90% of growth inhibition; NTM, nontuberculous mycobacterial; REMA, resazurin microtiter assay; RFU%, relative fluorescence units

■ REFERENCES

(1) WHO, Global tuberculosis report. 2022, https://www.who.int/teams/global-tuberculosis-programme/data.

(2) Aubry, A.; Mougari, F.; Reibel, F.; Cambau, E. Mycobacterium marinum. *Microbiol. Spectr.* **2017**, *5* (2), DOI: 10.1128/microbiolspec.TNMI7-0038-2016.

(3) Stout, J. E.; Koh, W. J.; Yew, W. W. Update on pulmonary disease due to non-tuberculous mycobacteria. *Int. J. Infect. Dis.* **2016**, *45*, 123−134.

(4) Swenson, C.; Zerbe, C. S.; Fennelly, K. Host Variability in NTM Disease: Implications for Research Needs. *Front. Microbiol.* **2018**, *9*, 2901.

(5) Tortoli, E.; Fedrizzi, T.; Meehan, C. J.; Trovato, A.; Grottola, A.; Giacobazzi, E.; Serpini, G. F.; Tagliazucchi, S.; Fabio, A.; Bettua, C.;

Bertorelli, R.; Frascaro, F.; De Sanctis, V.; Pecorari, M.; Jousson, O.; Segata, N.; Cirillo, D. M. The new phylogeny of the genus Mycobacterium: The old and the news. *Infect. Genet. Evol.* **2017**, *56*, 19−25.
(6) van Ingen, J.; Wagner, D.; Gallagher, J.; Morimoto, K.; Lange, C.; Haworth, C. S.; Floto, R. A.; Adjemian, J.; Prevots, D. R.; Griffith, D. E.; Ntm, N. E. T. Poor adherence to management guidelines in nontuberculous mycobacterial pulmonary diseases. *Eur. Respir. J.* **2017**, *49*, 1601855.
(7) Schiff, H. F.; Jones, S.; Achaiah, A.; Pereira, A.; Stait, G.; Green, B. Clinical relevance of non-tuberculous mycobacteria isolated from respiratory specimens: seven year experience in a UK hospital. *Sci. Rep.* **2019**, *9*, 1730.
(8) Wetzstein, N.; Geil, A.; Kann, G.; Lehn, A.; Schuttfort, G.; Kessel, J.; Bingold, T. M.; Kupper-Tetzel, C. P.; Haberl, A.; Graf, C.; Vehreschild, M.; Stephan, C.; Hogardt, M.; Wichelhaus, T. A.; Wolf, T. Disseminated disease due to non-tuberculous mycobacteria in HIV positive patients: A retrospective case control study. *PLoS One* **2021**, *16*, No. e0254607.
(9) Roux, A. L.; Catherinot, E.; Ripoll, F.; Soismier, N.; Macheras, E.; Ravilly, S.; Bellis, G.; Vibet, M. A.; Le Roux, E.; Lemonnier, L.; Gutierrez, C.; Vincent, V.; Fauroux, B.; Rottman, M.; Guillemot, D.; Gaillard, J. L.; Jean-Louis Herrmann for the OMA Group. Multicenter study of prevalence of nontuberculous mycobacteria in patients with cystic fibrosis in france. *J. Clin. Microbiol.* **2009**, *47*, 4124−4128.
(10) Leung, J. M.; Olivier, K. N. Nontuberculous mycobacteria in patients with cystic fibrosis. *Semin. Respir. Crit. Care Med.* **2013**, *34*, 124−134.
(11) Park, I.; Olivier, K. Nontuberculous mycobacteria in cystic fibrosis and non-cystic fibrosis bronchiectasis. *Semin. Respir. Crit. Care Med.* **2015**, *36*, 217−224.
(12) Roux, A. L.; Viljoen, A.; Bah, A.; Simeone, R.; Bernut, A.; Laencina, L.; Deramaudt, T.; Rottman, M.; Gaillard, J. L.; Majlessi, L.; Brosch, R.; Girard-Misguich, F.; Vergne, I.; de Chastellier, C.; Kremer, L.; Herrmann, J. L. The distinct fate of smooth and rough *Mycobacterium abscessus* variants inside macrophages. *Open Biol.* **2016**, *6*, No. 160185.
(13) Boudehen, Y. M.; Kremer, L. Mycobacterium abscessus. *Trends Microbiol.* **2021**, *29*, 951−952.
(14) Johansen, M. D.; Herrmann, J. L.; Kremer, L. Non-tuberculous mycobacteria and the rise of *Mycobacterium abscessus*. *Nat. Rev. Microbiol.* **2020**, *18*, 392−407.
(15) Catherinot, E.; Clarissou, J.; Etienne, G.; Ripoll, F.; Emile, J. F.; Daffe, M.; Perronne, C.; Soudais, C.; Gaillard, J. L.; Rottman, M. Hypervirulence of a rough variant of the *Mycobacterium abscessus* type strain. *Infect. Immun.* **2007**, *75*, 1055−1058.
(16) Catherinot, E.; Roux, A. L.; Macheras, E.; Hubert, D.; Matmar, M.; Dannhoffer, L.; Chinet, T.; Morand, P.; Poyart, C.; Heym, B.; Rottman, M.; Gaillard, J. L.; Herrmann, J. L. Acute respiratory failure involving an R variant of *Mycobacterium abscessus*. *J. Clin. Microbiol.* **2009**, *47*, 271−274.
(17) Jönsson, B. E.; Gilljam, M.; Lindblad, A.; Ridell, M.; Wold, A. E.; Welinder-Olsson, C. Molecular epidemiology of *Mycobacterium abscessus*, with focus on cystic fibrosis. *J. Clin. Microbiol.* **2007**, *45*, 1497−1504.
(18) Surette, M. G. The cystic fibrosis lung microbiome. *Ann. Am. Thorac. Soc.* **2014**, *11*, S61−S65.
(19) Kiedrowski, M. R.; Bomberger, J. M. Viral-Bacterial Co-infections in the Cystic Fibrosis Respiratory Tract. *Front. Immunol.* **2018**, *9*, 3067.
(20) Lim, A. Y. H.; Chotirmall, S. H.; Fok, E. T. K.; Verma, A.; De, P. P.; Goh, S. K.; Puah, S. H.; Goh, D. E. L.; Abisheganaden, J. A. Profiling non-tuberculous mycobacteria in an Asian setting: characteristics and clinical outcomes of hospitalized patients in Singapore. *BMC Pulm. Med.* **2018**, *18*, 85−85.
(21) Pierre-Audigier, C.; Ferroni, A.; Sermet-Gaudelus, I.; Le Bourgeois, M.; Offredo, C.; Vu-Thien, H.; Fauroux, B.; Mariani, P.; Munck, A.; Bingen, E.; Guillemot, D.; Quesne, G.; Vincent, V.; Berche, P.; Gaillard, J. L. Age-related prevalence and distribution of non-tuberculous mycobacterial species among patients with cystic fibrosis. *J. Clin. Microbiol.* **2005**, *43*, 3467−3470.
(22) Nessar, R.; Cambau, E.; Reyrat, J. M.; Murray, A.; Gicquel, B. *Mycobacterium abscessus*: a new antibiotic nightmare. *J. Antimicrob. Chemother.* **2012**, *67*, 810−818.
(23) Osmani, M.; Sotello, D.; Alvarez, S.; Odell, J. A.; Thomas, M. *Mycobacterium abscessus* infections in lung transplant recipients: 15-year experience from a single institution. *Transpl. Infect. Dis.* **2018**, *20*, No. e12835.
(24) Cavalier, J. F.; Spilling, C. D.; Durand, T.; Camoin, L.; Canaan, S. Lipolytic enzymes inhibitors: A new way for antibacterial drugs discovery. *Eur. J. Med. Chem.* **2021**, *209*, No. 112908.
(25) Nguyen, P. C.; Delorme, V.; Bénarouche, A.; Martin, B. P.; Paudel, R.; Gnawali, G. R.; Madani, A.; Puppo, R.; Landry, V.; Kremer, L.; Brodin, P.; Spilling, C. D.; Cavalier, J.-F.; Canaan, S. Cyclipostins and Cyclophostin analogs as promising compounds in the fight against tuberculosis. *Sci. Rep.* **2017**, *7*, 11751.
(26) Nguyen, P. C.; Madani, A.; Santucci, P.; Martin, B. P.; Paudel, R. R.; Delattre, S.; Herrmann, J. L.; Spilling, C. D.; Kremer, L.; Canaan, S.; Cavalier, J. F. Cyclophostin and Cyclipostins analogues, new promising molecules to treat mycobacterial-related diseases. *Int. J. Antimicrob. Agents* **2018**, *51*, 651−654.
(27) Madani, A.; Ridenour, J. N.; Martin, B. P.; Paudel, R. R.; Abdul Basir, A.; Le Moigne, V.; Herrmann, J. L.; Audebert, S.; Camoin, L.; Kremer, L.; Spilling, C. D.; Canaan, S.; Cavalier, J. F. Cyclipostins and Cyclophostin Analogues as Multitarget Inhibitors That Impair Growth of *Mycobacterium abscessus*. *ACS Infect. Dis.* **2019**, *5*, 1597−1608.
(28) Point, V.; Malla, R. K.; Diomande, S.; Martin, B. P.; Delorme, V.; Carriere, F.; Canaan, S.; Rath, N. P.; Spilling, C. D.; Cavalier, J. F. Synthesis and kinetic evaluation of cyclophostin and cyclipostins phosphonate analogs as selective and potent inhibitors of microbial lipases. *J. Med. Chem.* **2012**, *55*, 10204−10219.
(29) Point, V.; Malla, R. K.; Carriere, F.; Canaan, S.; Spilling, C. D.; Cavalier, J. F. Enantioselective inhibition of microbial lipolytic enzymes by nonracemic monocyclic enolphosphonate analogues of cyclophostin. *J. Med. Chem.* **2013**, *56*, 4393−4401.
(30) Viljoen, A.; Richard, M.; Nguyen, P. C.; Fourquet, P.; Camoin, L.; Paudal, R. R.; Gnawali, G. R.; Spilling, C. D.; Cavalier, J. F.; Canaan, S.; Blaise, M.; Kremer, L. Cyclipostins and cyclophostin analogs inhibit the antigen 85C from *Mycobacterium tuberculosis* both in vitro and in vivo. *J. Biol. Chem.* **2018**, *293*, 2755−2769.
(31) Spilling, C. D.; Martin, B. P.; Canaan, S.; Cavalier, J.-F. Fluorescent Labeled Inhibitors. US10047112B2, August 14, 2018, 2018.
(32) Susani-Etzerodt, H.; Schmidinger, H.; Riesenhuber, G.; Birner-Gruenberger, R.; Hermetter, A. A versatile library of activity-based probes for fluorescence detection and/or affinity isolation of lipolytic enzymes. *Chem. Phys. Lipids* **2006**, *144*, 60−68.
(33) Dutta, S.; Malla, R. K.; Bandyopadhyay, S.; Spilling, C. D.; Dupureur, C. M. Synthesis and kinetic analysis of some phosphonate analogs of cyclophostin as inhibitors of human acetylcholinesterase. *Bioorg. Med. Chem.* **2010**, *18*, 2265−2274.
(34) Malla, R. K.; Bandyopadhyay, S.; Spilling, C. D.; Dutta, S.; Dupureur, C. M. The first total synthesis of (+/−)-cyclophostin and (+/−)-cyclipostin P: inhibitors of the serine hydrolases acetyl cholinesterase and hormone sensitive lipase. *Org. Lett.* **2011**, *13*, 3094−3097.
(35) Vasilieva, E.; Dutta, S.; Malla, R. K.; Martin, B. P.; Spilling, C. D.; Dupureur, C. M. Rat hormone sensitive lipase inhibition by cyclipostins and their analogs. *Bioorg. Med. Chem.* **2015**, *23*, 944−952.
(36) Blanot, D.; Lee, J.; Girardin, S. E. Synthesis and biological evaluation of biotinyl hydrazone derivatives of muramyl peptides. *Chem. Biol. Drug Des.* **2012**, *79*, 2−8.
(37) Huang, J.; Liu, M.; Ma, X.; Dong, Q.; Ye, B.; Wang, W.; Zeng, W. A highly selective turn-off fluorescent probe for Cu(ii) based on a dansyl derivative and its application in living cell imaging. *RSC Adv.* **2014**, *4*, 22964−22970.

https://doi.org/10.1021/acsinfecdis.2c00448
ACS Infect. Dis. 2022, 8, 2564−2578

(38) Hanson, P. R.; Chegondi, R.; Nguyen, J.; Thomas, C. D.; Waetzig, J. D.; Whitehead, A. Total synthesis of dolabelide C: a phosphate-mediated approach. *J. Org. Chem.* **2011**, *76*, 4358−4370.
(39) Sauer, R.; Turshatov, A.; Baluschev, S.; Landfester, K. One-Pot Production of Fluorescent Surface-Labeled Polymeric Nanoparticles via Miniemulsion Polymerization with Bodipy Surfmers. *Macromolecules* **2012**, *45*, 3787−3796.
(40) Fletcher, D. I.; Ganellin, C. R.; Piergentili, A.; Dunn, P. M.; Jenkinson, D. H. Synthesis and pharmacological testing of polyaminoquinolines as blockers of the apamin-sensitive Ca^{2+}-activated K^+ channel (SK(Ca)). *Bioorg. Med. Chem.* **2007**, *15*, 5457−5479.
(41) Ing, H. R.; Manske, R. H. F. CCCXII.—A modification of the Gabriel synthesis of amines. *J. Chem. Soc.* **1926**, *129*, 2348−2351.
(42) Niwa, M.; Morikawa, M.-A.; Nabeta, T.; Higashi, N. Preparation of Anthryl Group-Tagged Helical Poly(γ-benzyl l-glutamate) Self-Assembled Film on Gold Surface and Its Interaction with DNA. *Macromolecules* **2002**, *35*, 2769−2775.
(43) O'Brien, J.; Wilson, I.; Orton, T.; Pognan, F. Investigation of the Alamar Blue (resazurin) fluorescent dye for the assessment of mammalian cell cytotoxicity. *Eur. J. Biochem.* **2000**, *267*, 5421−5426.
(44) Christophe, T.; Jackson, M.; Jeon, H. K.; Fenistein, D.; Contreras-Dominguez, M.; Kim, J.; Genovesio, A.; Carralot, J. P.; Ewann, F.; Kim, E. H.; Lee, S. Y.; Kang, S.; Seo, M. J.; Park, E. J.; Skovierova, H.; Pham, H.; Riccardi, G.; Nam, J. Y.; Marsollier, L.; Kempf, M.; Joly-Guillou, M. L.; Oh, T.; Shin, W. K.; No, Z.; Nehrbass, U.; Brosch, R.; Cole, S. T.; Brodin, P. High content screening identifies decaprenyl-phosphoribose 2′ epimerase as a target for intracellular antimycobacterial inhibitors. *PLoS Pathog.* **2009**, *5*, No. e1000645.
(45) Le Moigne, V.; Blouquit-Laye, S.; Desquesnes, A.; Girard-Misguich, F.; Herrmann, J. L. Liposomal amikacin and *Mycobacterium abscessus*: intimate interactions inside eukaryotic cells. *J. Antimicrob. Chemother.* **2022**, dkac348.
(46) Takano, K.; Shimada, D.; Kashiwagura, S.; Kamioka, Y.; Hariu, M.; Watanabe, Y.; Seki, M. Severe Pulmonary *Mycobacterium abscessus* Cases Due to Co-Infection with Other Microorganisms Well Treated by Clarithromycin and Sitafloxacin in Japan. *Int. Med. Case Rep. J.* **2021**, *14*, 465−470.
(47) Wynn, T. A.; Chawla, A.; Pollard, J. W. Macrophage biology in development, homeostasis and disease. *Nature* **2013**, *496*, 445−455.
(48) Huss, M.; Ingenhorst, G.; Konig, S.; Gassel, M.; Drose, S.; Zeeck, A.; Altendorf, K.; Wieczorek, H. Concanamycin A, the specific inhibitor of V-ATPases, binds to the V(o) subunit c. *J. Biol. Chem.* **2002**, *277*, 40544−40548.
(49) Griffith, D. E. *Mycobacterium abscessus* and Antibiotic Resistance: Same As It Ever Was. *Clin. Infect. Dis.* **2019**, *69*, 1687−1689.
(50) Shaw, L. P.; Doyle, R. M.; Kavaliunaite, E.; Spencer, H.; Balloux, F.; Dixon, G.; Harris, K. A. Children With Cystic Fibrosis Are Infected With Multiple Subpopulations of *Mycobacterium abscessus* With Different Antimicrobial Resistance Profiles. *Clin. Infect. Dis.* **2019**, *69*, 1678−1686.
(51) Barelier, S.; Avellan, R.; Gnawali, G. R.; Fourquet, P.; Roig-Zamboni, V.; Poncin, I.; Point, V.; Bourne, Y.; Audebert, S.; Camoin, L.; Spilling, C. D.; Canaan, S.; Cavalier, J. F.; Sulzenbacher, G. Direct capture, inhibition and crystal structure of HsaD (Rv3569c) from *M. tuberculosis*. *FEBS J.* **2022**, DOI: 10.1111/febs.16645.
(52) Greenwood, D. J.; Dos Santos, M. S.; Huang, S.; Russell, M. R. G.; Collinson, L. M.; MacRae, J. I.; West, A.; Jiang, H.; Gutierrez, M. G. Subcellular antibiotic visualization reveals a dynamic drug reservoir in infected macrophages. *Science* **2019**, *364*, 1279−1282.
(53) Santucci, P.; Greenwood, D. J.; Fearns, A.; Chen, K.; Jiang, H.; Gutierrez, M. G. Intracellular localisation of *Mycobacterium tuberculosis* affects efficacy of the antibiotic pyrazinamide. *Nat. Commun.* **2021**, *12*, 3816.
(54) Schump, M. D.; Fox, D. M.; Bertozzi, C. R.; Riley, L. W. Subcellular Partitioning and Intramacrophage Selectivity of Antimicrobial Compounds against *Mycobacterium tuberculosis*. *Antimicrob. Agents Chemother.* **2017**, *61*, e01639−e01616.
(55) Sambandamurthy, V. K.; Derrick, S. C.; Hsu, T.; Chen, B.; Larsen, M. H.; Jalapathy, K. V.; Chen, M.; Kim, J.; Porcelli, S. A.; Chan, J.; Morris, S. L.; Jacobs, W. R. *Mycobacterium tuberculosis* DeltaRD1 DeltapanCD: a safe and limited replicating mutant strain that protects immunocompetent and immunocompromised mice against experimental tuberculosis. *Vaccine* **2006**, *24*, 6309−6320.
(56) Bernut, A.; Herrmann, J. L.; Kissa, K.; Dubremetz, J. F.; Gaillard, J. L.; Lutfalla, G.; Kremer, L. *Mycobacterium abscessus* cording prevents phagocytosis and promotes abscess formation. *Proc. Natl. Acad. Sci. U. S. A.* **2014**, *111*, E943−E952.
(57) Palomino, J. C.; Martin, A.; Camacho, M.; Guerra, H.; Swings, J.; Portaels, F. Resazurin microtiter assay plate: simple and inexpensive method for detection of drug resistance in *Mycobacterium tuberculosis*. *Antimicrob. Agents Chemother.* **2002**, *46*, 2720−2722.
(58) Rybniker, J.; Vocat, A.; Sala, C.; Busso, P.; Pojer, F.; Benjak, A.; Cole, S. T. Lansoprazole is an antituberculous prodrug targeting cytochrome bc1. *Nat. Commun.* **2015**, *6*, 7659.
(59) Wiegand, I.; Hilpert, K.; Hancock, R. E. W. Agar and broth dilution methods to determine the minimal inhibitory concentration (MIC) of antimicrobial substances. *Nat. Protoc.* **2008**, *3*, 163−175.
(60) Santucci, P.; Dedaki, C.; Athanasoulis, A.; Gallorini, L.; Munoz, A.; Canaan, S.; Cavalier, J.-F.; Magrioti, V. Synthesis of long chain β-lactones and their antibacterial activities against pathogenic mycobacteria. *ChemMedChem* **2019**, *14*, 349−358.
(61) Dupont, C.; Viljoen, A.; Dubar, F.; Blaise, M.; Bernut, A.; Pawlik, A.; Bouchier, C.; Brosch, R.; Guerardel, Y.; Lelievre, J.; Ballell, L.; Herrmann, J. L.; Biot, C.; Kremer, L. A new piperidinol derivative targeting mycolic acid transport in *Mycobacterium abscessus*. *Mol. Microbiol.* **2016**, *101*, 515−529.
(62) Waskom, M. seaborn: statistical data visualization. *J. Open Source Softw.* **2021**, *6*, 3021.
(63) Postma, M.; Goedhart, J. PlotsOfData—A web app for visualizing data together with their summaries. *PLoS Biol.* **2019**, *17*, No. e3000202.

Recommended by ACS

Pyrrolopyrimidine Bumped Kinase Inhibitors for the Treatment of Cryptosporidiosis
Matthew A. Hulverson, Wesley C. Van Voorhis, *et al.*
FEBRUARY 10, 2021
ACS INFECTIOUS DISEASES
READ

Identification and Biochemical Characterization of Pyrrolidinediones as Novel Inhibitors of the Bacterial Enzyme MurA
Reem K. Fathalla, Matthias Engel, *et al.*
OCTOBER 21, 2022
JOURNAL OF MEDICINAL CHEMISTRY
READ

6-Halopyridylmethylidene Penicillin-Based Sulfones Efficiently Inactivate the Natural Resistance of *Pseudomonas aeruginosa* to β-Lactam Antibiotics
Juan C. Vázquez-Ucha, Alejandro Beceiro, *et al.*
APRIL 29, 2021
JOURNAL OF MEDICINAL CHEMISTRY
READ

Novel Thienopyrimidine Inhibitors of *Leishmania N*-Myristoyltransferase with On-Target Activity in Intracellular Amastigotes
Andrew S. Bell, Edward W. Tate, *et al.*
JUNE 24, 2020
JOURNAL OF MEDICINAL CHEMISTRY
READ

Get More Suggestions >

SUPPORTING INFORMATION

Synthesis and Biological characterization of Fluorescent Cyclipostins & Cyclophostin Analogs: new Insights for the Diagnosis of Mycobacterial-related Diseases

Morgane Sarrazin,[a,#] Benjamin P. Martin,[b,#] Romain Avellan,[a,#] Giri Raj Gnawali,[b,#] Isabelle Poncin,[a] Hugo Le Guenno,[c] Christopher D. Spilling,[b,*] Jean-François Cavalier,[a,*] Stéphane Canaan[a,*]

[a] Aix-Marseille Univ, CNRS, LISM, IMM FR3479, Marseille, France

[b] Department of Chemistry & Biochemistry, University of Missouri St. Louis, One University Boulevard, St. Louis, MO 63121.

[c] Microscopy Core Facility, IMM FR3479, CNRS, Aix-Marseille Univ, Marseille, France

[#] These authors should be considered as equal first authors.

* To whom correspondence should be addressed:

E-mail address: canaan@imm.cnrs.fr (S. Canaan); jfcavalier@imm.cnrs.fr (JF Cavalier); SpillingC@msx.umsl.edu (C.D. Spilling)

Table of contents

Chemistry - synthesis of compounds S2

^{1}H, ^{13}C and ^{31}P NMR spectra S18

Figures S1-S8 S30

CHEMISTRY - SYNTHESIS OF COMPOUNDS

General Experimental. All reactions were carried out in oven dried glassware under an atmosphere of argon unless otherwise noted. THF was distilled from sodium and benzophenone, CH_2Cl_2 and CH_3CN were distilled from CaH_2, and MeOH and *i*-PrOH were distilled from magnesium. All chemicals and reagents were purchased from commercial suppliers and used directly unless otherwise noted. ^{1}H ^{13}C and ^{31}P NMR spectra were recorded at 300, 75 and 121 MHz, respectively. ^{1}H NMR spectra are referenced to $CDCl_3$ (7.27 ppm), ^{13}C NMR spectra are referenced to $CDCl_3$ (77.23 ppm), and ^{31}P NMR spectra are referenced to external H_3PO_4. Target compounds were purified by chromatography (see below) and have purity of ≥ 95%.

Unlabeled **CyC_{31}** and **CyC_{32}** compounds were synthesized as described in reference [1].

Preparative HPLC Specifications and Conditions. Manual Preparative injector: Rheodyne 1700 (3725i-119) with 20 mL loop; Solvent A – MeOH; Solvent B – H_2O; Varian ProStar Model 210 pumps equipped with 25 mL/min Rainin/Gilson type pump heads. Kromasil 100-10C18-2025 column; 10 μm particle diameter; 250 mm × 20 mm i.d. Spectra-Physics Spectra 100 UV detector with prep cell. LKB 2211 Superac fraction collector. 50% MeOH/50% H_2O to 100% MeOH from 12 min to 60 min at a flow rate of 10 mL/min.

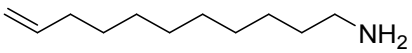

Undec-10-en-1-amine (2). Undec-10-enoic acid (20.25 g, 109.9 mmol) was dissolved in thionyl chloride (136 mL). The solution was heated at reflux for 1 h, and then concentrated by distillation of the remaining thionyl chloride. The resulting oil was dissolved in CH_2Cl_2 and added dropwise to concentrated aqueous NH_4OH at 0 °C. The mixture was diluted with water and CH_2Cl_2 until two clear layers formed. The organic phase was washed with 1N HCl and brine was added to aid the separation. The organic phase was dried over anhydrous Na_2SO_4 and concentrated *in vacuo* giving the amide (19.91 g, 99%) as a pale pink solid. ^{1}H NMR (300 MHz,

$CDCl_3$) δ 5.82 (ddt, J_{HH} = 17.1, 10.2, 6.8 Hz, 1H), 5.38 (br s, 2H), 4.98 (m, 2H), 2.23 (t, J_{HH} = 7.5 Hz, 2H), 2.04 (q, J_{HH} = 6.9 Hz, 2H), 1.64 (p, J_{HH} = 7.5 Hz, 2H), 1.31 (m, 12H).

$LiAlH_4$ (2.3 g, 60.6 mmol) was slowly added to the flask containing THF (50 mL). The suspension was heated at reflux for 30 min. The mixture was cooled to room temperature and a solution of the amide (5.0 g, 27.3 mmol) in THF (100 mL) was added dropwise. The mixture was again heated at reflux for 24 h. EtOAc (20 mL) was added dropwise and then the mixture was cooled to 0°C in an ice water bath. Saturated aqueous Na_2SO_4 (40 mL) was added slowly and the resulting white suspension was filtered, rinsing 5 times with EtOAc (20 mL each). The organic phase was separated, dried, and concentrated *in vacuo*. The resulting oil was distilled (kugelrohr oven) to give amine **5** (3.12 g, 68%) as a green oil. ^{1}H NMR (300 MHz, $CDCl_3$) δ 5.82 (ddt, J_{HH} = 17.0, 10.1, 6.7 Hz, 1H), 4.97 (m, 2H), 2.68 (t, J_{HH} = 6.9 Hz, 2H), 2.05 (q, J_{HH} = 7.0 Hz, 2H), 1.29 (m, 14H).

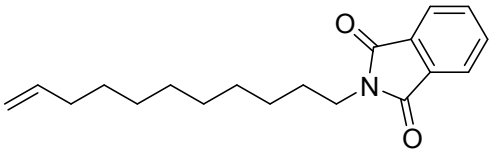

2-(Undec-10-en-1-yl)isoindoline-1,3-dione (3). To a solution of amine **2** (333 mg, 1.97 mmol) in toluene (5 mL) was added phthalic anhydride (291 mg, 1.96 mmol) and the resulting solution was heated at reflux for 16 h. The mixture was concentrated *in vacuo* and the crude material was purified by column chromatography (SiO_2, 5% EtOAc in hexanes) to give the phthalimide **6** (464 mg, 79%) as a white solid. ^{1}H NMR (300 MHz, $CDCl_3$) δ 7.87 – 7.75 (m, 2H), 7.75 – 7.60 (m, 2H), 5.79 (ddt, J_{HH} = 17.0, 10.2, 6.7 Hz, 1H), 5.03 – 4.82 (m, 1H), 3.67 (t, J_{HH} = 7.3 Hz, 2H), 2.02 (q, J_{HH} = 6.8 Hz, 2H), 1.72 – 1.55 (m, 2H), 1.39 – 1.16 (m, 12H).

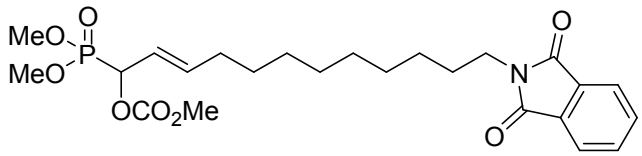

(±)-(*E*)-1-(Dimethoxyphosphoryl)-12-(1,3-dioxoiso indolin-2-yl)dodec-2-en-1-yl methyl carbonate (5). To a solution of phthalimide **3** (2.06 g, 6.88 mmol) and phosphonate **4** (2.00 g, 8.92 mmol) in CH_2Cl_2 (17.2 mL), was added CuI (66 mg, 0.35 mmol) and Grubbs 2nd generation catalyst (292 mg, 0.344 mmol). The mixture was heated at reflux for 4 h, and then cooled and concentrated

in vacuo. The crude material was purified by column chromatography (SiO_2, 30–50% EtOAc in hexanes) to remove nonpolar impurities and then by preparative reverse phase HPLC to give **5** (2.75 g, 81%) as a yellow oil. IR (neat, NaCl) 3006, 2928, 2855, 1755, 1713, 1615 cm^{-1}; ^1H NMR (300 MHz, $CDCl_3$) δ 7.80 – 7.73 (m, 2H), 7.69 – 7.61 (m, 2H), 5.97 – 5.81 (m, 1H), 5.55 – 5.43 (m, 1H), 5.37 (m, 1H), 3.75 (m, 9H), 3.60 (t, J_{HH} = 7.3 Hz 2H), 2.07 – 1.95 (m, 2H), 1.61 (m, 2H), 1.25 (m, 12H). ^{13}C NMR (75 MHz, $CDCl_3$) δ 168.4, 155.9 (d, J_{CP} = 9.6 Hz), 138.9 (d, J_{CP} = 12.6 Hz), 133.9, 132.3, 123.15, 120.4 (d, J_{CP} = 3.5 Hz), 73.2 (d, J_{CP} = 171.2 Hz), 55.3, 53.8 (d, J_{CP} = 10.6 Hz), 53.7 (d, J_{CP} = 9.5 Hz), 38.0, 32.4, 29.4, 29.3, 29.2, 29.1, 29.0, 28.6, 26.9; ^{31}P NMR (121 MHz, $CDCl_3$) δ 20.1, 19.8 (*Z*:*E* = 1:11); HRMS (FAB, NBA, MH^+) calcd for $C_{24}H_{35}NO_8P$: 496.2100, found 496.2117.

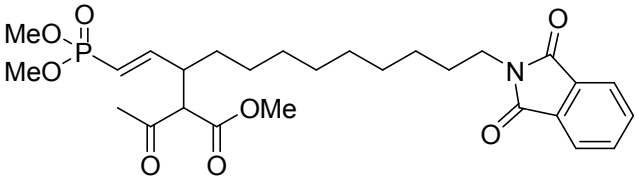

(±)-(*E*)-Methyl 2-acetyl-3-(2-(dimethoxyphosphoryl) vinyl)-12-(1,3-dioxoisoindolin-2-yl) dodecanoate (6). To a solution of carbonate **5** (300 mg, 0.605 mmol) and methyl acetoacetate (200 µL, 1.8 mmol) in dry THF (750 µL) was added a solution of $Pd_2(dba)_3$ (11 mg, 0.012 mmol) and dppe (12 mg, 0.030 mmol) in dry THF (500 µL) by cannula rinsing with additional dry THF (250 µL). The resulting green solution was heated in oil bath at 40˚C for 2 h and then concentrated *in vacuo*. The crude mixture was purified by column chromatography (SiO_2, 70–85% EtOAc in hexanes) to give **6** (229 mg, 71%) as a pale-yellow oil (1:1 mixture of diastereoisomers). IR (neat, NaCl) 2930, 2855, 1772, 1713, 1633 cm^{-1}; ^1H NMR (300 MHz, $CDCl_3$) δ 7.89 – 7.70 (m, 2H), 7.75 – 7.64 (m, 2H), 6.49 (m, 1H), 5.82 – 5.50 (m, 1H), 3.79 – 3.61 (m, 11 H), 3.51 (m, 1H), 3.07 – 2.83 (m, 1H), 2.18 (d, *J* = 17.7 Hz, 3H), 1.71 – 1.55 (m, 2H), 1.42 – 1.10 (m, 14H); ^{13}C NMR (75 MHz, $CDCl_3$) δ 201.3, 168.6, 153.3, 134.0, 132.3, 123.2, 118.8 (118.6) (d, J_{CP} = 185.7 Hz), 63.8 (63.7), 52.7 (52.5), 52.4 (d, J_{CP} = 5.6 Hz), 44.2 (43.9), 38.1, 31.8 (31.7), 30.2, 30.0, 29.8, 29.5, 29.4, 29.3, 29.2, 28.7, 27.2, 27.0, 26.9; ^{31}P NMR (121 MHz, $CDCl_3$) δ 20.0, 19.9; HRMS (FAB, NBA, MH^+) calcd for $C_{27}H_{39}NO_8P$: 536.2413, found 536.2428.

To a solution of **6** (1.65 g, 3.08 mmol) in MeOH (7.7 mL) was added palladium on carbon (10%, 328 mg) and the resulting mixture was stirred under hydrogen atmosphere until the reaction was complete (^{31}P NMR). The catalyst was removed by filtration through Celite and the solution was concentrated *in vacuo* to give a 7.8:1 mixture **7** and **8** (1.65 g, 100%) as a colorless oil. The compounds were separated by preparative HPLC for characterization.

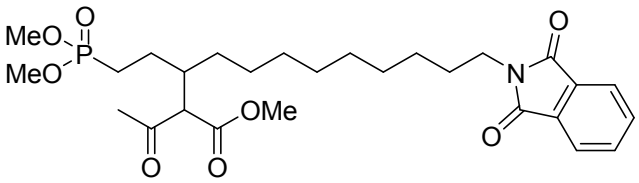

(±)-Methyl 2-acetyl-3-(2-(dimethoxyphosphoryl) ethyl)-12-(1,3-dioxoisoindolin-2-yl)dodecanoate (7). (1:1 mixture of diastereoisomers). IR (neat, NaCl) 2929, 2855, 1772, 1713 cm^{-1}; ^{1}H NMR (300 MHz, $CDCl_3$) δ 7.79 (m, 2H), 7.67 (m, 2H), 3.68 (m, 9H), 3.62 (t, J_{HH} = 7.3 Hz, 2H), 3.42 (d, J_{HH} = 8.3 Hz, 1H), 2.18 (m, 4H), 1.62 (m, 6H), 1.23 (m, 14H); ^{13}C NMR (75 MHz, $CDCl_3$) δ 202.90 (202.87), 169.62 (169.60), 168.5, 134.0, 132.2, 123.2, 63.0, 52.5 (d, J_{CP} = 5.7 Hz), 38.1, 37.9, 30.5 (30.4), 29.8 (29.7), 29.6, 29.5, 29.2, 28.7, 26.9 (26.3), 23.5 (23.4) (d, J_{CP} = 5.9 Hz), 21.7 (21.5) (d, J_{CP} = 141.2 Hz); ^{31}P NMR (121 MHz, $CDCl_3$) δ 34.4, 34.2; HRMS (FAB, NBA, MNa^+) calcd for $C_{27}H_{40}NO_8PNa^+$: 560.2389, found 560.2394.

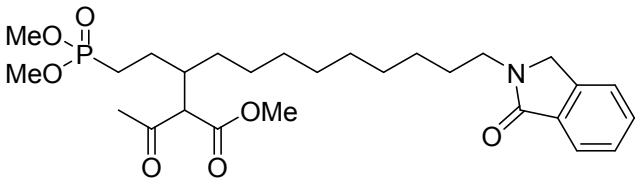

Methyl 2-acetyl-3-(2-(dimethoxyphosphoryl)ethyl)-12-(1-oxoisoindolin-2-yl)dodecanoate (8). (1:1 mixture of diastereoisomers). IR (neat, NaCl) 2928, 2854, 1712, 1678 cm^{-1}; ^{1}H NMR (300 MHz, $CDCl_3$) δ 7.85 (m, 1H), 7.49 (m, 3H), 4.38 (s, 2H), 3.77 – 3.67 (m, 9H), 3.61 (t, J_{HH} = 7.3 Hz, 2H), 3.46 (d, J = 8.2 Hz, 1H), 2.23 (s, 4H), 1.81 – 1.57 (m, 6H), 1.28 (m, 14H); ^{13}C NMR (75 MHz, $CDCl_3$) δ 203.03 (203.01), 169.74 (169.71), 168.6, 141.3, 133.3, 131.3, 128.2, 123.8, 122.8, 63.14 (63.11), 52.62, 52.58, 52.5, 50.1, 42.6, 38.2 (38.0), 30.6 (30.5), 29.9 (29.8), 29.7, 29.6, 29.5, 28.7, 27.0, 26.5, 23.62 (23.55), 21.8 (21.7) (d, J_{CP} = 141.4 Hz), 9.8; ^{31}P NMR (121 MHz, $CDCl_3$) δ 34.4, 34.2; HRMS (FAB, NBA, MH^+) calcd for $C_{27}H_{43}NO_7P$: 524.2777, found 524.2786.

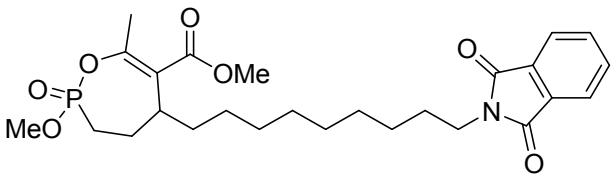

(±)-Methyl-5-(9-(1,3-dioxoisoindolin-2-yl)nonyl)-2-methoxy-7-methyl-2,3,4,5-tetrahydro-1,2-oxaphosphepine-6-carboxylate 2-oxide (9α and 9β). To a solution of **7** and **8** (7.8:1, 528 mg, 0.98 mmol) in dry CH_3CN (500 µL) was added NaI (162 mg, 1.08 mmol). The solution was heated at reflux until the reaction was complete (^{31}P NMR). The mixture was concentrated *in vacuo*. The resulting solid was dissolved in dry DMF (4 mL) and Hunig's base (260 µL, 1.5 mmol) was added followed by HBTU (559 mg, 1.47 mmol). After 2 h, the red solution was partitioned between 1N HCl and CH_2Cl_2 and then extracted twice more with CH_2Cl_2. The combined organic layers were washed with saturated aqueous $NaHCO_3$ and brine and concentrated *in vacuo*. The crude material was purified by preparative HPLC to give **9** (310 mg, 62%, 1:1.8 mixture of diastereomers) as a yellow oil. Further chromatographic separation of the diastereomers gave **9α** and **9β** as a yellow oil.

9α: IR (neat, NaCl) 2928, 2855, 1773, 1718 cm^{-1}; ^1H NMR (300 MHz, $CDCl_3$) δ 7.77 (m, 2H), 7.66 (m, 2H), 3.77 (d, J_{HP} = 11.2 Hz, 3H), 3.69 (s, 3H), 3.61 (t, J_{HH} = 7.3 Hz, 2H), 2.92 (m, 1H), 2.17 (d, J_{HP} = 1.6 Hz, 3H), 2.15–1.78 (m, 4H), 1.58 (m, 3H), 1.40 (m, 1H), 1.57 (m, 12H); ^{13}C NMR (75.4 MHz, $CDCl_3$) δ 169.0 (d, J_{CP} = 1.7 Hz), 168.5, 155.7 (d, J_{CP} = 7.3 Hz), 133.9, 132.2 123.2, 123.1, 52.1 (d, J_{CP} = 7.1 Hz), 38.1, 37.2 (d, J_{CP} = 1.5 Hz), 30.7, 29.6, 29.4, 29.2, 28.6, 27.7, 26.9, 24.9 (d, J_{CP} = 6.9 Hz), 21.9 (d, J_{CP} = 135.1 Hz), 21.4 (d, J_{CP} = 1.2 Hz); ^{31}P NMR (121.4 MHz, $CDCl_3$) δ 26.1; HRMS (FAB, NBA, MNa^+) calcd for $C_{26}H_{36}NO_7PNa^+$: 528.2128, found 528.2139.

9β: IR (neat, NaCl) 2928, 2855, 1771, 1712 cm^{-1}; ^1H NMR (300 MHz, $CDCl_3$) δ 7.73 (m, 1H), 7.62 (m, 3H), 3.73 (d, J_{HP} = 11.0 Hz, 3H), 3.65 (s, 3H), 3.56 (t, J_{HH} = 7.3 Hz, 2H), 2.78 (m, 1H), 2.13–1.76 (m, 4H), 2.08 (d, J_{HP} = 0.8 Hz, 3H), 1.56 (m, 3H), 1.40 (m, 1H), 1.17 (m, 12H); ^{13}C NMR (75.4 MHz, $CDCl_3$) δ 169.0 (d, J_{CP} = 1.6 Hz), 168.3, 154.8 (d, J_{CP} = 9.4 Hz), 133.8, 132.1, 123.1, 123.0, 52.5 (d, J_{CP} = 6.8 Hz), 51.9, 37.9, 37.0, 30.8, 29.4, 29.3, 29.1, 28.5, 27.5, 26.8, 25.1 (d, J_{CP} = 7.9 Hz), 25.1 (d, J_{CP} = 134.0 Hz), 21.0 (d, J_{CP} = 2.0 Hz); ^{31}P NMR (121.4 MHz, $CDCl_3$) δ 23.4; HRMS (FAB, NBA, MNa^+) calcd for $C_{26}H_{36}NO_7PNa^+$: 528.2127, found 528.2126.

Deprotection and dansylation. To a solution of the α-phthalimide **9β** (134 mg, 0.265 mmol) in isopropyl alcohol/water (6:1, 2.7 mL) was added sodium borohydride (50 mg, 1.32 mmol). The solution was stirred for 2 h and then the reaction was quenched by the addition of 1N HCl. The reaction mixture was extracted with CH_2Cl_2 and the extract was dried over sodium sulfate and concentrated in *vacuo*. The residue was re-dissolved in isopropyl alcohol (2.7 mL) and acetic acid (30 μL, 1.05 mmol) was added. The resulting solution was heated at reflux for 24 h. The solution was cooled to room temperature and DMF (1.3 mL) was added. The solution was concentrated under reduced pressure to remove the isopropyl alcohol and then and Hunig's base (140 μL, 0.804 mmol) was added with stirring followed by Dansyl-chloride (107 mg, 0.397 mmol) in DMF (1.4 mL). The solution was stirred for 24 h and then it was concentrated *in vacuo*. The residue was purified by column chromatography (SiO_2, 55% EtOAc in hexanes) to give the Dansylamide (21.6 mg, 13%). Reverse phase HPLC gave the pure **CyC$_{7β\text{-Dansyl}}$** diastereoisomer (^{31}P NMR 26.2 ppm) (7.1 mg 4%). (see below for full characterization data).

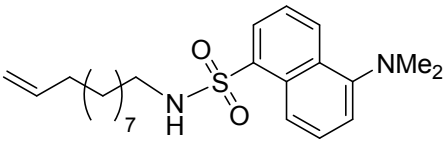

5-(dimethylamino)-N-(undec-10-en-1-yl)naphthalene-1-sulfonamide (11). To the solution of **2** (2.0 g, 11.82 mmol) in 2 mL dry DCM was added DIPEA (4.3 mL, 24.882 mmol) followed by the addition of Dansyl-chloride (3.49 g, 13 mmol) dissolved in 5 mL DCM slowly, over five minutes. The reaction mixture was stirred for 72 hours at room temperature. Then 137 mL of brine was added followed by addition of 500 mL of EtOAc and washed several times with water to bring to neutral PH. Finally washed with brine and the organic phase was evaporated *in vacuo*. The crude mixture was purified by column chromatography (SiO_2, 5-15 % EtOAc in Hexane) to get green viscous liquid (3.845 g, 81%). IR (neat) 3291, 3071, 2921, 2850 cm^{-1} ; ^{1}H NMR (300 MHz, $CDCl_3$) δ 8.55 (d, J_{HH} = 8.5 Hz, 1H), 8.30 (d, J_{HH} = 8.7 Hz, 1H), 8.26 (dd, J_{HH} = 7.3, 1.2 Hz, 1H), 7.57 (m, 2H), 7.21 (s, 1H), 5.80 (ddt, J_{HH} = 16.9, 10.2, 6.7 Hz, 1H), 5.06 – 4.80 (m, 2H), 4.64 (t, J_{HH} = 6.0 Hz, 1H), 2.95 – 2.84 (m, 8H), 2.06 –

1.90 (m, 2H), 1.35 – 1.09 (m, 14H); ^{13}C NMR (75 MHz, $CDCl_3$) δ 152.2, 139.4, 139.0, 134.9, 130.6, 130.0, 129.9, 129.8, 128.6, 123.4, 118.9, 115.3, 114.3, 45.6, 43.5, 33.9, 29.7, 29.5, 29.2, 29.1, 29.0, 26.6. HRMS (FAB, NBA, MNa^+) calcd for $C_{23}H_{34}N_2O_2SNa^+$: 425.2238, found 425.2238.

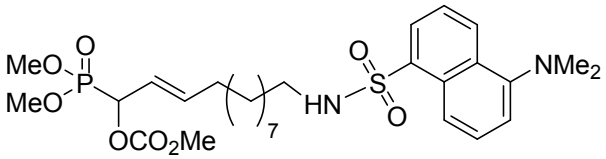

(±)-(*E*)-1-(dimethoxyphosphoryl)-12-((5-(dimethylamino)naphthalene)-1-sulfonamido) dodec-2-en-1-yl methyl carbonate (12). To the solution of **11** (2.58 g, 6.409 mmol) in dry DCM, vinyl carbonate **4** (2.88 g, 12.818 mmol). Then Grubbs 2nd generation catalyst (326 mg, 0.385 mmol) and CuI (98 mg, 0.512 mmol) were added. The mixture was heated at reflux for 5 hours. The completion of reaction was checked by TLC and ^{31}P NMR. The reaction mixture was cooled and concentrated *in vacuo* and then purified by Column Chromatography (SiO_2, 70% EtOAc in Hexane) to give viscous green product **12** (3.45 g, 90%). IR(neat) 3175, 2924, 2851, 1750 cm^{-1}; ^{1}H NMR (300 MHz, $CDCl_3$) δ 8.51 (d, J = 8.5 Hz, 1H), 8.31 (d, J_{HH} = 8.7 Hz, 1H), 8.23 (dd, J_{HH} = 7.3, 1.1 Hz, 1H), 7.60 – 7.44 (m, 2H), 7.16 (d, J_{HH} = 7.5 Hz, 1H), 5.93 (m, 1H), 5.61 – 5.35 (m, 2H), 5.02 (t, J_{HH} = 6.0 Hz, 1H), 3.85 – 3.74 (m, 9H), 2.86 (m, 8H), 2.05 (m, 2H), 1.40 – 1.26 (m, 4H), 1.25 – 0.99 (m, 10H). ^{13}C NMR (75 MHz, $CDCl_3$) δ 154.8 (d, J_{CP} = 9.8 Hz), 152.0, 139.1 (d, J_{CP} = 12.5 Hz), 135.0, 130.4, 129.9, 129.7, 129.6, 128.37 (s), 123.3, 120.2 (d, J_{CP} = 3.8 Hz), 118.9, 115.2, 73.1 (d, J_{CP} = 171.1 Hz), 55.4, 53.9 (d, J_{CP} = 7.1 Hz), 53.8 (d, J_{CP} = 6.5 Hz), 45.5, 43.4, 32.4, 29.6, 29.3, 29.2, 29.0, 28.9, 26.4. ^{31}P NMR (121 MHz, $CDCl_3$) δ 19.9; HRMS (FAB, NBA, MNa^+) calcd for $C_{28}H_{43}N_2O_8PSNa^+$: 621.2375, found 621.2367.

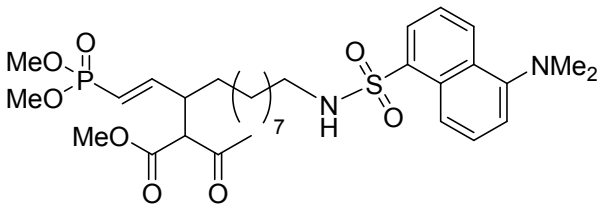

(±)-Methyl (*E*)-2-acetyl-3-(2-(dimethoxyphosphoryl) vinyl)-12-((5-(dimethylamino) naphthalene)-1-sulfonamido) dodecanoate (13). To an oven dried RB flask, $Pd_2(dba)_3$ (111.0 mg, 0.121mmol) and dppe (121.0 mg, 0.303 mmol) were added. To this flask 2 mL of dry THF was added and the mixture was stirred for 10 minutes at room temperature under

Argon atmosphere. Then methyl acetoacetate (3 equivalent, 9.11 mmol, 1mL) was added and left stirring for about 5 minutes. To this mixture the solution of **12** (1.82 g, 3.4 mmol) in THF (5 mL/mmol) was added through canula and rinsed with additional 0.5 mL THF, and the reaction mixture was heated at reflux for 4 hours till completion, which was checked by TLC and ^{31}P NMR. The reaction mixture was extracted with EtOAc and washed with brine and dried over Na_2SO_4. Solvents were removed under reduced pressure and the pure product was isolated by column chromatography (SiO_2, 20-40% Acetone in Hexane) to get viscous green product **13** (1.645 g, 85%). IR (neat) 3161, 2924, 2851, 1738, 1713 cm^{-1}; ^1H NMR (300 MHz, $CDCl_3$) δ 8.49 (d, J_{HH} = 8.5 Hz, 1H), 8.30 (d, J_{HH} = 8.7 Hz, 1H), 8.20 (dd, J_{HH} = 7.3, 1.2 Hz, 1H), 7.49 (dt, J_{HH} = 8.6, 7.6 Hz, 2H), 7.14 (d, J_{HH} = 7.4 Hz, 1H), 6.51 (m, 1H), 5.74 – 5.54 (m, 1H), 5.27 (t, J_{HH} = 5.7 Hz, 1H), 3.72 – 3.61 (m, 9H), 3.52 (m, 1H), 3.00 – 2.77 (m, 9H), 2.17 (m, 3H), 1.46 – 1.24 (m, 4H), 1.05 (m, 12H). ^{13}C NMR (75 MHz, $CDCl_3$) δ 201.4 (d, J_{CP} = 2.5 Hz), 168.4 (d, J_{CP} = 12.2 Hz), 153.4 (d, J_{CP} = 4.5 Hz),151.9, 135.0, 130.2, 129.9, 129.7, 129.5, 128.2, 123.2, 118.9, 118.6 (d, J_{CP} = 184.5 Hz), 115.1, 63.6 (d, J_{CP} = 8.5 Hz), 52.7, 52.4 (d, J_{CP} = 3.75 Hz) 45.4, 44.0 (43.7) (d, J_{CP} = 3.9 Hz), 43.3, 31.6, 31.5 (d, J_{CP} = 10.8 Hz), 31.5, 30.2 , 29.9, 29.5, 29.1, 29.0, 28.8, 26.8 (d, J_{CP} = 10.4 Hz), 26.4; ^{31}P NMR (121 MHz, $CDCl_3$) δ 19.9, 20.0; HRMS (FAB, NBA, MNa^+) calcd for $C_{31}H_{47}N_2O_8PSNa^+$: 661.2684, found 661.2682.

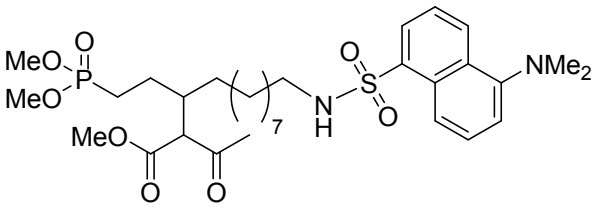

(±)-Methyl 2-acetyl-3-(2-(dimethoxyphosphoryl)ethyl)-12-((5-(dimethylamino)naphthalene)-1-sulfonamido) dodecanoate (14). To a solution of **13** (1.139 g, 1.78 mmol) in Methanol (3 mL/mmol) were added 10% palladium on charcoal (0.05 g/mmol). The solution was first flushed with Argon followed by H_2 (balloon pressure). H_2 pressure was maintained, while the reaction mixture was vigorously stirred. The completion of reaction was observed by ^{31}P NMR analysis. After complete reduction (4 h), the reaction mixture was filtered through Celite and washed with CH_2Cl_2, solvent removed under reduced pressure to get mixture of saturated

phosphonate **14** in quantitative yield. IR (neat): 3159, 3144, 2924, 2850, 1734, 1709 cm^{-1}; ^{1}H NMR (300 MHz, $CDCl_3$) δ 8.45 (d, J_{HH} = 8.5 Hz, 1H), 8.25 (d, J_{HH} = 8.7 Hz, 1H), 8.16 (dd, J_{HH} = 7.3, 1.2 Hz, 1H), 7.54 – 7.37 (m, 2H), 7.10 (d, J_{HH} = 7.5 Hz, 1H), 5.19 (t, J_{HH} = 6.0 Hz, 1H), 3.70 – 3.59 (m, 9H), 3.39 (m, 1H), 2.87 – 2.74 (m, 8H), 2.20 (m 4H), 1.71 – 1.48 (m, 4H), 1.34 – 0.95 (m, 16H); ^{13}C NMR (75 MHz, $CDCl_3$) δ 202.8 (d, J_{CP} = 3.0 Hz), 169.5 (d, J_{CP} = 2.9 Hz), 151.9, 135.0, 130.2, 129.9, 129.7, 129.4, 128.2, 123.2, 118.9, 115.1, 62.8 (d, J_{CP} = 6.7 Hz), 52.4 (d, J_{CP} = 6.6 Hz), 52.3, 45.4, 43.2, 37.9, 37.7, 30.3 (d, J_{CP} = 8.9 Hz), 29.7 (29.13), 27.6 (d, J_{CP} = 188.0 Hz 26.1 (d, J_{CP} = 3.4 Hz), 23.4 (d, J_{CP} = 4.7 Hz), 23.2 (d, J_{CP} = 4.6 Hz), 23.4 (23.23), 22.4 (d, J_{CP} = 4.5 Hz), 20.5 (d, J_{CP} = 4.5 Hz). ^{31}P NMR (121 MHz, $CDCl_3$) δ 34.4, 34.2; HRMS (FAB, NBA, MNa^+) calcd for $C_{31}H_{49}N_2O_8PSNa^+$: 663.2844, found 663.2842.

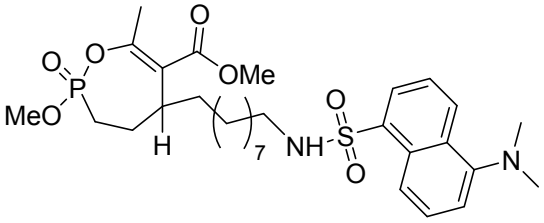

(±)-Methyl 5-(9-((5-(dimethylamino)naphthalene)-1-sulfonamido)nonyl)-2-methoxy-7-methyl-3,4,5-trihydro-1,2-oxaphosphepine-6-carboxylate 2-oxide (racemic $CyC_{7\text{-}Dansyl}$). To a solution of **14** (3.1 g, 4.9 mmol) in CH_3CN (2.4 mL/mmol) in an oven dried RB flask, NaI (0.809 g, 5.402 mmol) was added. This solution was refluxed at 80°C for 24 hours. The completion of reaction was observed through ^{31}P NMR. The resulting sodium salt was dried under reduced pressure. The solid sodium salt of phosphonate was dissolved in 20 ml of DMF (4ml/mmol) with 1.5 mL of diisopropyl ethyl amine (0.3 mL/mol). Then HBTU (2.80 g, 7.36 mmol) was added. After three hours the red solution was then partitioned between saturated NH_4Cl and CH_2Cl_2. The organic layer was then washed with $NaHCO_3$ and brine and concentrated *in vacuo*. The crude product was chromatographed (SiO_2, 20-30% Acetone in Hexane) to get viscous, sticky green liquid of diastereomer $\mathbf{CyC_{7\text{-}Dansyl}}$ (1.819 g, 2.98 mmol, 61%), further separated to give $\mathbf{CyC_{7\alpha\text{-}Dansyl}}$ and $\mathbf{CyC_{7\beta\text{-}Dansyl}}$.

$\mathbf{CyC_{7\alpha\text{-}Dansyl}}$: IR (neat) 3175, 2923, 2851, 1711 cm^{-1}; ^{1}H NMR (300 MHz, $CDCl_3$) δ 8.59 (d, J_{HH} = 8.5 Hz, 1H), 8.34 (d, J_{HH} = 8.7 Hz, 1H), 8.29 (dd, J_{HH} = 7.3, 1.2 Hz, 1H), 7.65 – 7.53 (m, 2H), 7.23

(d, J_{HH} = 7.4 Hz, 1H), 4.75 (t, J_{HH} = 6.1 Hz, 1H), 3.86 (d, J_{HP} = 11.2 Hz, 3H), 3.78 (s, 3H), 3.02 – 2.88 (m, 9H), 2.27 (m, 3H), 2.13 – 1.75 (m, 4H), 1.51 (m, 4H), 1.28 – 1.12 (m, 12H); ^{13}C NMR (75 MHz, $CDCl_3$) δ 168.9 (d, J_{CP} = 1.7 Hz), 155.6 (d, J_{CP} = 7.3 Hz), 151.9, 135.0, 130.2, 129.8, 129.6, 129.4, 128.2, 123.2, 123.0 (d, J_{CP} = 5.3 Hz), 118.9, 115.1, 52.0 (d, J_{CP} = 7.1 Hz), 51.9, 45.4, 43.2, 37.1, 30.6, 29.5, 29.2, 28.9, 27.6, 26.3, 24.9 (d, J_{CP} = 6.9 Hz), 21.8 (d, J_{CP} = 134.21 Hz), 21.2 (d, J_{CP} = 1.4 Hz); ^{31}P NMR (121 MHz, $CDCl_3$) δ 26.2; HRMS (FAB, NBA, MNa^+) calcd for $C_{30}H_{45}N_2O_7PSNa^+$: 631.2582, found 631.2581.

CyC$_{7\beta\text{-Dansyl}}$: IR(neat) 3163, 2921, 2849, 1712, cm^{-1}; H NMR (300 MHz, $CDCl_3$) δ 8.51 (d, J_{HH} = 8.4 Hz, 1H), 8.30 (d, J_{HH} = 8.6 Hz, 1H), 8.22 (d, J_{HH} = 7.2 Hz, 1H), 7.60 – 7.42 (m, 2H), 7.16 (d, J_{HH} = 7.5 Hz, 1H), 5.05 (t, J_{HH} = 6.0 Hz, 1H), 3.81 (d, J_{HP} = 2.4 Hz, 3H), 3.73 (s, 3H), 2.87 (s, 8H), 2.26 – 2.11 (m, 4H), 1.98 (m, 4H), 1.53 (m, 2H), 1.33 (m, 2H), 1.28 – 1.04 (m, 12H); ^{13}C NMR (75 MHz, $CDCl_3$) δ 169.5, 156.2 (d, J_{CP} = 7.3 Hz), 135.4, 130.9, 130.4, 130.2, 128.9, 123.8, 123.6 (d, J = 5.2 Hz), 119.34, 115.7, 52.6 (d, J = 7.1 Hz), 52.5, 46.0, 43.9, 37.7, 31.2, 30.0 (d, J_{CP} = 3.2 Hz), 29.8, 29.5, 28.1, 26.9, 25.4 (d, J_{CP} = 6.8 Hz), 23.4 (d, J_{CP} = 134.25 Hz), 21.8 (d, J_{CP} = 1.5 Hz); ^{31}P NMR (121 MHz, $CDCl_3$) δ 23.5; HRMS (FAB, NBA, MNa^+) calcd for $C_{30}H_{45}N_2O_7PSNa$: 631.2582, found 631.2593.

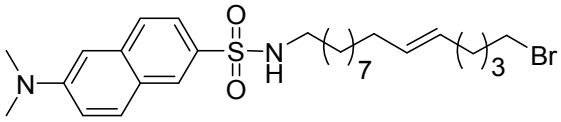

N-(15-bromopentadecyl)-6-(dimethylamino) naphthalene-2-sulfonamide (15): To the solution of **11** (0.300 g, 0.745 mmol) in dry DCM (2 mL), 5-bromo-Hex-1-ene (6 equivalent, 0.729 g, 4.48 mmol) was added in the RB flask under Argon pressure. Then Grubbs 2nd generation catalyst (0.038 g, 0.0447 mmol) was added, followed by the addition of CuI (0.011 g, 0.0596 mmol). The flask was then placed in the preheated Sand bath and refluxed for 6 hours. Completion of reaction was checked by TLC. The reaction mixture was dried and then purified by Column Chromatography (SiO_2, 5-10% EtOAc in Hexane) to get green viscous liquid **15** (0.295 g, 74%. IR(neat) 3297, 22920, 2849, 2784, 1308 cm^{-1}; ^{1}H NMR (300 MHz, $CDCl_3$) δ 8.56 (d, J_{HH} = 8.5 Hz, 1H), 8.28 (dd, J_{HH} = 14.4, 7.9 Hz, 2H), 7.56

(dt, J_{HH} = 10.3, 8.0 Hz, 2H), 7.20 (d, J_{HH} = 7.5 Hz, 1H), 5.50 – 5.23 (m, 2H), 4.65 (t, J_{HH} = 6.0 Hz, 1H), 3.41 (m, 2H), 2.93 – 2.82 (m, 8H), 2.14 – 1.74 (m, 6H), 1.49 (m, 2H), 1.41 – 1.03 (m, 14H); ^{13}C NMR (75 MHz, $CDCl_3$) δ 153.4, 134.7, 131.3, 130.5, 129.9, 129.8, 129.7, 129.4, 128.5, 123.3, 118.7, 115.2, 45.5, 43.4, 34.0, 32.6, 32.3, 31.7, 29.6, 29.4, 29.7, 28.7, 26.5; HRMS (ESI, M^+) calcd for $C_{27}H_{42}BrN_2O_2S$: 537.2150, found 537.2145.

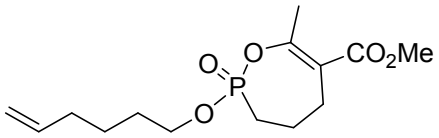

Methyl 2-(hex-5-en-1-yloxy)-7-methyl-3,4,5-trihydro-1,2-oxaphosphepine-6-carboxylate 2-oxide (17). To the solution of **CyC$_4$** (0.468 g, 1.99 mmol) in 2 ml of Toluene (distilled over CaH_2 and placed in 4 Å molecular sieves for 1 h) was added TBAI (0.074 g, 0.199 mmol) followed by the addition of 6-bromo-hexene (3.24 g, 19.9 mmol) through syringe. The reaction mixture was refluxed till completion, which was monitored by TLC and ^{31}PNMR. The reaction mixture was dried over reduced pressure and purified by column chromatography (SiO_2 30-50% EtOAc in Hexane) to get **17** (0.450 g, 75%). IR (neat) 3073, 2931, 2862, 1711, 1639 cm^{-1}; ^{1}H NMR (300 MHz, $CDCl_3$) δ 5.74 (ddt, J_{HP} = 16.9, J_{HH} = 10.2, 6.7 Hz, 1H), 5.08 – 4.82 (m, 2H), 4.25 – 4.01 (m, 2H), 3.70 (s, 3H), 2.69 – 2.37 (m, 2H), 2.28 (s, 3H), 2.13 – 1.95 (m, 4H), 1.94 – 1.79 (m, 2H), 1.67 (m, 2H), 1.50 – 1.38 (m, 2H); ^{13}C NMR (75 MHz, $CDCl_3$) δ 168.2 (d, J_{CP} = 1.8 Hz), 159.4 (d, J_{CP} = 7.8 Hz), 138.4 (s), 119.3 (d, J_{CP} = 4.6 Hz), 115.2, 66.0 (d, J_{CP} = 7.0 Hz), 52.1, 33.3, 29.9 (d, J_{CP} = 6.2 Hz), 26.8 (d, J_{CP} = 133.5 Hz) 26.4 (d, J_{CP} = 2.7 Hz), 24.9, 21.3 (d, J_{CP} = 7.5 Hz), 21.2 (d, J_{CP} = 1.7 Hz); ^{31}P NMR (121 MHz, $CDCl_3$) δ 23.2; HRMS (FAB, NBA, MNa^+) calcd for $C_{14}H_{23}O_5PNa$: 325.1180, found 325.1186.

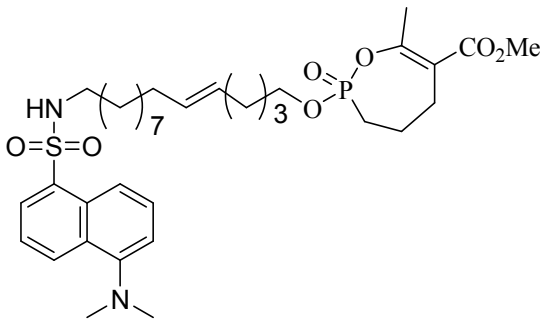

Methyl (*E*)-2-((15-((5-(dimethylamino)naphthalene)-1-sulfonamido)pentadec-5-en-1-yl)oxy)-7-methyl-3,4,5-trihydro-1,2-oxaphosphepine-6-carboxylate 2-oxide (16). To the solution of **17** (0.081 g, 0.267 mmol) in dry DCM (2 mL), labeled alkene **11** (0.324 g, 0.803 mmol) was added in the RB flask under Argon pressure. Then

Hoveyda Grubbs catalyst II (0.009 g, 0.00405 mmol) was added. The flask was placed in the preheated Sand bath and refluxed for 6 hours. The completion of reaction was checked by TLC and ^{31}P NMR. The reaction mixture was dried and then purified by Column Chromatography (SiO_2, 30-50% EtOAc in Hexane) to get green viscous liquid **16** (0.089 g, 49.2%). IR (neat): 3172, 2921, 2850, 2785, 1713, 1643 cm^{-1}; ^1H NMR (300 MHz, $CDCl_3$) δ 8.48 (d, J_{HH} = 8.5 Hz, 1H), 8.27 (d, J_{HH} = 8.6 Hz, 1H), 8.23 – 8.15 (m, 1H), 7.55 – 7.41 (m, 2H), 7.13 (d, J_{HH} = 7.5 Hz, 1H), 5.43 – 5.22 (m, 2H), 4.97 (t, J_{HH} = 6.0 Hz, 1H), 4.10 (m, 2H), 3.70 (s, 3H), 2.88 – 2.76 (m, 8H), 2.55 (m, 2H), 2.28 (s, 3H), 2.01 (m, 8H), 1.67 (m, 2H), 1.46 – 1.00 (m, 16H); ^{13}C NMR (75 MHz, $CDCl_3$) δ 168.2 (d, J_{CP} = 1.8 Hz), 159.3 (d, J_{CP} = 7.8 Hz), 152.0, 134.9, 131.3, 130.4, 129.9, 129.7, 129.6, 128.4, 123.3, 119.1 (d, J_{CP} = 4.6 Hz), 118.9, 115.2, 66.0 (d, J_{CP} = 7.0 Hz), 52.0 (s), 45.5, 43.4, 32.6, 32.0, 29.9 (d, J_{CP} = 6.2 Hz), 29.6, 29.5, 29.4, 29.4, 29.1, 29.0, 26.6 (d, J_{CP} = 133.5 Hz), 26.5, 26.3 (d, J_{CP} = 2.7 Hz), 25.5, 21.2 (d, J_{CP} = 7.5 Hz), 21.0 (d, J_{CP} = 1.7 Hz); ^{31}P NMR (121 MHz, $CDCl_3$) δ 23.3. HRMS (FAB, NBA, MH^+) calcd for $C_{35}H_{54}N_2O_7PS$: 677.3389, found 677.3400.

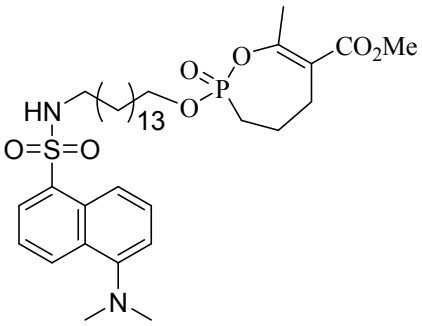

Methyl 2-((15-((5-(dimethylamino)naphthalene)-1-sulfonamido)pentadecyl)oxy)-7-methyl-3,4,5-trihydro-1,2-oxaphosphepine-6-carboxylate 2-oxide ($CyC_{11\text{-}Dansyl}$). To a solution of **16** (0.089 g, 0.131mmol) in methanol (2 mL/mmol) were added 10% palladium on charcoal (0.05 g/mmol, 0.007 g). The solution was first flushed with Argon and with hydrogen gas filled in the balloon. The reaction was stirred for 3 hours till completion. After the completion of reaction, the reaction mixture was filtered through Celite and washed with CH_2Cl_2. Solvents were removed *in vaccuo* to get saturated phosphonate **$CyC_{11\text{-}Dansyl}$** in quantitative yield. IR (neat): 3281,3172, 2920, 2850, 2784, 1713 ,1643 cm^{-1}; ^1H NMR (300 MHz, $CDCl_3$) δ 8.53 (d, J_{HH} = 8.5 Hz, 1H), 8.29 (d, J_{HH} = 8.6 Hz, 1H), 8.24 (d, J_{HH} = 7.2 Hz, 1H), 7.53 (m, 2H), 7.17 (d, J_{HH} = 7.5 Hz, 1H), 4.86 (t, J_{HH} = 5.7 Hz, 1H), 4.23 – 4.04 (m, 2H), 3.74 (s, 3H), 2.93 – 2.82 (m, 8H), 2.58 (m, 2H), 2.32 (s, 3H), 2.20 – 2.01 (m, 2H), 1.95 (m, 2H), 1.67 (m, 2H), 1.38 – 1.03 (m, 24H); ^{13}C NMR

(75 MHz, $CDCl_3$) δ 168.3, 159.4 (d, J_{CP} = 7.8 Hz), 152.1, 134.9, 130.5, 130.0, 129.8, 128.5, 123.4, 119.2 (d, J_{CP} = 4.6 Hz), 118.9, 115.3, 66.3 (d, J_{CP} = 7.1 Hz), 52.1, 45.6, 43.5, 30.6 (d, J_{CP} = 6.1 Hz), 29.7, 29.7, 29.6, 29.5, 29.2, 29.1, 26.76 (d, J_{CP} = 132.75 Hz), 26.57 (s), 26.40 (d, J_{CP} = 2.6 Hz), 25.62 (s), 21.28 (d, J_{CP} = 7.5 Hz), 21.15 (d, J_{CP} = 1.6 Hz). ^{31}P NMR (121 MHz, $CDCl_3$) δ 23.2. HRMS (FAB, NBA, MNa^+) calcd for $C_{35}H_{55}N_2O_7PSNa^+$: 701.3365, found 701.3344.

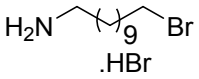

11-bromoundecan-1-amine (20) was prepared following the literature method. The spectral data were in accordance to the cited literature.[2-5] ^1H NMR (300 MHz, $CDCl_3$) δ 8.04 (br, 3H), 3.43 (t, J = 6.9 Hz, 2H), 3.11 – 3.01 (m, 2H), 1.86 (m, 4H), 1.36 (d, J = 37.9 Hz, 14H); ^{13}C NMR (75 MHz, $CDCl_3$) δ 40.1, 34.0, 32.8, 29.4, 29.3, 28.9, 28.7, 28.1, 27.6, 26.5.

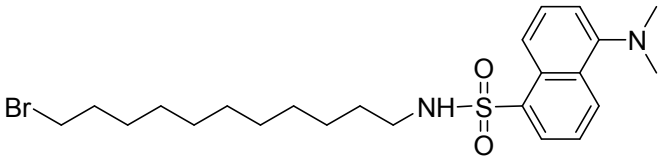

N-(11-bromoundecyl)-5-(dimethylamino) naphthalene-1-sulfonamide (21). To a solution of 11-bromoundecan-1-amine **20** (0.200 g, 0.802 mmol) in dry DCM (3 mL), Dansyl-chloride was added (0.238 g, 0.883 mmol) slowly followed by the addition of DIPEA (0.294 mL, 1.686 mmol) and stirred for 6 hours at room temperature. To the reaction mixture brine was added followed by the addition of EtOAc and washed with water several times. Finally washed with brine and dried over $MgSO_4$. The solvents were removed under reduced pressure. The crude mixture was purified by column chromatography (SiO_2; 10-20% EtOAc in Hexane) to give **21** as a viscous green liquid. (0.216 g, 55%). IR (neat) 3293, 3078, 2921, 2849, 1610, 1572 cm^{-1}; ^1H NMR (300 MHz, $CDCl_3$) δ 8.53 (d, J_{HH} = 8.5 Hz, 1H), 8.33 (d, J_{HH} = 8.6 Hz, 1H), 8.25 (d, J_{HH} = 7.2 Hz, 1H), 7.61 – 7.44 (m, 2H), 7.17 (d, J = 7.6 Hz, 1H), 5.01 (t, J = 6.0 Hz, 1H), 3.39 (t, J_{HH} = 6.8 Hz, 2H), 2.97 – 2.80 (m, 8H), 1.79 (m, 2H), 1.35 (m, 4H), 1.30 – 1.00 (m, 12H); ^{13}C NMR (75 MHz, $CDCl_3$) δ 152.0, 134.9, 130.4, 129.9, 129.7, 129.7, 128.5, 123.3, 118.9, 115.2, 45.5, 43.4, 34.3, 32.9, 29.5, 29.4, 29.3, 29.0, 28.8, 28.2, 26.4; HRMS (FAB, NBA, MNa^+) calcd for $C_{23}H_{35}BrN_2O_2SNa^+$: 505.1482, found 505.1509.

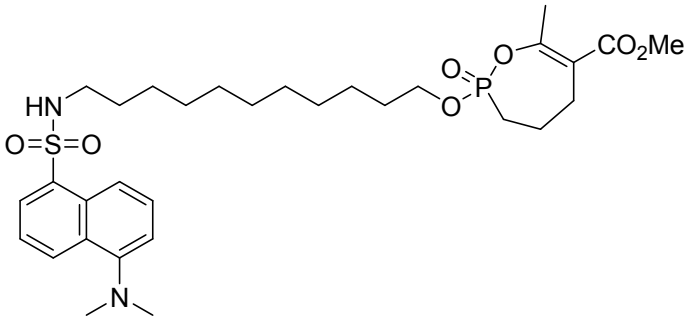

Methyl 2-((9-((5-(dimethylamino)naphthalene)-1-sulfonamido)nonyl)oxy)-7-methyl-3,4,5-trihydro-1,2-oxaphosphepine-6-carboxylate 2-oxide ($CyC_{32\text{-}Dansyl}$). To a solution of monocyclic phosphonate ester **CyC_4** (0.100 g, 0.4272 mmol) in dry toluene 1 ml (distilled) was added solution of solution **21** (226 mg, 0.4699 mmol) in dry toluene 1 mL followed by the addition of TBAI (0.021 g, 0.043 mmol) and heated in reflux for 7 h till the completion of reaction as observed by TLC and ^{31}P NMR. Solvents were removed, and the crude mixture was purified through column chromatography (SiO_2, 50% EtOAc in Hexane) to give **$CyC_{32\text{-}Dansyl}$** as a viscous green liquid (0.114 mg, 43%). IR (neat) 3283, 3165, 2923, 2851, 1712, 1643 cm^{-1}; ^1H NMR (300 MHz, $CDCl_3$) δ 8.51 (d, J_{HH} = 8.5 Hz, 1H), 8.29 (d, J_{HH} = 8.7 Hz, 1H), 8.22 (dd, J_{HH} = 7.3, 1.2 Hz, 1H), 7.56 – 7.46 (m, 2H), 7.17 (d, J_{HH} = 7.1 Hz, 1H), 4.91 (t, J_{HH} = 6.1 Hz, 1H), 4.16 – 4.00 (m, 2H), 3.73 (s, 3H), 2.90 – 2.79 (m, 8H), 2.70 – 2.43 (m, 2H), 2.31 (s, 3H), 2.17 – 1.81 (m, 4H), 1.65 (m, 2H), 1.38 – 1.05 (m, 16H); ^{13}C NMR (75 MHz, $CDCl_3$) δ 168.2, 159.3 (d, J_{CP} = 7.8 Hz), 152.0, 134.9, 130.4, 129.9, 129.76, 129.7, 128.4, 123.34, 119.2 (d, J_{CP} = 4.6 Hz), 118.9, 115.2, 66.2 (d, J_{CP} = 7.1 Hz), 52.0, 45.5, 43.4, 30.5 (d, J = 6.2 Hz), 29.6, 29.5, 29.4, 29.1, 29.0, 26.7 (d, J_{CP} = 132.75 Hz), 26.5, 26.3 (d, J_{CP} = 2.7 Hz), 25.52, 21.2 (d, J_{CP} = 7.4 Hz), 21.0 (d, J_{CP} = 1.7 Hz). ^{31}P NMR (121 MHz, $CDCl_3$) δ 23.2. HRMS (FAB, NBA, MNa^+) calcd for $C_{31}H_{47}N_2O_7PSNa^+$ 645.2739 found 645.2751.

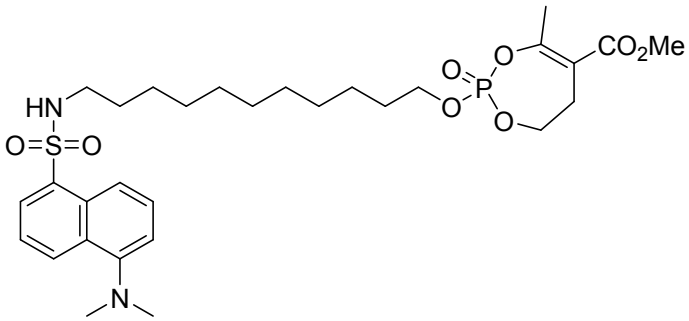

Methyl 2-((11-((5-(dimethylamino)naphthalene)-1-sulfonamido)undecyl)oxy)-4-methyl-6,7-dihydro-1,3,2-dioxaphosphepine-5-carboxylate 2-oxide ($CyC_{31\text{-}Dansyl}$). To a solution of monocyclic phosphate ester **CyC_{16}** (0.099 g, 0.4176 mmol) in dry dioxane (1 mL) was added **21** (0.226 g, 0.4699 mmol) dissolved in dioxane through canula followed by the addition of TBAI (0.016 g, 0.042 mmol),

and refluxed for 7 h till the completion of reaction. The reaction mixture was evaporated to remove the solvents and the crude mixture was purified through column chromatography (SiO_2, 30-50% EtOAc in Hexane) to give **$CyC_{31\text{-}Dansyl}$** as a viscous green liquid (0.114 g, 43%). IR(neat) 3276, 3208, 2922, 2851, 1715, 1645 cm^{-1}; ^1H NMR (300 MHz, $CDCl_3$) δ 8.52 (d, J_{HH} = 8.5 Hz, 1H), 8.29 (d, J_{HH} = 8.6 Hz, 1H), 8.23 (dd, J_{HH} = 7.2, 0.7 Hz, 1H), 7.58 – 7.46 (m, 2H), 7.17 (d, J_{HH} = 7.5 Hz, 1H), 4.84 (t, J_{HH} = 6.0 Hz, 1H), 4.36 (m, 1H), 4.21 – 4.09 (m, 3H), 3.75 (s, 3H), 3.05 – 2.77 (m, 10H), 2.34 (s, 3H), 1.75 – 1.62 (m, 2H), 1.33 (m, 4H), 1.28 – 1.05 (m, 12H); ^{13}C NMR (75 MHz, $CDCl_3$) δ 167.3, 161.1 (d, J_{CP} = 9.6 Hz), 152.2, 135.0, 130.5, 130.0, 129.8, 129.8, 128.5, 123.4, 118.9, 115.5 (d, J_{CP} = 3.8 Hz), 115.3, 69.2 (d, J_{CP} = 6.1 Hz), 68.4 (d, J_{CP} = 6.8 Hz), 52.3, 45.6, 43.5, 30.4 (d, J_{CP} = 6.6 Hz), 29.7, 29.5, 29.4, 29.1 (d, J_{CP} = 5.1 Hz), 28.3, 26.5, 25.4, 20.5 (d, J_{CP} = 3.9 Hz); ^{31}P NMR (121 MHz, $CDCl_3$) δ -10.8; HRMS (ESI, MNa^+) calcd for $C_{30}H_{45}N_2O_8PSNa^+$ 647.2514, found 647.2526.

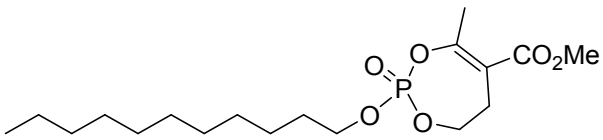

Methyl 4-methyl-2-(undecyloxy)-6,7-dihydro-1,3,2-dioxaphosphepine-5-carboxylate 2-oxide (CyC$_{31}$).[1] To a solution of monocyclic phosphate ester **CyC_{16}** (0.100 g, 0.421 mmol) in 1,4-dioxane (1 mL) was added a solution of bromoundecane (0.366 mL, 1.63 mmol) followed by the addition of *n*Bu_4NI (0.020 g, 0.054 mmol) in 1,4-dioxane (1 mL). The resulting solution was heated to reflux for 4 hours when the completion of reaction was observed by TLC and ^{31}P NMR spectroscopy. The solution was concentrated *in vacuo* and the residue was purified using column chromatography (SiO_2, 50% EtOAc in hexane) to give CyC_{31} viscous liquid (0.059 mg, 38%). IR (neat) 2921, 2851, 1717, 1644, 1287 cm^{-1}; ^1H NMR (300 MHz, $CDCl_3$) δ 4.434-4.28 (m, 1H), 4.23-4.08 (m, 3H), 3.75 (s, 3H), 3.06-2.76 (m, 2H), 1.76-1.64 (m, 2H), 1.40-1.17 (m, 16H), 0.86 (d, J_{HH} = 6.4 Hz, 3H); ^{13}C NMR (75 MHz, $CDCl_3$) δ 167.2 (d, J_{HP} = 1.9 Hz), 161.1 (d, J_{HP} = 9.6 Hz), 115.4 (d, J_{HP} = 3.8 Hz), 84.8, 69.2 (d, J_{HP} = 6.0 Hz), 68.2, 68.2, 52.2, 31.9, 30.3 (d, J_{CP} = 6.6 Hz), 29.6, 29.5, 29.4, 29.1, 28.2, 22.7, 20.4 (d, J_{CP} = 3.8 Hz), 14.2; ^{31}P NMR (121 MHz, $CDCl_3$); δ -10.8; HRMS (ESI, MH^+) calcd for $C_{18}H_{34}O_6P$ 377.2093, found 377.2088.

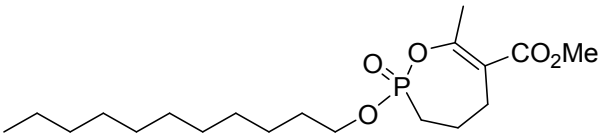

Methyl 7-methyl-2-(undecyloxy)-3,4,5-trihydro-1,2-oxaphosphepine-6-carboxylate 2-oxide (CyC$_{32}$).[1] To a solution of monocyclic phosphonate ester **CyC$_4$** (0.145 g, 0.619 mmol) in toluene (1 mL) was added a solution of bromoundecane (0.0.415 mL, 1.85 mmol) followed by the addition of *n*Bu$_4$NI (0.023 g, 0.062 mmol) in toluene (1 mL). The resulting solution was heated to reflux for 4 hours when the completion of reaction was observed by TLC and ^{31}P NMR spectroscopy. The solution was concentrated *in vacuo* and the residue was purified using column chromatography (SiO$_2$, 50% EtOAc in hexane) to give CyC$_{32}$ viscous liquid (0.097 g, 42%). IR (neat) 2921, 2852, 1714, 1644 cm^{-1}; ^{1}H NMR (300 MHz, CDCl$_3$) δ 4.20-4.03 (m, 3H), 3.72 (s, 3H), 2.69-2.48 (m, 2H), 2.38 (s, 3H), 2.30-1.82 (m, 5H), 1.71 – 1.59 (m, 3H), 1.21 (m, 16H), 0.86 (d, J_{HH} = 6.4 Hz, 3H); ^{13}C NMR (75 MHz, CDCl$_3$) δ 186.1, 159.4 (d, J_{HP} = 7.8 Hz), 119.1 (d, J_{HP} = 4.7 Hz), 66.2 (d, J_{HP} = 6.9 Hz), 51.9, 30.5 (d, J_{CP} = 6.0 Hz), 29.7, 29.63, 29.57, 29.4, 29.3, 29.2, 27.0 (d, J_{CP} = 93 Hz) , 25.5, 22.8, 21.2, 21.1, 22.0, 14.2; ^{31}P NMR (121 MHz, CDCl$_3$); δ 23.2; HRMS (ESI, MH$^+$) calcd for C$_{19}$H$_{36}$O$_5$P 375.2300, found 375.2296.

References

(1) Barelier, S.; Avellan, R.; Gnawali, G. R.; Fourquet, P.; Roig-Zamboni, V.; Poncin, I.; Point, V.; Bourne, Y.; Audebert, S.; Camoin, L.; Spilling, C. D.; Canaan, S.; Cavalier, J. F.; Sulzenbacher, G., Direct capture, inhibition and crystal structure of HsaD (Rv3569c) from M. tuberculosis. *FEBS J* **2022**, https://doi.org/10.1111/febs.16645.

(2) Cheng, K.; Landry, C. C., Diffusion-based deprotection in mesoporous materials: a strategy for differential functionalization of porous silica particles. *J Am Chem Soc* **2007,** *129* (31), 9674-85.

(3) Mes, T.; van der Weegen, R.; Palmans, A. R.; Meijer, E. W., Single-chain polymeric nanoparticles by stepwise folding. *Angew Chem Int Ed Engl* **2011,** *50* (22), 5085-9.

(4) Sauer, R.; Turshatov, A.; Baluschev, S.; Landfester, K., One-Pot Production of Fluorescent Surface-Labeled Polymeric Nanoparticles via Miniemulsion Polymerization with Bodipy Surfmers. *Macromolecules* **2012,** *45* (9), 3787-3796.

(5) Tanahashi, M.; Matsuda, T., Surface functional group dependence on apatite formation on self-assembled monolayers in a simulated body fluid. *J Biomed Mater Res* **1997,** *34* (3), 305-15.

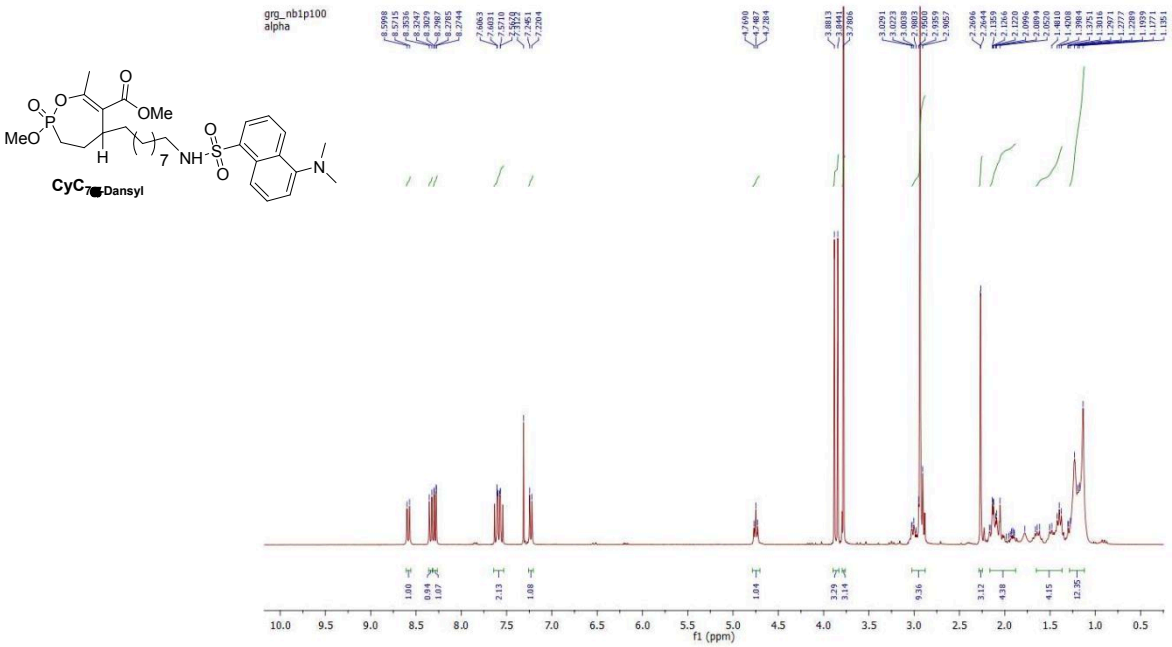

^{1}HNMR spectrum (300 MHz, CDCl3)

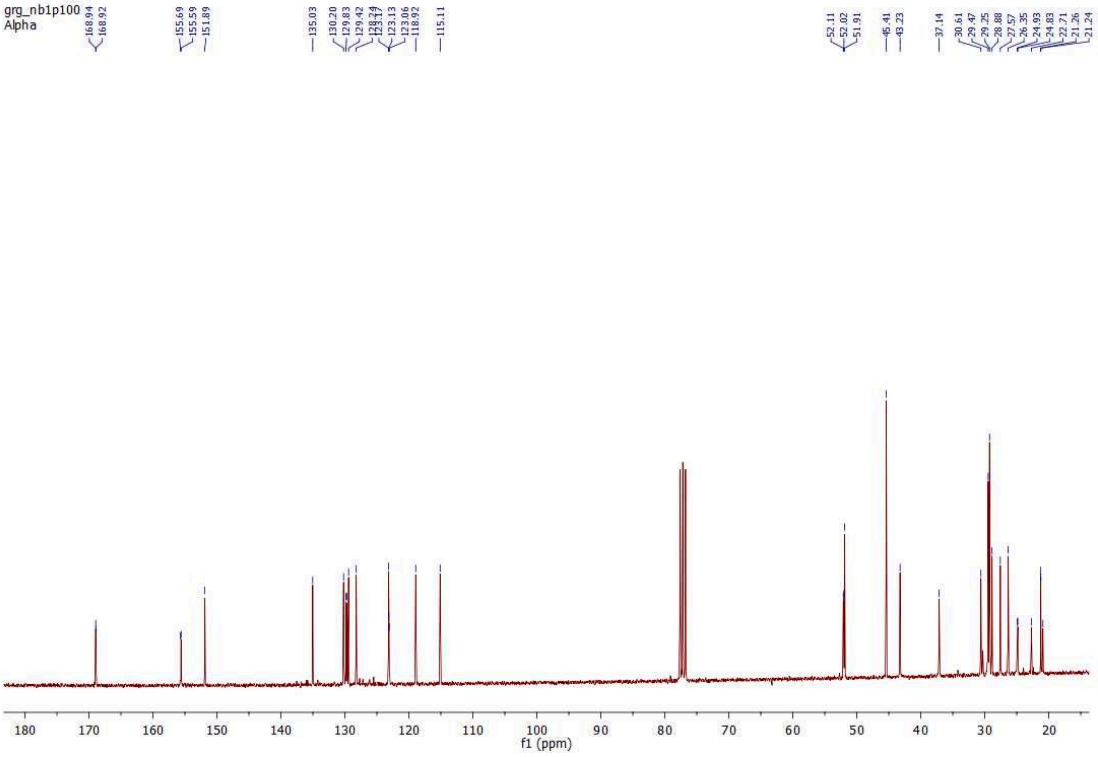

^{13}C NMR spectrum

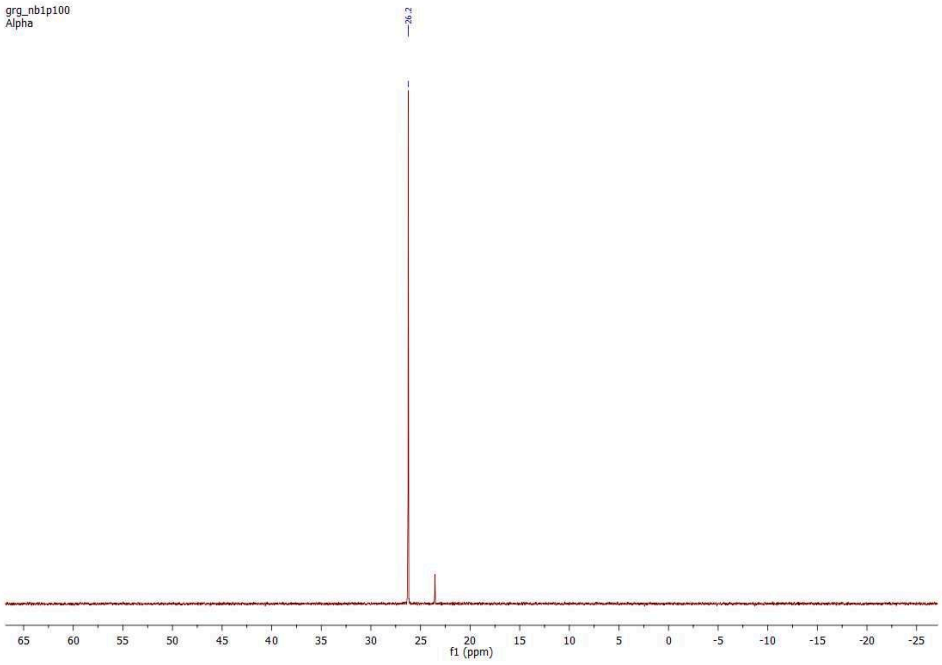

^{31}P NMR spectrum

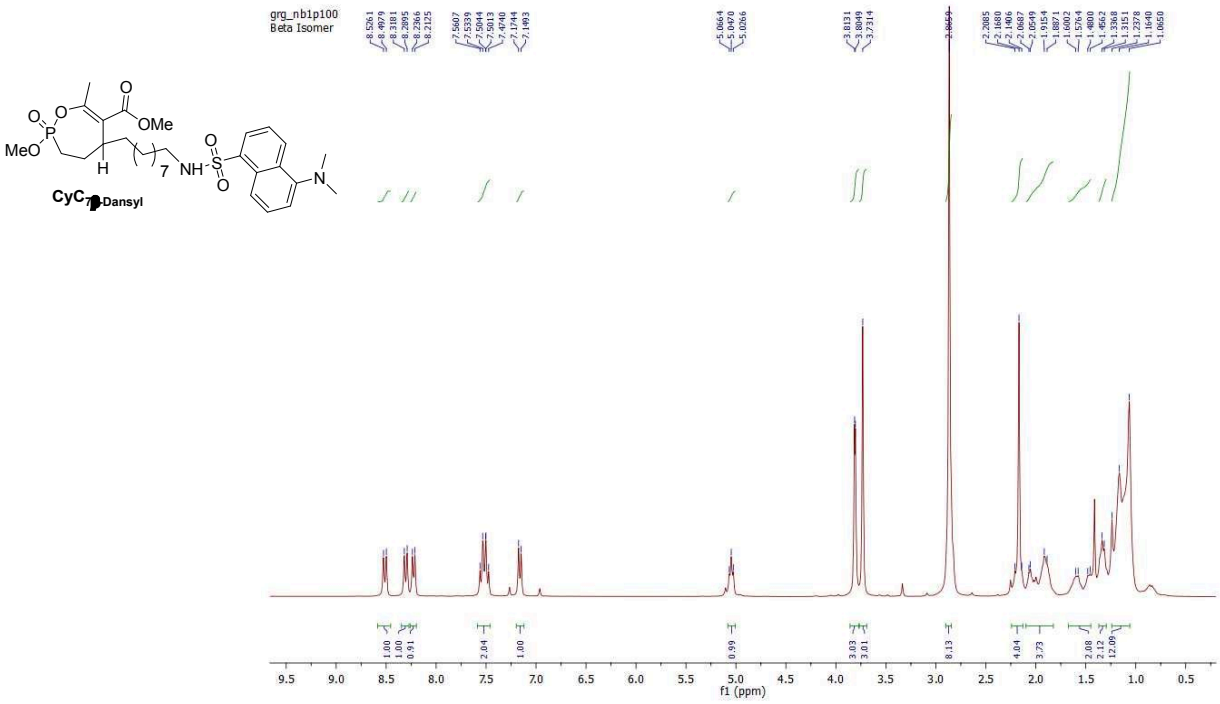

^{1}HNMR spectrum (300 MHz, CDCl3)

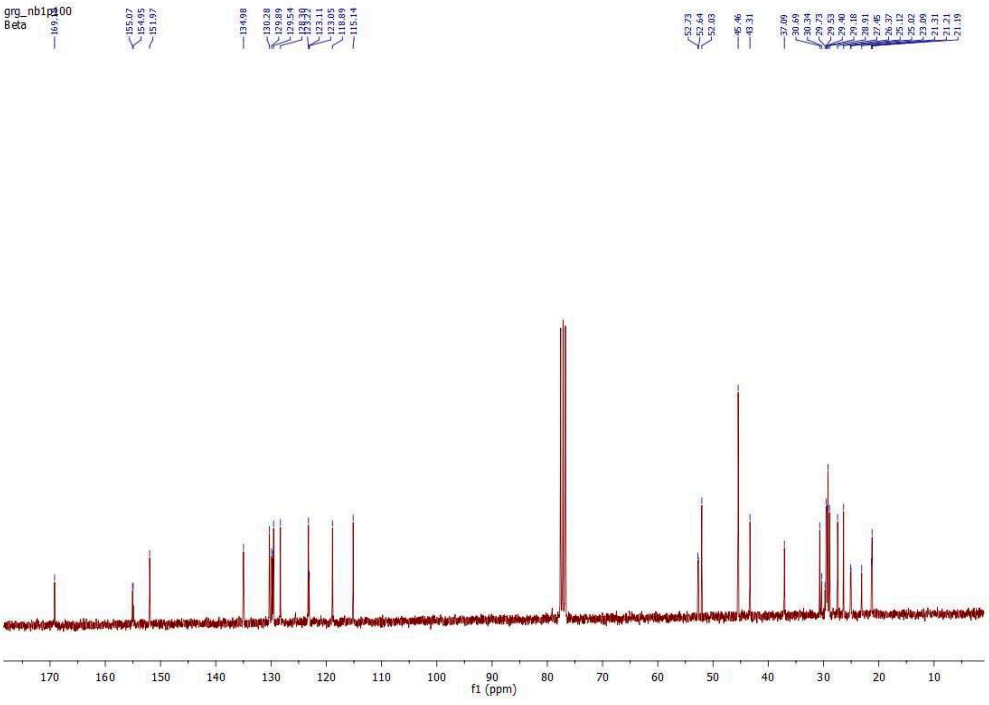

^{13}C NMR spectrum

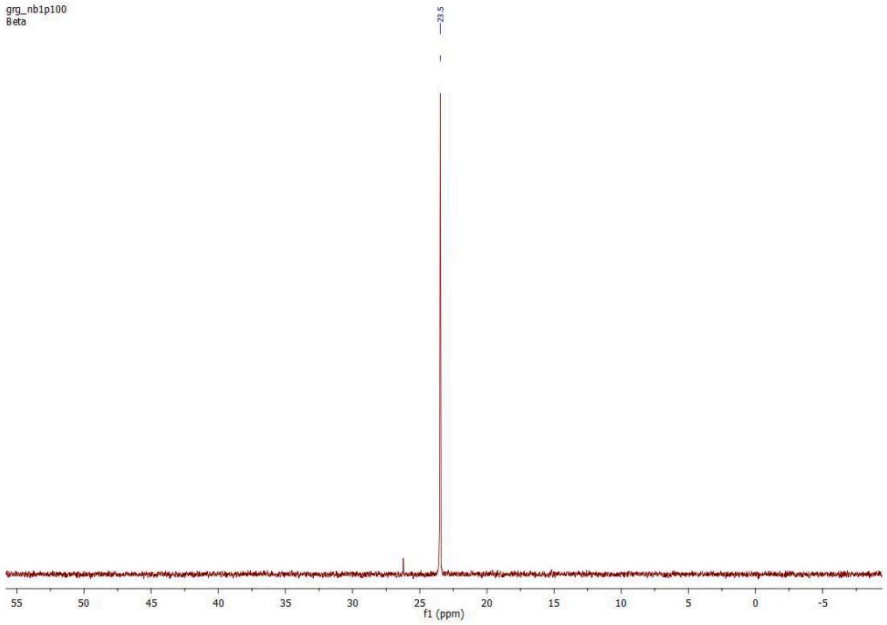

^{31}P NMR spectrum

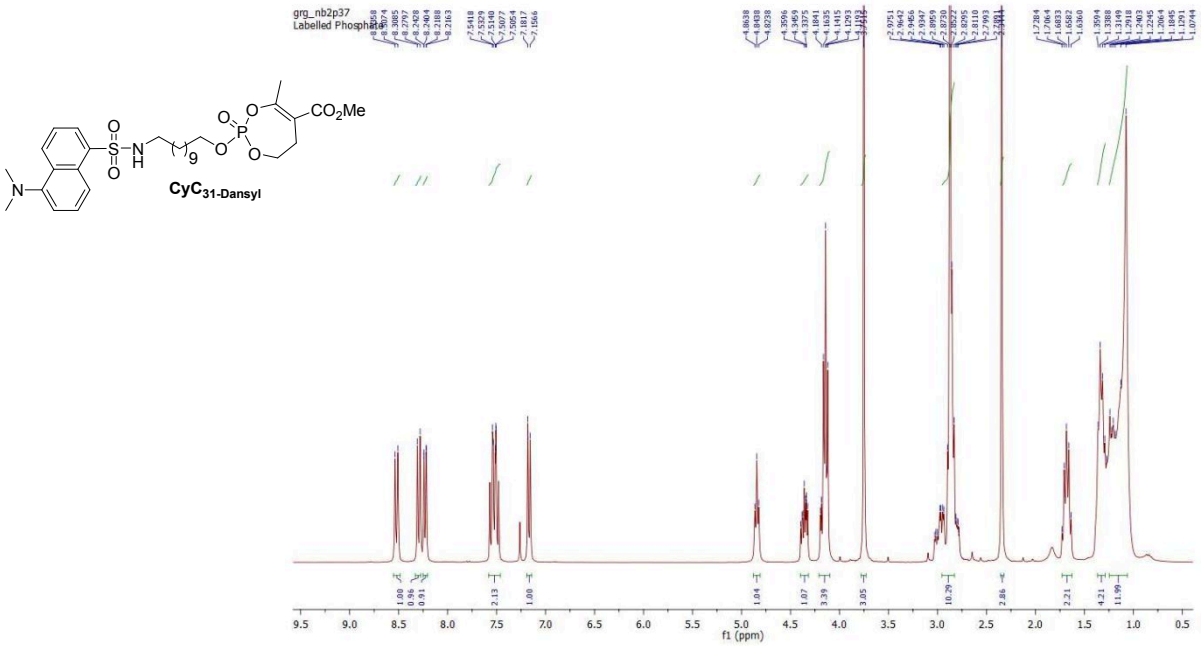

^{1}H NMR Spectrum (300 MHz, $CDCl_3$)

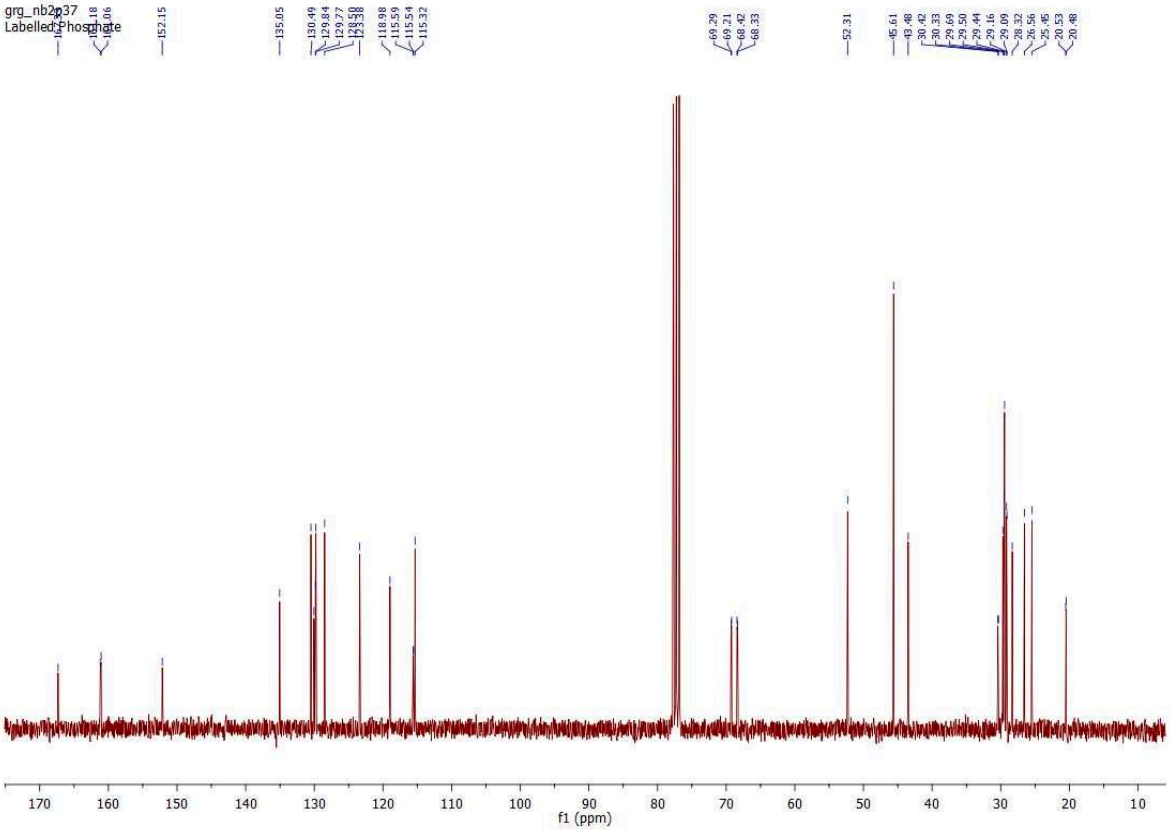

^{13}C NMR spectrum

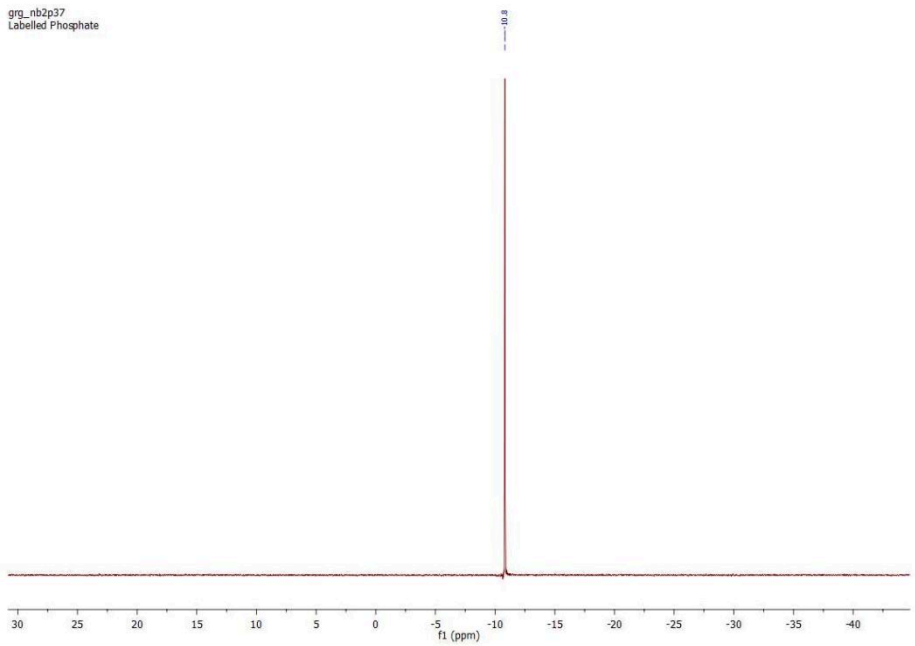

^{31}P NMR spectrum

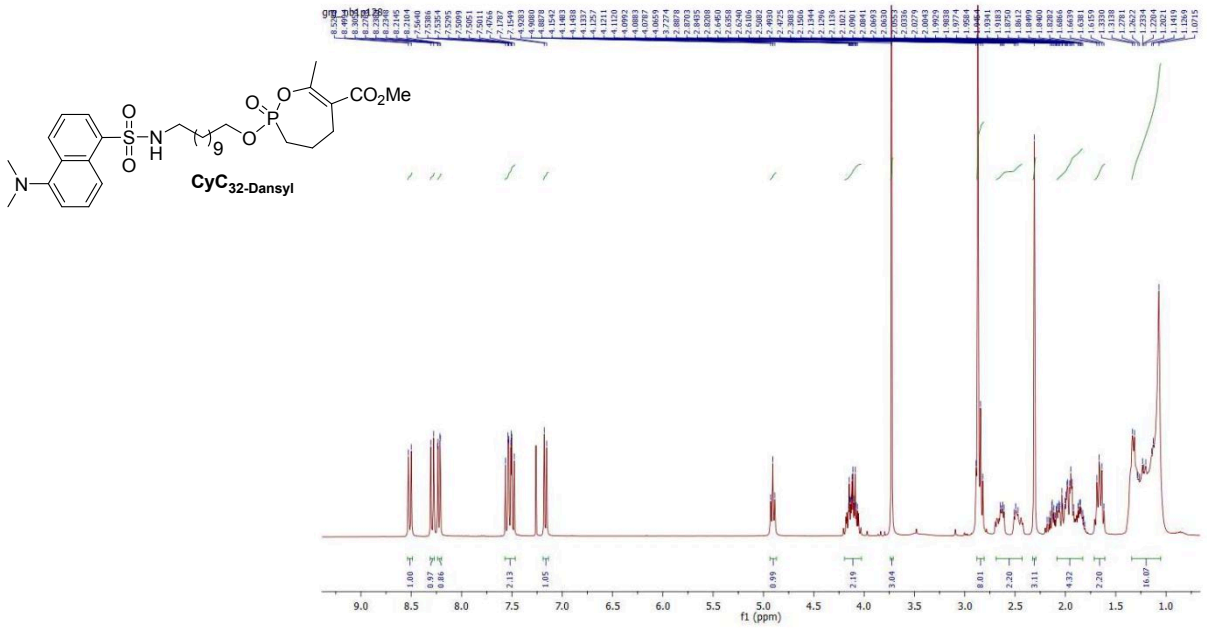

^{1}H NMR Spectrum (300 MHz, $CDCl_3$)

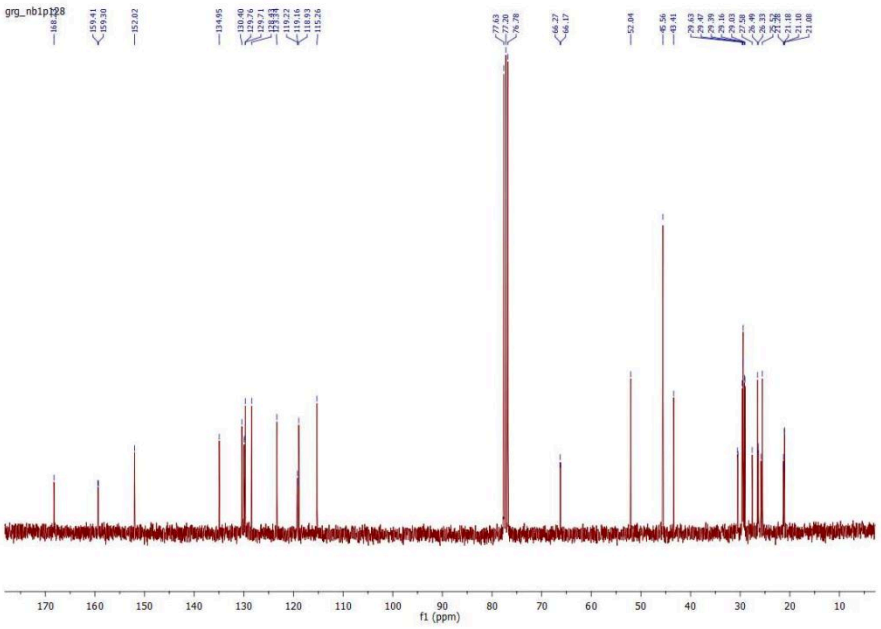

^{13}C NMR spectrum

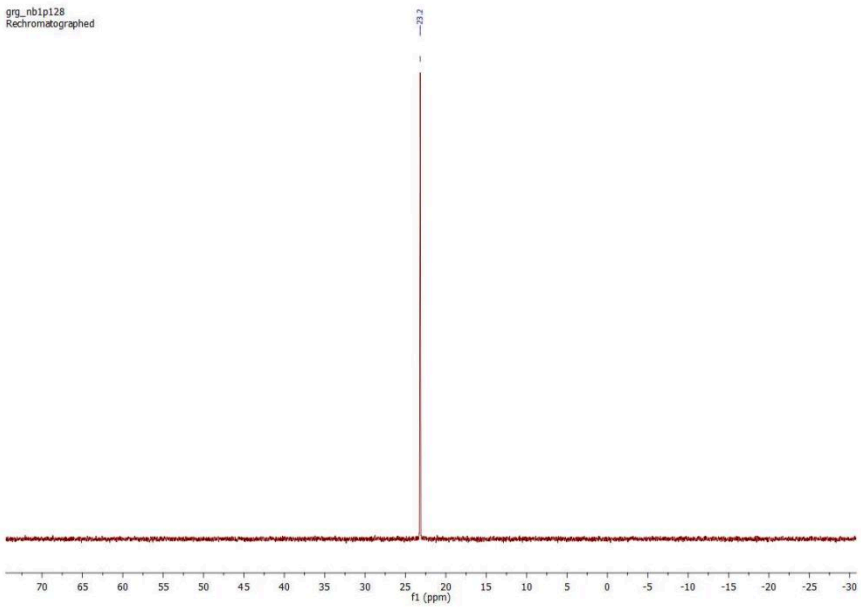

^{31}P NMR spectrum

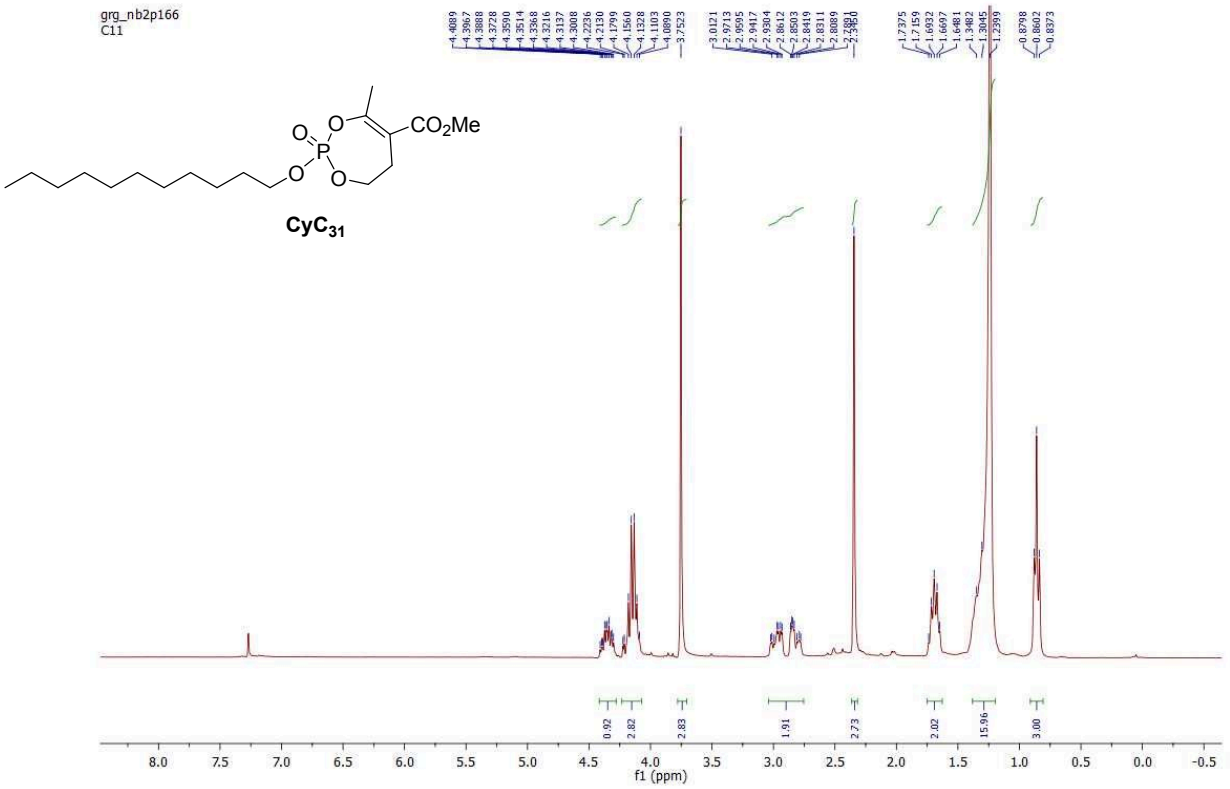

^{1}H NMR Spectrum (300 MHz, $CDCl_3$)

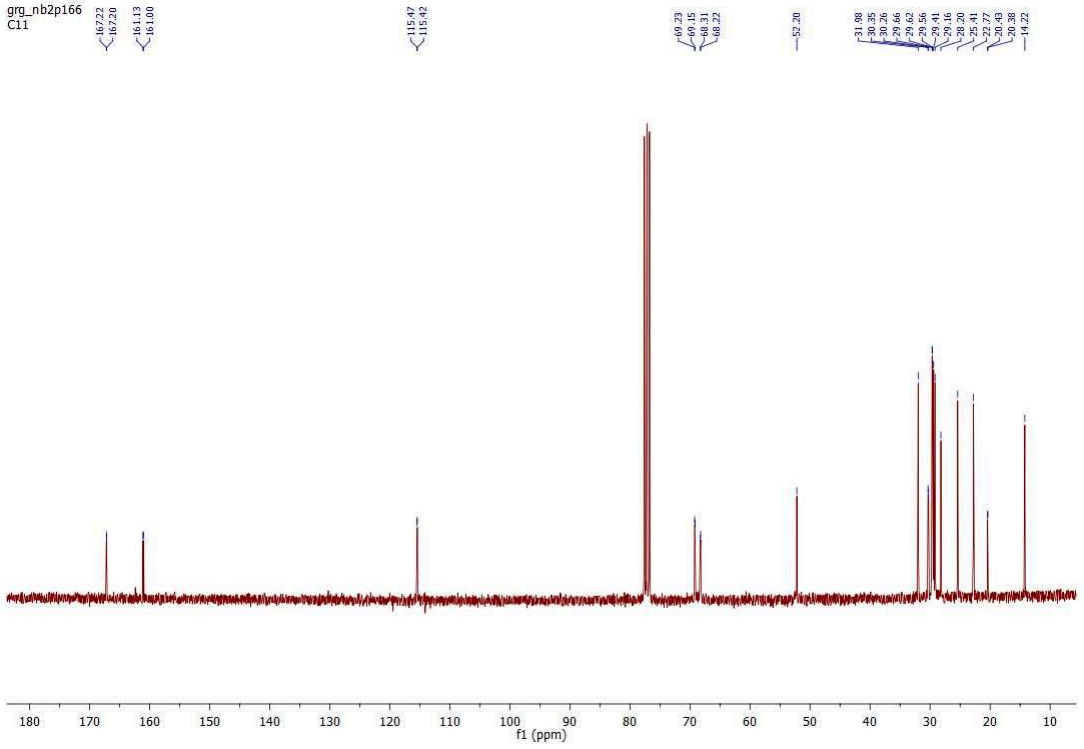

^{13}C NMR Spectrum (300 MHz, $CDCl_3$)

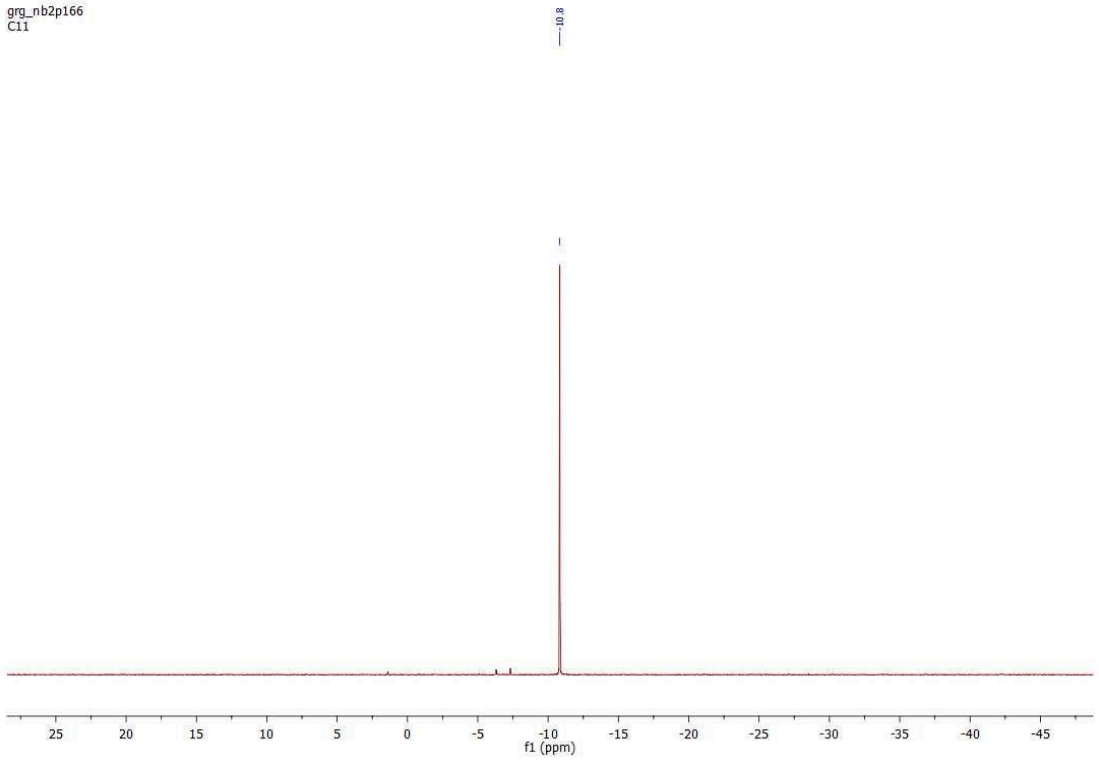

^{31}P NMR Spectrum (300 MHz, $CDCl_3$)

(CyC_{32})

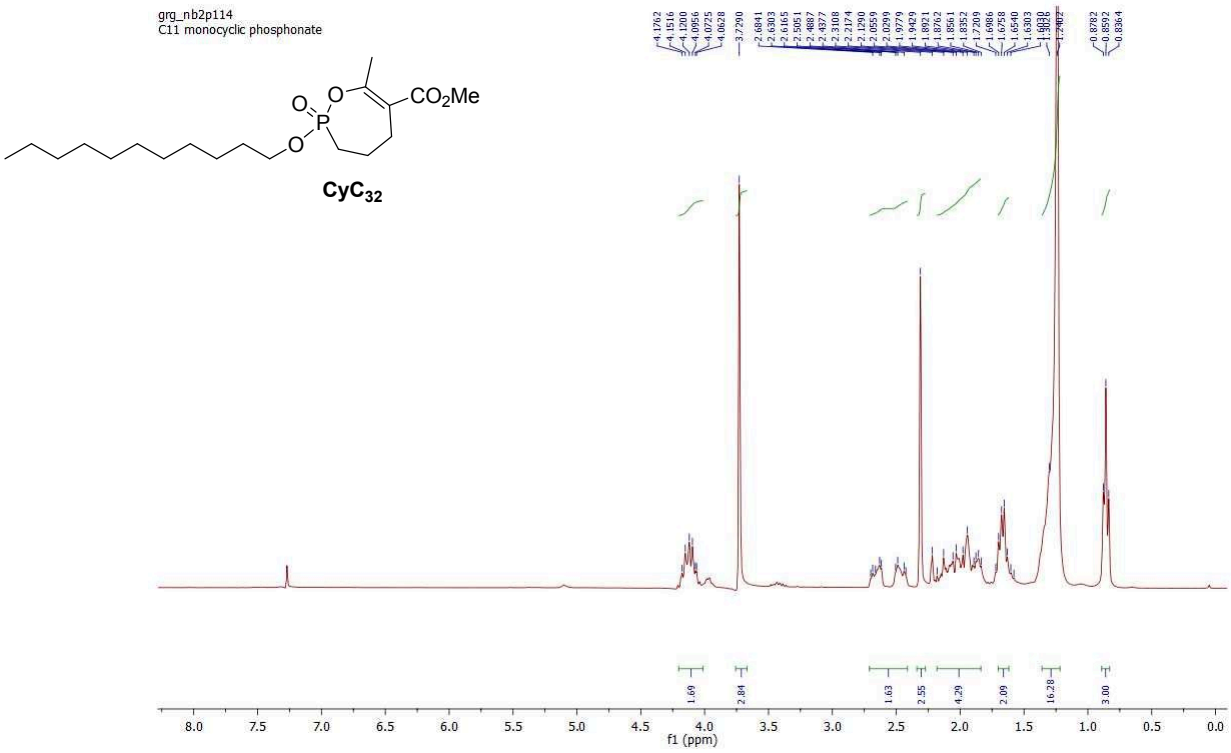

^{1}H NMR Spectrum (300 MHz, $CDCl_3$)

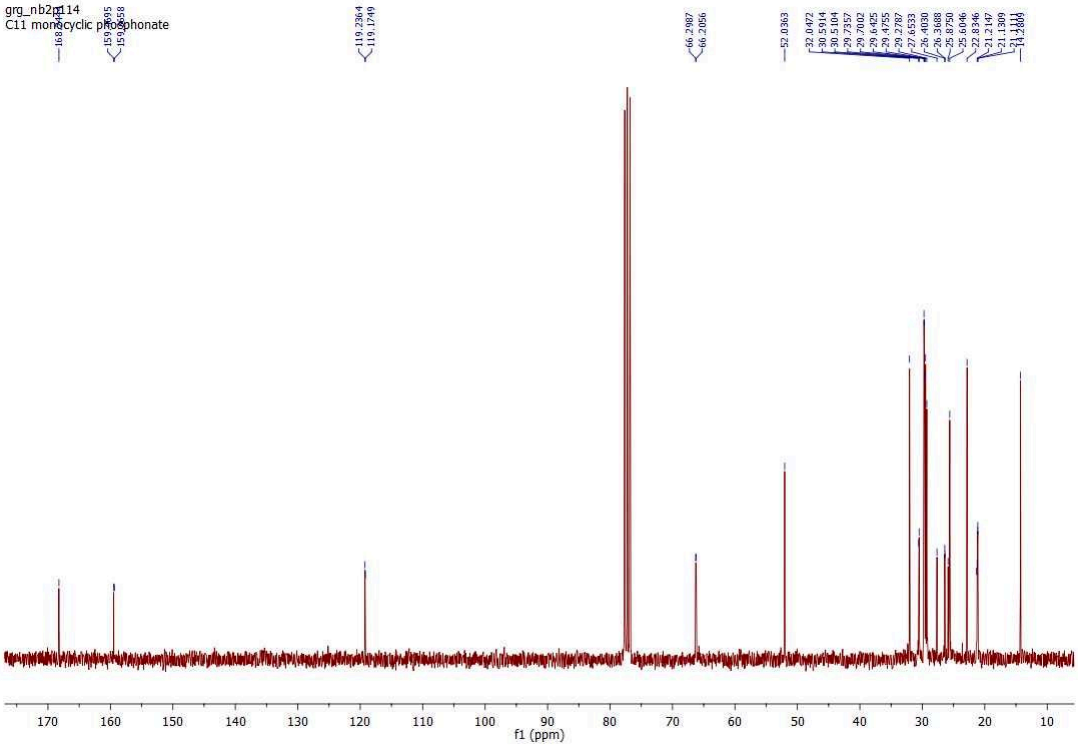

^{13}C NMR Spectrum (300 MHz, $CDCl_3$)

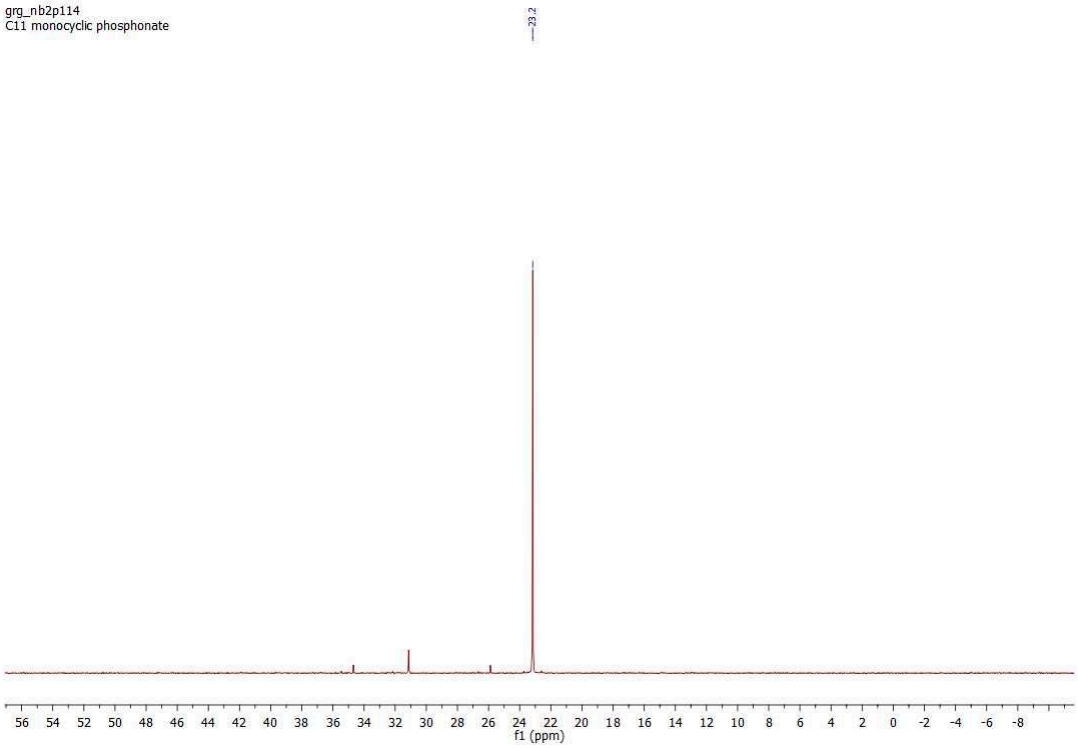

^{31}P NMR Spectrum (300 MHz, $CDCl_3$)

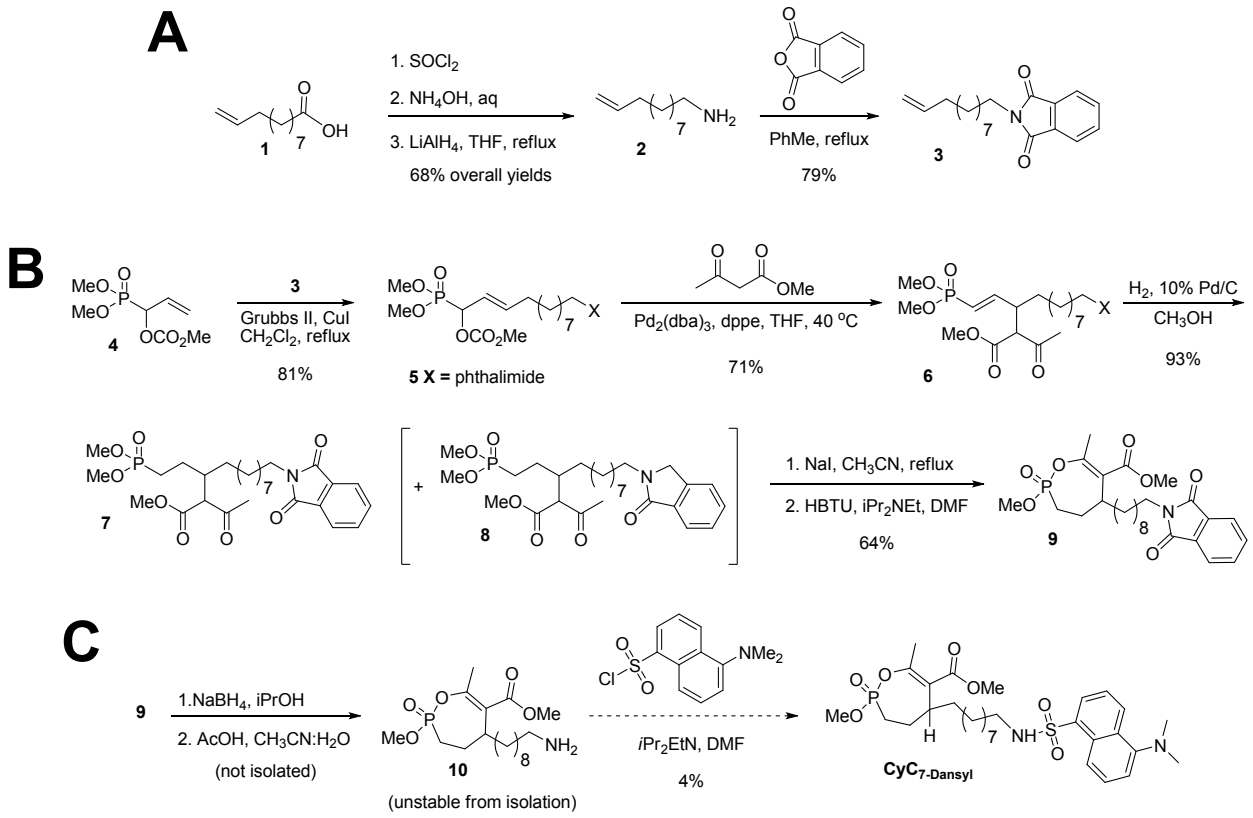

Figure S1. First synthetic route for the obtention of racemic **CyC$_{7\text{-Dansyl}}$**.

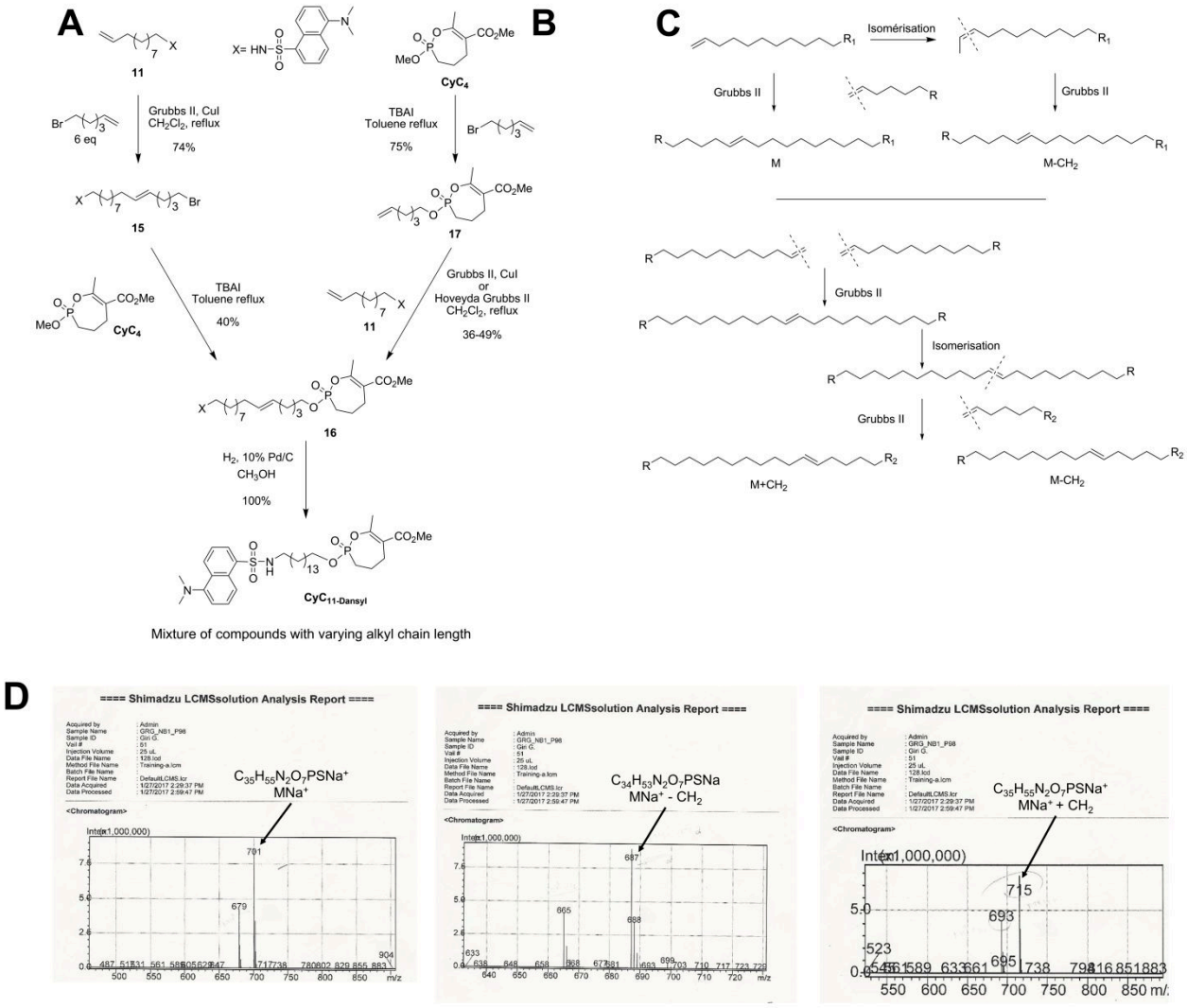

Figure S2. (A-B) Cross metathesis pathway for the obtention of **$CyC_{11\text{-}Dansyl}$**, and **(C)** probable isomerization of double bonds during the metathesis reaction, and **(D)** LC-MS spectra of final product.

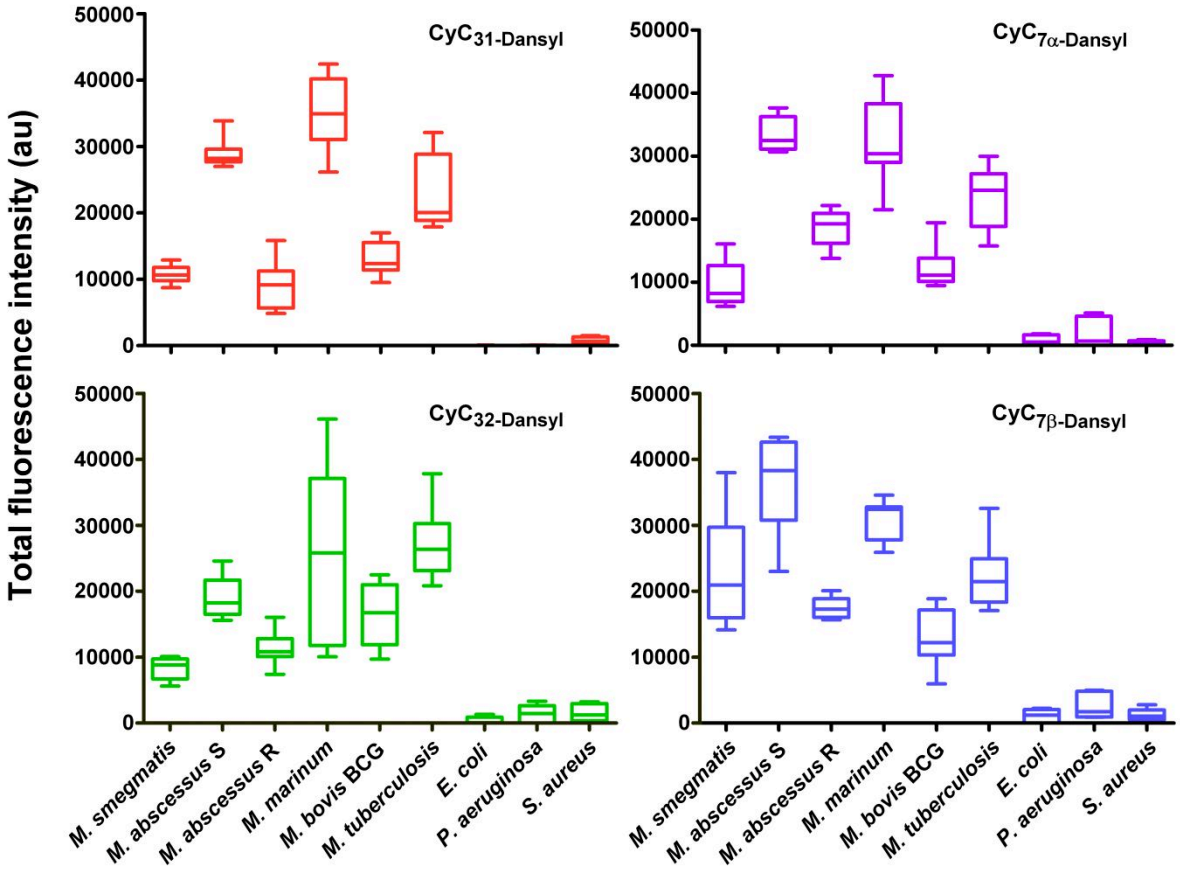

Figure S3. Total fluorescence intensity profile of each CyC$_{\text{-Dansyl}}$-treated bacteria expressed as arbitrary units (au). For each **CyC** probe, boxplot representation of the Dansyl total fluorescence intensity measured for *M. smegmatis*, *M. abscessus* S & R, *M. marinum*, *M. bovis* BCG, *M. tuberculosis*, *E. coli*, *P. aeruginosa*, *S. aureus* strains. Values are from **Figure 2B** and **Figure S4B**.

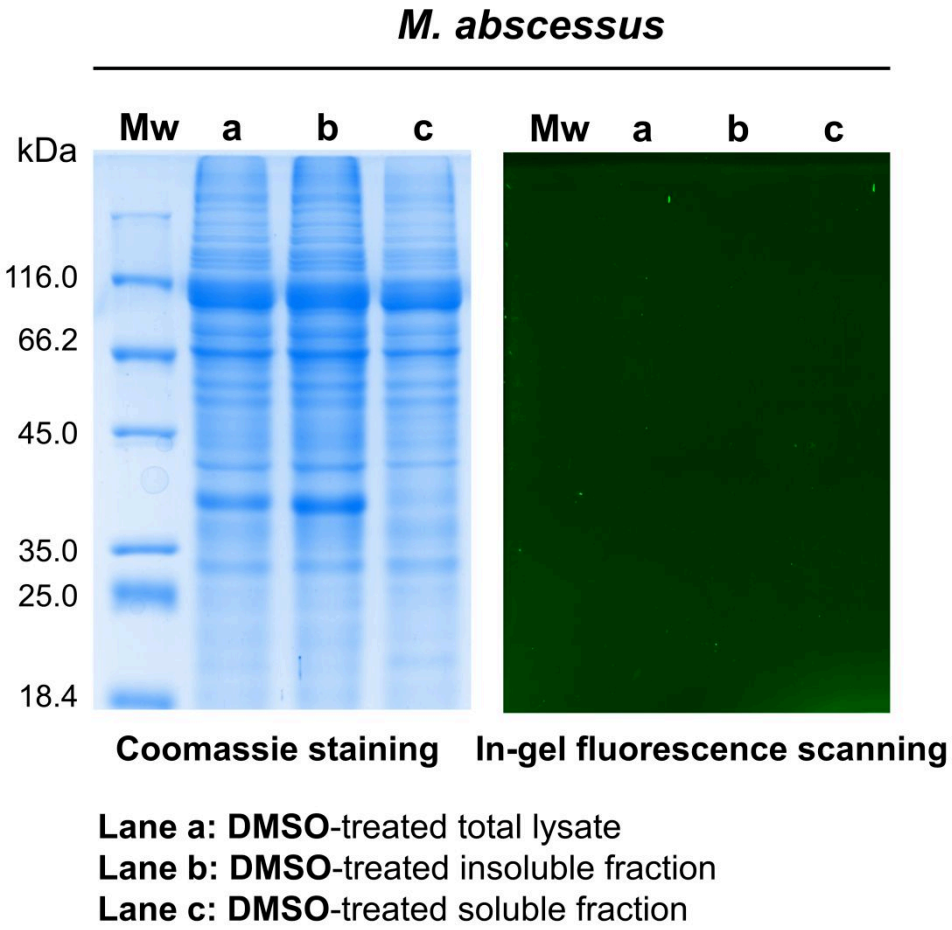

Figure S4. **SDS-PAGE gel of DMSO-treated *M. abscessus* total lysate.** The bacteria were exposed to DMSO for 3 h, then washed and lysed. Equal amounts of proteins (50 µg) were separated by 12% SDS-PAGE and visualized by Coomassie blue staining (*left*) and in-gel fluorescence for Dansyl detection (*right*). Fluorescent gel scanning was done using trans-UV illumination (λ_{ex} 302 nm) as excitation source, and as emission the 530/28 filter of a ChemiDoc MP Imager (Bio-Rad) before staining of the gels with Coomassie Brilliant Blue dye.

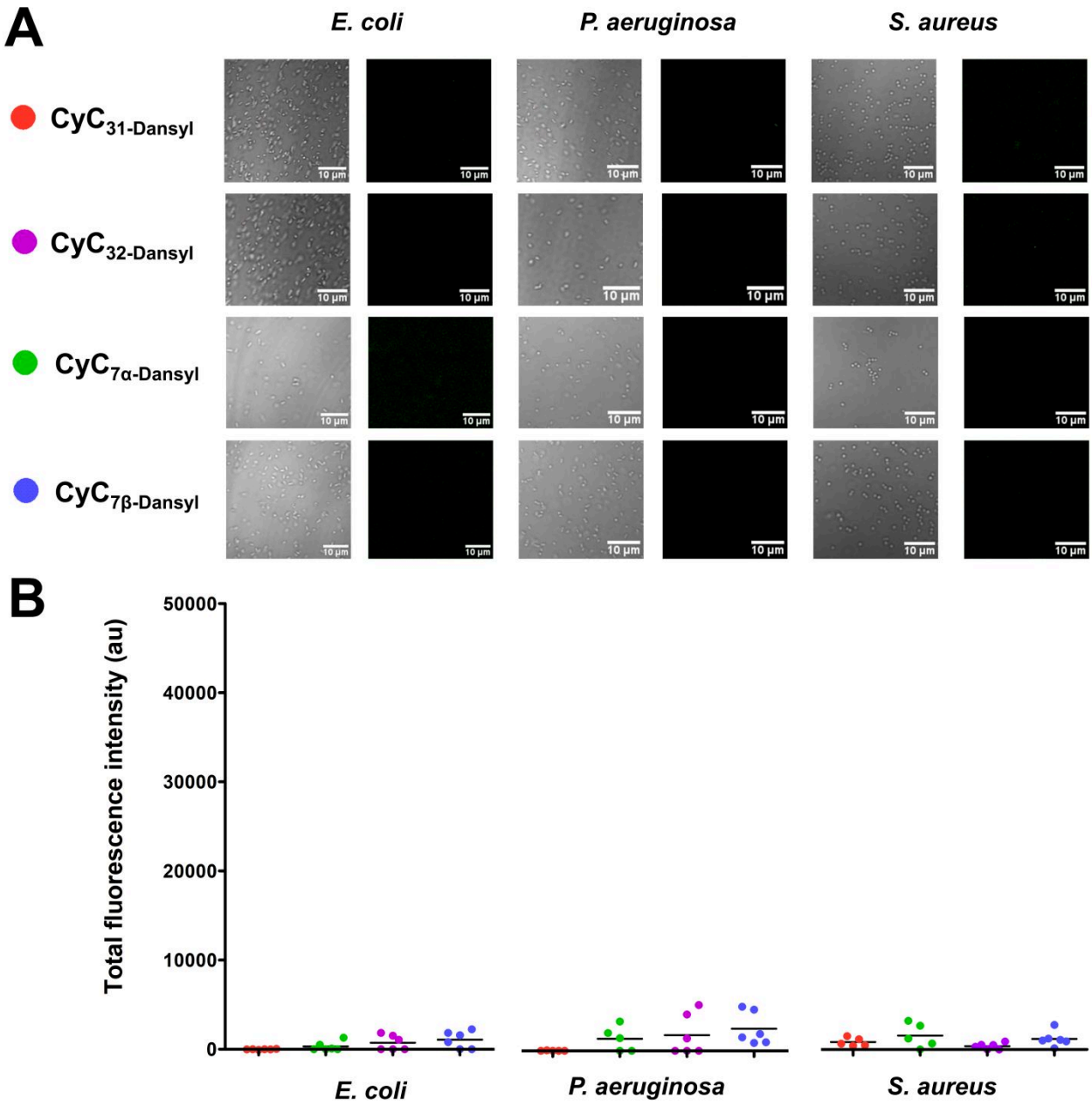

Figure S5. **The CyCs are unable to cross the cell wall of Gram-positive and Gram-negative bacteria.** **(A)** Representative fluorescence images of *E. coli*, *P. aeruginosa* and *S. aureus* strains in presence of fluorescent **CyCs**. Bacterial suspension corresponding to 1.5×10^{10} cells/mL in PBS-T were exposed to 200 µM **CyC$_{\text{-Dansyl}}$** for 3 h, then washed and fixed with 4% paraformaldehyde. Fixed bacteria were imaged using an Olympus IX81 confocal microscope. The same results were also obtained when using PBS in absence of Tween 20 detergent (*data not shown*). Scale bars correspond to 5 µm. **(B)** Total fluorescence intensity of each **CyC$_{\text{-Dansyl}}$**-treated bacteria expressed as arbitrary units (au). For the sake of comparison, the *y*-axis has been scaled to the one reported in **Figure 2**. Compounds color code is indicated in panel (**A**). Results are corresponding to $n = 3$ biologically independent experiments performed in triplicate.

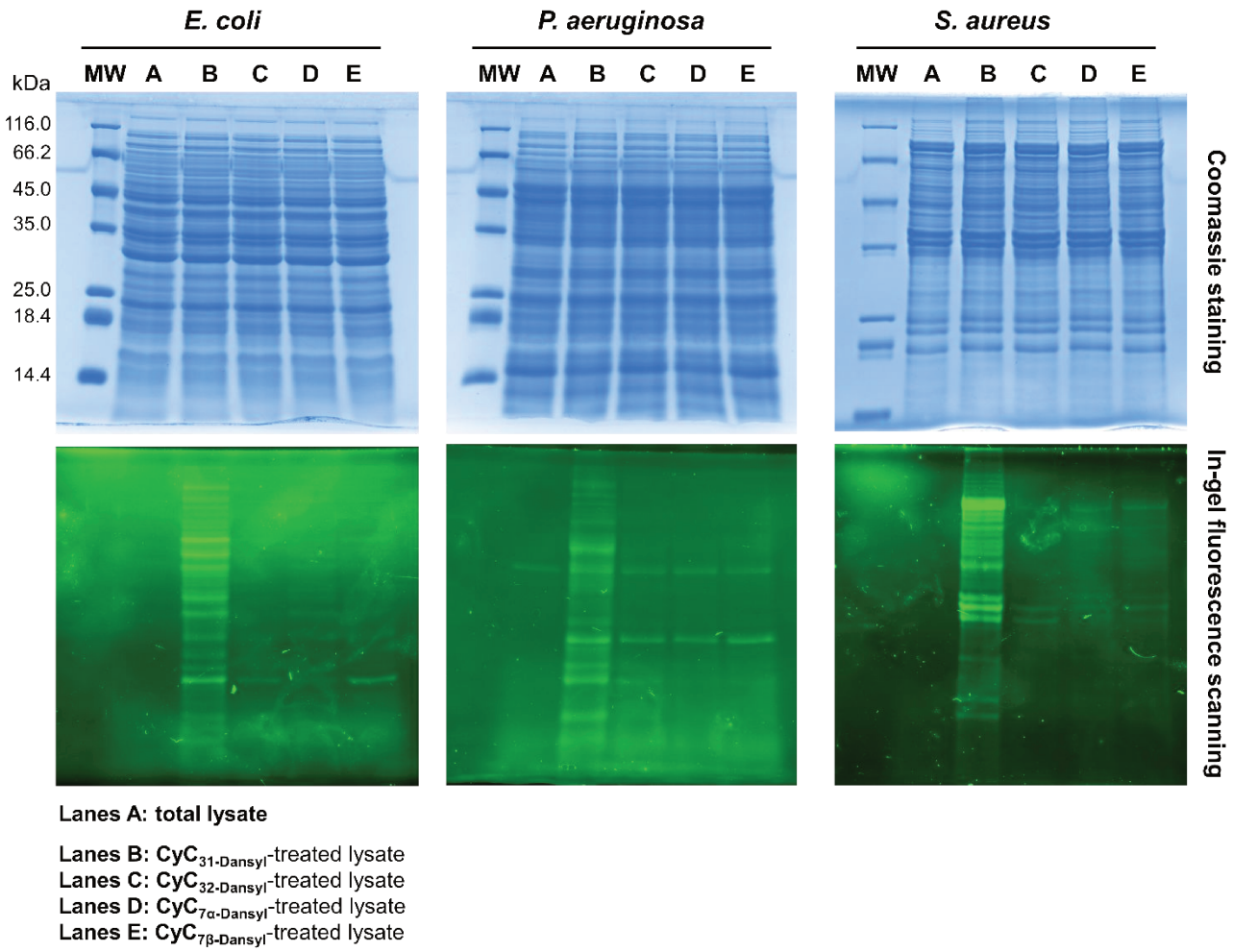

Figure S6. The CyCs are able to react with Gram-positive and Gram-negative bacterial (Ser/Cys)-base enzymes when incubated with total lysate. A sample of *E. coli*, *P. aeruginosa* or *S. aureus* total lysate (1 mg/mL - 50 µL final volume) was pre-incubated for 3 h with 200 µM **CyC$_{\text{-Dansyl}}$** or DMSO. The reaction was stopped by adding 5X Laemmli reducing buffer followed by boiling, and equal amounts of proteins (50 µg) were separated by 12% SDS-PAGE and visualized by Coomassie blue staining (*top*) and in-gel fluorescence visualization (*bottom*). The various **CyC$_{\text{-Dansyl}}$** compounds are able to covalently label bacterial (Ser/Cys)-base enzymes, as evidenced by the occurrence of various fluorescent bands in ***lanes B-E***.
The **CyC$_{\text{-Dansyl}}$**-labeled proteins were detected by fluorescent gel scanning using trans-UV illumination (λ_{ex} 302 nm) as excitation source and as emission the 530/28 filter of a ChemiDoc MP Imager (Bio-Rad) before staining of the gels with Coomassie Brilliant Blue dye.

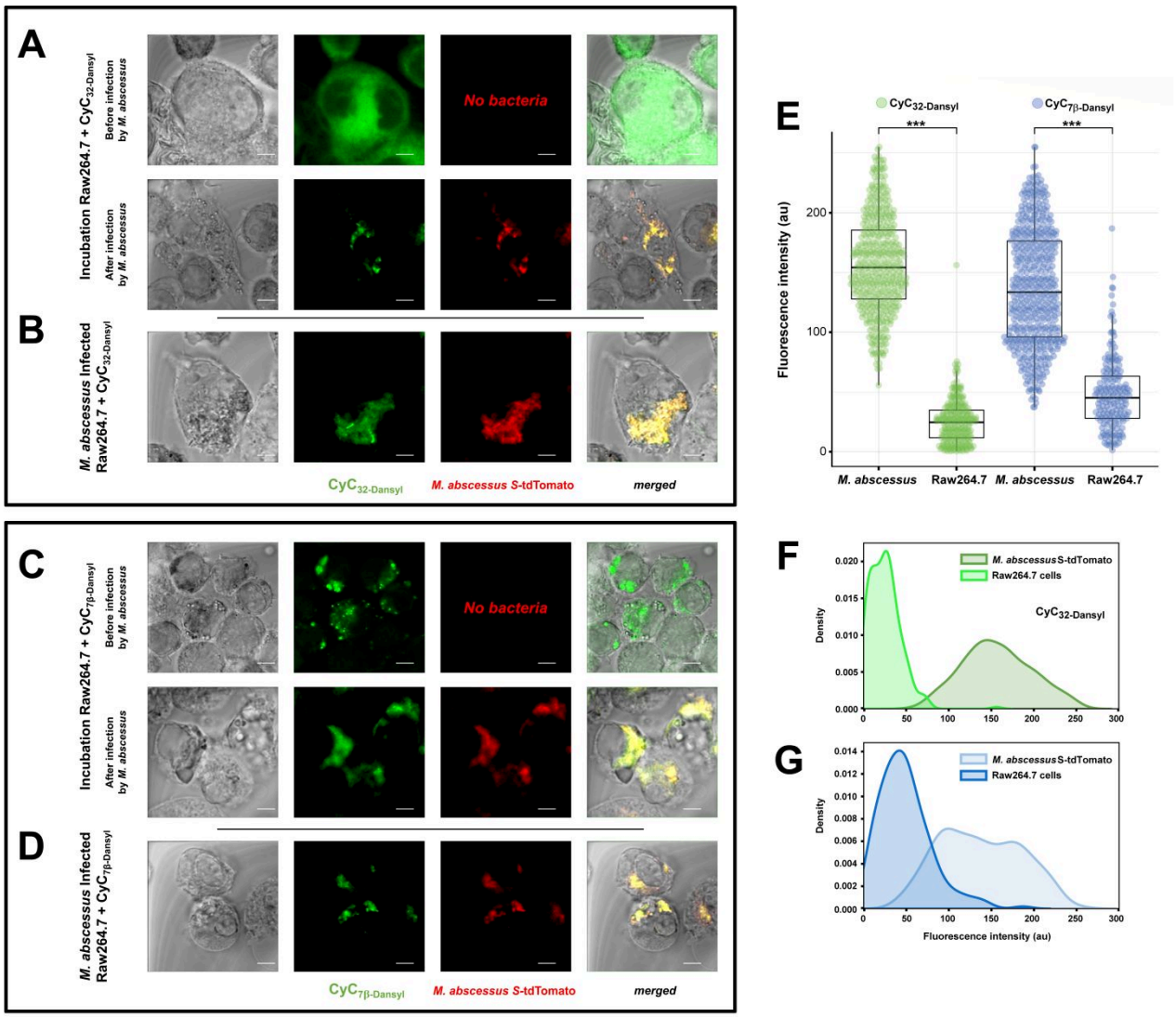

Figure S7. The $CyC_{32\text{-}Dansyl}$ and $CyC_{7\beta\text{-}Dansyl}$ specifically localized on *M. abscessus* S inside infected Raw264.7 macrophages. (**A, C**) Raw264.7 macrophages were preincubated with 100 µM **$CyC_{32\text{-}Dansyl}$** (**A**) or **$CyC_{7\beta\text{-}Dansyl}$** (**C**) for 24 h prior to be infected with *M. abscessus* S-tdTomato (MOI 10) for another 24 h. (**B, D**) Alternatively, *M. abscessus* S-dtTomato infected Raw264.7 were treated with each probe for 24 h before chemical fixation and confocal fluorescence imaging. Scale bars correspond to 5 µm. Micrographs are representative of 2 independent experiments. (**E**) Quantitative analysis of the Dansyl fluorescence signal per bacterium and Raw264.7 cell positive area shown as a sinaplot-boxplot and expressed as arbitrary units (au). Results are from two biologically independent experiments. 185 to 251 cells were observed resulting in 451 to 511 segmented intracellular *M. abscessus* S-dtTomato positive regions. The *p*-values were calculated by using a two-tailed *t*-statistic test with Prism 4.0 (Graphpad, Inc): *** *p*-value < 0.001. **(F-G)** Analysis of the Dansyl-fluorescent signal profile of *M. abscessus* S-tdTomato and Raw264.7 positive cells reported as density plot.

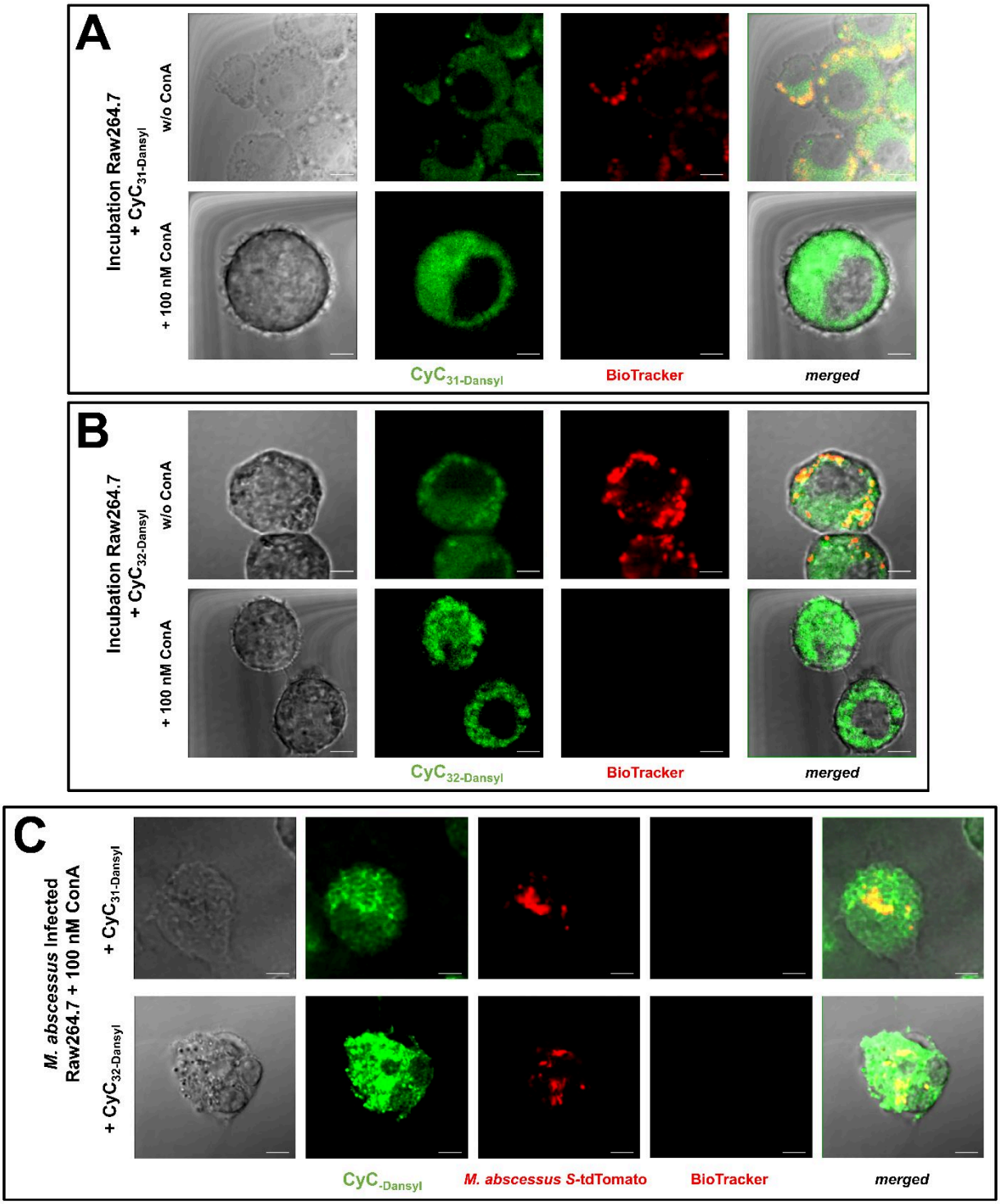

Figure S8. The $CyC_{31/32\text{-}Dansyl}$ do not accumulate mainly in acidic compartments inside Raw264.7 macrophages. Raw264.7 macrophages were preincubated with 100 µM **$CyC_{31\text{-}Dansyl}$ (A)** or **$CyC_{32\text{-}Dansyl}$ (B)** for 24 h in presence or absence of 100 nM Concanamycin A (ConA) prior to be stained with 1X BioTracker™ NIR633 Lysosome Dye (Sigma Aldrich) and processed for confocal fluorescence imaging. Micrographs are representative of 106 to 136 observed cells from two biologically independent experiments. (**C**) **Disruption of endolysosomal acidification impairs $CyC_{\text{-}Dansyl}$ colocalization with *M. abscessus* cells inside infected Raw264.7 macrophages**. *M. abscessus* S-dtTomato infected Raw264.7 macrophages treated with 100 nM Concanamycin A (ConA) were further preincubated with 100 µM **$CyC_{31\text{-}Dansyl}$** or **$CyC_{32\text{-}Dansyl}$** for 24 h prior to be stained with 1X BioTracker™ NIR633 dye and processed for confocal fluorescence imaging. Micrographs are representative of around 120 observed cells from two biologically independent experiments. Scale bars: 5 µm.

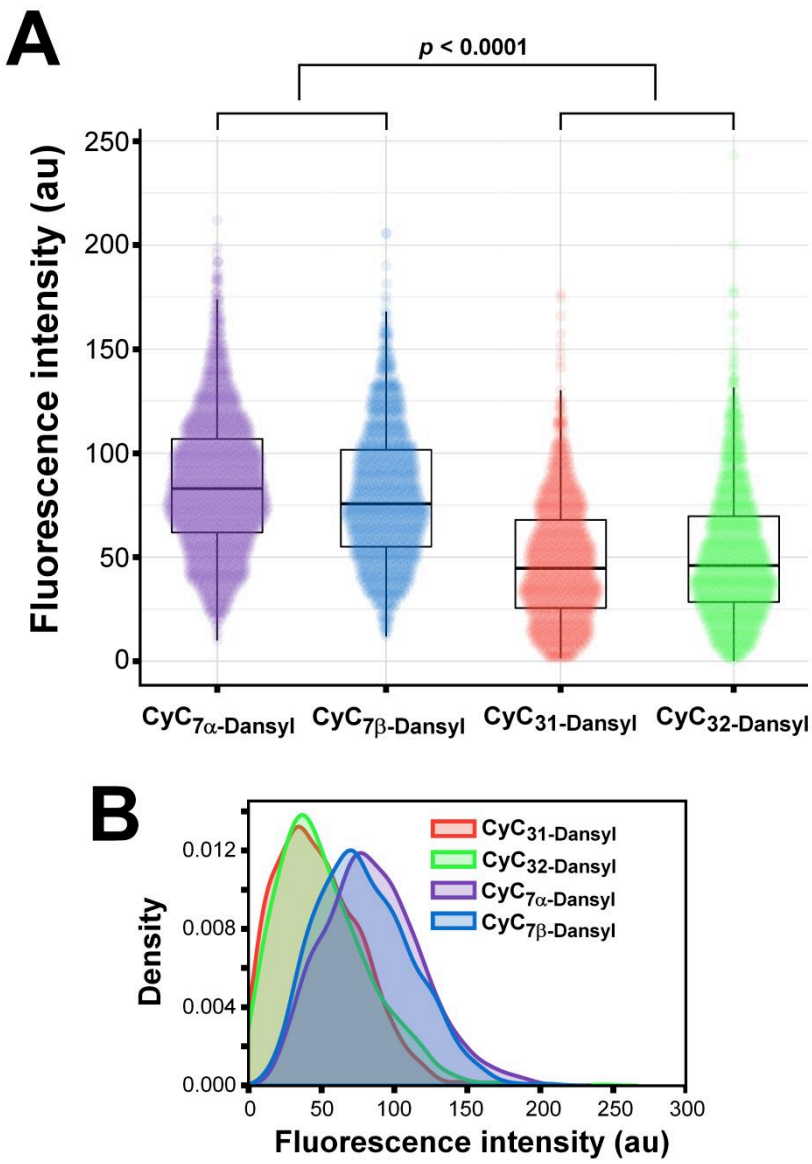

Figure S9. The $CyC_{7(\alpha,\beta)\text{-Dansyl}}$ accumulates in acidic compartments inside Raw264.7 macrophages. Raw264.7 macrophages were incubated with 100 µM **$CyC_{31\text{-Dansyl}}$**, **$CyC_{32\text{-Dansyl}}$**, **$CyC_{7\alpha\text{-Dansy}}$** or **$CyC_{7\beta\text{-Dansyl}}$** for 24 h before being stained with 1X BioTracker™ NIR633 Lysosome Dye (Sigma Aldrich) and processed for confocal fluorescence imaging. Quantitative analysis of the Dansyl fluorescent signal was performed on the BioTracker positive regions for each compound and plotted **(A)** as sinaplot-boxplot and expressed as arbitrary units (au), and **(B)** as density plot. Result are from 106 to 136 observed cells resulting in 1183 to 1955 segmented BioTracker positive regions. The *p*-value was calculated by using a two-tailed *t*-statistic test with Prism 4.0 (Graphpad, Inc).

Article III

Direct capture, inhibition and crystal structure of HsaD (Rv3965c) from *M. tuberculosis*

S. Barelier, **R. Avellan**, G.R. Gnawali, P. Fourquet, V. Roig-Zamboni, I. Poncin, V. Point, Y. Bourne, S. Audebert, L. Camoin, C.D. Spilling, S. Canaan, J.-F. Cavalier, G. Sulzenbacher

FEBS J. 2023, 290(6), 1563-1582
https://doi.org/10.1111/febs.16645

La tuberculose est une maladie causée par *M. tb* qui représente aujourd'hui un problème de santé majeur avec près de 10.6 millions de nouveaux cas et 1.3 millions de morts dans le monde en 2022 [19]. Un des éléments clef de la pathogénie de *M. tb* est sa capacité à survivre dans les macrophages et à s'y reproduire, mais également à utiliser les lipides de l'hôte comme les acides gras et le cholestérol comme source de carbone pour persister au sein des macrophages et du granulome [40, 257, 358, 366].

En effet, au cours d'une infection à *M. tb*, les bactéries sont capables d'hydrolyser les lipides de l'hôte et de les stocker dans leur propre cytoplasme sous forme d'ILI de façon à s'en servir comme source de carbone pour l'entrée en dormance et la réactivation de l'infection [40]. Le catabolisme du cholestérol joue également un rôle important dans les infections à *M. tb* [254, 401] car il sert de source de carbone pour la survie des bactéries dans les macrophages [401, 402]. L'acquisition de lipides et du cholestérol de l'hôte est donc essentielle pour la persistance à long terme des infections à *M. tb* [359, 403].

Les enzymes mycobactériennes impliquées dans le métabolisme des lipides représentent donc des cibles thérapeutiques intéressantes pour la recherche et l'optimisation de nouvelles molécules antituberculeuses. La plupart de ces enzymes appartiennent à la familles des α/β-hydrolases [198] qui possèdent une sérine ou une cystéine catalytique dans leur site actif [404].

Dans ce contexte, la découverte d'inhibiteurs covalents de ces enzymes à sérine ou cystéine catalytique a permis le développement de nouvelle sonde d'ABPP pour les identifier au sein d'un protéome complexe [377]. Notre équipe a précédemment développé une nouvelle famille d'analogues de Cyclophostines et de Cyclipostins (**CyC**) qui sont des inhibiteurs covalents de ces enzymes [330, 338]. Parmi les 38 **CyC** testés, le **CyC$_{17}$** est le meilleur inhibiteur de la croissance extracellulaire de *M. tb* avec une CMI$_{90}$ de 2.6 µM, mais est totalement inactif contre la croissance intracellulaire dans un modèle d'infection de macrophages Raw264.7. Par contre, les **CyC$_{7\beta}$** et **CyC$_{7\beta}$** ont montré une activité contre la croissance intracellulaire de *M. tb* avec respectivement des CMI$_{50}$ de 5.0 et 13.9 µM [330, 336].

Une approche d'ABPP compétitive a déjà été effectuée pour identifier les cibles du **CyC$_{17}$** chez *M. tb* par compétition d'inhibition avec un fluorophosphonate, la Desthiobiotine-FP. Cette approche a permis d'identifier 23 protéines comme cibles potentielles du **CyC$_{17}$**, qui sont

toutes des enzymes à sérine ou cystéine et dont la plupart sont impliquées dans le métabolisme des lipides et du cholestérol [330, 336].

Parmi ces 23 cibles identifiées, on retrouve HsaD (2-hydroxy-6-oxo-6-phenylhexa-2,4-dienoate hydrolase, Rv3569c). Cette protéine est impliquée dans le catabolisme du cholestérol, où elle catalyse la rupture d'une liaison carbone-carbone du produit de métaclivage 4,5-9,10-diseco-3- hydroxy-5,9,17-trioxoandrosta-1(10),2-diene-4-oic acid (4,9-DHSA) [402]. HsaD fait partie d'un ensemble de quatre enzymes clefs dans la dégradation du cycle A/B du cholestérol : HsaA - Rv3567 ; HsaB - Rv3570 ; HsaC - Rv3568 ; et HsaD (**Figure 43**). Des études de mutagenèse par transposon ont de plus montré que HsaD est essentielle pour la survie de *M. tb* dans les macrophages [359, 366].

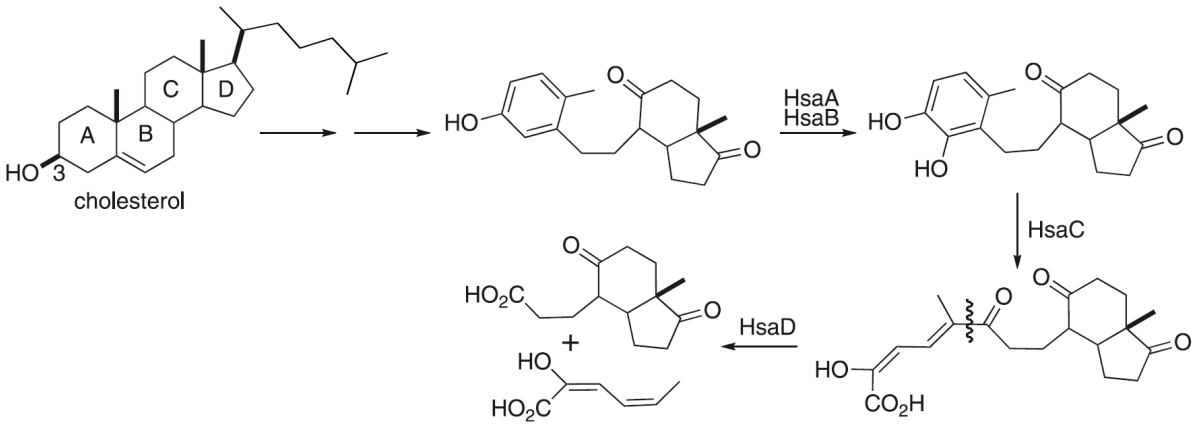

Figure 43. Réactions successives catalysées par HsaA-HsaD dans le catabolisme du cholestérol chez *M. tb*. Adapté de [367]

L'approche d'ABPP compétitive utilisée pour identifier ces cibles avait été effectuée sur un lysat cellulaire [336] ce qui induit un biais dû à l'aspect indirect de la méthode, mais également sur le fait que les cibles identifiées en lysat ne sont pas forcément des cibles effectives en cellule entière.

Dans cette étude nous reportons la synthèse de nouveaux analogues du **CyC$_{17}$** qui contiennent un groupement alcyne terminal afin d'effectuer la capture directe de leurs cibles chez *M. tb* par une approche d'ABPP par chimie-click (CC-ABPP) [360, 376, 405, 406]. Le fait qu'HsaD ait également été identifiée comme cible de ces nouvelles sondes **CyC**-alcyne, et qu'elle représente une cible thérapeutique d'intérêt [368] nous a donc conduit à la valider comme

cible effective de nos composés afin d'établir une preuve de concept de la CC-ABPP avec nos inhibiteurs. Pour ce faire, nous avons produit et purifié de façon recombinante HsaD de *M. tb*, puis réalisé les tests d'inhibition avec différents **CyC**. Les résultats obtenus ont confirmé que HsaD était bien inhibée par nos composés. De plus, l'obtention des structures cristallines de divers complexes **CyC**-HsaD ont clairement démontré le caractère covalent de la liaison entre les **CyC** et la sérine catalytique Ser^{114} de HsaD.

Ce travail a permis de valider la démarche de CC-ABPP avec les sondes **CyC**-alcyne et a ouvert la voie à l'utilisation de nos inhibiteurs en tant que sondes pour identifier de nouvelles cibles thérapeutiques potentielles dans la lutte contre les mycobactéries.

Check for updates

The FEBS Journal

FEBS PRESS science publishing by scientists

Direct capture, inhibition and crystal structure of HsaD (Rv3569c) from *M. tuberculosis*

Sarah Barelier[1], Romain Avellan[2], Giri Raj Gnawali[3], Patrick Fourquet[4], Véronique Roig-Zamboni[1], Isabelle Poncin[2], Vanessa Point[2], Yves Bourne[1], Stéphane Audebert[4], Luc Camoin[4], Christopher D. Spilling[3], Stéphane Canaan[2], Jean-François Cavalier[2] and Gerlind Sulzenbacher[1]

1 CNRS, AFMB, Aix-Marseille University, France
2 CNRS, LISM, IMM FR3479, Aix-Marseille University, France
3 Department of Chemistry and Biochemistry, University of Missouri-St. Louis, MO, USA
4 INSERM, CNRS, Institut Paoli-Calmettes, CRCM, Marseille Protéomique, Aix-Marseille University, France

Keywords
activity-based protein profiling; anti-tuberculous molecules; cholesterol metabolism; Cyclipostins & Cyclophostin; inhibition mechanism

Correspondence
J.-F. Cavalier, CNRS, LISM, IMM FR3479, Aix-Marseille University, Marseille, France
Tel: +33 491164093
E-mail: jfcavalier@imm.cnrs.fr
and
G. Sulzenbacher, CNRS, AFMB, Aix-Marseille University, Marseille, France
Tel: +33 491825566
E-mail: gerlind.sulzenbacher@univ-amu.fr

(Received 25 August 2022, revised 20 September 2022, accepted 4 October 2022)

doi:10.1111/febs.16645

A hallmark of *Mycobacterium tuberculosis* (*M. tb*), the aetiologic agent of tuberculosis, is its ability to metabolise host-derived lipids. However, the enzymes and mechanisms underlying such metabolism are still largely unknown. We previously reported that the Cyclophostin & Cyclipostins (**CyC**) analogues, a new family of potent antimycobacterial molecules, react specifically and covalently with (Ser/Cys)-based enzymes mostly involved in bacterial lipid metabolism. Here, we report the synthesis of new **CyC** alkyne-containing inhibitors (**CyC$_{yne}$**) and their use for the direct fishing of target proteins in *M. tb* culture via bio-orthogonal click-chemistry activity-based protein profiling (CC-ABPP). This approach led to the capture and identification of a variety of enzymes, and many of them involved in lipid or steroid metabolisms. One of the captured enzymes, HsaD (Rv3569c), is required for the survival of *M. tb* within macrophages and is thus a potential therapeutic target. This prompted us to further explore and validate, through a combination of biochemical and structural approaches, the specificity of HsaD inhibition by the **CyC** analogues. We confirmed that the **CyC** bind covalently to the catalytic Ser^{114} residue, leading to a total loss of enzyme activity. These data were supported by the X-ray structures of four HsaD-**CyC** complexes, obtained at resolutions between 1.6 and 2.6 Å. The identification of mycobacterial enzymes directly captured by the **CyC$_{yne}$** probes through CC-ABPP paves the way to better understand and potentially target key players at crucial stages of the bacilli life cycle.

Introduction

Tuberculosis (TB), caused by *Mycobacterium tuberculosis* (*M. tb*), is still one of to the top 10 causes of death worldwide triggered by a bacterial pathogen. In 2020, nearly 1.5 million people died from TB and an additional 9.9 million contracted the disease [1].

A key feature of *M. tb* pathogenesis, as well as other pathogenic mycobacteria, is its ability to survive within macrophages. Numerous studies have highlighted the critical role of host-derived carbon sources, such as fatty acids and/or cholesterol, for *M. tb* to persist and

Abbreviations
ABPP, activity-based protein profiling; au, arbitrary unit; CC-ABPP, click-chemistry ABPP; CyC, Cyclipostins and Cyclophostin analogues; HOPDA, 2-hydroxy-6-oxo-6-phenylhexa-2,4-dienoic acid; ILI, intrabacterial lipid inclusion; INH, isoniazid; MIC_{90}, minimal inhibitory concentration leading to 90% bacterial growth inhibition; REMA, resazurin microtiter assay; RMSD, root-mean-square deviation; TAG, triacylglycerols; TB, tuberculosis; TLC, thin-layer chromatography; x_I, inhibitor molar excess related to 1 mol of enzyme; x_{I50}, inhibitor molar excess leading to 50% enzyme inhibition.

This is an open access article under the terms of the Creative Commons Attribution License, which permits use, distribution and reproduction in any medium, provided the original work is properly cited.

17424658, 2023, 6, Downloaded from https://febs.onlinelibrary.wiley.com/doi/10.1111/febs.16645 by Cochrane France, Wiley Online Library on [16/03/2023]. See the Terms and Conditions (https://onlinelibrary.wiley.com/terms-and-conditions) on Wiley Online Library for rules of use; OA articles are governed by the applicable Creative Commons License

replicate inside macrophages [2–5]. Accordingly, during infection, *M. tb* is able to hydrolyse host lipids, and to store them as triacylglycerols (TAG) in its own cytoplasm as intrabacterial lipid inclusions (ILIs). These ILI will then serve as a source of carbon and energy to sustain bacterial survival [2]. In addition to TAG, cholesterol catabolism also plays a central role in the infection process of *M. tb* [6,7], as cholesterol is used as a carbon source during the survival of the bacillus inside macrophages [5,8].

Collectively, the acquisition of lipids and cholesterol is essential for the long-term survival and persistence of *M. tb* [9,10]. Consequently, the mycobacterial enzymes involved in such metabolisms are considered potential targets for TB drug discovery.

Most of these enzymes belong to the α/β-hydrolase fold superfamily [11], which includes hydrolases, oxidoreductases, transferases, lyases, ligases and isomerases. The hydrolase class covers a wide variety of enzymes, such as esterases, lipases, thioesterases, dienelactone hydrolases, epoxide hydrolases, peptidases, a 2-hydroxy-6-oxo-6-phenylhexa-2,4 dienoate hydrolase and haloalkane dehalogenases [11]. A conserved structural feature of these enzymes is the presence of a catalytic serine or cysteine residue in their active site.

Such (Ser/Cys)-based mycobacterial enzymes represent a promising class of potential therapeutic targets in the fight against TB [12]. Therefore, finding ways to identify, inhibit or control their activity may open the way to new chemotherapeutic developments against mycobacterial infections.

In this context, the discovery of covalent inhibitors has led to the development of a powerful chemoproteomic approach, termed activity-based protein profiling (ABPP), allowing the identification of bacterial (Ser/Cys)-based enzymes in complex proteomes [13].

We previously reported the development of Cyclophostin & Cyclipostins (**CyC**) analogues, a new family of potent antimycobacterial molecules reacting specifically and covalently with (Ser/Cys)-based enzymes [14,15]. Among a set of 38 **CyC** analogues tested against *M. tb*, the Cyclophostin analogues $\mathbf{CyC_{7\beta}}$ and $\mathbf{CyC_{8\beta}}$ as well as the Cyclipostins analog $\mathbf{CyC_{17}}$ displayed potent anti-tubercular activity. Whereas $\mathbf{CyC_{7\beta}}$ exhibited promising activity against both extracellular and intracellular mycobacteria (MIC_{90} of 37.2 and 5.0 μM, respectively), $\mathbf{CyC_{8\beta}}$ was mostly found to be active against intracellular bacteria (MIC_{90} ~ 13.9 μM). Conversely, $\mathbf{CyC_{17}}$ was a potent inhibitor of extracellular growth (MIC_{90} ~ 2.6 μM) with no activity against intracellular bacilli [15,16]. A competitive ABPP approach using $\mathbf{CyC_{17}}$-pretreated *M. tb* lysate and the ActivX™ Desthiobiotin-FP probe led to the identification of 23 distinct proteins as potential targets of this inhibitor, which were all (Ser/Cys)-based enzymes, most of them participating in *M. tb* lipid or cholesterol metabolism and cell wall biosynthesis [15,16]. In particular, HsaD (2-hydroxy-6-oxo-6-phenylhexa-2,4-dienoate hydrolase, Rv3569c) was identified as a potential target of $\mathbf{CyC_{17}}$. This protein catalyses the hydrolytic cleavage of carbon–carbon bonds of the *meta*-cleavage product 4,5-9,10-diseco-3-hydroxy-5,9,17-trioxoandrosta-1(10),2-diene-4-oic acid (4,9-DHSA) in the cholesterol metabolic pathway [8] and is one of the four key enzymes involved in the degradation of the A/B rings of cholesterol (i.e. HsaA, Rv3567; HsaB, Rv3570; HsaC, Rv3568; and HsaD) [8]. Moreover, studies using transposon mutagenesis have shown that HsaD was required for the survival of *M. tb* within macrophages [3,9].

However, this latter competitive ABPP approach for target identification in cell lysates [16] presented the major disadvantage of being indirect and not applied on living cells, with the risk of identifying proteins present in the lysate but not targeted *in vivo*.

Here, we report the synthesis of two new analogues of $\mathbf{CyC_{17}}$ containing a terminal alkyne function (i.e. $\mathbf{CyC_{yne}}$) and describe their use for the direct capture of target proteins in a living *M. tb* culture using a direct click-chemistry ABPP approach (CC-ABPP) [17–20]. Since HsaD appeared also as a target of these new $\mathbf{CyC_{yne}}$ probes, and given its potential as therapeutic target [21], we further explore and validate, through a combination of biochemical and structural approaches, the specificities of HsaD inhibition by the **CyC** analogues.

Results

Synthesis, antibacterial activity and target enzyme identification via activity-based protein profiling using $\mathbf{CyC_{yne}}$ probes

The monocyclic enol-phosphate $\mathbf{CyC_{31yne}}$ and phosphonate $\mathbf{CyC_{32yne}}$ probes were prepared using the transesterification protocol, as previously published [22]. The ester exchange reaction process with the monocyclic phosphate $\mathbf{CyC_{16}}$ [15,23] or phosphonate $\mathbf{CyC_4}$ [15,22] methyl ester was achieved in the presence of excess of 11-bromoundec-1-yne **1** [24] and TBAI in refluxing toluene or 1,4-dioxane to give the corresponding alkynyl phosphate $\mathbf{CyC_{31yne}}$ or phosphonate $\mathbf{CyC_{32yne}}$ derivative in 43–44% yields (Fig. 1A). The corresponding alkyl parent molecules, $\mathbf{CyC_{31}}$ and $\mathbf{CyC_{32}}$, were obtained from similar reaction with 1-bromoundecane in 38–42% yields.

17424658, 2023, 6, Downloaded from https://febs.onlinelibrary.wiley.com/doi/10.1111/febs.16645 by Cochrane France, Wiley Online Library on [16/03/2023]. See the Terms and Conditions (https://onlinelibrary.wiley.com/terms-and-conditions) on Wiley Online Library for rules of use; OA articles are governed by the applicable Creative Commons License

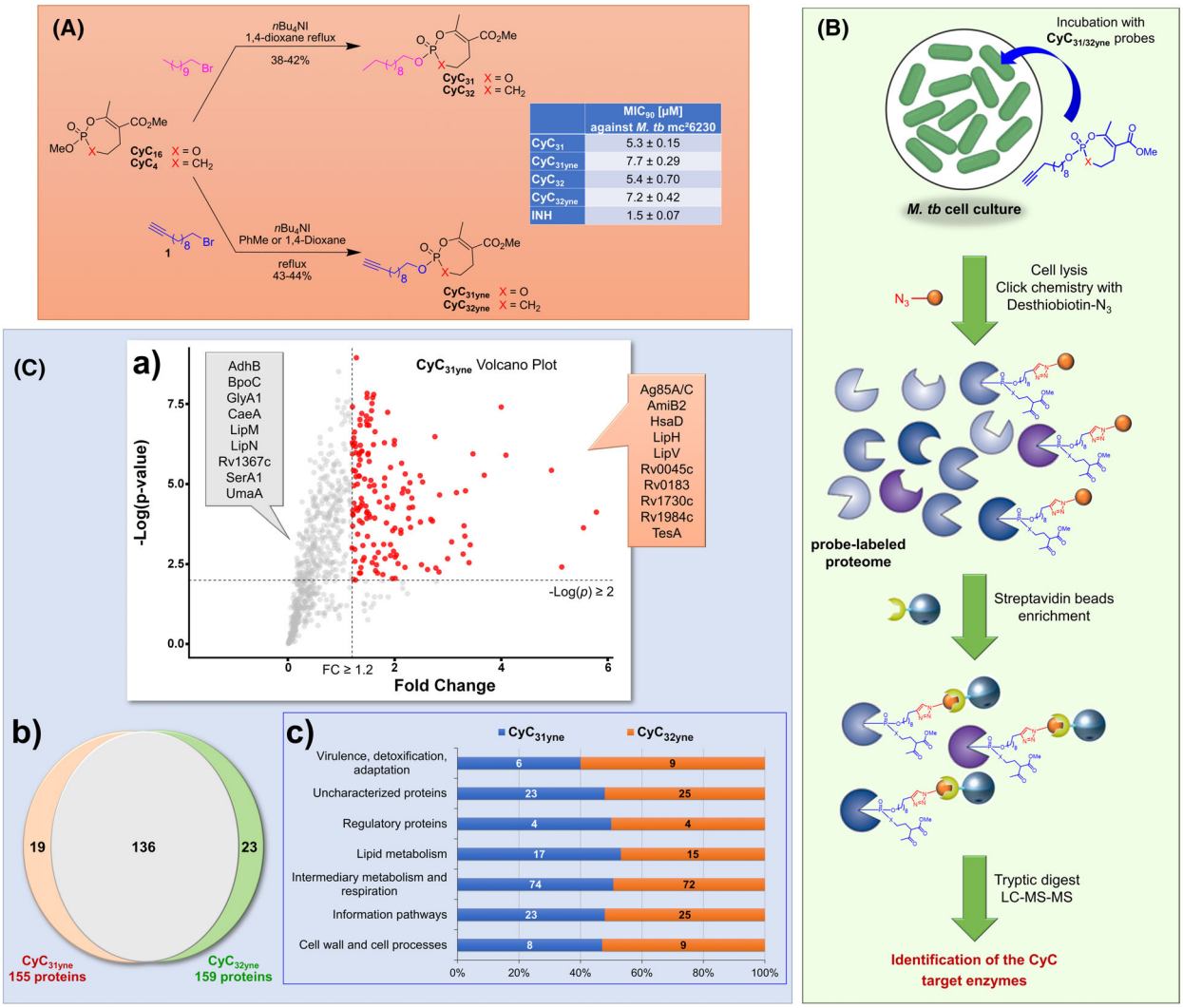

Fig. 1. Click-chemistry activity-based protein profiling on a *M. tb* living culture. (A) Synthesis of the monocyclic phosphate **CyC$_{31}$** and phosphonate **CyC$_{32}$**, as well as the corresponding alkyne derivatives **CyC$_{31yne}$** and **CyC$_{32yne}$**. The inserted table depicts the antibacterial activity of the four **CyC** derivatives against *M. tb* mc^{2}6230 growth in broth medium, reported as MIC$_{90}$. Values are mean of at least two independent assays performed in triplicate. INH, isoniazid used as control drug. (B) Click-chemistry activity-based protein profiling (CC-ABPP) typical workflow for the identification of proteins covalently bound to **CyC$_{yne}$** inhibitors. Exponential growth phase culture of *M. tb* mc^{2}6230 was pre-treated with either **CyC$_{31yne}$** or **CyC$_{32yne}$** prior to cell lysis and subsequent click-reaction with Azide-PEG$_3$-Desthiobiotin reporter. Samples were then treated with streptavidin-agarose beads for the capture and enrichment of labelled proteins, followed by tryptic digestion. Tandem mass spectrometry analyses and subsequent differential peptides analysis allowed the identification of the **CyC** target enzymes. (C) Proteomics analysis of CC-ABPP applied to a *M. tb* mc^{2}6230 culture. (a) Volcano plot of the proteomic analysis of **CyC$_{31yne}$** showing the significance of two-sample *t*-test (−Log(*P*-value)) versus fold-change (Log$_2$(LFQ normalised intensity in **CyC$_{31yne}$** vs. non-specific condition)) on the *y* and *x* axes, respectively. Only proteins identified with a score threshold value ≥ 60 were considered. Here the plot is zoomed on the positive difference between the two conditions. The dashed lines indicate the threshold of *P*-value ≤ 0.01 and a fold-change ≥ 1.2. The two insets show the proteins already identified via competitive ABPP with **CyC$_{17}$** [16]. (b) Venn diagram showing the total number of proteins differentially captured with **CyC$_{31yne}$** and **CyC$_{32yne}$** at a *P*-value ≤ 0.01 and a fold-change ≥ 1.2. (c) Functional categories of *M. tb* proteins identified with **CyC$_{31yne}$** and **CyC$_{32yne}$**, respectively, according to the functional classification system of the Mycobrowser database [65]. The numbers correspond to the total number of identified proteins in each category. Proteins without functional annotation are denoted as uncharacterised proteins.

The antimicrobial potency of the two **CyC$_{yne}$** as compared with **CyC$_{31}$** and **CyC$_{32}$** was evaluated against *M. tb* mc^{2}6230. The minimal inhibitory concentration leading to 90% bacterial growth inhibition (i.e. MIC$_{90}$) was determined by the resazurin microtiter assay (REMA) [16,25,26]. Similar

17424658, 2023, 6, Downloaded from https://febs.onlinelibrary.wiley.com/doi/10.1111/febs.16645 by Cochrane France, Wiley Online Library on [16/03/2023]. See the Terms and Conditions (https://onlinelibrary.wiley.com/terms-and-conditions) on Wiley Online Library for rules of use; OA articles are governed by the applicable Creative Commons License

antibacterial activities against *M. tb* $mc^2$6230 were obtained for each pair, that is **CyC$_{31}$**/**CyC$_{31yne}$** (5.3/7.7 μM) and **CyC$_{32}$**/**CyC$_{32yne}$** (5.4/7.2 μM), respectively (Fig. 1A). Interestingly, **CyC$_{31}$** and **CyC$_{32}$** exhibited MIC_{90} values of the same order of magnitude than that of **CyC$_{17}$** (2.6 μM) against *M. tb* [16,26].

Based on these results, **CyC$_{31yne}$** and **CyC$_{32yne}$** were used as probes in a click-chemistry activity-based protein profiling (CC-ABPP) strategy (Fig. 1B) [27]. Each **CyC$_{yne}$** probe was first incubated with *M. tb* culture followed by cell lysis. Then, subsequent bio-orthogonal click-chemistry reaction led to the formation of a stable triazole cycle between the **CyC$_{yne}$**-enzyme complex and the Desthiobiotin-N_3 via the copper(I)-catalysed Huisgen's 1,3-dipolar cycloaddition reaction [28]. After enrichment on streptavidin agarose-beads, the mixtures were further digested with trypsin. The resulting peptides were analysed by liquid chromatography–tandem mass spectrometry (LC–MS/MS) followed by label-free quantification analysis. The comparative proteomic analysis between a control sample (i.e. DMSO-treated *M. tb* cells for non-specific binding to streptavidin agarose-beads) and **CyC$_{yne}$**-treated samples led to the identification of 155 and 159 target enzymes with **CyC$_{31yne}$** and **CyC$_{32yne}$**, respectively, when applying *P*-value ≤ 0.01 and fold-change ≥ 1.2 thresholds on the proteomics analysis results (Fig. 1C; Tables S1 and S2).

As expected from their closely related chemical structure and the well-known mechanism of action of such enolphosphorus derivatives [14,15], a comparable proteomic profile was obtained with the two **CyC$_{yne}$** probes (Fig. 1C; Tables S1 and S2), as depicted in the venn diagram and the protein functional categorisation (Fig. 1C-b,c; Table S3). Interestingly, while both inhibitors share 139 common targets, 19 and 23 additional specific target enzymes were obtained with **CyC$_{31yne}$** and **CyC$_{32yne}$**, respectively (Fig. 1C-b; Table S3), thereby demonstrating some degree of selectivity between the two **CyC** inhibitors. Noteworthily, as depicted in the Volcano Plot (Fig. 1C-a), 20 of the 23 (Ser/Cys)-based enzymes previously identified with **CyC$_{17}$** in a competitive ABPP approach [16] were also captured by the **CyC$_{31yne}$** probe. Notably, if nine enzymes (AdhB, BpoC, CaeA, GlyA1, LipM, LipN, Rv1367c, SerA1 and UmaA) were found below the 1.2-fold-change threshold, 11 proteins (Ag85A/C, AmiB2, HsaD, LipH, LipV, Rv0045c, Rv0183, Rv1730c, Rv1984c and TesA) were detected above this threshold (Fig. 1C-a). Eighteen of these latter 20 enzymes were also captured by **CyC$_{32yne}$** with a similar distribution using the same 1.2-fold-change threshold. Of interest, the carbon–carbon hydrolase HsaD involved in cholesterol metabolism was only captured by the alkylphosphate inhibitor **CyC$_{31yne}$** and not by its alkylphosphonate counterpart **CyC$_{32yne}$** (Table S3).

The fact that HsaD was found to be essential for intramacrophage survival of *M. tb* [3] and that its overexpression was associated with increased resistance levels to **CyC$_{17}$** [16] prompted us to further investigate its biochemical and structural interactions with **CyC$_{17}$**, the new **CyC$_{31}$** and **CyC$_{32}$**, as well as with two inhibitors of intracellular *M. tb* growth **CyC$_{7β}$** and **CyC$_{8β}$** [16].

Covalent inhibition of the HsaD MCP hydrolase activity

HsaD was previously characterised as a member of the *meta*-cleavage product (MCP) hydrolase class of enzymes that catalyses the hydrolytic cleavage of a carbon–carbon bond through a serine protease-like catalytic triad [29,30]. HsaD was reported to exhibit a high specificity for the steroid 4,9-DHSA within the cholesterol metabolic pathway [8].

To test the hypothesis that the **CyC** analogues inhibit HsaD activity, we first cloned *hsaD* (*rv3569c*) into a pVV16 vector, and the recombinant protein was produced in *Mycobacterium smegmatis*. HsaD was purified to homogeneity by successive nickel affinity and size-exclusion chromatography steps, leading to 5–10 mg of pure recombinant protein per litre of culture. The protein was further concentrated up to 7.5 $mg{\cdot}mL^{-1}$, the highest concentration used for crystallographic experiments. Its purity and the expected molecular weight (~ 33 kDa) were confirmed by 15% SDS/PAGE (Fig. 2A) and global mass spectrometry (Fig. 2D).

To investigate the inhibitory potency of **CyC$_{17}$**, **CyC$_{31}$**, **CyC$_{32}$**, as well as **CyC$_{7β}$** and **CyC$_{8β}$** (Fig. 2B), the purified protein was incubated at room temperature with each inhibitor at various inhibitor molar excess (x_I). The residual enzyme activity was then measured using a MCP hydrolase activity assay with the synthetic substrate 2-hydroxy-6-oxo-6-phenylhexa-2,4-dienoic acid (HOPDA) [30]. The variation in HsaD residual activity allowed determination of the inhibitor molar excess leading to 50% enzyme inhibition, that is x_{I50} value [31,32]. Thereby, a x_{I50} value of 0.5 is synonymous with a 1 : 1 stoichiometric ratio between the inhibitor and the enzyme and is therefore the highest level of inhibitory activity that can be achieved. In good agreement with the CC-ABPP results, **CyC$_{32}$** failed to inhibit HsaD activity even at high molar excess x_I of 80 (i.e. 14.4 ± 0.10% inhibition). On the contrary, a dose-dependent inhibition was observed with all the other four **CyC** compounds (Fig. 2C). In

17424658, 2023, 6, Downloaded from https://febs.onlinelibrary.wiley.com/doi/10.1111/febs.16645 by Cochrane France, Wiley Online Library on [16/03/2023]. See the Terms and Conditions (https://onlinelibrary.wiley.com/terms-and-conditions) on Wiley Online Library for rules of use; OA articles are governed by the applicable Creative Commons License

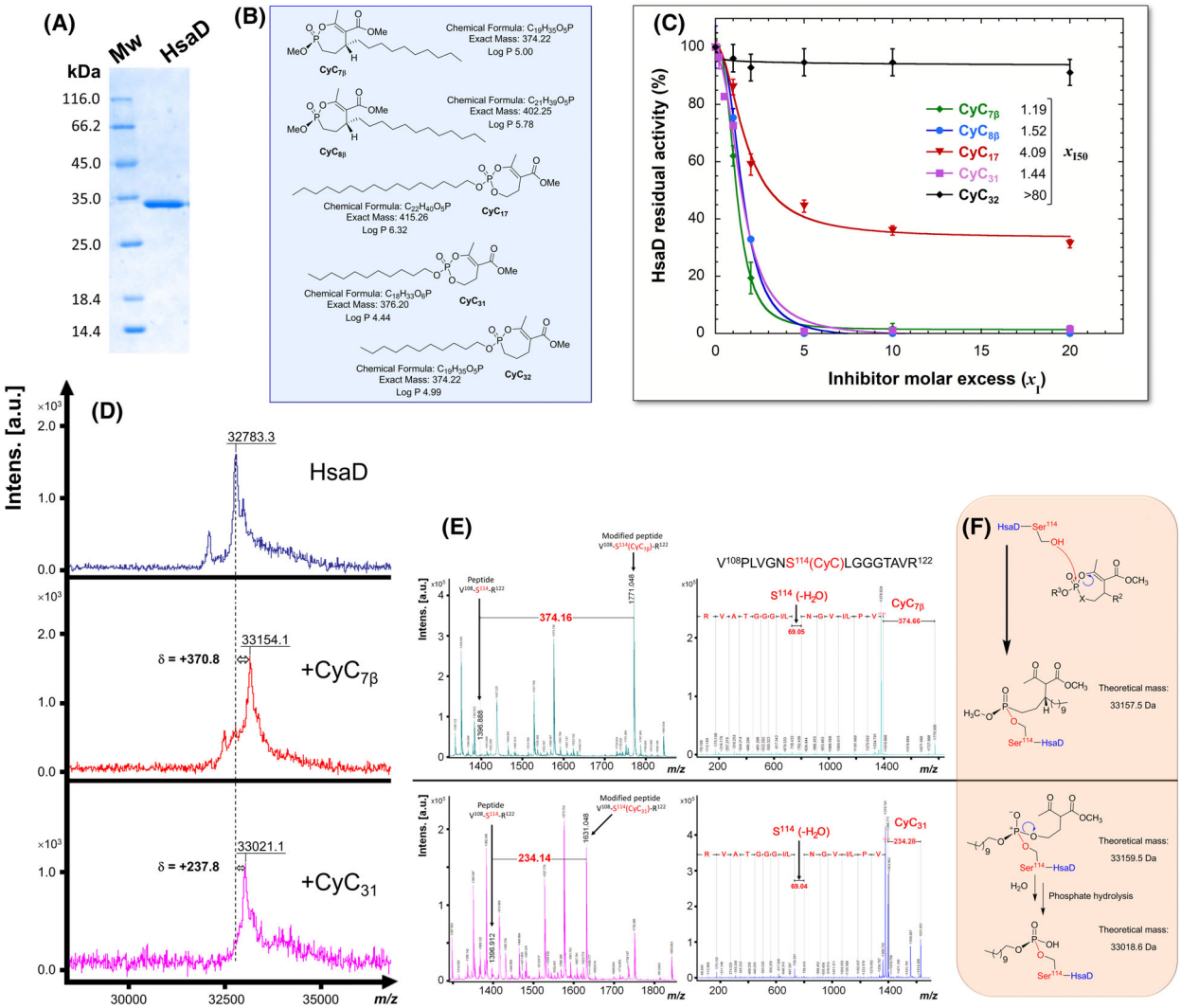

Fig. 2. Covalent binding to HsaD and inhibition by **CyC** compounds. (A) HsaD purification. Mw, standard from Euromedex; purified HsaD, 2.3 μg loaded. (B) Chemical structures of **CyC7β** and **CyC8β**, *cis*-monocyclic enol phosphonate analogues of Cyclophostin, and **CyC17**, **CyC31** and **CyC32**, monocyclic enol phosphate analogues of Cyclipostins. (C) Inhibition of the HsaD MCP hydrolase activity is mediated by the covalent binding of **CyC** analogues. Dose–response curves for **CyC7β**, **CyC8β**, **CyC17**, **CyC31** and **CyC32** showing the decrease in HsaD enzymatic activity on the HOPDA substrate, with the calculated x_{I50} values. (D) Global mass modification of HsaD pre-incubated with **CyC7β** and **CyC31** as determined by MALDI-TOF mass spectrometry. (E) Peptide mass fingerprint (1300–1900 Da zone) of the digested HsaD pre-incubated with **CyC7β** and **CyC31** showing a signal corresponding to the modified catalytic peptide resulting from the covalent binding of each **CyC** to the catalytic Ser^{114} (left panels); and MS/MS spectrum of the modified $V^{108}PLVGNS^{114}LGGGTAVR^{122}$ peptide (right panels). The sequence of each peptide is shown from C-terminal to N-terminal (from left to right) with a gap at the Ser^{114} place corresponding to the remaining serine structure without the hydroxyl moiety (~ 69 Da) and the neutral loss corresponding to **CyC7β** and **CyC31** binding, thus confirming the covalent adduct. (F) Mechanism of HsaD inhibition by the phosphonate **CyC7β** and the phosphate analog **CyC31** based on mass spectrometry analyses. a.u., arbitrary units.

terms of molar excess of inhibitor, the **CyC7β**, **CyC8β** and **CyC31** were 2.7–3.4 times more active towards HsaD than **CyC17**, as judged by their respective x_{150} values of 1.19, 1.52, 1.44 and 4.09, respectively.

Next, we confirmed the covalent nature of the inhibition using MALDI-TOF mass spectrometry. In the presence of **CyC7β** (374.2 Da), a mass increment of +370.8 was observed as compared with the global mass of untreated HsaD (Fig. 2D). Mass spectra of tryptic digestion in the 1300–1900 Da interval further confirmed the covalent binding by highlighting the $V^{108}PLVGNS^{114}LGGGTAVR^{122}$ peptide, which contains the catalytic Ser^{114} in its native ($[M + H]^+$ =1396.888 Da) and modified ($[M + H]^+$ =

17424658, 2023, 6, Downloaded from https://febs.onlinelibrary.wiley.com/doi/10.1111/febs.16645 by Cochrane France, Wiley Online Library on [16/03/2023]. See the Terms and Conditions (https://onlinelibrary.wiley.com/terms-and-conditions) on Wiley Online Library for rules of use; OA articles are governed by the applicable Creative Commons License

1771.089 Da) forms (Fig. 2E). Additionally, MS/MS spectrum of the modified peptide confirmed the specific coupling of **CyC$_{7\beta}$** to the Ser^{114} residue with a gap of ~ 69 Da corresponding to Ser^{114} without the hydroxyl group as well as a neutral loss of around +374.4 Da. These data clearly support the formation of a covalent HsaD-**CyC$_{7\beta}$** complex at the catalytic Ser^{114} (Fig. 2F). Similar results were obtained with **CyC$_{8\beta}$** following tryptic digestion, with a mass difference between the native and modified peptides of +402.23 Da (Fig. 3A). These results are consistent with the known and irreversible mechanism of action of such phosphonate compounds, as previously demonstrated using pure mycobacterial lipolytic enzymes [32–34].

With respect to the phosphate analog **CyC$_{31}$**, the observed +237.8 Da mass shift increment was 138.4 Da lower than its theoretical molecular mass of 376.2 Da (Fig. 2D). Peptide mass fingerprinting of the HsaD-**CyC$_{31}$** adduct followed by the MS/MS analysis of the V^{108}-R^{122} modified peptide (Fig. 2E) confirmed the covalent binding to Ser^{114} as well as the mass difference of around +234.2 Da. Such a difference in mass, also observed with **CyC$_{17}$** (304.2 Da *vs.* 446.28 Da – Fig. 3B), is in agreement with previous studies of the thioesterase TesA and the Antigen 85 complex [33,34]. Here, after phosphorylation of the HsaD-Ser^{114} catalytic serine by **CyC$_{31}$** or **CyC$_{17}$**, further rearrangement of the covalently bound inhibitor occurs, resulting in the loss of the methyl 2-acetyl-4-hydroxybutanoate moiety to reach a stable thermodynamic state (Figs 2F and 3B). In addition, this mechanism is not only perfectly in line with the data generated by the proteomic experiments, but above all, it was further corroborated by the crystal structure of the **CyC$_{31}$**-HsaD complex as outlined below.

Crystal structures of HsaD

The structure of native HsaD was solved at a high resolution (1.96 Å) and is identical to the one described by Lack et al. (PDB: 2VF2) [21,35], with a root-mean-square deviation (RMSD) of 0.317 over 259 alpha carbon atoms; making our HsaD structure the best resolution obtained so far. Crystals of native HsaD belong to space group $P222_1$ with average unit cell axes of 76.8 × 87.4 × 106.2 Å and two molecules per asymmetric unit. The biological assembly is a homotetramer, which can be generated by application of a crystallographic twofold axis. The two monomers present in the asymmetric unit are nearly identical (RMSD 0.248 Å over 266 alpha carbon atoms) and display an α/β-hydrolase fold, which contains the active site made-up by the catalytic triad Ser^{114}, Asp^{241} and His^{269} [30]. Residues 7–290 were built in both chains, while the first six residues as well as the 6×His-tag at the C-terminus were not modelled due to lack of experimental evidence.

Structural studies of HsaD in the presence of **CyC$_{7\beta}$**, **CyC$_{8\beta}$**, **CyC$_{17}$** and **CyC$_{31}$** led to well-defined structures of enzyme-inhibitor complexes with very high resolutions in the 1.62–2.20 Å range. Crystals of HsaD in complex with **CyC$_{8\beta}$**, **CyC$_{17}$** and **CyC$_{31}$** belong to the same space group as native HsaD with similar unit cell axes and two molecules per asymmetric unit. By contrast, crystals of HsaD in complex with **CyC$_{7\beta}$** belong to space group $P2_12_12$ with unit cell axes of 76.9 × 78.4 × 92 Å. Data collection and refinement statistics for all structures are shown in Table 1.

The crystal structures of each complex were compared with that of native HsaD. No major conformational changes induced by inhibitor-binding could be observed (overall RMSD with respect to native HsaD of 0.09–0.12 Å for **CyC$_{8\beta}$**, **CyC$_{17}$** and **CyC$_{31}$**, and 0.47 Å for **CyC$_{7\beta}$**, which belongs to a different space group) (Fig. 4A). The three catalytic residues Ser^{114}, Asp^{241} and His^{269} adopt the same conformations in all complexes (Fig. 4B). The main differences are observed at the level of the side-chains of Asn^{54}, Asn^{113}, Leu^{158} and Met^{177} that are within close proximity of the catalytic serine Ser^{114}. Additionally, the large movement of Met^{177} in the HsaD-**CyC$_{7\beta}$** complex induces a cascade of conformational changes which pushes away the oppositely lying side-chains of Ser^{56} and Arg^{57} and leads to the fusion of two short helices into a single, bent helix (Fig. 4C). However, these differences, which are not caused by crystal packing artefacts, do not affect the overall structure of the active site of HsaD.

Covalent binding of all **CyC** compounds to Ser^{114} was confirmed by careful examination of the electron density around Ser^{114}. In all four complexes, electron density for the phosphate group covalently linked to Ser^{114} was clearly visible in both chain A and chain B.

Clear electron density can be seen for nearly the entire structure of the Cyclophostin analog **CyC$_{7\beta}$** in both monomers, although the end of the alkyl chain cannot be modelled with certainty (Fig. 5A). The observed electron density agrees with ring aperture, confirming that the compound has reacted with Ser^{114} (Fig. 2F). The observed distance of about 1.5 Å between the phosphorus atom of **CyC$_{7\beta}$** and the side-chain oxygen of Ser^{114} clearly attests that in the crystal, the ligand is covalently bound. The phosphonate group of **CyC$_{7\beta}$** forms hydrogen-bonds with the backbone atoms of Gly^{45} and Leu^{115}, and with the side-chain of His^{269}, which in turn is stabilised via hydrogen-bonding to Asp^{241} (Fig. 5B–D). The rest of the molecule forms few interactions with

17424658, 2023, 6, Downloaded from https://febs.onlinelibrary.wiley.com/doi/10.1111/febs.16645 by Cochrane France, Wiley Online Library on [16/03/2023]. See the Terms and Conditions (https://onlinelibrary.wiley.com/terms-and-conditions) on Wiley Online Library for rules of use; OA articles are governed by the applicable Creative Commons License

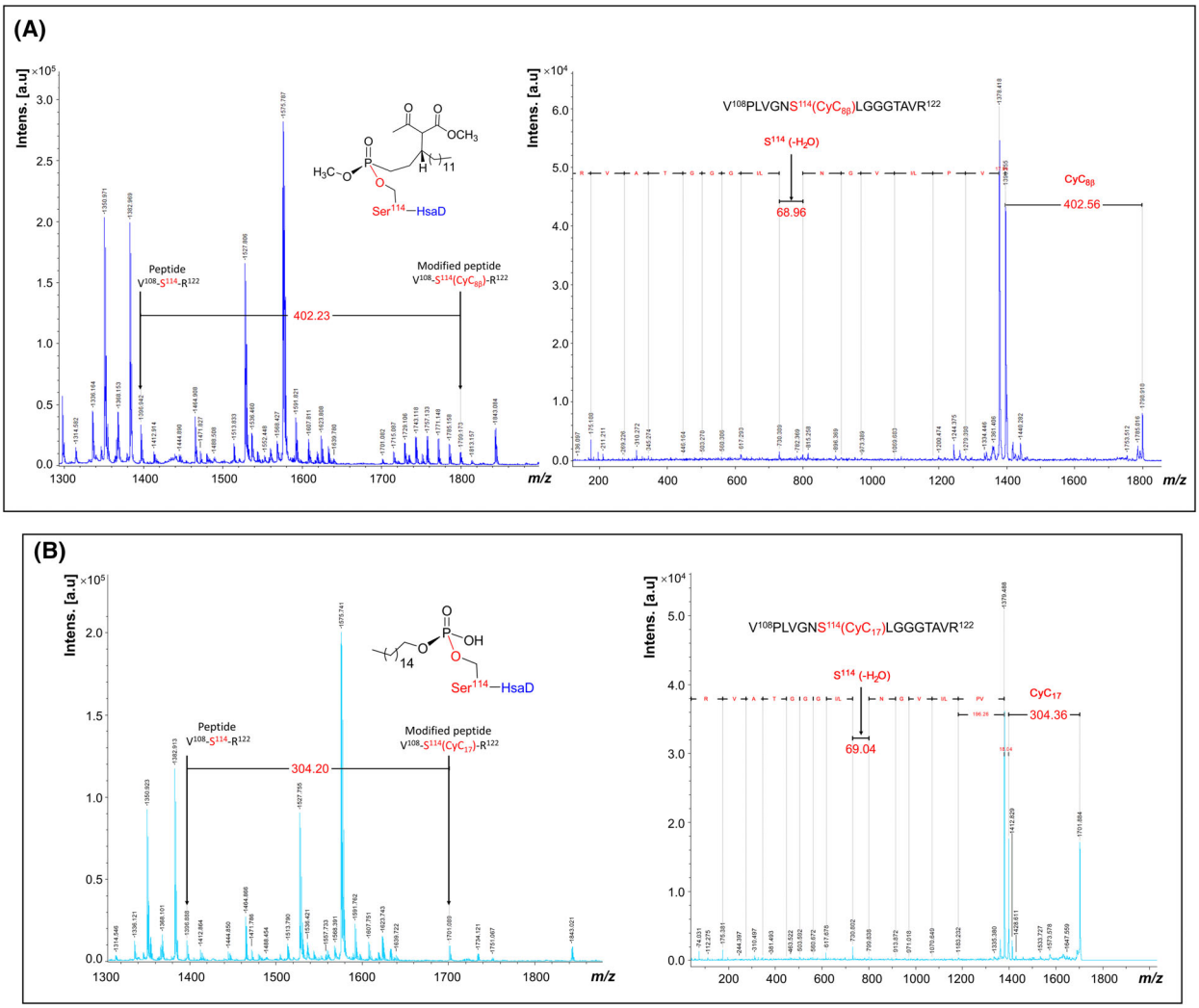

Fig. 3. Peptide mass fingerprint (1300–1900 Da zone) of the digested HsaD pre-incubated with (A) **CyC$_{8\beta}$** and (B) **CyC$_{17}$** showing a signal corresponding to the modified catalytic peptide resulting from the covalent binding of each **CyC** to the catalytic Ser^{114} (left panels); and MS/MS spectrum of the modified V^{108}PLVGNS^{114}LGGGTAVR^{122} peptide (right panels). The sequence of each peptide is shown from C-terminal to N-terminal (from left to right) with a gap at the Ser^{114} place corresponding to the remaining serine structure without the hydroxyl moiety (~ 69 Da) and the neutral loss corresponding to **CyC$_{8\beta}$** and **CyC$_{17}$** binding, thus confirming the covalent adduct.

the enzyme, except for a hydrogen bond between a carbonyl of **CyC$_{7\beta}$** and the backbone of Gly^{141}. The long aliphatic chain of **CyC$_{7\beta}$** is stabilised by hydrophobic interactions involving in particular the side-chains of Leu^{158}, Met^{208} and Phe^{212}.

For **CyC$_{8\beta}$**, which differs from **CyC$_{7\beta}$** only by two extra carbon atoms, only the covalent phosphonate head with its methoxy group was modelled, as the observed electron density was incomplete. The position of the phosphonate confirms the covalent nature of the [Ser^{114}-Oγ/P] bond (1.6 Å) and is compatible with a binding comparable to that of **CyC$_{7\beta}$**. Interactions similar to the HsaD-**CyC$_{7\beta}$** complex are observed between the phosphonate head of the compound and the active site residues. Finally, crystals of the HsaD-**CyC$_{8\beta}$** complex that were resolubilised and subjected to mass spectrometry analysis, show a shift corresponding to **CyC$_{8\beta}$** molecular weight (+402.23 Da – Fig. 3A), indicating that the compound is present in full-length within the crystal, even though it was not observed entirely in the electron density, possibly due to radiation damage or conformational flexibility.

Regarding the Cyclipostins analog **CyC$_{17}$**, again the electron density does not allow confident placement of the entire compound in the electron density and only the phosphate head covalently bound to Ser^{114} was

17424658, 2023, 6, Downloaded from https://febs.onlinelibrary.wiley.com/doi/10.1111/febs.16645 by Cochrane France, Wiley Online Library on [16/03/2023]. See the Terms and Conditions (https://onlinelibrary.wiley.com/terms-and-conditions) on Wiley Online Library for rules of use; OA articles are governed by the applicable Creative Commons License

Table 1. Data collection and refinement statistics (molecular replacement). Values in parentheses are for the highest-resolution shell.

	Native HsaD	HsaD-**CyC$_{7\beta}$**	HsaD-**CyC$_{8\beta}$**	HsaD-**CyC$_{17}$**	HsaD-**CyC$_{31}$**
Data collection					
Space group	$P222_1$	$P2_12_12$	$P222_1$	$P222_1$	$P222_1$
Cell dimensions *a*, *b*, *c* (Å)	76.8, 87.4, 106.2	76.9, 78.4, 92.0	76.8, 87.2, 105.9	77.0, 87.4, 106.1	76.7, 87.2, 105.6
Resolution (Å)	45.38–1.96 (2.01–1.96)	47.14–2.15 (2.22–2.15)	45.26–2.20 (2.27–2.20)	45.36–1.81 (1.85–1.81)	45.21–1.62 (1.64–1.62)
No. reflections	51 930 (3434)	30 915 (2594)	36 843 (3132)	66 020 (3704)	91 211 (4202)
R_{merge}	0.148 (1.165)	0.158 (0.996)	0.157 (1.349)	0.118 (1.390)	0.081 (1.466)
R_{pim}	0.047 (0.378)	0.058 (0.373)	0.048 (0.413)	0.033 (0.404)	0.023 (0.424)
CC (1/2)	0.998 (0.653)	0.996 (0.769)	0.998 (0.696)	0.999 (0.638)	0.999 (0.738)
I/σ_I	13.8 (2.1)	11.7 (2.4)	12.4 (2.4)	16.5 (2.0)	17.2 (1.9)
Completeness (%)	99.6 (94.4)	99.8 (98.5)	100.0 (99.8)	99.8 (96.0)	99.7 (94.7)
Multiplicity	10.5 (9.9)	8.1 (7.8)	11.4 (11.4)	13.4 (12.4)	13.5 (12.3)
Wilson B (Å^2)	14.8	17.4	30.4	19.1	19.6
Refinement					
R_{work} (%)	18.31	18.14	17.54	18.23	18.36
R_{free} (%)	21.89	21.18	22.36	21.32	20.22
No. atoms					
Protein	4388	4388	4388	4388	4388
Ligand/ions	11	75	35	20	35
Water	293	125	108	336	377
R.m.s. deviations					
Bond lengths (Å)	0.0099	0.0133	0.0139	0.0087	0.0067
Bond angles (°)	1.5555	1.7584	1.8079	1.5172	1.3682
Ramachandran					
Favoured (%)	96.99	95.74	96.45	97.87	98.05
Outliers (%)	0	0	0	0	0
PDB code	7ZJT	7ZM1	7ZM2	7ZM3	7ZM4

modelled ([Ser^{114}-Oγ/P] distance ~ 1.5 Å). Finally, in the HsaD-**CyC$_{31}$** complex, the crystal structure confirmed the mass spectrometry data (Fig. 2D–F). Indeed, the inhibitor, whose aliphatic chain contains five carbon atoms less than **CyC$_{17}$**, has lost its β-ketoester moiety. The hydrolysed molecule is clearly visible in the electron density (Fig. 5A), and covalent binding is confirmed ([Ser^{114}-Oγ/P] distance ~ 1.5 Å). Here, the phosphate head hydrogen-bonds with the backbones of Gly^{45} and Leu^{115}, with the side-chain of His^{269}, itself stabilised by Asp^{241} and with two water molecules. The long aliphatic chain is stabilised by hydrophobic interaction with the side-chains of Leu^{158}, Met^{208} and Phe^{212} (Fig. 5B–D).

Overall, the binding modes are highly similar between the Cyclophostin analog **CyC$_{7\beta}$** and the Cyclipostins analog **CyC$_{31}$**, involving the same active site residues.

In silico molecular docking study

In order to better understand the absence of inhibitory activity of **CyC$_{32}$** at the molecular level, complementary *in silico* molecular docking experiments were conducted as described previously [16,32] using our HsaD-**CyC$_{31}$** crystal structure (PDB ID: 7ZM4) as receptor (Fig. 6). Docking runs were performed using the AUTODOCK VINA program [36] after removing the bound **CyC$_{31}$** and replacing the catalytic Ser^{114} by a glycine residue in order to enable the docked inhibitor to adopt a suitable position corresponding to the pre-bound intermediate before the nucleophilic attack in the active site [16,32].

For **CyC$_{32}$**, the best scoring position obtained (i.e. lowest energy complex) places this compound at the entrance of the active site cleft, with a predicted binding energy value $\Delta E_{\mathbf{CyC_{32}}} = -7.3$ kcal·mol^{-1} (Fig. 6A). In this nonproductive orientation, the phosphorus atom of the docked **CyC$_{32}$** would indeed be found in an opposite and unfavourable position at a 9.5 Å distance from the catalytic Ser^{114}, thus excluding the occurrence of any covalent interaction (Fig. 6B). By contrast, the same *in silico* docking experiment performed with **CyC$_{31}$** resulted in a best scoring position showing the reactive phosphorus atom at a 1.6 Å distance from the catalytic Ser^{114}, therefore facilitating the formation of a covalent bond, with a predicted

17424658, 2023, 6, Downloaded from https://febs.onlinelibrary.wiley.com/doi/10.1111/febs.16645 by Cochrane France, Wiley Online Library on [16/03/2023]. See the Terms and Conditions (https://onlinelibrary.wiley.com/terms-and-conditions) on Wiley Online Library for rules of use; OA articles are governed by the applicable Creative Commons License

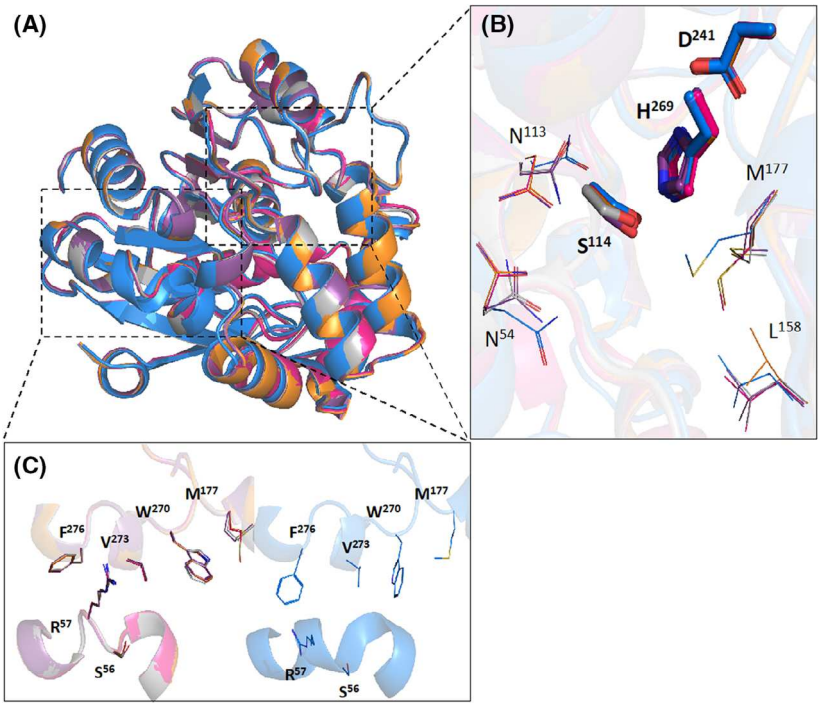

Fig. 4. Comparison of native HsaD and HsaD-**CyC** crystal structures. (A) Superposition of the crystal structures of native HsaD and HsaD in complex with the different **CyC** compounds. Native HsaD is in light grey cartoon, HsaD in complex with $\mathbf{CyC_{7\beta}}$, $\mathbf{CyC_{8\beta}}$, $\mathbf{CyC_{17}}$ and $\mathbf{CyC_{31}}$ are in blue, purple, orange and pink, respectively. For clarity, the coordinates of the **CyC** compounds have been omitted. (B) Close up view of the HsaD active site. The catalytic residues Ser^{114}, Asp^{241} and His^{269} are shown as sticks, the active site residues displaying conformational changes are shown as lines. (C) Close up view comparing the superposed structures of native HsaD, HsaD-$\mathbf{CyC_{8\beta}}$, HsaD-$\mathbf{CyC_{17}}$, and HsaD-$\mathbf{CyC_{31}}$ (left) as well as the structure of HsaD-$\mathbf{CyC_{7\beta}}$ (right), showing the fusion of two helices into one in the latter complex. Structures were drawn with PYMOL molecular graphics system (version 2; Schrödinger, LLC).

binding energy value $\Delta E_{\mathbf{CyC_{31}}docked} = -7.8$ kcal·mol^{-1} (Fig. 6B). Comparison of this generated $\mathbf{CyC_{31}}docked$ top ranked docking pose with the binding geometry observed in the HsaD-$\mathbf{CyC_{31}}$ crystal structure revealed of 0.7 Å deviation between the two reactive phosphorus atoms (Fig. 6C). This redocking/cross-docking experiment thus confirms the validity and reliability of our computational approach. In addition, using a similar *in silico* approach with the reported crystal structure of HsaD bound to 3,5-dichloro-4-hydroxybenzoic acid (PDB: 5JZS – 2.27 Å resolution [21]), we had previously demonstrated that $\mathbf{CyC_{17}}$ adopted a productive orientation close to the catalytic Ser^{114} ($\Delta E_{\mathbf{CyC17}} = -7.4$ kcal·mol^{-1}; [Ser^{114}-Oγ/P] distance ~ 2.3 Å) [16]. A good level of concordance was also observed between the favourable docked conformation of $\mathbf{CyC_{17}}$ and the 3D structure of the covalently bound $\mathbf{CyC_{31}}$-Ser^{114} in HsaD active site (Fig. 6D).

Overall, such *in silico* molecular docking results not only corroborate our experimental biochemical data but also provide some clues that may explain the absence of inhibitory activity of $\mathbf{CyC_{32}}$ towards HsaD.

Discussion

Compounds that specifically target mycobacterial (Ser/Cys)-based enzymes represent novel and promising antibacterial agents, offering supplementary therapeutic options [15,20,37]. In this regard, we have shown that Cyclophostin & Cyclipostins analogues (**CyC**) are potent antimycobacterial multitarget compounds leading to the arrest of *M. tb* growth either in broth medium or inside infected macrophages, by impairing simultaneously the activity of various (Ser/Cys)-based enzymes participating in important physiological processes related to lipid metabolism [15]. More specifically, the physiological processes related to host-lipid metabolism (cholesterol and fatty acids) are critical to the *M. tb* infectious life cycle for propagation of the infection, establishment of the dormancy state and reactivation of the disease [2,38]. Therefore, finding ways to identify and inhibit the enzymes involved in such metabolic processes in *M. tb* would open new opportunities to treat TB.

To address this vital issue, we synthesised novel **CyC** alkyne-containing inhibitors (i.e. $\mathbf{CyC_{yne}}$), analogous of the best $\mathbf{CyC_{17}}$ extracellular growth inhibitor [15]. We showed that these new activity-based probes represent very powerful and highly valuable tools to identify mycobacterial (Ser/Cys)-based enzyme by fishing them directly from a living *M. tb* culture. Our endeavour was comforted by the fact that both phosphate $\mathbf{CyC_{31yne}}$ and phosphonate $\mathbf{CyC_{32yne}}$ analogues share 136 common targets. Notably, most of the 23 (Ser/Cys)-based enzymes previously identified through competitive ABPP with $\mathbf{CyC_{17}}$ and the ActivX™ Desthiobiotin-FP probe [16] were also captured, confirming the robustness of this bio-orthogonal click-chemistry ABPP direct approach. Such a result was,

17424658, 2023, 6, Downloaded from https://febs.onlinelibrary.wiley.com/doi/10.1111/febs.16645 by Cochrane France, Wiley Online Library on [16/03/2023]. See the Terms and Conditions (https://onlinelibrary.wiley.com/terms-and-conditions) on Wiley Online Library for rules of use; OA articles are governed by the applicable Creative Commons License

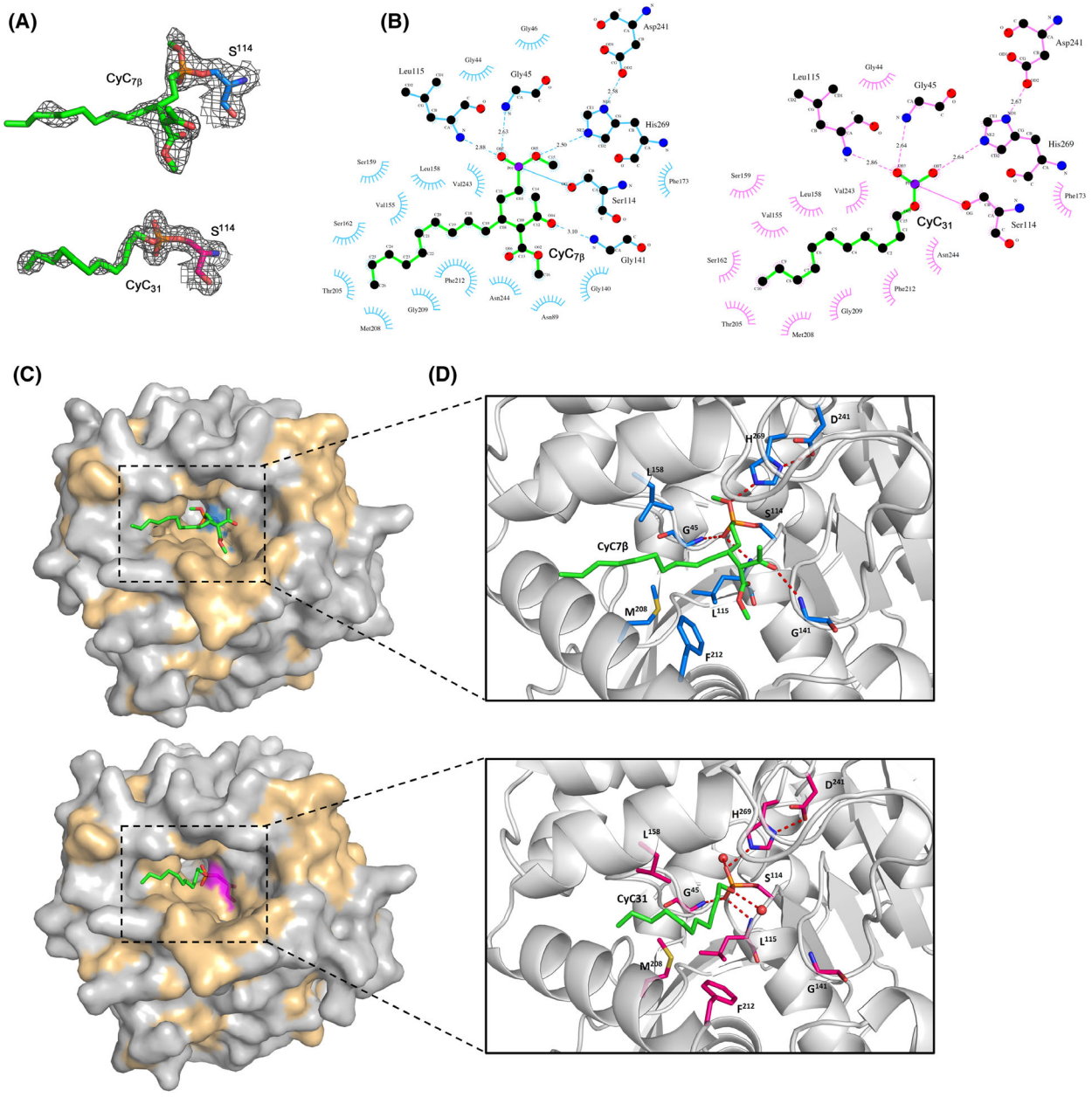

Fig. 5. Structural characterisation of HsaD-**CyC** complexes. (A) 2Fo-Fc electron density maps for two HsaD-**CyC** complexes. Ligands are depicted with green sticks and the catalytic Ser^{114} with blue and pink sticks for the HsaD-$\mathbf{CyC_{7\beta}}$ and HsaD-$\mathbf{CyC_{31}}$ complexes, respectively. Density maps are contoured at 1σ level. (B) LIGPLOT+ representation of the HsaD-$\mathbf{CyC_{7\beta}}$ (left) and HsaD-$\mathbf{CyC_{31}}$ (right) complexes. Hydrogen-bonds, hydrophobic interactions and the covalent Ser^{114}-**CyC** bond are shown. (C) X-ray structures of **CyC** compounds bound to HsaD. $\mathbf{CyC_{7\beta}}$ (top), $\mathbf{CyC_{31}}$ (bottom) and the catalytic Ser^{114} are shown as sticks, the protein surface is coloured in grey with hydrophobic residues highlighted in pale orange. (D) Close-up view of HsaD active site containing the bound inhibitors. $\mathbf{CyC_{7\beta}}$ (top), $\mathbf{CyC_{31}}$ (bottom) and the main active site residues are shown as sticks. Red dashes represent hydrogen-bonds, water molecules are represented by red spheres. Structures were drawn with PYMOL Molecular Graphics System (version 2; Schrödinger, LLC).

however, expected due to the very close chemical structure with similar hydrophobic properties (i.e. mean Log $P = 4.72 \pm 0.28$ – Fig. 2B), and identical mechanism of inhibition of $\mathbf{CyC_{31yne}}$ and $\mathbf{CyC_{32yne}}$. Nevertheless, a set of 19 and 23 specific targets for $\mathbf{CyC_{31yne}}$ and $\mathbf{CyC_{32yne}}$, respectively, were also obtained (Fig. 1A). The fact that some enzymes were captured with one $\mathbf{CyC_{yne}}$ and not the other will be

17424658, 2023, 6, Downloaded from https://febs.onlinelibrary.wiley.com/doi/10.1111/febs.16645 by Cochrane France, Wiley Online Library on [16/03/2023]. See the Terms and Conditions (https://onlinelibrary.wiley.com/terms-and-conditions) on Wiley Online Library for rules of use; OA articles are governed by the applicable Creative Commons License

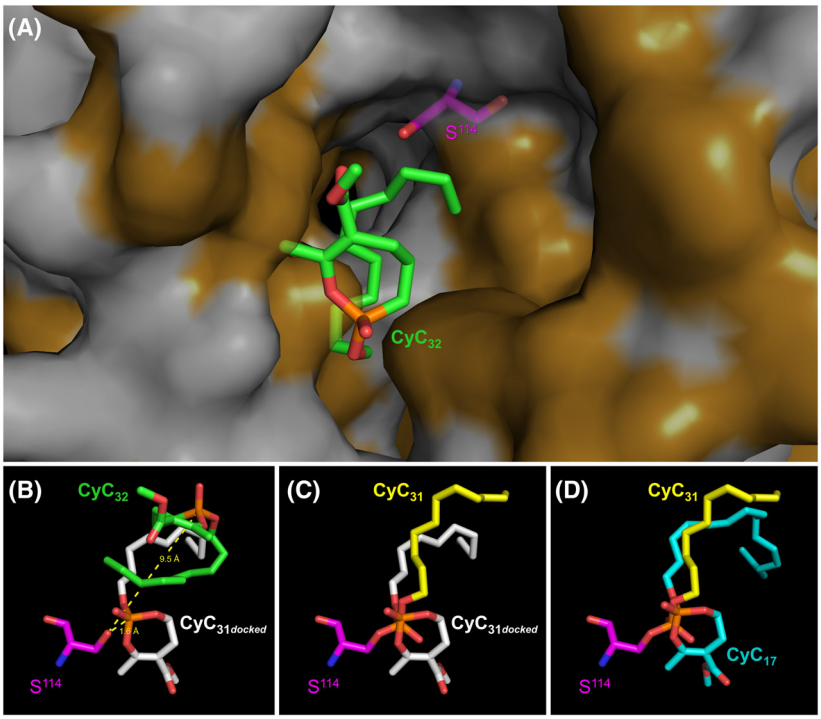

Fig. 6. *In silico* molecular docking experiments. (A) Top-scoring docking position of **CyC$_{32}$** (green) with the crystal structure of HsaD in van der Waals surface representation. Hydrophobic residues are highlighted in bright orange. (B) Distances between the catalytic Ser^{114}-Oγ residue and the **CyC** reactive phosphorus atom. The distances were calculated from the top-scoring docking positions of **CyC$_{32}$** (green) and **CyC$_{31docked}$** (white). **(**C, D**)** Top-scoring docking position of **CyC$_{31docked}$** and **CyC$_{17}$**. Superimposition of the top-scoring docking position of **CyC$_{31docked}$** (white – **C**) and **CyC$_{17}$** [16] (cyan – **D**) with the crystal structure of S^{114}-**CyC$_{31}$** (yellow). Each inhibitor is in stick representation with the following atom colour-code: oxygen, red; phosphorus, orange; carbon, green, white, yellow or cyan. The catalytic Ser^{114} residue is coloured in magenta. Structures were drawn with PYMOL Molecular Graphics System (version 1.4; Schrödinger, LLC) using the PDB file 7ZM4.

due to the chemical properties of the phosphate *vs.* phosphonate chemical groups, thus emphasizing some selective inhibitory activity.

Among the **CyC** target enzymes, HsaD (Rv3569c) which is involved in the cholesterol metabolism pathway [8] and is also essential for *M. tb* survival inside macrophages [3,9], was specifically captured, first by **CyC$_{17}$** [16], and here by **CyC$_{31yne}$**, but not by **CyC$_{32yne}$**. This guided our biochemical and structural research effort to investigate the interactions of HsaD with the Cyclipostins analogues **CyC$_{17}$**, **CyC$_{31}$** and **CyC$_{32}$**, as well as with the Cyclophostin analogues **CyC$_{7β}$** and **CyC$_{8β}$** that previously showed promising activity against intracellular mycobacteria [16].

Here, a combination of complementary and orthogonal approaches provides a clear overview of the interactions between HsaD and the five **CyC** compounds. We demonstrated that HsaD is not inhibited by **CyC$_{32}$** (Fig. 2C) and provided clues that this lack of inhibition may result from a nonproductive binding of the enolphosphorus core of **CyC$_{32}$** located at the entrance of the active site crevice, opposite Ser^{114} (Fig. 6A,B). Such positioning would thus prevent any reaction with the catalytic serine, in agreement with the CC-ABPP experiment (Fig. 1). By contrast, biochemical and mass spectrometry experiments have confirmed the covalent binding of the two Cyclipostins analogues **CyC$_{17}$** and **CyC$_{31}$**, but also of the Cyclophostin analogues **CyC$_{7β}$** and **CyC$_{8β}$** to the catalytic Ser^{114}, leading to full inhibition of HsaD enzymatic activity (Fig. 2). The observation of *in vitro* inhibition of HsaD by **CyC$_{7β}$** and **CyC$_{8β}$** strengthens our previous findings pointing towards *M. tb* bacterial clearance from infected macrophages, as observed in *ex vivo* experiments in the presence of these two inhibitors [16]. Indeed, it is tempting to consider that intracellular *M. tb* growth inhibition may result at least in part from the inactivation of this enzyme, which is essential for intramacrophagic bacterial survival [3].

Moreover, all data (dose response curves, global mass modification and peptide mass fingerprint on the digested HsaD-**CyC** adducts, as well as the corresponding crystal structures) converge to the same mechanism of covalent inhibition through phosphorylation of the catalytic Ser^{114}, thereby abolishing HsaD enzymatic activity. Remarkably, and as previously observed in the inhibited Ag85C-**CyC$_{17}$** and TesA-**CyC$_{17}$** complexes [33,34], after phosphorylation of the serine by **CyC$_{17}$** or **CyC$_{31}$**, the two phosphates undergo a partial hydrolysis resulting in rearrangement of the inner structure of the bound inhibitors and the release of their methyl 2-acetyl 4-hydroxybutyrate group. Such chemical modification can undoubtedly be considered as the signature of the reactivity of these Cyclipostins phosphate analogues with (Ser/Cys)-based enzymes.

Finally, in this study, a click-chemistry ABPP approach using newly synthesised **CyC$_{yne}$** probes has

17424658, 2023, 6, Downloaded from https://febs.onlinelibrary.wiley.com/doi/10.1111/febs.16645 by Cochrane France, Wiley Online Library on [16/03/2023]. See the Terms and Conditions (https://onlinelibrary.wiley.com/terms-and-conditions) on Wiley Online Library for rules of use; OA articles are governed by the applicable Creative Commons License

allowed the direct capture of enzymes playing a crucial role in lipid or steroid metabolism in *M. tb* life cycle. The structural results also underline the potency and the added value of using the **CyC$_{yne}$** probes to identify, via activity-based profiling approaches, novel targets to fight TB infection.

Overall, our results confirm that the **CyC** inhibitors are multitarget compounds leading to the inhibition of *M. tb* growth through the inhibition of various mycobacterial (Ser/Cys)-based enzymes involved in important physiological processes. Moreover, given their nontoxicity towards mammalian cells at concentrations up to 100 μM [16], the **CyC$_{yne}$** activity-based probes represent useful tools to better understand the metabolic pathways used by *M. tb* to catabolise host-derived lipids (cholesterol and fatty acids) for its survival. Notably, the identification of key enzymes inactivated by our probes and involved in the accumulation and consumption of ILI at key stages of bacterial development [2] will provide highly valuable data and reveal new potential therapeutic targets for the elimination of actively replicating or latent bacilli from infected individuals.

Materials and methods

Compound synthesis

General experimental

All reactions were carried out in oven dried glassware under an atmosphere of argon unless otherwise noted. ^{1}H ^{13}C and ^{31}P NMR spectra were recorded at 300, 75 and 121 MHz, respectively. ^{1}H NMR spectra are referenced to $CDCl_3$ (7.27 p.p.m.), ^{13}C NMR spectra are referenced to $CDCl_3$ (77.23 p.p.m.), and ^{31}P NMR spectra are referenced to external H_3PO_4. Coupling constants, *J*, are reported in Hz. Analytical thin-layer chromatography (TLC) analyses were performed on silica gel plates 60PF$_{254}$. Visualisation was accomplished with UV light, $KMnO_4$ solution or iodine. The **CyC$_{7β}$**, **CyC$_{8β}$** and **CyC$_{17}$** were synthesised as described previously [23,32]. Stock solutions (10 mM) of the **CyC** compounds were prepared in dimethyl sulfoxide (DMSO) and stored at 4 °C.

Methyl 4-methyl-2-(undec-10-yn-1-yloxy)-6,7-dihydro-1,3,2-dioxaphosphepine-5-carboxylate 2-oxide (CyC$_{31yne}$)

To a solution of monocyclic phosphate ester **CyC$_{16}$** [15,23] (0.100 g, 0.421 mmol) in 1,4-dioxane (1 mL) was added the solution of 11-bromoundec-1-yne (**1**) [24] (215 mg, 0.928 mmol) in 1,4-dioxane (1 mL). Solid *n*Bu$_4$NI (0.016 g, 0.042 mmol) was added, and the solution was heated to reflux for 7 h when completion of reaction was observed by TLC and ^{31}P NMR spectroscopy. The solution was concentrated under reduced pressure and the crude mixture was purified using column chromatography (SiO_2, 50% EtOAc in hexane) to give the title compound (0.067 g, 43%) viscous green liquid. IR (neat) 2925, 2853, 1716, 1644, 1284 cm^{-1}; ^{1}H NMR (300 MHz, $CDCl_3$) δ 4.44–4.30 (m, 1H), 4.26–4.09 (m, 3H), 3.78 (s, 3H), 3.10–2.76 (m, 2H), 2.37 (s, 3H), 2.19 (td, J_{HH} = 7.0, 2.6 Hz, 2H), 1.95 (t, J_{HH} = 2.6 Hz, 1H), 1.76–1.66 (m, 2H), 1.55–1.47 (m, 2H), 1.43–1.22 (m, 10H); ^{13}C NMR (75 MHz, $CDCl_3$) δ 167.2 (d, J_{HP} = 1.8 Hz), 161.1 (d, J_{CP} = 9.6 Hz), 115.5 (d, J_{CP} = 3.8 Hz), 84.8, 69.2 (d, J_{CP} = 6.1 Hz), 68.3, 68.2, 52.2, 30.3 (d, J_{CP} = 6.6 Hz), 29.4, 29.1, 29.1, 28.8, 28.5, 28.2, 25.4, 20.4 (d, J_{CP} = 3.8 Hz), 18.5; ^{31}P NMR (121 MHz, $CDCl_3$); δ −10.77; HRMS (ESI, MH$^+$) calcd for $C_{18}H_{30}O_6P$ 373.1780, found 373.1775 and (MNa$^+$) calcd for $C_{18}H_{29}O_6PNa$ 395.1599 found 395.1594.

Methyl 4-methyl-2-(undecyloxy)-6,7-dihydro-1,3,2-dioxaphosphepine-5-carboxylate 2-oxide (CyC$_{31}$)

To a solution of monocyclic phosphate ester **CyC$_{16}$** (0.100 g, 0.421 mmol) in 1,4-dioxane (1 mL) was added a solution of bromoundecane (0.366 mL, 1.63 mmol) followed by the addition of *n*Bu$_4$NI (0.020 g, 0.054 mmol) in 1,4-dioxane (1 mL). The resulting solution was heated to reflux for 4 h when the completion of reaction was observed by TLC and ^{31}P NMR spectroscopy. The solution was concentrated *in vacuo* and the residue was purified using column chromatography (SiO_2, 50% EtOAc in hexane) to give **CyC$_{31}$** viscous liquid (0.059 mg, 38%). IR (neat) 2921, 2851, 1717, 1644, 1287 cm^{-1}; ^{1}H NMR (300 MHz, $CDCl_3$) δ 4.434–4.28 (m, 1H), 4.23–4.08 (m, 3H), 3.75 (s, 3H), 3.06–2.76 (m, 2H), 1.76–1.64 (m, 2H), 1.40–1.17 (m, 16H), 0.86 (d, J_{HH} = 6.4 Hz, 3H); ^{13}C NMR (75 MHz, $CDCl_3$) δ 167.2 (d, J_{HP} = 1.9 Hz), 161.1 (d, J_{HP} = 9.6 Hz), 115.4 (d, J_{HP} = 3.8 Hz), 84.8, 69.2 (d, J_{HP} = 6.0 Hz), 68.2, 68.2, 52.2, 31.9, 30.3 (d, J_{CP} = 6.6 Hz), 29.6, 29.5, 29.4, 29.1, 28.2, 22.7, 20.4 (d, J_{CP} = 3.8 Hz), 14.2; ^{31}P NMR (121 MHz, $CDCl_3$); δ −10.8; HRMS (ESI, MH$^+$) calcd for $C_{18}H_{34}O_6P$ 377.2093, found 377.2088.

Methyl 7-methyl-2-(undec-10-yn-1-yloxy)-3,4,5-trihydro-1,2-oxaphosphepine-6-carboxylate 2-oxide (CyC$_{32yne}$)

To a solution of monocyclic phosphonate ester **CyC$_4$** [15,22] (0.085 g, 0.363 mmol) in dry toluene (1 mL) was added a solution of solution 11-bromoundec-1-yne (**1**) [24] (0.185 g, 0.798 mmol) in dry toluene (1 mL). Solid *n*Bu$_4$NI (0.013 g, 0.036 mmol) was added and heated the mixture was heated to reflux for 4 h when completion of reaction was observed by TLC and ^{31}P NMR spectroscopy. The solution was concentrated under reduced pressure and the crude mixture was purified using column chromatography (SiO_2, 50% EtOAc in hexanes) to give the title compound

17424658, 2023, 6, Downloaded from https://febs.onlinelibrary.wiley.com/doi/10.1111/febs.16645 by Cochrane France, Wiley Online Library on [16/03/2023]. See the Terms and Conditions (https://onlinelibrary.wiley.com/terms-and-conditions) on Wiley Online Library for rules of use; OA articles are governed by the applicable Creative Commons License

(0.059 g, 44%) as viscous liquid. IR (neat) 2926, 2854, 1713, 1643 cm^{-1}; ^{1}H NMR (300 MHz, $CDCl_3$) δ 4.19–4.05 (m, 2H), 3.73 (s, 3H), 2.68–2.42 (m, 2H), 2.31 (s, 3H), 2.18–2.08 (m, 3H), 2.06–2.00 (m, 1H), 1.96–1.85 (m, 3H), 1.74–1.60 (m, 2H), 1.58–1.42 (m, 2H), 1.34–1.28 (br, 10H); ^{13}C NMR (75 MHz, $CDCl_3$) δ 168.2, 159.4 (d, J_{CP} = 7.8 Hz), 119.2 (d, J_{CP} = 4.6 Hz), 84.8, 68.3, 66.2 (d, J_{CP} = 7.1 Hz), 52.0, 30.5 (d, J_{CP} = 6.1 Hz), 29.5, 29.2, 29.1, 28.8, 28.6, 27.7, 26.4 (d, J_{CP} = 2.5 Hz), 25.9, 25.6, 21. (d, J_{CP} = 7.5 Hz), 21.1 (d, J_{CP} = 1.6 Hz), 18.5; ^{31}P NMR (121 MHz, $CDCl_3$) δ 23.2; HRMS (ESI, MH^+) calcd for $C_{19}H_{32}O_5P$ 371.1987 found 371.1984 and (MNa^+) calcd for $C_{19}H_{31}O_5PNa$ 393.1807 found 393.1801.

Methyl 7-methyl-2-(undecyloxy)-3,4,5-trihydro-1,2-oxaphosphepine-6-carboxylate 2-oxide (CyC_{32})

To a solution of monocyclic phosphonate ester **CyC_4** (0.145 g, 0.619 mmol) in toluene (1 mL) was added a solution of bromoundecane (0.0.415 mL, 1.85 mmol) followed by the addition of nBu_4NI (0.023 g, 0.062 mmol) in toluene (1 mL). The resulting solution was heated to reflux for 4 h when the completion of reaction was observed by TLC and ^{31}P NMR spectroscopy. The solution was concentrated *in vacuo*, and the residue was purified using column chromatography (SiO_2, 50% EtOAc in hexane) to give **CyC_{32}** viscous liquid (0.097 g, 42%). IR (neat) 2921, 2852, 1714, 1644 cm^{-1}; ^{1}H NMR (300 MHz, $CDCl_3$) δ 4.20–4.03 (m, 3H), 3.72 (s, 3H), 2.69–2.48 (m, 2H), 2.38 (s, 3H), 2.30–1.82 (m, 5H), 1.71–1.59 (m, 3H), 1.21 (m, 16H), 0.86 (d, J_{HH} = 6.4 Hz, 3H); ^{13}C NMR (75 MHz, $CDCl_3$) δ 186.1, 159.4 (d, J_{HP} = 7.8 Hz), 119.1 (d, J_{HP} = 4.7 Hz), 66.2 (d, J_{HP} = 6.9 Hz), 51.9, 30.5 (d, J_{CP} = 6.0 Hz), 29.7, 29.63, 29.57, 29.4, 29.3, 29.2, 27.0 (d, J_{CP} = 93 Hz), 25.5, 22.8, 21.2, 21.1, 22.0, 14.2; ^{31}P NMR (121 MHz, $CDCl_3$); δ 23.2; HRMS (ESI, MH^+) calcd for $C_{19}H_{36}O_5P$ 375.2300, found 375.2296.

MIC determination

The antibacterial activity of the **CyC_{31yne}** and **CyC_{32yne}** probes as compared with the parent **CyC_{31}** and **CyC_{32}** against *M. tb* mc^26230 was assessed by determining their MICs in 96-well flat-bottom Nunclon Delta Surface microplates with lid (Thermo-Fisher Scientific, Illkirch, France) using the REMA assay [39,40]. Briefly, a log-phase *M. tb* mc^26230 culture was diluted to a cell density of 5×10^6 cells·mL^{-1} in 7H9 broth (BD Difco, Le Pont de Claix, France) supplemented with 0.2% glycerol, 0.05% Tween 80 (Sigma-Aldrich, St. Quentin Fallavier, France) and 10% oleic acid, albumin, dextrose, catalase (OADC enrichment; BD Difco) and 24 μg·mL^{-1} D-panthothenate (Sigma-Aldrich) (7H9-S^{OADC}). Then, 100 μL of the above inoculum (i.e. 5×10^5 cells per well) were added to 100 μL of a serial twofold dilutions of each **CyC** compound (or DMSO as control) in 7H9-S^{OADC} medium, to a final volume of 200 μL per well of the 96-well plates [16,33]. Plates were incubated at 37 °C for 10–14 days. Then, 20 μL of a 0.025% (*w*/*v*) resazurin solution was added to each well, and the plates were incubated at 37 °C for colour change from blue to pink or violet and for a reading of fluorescence units (FU). Fluorescence corresponding to the resazurin reduction to its metabolite resorufin was quantified using a Tecan Spark 10M multimode microplate reader (Tecan Group Ltd, Lyon, France) with excitation at 530 nm and emission at 590 nm. MIC values were determined by fitting the relative fluorescence unit (RFU%) sigmoidal dose–response curves in KALEIDAGRAPH 4.2 software (Synergy Software, Reading, PA, USA). The lowest drug concentration inhibiting 90% of *M. tb* growth was defined as the MIC_{90}. Isoniazid (INH) was used as reference drug.

Activity-based protein profiling – adapted from [18,19]

Capture of *M. tb* mc^26230 potential target enzymes from CyC_{yne}-treated culture

From 1 L of culture at the logarithmic growth stage (OD_{600} ~ 1.5), *M. tb* mc^26230 cells were harvested by centrifugation at 5000 ***g*** for 15 min, and resuspended in 7H9-S^{OADC} at a final theoretical OD_{600} of 40. One mL sample of this homogeneous bacterial suspension was incubated with **CyC_{31yne}**, **CyC_{32yne}** (500 μM final concentration) or DMSO (control) at 37 °C for 4 h under gentle shaking at 75 r.p.m. Bacteria were harvested (16 200 ***g***, 4 °C, 15 min) and washed with 3× 500 μL PBS. Cell pellets were resuspended in 750 μL PBS supplemented with EDTA-free protease inhibitors (cOmplete Mini, EDTA-free; Roche, Mannheim, Germany) at a 1 : 1 (*w*/*v*) ratio. The bacterial cells were then mixed with 350 μL of 0.1 mm diameter glass beads (BioSpec) in a 2-mL Eppendorf tube and disrupted during 2 × 4 min of violent shaking, with ice cooling between each run, using Mini-Beadbeater-96 (BioSpec, Bartlesville, OK, USA). The lysate was cooled down in ice for 5 min and then centrifuged at 4 °C and at 200 ***g*** for 10 min to remove the cell debris and unbroken cells. The concentration of total proteins in the supernatants was determined via the Bradford method, adjusted to a concentration of 1 mg·mL^{-1}, snap frozen in liquid nitrogen and stored at −80 °C until further use.

Both **CyC_{31yne}**- and **CyC_{32yne}**-treated *M. tb* and DMSO-control lysate samples (500 μL – 0.5 mg total proteins) were subjected to click-chemistry reaction by addition of 8 μL Desthiobiotin-PEG_3-N_3 (Jena Bioscience, Jena, Germany, CLK-AZ104P4–100; 40 mM in DMSO), 48.1 μL TBTA ligand (1.667 mM in *t*BuOH/DMSO 8 : 2 *v*/*v*) and 20 μL fresh TCEP solution (50 mM in H_2O) to the cells. The final concentrations were: 640 μM Desthiobiotin-PEG_3-N_3, 1.6 mM TCEP and 160 μM TBTA ligand. After gently

17424658, 2023, 6, Downloaded from https://febs.onlinelibrary.wiley.com/doi/10.1111/febs.16645 by Cochrane France, Wiley Online Library on [16/03/2023]. See the Terms and Conditions (https://onlinelibrary.wiley.com/terms-and-conditions) on Wiley Online Library for rules of use; OA articles are governed by the applicable Creative Commons License

vortexing of the samples, the cycloaddition reaction was initiated by addition of 16 µL $CuSO_4$ solution (50 mM in H_2O – final concentration: 1.6 mM). The lysates were mixed by vortexing again and incubated for 2 h under gentle rotative agitation (15 r.p.m.) at room temperature in the dark. The proteins were further precipitated overnight at −20 °C by adding 4 mL ice-cold acetone, and pelletised by centrifugation (16 200 ***g***, 4 °C, 15 min). The supernatant was discarded and the proteins were washed with 2 × 500 µL cold MeOH (resuspension by sonication, 1 × 10 s, 10% max. intensity). After centrifugation (16 200 ***g***, 4 °C, 10 min), the pellets were resuspended in 0.2% (*w*/*v*) SDS in PBS (250 µL) at room temperature by mild sonication (4 × 10 s, 10% max. intensity). Affinity enrichment was performed with 25 µL Pierce™ High Capacity Streptavidin Agarose Resin (Thermo Scientific ref. 20359; prewashed 3 × 500 µL 0.4% SDS solution, centrifugation was performed at 2000 ***g*** for 2 min). Each *M. tb* treated-lysate was enriched for labelled proteins by transfer to the previously washed beads (around 250 µg) and incubated under gentle rotative agitation (15 r.p.m.) at room temperature for 3 h. Beads were stringently washed following pull-down (1 mL each time): 2× 0.4% (*w*/*v*) SDS in PBS, and 1× 10 M urea in PBS. All centrifugation steps were conducted at 2000 ***g*** for 2 min at room temperature. The beads containing bound, biotinylated proteins were resuspended in 60 µL PBS buffer pH 7.4 containing 50 mM free D-biotin.

The resulting solution was mixed with 5× Laemmli reducing sample buffer, and heated at 95 °C for 5 min. This step allowed the recovery of the captured labelled proteins by exchanging the initially captured Desthiobiotin/streptavidin complex to the greater affinity biotin/streptavidin complex. Each sample was snap frozen in liquid nitrogen and stored at −80 °C before mass spectrometry experiments.

To check for unspecific binding, the DMSO-treated lysate sample was also incubated with the streptavidin-agarose beads, and processed as described above.

Mass spectrometry analysis

The protein isolates were loaded on NuPAGE™ 4–12% Bis–tris acrylamide gels according to the manufacturer's instructions (Invitrogen, Life Technologies, Carlsbad, CA, USA). Running of samples was stopped as soon as proteins stacked as a single band. Protein containing bands were stained with Thermo Scientific Imperial Blue, cut from the gel, and following reduction and iodoacetamide alkylation, digested with high-sequencing grade trypsin (Promega, Madison, WI, USA) [25,41]. Extracted peptides were concentrated before mass spectrometry analysis. Samples were reconstituted with 0.1% trifluoroacetic acid in 2% acetonitrile and analysed by liquid chromatography (LC)-tandem MS (MS/MS) using a Q Exactive Plus Hybrid Quadrupole-Orbitrap online with a nanoLC Ultimate 3000 chromatography system (Thermo Fisher Scientific™, San Jose, CA, USA). For each biological sample, 5 µL corresponding to 25% of digested sample was injected in duplicate on the system. After preconcentration and washing of the sample on a Acclaim PepMap 100 column (C18, 2 cm × 100 µm i.d. 100 Å pore size, 5 µm particle size), peptides were separated on a LC EASY-Spray column (C18, 50 cm × 75 µm i.d., 100 Å, 2 µm, 100 Å particle size) at a flow rate of 300 nL·min^{-1} with a two-step linear gradient (2–22% acetonitrile/H_2O; 0.1% formic acid for 100 min and 22–32% acetonitrile/H_2O; 0.1% formic acid for 20 min). For peptide ionisation in the EASY-Spray source, spray voltage was set at 1.9 kV and the capillary temperature at 250 °C. All samples were measured in a data-dependent acquisition mode. Each run was preceded by a blank MS run in order to monitor system background. The peptide masses were measured in a survey full scan (scan range 375–1500 m/z, with 70 K FWHM resolution at $m/z = 400$, target AGC value of 3.00×10^6 and maximum injection time of 100 ms). Following the high-resolution full scan in the Orbitrap, the 10 most intense data-dependent precursor ions were successively fragmented in HCD cell and measured in Orbitrap (normalised collision energy of 25%, activation time of 10 ms, target AGC value of 1.00×10^5, intensity threshold 1.00×10^4 maximum injection time 100 ms, isolation window 2 m/z, 17.5 K FWHM resolution, scan range 200–2000 m/z). Dynamic exclusion was implemented with a repeat count of 1 and exclusion duration of 20 s.

Protein identification and quantification

Relative intensity-based label-free quantification (LFQ) was processed using the MAXLFQ algorithm [42] from the freely available MAXQUANT computational proteomics platform, version 1.6.3.4 [43]. Analysis was made on two biological replicates, each injected two times on mass spectrometers. The acquired raw LC Orbitrap MS data were first processed using the integrated Andromeda search engine [44]. Spectra were searched against the *Mycobacterium tuberculosis* database extracted from UniProt (date 2021-03-10; 3993 entries) [45]. The false discovery rate (FDR) at the peptide and protein levels were set to 1% and determined by searching a reverse database. For protein grouping, all proteins that could not be distinguished based on their identified peptides were assembled into a single entry according to the MAXQUANT rules. The statistical analysis was made with PERSEUS program (version 1.6.15) from the MAXQUANT environment (www.maxquant.org). Quantifiable proteins were defined as those detected in above three of four samples in one condition or more. Protein LFQ normalised intensities were base 2 logarithmised to obtain a normal distribution. Missing values were replaced using data imputation by randomly selecting from a normal distribution centred on the lower edge of the intensity values that simulates signals of low abundant proteins using default

17424658, 2023, 6, Downloaded from https://febs.onlinelibrary.wiley.com/doi/10.1111/febs.16645 by Cochrane France, Wiley Online Library on [16/03/2023]. See the Terms and Conditions (https://onlinelibrary.wiley.com/terms-and-conditions) on Wiley Online Library for rules of use; OA articles are governed by the applicable Creative Commons License

parameters (a downshift of 1.8 standard deviation and a width of 0.3 of the original distribution). To determine whether a given detected protein was specifically differential, a two-sample *t*-test wascarried out using permutation-based FDR-controlled at 1% and employing 250 permutations. The *P*-value was adjusted using a scaling factor s0 with a value of 1 [46].

The mass spectrometry proteomics data have been deposited to the ProteomeXchange Consortium (www.proteomexchange.org) [47] via the PRIDE partner repository [48] with the dataset identifier PXD034921.

Cloning, expression and purification of HsaD

The *rv3569c* gene encoding HsaD was amplified by PCR using *M. tuberculosis* H37Rv genomic DNA and specific forward (*hsaD*-Fwd: 5′-CCAGCATATGACAGCTACCGAGG AATTGACGT-3′) and reverse (*hsaD*-Rev: 5′-CCAGAAG CTTTCTGCCACCTCCCAGAAATTCAATC-3′) primers. The PCR product was cloned into a pVV16 vector following digestion with NdeI and BamHI restriction sites in 5′ and 3′ ends, respectively, enabling the incorporation of a 6×His-tag in the C-terminus of the HsaD protein. Sequence integrity of the construct was confirmed by DNA sequencing (Eurofins Genomics, Ebersberg, Germany).

Mycobacterium smegmatis mc^2155 electrocompetent cells were prepared as previously described [49], and electroporation procedure was performed as in [16]. Transformants were selected on Middlebrook 7H9 agar plates supplemented with 50 $\mu g \cdot mL^{-1}$ hygromycin. Plates were incubated at 37 °C for 3–5 days. *M. smegmatis* mc^2155 carrying *pVV16::hsaD* was cultured in Middlebrook 7H9 broth (BD Difco, Le Pont-de-Claix, France) supplemented with 0.05% (*v*/*v*) Tween-80, 0.2% (*v*/*v*) glycerol, 10% (*v*/*v*) ADS (0.5% albumin, 0.2% dextrose, 0.085% NaCl) and 50 $\mu g \cdot mL^{-1}$ hygromycin at 37 °C and 220 r.p.m. When OD_{600} reached 3, bacterial cells were harvested by centrifugation (8000 ***g***, 4 °C, 1 h), resuspended in lysis buffer (50 m M Tris–HCl, pH 8.0, 1 M NaCl, 0.1% Triton X-100; 30 mL per litre of culture) and disrupted by sonication on ice. After centrifugation, the supernatant was recovered and loaded onto a nickel-chelate affinity resin. The resin was washed with buffer A (50 m M Tris–HCl pH 8, 1 M NaCl, 10 m M imidazole). The protein was eluted with buffer B (50 m M Tris–HCl pH 8, 1 M NaCl, 250 m M imidazole), concentrated and further purified by size-exclusion chromatography on a Superdex 200 16/60 column (GE-Healthcare, Buc, France) equilibrated with buffer C (50 m M Tris–HCl pH 8, 1 M NaCl). Pure fractions of HsaD, as analysed by SDS/PAGE electrophoresis, were pooled and concentrated to 7.0–7.5 $mg \cdot mL^{-1}$ using a 10 kDa cut-off ultracentrifugation membrane (Thermo Scientific). HsaD was stored at −80 °C. Theoretical physical properties (molecular mass, extinction coefficient at 280 nm, and isoelectric point) of HsaD containing the 6×His tag at the C-terminal position were computed with the PROTPARAM tool [50] (https://web.expasy.org/protparam/).

Inhibition assays

The lipase-inhibitor pre-incubation method was used to test, in aqueous medium and in the absence of substrate, the possible direct reactions between the enzyme and the **CyC** inhibitors as already reported [32,34]. Briefly, each inhibitor was incubated overnight at 23 °C with HsaD (12 µM final concentration in 50 mM Tris–HCl buffer pH 8, 67 mM NaCl) at varying inhibitor molar excess (x_I) [32] ranging from 0.2 to 80 related to 1 mol of enzyme, in a final volume of 100 µL. After the incubation period, the residual HsaD activity was measured via monitoring the degradation of the synthetic substrate HOPDA (200 µM final concentration) at $OD_{450\ nm}$ using a microtiter plate scanning spectrophotometer (PowerWave™; Bio-Tek Instrument, Les Ulis, France) as described in [21]. The variation in the residual enzyme activity allowed the determination of the inhibitor molar excess that reduces the enzyme activity to 50% of its initial value (x_{I50}) [32,34]. Dose response curves were fitted using KALEIDAGRAPH v.4.03 (Synergy Software). Results are expressed as mean values ± SD of two independent assays.

Mass-spectrometry analysis of HsaD-CyC complexes

Intact protein mass analysis

Protein masses were determined on purified solution samples. To this end, the proteins in 10 µL of 50 mM Tris pH 8, 100 mM NaCl buffer were desalted on ZipTip C4 (Millipore, Molsheim, France) and eluted by 3 µL of sinapinic acid matrix solution in 0.3% TFA/CH_3CN (50 : 50 *v*/*v*). One microlitre of the mix was spotted on the target and analysed by MALDI-TOF on an Ultraflex III spectrometer (Bruker Daltonics, Wissembourg, France) controlled by the FLEXCONTROL 3.0 package (Build 51) and operated in the linear mode, using a maximum accelerating potential of 25 kV and a 20 000–100 000 *m*/*z* range (LP_66kDa method). The laser frequency was fixed to 100 Hz and ~ 1000 shots per sample were cumulated. Four external standards (Protein Calibration Standard II; Bruker Daltonics) were used to calibrate each spectrum to a mass accuracy within 100 p.p.m. Peak picking was performed using the FLEXANALYSIS 3.0 software with an adapted analysis method. Parameters used were as follows: centroid peak detection algorithm, S/N threshold fixed to 5 and a quality factor threshold of 30.

Peptide mass fingerprinting

Proteins in SDS/PAGE gel-excised bands were submitted to trypsin digestion using a slightly modified Shevchenko

17424658, 2023, 6, Downloaded from https://febs.onlinelibrary.wiley.com/doi/10.1111/febs.16645 by Cochrane France, Wiley Online Library on [16/03/2023]. See the Terms and Conditions (https://onlinelibrary.wiley.com/terms-and-conditions) on Wiley Online Library for rules of use; OA articles are governed by the applicable Creative Commons License

protocol [41]. Briefly, the bands were washed and destained using 100 mM NH_4HCO_3 (pH 8.0), reduced using DTT 10 mM (56 °C, 45 min) and alkylated with 55 mM iodoacetamide (25 °C, 30 min in the dark), both in 100 mM NH_4HCO_3 (pH 8.0), dried at room temperature, and reswollen into 25 mM NH_4HCO_3 supplemented with 12.5 ng·μL^{-1} trypsin (V5111; Promega) overnight at 37 °C. Peptide extracts collected from the digestion solution, from a first extract by sonication in 5% formic acid, and from a second one in 5% formic acid/CH_3CN (40 : 60 *v*/*v*) were pooled and dried in a centrifugal vacuum system.

Peptides were then resuspended in a α-cyano-4-hydroxycinnamic acid matrix solution (saturated solution in 50% acetonitrile/0.3% TFA), and 1 μL was spotted on the Maldi metal target. Mass analyses were performed on a MALDI-TOF-TOF Ultraflex III spectrometer (Bruker Daltonics) controlled by the FLEXCONTROL 3.0 package (Build 51). This instrument was used at a maximum accelerating potential of 25 kV and was operated in reflector mode and the *m*/*z* range from 600 to 3500. Six external standards (Peptide Calibration Standard II; Bruker Daltonics) were used to calibrate each spectrum to a mass accuracy within 10 p.p.m. with a minimal resolution of 10 000 for the angiotensin II peak (Monoisotopic mass = 1046.542 Da). Peak picking was performed with FLEXANALYSIS 3.0 software (Bruker) with an adapted analysis method. Parameters used were as follows: SNAP peak detection algorithm, S/N threshold fixed to 6 and a quality factor threshold of 30. The peaks obtained were then compared with the theoretical digestion peaks list of the total protein with BIOTOOLS software (Bruker).

MS/MS analyses

Sequences of modified peptides were confirmed by MS/MS analyses on the Maldi TOF-TOF Ultraflex III spectrometer (Bruker Daltonics) using the LIFT_2017 method after calibration. LIFT mass spectra were acquired in the positive ion mode. Metastable fragmentation was induced by a nitrogen laser (337 nm) without the further use of collision gas. Precursor ions were accelerated to 8 kV and selected in a timed ion gate. In the LIFT-cell, the fragments were further accelerated to 19.07 kV. The reflector potential was 29.6 kV [51].

Crystallisation, data collection and processing

Crystallisation trials on the native form of HsaD were performed by the sitting-drop vapour-diffusion method using a TECAN EVO pipetting robot to fill Greiner plates with commercial screens and a Mosquito® (TTP Labtech, Melbourn, England) crystallisation robot to dispense the protein and reservoir solutions. Crystal hits emerged from a condition of the AmSO4 suite (NeXtal) containing 2 M $(NH_4)_2SO_4$, 0.1 M MES-Na pH 6.5 and 5% (*v*/*v*) PEG400 and after several optimisation rounds well diffracting crystals were obtained by the hanging-drop vapour-diffusion method in Linbro plates by mixing 1 μL protein solution at 7.5 mg·mL^{-1} with 0.5 μL reservoir solution composed of 1.5–1.7 M $(NH_4)_2SO_4$, 0.1 M MES-Na pH 6.5 and 5 to 10% (*v*/*v*) PEG400.

To obtain the structure of HsaD in complex with the **CyC** inhibitors, the protein at 7.5 mg·mL^{-1} was mixed either with each of the **CyC$_{7\beta}$**, **CyC$_{8\beta}$** and **CyC$_{17}$** inhibitors dissolved in Transcutol® HP (Gattefossé SAS, Saint-Priest, France) at a molar excess $x_I = 100$ and incubated at room temperature for 2 h, or with **CyC$_{31}$** dissolved in DMSO at a molar excess $x_I = 2.5$ and incubated at room temperature for 24 h.

Crystallisation of HsaD in complex with the **CyC** inhibitors was performed as outlined above for the native form of HsaD. Crystals of native HsaD, and HsaD in complex with the **CyC** inhibitors were cryo-protected with reservoir solution supplemented with 30% (*v*/*v*) glycerol prior flash-freezing in liquid nitrogen. X-ray diffraction data were acquired at beam lines Proxima1 and Proxima2a at the Synchrotron Soleil, Gif-sur-Yvette. Diffraction data were processed with XDS [52] and scaled and merged using the CCP4 suite [53,54] of programs POINTLESS [55], AIMLESS [56] and TRUNCATE [57].

The structure of native HsaD was solved by molecular replacement with the program PHASER [58] using the structural coordinates of the same protein (PDB: 2VF2 – 2.35 Å resolution [35], 100% sequence identity) as the search model. The complex HsaD-**CyC** structures were solved by molecular replacement using the coordinates of native HsaD as the search model. Refinement and model adjustment were carried out with the programs REFMAC [59] and COOT [60], respectively. Random sets of ~ 5% of reflections, depending on the resolution limit, were set-aside for cross-validation purposes. The composition of cross-validation data sets was systematically taken over from the parent data set, except for the complex HsaD-**CyC$_{7\beta}$**, which belongs to a different space group. The covalent link between the **CyC** ligands and the catalytic serine S^{114}, and stereochemical restraints for the inhibitors, were generated by JLIGAND [61]. Model quality was assessed with internal modules of COOT [60] and with the MOLPROBITY server [62]. Ligands were fitted into unbiased Fo–Fc difference electron density maps calculated after 5–7 cycles of restrained refinement with REFMAC [59]. Figures representing structural renderings were generated with the PYMOL Molecular Graphics System (Version 2; Schrödinger, LLC, Mannheim, Germany).

In silico molecular docking experiments

AUTODOCK VINA [36] was used as previously reported [16,20,63] to generate the putative binding modes of the various **CyC** inhibitors into the active site of HsaD. The PYMOL Molecular Graphics System (version 1.4; Schrödinger, LLC) was used as the working environment with an in-house

17424658, 2023, 6, Downloaded from https://febs.onlinelibrary.wiley.com/doi/10.1111/febs.16645 by Cochrane France, Wiley Online Library on [16/03/2023]. See the Terms and Conditions (https://onlinelibrary.wiley.com/terms-and-conditions) on Wiley Online Library for rules of use; OA articles are governed by the applicable Creative Commons License

version of the AUTODOCK/VINA PYMOL plugin [63]. The X-ray crystallographic structure of HsaD in complex with the $\mathbf{CyC_{31}}$ inhibitor (PDB: 7ZM4) was used as the receptor. Docking runs were performed after removing the bound $\mathbf{CyC_{31}}$ from the enzyme active site, and replacing the catalytic Ser^{114} with a glycine residue to enable the ligand (i.e. the inhibitor) to adopt a suitable position corresponding to the prebound intermediate before the nucleophilic attack in the enzyme active site. The box size used was chosen to fit the whole enzyme's active site cleft and allowed non-constructive binding positions. The three-dimensional structures of the **CyC** compounds were constructed using CHEM3D ULTRA 11.0 software, and their geometry was refined using the Avogadro open-source molecular builder and visualisation tool (version 1.2.0. http://avogadro.cc/) [64].

Acknowledgements

This work was supported by the CNRS, Aix Marseille University, and the Agence Nationale de la Recherche (grant no. ANR-19-CE44-0011) and by the French Infrastructure for Integrated Structural Biology (FRISBI) (grant no. ANR-10-INSB-05-01). Proteomics analyses were done using the mass spectrometry facility of Marseille Proteomics (marseille-proteomique.univ-amu.fr) supported by IBISA, the Cancéropôle PACA, the Provence-Alpes-Côte d'Azur Région, the Institut Paoli-Calmettes, and Fonds Europeen de Développement Régional (FEDER). We thank Synchrotron Soleil for beamtime allocation and beam line staff for assistance with data collection. The synthetic substrate HOPDA was kindly provided to us by Prof Edith Sim (Oxford University) and Dr Ali Ryan (Northumbria University).

Conflict of interest

The authors declare no conflict of interest.

Author contributions

SB, GS and J-FC involved in conceptualisation; SB, PF, SA, LC and GS involved in data curation; SB, RA, PF, VR-Z, IP, VP, SA and LC involved in the investigation; SB, RA, PF, VR-Z, IP, VP, SA and LC involved in the methodology; GRG and CDS involved in resources; SB, RA, CDS, SC, GS and J-FC involved in formal analysis; SB, RA, PF and J-FC involved in visualisation; SB and J-FC involved in writing—original draft; SB, YB, CDS, PF, SC, LC, GS and J-FC involved in writing–review and editing. GS and J-FC involved in the supervision; J-FC involved in funding acquisition; J-FC involved in validation; J-FC involved in project administration. All authors have given approval to the final version of the manuscript.

Peer review

The peer review history for this article is available at https://publons.com/publon/10.1111/febs.16645.

Data availability statement

The atomic coordinates and structure factors (PDB: 7ZJT, 7ZM1, 7ZM2, 7ZM3 and 7ZM4) have been deposited in the Protein Data Bank (https://www.wwpdb.org/).

References

1 WHO. Global tuberculosis report. 2021 [cited xxxx xxx xx]. Available from: https://www.who.int/teams/global-tuberculosis-programme/data
2 Mallick I, Santucci P, Poncin I, Point V, Kremer L, Cavalier JF, et al. Intrabacterial lipid inclusions in mycobacteria: unexpected key players in survival and pathogenesis? *FEMS Microbiol Rev*. 2021;**45**:fuab029.
3 Rengarajan J, Bloom BR, Rubin EJ. Genome-wide requirements for *Mycobacterium tuberculosis* adaptation and survival in macrophages. *Proc Natl Acad Sci USA*. 2005;**102**:8327–32.
4 Sassetti CM, Rubin EJ. Genetic requirements for mycobacterial survival during infection. *Proc Natl Acad Sci USA*. 2003;**100**:12989–94.
5 Pandey AK, Sassetti CM. Mycobacterial persistence requires the utilization of host cholesterol. *Proc Natl Acad Sci USA*. 2008;**105**:4376–80.
6 Ouellet H, Johnston JB, de Montellano PR. Cholesterol catabolism as a therapeutic target in *Mycobacterium tuberculosis*. *Trends Microbiol*. 2011;**19**:530–9.
7 Lovewell RR, Sassetti CM, VanderVen BC. Chewing the fat: lipid metabolism and homeostasis during *M. tuberculosis* infection. *Curr Opin Microbiol*. 2016;**29**:30–6.
8 Van der Geize R, Yam K, Heuser T, Wilbrink MH, Hara H, Anderton MC, et al. A gene cluster encoding cholesterol catabolism in a soil actinomycete provides insight into *Mycobacterium tuberculosis* survival in macrophages. *Proc Natl Acad Sci USA*. 2007;**104**:1947–52.
9 Griffin JE, Gawronski JD, Dejesus MA, Ioerger TR, Akerley BJ, Sassetti CM. High-resolution phenotypic profiling defines genes essential for mycobacterial growth and cholesterol catabolism. *PLoS Pathog*. 2011;**7**:e1002251.
10 Singh G, Singh G, Jadeja D, Kaur J. Lipid hydrolizing enzymes in virulence: *Mycobacterium tuberculosis* as a model system. *Crit Rev Microbiol*. 2010;**36**:259–69.
11 Johnson G. The alpha/beta hydrolase fold proteins of *Mycobacterium tuberculosis*, with reference to their

17424658, 2023, 6, Downloaded from https://febs.onlinelibrary.wiley.com/doi/10.1111/febs.16645 by Cochrane France, Wiley Online Library on [16/03/2023]. See the Terms and Conditions (https://onlinelibrary.wiley.com/terms-and-conditions) on Wiley Online Library for rules of use; OA articles are governed by the applicable Creative Commons License

contribution to virulence. *Curr Protein Pept Sci*. 2017;**18**:190–210.
12 Dedieu L, Serveau-Avesque C, Kremer L, Canaan S. Mycobacterial lipolytic enzymes: a gold mine for tuberculosis research. *Biochimie*. 2013;**95**:66–73.
13 Keller LJ, Babin BM, Lakemeyer M, Bogyo M. Activity-based protein profiling in bacteria: applications for identification of therapeutic targets and characterization of microbial communities. *Curr Opin Chem Biol*. 2019;**54**:45–53.
14 Spilling CD. The chemistry and biology of Cyclophostin, the Cyclipostins and related compounds. *Molecules*. 2019;**24**:2579.
15 Cavalier JF, Spilling CD, Durand T, Camoin L, Canaan S. Lipolytic enzymes inhibitors: a new way for antibacterial drugs discovery. *Eur J Med Chem*. 2021;**209**:112908.
16 Nguyen PC, Delorme V, Bénarouche A, Martin BP, Paudel R, Gnawali GR, et al. Cyclipostins and Cyclophostin analogs as promising compounds in the fight against tuberculosis. *Sci Rep*. 2017;**7**:11751.
17 Cravatt BF, Wright AT, Kozarich JW. Activity-based protein profiling: from enzyme chemistry to proteomic chemistry. *Annu Rev Biochem*. 2008;**77**:383–414.
18 Krysiak J, Sieber SA. Activity-based protein profiling in bacteria. In: Overkleeft HS, Florea BI, editors. Activity-based proteomics: methods and protocols. New York: Springer; 2017. p. 57–74.
19 Lehmann J, Cheng TY, Aggarwal A, Park AS, Zeiler E, Raju RM, et al. An antibacterial beta-lactone kills *Mycobacterium tuberculosis* by disrupting mycolic acid biosynthesis. *Angew Chem Int Ed Engl*. 2018;**57**:348–53.
20 Li M, Patel HV, Cognetta AB, Smith TC, Mallick I, Cavalier J-F, et al. Identification of cell wall synthesis inhibitors active against *Mycobacterium tuberculosis* by competitive activity-based protein profiling. *Cell Chem Biol*. 2022;**29**:883–96.e5.
21 Ryan A, Polycarpou E, Lack NA, Evangelopoulos D, Sieg C, Halman A, et al. Investigation of the mycobacterial enzyme HsaD as a potential novel target for anti-tubercular agents using a fragment-based drug design approach. *Br J Pharmacol*. 2017;**174**:2209–24.
22 Dutta S, Malla RK, Bandyopadhyay S, Spilling CD, Dupureur CM. Synthesis and kinetic analysis of some phosphonate analogs of cyclophostin as inhibitors of human acetylcholinesterase. *Bioorg Med Chem*. 2010;**18**:2265–74.
23 Vasilieva E, Dutta S, Malla RK, Martin BP, Spilling CD, Dupureur CM. Rat hormone sensitive lipase inhibition by cyclipostins and their analogs. *Bioorg Med Chem*. 2015;**23**:944–52.
24 Neef AB, Schultz C. Selective fluorescence labeling of lipids in living cells. *Angew Chem Int Ed Engl*. 2009;**48**:1498–500.
25 Madani A, Ridenour JN, Martin BP, Paudel RR, Abdul Basir A, Le Moigne V, et al. Cyclipostins and cyclophostin analogues as multitarget inhibitors that impair growth of *Mycobacterium abscessus*. *ACS Infect Dis*. 2019;**5**:1597–608.
26 Nguyen PC, Madani A, Santucci P, Martin BP, Paudel RR, Delattre S, et al. Cyclophostin and Cyclipostins analogs, new promising molecules to treat mycobacterial-related diseases. *Int J Antimicrob Agents*. 2018;**51**:651–4.
27 Niphakis MJ, Cravatt BF. Enzyme inhibitor discovery by activity-based protein profiling. *Annu Rev Biochem*. 2014;**83**:341–77.
28 Díez-González S. Chapter three – Copper(I)–acetylides: access, structure, and relevance in catalysis. In: Pérez PJ, editor. Advances in organometallic chemistry. Cambridge: Academic Press; 2016. p. 93–141.
29 Lack NA, Kawamura A, Fullam E, Laurieri N, Beard S, Russell AJ, et al. Temperature stability of proteins essential for the intracellular survival of *Mycobacterium tuberculosis*. *Biochem J*. 2009;**418**:369–78.
30 Lack NA, Yam KC, Lowe ED, Horsman GP, Owen RL, Sim E, et al. Characterization of a carbon-carbon hydrolase from *Mycobacterium tuberculosis* involved in cholesterol metabolism. *J Biol Chem*. 2010;**285**:434–43.
31 Nguyen PC, Delorme V, Benarouche A, Guy A, Landry V, Audebert S, et al. Oxadiazolone derivatives, new promising multi-target inhibitors against *M. tuberculosis*. *Bioorg Chem*. 2018;**81**:414–24.
32 Point V, Malla RK, Diomande S, Martin BP, Delorme V, Carriere F, et al. Synthesis and kinetic evaluation of Cyclophostin and Cyclipostins phosphonate analogs as selective and potent inhibitors of microbial lipases. *J Med Chem*. 2012;**55**:10204–19.
33 Nguyen PC, Nguyen VS, Martin BP, Fourquet P, Camoin L, Spilling CD, et al. Biochemical and structural characterization of TesA, a major thioesterase required for outer-envelope lipid biosynthesis in *M. tuberculosis*. *J Mol Biol*. 2018;**430**:5120–36.
34 Viljoen A, Richard M, Nguyen PC, Fourquet P, Camoin L, Paudal RR, et al. Cyclipostins and Cyclophostin analogs inhibit the antigen 85C from *mycobacterium tuberculosis* both *in vitro* and *in vivo*. *J Biol Chem*. 2018;**293**:2755–69.
35 Lack N, Lowe ED, Liu J, Eltis LD, Noble MEM, Sim E, et al. Structure of HsaD, a steroid-degrading hydrolase, from *Mycobacterium tuberculosis*. *Acta Crystallogr Sect F*. 2008;**64**:2–7.
36 Trott O, Olson AJ. AutoDock Vina: improving the speed and accuracy of docking with a new scoring function, efficient optimization, and multithreading. *J Comput Chem*. 2010;**31**:455–61.

17424658, 2023, 6, Downloaded from https://febs.onlinelibrary.wiley.com/doi/10.1111/febs.16645 by Cochrane France, Wiley Online Library on [16/03/2023]. See the Terms and Conditions (https://onlinelibrary.wiley.com/terms-and-conditions) on Wiley Online Library for rules of use; OA articles are governed by the applicable Creative Commons License

37 Babin BM, Keller LJ, Pinto Y, Li VL, Eneim AS, Vance SE, et al. Identification of covalent inhibitors that disrupt *M. tuberculosis* growth by targeting multiple serine hydrolases involved in lipid metabolism. *Cell Chem Biol*. 2022;**29**:897–909.e7.
38 Rohde KH, Abramovitch RB, Russell DG. *Mycobacterium tuberculosis* invasion of macrophages: linking bacterial gene expression to environmental cues. *Cell Host Microbe*. 2007;**2**:352–64.
39 Palomino JC, Martin A, Camacho M, Guerra H, Swings J, Portaels F. Resazurin microtiter assay plate: simple and inexpensive method for detection of drug resistance in *Mycobacterium tuberculosis*. *Antimicrob Agents Chemother*. 2002;**46**:2720–2.
40 Rybniker J, Vocat A, Sala C, Busso P, Pojer F, Benjak A, et al. Lansoprazole is an antituberculous prodrug targeting cytochrome bc1. *Nat Commun*. 2015;**6**:7659.
41 Shevchenko A, Wilm M, Vorm O, Mann M. Mass spectrometric sequencing of proteins silver-stained polyacrylamide gels. *Anal Chem*. 1996;**68**:850–8.
42 Cox J, Hein MY, Luber CA, Paron I, Nagaraj N, Mann M. Accurate proteome-wide label-free quantification by delayed normalization and maximal peptide ratio extraction, termed MaxLFQ. *Mol Cell Proteomics*. 2014;**13**:2513–26.
43 Cox J, Mann M. MaxQuant enables high peptide identification rates, individualized p.p.b.-range mass accuracies and proteome-wide protein quantification. *Nat Biotechnol*. 2008;**26**:1367–72.
44 Cox J, Neuhauser N, Michalski A, Scheltema RA, Olsen JV, Mann M. Andromeda: a peptide search engine integrated into the MaxQuant environment. *J Proteome Res*. 2011;**10**:1794–805.
45 The UniProt Consortium. UniProt: the universal protein knowledgebase. *Nucleic Acids Res*. 2017;**45**:D158–69.
46 Tusher VG, Tibshirani R, Chu G. Significance analysis of microarrays applied to the ionizing radiation response. *Proc Natl Acad Sci USA*. 2001;**98**:5116–21.
47 Deutsch EW, Bandeira N, Sharma V, Perez-Riverol Y, Carver JJ, Kundu DJ, et al. The ProteomeXchange consortium in 2020: enabling 'big data' approaches in proteomics. *Nucleic Acids Res*. 2020;**48**:D1145–52.
48 Perez-Riverol Y, Bai J, Bandla C, Garcia-Seisdedos D, Hewapathirana S, Kamatchinathan S, et al. The PRIDE database resources in 2022: a hub for mass spectrometry-based proteomics evidences. *Nucleic Acids Res*. 2022;**50**:D543–52.
49 Goude R, Roberts DM, Parish T. Electroporation of mycobacteria. In: Parish T, Roberts DM, editors. Mycobacteria protocols. New York: Springer; 2015. p. 117–30.
50 Gasteiger E, Hoogland C, Gattiker A, Duvaud SE, Wilkins MR, Appel RD, et al. Protein identification and analysis tools on the ExPASy server. In: Walker JM, editor. The proteomics protocols handbook. Totowa: Humana Press; 2005. p. 571–607.
51 Suckau D, Resemann A, Schuerenberg M, Hufnagel P, Franzen J, Holle A. A novel MALDI LIFT-TOF/TOF mass spectrometer for proteomics. *Anal Bioanal Chem*. 2003;**376**:952–65.
52 Kabsch W. Integration, scaling, space-group assignment and post-refinement. *Acta Crystallogr D Biol Crystallogr*. 2010;**66**:133–44.
53 Potterton E, Briggs P, Turkenburg M, Dodson E. A graphical user interface to the CCP4 program suite. *Acta Crystallogr D Biol Crystallogr*. 2003;**59**:1131–7.
54 Winn MD, Ballard CC, Cowtan KD, Dodson EJ, Emsley P, Evans PR, et al. Overview of the CCP4 suite and current developments. *Acta Crystallogr D Biol Crystallogr*. 2011;**67**:235–42.
55 Evans PR. An introduction to data reduction: space-group determination, scaling and intensity statistics. *Acta Crystallogr D Biol Crystallogr*. 2011;**67**: 282–92.
56 Evans PR, Murshudov GN. How good are my data and what is the resolution? *Acta Crystallogr D Biol Crystallogr*. 2013;**69**:1204–14.
57 French S, Wilson K. On the treatment of negative intensity observations. *Acta Crystallogr A*. 1978;**34**: 517–25.
58 McCoy AJ, Grosse-Kunstleve RW, Adams PD, Winn MD, Storoni LC, Read RJ. Phaser crystallographic software. *J Appl Cryst*. 2007;**40**:658–74.
59 Murshudov GN, Skubák P, Lebedev AA, Pannu NS, Steiner RA, Nicholls RA, et al. REFMAC5 for the refinement of macromolecular crystal structures. *Acta Crystallogr D Biol Crystallogr*. 2011;**67**:355–67.
60 Emsley P, Cowtan K. Coot: model-building tools for molecular graphics. *Acta Crystallogr D Biol Crystallogr*. 2004;**60**:2126–32.
61 Lebedev AA, Young P, Isupov MN, Moroz OV, Vagin AA, Murshudov GN. JLigand: a graphical tool for the CCP4 template-restraint library. *Acta Crystallogr D Biol Crystallogr*. 2012;**68**:431–40.
62 Williams CJ, Headd JJ, Moriarty NW, Prisant MG, Videau LL, Deis LN, et al. MolProbity: more and better reference data for improved all-atom structure validation. *Protein Sci*. 2018;**27**:293–315.
63 Seeliger D, de Groot BL. Ligand docking and binding site analysis with PyMOL and Autodock/Vina. *J Comput Aided Mol Des*. 2010;**24**:417–22.
64 Hanwell MD, Curtis DE, Lonie DC, Vandermeersch T, Zurek E, Hutchison GR. Avogadro: an advanced semantic chemical editor, visualization, and analysis platform. *J Chem*. 2012;**4**:17.
65 Kapopoulou A, Lew JM, Cole ST. The MycoBrowser portal: a comprehensive and manually annotated

17424658, 2023, 6, Downloaded from https://febs.onlinelibrary.wiley.com/doi/10.1111/febs.16645 by Cochrane France, Wiley Online Library on [16/03/2023]. See the Terms and Conditions (https://onlinelibrary.wiley.com/terms-and-conditions) on Wiley Online Library for rules of use; OA articles are governed by the applicable Creative Commons License

resource for mycobacterial genomes. *Tuberculosis (Edinb)*. 2011;**91**:8–13.

Supporting information

Additional supporting information may be found online in the Supporting Information section at the end of the article.

Fig. S1. ^{1}H, ^{13}C and ^{31}P NMR spectra of the $\mathbf{CyC_{31}}$, $\mathbf{CyC_{32}}$, $\mathbf{CyC_{31yne}}$ and $\mathbf{CyC_{32yne}}$ compounds.

Table S1. $\mathbf{CyC_{31yne}}$ target proteins identified in *M. tb* $mc^{2}6230$ culture through CC-ABPP by LC-ESI-MS/MS analysis.

Table S2. $\mathbf{CyC_{32yne}}$ target proteins identified in *M. tb* $mc^{2}6230$ culture through CC-ABPP by LC-ESI-MS/MS analysis.

Table S3. Proteins differentially captured with $\mathbf{CyC_{31yne}}$ and $\mathbf{CyC_{32yne}}$ at a p-value ≤ 0.01 and a fold-change ≥ 1.2.

17424658, 2023, 6, Downloaded from https://febs.onlinelibrary.wiley.com/doi/10.1111/febs.16645 by Cochrane France, Wiley Online Library on [16/03/2023]. See the Terms and Conditions (https://onlinelibrary.wiley.com/terms-and-conditions) on Wiley Online Library for rules of use; OA articles are governed by the applicable Creative Commons License

Supporting Information

Direct capture, inhibition and crystal structure of HsaD (Rv3569c) from *M. tuberculosis*

Sarah Barelier[a], Romain Avellan[b], Giri Raj Gnawali[c], Patrick Fourquet[d], Véronique Roig-Zamboni[a], Isabelle Poncin[b], Vanessa Point[b], Yves Bourne[a], Stéphane Audebert[d], Luc Camoin[d], Christopher D. Spilling[c], Stéphane Canaan[b], Jean-François Cavalier[b,*], Gerlind Sulzenbacher[a,*]

[a] Aix-Marseille Univ., CNRS, AFMB UMR 7257, Marseille, France

[b] Aix-Marseille Univ., CNRS, LISM, IMM FR3479, Marseille, France

[c] Department of Chemistry and Biochemistry, University of Missouri-St. Louis, One University Boulevard, St. Louis, Missouri, 63121, United States

[d] Aix-Marseille Univ., INSERM, CNRS, Institut Paoli-Calmettes, CRCM, Marseille Protéomique, Marseille, France

* To whom correspondence should be addressed

E-mail address: jfcavalier@imm.cnrs.fr (J.-F. Cavalier); https://orcid.org/0000-0003-0864-8314

E-mail address: gerlind.sulzenbacher@univ-amu.fr (G. Sulzenbacher); https://orcid.org/0000-0003-4844-2820

Table of contents

Table S1. CyC$_{31yne}$ target proteins identified in *M. tb* mc²6230 culture through CC-ABPP by LC-ESI-MS/MS analysis. Only positive hits with a *p*-value <0.01 and a fold-change ≥1.2 are reported

Table S2. **CyC$_{32yne}$** target proteins identified in *M. tb* mc²6230 culture through CC-ABPP by LC-ESI-MS/MS analysis. Only positive hits with a *p*-value <0.01 and a fold-change ≥1.2 are reported

Table S3. Proteins differentially captured with **CyC$_{31yne}$** and **CyC$_{32yne}$** at a *p*-value ≤ 0.01 and a fold-change ≥ 1.2

Fig. S1. ^{1}H, ^{13}C and ^{31}P NMR spectra

Table S1. **CyC_{31yne} target proteins identified in *M. tb* mc²6230 culture through CC-ABPP by LC-ESI-MS/MS analysis. Only positive hits with a *p*-value <0.01 and a fold-change ≥1.2 are reported.**

Pathway/Functional category	Protein IDs	Gene names	Essentiality	Change	Fold Change (log2)	-LOG(p-value)	Manhattan distance	Unique peptides	Unique sequence coverage [%]	Mol. weight [kDa]	Q-value	Score	Intensity	MS/MS count	Protein names
Intermediary metabolism and respiration	P9WKL5	htm Rv0560c	Non-Essential	Increased	5.786037922	4.118003579	9.904041501	11	81.3	25.945	0	236.39	1496400000	185	2-heptyl-1-hydroxyquinolin-4(1H)-one methyltransferase (HQNO methyltransferase)
Intermediary metabolism and respiration	P71668	lipI Rv1400c	Non-Essential	Increased	5.544583797	3.636842818	9.181426615	11	62.8	34.052	0	196.79	3692100000	161	Esterase LipI
Lipid metabolism	I6XU97	Rv0045c	Non-Essential	Increased	5.136509418	2.411832965	7.548342383	12	60.4	32.131	0	158.22	1134900000	149	Esterase Rv0045c
Cell wall and cell processes	P9WP43	cut7 Rv1984c	Growth-Advantage	Increased	4.943463326	5.426353158	10.36981648	4	30.9	21.782	0	249.99	1758900000	94	Carboxylesterase Culp1
Intermediary metabolism and respiration	P9WIV5	nuoE Rv3149	Non-Essential	Increased	4.08878994	5.901340563	9.990130503	8	47.2	27.197	0	104.83	1665600000	169	NADH-quinone oxidoreductase subunit E
Uncharacterized protein	O53672	Rv0250c	Non-Essential	Increased	4.000836849	7.406453506	11.40729036	5	63.9	10.896	0	109.29	1183800000	147	Uncharacterized protein Rv0250c
Uncharacterized protein	I6YA17	Rv2699c	Essential	Increased	3.682217121	5.273023154	8.955240275	4	75	10.916	0	109.48	833630000	120	Uncharacterized protein
Intermediary metabolism and respiration	P9WKB7	nlhH lipH Rv1399c	Non-Essential	Increased	3.469993591	5.94020195	9.410195541	7	30.1	33.906	0	70.833	884740000	168	Carboxylesterase NlhH
Cell wall and cell processes	P71988	Rv1730c	Non-Essential	Increased	3.418309212	3.104246164	6.522555376	12	30.2	55.8	0	85.77	409610000	78	Possible penicillin-binding protein
Intermediary metabolism and respiration	P9WKD7	rpiB Rv2465c	Essential	Increased	3.396066189	2.546470647	5.942536836	10	75.3	17.277	0	160.26	2766500000	285	Ribose-5-phosphate isomerase B
Intermediary metabolism and respiration	P9WN21	glpX Rv1099c	Non-Essential	Increased	3.329022408	4.785262711	8.114285119	19	62.7	38.084	0	323.31	6253200000	412	Fructose-1,6-bisphosphatase class 2 (FBPase class 2)
Information pathways	P9WGH9	sigH rpoE Rv3223c	Non-Essential	Increased	3.317800522	3.377405128	6.69520565	9	64.8	24.225	0	96.283	719550000	153	ECF RNA polymerase sigma factor SigH
Uncharacterized protein	P71990	Rv1732c	Non-Essential	Increased	3.302349567	3.699920072	7.002269639	8	43.4	19.399	0	154.27	1498800000	244	Conserved protein
Information pathways	P9WNM9	Rv0120c	Non-Essential	Increased	3.285088062	2.816658695	6.101746757	21	37.8	75.63	0	120.23	1890300000	217	Elongation factor G-like protein
Uncharacterized protein	O07173	Rv0123	Non-Essential	Increased	3.160677433	4.728247657	7.88892509	7	65.6	13.623	0	144.29	817970000	79	Uncharacterized protein
Uncharacterized protein	O06154	Rv1637c	Non-Essential	Increased	3.069756985	3.197053448	6.266810433	7	43.6	27.936	0	82.99	1265900000	180	Conserved protein
Information pathways	P9WHJ7	rbfA Rv2838c	Non-Essential	Increased	2.993652821	2.672148689	5.66580151	8	72.7	18.998	0	214.51	1253800000	103	Ribosome-binding factor A
Uncharacterized protein	P95198	Rv0390	Non-Essential	Increased	2.843595982	4.656884186	7.500480168	6	55.7	15.392	0	92.177	1119800000	154	Conserved protein
Uncharacterized protein	P9WL15	Rv2927c	Essential	Increased	2.832271099	2.255673694	5.087944793	12	49.4	26.986	0	166.95	2310800000	236	Uncharacterized protein Rv2927c
Uncharacterized protein	P9WFM1	Rv2230c	Non-Essential	Increased	2.774307251	2.379485521	5.153792772	12	50.4	39.597	0	84.339	1221400000	75	GTP cyclohydrolase 1 type 2 homolog
Cell wall and cell processes	P9WJD9	espB Rv3881c	Growth-Advantage	Increased	2.756381035	6.478589908	9.234970943	18	58.5	47.593	0	323.31	4398200000	631	ESX-1 secretion-associated protein EspB (Antigen MTB48)
Intermediary metabolism and respiration	P9WKG1	ispH2 lytB2 Rv1110	Essential	Increased	2.710473537	3.846191936	6.556665473	10	42.1	36.297	0	61.329	763100000	184	4-hydroxy-3-methylbut-2-enyl diphosphate reductase 2 (HDR 2)
Intermediary metabolism and respiration	I6YGL1	Rv3591c	Non-Essential	Increased	2.680040359	3.895699602	6.575739961	9	46.3	28.542	0	124.8	778130000	161	Possible hydrolase
Uncharacterized protein	I6XF60	Rv2731	Non-Essential	Increased	2.617456436	2.331112033	4.948568469	22	56.4	49.795	0	323.31	4056600000	403	Conserved alanine and arginine rich protein
Uncharacterized protein	O53531	Rv2257c	Non-Essential	Increased	2.52463007	5.061343775	7.585973845	9	56.6	28.385	0	95.268	593810000	116	Conserved protein
Lipid metabolism	O86318	accD2 Rv0974c	Non-Essential	Increased	2.503325939	2.483698746	4.987024685	11	27.6	56.256	0	67.036	544510000	116	Probable biotin-dependent acyl-coenzyme A carboxylase beta2 subunit
Virulence, detoxification, adaptation	P9WG35	tpx Rv1932	Non-Essential	Increased	2.483623981	3.814202045	6.297826026	6	69.7	16.896	0	323.31	10137000000	382	Thiol peroxidase (Tpx)
Intermediary metabolism and respiration	P9WMP3	hemC Rv0510	Essential	Increased	2.478846073	5.26015399	7.739000063	10	40.8	31.938	0	97.706	849500000	157	Porphobilinogen deaminase (PBG)
Intermediary metabolism and respiration	P9WMR7	Rv1341	Non-Essential	Increased	2.370626926	6.5817477	8.952374626	13	40	48.142	0	174.08	2269300000	284	dITP/XTP pyrophosphatase
Lipid metabolism	P9WQP1	fbpB Rv1886c	Growth-Advantage	Increased	2.298300743	3.651520066	5.949820809	5	21.8	34.58	0	290.36	10531000000	319	Diacylglycerol acyltransferase/mycolyltransferase Ag85B (FbpB)
Intermediary metabolism and respiration	L0TC47	lipV Rv3203	Non-Essential	Increased	2.286476612	5.038909798	7.32538641	11	60.2	27.868	0	132.66	1003900000	106	Lipase LipV
Intermediary metabolism and respiration	I6X9R9	aldA Rv0768	Non-Essential	Increased	2.272338867	4.253093685	6.525432552	7	21.7	51.183	0	86.869	357980000	49	Probable aldehyde dehydrogenase NAD dependent AldA
Regulatory proteins	P9WMC1	ethR Rv3855	Non-Essential	Increased	2.260409832	3.924594972	6.185004804	5	31.9	23.756	0	63.392	529830000	93	HTH-type transcriptional regulator EthR
Lipid metabolism	P9WQP3	fbpA Rv3804c	Non-Essential	Increased	2.249478817	4.767489826	7.016968643	11	45	35.686	0	323.31	22480000000	858	Diacylglycerol acyltransferase/mycolyltransferase Ag85A (FbpA)
Information pathways	P9WIP7	lsr2 Rv3597c	Growth-Defect	Increased	2.198446274	5.312577233	7.511023507	5	30.4	12.098	0	88.525	3275100000	512	Nucleoid-associated protein Lsr2
Intermediary metabolism and respiration	P9WMM5	hisA Rv1603	Essential	Increased	2.193735123	2.400166902	4.593902025	13	75	25.632	0	289.37	2168700000	306	Phosphoribosyl isomerase A [1-(5-phosphoribosyl)-5-[(5-phosphoribosylamino)methylideneamino] imidazole-4-carboxamide isomerase]
Lipid metabolism	P9WQD5	tesA Rv2928	Non-Essential	Increased	2.165913582	4.851389712	7.017303294	19	76.2	29.151	0	209.19	9833200000	709	Thioesterase TesA
Information pathways	P9WH53	rpsP Rv2909c	Growth-Defect	Increased	2.142980576	4.7142933	6.857273876	12	75.3	17.437	0	323.31	39693000000	944	30S ribosomal protein S16
Information pathways	P9WHG1	prfB Rv3105c	Essential	Increased	2.130598545	5.647978035	7.77857658	18	56.1	41.473	0	319.52	4657400000	415	Peptide chain release factor 2 (RF-2)
Intermediary metabolism and respiration	P9WG59	thrC Rv1295	Essential	Increased	2.116921425	3.467989094	5.584910519	18	86.9	37.321	0	323.31	8237200000	547	Threonine synthase (TS)
Intermediary metabolism and respiration	P9WP27	aao Rv1905c	Non-Essential	Increased	2.116910934	3.565089537	5.682000471	13	58.4	34.108	0	85.226	980770000	127	Probable D-amino-acid oxidase (DAAO)
Intermediary metabolism and respiration	P71805	Rv1377c	Non-Essential	Increased	2.064102173	2.517913981	4.582016154	7	44.3	22.815	0	79.441	574190000	108	Putative transferase
Intermediary metabolism and respiration	P9WIM1	pafB Rv2096c	Non-Essential	Increased	2.033325195	2.791835724	4.825160919	10	46.4	35.3	0	112.99	635160000	114	Protein PafB (Proteasome accessory factor B)
Intermediary metabolism and respiration	P96826	Rv0149	Growth-Advantage	Increased	2.009970665	2.056853514	4.066824179	7	41	33.278	0	125.05	1789100000	197	Possible quinone oxidoreductase (NADPH:quinone oxidoreductase) (Zeta-crystallin)
Intermediary metabolism and respiration	P9WHL3	pyrC Rv1381	Essential	Increased	2.00991869	2.723351047	4.733269737	11	33	45.192	0	103.28	1420200000	207	Dihydroorotase (DHOase)
Intermediary metabolism and respiration	P9WKZ7	Rv3400	Non-Essential	Increased	2.005986691	3.628477806	5.634464497	17	66.4	28.227	0	161.22	3860700000	245	Uncharacterized protein Rv3400
Lipid metabolism	I6YBZ8	htdY Rv3389c	Non-Essential	Increased	1.996554375	6.360019791	8.356574166	19	72.4	30.296	0	323.31	13120000000	776	3-hydroxyacyl-thioester dehydratase Y
Information pathways	P9WHC7	rplA Rv0641	Essential	Increased	1.992814064	6.23640838	8.229222444	13	63.8	24.756	0	323.31	38635000000	1179	50S ribosomal protein L1
Regulatory proteins	P9WHR7	lexA Rv2720	Growth-Defect	Increased	1.979640961	2.905286303	4.884927264	8	50.4	24.841	0	179.37	1591000000	211	LexA repressor
Intermediary metabolism and respiration	O07427	Rv0183	Non-Essential	Increased	1.973363876	4.335331492	6.308695368	15	69.9	30.261	0	323.31	11372000000	711	Monoacylglycerol lipase (MGL)
Information pathways	P9WHG3	prfA Rv1299	Essential	Increased	1.963119984	3.547151165	5.510271149	7	33.9	39.036	0	174.69	603890000	98	Peptide chain release factor 1 (RF-1)
Uncharacterized protein	O07738	Rv1894c	Non-Essential	Increased	1.955036163	2.049304638	4.004340801	11	34.8	40.185	0	84.959	1471900000	150	NMO domain-containing protein
Information pathways	P9WHW3	ppiA Rv0009	Non-Essential	Increased	1.953566074	4.227682742	6.181248816	8	74.7	19.239	0	323.31	7018300000	475	Peptidyl-prolyl cis-trans isomerase A
Cell wall and cell processes	P9WJD5	espD Rv3614c	Non-Essential	Increased	1.922756195	2.767616643	4.690372838	6	40.8	19.834	0	88.008	805010000	88	ESX-1 secretion-associated protein EspD
Lipid metabolism	P96202	ppsC Rv2933	Non-Essential	Increased	1.922693253	5.51624264	7.438935893	36	24.9	230.62	0	191.02	1787100000	321	Phenolphthiocerol/phthiocerol polyketide synthase subunit C
Intermediary metabolism and respiration	P9WIU1	pdxH Rv2607	Non-Essential	Increased	1.921628952	3.112992196	5.034621148	12	68.8	25.186	0	186.59	1927600000	258	Pyridoxine 5'-phosphate oxidase (PNP oxidase)
Information pathways	P9WH31	rpsF Rv0053	Essential	Increased	1.868440151	7.241812412	9.110252563	7	75	10.935	0	87.952	7913600000	323	30S ribosomal protein S6
Uncharacterized protein	O69667	Rv3699	Non-Essential	Increased	1.858729839	4.279913189	6.138643028	8	64.4	24.998	0	272.88	3091800000	229	Conserved protein
Intermediary metabolism and respiration	O50433	fdxC Rv1177	Essential	Increased	1.858028412	4.575886042	6.433914454	5	38.9	11.839	0	87.172	1026900000	123	Ferredoxin
Lipid metabolism	P9WQN9	fbpC Rv0129c	Non-Essential	Increased	1.845247746	3.790455823	5.635703569	10	35.6	36.771	0	118.43	7387400000	399	Diacylglycerol acyltransferase/mycolyltransferase Ag85C (FbpC)
Intermediary metabolism and respiration	Q6MX51	Rv0296c	Non-Essential	Increased	1.818379879	2.672392588	4.490772467	21	64.3	51.845	0	222.49	2846700000	326	Probable sulfatase
Regulatory proteins	P9WMH1	ideR Rv2711	Essential	Increased	1.813466072	5.186402693	6.999868765	12	70.4	25.233	0	253.77	3942400000	252	Iron-dependent repressor IdeR
Uncharacterized protein	O07196	Rv2694c	Non-Essential	Increased	1.808377266	6.289433758	8.097811024	9	66.4	13.57	0	174.26	1063300000	98	Conserved protein
Intermediary metabolism and respiration	P0CG96	sseC1	Growth-Advantage	Increased	1.805895329	4.945687316	6.751582645	7	92	10.165	0	243.5	7101400000	436	Uncharacterized protein Rv3118
Intermediary metabolism and respiration	P9WPQ9	bfr Rv1876	Growth-Advantage	Increased	1.793398857	3.118854329	4.912253186	10	81.8	18.34	0	323.31	5975300000	376	Bacterioferritin (BFR)
Intermediary metabolism and respiration	I6XHH5	hsaE Rv3536c	Non-Essential	Increased	1.779067993	2.175102916	3.954170909	9	47.1	27.891	0	137.09	1097900000	106	Probable hydratase
Information pathways	P9WHB7	rplX Rv0715	Essential	Increased	1.712803841	4.436627796	6.149431637	8	70.5	11.475	0	95.429	18183000000	487	50S ribosomal protein L24
Intermediary metabolism and respiration	P9WL31	Rv2895c	Non-Essential	Increased	1.693223476	2.866915083	4.560138559	11	50.9	30.602	0	121.8	1953200000	163	Uncharacterized protein Rv2895c
Lipid metabolism	P9WQE3	Rv2934	Non-Essential	Increased	1.678764343	2.219958781	3.898723124	23	16.2	193.31	0	121.58	1780100000	182	Phenolphthiocerol/phthiocerol polyketide synthase subunit D (PpsD)
Intermediary metabolism and respiration	P9WMM3	hisF Rv1605	Essential	Increased	1.659536362	2.478543245	4.138079607	11	56.6	27.221	0	62.854	1055200000	170	Imidazole glycerol phosphate synthase subunit HisF
Intermediary metabolism and respiration	L7N690	amiB1 Rv3306c	Non-Essential	Increased	1.641599178	2.296105655	3.937704833	11	36.8	40.74	0	67.803	995260000	97	Peptidase M20 domain-containing protein 2
Information pathways	P9WQ13	end nfo Rv0670	Non-Essential	Increased	1.630804062	6.634233496	8.265037558	13	61.9	26.845	0	221.36	3339000000	312	Probable endonuclease 4 (EC 3.1.21.2) (Endodeoxyribonuclease IV) (Endonuclease IV)
Intermediary metabolism and respiration	P9WK35	ribC Rv1412	Non-Essential	Increased	1.629113197	4.77126436	6.400377557	8	51.7	21.32	0	192.06	1514200000	183	Riboflavin synthase (RS)
Lipid metabolism	I6X9J0	fadE8 Rv0672	Non-Essential	Increased	1.628101349	2.704342869	4.332444218	19	47	58.534	0	238.95	3791900000	364	Probable acyl-CoA dehydrogenase FadE8
Intermediary metabolism and respiration	P9WJQ9	mobA Rv2453c	Non-Essential	Increased	1.625932693	3.938084769	5.564017462	6	43.8	21.084	0	85.717	700480000	98	Probable molybdenum cofactor guanylyltransferase (MoCo guanylyltransferase)
Intermediary metabolism and respiration	P9WP55	cysK1 Rv2334	Non-Essential	Increased	1.613677502	4.960608703	6.574286205	12	56.5	32.752	0	104.78	2653600000	286	O-acetylserine sulfhydrylase (OAS sulfhydrylase) (OASS)
Intermediary metabolism and respiration	P9WK17	glcB Rv1837c	Essential	Increased	1.607802868	7.799451565	9.407254433	40	55.9	80.402	0	323.31	52983000000	2042	Malate synthase G
Lipid metabolism	O33194	Rv1692	Non-Essential	Increased	1.606084347	3.108531692	4.714616039	10	40.5	37.01	0	103.68	1242800000	128	D-glycerol 3-phosphate phosphatase (D,L-glycerol 3-phosphate phosphatase) (G3P phosphatase)
Intermediary metabolism and respiration	P9WPJ7	canA Rv1284	Non-Essential	Increased	1.602204323	6.230030184	7.832234507	10	67.5	18.189	0	200.5	5047400000	300	Beta-carbonic anhydrase 1 (mtCA 1)
Intermediary metabolism and respiration	O53554	ilvX Rv3509c	Non-Essential	Increased	1.5879035	7.701533788	9.289437288	25	64.7	52.072	0	323.31	12425000000	918	Putative acetolactate synthase large subunit IlvX (ALS)
Intermediary metabolism and respiration	P9WHF5	sseB Rv2291	Non-Essential	Increased	1.578984261	2.549066797	4.128051058	6	42.6	29.4	0	80.367	745990000	123	Putative thiosulfate sulfurtransferase SseB
Virulence, detoxification, adaptation	P9WNV9	dnaJ1 Rv0352	Non-Essential	Increased	1.575582504	7.520792877	9.096375381	22	66.6	41.345	0	323.31	7297300000	748	Chaperone protein DnaJ 1
Lipid metabolism	O33332	ltp1 Rv2790c	Non-Essential	Increased	1.567272186	7.292147958	8.859420144	9	40.1	42.904	0	289.27	1012100000	153	Probable lipid-transfer protein Ltp1
Uncharacterized protein	P9WFN1	Rv2140c	Non-Essential	Increased	1.552670956	5.113639421	6.666310377	9	71.6	18.634	0	201.56	5436100000	261	UPF0098 protein Rv2140c

Table S1. **CyC_{31yne} target proteins identified in *M. tb* mc²6230 culture through CC-ABPP by LC-ESI-MS/MS analysis. Only positive hits with a *p*-value <0.01 and a fold-change ≥1.2 are reported.**

Pathway/Functional category	Protein IDs	Gene names	Essentiality	Change	Fold Change (log2)	-LOG(p-value)	Manhattan distance	Unique peptides	Unique sequence coverage [%]	Mol. weight [kDa]	Q-value	Score	Intensity	MS/MS count	Protein names
Intermediary metabolism and respiration	P9WKG3	gcpE Rv2868c	Essential	Increased	1.547883511	7.032795747	8.580679258	19	72.4	40.482	0	323.31	14215000000	965	4-hydroxy-3-methylbut-2-en-1-yl diphosphate synthase (flavodoxin)
Uncharacterized protein	O06310	Rv0360c	Non-Essential	Increased	1.537196159	3.965280815	5.502476974	6	41.4	15.329	0	77.241	1665900000	181	Conserved protein
Intermediary metabolism and respiration	P9WG95	ilvA Rv1559	Essential	Increased	1.528332233	4.92820069	6.456532923	13	34.7	45.04	0	247.37	2919000000	319	L-threonine dehydratase biosynthetic IlvA
Uncharacterized protein	I6Y946	Rv0925c	Non-Essential	Increased	1.522557735	5.705353404	7.227911139	11	62	26.944	0	217.91	5103700000	414	Conserved protein
Intermediary metabolism and respiration	P9WQA5	Rv2971	Essential	Increased	1.517558575	6.837123403	8.354681978	16	77.3	30.364	0	323.31	29840000000	1139	Uncharacterized oxidoreductase Rv2971
Intermediary metabolism and respiration	I6X8S7	Rv0223c	Non-Essential	Increased	1.517125607	4.056449975	5.573575582	10	28.5	51.157	0	129.54	1246300000	139	Probable aldehyde dehydrogenase
Intermediary metabolism and respiration	P9WJH7	ndkA Rv2445c	Non-Essential	Increased	1.503061771	5.959943148	7.463004919	7	83.8	14.507	0	240.09	3170100000	420	Nucleoside diphosphate kinase (NDK)
Intermediary metabolism and respiration	P9WP51	cbs Rv1077	Non-Essential	Increased	1.498043537	5.917974021	7.416017558	19	69	48.635	0	323.31	7763600000	681	Putative cystathionine beta-synthase Rv1077
Information pathways	P9WFC7	uvrB Rv1633	Non-Essential	Increased	1.490061283	3.370636482	4.860697765	22	33.2	80.406	0	96.106	1508500000	243	UvrABC system protein B (Protein UvrB) (Excinuclease ABC subunit B)
Intermediary metabolism and respiration	P9WHF9	cysA1 Rv3117	Growth-Advantage	Increased	1.482728958	7.835196495	9.317925453	32	92.1	31.014	0	323.31	85994000000	2304	Putative thiosulfate sulfurtransferase (Rhodanese-like protein)
Lipid metabolism	P9WNG3	fabH Rv0533c	Non-Essential	Increased	1.48261261	4.13547188	5.61808449	10	58.2	34.872	0	139.14	1236900000	127	3-oxoacyl-[acyl-carrier-protein] synthase 3 (KAS III) (MtFabH)
Information pathways	P9WNM1	tsf Rv2889c	Essential	Increased	1.481397152	7.704732199	9.186129351	24	79.3	28.754	0	323.31	48000000000	1909	Elongation factor Ts (EF-Ts)
Intermediary metabolism and respiration	P9WIT1	Rv2280	Non-Essential	Increased	1.480064392	6.84111639	8.321180782	15	59.5	48.051	0	323.31	13720000000	821	Uncharacterized FAD-linked oxidoreductase Rv2280
Intermediary metabolism and respiration	P9WPC5	clpP1 Rv2461c	Essential	Increased	1.47578907	4.09763756	5.57342663	10	60.5	21.707	0	323.31	20440000000	656	ATP-dependent Clp protease proteolytic subunit 1 (Endopeptidase Clp 1)
Lipid metabolism	I6X8D2	pks13 Rv3800c	Essential	Increased	1.475198746	3.928367502	5.403566248	87	74.6	186.44	0	323.31	95999000000	4822	Polyketide synthase Pks13
Virulence, detoxification, adaptation	P9WIE1	bcp2 Rv2521	Non-Essential	Increased	1.47120142	6.96329132	8.43449274	12	75.8	17.077	0	323.31	5389000000	375	Putative peroxiredoxin Rv2521
Intermediary metabolism and respiration	P9WHH1	trxB2 Rv3913	Essential	Increased	1.468574524	7.125027814	8.593602338	14	61.8	35.643	0	323.31	5188100000	586	Thioredoxin reductase (TR)
Virulence, detoxification, adaptation	P9WQB7	ahpC Rv2428	Non-Essential	Increased	1.459630966	4.307575107	5.767206073	8	56.4	21.566	0	133.35	762220000	114	Alkyl hydroperoxide reductase C (MtAhpC)
Intermediary metabolism and respiration	I6Y276	Rv2993c	Non-Essential	Increased	1.435403347	5.1571145	6.592517847	9	65.3	25.341	0	155.8	3613100000	294	Possible 2-hydroxyhepta-2,4-diene-1,7-dioate isomerase (HHDD isomerase)
Intermediary metabolism and respiration	P9WG67	Rv3914	Non-Essential	Increased	1.425992489	2.705424791	4.13141728	5	62.9	12.544	0	107.01	1654100000	128	Thioredoxin (Trx) (MPT46)
Virulence, detoxification, adaptation	P9WFD9	Rv2028c	Non-Essential	Increased	1.404054165	3.082649002	4.486703167	11	62	29.441	0	121.72	1871700000	124	Universal stress protein Rv2028c (USP Rv2028c)
Uncharacterized protein	P9WJA3	hrp1 Rv2626c	Non-Essential	Increased	1.401695728	2.62444789	4.026143618	7	69.2	15.518	0	87.407	2293300000	214	Hypoxic response protein 1 (HRP1)
Intermediary metabolism and respiration	P9WP85	cobT Rv2207	Non-Essential	Increased	1.389843941	3.793270542	5.183114483	7	23.8	36.411	0	110.37	942450000	153	Nicotinate-nucleotide--dimethylbenzimidazole phosphoribosyltransferase (NN:DBI PRT)
Information pathways	P9WH51	rpsQ Rv0710	Essential	Increased	1.38792181	4.405456062	5.793377872	10	58.5	14.741	0	188.96	25720000000	718	30S ribosomal protein S17
Uncharacterized protein	P9WMN5	Rv2204c	Non-Essential	Increased	1.384844303	6.026899374	7.411743677	9	93.2	12.544	0	181.59	2364000000	308	Protein Rv2204c
Intermediary metabolism and respiration	P9WFE3	ureG Rv1852	Non-Essential	Increased	1.382813454	6.024638147	7.407451601	9	47.3	23.348	0	215.24	1507400000	139	Urease accessory protein UreG
Intermediary metabolism and respiration	O53311	Rv3161c	Non-Essential	Increased	1.382339954	7.204186976	8.58652693	18	59.2	42.504	0	323.31	12632000000	749	Possible dioxygenase
Virulence, detoxification, adaptation	P9WPE7	groEL2 Rv0440	Essential	Increased	1.373822212	4.548935401	5.922757613	51	84.8	56.726	0	323.31	8.3966E+11	8413	Chaperonin GroEL 2
Uncharacterized protein	O50398	Rv3369	Non-Essential	Increased	1.367909431	2.39504372	3.762953151	4	29.2	15.718	0	68.22	1642200000	81	Conserved protein
Intermediary metabolism and respiration	P9WQ97	amiB2 Rv1263	Non-Essential	Increased	1.364027977	4.300808313	5.66483629	21	65.2	49.08	0	206.39	2613300000	409	Putative amidase AmiB2
Regulatory proteins	P9WGL7	Rv3143	Non-Essential	Increased	1.360807896	2.223415073	3.584222969	5	63.9	14.386	0	69.438	971600000	97	Uncharacterized response regulatory protein Rv3143
Information pathways	P9WNN1	tuf Rv0685	Essential	Increased	1.356069565	6.209525085	7.56559465	29	86.4	43.593	0	323.31	1.3441E+11	3465	Elongation factor Tu (EF-Tu)
Lipid metabolism	O53422	fadA3 Rv1074c	Growth-Advantage	Increased	1.353399754	5.756874235	7.110273989	22	75.6	42.655	0	323.31	35707000000	1576	Probable beta-ketoacyl CoA thiolase FadA3
Intermediary metabolism and respiration	P9WQA3	fba Rv0363c	Essential	Increased	1.352650166	6.840715864	8.19336603	24	82.3	36.544	0	323.31	24083000000	1312	Fructose-bisphosphate aldolase (FBP aldolase) (FBPA)
Information pathways	P9WGZ1	rpoA Rv3457c	Essential	Increased	1.348324299	7.016413319	8.364737618	25	77.5	37.706	0	323.31	41301000000	1601	DNA-directed RNA polymerase subunit alpha (RNAP subunit alpha)
Intermediary metabolism and respiration	P9WQB9	adhD Rv3086	Non-Essential	Increased	1.341504574	5.969908309	7.311412883	9	40.5	38.341	0	253.9	2640100000	287	Putative alcohol dehydrogenase D
Intermediary metabolism and respiration	O86374	Rv3257c	Essential	Increased	1.340111527	2.221507545	3.561819072	10	34.4	49.04	0	77.754	1173900000	161	Probable phosphomannomutase PmmA (PMM) (Phosphomannose mutase)
Information pathways	P9WHD3	rplQ Rv3456c	Growth-Defect	Increased	1.340217113	3.853778426	5.193995539	15	72.2	19.475	0	323.31	34848000000	1004	50S ribosomal protein L17
Uncharacterized protein	I6X540	Rv2683	Non-Essential	Increased	1.338754654	5.242647311	6.581401965	7	51.5	17.729	0	87.011	1212700000	90	Conserved protein
Intermediary metabolism and respiration	P9WNX5	asd Rv3708c	Growth-Defect	Increased	1.332257748	5.912138618	7.244396366	16	59.1	36.23	0	323.31	11487000000	664	Aspartate-semialdehyde dehydrogenase (ASA dehydrogenase) (ASADH)
Cell wall and cell processes	P9WQN5	mpa Rv2115c	Non-Essential	Increased	1.330803871	5.589252653	6.920056524	29	59.3	67.4	0	323.31	8745700000	834	Proteasome-associated ATPase (ARC) (Mycobacterial proteasome ATPase)
Cell wall and cell processes	P9WMU1	wag31 ag84 Rv2145c	Essential	Increased	1.328158855	4.240071653	5.568230508	9	44.2	28.277	0	120.57	989000000	178	Cell wall synthesis protein Wag31 (Antigen 84)
Intermediary metabolism and respiration	P9WHL7	purL Rv0803	Essential	Increased	1.327511311	5.25040329	6.577914601	36	54.4	80.801	0	323.31	12662000000	874	Phosphoribosylformylglycinamidine synthase subunit PurL (FGAM synthase)
Intermediary metabolism and respiration	O53533	mscR Rv2259	Non-Essential	Increased	1.306638241	3.439092153	4.745730394	9	29.6	37.888	0	85.738	1801000000	237	S-nitrosomycothiol reductase MscR
Information pathways	P9WHD7	rplO Rv0723	Uncertain	Increased	1.30601263	4.170193387	5.476206017	8	50.7	15.533	0	174.25	13757000000	606	50S ribosomal protein L15
Intermediary metabolism and respiration	P9WIK3	cysH Rv2392	Growth-Defect	Increased	1.301439285	4.994230343	6.295669628	11	50	27.423	0	112.54	2538900000	409	Adenosine 5'-phosphosulfate reductase (APS reductase)
Intermediary metabolism and respiration	P9WIK1	nadA Rv1594	Essential	Increased	1.281888008	8.948527292	10.2304153	15	70.5	37.408	0	323.31	7085300000	614	Quinolinate synthase
Cell wall and cell processes	P96281	Rv0435c	Non-Essential	Increased	1.276519299	4.248635678	5.525154977	23	48.5	75.345	0	251.75	3672900000	386	Putative conserved ATPase
Lipid metabolism	P9WFI9	Rv0281	Non-Essential	Increased	1.27432251	5.228012768	6.502335278	15	57.3	32.998	0	284.8	7686200000	631	Putative S-adenosyl-L-methionine-dependent methyltransferase Rv0281
Information pathways	P9WI57	pnp Rv2783c	Essential	Increased	1.267739296	5.981150924	7.24889022	36	56.2	79.734	0	323.31	37869000000	1928	Polyribonucleotide nucleotidyltransferase
Uncharacterized protein	P9WME3	Rv1287	Non-Essential	Increased	1.264708519	2.003331719	3.268040238	4	49.1	17.209	0	67.241	343050000	57	Putative HTH-type transcriptional regulator Rv1287
Intermediary metabolism and respiration	P95034	Rv0688	Non-Essential	Increased	1.264598846	6.164718633	7.429317479	17	54.2	43.017	0	284.05	6941200000	574	Putative ferredoxin reductase
Intermediary metabolism and respiration	P9WQC5	adhC adh Rv3045	Non-Essential	Increased	1.262573242	5.400468923	6.663042165	17	55.8	37.075	0	323.31	20747000000	1030	NADP-dependent alcohol dehydrogenase C
Uncharacterized protein	O06578	Rv1126c	Non-Essential	Increased	1.255358219	2.58944815	3.844806369	7	47.8	22.197	0	117.77	431710000	82	Conserved protein
Intermediary metabolism and respiration	P9WNW9	hisD Rv1599	Essential	Increased	1.254595757	6.28154398	7.536139737	10	35.6	46.302	0	122.43	2097500000	213	Histidinol dehydrogenase (HDH)
Intermediary metabolism and respiration	P9WNH5	hsaD Rv3569c	Non-Essential	Increased	1.252779961	2.962565901	4.215345862	15	54	31.875	0	104.93	2017400000	321	4,5:9,10-diseco-3-hydroxy-5,9,17-trioxoandrosta-1(10),2-diene-4-oate hydrolase (MCP hydrolase)
Intermediary metabolism and respiration	P9WQH7	accD5 Rv3280	Essential	Increased	1.246607304	6.625911367	7.872518671	27	56.4	59.354	0	323.31	33559000000	2199	Biotin-dependent acetyl-/propionyl-coenzyme A carboxylase beta5 subunit (Acetyl-CoA carboxylase) (ACC)
Intermediary metabolism and respiration	P9WNG7	fixA Rv3029c	Growth-Defect	Increased	1.236661434	4.946724591	6.183386025	14	67.7	28.08	0	323.31	8521700000	566	Electron transfer flavoprotein subunit beta (Beta-ETF)
Information pathways	P9WH85	rplD Rv0702	Essential	Increased	1.236468792	4.398404264	5.634873056	10	52	23.743	0	272.24	26433000000	805	50S ribosomal protein L4
Intermediary metabolism and respiration	P9WQB3	leuA Rv3710	Essential	Increased	1.23295087	6.442831257	7.675781944	35	73.6	70.113	0	323.31	18661000000	1326	2-isopropylmalate synthase
Information pathways	P9WH79	rplI Rv0056	Non-Essential	Increased	1.225336552	5.426639909	6.651976461	9	44.7	16.169	0	164.51	7094000000	311	50S ribosomal protein L9
Intermediary metabolism and respiration	P9WM23	Rv1333	Non-Essential	Increased	1.224698544	2.025487953	3.250186497	4	15.4	33.952	0	62.119	192790000	18	Uncharacterized aminopeptidase Rv1333
Uncharacterized protein	P9WL63	Rv2629	Non-Essential	Increased	1.220798969	6.210431805	7.431230774	22	75.9	40.839	0	323.31	6398200000	649	Uncharacterized protein Rv2629
Information pathways	P9WH43	rpsA Rv1630	Essential	Increased	1.218367577	4.048168339	5.266535916	29	73	53.201	0	323.31	23602000000	1298	30S ribosomal protein S1
Cell wall and cell processes	P9WG55	tig Rv2462c	Non-Essential	Increased	1.217750549	4.030911501	5.24866205	16	43.3	50.615	0	244.83	3386400000	507	Trigger factor (TF)
Lipid metabolism	O53901	pks5 Rv1527c	Non-Essential	Increased	1.213652611	4.170032119	5.38368473	27	17.3	223.89	0	138.53	1299100000	271	Mycocerosic acid synthase-like polyketide synthase (MAS-like PKS)
Intermediary metabolism and respiration	P9WNE5	bfrB Rv3841	Non-Essential	Increased	1.212513924	3.691481644	4.903995568	12	76.2	20.442	0	321.27	40922000000	738	Ferritin BfrB
Intermediary metabolism and respiration	P9WG81	folD Rv3356c	Essential	Increased	1.208316803	7.413240345	8.621557148	18	66.9	29.483	0	266.22	5560700000	562	Bifunctional protein FolD
Intermediary metabolism and respiration	P9WMS7	guaA Rv3396c	Essential	Increased	1.206840992	5.940571627	7.147412619	21	57.5	56.059	0	323.31	9469900000	752	GMP synthase [glutamine-hydrolyzing]
Intermediary metabolism and respiration	P9WNL1	eno Rv1023	Growth-Defect	Increased	1.205562592	6.290448714	7.496011306	17	56.6	44.961	0	323.31	18393000000	828	Enolase
Intermediary metabolism and respiration	P9WHS9	dapE Rv1202	Essential	Increased	1.200644493	3.007239638	4.207884131	12	51.1	37.273	0	170.99	2205600000	160	Putative succinyl-diaminopimelate desuccinylase DapE (SDAP desuccinylase)

Table S2. **CyC_{32yne} target proteins identified in *M. tb* mc²6230 culture through CC-ABPP by LC-ESI-MS/MS analysis. Only positive hits with a *p*-value <0.01 and a fold-change ≥1.2 are reported.**

Functional category	Protein IDs	Gene names	Essentiality	Change	Fold change (log2)	-LOG(p-value)	Manhattan distance	Unique peptides	Unique sequence coverage [%]	Mol. weight [kDa]	Q-value	Score	Intensity	MS/MS count	Protein names
Cell wall and cell processes	P9WP43	cut7 Rv1984c	Growth-Advantage	Increased	5.864572525	4.976765729	10.84133825	4	30.9	21.782	0	249.99	1758900000	94	Carboxylesterase Culp1
Intermediary metabolism and respiration	P71668	lipI Rv1400c	Non-Essential	Increased	5.414610863	3.563300813	8.977911676	11	62.8	34.052	0	196.79	3692100000	161	Esterase LipI
Intermediary metabolism and respiration	P9WKL5	htrn Rv0560c	Non-Essential	Increased	5.325745583	3.917569011	9.243314594	11	81.3	25.945	0	236.39	1496400000	185	2-heptyl-1-hydroxyquinolin-4(1H)-one methyltransferase (HQNO methyltransferase)
Intermediary metabolism and respiration	P9WKB7	nlhH lipH Rv1399c	Non-Essential	Increased	4.446006775	5.499184478	9.945191253	7	30.1	33.906	0	70.833	884740000	168	Carboxylesterase NlhH
Intermediary metabolism and respiration	P9WIV5	nuoE Rv3149	Non-Essential	Increased	4.048645496	5.788751063	9.837396559	8	47.2	27.197	0	104.83	1665600000	169	NADH-quinone oxidoreductase subunit E (NDH-1 subunit E)
Uncharacterized protein	O53672	Rv0250c	Non-Essential	Increased	3.57204628	5.828411162	9.400457442	5	63.9	10.896	0	109.29	1183800000	147	Uncharacterized protein Rv0250c
Information pathways	P9WGH9	sigH rpoE Rv3223c	Non-Essential	Increased	3.484445095	3.521156304	7.005601399	9	64.8	24.225	0	96.283	719550000	153	ECF RNA polymerase sigma factor SigH (ECF sigma factor SigH)
Intermediary metabolism and respiration	P9WKD7	rpiB Rv2465c	Essential	Increased	3.390566349	2.496127297	5.886693646	10	75.3	17.277	0	160.26	2766500000	285	Ribose-5-phosphate isomerase B (Phosphoriboisomerase B)
Intermediary metabolism and respiration	P9WN21	glpX Rv1099c	Non-Essential	Increased	3.308312416	4.842266037	8.150578453	19	62.7	38.084	0	323.31	6253200000	412	Fructose-1,6-bisphosphatase class 2 (FBPase class 2)
Uncharacterized protein	I6YA17	Rv2699c	Essential	Increased	3.229794025	5.185957329	8.415751354	4	75	10.916	0	109.48	833630000	120	Uncharacterized protein
Information pathways	P9WNM9	Rv0120c	Non-Essential	Increased	3.222065449	2.78636621	6.008431659	21	37.8	75.63	0	120.23	1890300000	217	Elongation factor G-like protein
Regulatory proteins	P9WMC1	ethR etaR Rv3855	Non-Essential	Increased	3.135175705	4.211863961	7.347039666	5	31.9	23.756	0	63.392	529830000	93	HTH-type transcriptional regulator EthR
Cell wall and cell processes	O53149	Rv1458c	Growth-Defect	Increased	3.086162567	3.99664952	7.082812087	4	15.3	33.758	0	79.719	447690000	56	Probable unidentified antibiotic-transport ATP-binding protein ABC transporter
Uncharacterized protein	O06154	Rv1637c	Non-Essential	Increased	3.039237499	3.131580213	6.170817712	7	43.6	27.936	0	82.99	1265900000	180	Conserved protein
Uncharacterized protein	P71990	Rv1732c	Non-Essential	Increased	3.018773556	3.387270693	6.406044249	8	43.4	19.399	0	154.27	1498800000	244	Conserved protein
Information pathways	P9WHJ7	rbfA Rv2838c	Non-Essential	Increased	2.98382616	2.509295882	5.493122042	8	72.7	18.998	0	214.51	1253800000	103	Ribosome-binding factor A
Uncharacterized protein	P9WFM1	Rv2230c	Non-Essential	Increased	2.90926981	2.507850159	5.417119969	12	50.4	39.597	0	84.339	1221400000	75	GTP cyclohydrolase 1 type 2 homolog
Uncharacterized protein	O07173	Rv0123	Non-Essential	Increased	2.887873173	4.632873926	7.520747099	7	65.6	13.623	0	144.29	817970000	79	Uncharacterized protein
Uncharacterized protein	P95198	Rv0390	Non-Essential	Increased	2.737447262	4.383440309	7.120887571	6	55.7	15.392	0	92.177	1119800000	154	Conserved protein
Cell wall and cell processes	P9WJD9	espB mtb48 Rv3881c	Growth-Advantage	Increased	2.71696806	6.48138069	9.19834875	18	58.5	47.593	0	323.31	4398200000	631	ESX-1 secretion-associated protein EspB (Antigen MTB48)
Intermediary metabolism and respiration	P9WKG1	ispH2 lytB2 Rv1110	Essential	Increased	2.681500912	3.894123485	6.575624397	10	42.1	36.297	0	61.329	763100000	184	4-hydroxy-3-methylbut-2-enyl diphosphate reductase 2 (HDR 2)
Intermediary metabolism and respiration	P9WIM1	pafB Rv2096c	Non-Essential	Increased	2.654271603	3.343304595	5.997576198	10	46.4	35.3	0	112.99	635160000	114	Protein PafB (Proteasome accessory factor B)
Uncharacterized protein	P9WL15	Rv2927c	Essential	Increased	2.565018654	2.049918425	4.614937079	12	49.4	26.986	0	166.95	2310800000	236	Uncharacterized protein Rv2927c
Uncharacterized protein	I6XF60	Rv2731	Non-Essential	Increased	2.555454254	2.283047447	4.838501701	22	56.4	49.795	0	323.31	4056600000	403	Conserved alanine and arginine rich protein
Lipid metabolism	O86318	accD2 Rv0974c	Non-Essential	Increased	2.507756233	2.492210086	4.999966319	11	27.6	56.256	0	67.036	544510000	116	Probable biotin-dependent acyl-coenzyme A carboxylase beta2 subunit
Intermediary metabolism and respiration	P9WMP3	hemC Rv0510	Essential	Increased	2.408607006	4.521314368	6.929921374	10	40.8	31.938	0	97.706	849500000	157	Porphobilinogen deaminase (PBG)
Information pathways	P9WGW3	ruvA Rv2593c	Growth-Defect	Increased	2.407989979	2.029823657	4.437813636	6	46.9	20.189	0	79.28	536630000	93	Holliday junction ATP-dependent DNA helicase RuvA
Virulence, detoxification, adaptation	P9WG35	tpx Rv1932	Non-Essential	Increased	2.321673393	3.582438751	5.904112144	6	69.7	16.896	0	323.31	10137000000	382	Thiol peroxidase (Tpx)
Information pathways	P9WH53	rpsP Rv2909c	Growth-Defect	Increased	2.225661278	5.735386148	7.961047426	12	75.3	17.437	0	323.31	39693000000	944	30S ribosomal protein S16
Uncharacterized protein	L7N684	Rv2141c	Non-Essential	Increased	2.22158289	4.341350569	6.562933459	13	40	48.142	0	174.08	2269300000	284	Conserved protein
Intermediary metabolism and respiration	P9WMM5	hisA Rv1603	Essential	Increased	2.204256058	2.406979582	4.61123564	13	75	25.632	0	289.37	2168700000	306	Phosphoribosyl isomerase A (1-(5-phosphoribosyl)-5-[(5-phosphoribosylamino)methylideneamino] imidazole-4-carboxamide isomerase)
Intermediary metabolism and respiration	P96826	Rv0149	Growth-Advantage	Increased	2.197679996	2.169883388	4.367563384	7	41	33.278	0	125.05	1789100000	197	Possible quinone oxidoreductase (NADPH:quinone oxidoreductase) (Zeta-crystallin)
Virulence, detoxification, adaptation	P9WIR3	Rv0577	Non-Essential	Increased	2.173385143	4.087804176	6.261189319	5	37.5	27.343	0	323.31	1751200000	208	Putative glyoxylase CFP32 (27 kDa antigen Cfp30B)
Intermediary metabolism and respiration	P9WG59	thrC Rv1295	Essential	Increased	2.160535336	3.473021069	5.633556405	18	86.9	37.321	0	323.31	8237200000	547	Threonine synthase (TS)
Information pathways	P9WHW3	ppiA Rv0009	Non-Essential	Increased	2.152626514	6.640704345	8.793330859	8	74.7	19.239	0	323.31	7018300000	475	Peptidyl-prolyl cis-trans isomerase A (PPIase A)
Information pathways	P9WH31	rpsF Rv0053	Essential	Increased	2.113023758	7.090426287	9.203450045	7	75	10.935	0	87.952	7913600000	323	30S ribosomal protein S6
Information pathways	P9WHG3	prfA Rv1299	Essential	Increased	2.10341835	3.730074243	5.833492593	7	33.9	39.036	0	174.69	603890000	98	Peptide chain release factor 1 (RF-1)
Information pathways	P9WIP7	lsr2 Rv3597c	Growth-Defect	Increased	2.099945545	5.604350557	7.704296102	5	30.4	12.098	0	88.525	32751000000	512	Nucleoid-associated protein Lsr2
Information pathways	P9WHC7	rplA Rv0641	Essential	Increased	2.09340477	6.024031504	8.117436274	13	63.8	24.756	0	323.31	38635000000	1179	50S ribosomal protein L1
Intermediary metabolism and respiration	P9WKZ7	Rv3400	Non-Essential	Increased	2.082166195	3.651430426	5.733596621	17	66.4	28.227	0	161.22	3860700000	245	Uncharacterized protein Rv3400
Intermediary metabolism and respiration	P9WP27	aao Rv1905c	Non-Essential	Increased	2.061562061	3.495350768	5.556912829	13	58.4	34.108	0	85.226	980770000	127	Probable D-amino-acid oxidase (DAAO) (DAMOX) (DAO)
Intermediary metabolism and respiration	P9WHL3	pyrC Rv1381	Essential	Increased	2.057533264	2.778904875	4.836438139	11	33	45.192	0	103.28	1420200000	207	Dihydroorotase (DHOase)
Information pathways	P9WHG1	prfB Rv3105c	Essential	Increased	2.049877167	5.451673159	7.501550326	18	56.1	41.473	0	319.52	4657400000	415	Peptide chain release factor 2 (RF-2)
Uncharacterized protein	O07738	Rv1894c	Non-Essential	Increased	2.041158676	2.099410363	4.140569039	11	34.8	40.185	0	84.959	1471900000	150	NMO domain-containing protein
Uncharacterized protein	O53531	Rv2257c	Non-Essential	Increased	2.038984776	6.151534879	8.190519655	9	56.6	28.385	0	95.268	593810000	116	Conserved protein
Intermediary metabolism and respiration	I6X9R9	aldA Rv0768	Non-Essential	Increased	2.038165092	3.165126357	5.203291449	7	21.7	51.183	0	86.869	357980000	49	Probable aldehyde dehydrogenase NAD dependent AldA (Aldehyde dehydrogenase [NAD+])
Lipid metabolism	I6Y8Z8	htdY Rv3389c	Non-Essential	Increased	2.005271435	6.136274264	8.141545699	19	72.4	30.296	0	323.31	13120000000	776	3-hydroxyacyl-thioester dehydratase Y (Enoyl-CoA hydratase 2)
Intermediary metabolism and respiration	P9WPQ9	bfr Rv1876	Growth-Advantage	Increased	1.977850914	3.300200785	5.278051699	10	81.8	18.34	0	323.31	5975300000	376	Bacterioferritin (BFR)
Regulatory proteins	P9WHR7	lexA Rv2720	Growth-Defect	Increased	1.973381042	2.86003511	4.833416152	8	50.4	24.841	0	179.37	1591000000	211	LexA repressor
Intermediary metabolism and respiration	P9WL31	Rv2895c	Non-Essential	Increased	1.964669704	3.202493371	5.167163075	11	50.9	30.602	0	121.8	1953200000	163	Uncharacterized protein Rv2895c
Intermediary metabolism and respiration	I6XHH5	hsaE Rv3536c	Non-Essential	Increased	1.955347061	2.370913113	4.326260174	9	47.1	27.891	0	137.09	1097900000	106	Probable hydratase
Intermediary metabolism and respiration	P71805	Rv1377c	Non-Essential	Increased	1.940551758	2.369532691	4.310084449	7	44.3	22.815	0	79.441	574190000	108	Putative transferase
Cell wall and cell processes	P9WJD5	espD Rv3614c	Non-Essential	Increased	1.92638731	2.674835707	4.601223017	6	40.8	19.834	0	88.008	805010000	88	ESX-1 secretion-associated protein EspD
Lipid metabolism	P9WQN9	fbpC Rv0129c	Non-Essential	Increased	1.921019077	3.207487644	5.128506721	10	35.6	36.771	0	118.43	7387400000	399	Diacylglycerol acyltransferase/mycolyltransferase Ag85C (DGAT)
Lipid metabolism	P96202	ppsC Rv2933	Non-Essential	Increased	1.866245747	5.771494551	7.637740298	36	24.9	230.62	0	191.02	1787100000	321	Phenolphthiocerol/phthiocerol polyketide synthase subunit C
Intermediary metabolism and respiration	P9WIJ1	pdxH Rv2607	Non-Essential	Increased	1.863657475	3.077927131	4.941584606	12	68.8	25.186	0	186.59	1927600000	258	Pyridoxine 5'-phosphate oxidase (PNP oxidase) (PNPOx)
Lipid metabolism	P9WHN9	php Rv0230c	Growth-Advantage	Increased	1.86165905	2.040712126	3.902371176	7	26.1	35.885	0	72.698	740750000	98	Phosphotriesterase homology protein
Intermediary metabolism and respiration	P9WQP5	devB Rv1445c	Non-Essential	Increased	1.853541374	2.649670198	4.503211572	7	34.8	25.804	0	80.965	896390000	94	6-phosphogluconolactonase (6PGL)
Uncharacterized protein	O69667	Rv3699	Non-Essential	Increased	1.841756344	4.294477413	6.136233757	8	64.4	24.998	0	272.88	3091800000	229	Conserved protein
Cell wall and cell processes	P71988	Rv1730c	Non-Essential	Increased	1.841503143	2.368620008	4.210123151	12	30.2	55.8	0	85.77	409610000	78	Possible penicillin-binding protein
Intermediary metabolism and respiration	I6YGL1	Rv3591c	Non-Essential	Increased	1.831168175	3.161366155	4.99253433	9	46.3	28.542	0	124.8	778130000	161	Possible hydrolase
Uncharacterized protein	P9WFN1	Rv2140c	Non-Essential	Increased	1.803235531	5.243319937	7.046555468	9	71.6	18.634	0	201.56	5436100000	261	UPF0098 protein Rv2140c
Intermediary metabolism and respiration	P9WJH7	ndkA ndk Rv2445c	Non-Essential	Increased	1.789879322	5.573120226	7.362999548	7	83.8	14.507	0	240.09	3170100000	420	Nucleoside diphosphate kinase (NDK) (NDKA) (NDP kinase)
Intermediary metabolism and respiration	Q6MX51	Rv0296c	Non-Essential	Increased	1.789088249	2.629538255	4.418626504	21	64.3	51.845	0	222.49	2846700000	326	Probable sulfatase
Regulatory proteins	P9WMH1	ideR Rv2711	Essential	Increased	1.779898167	3.913122365	5.693020532	12	70.4	25.233	0	253.77	3942400000	252	Iron-dependent repressor IdeR
Intermediary metabolism and respiration	P9WK35	ribE ribC Rv1412	Non-Essential	Increased	1.736850739	5.306868204	7.043718943	8	51.7	21.32	0	192.06	1514200000	183	Riboflavin synthase (RS)
Intermediary metabolism and respiration	P9WPJ7	mtcA1 canA Rv1284	Non-Essential	Increased	1.728070736	4.94720636	6.675277096	10	67.5	18.189	0	200.5	5047400000	300	Beta-carbonic anhydrase 1 (Beta-CA 1) (Carbonate dehydratase 1) (mtCA 1)
Intermediary metabolism and respiration	P0CG96;P0CG95	sseC1 Rv3118	Growth-Advantage	Increased	1.710254192	5.472001056	7.182255248	7	92	10.165	0	243.5	7101400000	436	Uncharacterized protein Rv3118
Intermediary metabolism and respiration	P9WP55	cysK1 cysK Rv2334	Non-Essential	Increased	1.662670135	5.14549221	6.808162345	12	56.5	32.752	0	104.78	2653600000	286	O-acetylserine sulfhydrylase (OAS sulfhydrylase) (OASS) (Cysteine synthase A)
Intermediary metabolism and respiration	O53311	Rv3161c	Non-Essential	Increased	1.658146858	8.890944067	10.54909093	18	59.2	42.504	0	323.31	12632000000	749	Possible dioxygenase
Lipid metabolism	P9WQD5	tesA Rv2928	Non-Essential	Increased	1.657240868	4.546645615	6.203886483	19	76.2	29.151	0	209.19	9833200000	709	Thioesterase TesA (EC 3.1.2.-) (Acetylesterase) (Palmitoyl-CoA hydrolase)
Information pathways	P9WNN1	tuf Rv0685	Essential	Increased	1.655775547	7.494156007	9.149931554	29	86.4	43.593	0	323.31	1.3441E+11	3465	Elongation factor Tu (EF-Tu)
Lipid metabolism	O33194	Rv1692	Non-Essential	Increased	1.633582115	2.847551962	4.481134077	10	40.5	37.01	0	103.68	1242800000	128	D-glycerol 3-phosphate phosphatase (D,L-glycerol 3-phosphate phosphatase) (G3P phosphatase)
Intermediary metabolism and respiration	O07427	Rv0183	Non-Essential	Increased	1.626428127	4.583235226	6.209663353	15	69.9	30.261	0	323.31	11372000000	711	Monoacylglycerol lipase (MGL)
Intermediary metabolism and respiration	P9WHH1	trxB trxB2 trxR Rv3913	Essential	Increased	1.618580818	6.664199149	8.282779967	14	61.8	35.643	0	323.31	5188100000	586	Thioredoxin reductase (TR) (TRXR)
Intermediary metabolism and respiration	P9WNE5	bfrB ftn Rv3841	Non-Essential	Increased	1.616090298	3.400905712	5.01699601	12	76.2	20.442	0	321.27	40922000000	738	Ferritin BfrB (Non-heme ferritin Ftn) (Nox19)
Intermediary metabolism and respiration	P9WK17	glcB Rv1837c	Essential	Increased	1.613258839	6.727290203	8.340549042	40	55.9	80.402	0	323.31	52983000000	2042	Malate synthase G
Intermediary metabolism and respiration	P9WHF9	cysA1 cysA Rv3117	Growth-Advantage	Increased	1.608123779	7.570898584	9.179022363	32	92.1	31.014	0	323.31	85994000000	2304	Putative thiosulfate sulfurtransferase (Rhodanese-like protein)
Virulence, detoxification, adaptation	P9WNV9	dnaJ1 Rv0352	Non-Essential	Increased	1.591628551	8.23985281	9.831481361	22	66.6	41.345	0	323.31	7297300000	748	Chaperone protein DnaJ 1
Information pathways	P9WNM1	tsf Rv2889c	Essential	Increased	1.58485651	6.914934979	8.499791489	24	79.3	28.754	0	323.31	48000000000	1909	Elongation factor Ts (EF-Ts)
Virulence, detoxification, adaptation	P9WPE7	groEL2 Rv0440	Essential	Increased	1.573252678	3.697999332	5.27125201	51	84.8	56.726	0	323.31	8.3966E+11	8413	Chaperonin GroEL 2
Intermediary metabolism and respiration	P9WJQ9	mobA Rv2453c	Non-Essential	Increased	1.564818382	3.723963964	5.288782346	6	43.8	21.084	0	85.717	700480000	98	Probable molybdenum cofactor guanylyltransferase (MoCo guanylyltransferase)
Lipid metabolism	P9WQE3	Rv2934	Non-Essential	Increased	1.562429905	2.135319093	3.697748998	23	16.2	193.31	0	121.58	1780100000	182	Phenolphthiocerol/phthiocerol polyketide synthase subunit D
Intermediary metabolism and respiration	P71853	Rv3548c	Non-Essential	Increased	1.560416222	2.408874123	3.969290345	6	28.9	31.07	0	101.99	167620000	41	Probable short-chain type dehydrogenase/reductase

Table S2. **CyC_{32yne} target proteins identified in *M. tb* mc²6230 culture through CC-ABPP by LC-ESI-MS/MS analysis. Only positive hits with a *p*-value <0.01 and a fold-change ≥1.2 are reported.**

Functional category	Protein IDs	Gene names	Essentiality	Change	Fold change (log2)	-LOG(p-value)	Manhattan distance	Unique peptides	Unique sequence coverage [%]	Mol. weight [kDa]	Q-value	Score	Intensity	MS/MS count	Protein names
Uncharacterized protein	I6Y946	Rv0925c	Non-Essential	Increased	1.559588909	4.999433699	6.559022608	11	62	26.944	0	217.91	5103700000	414	Conserved protein
Intermediary metabolism and respiration	P9WMM3	hisF Rv1605	Essential	Increased	1.559022427	2.320778454	3.879800881	11	56.6	27.221	0	62.854	1055200000	170	Imidazole glycerol phosphate synthase subunit HisF
Lipid metabolism	P9WQP3	fbpA Rv3804c	Non-Essential	Increased	1.536707878	3.631076348	5.167784226	11	45	35.686	0	323.31	22480000000	858	Diacylglycerol acyltransferase/mycolyltransferase Ag85A (DGAT)
Lipid metabolism	O33332	ltp1 Rv2790c	Non-Essential	Increased	1.53669405	6.119819101	7.656513151	9	40.1	42.904	0	289.27	1012100000	153	Probable lipid-transfer protein Ltp1
Uncharacterized protein	O50398	Rv3369	Non-Essential	Increased	1.535483837	2.69645941	4.231943247	4	29.2	15.718	0	68.22	1642200000	81	Conserved protein
Intermediary metabolism and respiration	O53554	ilvX Rv3509c	Non-Essential	Increased	1.533128262	6.810455562	8.343583824	25	64.7	52.072	0	323.31	12425000000	918	Putative acetolactate synthase large subunit IlvX (ALS) (Acetohydroxy-acid synthase large subunit) (AHAS)
Virulence, detoxification, adaptation	P9WQB7	ahpC Rv2428	Non-Essential	Increased	1.528003216	4.341049379	5.869052595	8	56.4	21.566	0	133.35	762220000	114	Alkyl hydroperoxide reductase C (MtAhpC) (Peroxiredoxin) (Thioredoxin peroxidase)
Lipid metabolism	I6X9J0	fadE8 Rv0672	Non-Essential	Increased	1.527789593	2.553871967	4.08166156	19	47	58.534	0	238.95	3791900000	364	Probable acyl-CoA dehydrogenase FadE8
Information pathways	P9WHB7	rplX Rv0715	Essential	Increased	1.526555538	4.455980727	5.982536265	8	70.5	11.475	0	95.429	18183000000	487	50S ribosomal protein L24
Uncharacterized protein	O06310	Rv0360c	Non-Essential	Increased	1.525137424	3.963027977	5.488165401	6	41.4	15.329	0	77.241	1665900000	181	Conserved protein
Intermediary metabolism and respiration	P9WKG3	ispG gcpE Rv2868c	Essential	Increased	1.517276764	7.112031009	8.629307773	19	72.4	40.482	0	323.31	14215000000	965	4-hydroxy-3-methylbut-2-en-1-yl diphosphate synthase (flavodoxin)
Uncharacterized protein	P9WFK3	Rv0504c	Non-Essential	Increased	1.510525227	5.251037192	6.761562419	12	89.8	18.36	0	85.137	3817000000	435	UPF0336 protein Rv0504c
Intermediary metabolism and respiration	P9WQA5	Rv2971	Essential	Increased	1.489521503	6.341149197	7.8306707	16	77.3	30.364	0	323.31	29840000000	1139	Uncharacterized oxidoreductase Rv2971
Virulence, detoxification, adaptation	P9WFD9	Rv2028c	Non-Essential	Increased	1.480623245	3.120141744	4.600764989	11	62	29.441	0	121.72	1871700000	124	Universal stress protein Rv2028c (USP Rv2028c)
Uncharacterized protein	O07196	Rv2694c	Non-Essential	Increased	1.475322723	5.670980116	7.146302839	9	66.4	13.57	0	174.26	1063300000	98	Conserved protein
Virulence, detoxification, adaptation	P9WIE1	bcp2 Rv2521	Non-Essential	Increased	1.475195885	7.426172013	8.901367898	12	75.8	17.077	0	323.31	5389000000	375	Putative peroxiredoxin Rv2521 (Thioredoxin-dependent peroxiredoxin Rv2521)
Uncharacterized protein	I6X540	Rv2683	Non-Essential	Increased	1.465690136	4.509901999	5.975592135	7	51.5	17.729	0	87.011	1212700000	90	Conserved protein
Lipid metabolism	P9WNG3	fabH Rv0533c	Non-Essential	Increased	1.462444305	3.956718925	5.41916323	10	58.2	34.872	0	139.14	1236900000	127	3-oxoacyl-[acyl-carrier-protein] synthase 3 (Beta-ketoacyl-ACP synthase III) (KAS III) (MtFabH)
Information pathways	P9WHB5	rplY Rv1015c	Growth-Defect	Increased	1.443259239	5.464394682	6.907653921	8	51.2	22.441	0	162.19	7020000000	382	50S ribosomal protein L25 (General stress protein CTC)
Uncharacterized protein	P9WME3	Rv1287	Non-Essential	Increased	1.443257332	2.053486081	3.496743413	4	49.1	17.209	0	67.241	343050000	57	Putative HTH-type transcriptional regulator Rv1287
Information pathways	P9WQ13	end nfo Rv0670	Non-Essential	Increased	1.442784786	6.364849842	7.807634628	13	61.9	26.845	0	221.36	3339000000	312	Probable endonuclease 4 (Endodeoxyribonuclease IV) (Endonuclease IV)
Intermediary metabolism and respiration	P9WG95	ilvA Rv1559	Essential	Increased	1.441131592	4.778570567	6.219702159	13	34.7	45.04	0	247.37	2919000000	319	L-threonine dehydratase biosynthetic IlvA (Threonine deaminase)
Intermediary metabolism and respiration	P9WP51	cbs Rv1077	Non-Essential	Increased	1.435930252	5.834255882	7.270186134	19	69	48.635	0	323.31	7763600000	681	Putative cystathionine beta-synthase Rv1077 (Serine sulfhydrase)
Information pathways	P9WFC7	uvrB Rv1633	Non-Essential	Increased	1.431797981	3.37479906	4.811277887	22	33.2	80.406	0	96.106	1508500000	243	UvrABC system protein B (Protein UvrB) (Excinuclease ABC subunit B)
Intermediary metabolism and respiration	P9WNX5	asd Rv3708c	Growth-Defect	Increased	1.423524857	5.203473558	6.626998415	16	59.1	36.23	0	323.31	11487000000	664	Aspartate-semialdehyde dehydrogenase (ASA dehydrogenase) (ASADH)
Intermediary metabolism and respiration	I6X857	Rv0223c	Non-Essential	Increased	1.412810802	3.957852822	5.370663624	10	28.5	51.157	0	129.54	1246300000	139	Probable aldehyde dehydrogenase
Regulatory proteins	P9WGL7	Rv3143	Non-Essential	Increased	1.411920071	2.284727479	3.69664755	5	63.9	14.386	0	69.438	971600000	97	Uncharacterized response regulatory protein Rv3143
Information pathways	P9WH43	rpsA Rv1630	Essential	Increased	1.410372257	3.931392028	5.341764285	29	73	53.201	0	323.31	23602000000	1298	30S ribosomal protein S1
Information pathways	P9WH85	rplD Rv0702	Essential	Increased	1.405642986	4.815563467	6.221206453	10	52	23.743	0	272.24	26433000000	805	50S ribosomal protein L4
Intermediary metabolism and respiration	P9WHT9	prcB Rv2110c	Essential	Increased	1.405330181	5.994341226	7.399671407	13	68	30.305	0	175.09	3584300000	415	Proteasome subunit beta
Uncharacterized protein	O06578	Rv1126c	Non-Essential	Increased	1.403783798	2.519333009	3.923116807	7	47.8	22.197	0	117.77	431710000	82	Conserved protein
Intermediary metabolism and respiration	P9WP85	cobT Rv2207	Non-Essential	Increased	1.402231216	3.625812722	5.028043938	7	23.8	36.411	0	110.37	942450000	153	Nicotinate-nucleotide--dimethylbenzimidazole phosphoribosyltransferase (NN:DBI PRT)
Lipid metabolism	O53422	fadA3 Rv1074c	Growth-Advantage	Increased	1.390129089	5.649729664	7.039858753	22	75.6	42.655	0	323.31	35707000000	1576	Probable beta-ketoacyl CoA thiolase FadA3
Intermediary metabolism and respiration	O86374	Rv3257c	Essential	Increased	1.388839722	2.300813296	3.689653018	10	34.4	49.04	0	77.754	1173900000	161	Probable phosphomannomutase PmmA (PMM) (Phosphomannose mutase)
Intermediary metabolism and respiration	P9WIT1	Rv2280	Non-Essential	Increased	1.387584209	7.631415603	9.018999812	15	59.5	48.051	0	323.31	13720000000	821	Uncharacterized FAD-linked oxidoreductase Rv2280
Intermediary metabolism and respiration	P9WNG7	etfB fixA Rv3029c	Growth-Defect	Increased	1.382524014	6.259246741	7.641770755	14	67.7	28.08	0	323.31	8521700000	566	Electron transfer flavoprotein subunit beta (Beta-ETF) (Electron transfer flavoprotein small subunit) (ETFSS)
Intermediary metabolism and respiration	P9WFE3	ureG Rv1852	Non-Essential	Increased	1.378807545	6.262832458	7.641640003	9	47.3	23.348	0	215.24	1507400000	139	Urease accessory protein UreG
Intermediary metabolism and respiration	I6Y276	Rv2993c	Non-Essential	Increased	1.374224663	4.452820703	5.827043566	9	65.3	25.341	0	155.8	3613100000	294	Possible 2-hydroxyhepta-2,4-diene-1,7-dioate isomerase (HHDD isomerase)
Information pathways	P9WGZ1	rpoA Rv3457c	Essential	Increased	1.361139774	5.852747156	7.21388693	25	77.5	37.706	0	323.31	41301000000	1601	DNA-directed RNA polymerase subunit alpha (RNAP subunit alpha)
Intermediary metabolism and respiration	I6XW38	Rv0730	Growth-Advantage	Increased	1.356253624	5.507171632	6.863425256	13	53.7	25.98	0	222.65	4732000000	355	DNA topoisomerase (ATP-hydrolyzing)
Intermediary metabolism and respiration	O50433	fdxC Rv1177	Essential	Increased	1.352934361	3.73044673	5.083381091	5	38.9	11.839	0	87.172	1026900000	123	Ferredoxin
Cell wall and cell processes	P9WQN5	mpa Rv2115c	Non-Essential	Increased	1.341079712	5.462645766	6.803725478	29	59.3	67.4	0	323.31	8745700000	834	Proteasome-associated ATPase (AAA ATPase forming ring-shaped complexes) (ARC) (Mycobacterial proteasome ATPase)
Intermediary metabolism and respiration	P9WHF5	sseB Rv2291	Non-Essential	Increased	1.341062069	2.183369734	3.524431803	6	42.6	29.4	0	80.367	745990000	123	Putative thiosulfate sulfurtransferase SseB
Information pathways	P9WHD3	rplQ Rv3456c	Growth-Defect	Increased	1.325903416	4.133423551	5.459326967	15	72.2	19.475	0	323.31	34848000000	1004	50S ribosomal protein L17
Intermediary metabolism and respiration	P9WQA3	fba Rv0363c	Essential	Increased	1.323069572	6.485383921	7.808453493	24	82.3	36.544	0	323.31	24083000000	1312	Fructose-bisphosphate aldolase (FBP aldolase) (FBPA)
Information pathways	P9WI57	pnp Rv2783c	Essential	Increased	1.308290958	5.537567202	6.84585816	36	56.2	79.734	0	323.31	37869000000	1928	Polyribonucleotide nucleotidyltransferase (Polynucleotide phosphorylase) (PNPase)
Intermediary metabolism and respiration	P9WHL7	purL Rv0803	Essential	Increased	1.306526661	5.1310187	6.437545361	36	54.4	80.801	0	323.31	12662000000	874	Phosphoribosylformylglycinamidine synthase subunit PurL (FGAM synthase)
Information pathways	P9WHD7	rplO Rv0723	Uncertain	Increased	1.293813229	3.900411929	5.194225158	8	50.7	15.533	0	174.25	13757000000	606	50S ribosomal protein L15
Uncharacterized protein	P9WL63	Rv2629	Non-Essential	Increased	1.287930965	6.378962805	7.66689377	22	75.9	40.839	0	323.31	6398200000	649	Uncharacterized protein Rv2629
Intermediary metabolism and respiration	P9WQ97	amiB2 Rv1263	Non-Essential	Increased	1.28298521	4.389474361	5.672459571	21	65.2	49.08	0	206.39	2613300000	409	Putative amidase AmiB2
Virulence, detoxification, adaptation	P9WMJ9	dnaK Rv0350	Essential	Increased	1.281809807	4.38609901	5.667908817	52	71.2	66.83	0	323.31	1.2183E+11	3416	Chaperone protein DnaK (HSP70)
Lipid metabolism	P9WFK1	hadA Rv0635	Essential	Increased	1.275116444	4.841212374	6.116328818	10	74.1	17.48	0	323.31	10835000000	571	UPF0336 protein Rv0635
Information pathways	P9WH79	rplI Rv0056	Non-Essential	Increased	1.274153233	5.31257368	6.586726913	9	44.7	16.169	0	164.51	7094000000	311	50S ribosomal protein L9
Uncharacterized protein	P9WJA3	hrp1 Rv2626c	Non-Essential	Increased	1.273047924	2.349850822	3.622898746	7	69.2	15.518	0	87.407	2293300000	214	Hypoxic response protein 1 (HRP1)
Intermediary metabolism and respiration	P9WIK3	cysH Rv2392	Growth-Defect	Increased	1.272475719	5.245759019	6.518234738	11	50	27.423	0	112.54	2538900000	409	Adenosine 5'-phosphosulfate reductase (APS reductase)
Information pathways	P9WH51	rpsQ Rv0710	Essential	Increased	1.271234035	3.695719044	4.966953079	10	58.5	14.741	0	188.96	25720000000	718	30S ribosomal protein S17
Lipid metabolism	P9WFI9	Rv0281	Non-Essential	Increased	1.270236969	5.300689264	6.570926233	15	57.3	32.998	0	284.8	7686200000	631	Putative S-adenosyl-L-methionine-dependent methyltransferase Rv0281
Cell wall and cell processes	P9WN95	ftsZ Rv2150c	Essential	Increased	1.264906883	4.590722573	5.855629456	17	44.3	38.755	0	172.25	3934300000	348	Cell division protein FtsZ
Cell wall and cell processes	P9628I	Rv0435c	Non-Essential	Increased	1.263228416	4.421361605	5.684590021	23	48.5	75.345	0	251.75	3672900000	386	Putative conserved ATPase
Lipid metabolism	P9WNG5	fabD Rv2243	Essential	Increased	1.256029606	5.721682262	6.977711868	8	42.1	30.788	0	84.896	1679800000	170	Malonyl CoA-acyl carrier protein transacylase (MCT)
Intermediary metabolism and respiration	P9WKI1	ino1 Rv0046c	Essential	Increased	1.25335598	6.729812604	7.983168584	20	61	40.093	0	323.31	7743400000	529	Inositol-3-phosphate synthase (IPS) (Myo-inositol 1-phosphate synthase) (MI-1-P synthase) (MIP synthase)
Intermediary metabolism and respiration	P9WPU7	atpA Rv1308	Essential	Increased	1.25289917	7.868112051	9.121011221	37	64.1	59.288	0	323.31	71480000000	2531	ATP synthase subunit alpha (ATP synthase F1 sector subunit alpha) (F-ATPase subunit alpha)
Intermediary metabolism and respiration	P9WIC9	gpm1 Rv0489	Non-Essential	Increased	1.249867439	5.859520046	7.109387485	14	75.9	27.215	0	323.31	8817000000	712	2,3-bisphosphoglycerate-dependent phosphoglycerate mutase (BPG-dependent PGAM) (PGAM) (Phosphoglyceromutase)
Intermediary metabolism and respiration	P9WPE1	citE Rv2498c	Non-Essential	Increased	1.245306015	4.766576346	6.011882361	11	48.4	28.885	0	174.59	3523900000	243	Citrate lyase subunit beta-like protein
Intermediary metabolism and respiration	P9WNW9	hisD Rv1599	Essential	Increased	1.24366045	5.208944557	6.452605007	10	35.6	46.302	0	122.43	2097500000	213	Histidinol dehydrogenase (HDH)
Intermediary metabolism and respiration	P9WNL1	eno Rv1023	Growth-Defect	Increased	1.233539581	6.559594301	7.793133882	17	56.6	44.961	0	323.31	18393000000	828	Enolase (2-phospho-D-glycerate hydro-lyase) (2-phosphoglycerate dehydratase)
Intermediary metabolism and respiration	P95034	Rv0688	Non-Essential	Increased	1.226113319	5.837335327	7.063448646	17	54.2	43.017	0	284.05	6941200000	574	Putative ferredoxin reductase
Intermediary metabolism and respiration	P9WG81	folD Rv3356c	Essential	Increased	1.22296524	5.775230348	6.998195588	18	66.9	29.483	0	266.22	5560700000	562	Bifunctional protein FolD [Includes: Methylenetetrahydrofolate dehydrogenase; Methenyltetrahydrofolate cyclohydrolase
Intermediary metabolism and respiration	P9WQB3	leuA Rv3710	Essential	Increased	1.218405247	6.237348856	7.455754103	35	73.6	70.113	0	323.31	18661000000	1326	2-isopropylmalate synthase (Alpha-IPM synthase) (Alpha-isopropylmalate synthase)
Virulence, detoxification, adaptation	P9WFC9	Rv1636	Essential	Increased	1.214326859	4.299955083	5.514281942	10	87	15.312	0	99.204	3008800000	380	Universal stress protein Rv1636 (USP Rv1636)
Intermediary metabolism and respiration	P9WGC7	sucD Rv0952	Essential	Increased	1.213413715	7.410160347	8.623574062	16	71.9	31.229	0	323.31	24686000000	951	Succinate--CoA ligase [ADP-forming] subunit alpha
Intermediary metabolism and respiration	P9WPZ7	argD Rv1655	Essential	Increased	1.20838213	2.097394074	3.305776204	14	41.5	40.909	0	102.27	2115600000	193	Acetylornithine aminotransferase (ACOAT)
Intermediary metabolism and respiration	P9WJK1	nadA Rv1594	Essential	Increased	1.206968784	8.152241247	9.359210031	15	70.5	37.408	0	323.31	7085300000	614	Quinolinate synthase
Cell wall and cell processes	P9WG55	tig Rv2462c	Non-Essential	Increased	1.204115391	4.024407921	5.228523312	16	43.3	50.615	0	244.83	3386400000	507	Trigger factor (TF) (PPIase)
Intermediary metabolism and respiration	P9WQB9	adhD Rv3086	Non-Essential	Increased	1.202385426	5.873431659	7.075817085	9	40.5	38.341	0	253.9	2640100000	287	Putative alcohol dehydrogenase D

Table S3. Proteins differentially captured with CyC_{31yne} and CyC_{32yne} at a *p*-value ≤ 0.01 and a fold-change ≥ 1.2

					CyC_{31yne} capture		CyC_{32yne} capture		
	Protein IDs	Functional category	Gene names	Essentiality	Fold change (log2)	-LOG(p-value)	Gene names	Essentiality	Fold change (log2)	-LOG(p-value)	Protein names
CyC_{31yne} specific target proteins	I6XU97	Lipid metabolism	Rv0045c	Non-Essential	5.136509418	2.411832965					Esterase Rv0045c
	P9WMR7	Intermediary metabolism and respiration	Rv1341	Non-Essential	2.370626926	6.5817477					dITP/XTP pyrophosphatase
	P9WQP1	Lipid metabolism	fbpB Rv1886c	Growth-Advantage	2.298300743	3.651520066					Diacylglycerol acyltransferase/mycolyltransferase Ag85B (FbpB)
	L0TC47	Intermediary metabolism and respiration	lipV Rv3203	Non-Essential	2.286476612	5.038909798					Lipase LipV
	P0CG96	Intermediary metabolism and respiration	sseC1	Growth-Advantage	1.805895329	4.945687316					Uncharacterized protein Rv3118
	L7N690	Intermediary metabolism and respiration	amiB1 Rv3306c	Non-Essential	1.641599178	2.296105655					Peptidase M20 domain-containing protein 2
	P9WPC5	Intermediary metabolism and respiration	clpP1 Rv2461c	Essential	1.47578907	4.09763756					ATP-dependent Clp protease proteolytic subunit 1 (Endopeptidase Clp 1)
	I6X8D2	Lipid metabolism	pks13 Rv3800c	Essential	1.475198746	3.928367502					Polyketide synthase Pks13
	P9WG67	Intermediary metabolism and respiration	Rv3914	Non-Essential	1.425992489	2.705424791					Thioredoxin (Trx) (MPT46)
	P9WMN5	Uncharacterized protein	Rv2204c	Non-Essential	1.384844303	6.026899374					Protein Rv2204c
	P9WMU1	Cell wall and cell processes	wag31 Rv2145c	Essential	1.328158855	4.240071653					Cell wall synthesis protein Wag31 (Antigen 84)
	O53533	Intermediary metabolism and respiration	mscR Rv2259	Non-Essential	1.306638241	3.439092153					S-nitrosomycothiol reductase MscR
	P9WQC5	Intermediary metabolism and respiration	adhC Rv3045	Non-Essential	1.262573242	5.400468923					NADP-dependent alcohol dehydrogenase C
	P9WNH5	**Intermediary metabolism and respiration**	**hsaD Rv3569c**	**Essential - survival in macrophage**	**1.252779961**	**2.962565901**					**4,5:9,10-diseco-3-hydroxy-5,9,17-trioxoandrosta-1(10),2-diene-4-oate hydrolase (MCP hydrolase)**
	P9WQH7	Intermediary metabolism and respiration	accD5 Rv3280	Essential	1.246607304	6.625911367					Biotin-dependent acetyl-/propionyl-coenzyme A carboxylase beta5 subunit (Acetyl-CoA carboxylase) (ACC)
	P9WM23	Intermediary metabolism and respiration	Rv1333	Non-Essential	1.224698544	2.025487953					Uncharacterized aminopeptidase Rv1333
	O53901	Lipid metabolism	pks5 Rv1527c	Non-Essential	1.213652611	4.170032119					Mycocerosic acid synthase-like polyketide synthase (MAS-like PKS)
	P9WMS7	Intermediary metabolism and respiration	guaA Rv3396c	Essential	1.206840992	5.940571627					GMP synthase [glutamine-hydrolyzing]
	P9WHS9	Intermediary metabolism and respiration	dapE Rv1202	Essential	1.200644493	3.007239638					Putative succinyl-diaminopimelate desuccinylase DapE (SDAP desuccinylase)
CyC_{31yne} and CyC_{32yne} shared target proteins	P9WKL5	Intermediary metabolism and respiration	htm Rv0560c	Non-Essential	5.786037922	4.118003579	htm Rv0560c	Non-Essential	5.325745583	3.917569011	2-heptyl-1-hydroxyquinolin-4(1H)-one methyltransferase (HQNO methyltransferase)
	P71668	Intermediary metabolism and respiration	lipI Rv1400c	Non-Essential	5.544583797	3.636842818	lipI Rv1400c	Non-Essential	5.414610863	3.563300813	Esterase LipI
	P9WP43	Cell wall and cell processes	cut7 Rv1984c	Growth-Advantage	4.943463326	5.426353158	cut7 Rv1984c	Growth-Advantage	5.864572525	4.976765729	Carboxylesterase Culp1
	P9WIV5	Intermediary metabolism and respiration	nuoE Rv3149	Non-Essential	4.08878994	5.901340563	nuoE Rv3149	Non-Essential	4.048645496	5.78875163	NADH-quinone oxidoreductase subunit E
	O53672	Uncharacterized protein	Rv0250c	Non-Essential	4.000836849	7.406453506	Rv0250c	Non-Essential	3.57204628	5.828411162	Uncharacterized protein Rv0250c
	I6YA17	Uncharacterized protein	Rv2699c	Essential	3.682217121	5.273023154	Rv2699c	Essential	3.229794025	5.185957329	Uncharacterized protein
	P9WKB7	Intermediary metabolism and respiration	nlhH lipH Rv1399c	Non-Essential	3.469993591	5.94020195	nlhH lipH Rv1399c	Non-Essential	4.446006775	5.499184478	Carboxylesterase NlhH
	P71988	Cell wall and cell processes	Rv1730c	Non-Essential	3.418309212	3.104246164	Rv1730c	Non-Essential	1.841503143	2.368620008	Possible penicillin-binding protein
	P9WKD7	Intermediary metabolism and respiration	rpiB Rv2465c	Essential	3.396066189	2.546470647	rpiB Rv2465c	Essential	3.390566349	2.496127297	Ribose-5-phosphate isomerase B
	P9WN21	Intermediary metabolism and respiration	glpX Rv1099c	Non-Essential	3.329022408	4.785262711	glpX Rv1099c	Non-Essential	3.308312416	4.842266037	Fructose-1,6-bisphosphatase class 2 (FBPase class 2)
	P9WGH9	Information pathways	sigH Rv3223c	Non-Essential	3.317800522	3.377405128	sigH rpoE Rv3223c	Non-Essential	3.484445095	3.521156304	ECF RNA polymerase sigma factor SigH
	P71990	Uncharacterized protein	Rv1732c	Non-Essential	3.302349567	3.699920072	Rv1732c	Non-Essential	3.018773556	3.387270693	Conserved protein
	P9WNM9	Information pathways	Rv0120c	Non-Essential	3.285088062	2.816658695	Rv0120c	Non-Essential	3.222065449	2.78636621	Elongation factor G-like protein
	O07173	Uncharacterized protein	Rv0123	Non-Essential	3.160677433	4.728247657	Rv0123	Non-Essential	2.887873173	4.632873926	Uncharacterized protein
	O06154	Uncharacterized protein	Rv1637c	Non-Essential	3.069756985	3.197053448	Rv1637c	Non-Essential	3.039237499	3.131580213	Conserved protein
	P9WHJ7	Information pathways	rbfA Rv2838c	Non-Essential	2.993652821	2.672148689	rbfA Rv2838c	Non-Essential	2.98382616	2.509295882	Ribosome-binding factor A
	P95198	Uncharacterized protein	Rv0390	Non-Essential	2.843595982	4.656884186	Rv0390	Non-Essential	2.737447262	4.383440309	Conserved protein
	P9WL15	Uncharacterized protein	Rv2927c	Essential	2.832271099	2.255673694	Rv2927c	Essential	2.565018654	2.049918425	Uncharacterized protein Rv2927c
	P9WFM1	Uncharacterized protein	Rv2230c	Non-Essential	2.774307251	2.379485521	Rv2230c	Non-Essential	2.90926981	2.507850159	GTP cyclohydrolase 1 type 2 homolog
	P9WJD9	Cell wall and cell processes	espB Rv3881c	Growth-Advantage	2.756381035	6.478589908	espB Rv3881c	Growth-Advantage	2.71696806	6.48138069	ESX-1 secretion-associated protein EspB (Antigen MTB48)
	P9WKG1	Intermediary metabolism and respiration	ispH2 lytB2 Rv1110	Essential	2.710473537	3.846191936	ispH2 lytB2 Rv1110	Essential	2.681500912	3.894123485	4-hydroxy-3-methylbut-2-enyl diphosphate reductase 2 (HDR 2)
	I6YGL1	Intermediary metabolism and respiration	Rv3591c	Non-Essential	2.680040359	3.895699602	Rv3591c	Non-Essential	1.831168175	3.161366155	Possible hydrolase
	I6XF60	Uncharacterized protein	Rv2731	Non-Essential	2.617456436	2.331112033	Rv2731	Non-Essential	2.555454254	2.283047447	Conserved alanine and arginine rich protein
	O53531	Uncharacterized protein	Rv2257c	Non-Essential	2.52463007	5.061343775	Rv2257c	Non-Essential	2.038984776	6.151534879	Conserved protein
	O86318	Lipid metabolism	accD2 Rv0974c	Non-Essential	2.503325939	2.483698746	accD2 Rv0974c	Non-Essential	2.507756233	2.492210086	Probable biotin-dependent acyl-coenzyme A carboxylase beta2 subunit
	P9WG35	Virulence, detoxification, adaptation	tpx Rv1932	Non-Essential	2.483623981	3.814202045	tpx Rv1932	Non-Essential	2.321673393	3.582438751	Thiol peroxidase (Tpx)
	P9WMP3	Intermediary metabolism and respiration	hemC Rv0510	Essential	2.478846073	5.26015399	hemC Rv0510	Essential	2.408607006	4.521314368	Porphobilinogen deaminase (PBG)
	I6X9R9	Intermediary metabolism and respiration	aldA Rv0768	Non-Essential	2.272338867	4.253093685	aldA Rv0768	Non-Essential	2.038165092	3.165126357	Probable aldehyde dehydrogenase NAD dependent AldA
	P9WMC1	Regulatory proteins	ethR Rv3855	Non-Essential	2.260409832	3.924594972	ethR Rv3855	Non-Essential	3.135175705	4.211863961	HTH-type transcriptional regulator EthR
	P9WQP3	Lipid metabolism	fbpA Rv3804c	Non-Essential	2.249478817	4.767489826	fbpA Rv3804c	Non-Essential	1.536707878	3.631076348	Diacylglycerol acyltransferase/mycolyltransferase Ag85A (FbpA)
	P9WIP7	Information pathways	lsr2 Rv3597c	Growth-Defect	2.198446274	5.312577233	lsr2 Rv3597c	Growth-Defect	2.099945545	5.604350557	Nucleoid-associated protein Lsr2
	P9WMM5	Intermediary metabolism and respiration	hisA Rv1603	Essential	2.193735123	2.400166902	hisA Rv1603	Essential	2.204256058	2.406979582	Phosphoribosyl isomerase A (1-(5-phosphoribosyl)-5-[(5-phosphoribosylamino)methylideneamino] imidazole-4-carboxamide isomerase)
	P9WQD5	Lipid metabolism	tesA Rv2928	Non-Essential	2.165913582	4.851389712	tesA Rv2928	Non-Essential	1.657240868	4.546645615	Thioesterase TesA
	P9WH53	Information pathways	rpsP Rv2909c	Growth-Defect	2.142980576	4.7142933	rpsP Rv2909c	Growth-Defect	2.225661278	5.735386148	30S ribosomal protein S16
	P9WHG1	Information pathways	prfB Rv3105c	Essential	2.130598545	5.647978035	prfB Rv3105c	Essential	2.049877167	5.451673159	Peptide chain release factor 2 (RF-2)
	P9WG59	Intermediary metabolism and respiration	thrC Rv1295	Essential	2.116921425	3.467989094	thrC Rv1295	Essential	2.160535336	3.473021069	Threonine synthase (TS)
	P9WP27	Intermediary metabolism and respiration	aao Rv1905c	Non-Essential	2.116910934	3.565089537	aao Rv1905c	Non-Essential	2.061562061	3.495350768	Probable D-amino-acid oxidase (DAAO)
	P71805	Intermediary metabolism and respiration	Rv1377c	Non-Essential	2.064102173	2.517913981	Rv1377c	Non-Essential	1.940551758	2.369532691	Putative transferase
	P9WIM1	Intermediary metabolism and respiration	pafB Rv2096c	Non-Essential	2.033325195	2.791835724	pafB Rv2096c	Non-Essential	2.654271603	3.343304595	Protein PafB (Proteasome accessory factor B)
	P96826	Intermediary metabolism and respiration	Rv0149	Growth-Advantage	2.009970665	2.056853514	Rv0149	Growth-Advantage	2.197679996	2.169883388	Possible quinone oxidoreductase (NADPH:quinone oxidoreductase) (Zeta-crystallin)
	P9WHL3	Intermediary metabolism and respiration	pyrC Rv1381	Essential	2.00991869	2.723351047	pyrC Rv1381	Essential	2.057533264	2.778904875	Dihydroorotase (DHOase)
	P9WKZ7	Intermediary metabolism and respiration	Rv3400	Non-Essential	2.005986691	3.628477806	Rv3400	Non-Essential	2.082166195	3.651430426	Uncharacterized protein Rv3400
	I6YBZ8	Lipid metabolism	htdY Rv3389c	Non-Essential	1.996554375	6.360019791	htdY Rv3389c	Non-Essential	2.005271435	6.136274264	3-hydroxyacyl-thioester dehydratase Y
	P9WHC7	Information pathways	rplA Rv0641	Essential	1.992814064	6.23640838	rplA Rv0641	Essential	2.09340477	6.024031504	50S ribosomal protein L1
	P9WHR7	Regulatory proteins	lexA Rv2720	Growth-Defect	1.979640961	2.905286303	lexA Rv2720	Growth-Defect	1.973381042	2.86003511	LexA repressor
	O07427	Intermediary metabolism and respiration	Rv0183	Non-Essential	1.973363876	4.335331492	Rv0183	Non-Essential	1.626428127	4.583235226	Monoacylglycerol lipase (MGL)
	P9WHG3	Information pathways	prfA Rv1299	Essential	1.963119984	3.547151165	prfA Rv1299	Essential	2.10341835	3.730074243	Peptide chain release factor 1 (RF-1)
	O07738	Uncharacterized protein	Rv1894c	Non-Essential	1.955036163	2.049304638	Rv1894c	Non-Essential	2.041158676	2.099410363	NMO domain-containing protein
	P9WHW3	Information pathways	ppiA Rv0009	Non-Essential	1.953566074	4.227682742	ppiA Rv0009	Non-Essential	2.152626514	6.640704345	Peptidyl-prolyl cis-trans isomerase A
	P9WJD5	Cell wall and cell processes	espD Rv3614c	Non-Essential	1.922756195	2.767616643	espD Rv3614c	Non-Essential	1.92638731	2.674835707	ESX-1 secretion-associated protein EspD
	P96202	Lipid metabolism	pgsC Rv2933	Non-Essential	1.922691253	5.51624264	pgsC Rv2933	Non-Essential	1.866245747	5.771494551	Phenolphthiocerol/phthiocerol polyketide synthase subunit C
	P9WU1	Intermediary metabolism and respiration	pdxH Rv2607	Non-Essential	1.921628952	3.112992196	pdxH Rv2607	Non-Essential	1.863657475	3.077927131	Pyridoxine 5'-phosphate oxidase (PNP oxidase)
	P9WH31	Information pathways	rpsF Rv0053	Essential	1.868440151	7.241812412	rpsF Rv0053	Essential	2.113023758	7.090426287	30S ribosomal protein S6
	O69667	Uncharacterized protein	Rv3699	Non-Essential	1.858729839	4.279913189	Rv3699	Non-Essential	1.841756344	4.294477413	Conserved protein
	O50433	Intermediary metabolism and respiration	fdxC Rv1177	Essential	1.858028412	4.575886042	fdxC Rv1177	Essential	1.352934361	3.73044673	Ferredoxin
	P9WQN9	Lipid metabolism	fbpC Rv0129c	Non-Essential	1.845247746	3.790455823	fbpC Rv0129c	Non-Essential	1.921019077	3.207487644	Diacylglycerol acyltransferase/mycolyltransferase Ag85C (FbpC)
	Q6MX51	Intermediary metabolism and respiration	Rv0296c	Non-Essential	1.818379879	2.672392588	Rv0296c	Non-Essential	1.789088249	2.629538255	Probable sulfatase
	P9WMH1	Regulatory proteins	ideR Rv2711	Essential	1.813466072	5.186402693	ideR Rv2711	Essential	1.779898167	3.913122365	Iron-dependent repressor IdeR
	O07196	Uncharacterized protein	Rv2694c	Non-Essential	1.808377266	6.289433758	Rv2694c	Non-Essential	1.475322723	5.670980116	Conserved protein
	P9WPQ9	Intermediary metabolism and respiration	bfr Rv1876	Growth-Advantage	1.793398857	3.118854329	bfr Rv1876	Growth-Advantage	1.977850914	3.300200785	Bacterioferritin (BFR)
	I6XHH5	Intermediary metabolism and respiration	hsaE Rv3536c	Non-Essential	1.779067993	2.175102916	hsaE Rv3536c	Non-Essential	1.955347061	2.370913113	Probable hydratase
	P9WHB7	Information pathways	rplX Rv0715	Essential	1.712803841	4.436627796	rplX Rv0715	Essential	1.526555538	4.455980727	50S ribosomal protein L24
	P9WL31	Intermediary metabolism and respiration	Rv2895c	Non-Essential	1.693223476	2.866915083	Rv2895c	Non-Essential	1.964669704	3.202493371	Uncharacterized protein Rv2895c
	P9WQE3	Lipid metabolism	Rv2934	Non-Essential	1.678764343	2.219958781	Rv2934	Non-Essential	1.562429905	2.135319093	Phenolphthiocerol/phthiocerol polyketide synthase subunit D (PpsD)
	P9WMM3	Intermediary metabolism and respiration	hisF Rv1605	Essential	1.659536362	2.478543245	hisF Rv1605	Essential	1.559022427	2.320778454	Imidazole glycerol phosphate synthase subunit HisF

Table S3. Proteins differentially captured with CyC_{31yne} and CyC_{32yne} at a *p*-value ≤ 0.01 and a fold-change ≥ 1.2

					CyC_{31yne} capture		CyC_{32yne} capture			
	Protein IDs	Functional category	Gene names	Essentiality	Fold change (log2)	-LOG(p-value)	Gene names	Essentiality	Fold change (log2)	-LOG(p-value)	Protein names
CyC31yne and CyC32yne shared target proteins	P9WQ13	Information pathways	end nfo Rv0670	Non-Essential	1.630804062	6.634233496	end nfo Rv0670	Non-Essential	1.442784786	6.364849842	Probable endonuclease 4 (Endodeoxyribonuclease IV) (Endonuclease IV)
	P9WK35	Intermediary metabolism and respiration	ribC Rv1412	Non-Essential	1.629113197	4.77126436	ribC Rv1412	Non-Essential	1.736850739	5.306868204	Riboflavin synthase (RS)
	I6X9J0	Lipid metabolism	fadE8 Rv0672	Non-Essential	1.628101349	2.704342869	fadE8 Rv0672	Non-Essential	1.527789593	2.553871967	Probable acyl-CoA dehydrogenase FadE8
	P9WJQ9	Intermediary metabolism and respiration	mobA Rv2453c	Non-Essential	1.625932693	3.938084769	mobA Rv2453c	Non-Essential	1.564818382	3.723963964	Probable molybdenum cofactor guanylyltransferase (MoCo guanylyltransferase)
	P9WP55	Intermediary metabolism and respiration	cysK1 Rv2334	Non-Essential	1.613677502	4.960608703	cysK1 Rv2334	Non-Essential	1.662670135	5.14549221	O-acetylserine sulfhydrylase (OAS sulfhydrylase) (OASS)
	P9WK17	Intermediary metabolism and respiration	glcB Rv1837c	Essential	1.607802868	7.799451565	glcB Rv1837c	Essential	1.613258839	6.727290203	Malate synthase G
	O33194	Lipid metabolism	Rv1692	Non-Essential	1.606084347	3.108531692	Rv1692	Non-Essential	1.633582115	2.847551962	D-glycerol 3-phosphate phosphatase (D,L-glycerol 3-phosphate phosphatase) (G3P phosphatase)
	P9WPJ7	Intermediary metabolism and respiration	canA Rv1284	Non-Essential	1.602204323	6.230030184	canA Rv1284	Non-Essential	1.728070736	4.94720636	Beta-carbonic anhydrase 1 (mtCA 1)
	O53554	Intermediary metabolism and respiration	ilvX Rv3509c	Non-Essential	1.5879035	7.701533788	ilvX Rv3509c	Non-Essential	1.533128262	6.810455562	Putative acetolactate synthase large subunit IlvX (ALS)
	P9WHF5	Intermediary metabolism and respiration	sseB Rv2291	Non-Essential	1.578984261	2.549066797	sseB Rv2291	Non-Essential	1.341062069	2.183369734	Putative thiosulfate sulfurtransferase SseB
	P9WNV9	Virulence, detoxification, adaptation	dnaJ1 Rv0352	Non-Essential	1.575582504	7.520792877	dnaJ1 Rv0352	Non-Essential	1.591628551	8.23985281	Chaperone protein DnaJ 1
	O33332	Lipid metabolism	ltp1 Rv2790c	Non-Essential	1.567272186	7.292147958	ltp1 Rv2790c	Non-Essential	1.53669405	6.119819101	Probable lipid-transfer protein Ltp1
	P9WFN1	Uncharacterized protein	Rv2140c	Non-Essential	1.552670956	5.113639421	Rv2140c	Non-Essential	1.803235531	5.243319937	UPF0098 protein Rv2140c
	P9WKG3	Intermediary metabolism and respiration	gcpE Rv2868c	Essential	1.547883511	7.032795747	gcpE Rv2868c	Essential	1.517276764	7.112031009	4-hydroxy-3-methylbut-2-en-1-yl diphosphate synthase (flavodoxin)
	O06310	Uncharacterized protein	Rv0360c	Non-Essential	1.537196159	3.965280815	Rv0360c	Non-Essential	1.525137424	3.963027977	Conserved protein
	P9WG95	Intermediary metabolism and respiration	ilvA Rv1559	Essential	1.528332233	4.92820069	ilvA Rv1559	Essential	1.441131592	4.778570567	L-threonine dehydratase biosynthetic IlvA
	I6Y946	Uncharacterized protein	Rv0925c	Non-Essential	1.522557735	5.705353404	Rv0925c	Non-Essential	1.559588909	4.999433699	Conserved protein
	P9WQA5	Intermediary metabolism and respiration	Rv2971	Essential	1.517558575	6.837123403	Rv2971	Essential	1.489521503	6.341149197	Uncharacterized oxidoreductase Rv2971
	I6X8S7	Intermediary metabolism and respiration	Rv0223c	Non-Essential	1.517125607	4.056449975	Rv0223c	Non-Essential	1.412810802	3.957852822	Probable aldehyde dehydrogenase
	P9WJH7	Intermediary metabolism and respiration	ndkA Rv2445c	Non-Essential	1.503061771	5.959943148	ndkA Rv2445c	Non-Essential	1.789879322	5.573120226	Nucleoside diphosphate kinase (NDK)
	P9WPS1	Intermediary metabolism and respiration	cbs Rv1077	Non-Essential	1.498043537	5.917974021	cbs Rv1077	Non-Essential	1.435930252	5.834255882	Putative cystathionine beta-synthase Rv1077
	P9WFC7	Information pathways	uvrB Rv1633	Non-Essential	1.490061283	3.370636482	uvrB Rv1633	Non-Essential	1.431797981	3.379479906	UvrABC system protein B (Protein UvrB) (Excinuclease ABC subunit B)
	P9WHF9	Intermediary metabolism and respiration	cysA1 Rv3117	Growth-Advantage	1.482728958	7.835196495	cysA1 Rv3117	Growth-Advantage	1.608123779	7.570898584	Putative thiosulfate sulfurtransferase (Rhodanese-like protein)
	P9WNG3	Lipid metabolism	fabH Rv0533c	Non-Essential	1.48261261	4.13547188	fabH Rv0533c	Non-Essential	1.462444305	3.956718925	3-oxoacyl-[acyl-carrier-protein] synthase 3 (KAS III) (MtFabH)
	P9WNM1	Information pathways	tsf Rv2889c	Essential	1.481397152	7.704732199	tsf Rv2889c	Essential	1.58485651	6.914934979	Elongation factor Ts (EF-Ts)
	P9WIT1	Intermediary metabolism and respiration	Rv2280	Non-Essential	1.480064392	6.84111639	Rv2280	Non-Essential	1.387584209	7.631415603	Uncharacterized FAD-linked oxidoreductase Rv2280
	P9WIE1	Virulence, detoxification, adaptation	bcp2 Rv2521	Non-Essential	1.47120142	6.96329132	bcp2 Rv2521	Non-Essential	1.475195885	7.426172013	Putative peroxiredoxin Rv2521
	P9WHH1	Intermediary metabolism and respiration	trxB2 Rv3913	Essential	1.468574524	7.125027814	trxB2 Rv3913	Essential	1.618580818	6.664199149	Thioredoxin reductase (TR)
	P9WQB7	Virulence, detoxification, adaptation	ahpC Rv2428	Non-Essential	1.459630966	4.307575107	ahpC Rv2428	Non-Essential	1.528003216	4.341049379	Alkyl hydroperoxide reductase C (MtAhpC)
	I6Y276	Intermediary metabolism and respiration	Rv2993c	Non-Essential	1.435403347	5.1571145	Rv2993c	Non-Essential	1.374224663	4.452820703	Possible 2-hydroxyhepta-2,4-diene-1,7-dioate isomerase (HHDD isomerase)
	P9WFD9	Virulence, detoxification, adaptation	Rv2028c	Non-Essential	1.404054165	3.082649002	Rv2028c	Non-Essential	1.480623245	3.120141744	Universal stress protein Rv2028c (USP Rv2028c)
	P9WJA3	Uncharacterized protein	hrp1 Rv2626c	Non-Essential	1.401695728	2.62444789	hrp1 Rv2626c	Non-Essential	1.273047924	2.349850822	Hypoxic response protein 1 (HRP1)
	P9WPB5	Intermediary metabolism and respiration	cobT Rv2207	Non-Essential	1.389843941	3.793270542	cobT Rv2207	Non-Essential	1.402231216	3.625812722	Nicotinate-nucleotide--dimethylbenzimidazole phosphoribosyltransferase (NN:DBI PRT)
	P9WH51	Information pathways	rpsQ Rv0710	Essential	1.38792181	4.405456062	rpsQ Rv0710	Essential	1.271234035	3.695719044	30S ribosomal protein S17
	P9WFE3	Intermediary metabolism and respiration	ureG Rv1852	Non-Essential	1.382813454	6.024638147	ureG Rv1852	Non-Essential	1.378807545	6.262832458	Urease accessory protein UreG
	O53311	Intermediary metabolism and respiration	Rv3161c	Non-Essential	1.382339954	7.204186976	Rv3161c	Non-Essential	1.658146858	8.890944067	Possible dioxygenase
	P9WPE7	Virulence, detoxification, adaptation	groEL2 Rv0440	Essential	1.373822212	4.548935401	groEL2 Rv0440	Essential	1.573252678	3.697999332	Chaperonin GroEL 2 (60 kDa chaperonin 2)
	O50398	Uncharacterized protein	Rv3369	Non-Essential	1.367909431	2.39504372	Rv3369	Non-Essential	1.535483837	2.69645941	Conserved protein
	P9WQ97	Intermediary metabolism and respiration	amiB2 Rv1263	Non-Essential	1.364027977	4.300808313	amiB2 Rv1263	Non-Essential	1.28298521	4.389474361	Putative amidase AmiB2
	P9WGL7	Regulatory proteins	Rv3143	Non-Essential	1.360807896	2.223415073	Rv3143	Non-Essential	1.411920071	2.284727479	Uncharacterized response regulatory protein Rv3143
	P9WNN1	Information pathways	tuf Rv0685	Essential	1.356069565	6.209525085	tuf Rv0685	Essential	1.655775547	7.494156007	Elongation factor Tu (EF-Tu)
	O53422	Lipid metabolism	fadA3 Rv1074c	Growth-Advantage	1.353399754	5.756874235	fadA3 Rv1074c	Growth-Advantage	1.390129089	5.649729664	Probable beta-ketoacyl CoA thiolase FadA3
	P9WQA3	Intermediary metabolism and respiration	fba Rv0363c	Essential	1.352650166	6.840715864	fba Rv0363c	Essential	1.323069572	6.485383921	Fructose-bisphosphate aldolase (FBP aldolase) (FBPA)
	P9WGZ1	Information pathways	rpoA Rv3457c	Essential	1.348324299	7.016413319	rpoA Rv3457c	Essential	1.361139774	5.852747156	DNA-directed RNA polymerase subunit alpha (RNAP subunit alpha)
	P9WQB9	Intermediary metabolism and respiration	adhD Rv3086	Non-Essential	1.341504574	5.969908309	adhD Rv3086	Non-Essential	1.202385426	5.873431659	Putative alcohol dehydrogenase D
	O86374	Intermediary metabolism and respiration	Rv3257c	Essential	1.340311527	2.221507545	Rv3257c	Essential	1.388839722	2.300813296	Probable phosphomannomutase PmmA (PMM) (Phosphomannose mutase)
	P9WHD3	Information pathways	rplQ Rv3456c	Growth-Defect	1.340217113	3.853778426	rplQ Rv3456c	Growth-Defect	1.325903416	4.133423551	50S ribosomal protein L17
	I6X540	Uncharacterized protein	Rv2683	Non-Essential	1.338754654	5.242647311	Rv2683	Non-Essential	1.465690136	4.509901999	Conserved protein
	P9WNX5	Intermediary metabolism and respiration	asd Rv3708c	Growth-Defect	1.332257748	5.912138618	asd Rv3708c	Growth-Defect	1.423524857	5.203473558	Aspartate-semialdehyde dehydrogenase (ASA dehydrogenase) (ASADH)
	P9WQN5	Cell wall and cell processes	mpa Rv2115c	Non-Essential	1.330803871	5.589252653	mpa Rv2115c	Non-Essential	1.341079712	5.462645766	Proteasome-associated ATPase (ARC) (Mycobacterial proteasome ATPase)
	P9WHL7	Intermediary metabolism and respiration	purL Rv0803	Essential	1.327511311	5.25040329	purL Rv0803	Essential	1.306526661	5.1310187	Phosphoribosylformylglycinamidine synthase subunit PurL (FGAM synthase)
	P9WHD7	Information pathways	rplO Rv0723	Uncertain	1.30601263	4.170193387	rplO Rv0723	Uncertain	1.293813229	3.900411929	50S ribosomal protein L15
	P9WIK3	Intermediary metabolism and respiration	cysH Rv2392	Growth-Defect	1.301439285	4.994230343	cysH Rv2392	Growth-Defect	1.272475719	5.245759019	Adenosine 5'-phosphosulfate reductase (APS reductase)
	P9WJK1	Intermediary metabolism and respiration	nadA Rv1594	Essential	1.281888008	8.948527292	nadA Rv1594	Essential	1.206968784	8.152241247	Quinolinate synthase
	P96281	Cell wall and cell processes	Rv0435c	Non-Essential	1.276519299	4.248635678	Rv0435c	Non-Essential	1.263228416	4.421361605	Putative conserved ATPase
	P9WFI9	Lipid metabolism	Rv0281	Non-Essential	1.27432251	5.228012768	Rv0281	Non-Essential	1.270236969	5.300689264	Putative S-adenosyl-L-methionine-dependent methyltransferase Rv0281
	P9WI57	Information pathways	pnp Rv2783c	Essential	1.267739296	5.981150924	pnp Rv2783c	Essential	1.308290958	5.537567202	Polyribonucleotide nucleotidyltransferase
	P9WME3	Uncharacterized protein	Rv1287	Non-Essential	1.264708519	2.003331719	Rv1287	Non-Essential	1.443257332	2.053486081	Putative HTH-type transcriptional regulator Rv1287
	P95034	Intermediary metabolism and respiration	Rv0688	Non-Essential	1.264598846	6.164718633	Rv0688	Non-Essential	1.226113319	5.837335327	Putative ferredoxin reductase
	O06578	Uncharacterized protein	Rv1126c	Non-Essential	1.255358219	2.58944815	Rv1126c	Non-Essential	1.403783798	2.519333009	Conserved protein
	P9WNW9	Intermediary metabolism and respiration	hisD Rv1599	Essential	1.254595757	6.281544398	hisD Rv1599	Essential	1.24366045	5.208944557	Histidinol dehydrogenase (HDH)
	P9WNG7	Intermediary metabolism and respiration	fixA Rv3029c	Growth-Defect	1.236661434	4.946724591	fixA Rv3029c	Growth-Defect	1.382524014	6.259246741	Electron transfer flavoprotein subunit beta (Beta-ETF)
	P9WH85	Information pathways	rplD Rv0702	Essential	1.236468792	4.398404264	rplD Rv0702	Essential	1.405642986	4.815563467	50S ribosomal protein L4
	P9WQB3	Intermediary metabolism and respiration	leuA Rv3710	Essential	1.232950687	6.442831257	leuA Rv3710	Essential	1.218405247	6.237348856	2-isopropylmalate synthase
	P9WH79	Information pathways	rplI Rv0056	Non-Essential	1.225336552	5.426639909	rplI Rv0056	Non-Essential	1.274153233	5.31257368	50S ribosomal protein L9
	P9WL63	Uncharacterized protein	Rv2629	Non-Essential	1.220798969	6.210431805	Rv2629	Non-Essential	1.287930965	6.378962805	Uncharacterized protein Rv2629
	P9WH43	Information pathways	rpsA Rv1630	Essential	1.218367577	4.048168339	rpsA Rv1630	Essential	1.410372257	3.931392028	30S ribosomal protein S1
	P9WG55	Cell wall and cell processes	tig Rv2462c	Non-Essential	1.217750549	4.030911501	tig Rv2462c	Non-Essential	1.204115391	4.024407921	Trigger factor (TF)
	P9WNE5	Intermediary metabolism and respiration	bfrB Rv3841	Non-Essential	1.212513924	3.691481644	bfrB Rv3841	Non-Essential	1.616090298	3.400905712	Ferritin BfrB
	P9WGB1	Intermediary metabolism and respiration	folD Rv3356c	Essential	1.208316803	7.413240345	folD Rv3356c	Essential	1.2296524	5.775230348	Bifunctional protein FolD
	P9WNL1	Intermediary metabolism and respiration	eno Rv1023	Growth-Defect	1.205562592	6.290448714	eno Rv1023	Growth-Defect	1.233539581	6.559594301	Enolase
CyC_{32yne} specific target proteins	O53149	Cell wall and cell processes					Rv1458c	Growth-Defect	3.086162567	3.99664952	Probable unidentified antibiotic-transport ATP-binding protein ABC transporter
	P9WGW3	Information pathways					ruvA Rv2593c	Growth-Defect	2.407989979	2.029823657	Holliday junction ATP-dependent DNA helicase RuvA
	L7N684	Uncharacterized protein					Rv2141c	Non-Essential	2.22158289	4.341350569	Conserved protein
	P9WIR3	Virulence, detoxification, adaptation					Rv0577	Non-Essential	2.173385143	4.087804176	Putative glyoxylase CFP32 (27 kDa antigen Cfp30B)
	P9WHN9	Lipid metabolism					php Rv0230c	Growth-Advantage	1.86165905	2.040712126	Phosphotriesterase homology protein
	P9WQP5	Intermediary metabolism and respiration					devB Rv1445c	Non-Essential	1.853541374	2.649670198	6-phosphogluconolactonase (6PGL)
	P0CG96;P0CG95	Intermediary metabolism and respiration					sseC1 Rv3118	Growth-Advantage	1.710254192	5.472001056	Uncharacterized protein Rv3118
	P71853	Intermediary metabolism and respiration					Rv3548c	Non-Essential	1.560416222	2.408874123	Probable short-chain type dehydrogenase/reductase
	P9WFK3	Uncharacterized protein					Rv0504c	Non-Essential	1.510525227	5.251037192	UPF0336 protein Rv0504c
	P9WHB5	Information pathways					rplY Rv1015c	Growth-Defect	1.443259239	5.464394682	50S ribosomal protein L25 (General stress protein CTC)
	P9WHT9	Intermediary metabolism and respiration					prcB Rv2110c	Essential	1.405330181	5.994341226	Proteasome subunit beta
	I6XW38	Intermediary metabolism and respiration					Rv0730	Growth-Advantage	1.356253624	5.507171632	DNA topoisomerase (ATP-hydrolyzing)
	P9WMJ9	Virulence, detoxification, adaptation					dnaK Rv0350	Essential	1.281809807	4.38609901	Chaperone protein DnaK (HSP70)
	P9WFK1	Lipid metabolism					hadA Rv0635	Essential	1.275116444	4.841212374	UPF0336 protein Rv0635
	P9WN95	Cell wall and cell processes					ftsZ Rv2150c	Essential	1.264906883	4.590722573	Cell division protein Fts2
	P9WNG5	Lipid metabolism					fabD Rv2243	Essential	1.256029606	5.721682262	Malonyl CoA-acyl carrier protein transacylase (MCT)
	P9WKI1	Intermediary metabolism and respiration					ino1 Rv0046c	Essential	1.25335598	6.729812604	Inositol-3-phosphate synthase (IPS) (Myo-inositol 1-phosphate synthase)
	P9WPU7	Intermediary metabolism and respiration					atpA Rv1308	Essential	1.25289917	7.868112051	ATP synthase subunit alpha (ATP synthase F1 sector subunit alpha) (F-ATPase subunit alpha)
	P9WIC9	Intermediary metabolism and respiration					gpm1 Rv0489	Non-Essential	1.249867439	5.859520046	2,3-bisphosphoglycerate-dependent phosphoglycerate mutase (BPG-dependent PGAM)
	P9WPE1	Intermediary metabolism and respiration					citE Rv2498c	Non-Essential	1.245306015	4.766576346	Citrate lyase subunit beta-like protein
	P9WFC9	Virulence, detoxification, adaptation					Rv1636	Essential	1.214326859	4.299955083	Universal stress protein Rv1636 (USP Rv1636)
	P9WGC7	Intermediary metabolism and respiration					sucD Rv0952	Essential	1.213413715	7.410160347	Succinate--CoA ligase [ADP-forming] subunit alpha
	P9WPZ7	Intermediary metabolism and respiration					argD Rv1655	Essential	1.20838213	2.097394074	Acetylornithine aminotransferase (ACOAT)

Fig. S1. ^{1}H, ^{13}C and ^{31}P NMR spectra

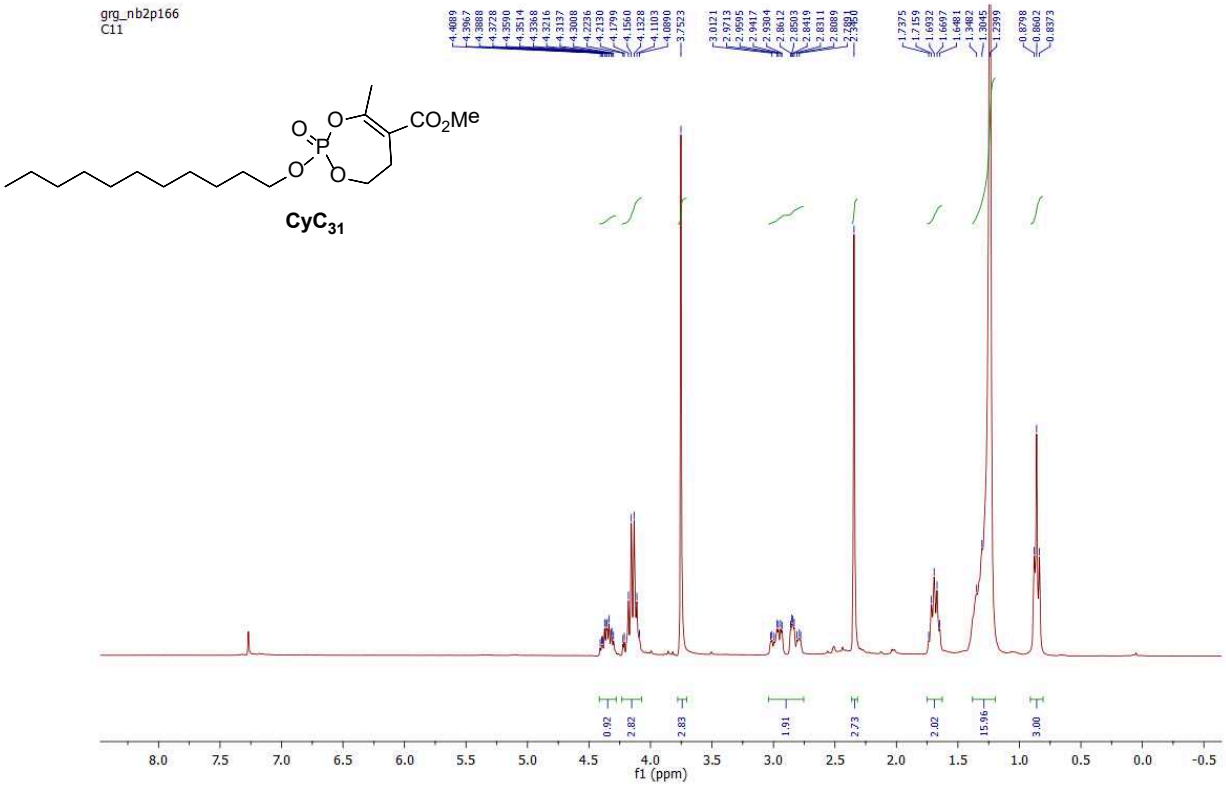

^{1}H NMR Spectrum (300 MHz, $CDCl_3$)

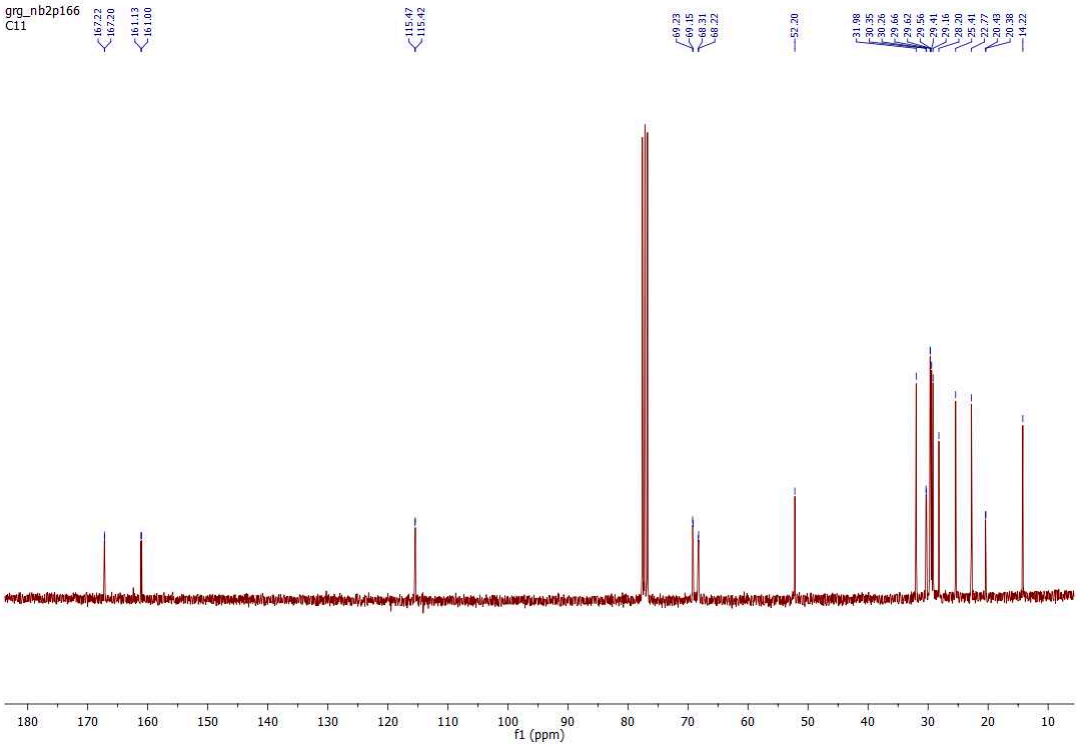

^{13}C NMR Spectrum (300 MHz, $CDCl_3$)

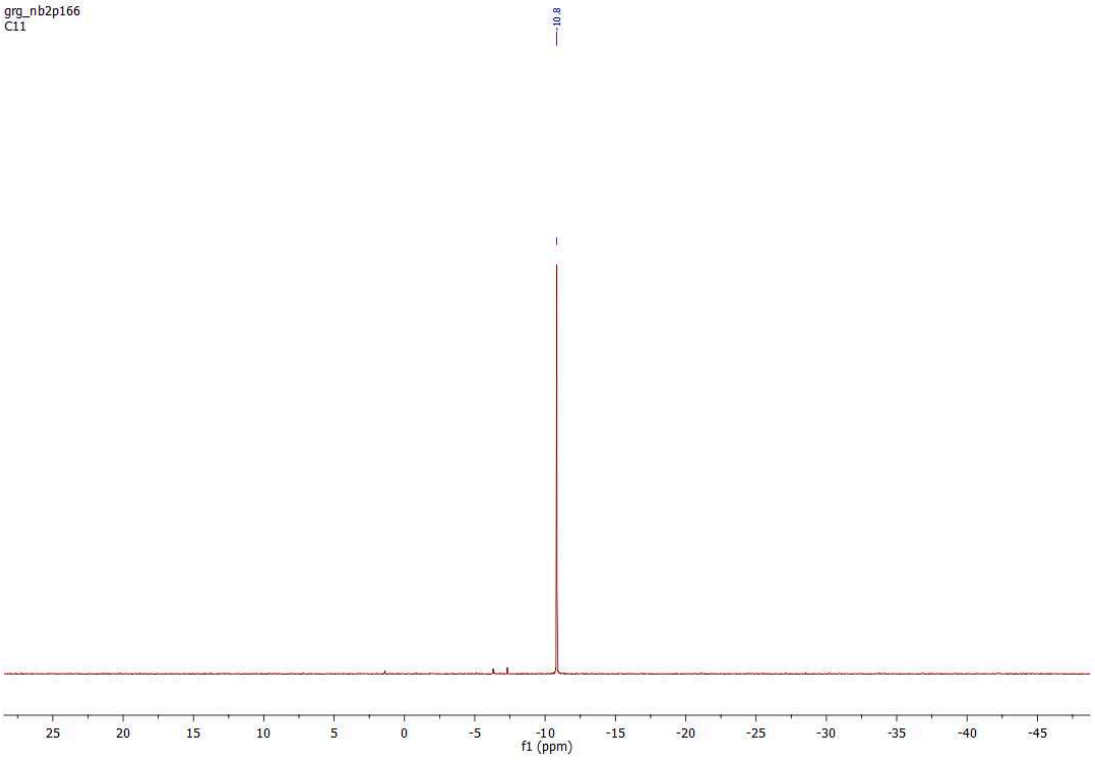

^{31}P NMR Spectrum (300 MHz, $CDCl_3$)

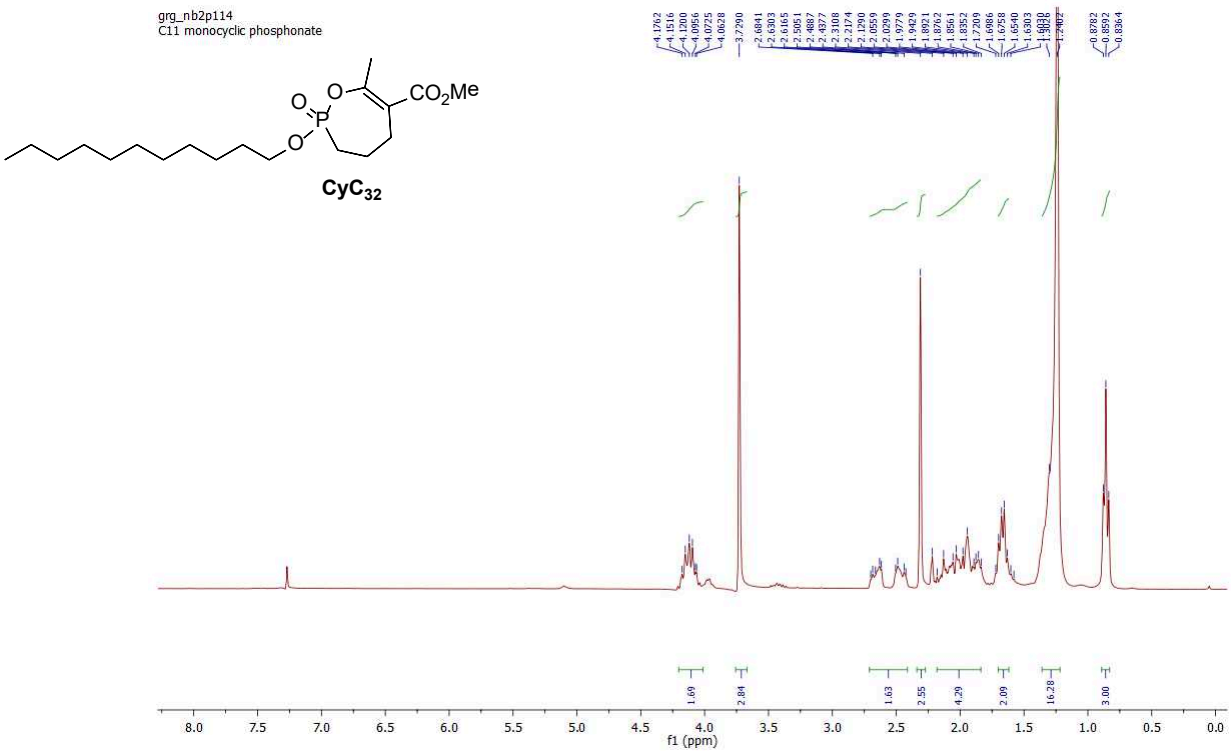

^{1}H NMR Spectrum (300 MHz, $CDCl_3$)

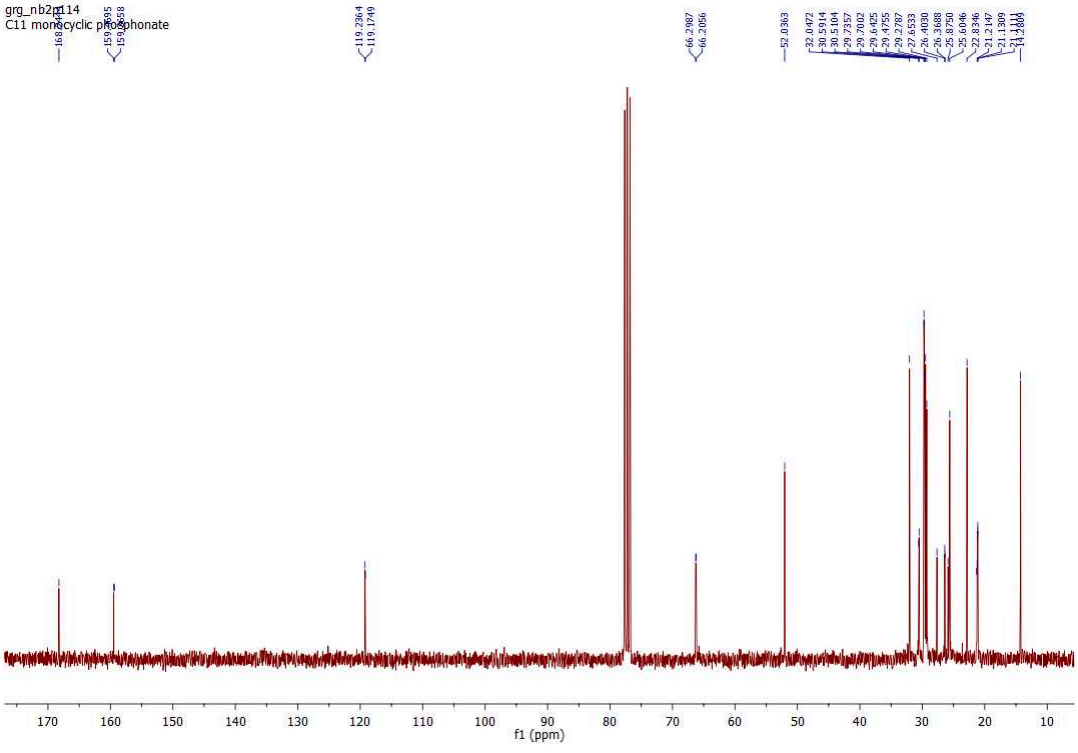

^{13}C NMR Spectrum (300 MHz, $CDCl_3$)

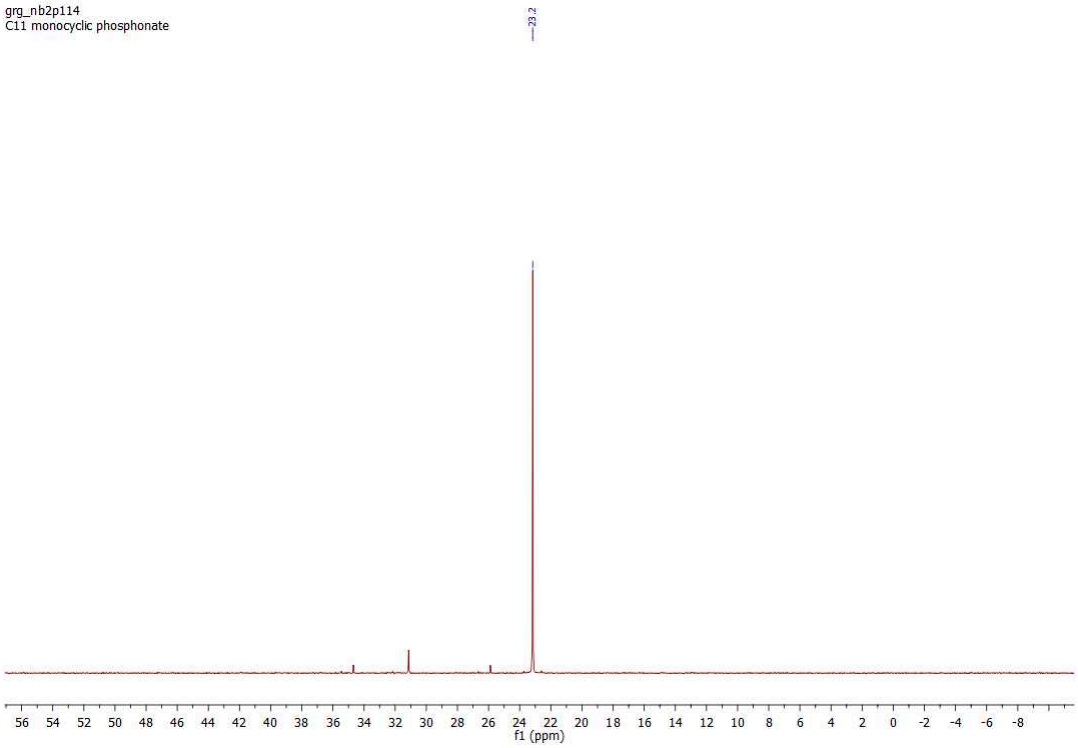

^{31}P NMR Spectrum (300 MHz, $CDCl_3$)

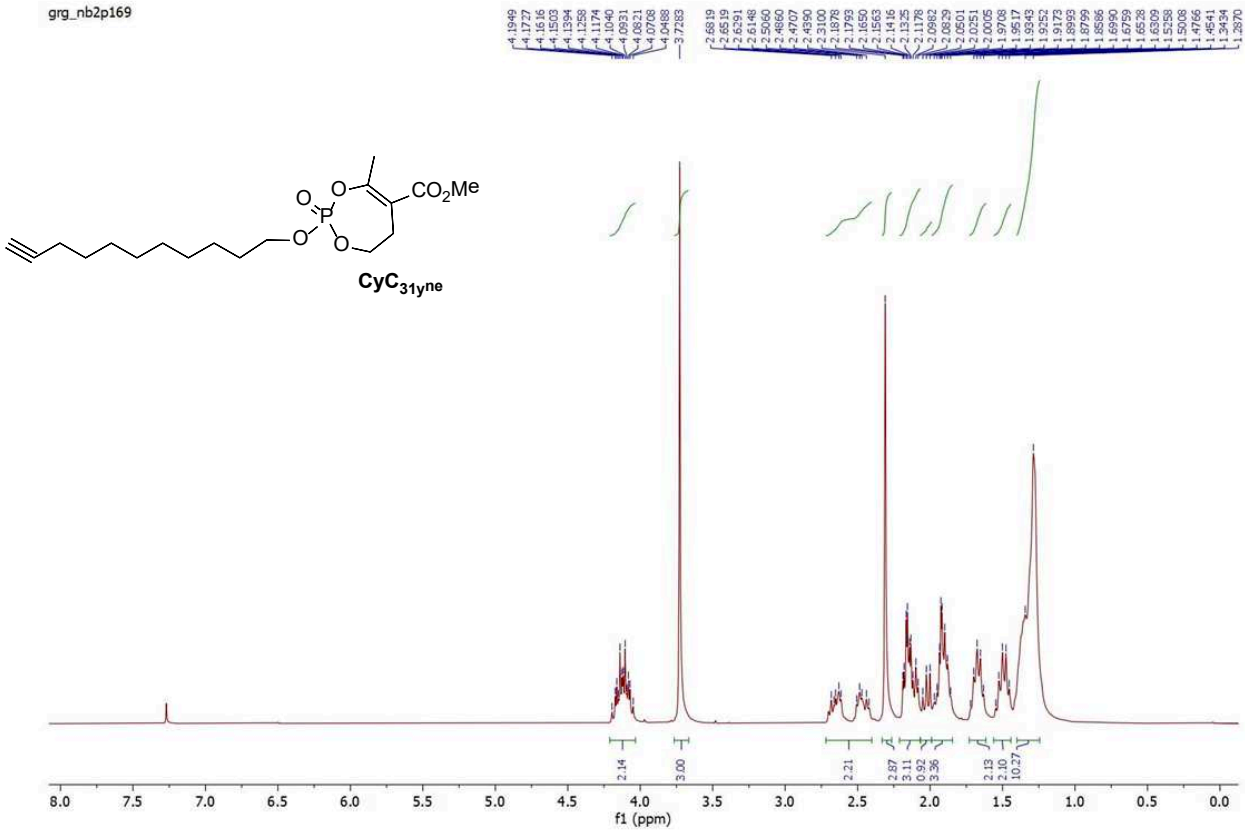

^{1}H NMR Spectrum (300 MHz, $CDCl_3$)

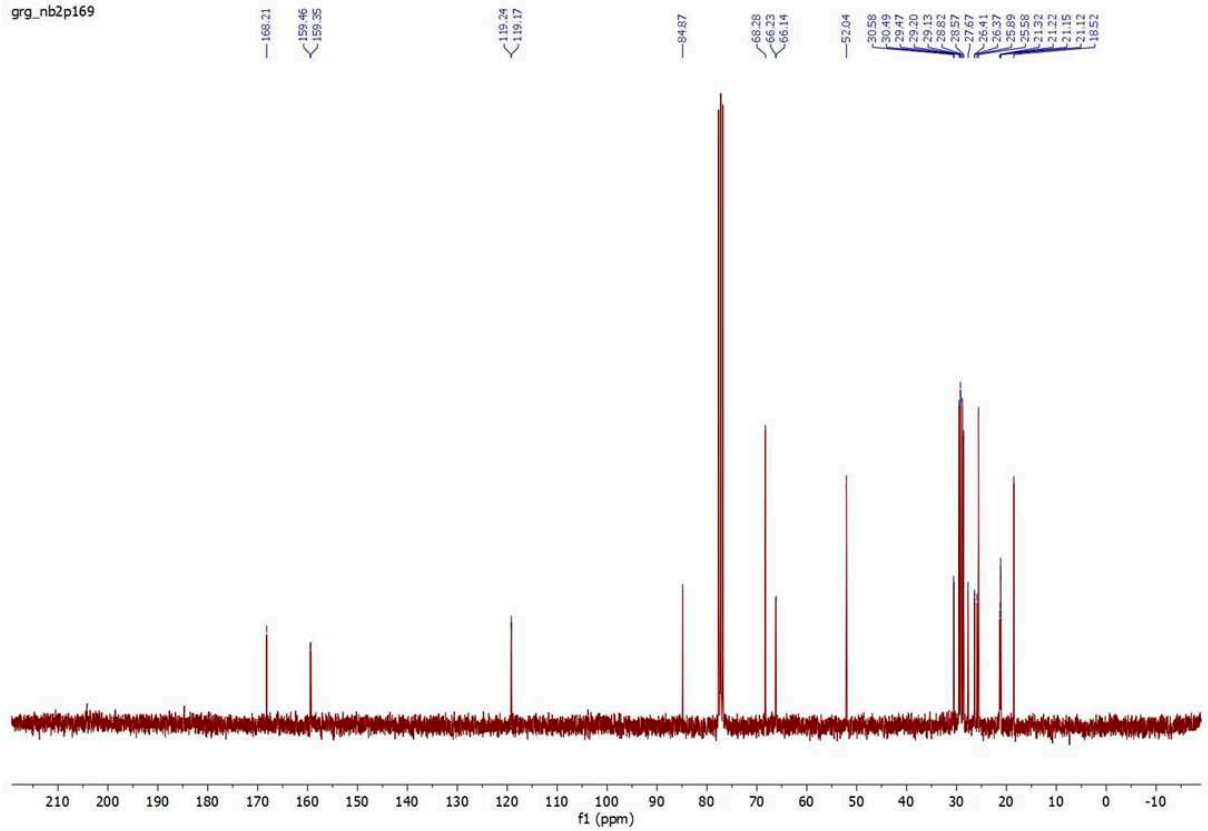

^{13}C NMR Spectrum (300 MHz, $CDCl_3$)

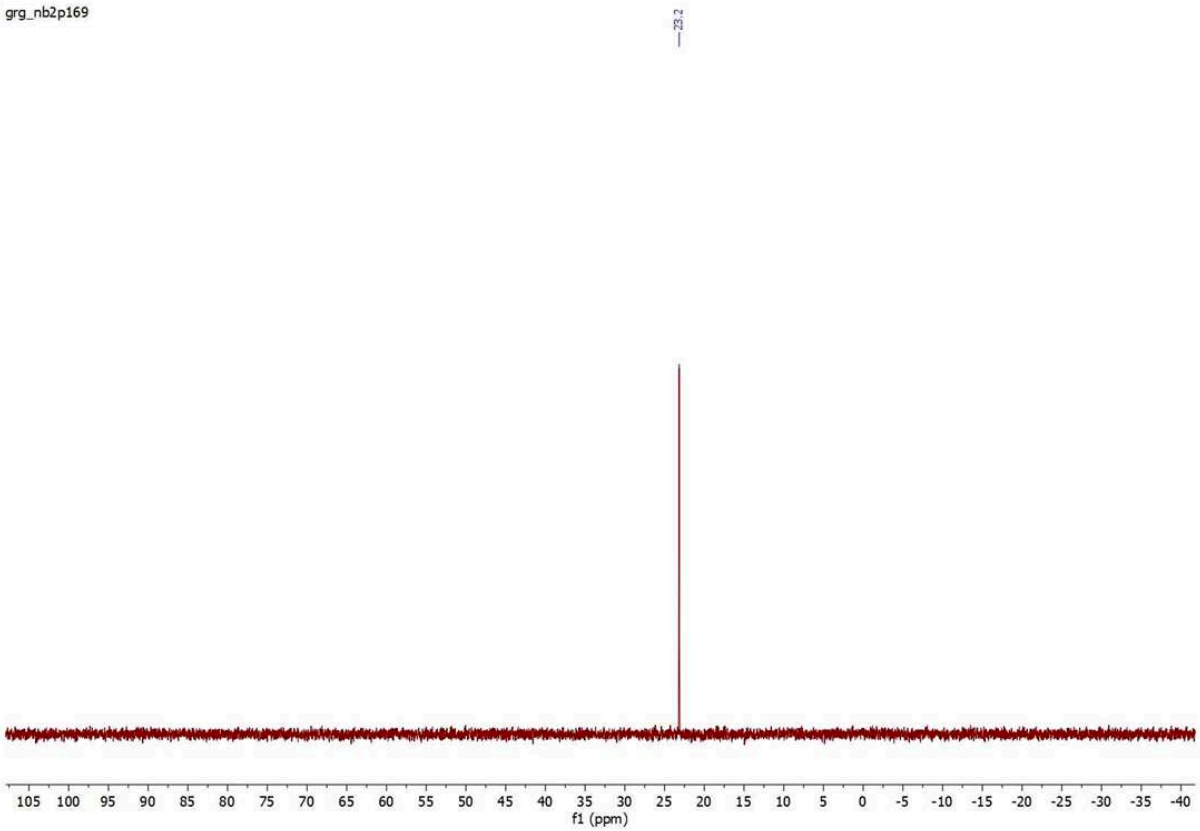

^{31}P NMR Spectrum (300 MHz, $CDCl_3$)

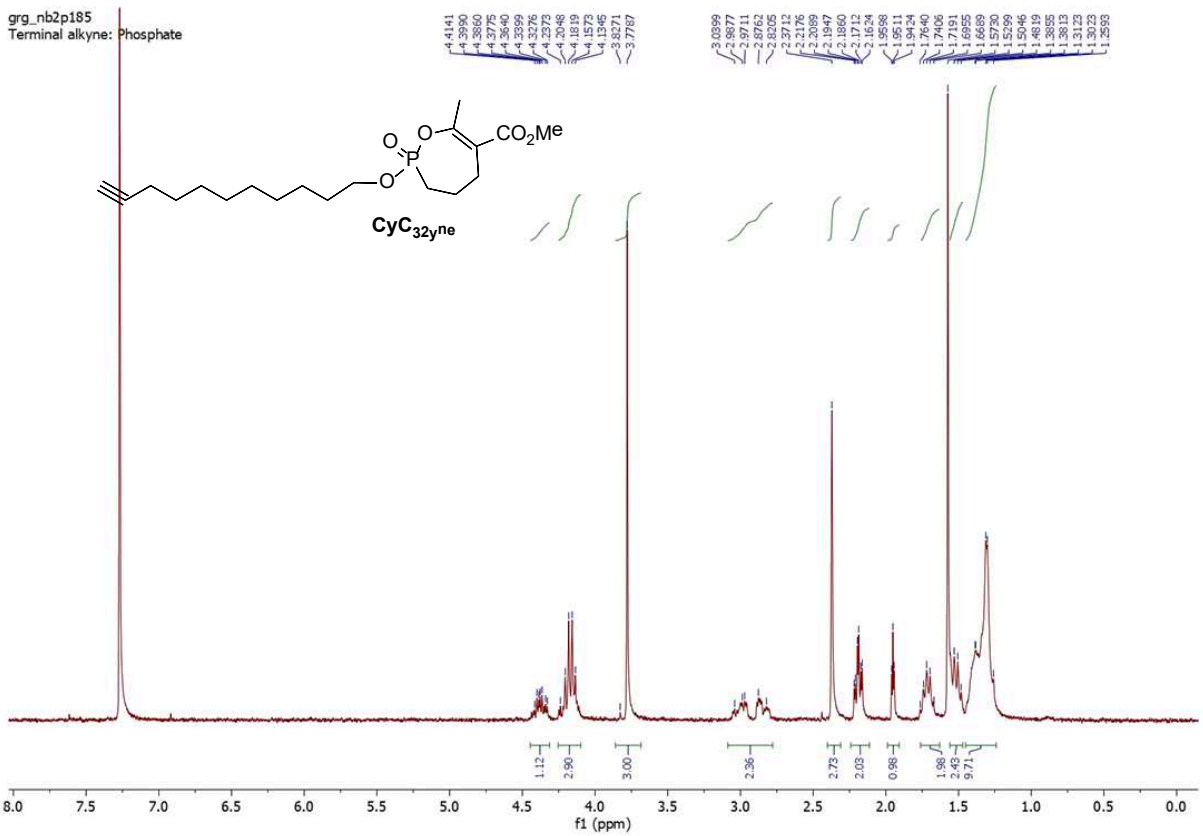

^{1}H NMR Spectrum (300 MHz, $CDCl_3$)

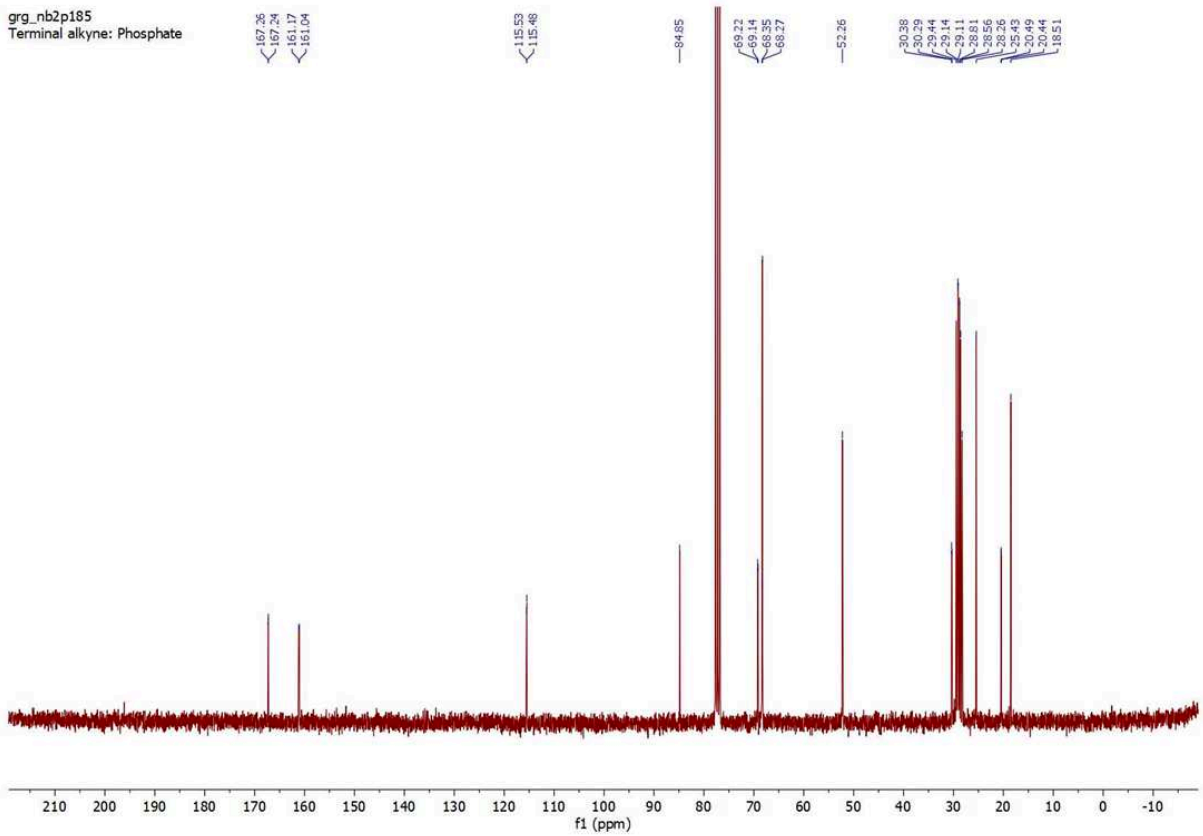

^{13}C NMR Spectrum (300 MHz, $CDCl_3$)

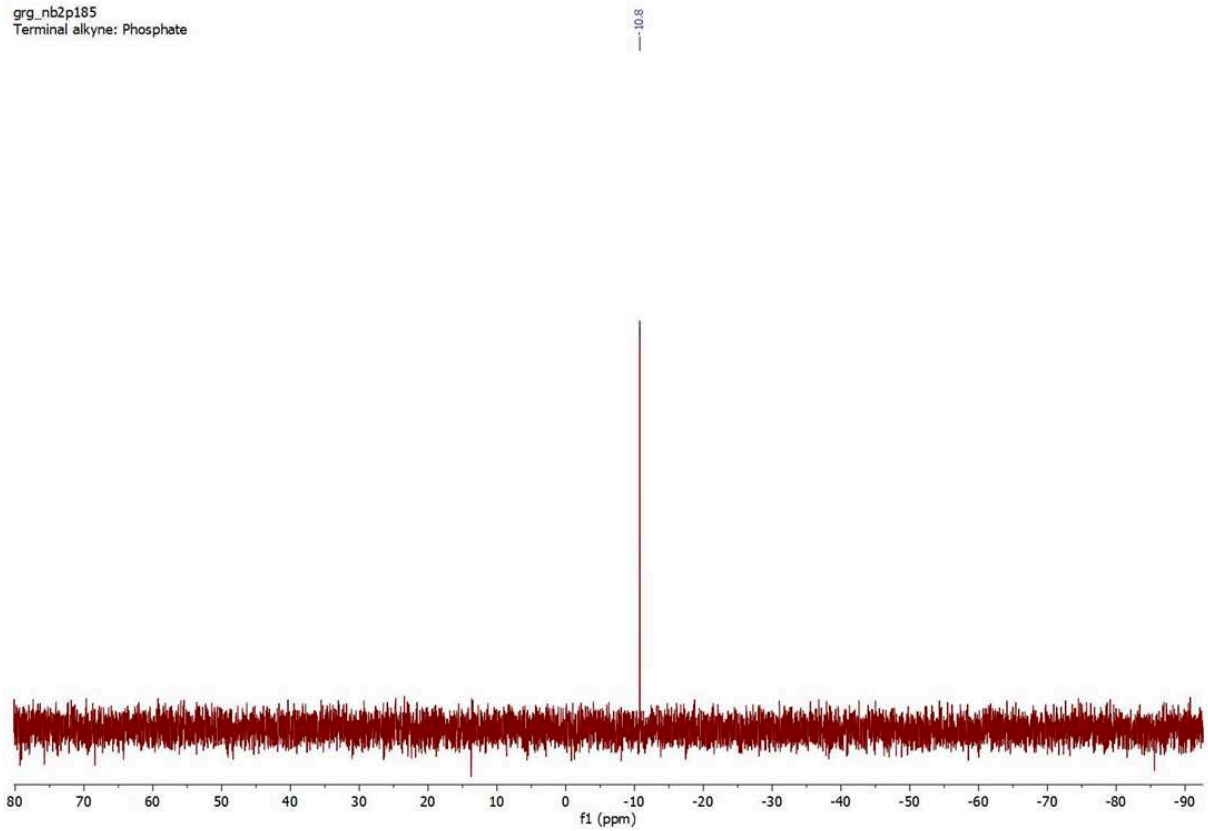

^{31}P NMR Spectrum (300 MHz, $CDCl_3$)

Article IV

Mapping of mycobacterial lipolytic enzymes involved in triacylglycerol accumulation as intrabacterial lipid inclusions using multi-target inhibitor-like affinity-based probes

---

R. Avellan*, J. Lehoux*, T. Dargham*, T. Francis, L. Celik, A. Guy, I. Poncin, V. Point, L. Kremer, T. Durand, S. Audebert, L. Camoin, C.D. Spilling, P. Santucci, C. Crauste, S. Canaan, J.-F. Cavalier

Manuscrit en préparation

* Contribution égale

Le métabolisme des lipides représente un aspect crucial dans la physiologie mycobactérienne. En effet, les mycobactéries possèdent une enveloppe complexe riche en lipides [407] qui joue un rôle central dans la résistance au stress ainsi que dans l'éviction de l'immunité des mycobactéries pathogènes. Un aspect fondamental des infections aux mycobactéries pathogènes réside dans leur capacité à métaboliser les lipides de l'hôte et à les accumuler dans leur propre cytoplasme sous forme d'inclusions lipidiques Intrabactériennes ou ILI [298, 408, 409]. Les ILI sont des organelles lipidiques constituées d'un cœur de lipides neutres (principalement des TAG) entouré d'une monocouche de phospholipides contenant de nombreuses protéines [205, 410-413]. Elles sont accumulées durant l'entrée en dormance et servent de stockage d'énergie, qui sera utilisé lors de la réactivation de l'infection, et permettent l'adaptation et la survie lors de divers stress environnementaux [39, 409, 414]. En particulier chez *M. tb*, les ILI jouent un rôle central dans la pathogénie en contribuant à l'installation d'infections latentes [224, 261, 414-416] et en induisant une résistance accrue aux antibiotiques de première ligne [261, 417, 418].

De plus, il a été montré que la présence d'ILI chez *M. abs* entraine une virulence accrue et une augmentation de la mortalité lors de l'infection d'embryons du poisson zèbre [218, 419].
Ainsi, si l'étude du métabolisme des ILI constitue une source de cibles thérapeutiques potentielles importante, les protéines impliquées dans ces processus restent cependant peu étudiées à ce jour. Bien que de nombreuses études sur des enzymes recombinantes purifiées existent [209, 330, 419, 420], les études dédiées à l'identification et la caractérisation du métabolisme des ILI restent rares.

Dans le but de pallier à ce manque, notre équipe a développé et validé un modèle expérimental simple d'induction de la synthèse des ILI par carence nutritive en azote chez *M. abs* et *M. smeg* : le milieu MSM-NL [218]. Nous avions également démontré que l'utilisation d'inhibiteurs d'enzymes à sérine ou cystéine permettait d'inhiber l'accumulation de TAG dans ce modèle, confirmant ainsi l'implication de ces enzymes dans la synthèse des TAG [218]. La plupart de ces enzymes à sérine ou cystéine présentent un repliement α/β-hydrolase [421, 422], et possèdent diverses activités : hydrolases, isomérases, lyases, ligases, oxydoréductases et transférases [421].

Nous avons précédemment développé et caractérisé deux familles d'inhibiteurs covalents de ces enzymes qui sont des analogues d'Oxadiazolones (**OX**) et de Cyclophostines/Cyclipostins

(**CyC**) [330]. Ces molécules sont des inhibiteurs multi-cibles qui forment une liaison covalente avec la sérine ou la cystéine catalytique de leurs enzymes cibles. Ces deux familles ont montré des activités antimycobactériennes intéressantes contre *M. tb* et *M. abs* à la fois *in vitro* et en contexte d'infection de macrophages par les mycobactéries. Enfin, ces molécules ne sont pas toxiques pour les macrophages [330, 336, 344, 348, 351, 354, 423].

Afin d'identifier les cibles enzymatiques de ces inhibiteurs chez *M. tb*, une première approche d'ABPP compétitive avait été utilisée en effectuant une compétition entre nos inhibiteurs et une sonde, l'ActivX^{TM} Desthiobiotin-FP, conduisant à identifier 18 et 23 cibles respectivement pour le **CyC$_{17}$** et l'**HPOX** [336, 348]. Cette même approche effectuée sur *M. abs* a mis en évidence 39 et 21 cibles respectivement pour le **CyC$_{17}$** et l'**iB*p*PPOX** [348, 354]. Parmi ces protéines identifiées, plusieurs ont été validées comme cibles effectives de nos inhibiteurs par des approches biochimiques et structurales. C'est le cas de la thioésterase-phospholipase LipG (Rv0646c) [371], de la mycolyltransférase Ag85C (Rv0129c & MAB_0175) [354, 369], de la thioésterase TesA (Rv2928) [370], et de l'hydrolase HsaD (Rv3569c) [424].

Tous ces résultats confirment que nos inhibiteurs ciblent de façon covalente des enzymes mycobactériennes à sérine et cystéine catalytiques impliquées dans le métabolisme des lipides. Dès lors, ces composés représentent des sondes ABP de choix pour étudier les mécanismes moléculaires utilisés par les mycobactéries dans l'acquisition des lipides de l'hôte, la synthèse et la consommation des ILI.

C'est donc dans ce contexte que nous avons synthétisé et caractérisé, lors des deux premières études présentées dans ce manuscrit de thèse, des sondes d'ABP CyC porteuses d'un fluorophore Dansyl (**CyC$_{31\text{-Dansyl}}$**) ou d'un alcyne terminal (**CyC$_{31yne}$**) de façon à marquer spécifiquement les mycobactéries dans une polyculture et également pour effectuer la capture directe des cibles de ce composé par CC-ABPP.

Dans le cadre de cette nouvelle étude, nous reportons la synthèse de deux nouvelles sondes ABP dérivées de l'**HPOX** [348, 354], l'une contenant un fluorophore NBD (**HP$_{\text{-NBD-}}$OX**) et la seconde un alcyne terminal (**HPOX$_{yne}$**). L'**HPOX** a été choisi car il présente une activité modérée contre *M. abs* (MIC_{50} / MIC_{90} = 92.9 / 99.9 µM).

Nous avons ensuite utilisé ces sondes ABP dérivées de **CyC** et d'**OX** afin d'étudier le métabolisme d'acquisition des ILI dans le modèle *in vitro* de carence en azote (MSM-NL).

Dans un premier temps nous avons montré que l'**HPOX$_{yne}$** et le **CyC$_{31yne}$** étaient capables d'inhiber partiellement la synthèse des TAG dans le modèle MSM-NL, et que les analogues fluorescents de ces deux composés étaient colocalisés avec les ILI dans ce modèle.
Par la suite, nous avons utilisé l'**HPOX$_{yne}$** et le **CyC$_{31yne}$** pour la capture directe de leurs cibles par CC-ABPP en condition d'accumulation des ILI (milieu MSM-NL) *vs*. en absence d'accumulation (milieu MSM). La comparaison des données de protéomique résultant de ces expériences a permis d'identifier 65 enzymes potentiellement impliquées dans le métabolisme de synthèse des ILI.

Parmi les cibles identifiées, la construction de souches de délétion, complémentation et de surexpression, nous a ensuite permis de valider la long-chain-fatty-acid--CoA ligase (MAB_1978/FadD15) comme directement impliquée dans la biogénèse des ILI chez *M. abs*. En effet, la souche de délétion a présenté un phénotype de 50% de réduction des TAG par rapport à la souche sauvage, avec une restauration du phénotype d'accumulation pour la souche de complémentation. De plus, la construction d'une souche reportrice de fusion *mab_1978c-sfGFP* nous a permis de confirmer la colocalisation de cette enzyme sur les ILI.

Il reste encore beaucoup de travail afin de caractériser et de valider l'ensemble des protéines identifiées par cette approche de CC-ABPP comme prenant part à la synthèse des ILI sous stress nutritif à l'azote. Ce travail permettra de mieux comprendre ce métabolisme clef dans les infections mycobactériennes et d'identifier de nouvelles cibles thérapeutiques pour lutter contre ces infections.

Mapping of mycobacterial lipolytic enzymes involved in triacylglycerol accumulation as intrabacterial lipid inclusions using activity-based multi-target inhibitor probes

Romain Avellan[1,#], Jordan Lehoux[2,#], Tonia Dargham[1,3,#], Thomas Francis[1], Léa Celik[1], Alexandre Guy[2], Isabelle Poncin[1], Vanessa Point[1], Laurent Kremer[4,5], Thierry Durand[2], Stéphane Audebert[6], Luc Camoin[6], Christopher D. Spilling[7], Pierre Santucci[1], Céline Crauste[2], Stéphane Canaan[1], Jean-François Cavalier[1]*

[1] Aix-Marseille Univ., CNRS, LISM UMR7255, IMM FR3479, Marseille, France

[2] IBMM, Univ Montpellier, CNRS, ENSCM, Montpellier, France

[3] IHU Méditerranée Infection, Aix-Marseille Univ., Marseille, France

[4] Centre National de la Recherche Scientifique UMR 9004, Institut de Recherche en Infectiologie de Montpellier (IRIM), Université de Montpellier, 1919 route de Mende, 34293, Montpellier, France

[5] INSERM, IRIM, 34293 Montpellier, France

[6] INSERM, CNRS, Institut Paoli-Calmettes, CRCM, Marseille Protéomique, Aix-Marseille Univ., France

[7] Department of Chemistry and Biochemistry, University of Missouri-St. Louis, MO, USA

[#] These authors contributed equally to this work, and should be considered as first co-authors

[*] Corresponding author: Jean-François Cavalier (jfcavalier@imm.cnrs.fr).

ABSTRACT

Mycobacterial lipids play a critical role in the physiology, life cycle and pathogenicity of mycobacteria-related diseases. They participate in host-pathogen interactions and fulfill important functions, related to virulence (reactivation and replication), adaptation to a non-replicating dormant form, cell wall biosynthesis, bacterial growth, lipid storage and degradation as intrabacterial lipid inclusions (ILI). They play also a major role in lipid metabolism for long-term survival and persistence but the enzymes involved in these processes remain largely undefined. Herein, we report the direct capture of target proteins in *Mycobacterium abscessus* growing under carbon excess and nitrogen-deprived *in vitro* conditions that promote triacylglycerol production and ILI formation. The method developed relies on bio-orthogonal click-chemistry activity-based protein profiling (CC-ABPP) of newly synthetized Oxadiazolone (**OX**), Cyclophostin and Cyclipostins (**CyC**) probes. This approach led to the identification of a set of 65 enzymes, potentially involved in the global processes related to ILI anabolism. Among these, the long-chain-fatty-acid-CoA ligase MAB_1978c/FadD15 has been validated as a pivotal enzyme that co-localizes on ILI and as a major contributor in ILI formation in *M. abscessus*.

KEYWORDS

Activity-based protein profiling; multitarget inhibitor-like affinity-based probes; lipid metabolism; Cyclipostins and Cyclophostin; Oxadiazolone; *M. abscessus*; triacylglycerol.

INTRODUCTION

Mycobacteria are known for their unique and complex cell wall architecture,[1] characterized by distinct lipid-rich outer layers, making lipid metabolism a central point of their physiological processes. One crucial aspect of all mycobacteria is their ability to metabolize host lipids and to accumulate the resulting neutral lipids in their own cytoplasm in the form of intrabacterial lipid inclusions (ILI).[2-4] These lipid-rich organelles consist of a hydrophobic core containing neutral lipids, essentially triacylglycerol (TAG), surrounded by a phospholipid monolayer, associated with numerous proteins.[5-9] These ILI not only serve as reservoirs for energy storage and provide a platform for the synthesis and maintenance of lipids, which are essential for the adaptability and survival of mycobacteria under various environmental stresses.[3, 10-11] This is particularly true in the case of *M. tuberculosis*, the causative agent of tuberculosis (TB), where ILI play a critical role in pathogenesis of the disease by contributing to the ability of the bacillus to establish and maintain infection[10, 12-15] and to induce increased tolerance to first-line anti-TB drugs.[13, 16-17]

ILI have been reported in all mycobacterial species; including pathogenic (*i.e.*, *M. canettii*[18], *M. leprae*,[19] *M. avium*,[11] *M. marinum*,[20] *M. ulcerans*,[21] and *M. tuberculosis*[7, 10, 13, 22-23]), non-tuberculous (*i.e.*, *M. abscessus*[24-25]), as well as saprophytic mycobacteria (*i.e.*, *M. smegmatis*[22, 24, 26-27]); suggests a conserved function of these organelles in the mycobacterial lifecycle and physiology.[28] Furthermore, zebrafish embryos infected with lipid-rich *M. abscessus* showed higher mortality, consistent with a role of ILI and host infection.[24-25] How these mycobacteria acquire host lipids and how ILI are formed remain largely unanswered questions. While these issues have been tackled, mostly by studying pure recombinant lipolytic enzymes secreted by mycobacteria,[23, 25, 29-30] studies dedicated to the identification and characterization of proteins involved in ILI accumulation and consumption remain scarce.[7, 26]

Stimulated by these observations, we developed two robust experimental models to report ILI formation and degradation, in order to mimic lipid metabolism during the dormancy and reactivation stages.[31] The first model is based on infected murine bone-marrow-derived

macrophages (mBMDM) fed with Very Low-Density Lipoproteins (VLDL) to trigger the differentiation of the macrophages into foamy macrophages.[11, 23] In this specific environment, mycobacteria are able to accumulate host lipids to form ILI, and further hydrolyze these stored ILI upon removal of VLDL from the culture medium, thus mimicking reactivation and propagation of the disease. The second one is an *in vitro* and reversible model based on carbon excess and nitrogen starvation allowing *in vitro* ILI biosynthesis and hydrolysis.[24] Interestingly, we demonstrated in both models that the presence of serine-hydrolase inhibitors impaired TAG accumulation in the form of ILI as well as their further hydrolysis, confirming the involvement of lipolytic enzymes in the ILI accumulation and consumption processes.[23-24] Most enzymes participating in ILI metabolism are members of the α/β-hydrolase fold superfamily,[32-34] consisting in hydrolases, isomerases, lyases, ligases, oxidoreductases and transferases. Moreover, the hydrolase class includes esterases, dienelactone hydrolases, epoxide hydrolases, haloalkane dehalogenases, lipases, thioesterases, and peptidases;[32, 34] all possessing a catalytic serine or cysteine residue in their active site, *i.e.*, (Ser/Cys)-based enzymes.

We have previously reported the potent antimycobacterial activity of two families of enzyme inhibitors, namely the Oxadiazolone compounds (**OX**) and the Cyclophostin & Cyclipostins analogs (**CyC**).[29] These molecules form a covalent bond with the catalytic serine or cysteine, thereby inhibiting the activity of the corresponding (Ser/Cys)-based enzyme.[29] Non-toxic to host cell macrophages (CC_{50}>100 µM), both **OX** and **CyC** efficiently inhibited the growth of *M. tuberculosis* and *M. abscessus* in broth medium and/or within infected macrophages.[29, 35-40]

A competitive activity-based protein profiling (ABPP) approach using either **CyC$_{17}$**- or **HPOX**-pre-treated *M. tuberculosis* cell culture, after enrichment with the ActivX^{TM} Desthiobiotin-FP probe, allowed the identification of 18 and 23 distinct target proteins, respectively.[37-38] A similar competitive ABPP strategy was further applied to *M. abscessus*, resulting in 39 and 21 potential target enzymes for **CyC$_{17}$** and **iB*p*PPOX**, respectively.[35, 37] Most of the identified proteins are (Ser/Cys)-based enzymes related to global lipid metabolism (cholesterol and free fatty acid) and

cell wall biosynthesis. Among them, the bifunctional thioesterase-phospholipase LipG (Rv0646c),[41] the mycolyltransferase Ag85C (Rv0129c & MAB_0175),[35, 42] the thioesterase TesA (Rv2928),[43] and the carbon-carbon hydrolase HsaD (Rv3569c)[44] have been validated as effective targets and subsequently confirmed by resolving their crystal structures in complex with **CyC$_{17}$**. Consequently, the use of these inhibitors as efficient activity-based probes (ABP) to decipher the metabolic pathways used by the mycobacteria to catabolize host derived lipids (cholesterol and fatty acids), notably by identifying key enzymes involved in the accumulation and consumption of ILI, will provide highly valuable data related to cellular and molecular mechanisms crucial for mycobacteria survival, persistence and virulence.[3] In addition, we have recently validated the use of new efficient **CyC** ABPs, obtained by direct introduction of either a Dansyl fluorescent moiety (*i.e.*, **CyC$_{31\text{-Dansyl}}$**[40]) or a terminal alkyne function (*i.e.*, **CyC$_{31\text{yne}}$**[44]), as a means to ***i)*** specifically label living mycobacterial species through the covalent binding to (Ser/Cys)-based enzymes,[40] and ***ii)*** capture target proteins in live mycobacteria through direct click-chemistry ABPP (CC-ABPP).[44] In the present study, we report the synthesis of two novel **OX** ABPs derived from the **HPOX** inhibitor,[35, 37] and containing either a terminal alkyne function (*i.e.*, **HPOX$_{\text{yne}}$**) or a fluorescent NBD tag (*i.e.*, **HP$_{\text{-NBD-}}$OX**). The **HPOX** derivative was selected based on its moderate antibacterial activity (MIC_{50} / MIC_{90} = 92.9 / 99.9 µM) against *M. abscessus* S growth. These four **OX** & **CyC** ABPs have been further exploited to decipher ILI formation in *M. abscessus* using the nitrogen-deprived (MSM-NL) *in vitro* model. Strikingly, the two alkyne-containing inhibitors, **HPOX$_{\text{yne}}$** and **CyC$_{31\text{yne}}$**, allowed the direct fishing of (Ser/Cys)-based target enzymes involved in these lipidic processes *via* bio-orthogonal CC-ABPP.

RESULTS AND DISCUSSION

Synthesis of New OX Affinity Probes. The Cyclipostins analog **CyC31**, as well as the corresponding **CyC31yne** and **CyC31-Dansyl** affinity probes were synthesized, as described previously.[40, 44] The new **HPOXyne** click-ready derivative was synthesized in a one-pot two-steps reaction using the methodology reported earlier to access the **HPOX** compound[37] (**Scheme 1A**).

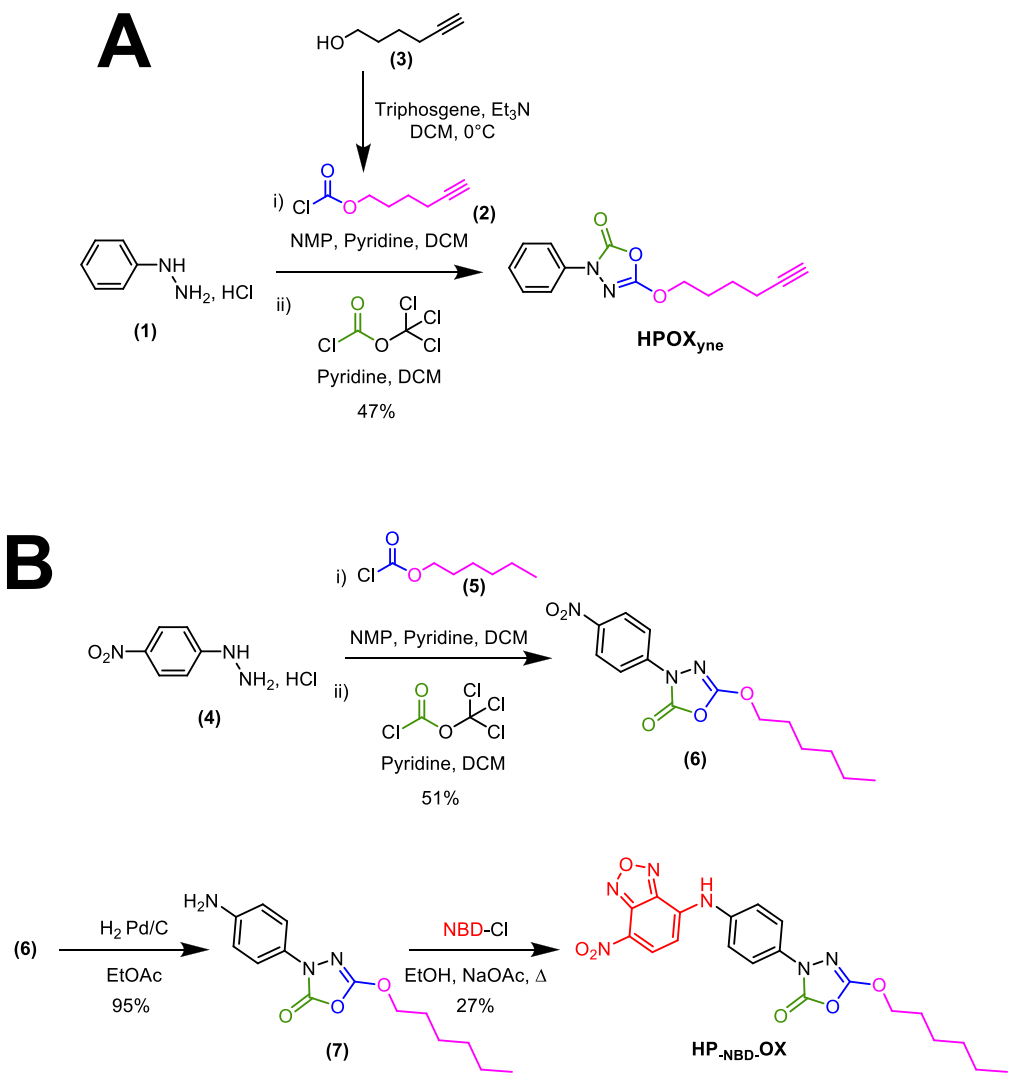

Scheme 1. General procedure for the synthesis of (**A**) **HPOXyne** and (**B**) **HP-NBD-OX**.

Briefly, commercially available phenylhydrazine hydrochloride (**1**) and hexyne chloroformate (**2**) formed *in situ* from 5-hexyn-1-ol (**3**) were used in basic conditions to produce a carbamate intermediate (*step i*) that was directly involved in the cyclization reaction in presence of diphosgene

(*step ii*) to obtain the desired **HPOX$_{yne}$** derivative in 47% yields.[37, 45] Incorporation of a fluorescent tag on the aromatic phenyl ring of the **HPOX** chemical structure was further achieved in 3 consecutive steps with introduction of the fluorescent NBD group after oxadiazolone ring formation (**Scheme 1B**). The synthesis started from commercially *p*-nitrophenyl hydrazine (**4**) that was engaged into the one-pot two-steps cyclisation process in presence of hexyl chloroformate (**5**). Catalytic hydrogenation of the nitro-oxadiazolone (**6**) over palladium led to the aniline derivative (**7**), which was further coupled through a nucleophilic substitution using NBD-chloride to afford the desire fluorescent **HP$_{-NBD-}$OX** in 13% overall yields.

The CyC and OX Affinity Probes Retain Antibacterial Activity comparable to their Parent Molecules. The antimicrobial potency of the selected **CyC** probes [**CyC$_{31yne}$** and **CyC$_{31-Dansyl}$**] as well as the new **OX** ABPs [**HPOX$_{yne}$** and **HP$_{-NBD-}$OX**] was next evaluated against the two variants S and R of *M. abscessus* and compared to that of their parent molecules, *i.e.*, **CyC$_{31}$** and **HPOX** (**Figure 1A**), respectively. The minimal inhibitory concentrations (MIC) leading to 50% and 90% bacterial growth inhibition (*i.e.*, MIC_{50}/MIC_{90}) were determined by the resazurin microtiter assay (REMA) and are reported in **Figure 1B**.[35-36, 40, 46] Importantly, **HPOX$_{yne}$** and **HP$_{-NBD-}$OX**, retained the same moderate antibacterial activity as the unmarked parent **HPOX** molecule against *M. abscessus*, with fold changes in MIC_{50} / MIC_{90} ranging from ×0.7-1.0 / ×1.3-2.0. Regarding the **CyC** probes, **CyC$_{31-Dansyl}$**, we had previously reported[40] that this fluorescent analog exhibited extracellular activity comparable to the parent unlabeled **CyC$_{31}$** compound, with very good (MIC_{50} = 1.4 µM / MIC_{90} = 6.1 µM) to moderate (MIC_{50} = 24.1 µM / MIC_{90} = 63.4 µM) anti-mycobacterial activity against *M. abscessus* S and R, respectively (**Figure 1B**). In addition, and as expected from our previous work on *M. tuberculosis*,[44] **CyC$_{31yne}$** showed similar antibacterial activities against *M. abscessus* S (MIC_{50} = 0.84 µM / MIC_{90} = 2.1 µM) and R (MIC_{50} = 10.3 µM / MIC_{90} = 18.5 µM) variants compared to unmodified **CyC$_{31}$**, with a fold change in MICs of ×0.7 to ×1.75 (**Figure 1B**).

Overall, these results indicate that incorporation of a fluorescent group or an alkyne bond does not alter the activity of the **OX** & **CyC** affinity-based probes. In addition to determining their MICs values, a prerequisite for using these ABPs to identify mycobacterial enzymes involved in ILI accumulation was to verify their ability to ***i)*** colocalize with ILI and ***ii)*** limit the total TAG content in *M. abscessus* S grown in nitrogen-limited MSM-NL.

Fluorescent OX and CyC Affinity probes colocalizes with ILI inside *M. abscessus*. In order to confirm the localization of **OX** & **CyC** ABPs inside lipid-rich bacteria, *M. abscessus* S cells were grown in MSM or MSM-NL for 24 h, harvested and resuspended in fresh medium in the presence of each fluorescent probe at a 100 µM final concentration for an additional 24 h. The **HP-$_{NBD}$-OX / CyC$_{31\text{-}Dansyl}$**-treated bacteria were stained with Nile Red for ILI labeling, as previously described[24] and further processed for fluorescent microscopy. As expected,[24] *M. abscessus* cultured in MSM-NL medium harbored clear, intense and compact cytoplasmic signal in the form of foci due to ILI staining. In both cases, a clear co-localization of the Dansyl and NBD fluorescent signal with Nile Red ILI' positive regions was observed (**Figure 1C**). Subsequent statistical analysis of the data resulted in Pearson's correlation coefficients and Manders' colocalization coefficients[47] (overlap of green and red pixel) of 0.788-0.808 as well as 0.845-1, respectively; together with a Costes *p*-value[48] of 1 and Li's ICQ value[49] of 0.280-0.324 (See **Methods** for parameters' detail).

In contrast, when cells were grown in MSM, the absence of ILI resulted in only low and mainly peripheral Nile Red staining corresponding to cell wall-associated lipids labeling (**Figure S1**). Consequently, as previously reported in the case of labeled **CyC-$_{Dansyl}$**-mycobacteria,[40] the diffuse fluorescence (*i.e.*, pale green and orange resulting colors) observed with the **HP-$_{NBD}$-OX** & **CyC$_{31\text{-}Dansyl}$**-treated *M. abscessus* strains grown in MSM is likely to results from a homogeneous distribution of the probes in the cell wall and/or the cytoplasm of the bacteria.

ILI accumulation is partially blocked by (Ser/Cys)-based enzyme inhibitors. (Ser/Cys)-based enzyme inhibitors can interfere with lipid metabolism by impairing the activity of lipolytic enzymes.[24, 27, 50-55] To confirm that such mycobacterial (Ser/Cys)-based enzyme are involved in ILI mobilization after a 24-hour culture of *M. abscessus* S in MSM-NL to induce ILI accumulation, lipid-rich mycobacteria were harvested, resuspended in fresh MSM-NL, and treated with either **HPOX$_{yne}$** or **CyC$_{31yne}$**. Apolar lipids were further extracted and the TAG content was analyzed by thin layer chromatography (TLC) (**Figure 1D**). Following 24 h incubation with **HPOX$_{yne}$** or **CyC$_{31yne}$**, a significant reduction in TAG levels of 28.6% and 22.6% (p-value < 0.01), respectively, was reached compared to the untreated bacteria.

These findings suggest that the two click-ready ABPs impair TAG production, presumably through the inhibition of (Ser/Cys)-based enzymes. As a consequence, they can be exploited as affinity probes in a click-chemistry activity-based protein profiling (CC-ABPP) strategy.

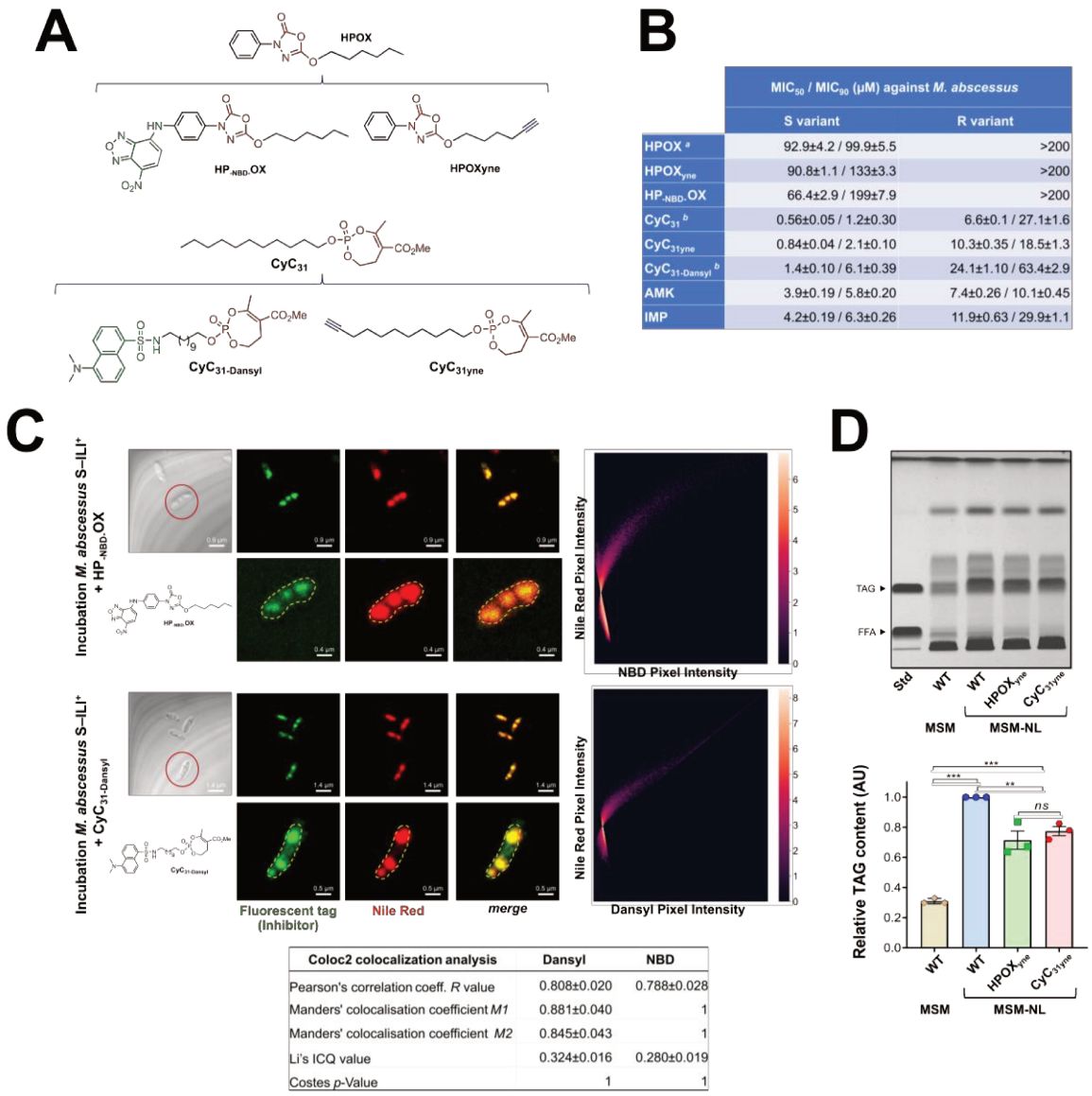

	MIC50 / MIC90 (µM) against *M. abscessus*	
	S variant	R variant
HPOX [a]	92.9±4.2 / 99.9±5.5	>200
$HPOX_{yne}$	90.8±1.1 / 133±3.3	>200
HP_{-NBD}-OX	66.4±2.9 / 199±7.9	>200
CyC_{31} [b]	0.56±0.05 / 1.2±0.30	6.6±0.1 / 27.1±1.6
CyC_{31yne}	0.84±0.04 / 2.1±0.10	10.3±0.35 / 18.5±1.3
$CyC_{31\text{-}Dansyl}$ [b]	1.4±0.10 / 6.1±0.39	24.1±1.10 / 63.4±2.9
AMK	3.9±0.19 / 5.8±0.20	7.4±0.26 / 10.1±0.45
IMP	4.2±0.19 / 6.3±0.26	11.9±0.63 / 29.9±1.1

Coloc2 colocalization analysis	Dansyl	NBD
Pearson's correlation coeff. *R* value	0.808±0.020	0.788±0.028
Manders' colocalisation coefficient *M1*	0.881±0.040	1
Manders' colocalisation coefficient *M2*	0.845±0.043	1
Li's ICQ value	0.324±0.016	0.280±0.019
Costes *p*-Value	1	1

Figure 1. OX & CyC inhibitors efficiently co-localize with ILI inside bacteria and partially block TAG accumulation. **(A)** Chemical structure of the fluorescent and click-ready **OX** & **CyC** activity-based probes as well as their respective parent molecules. **(B)** Antibacterial activity of the three **OX** and **CyC** derivatives against the two variants of *M. abscessus* in broth medium, expressed as the minimal concentration leading to 50% (MIC_{50}) or 90% (MIC_{90}) of growth inhibition, as determined by the REMA assay. [a] Data from Madani *et al.*[35] [b] Data from Sarrazin *et al.*[40] Values are mean of at least two independent assays performed in triplicate. IMP, imipenem; AMK, amikacin, used as control drugs. **(C)** The fluorescent **HP_{-NBD}-OX** and **$CyC_{31\text{-}Dansyl}$** specifically colocalized with ILI on *M. abscessus* S in nitrogen-limiting medium. Following a 24 h-culture of *M. abscessus* S in MSM-NL to induce ILI accumulation, lipid rich mycobacteria were harvested, re-suspended in fresh MSM-NL in presence of **HP_{-NBD}-OX** or **$CyC_{31\text{-}Dansyl}$** fluorescent probe for additional 24 h before chemical fixation, neutral lipids staining with Nile Red fluorescent dye, and confocal fluorescence imaging. Fluorescence controls are given in **Figure S2**. The Coloc2 plugin of ImageJ/Fiji was used to assess the colocalization between NBD or Dansyl fluorescent tag (*i.e.*, green channel) and Nile Red (*i.e.*, red channel), with the corresponding pixel intensity scatterplots shown on the right. Summary of the

correlation coefficients, including Pearson's correlation coefficient, Manders' coefficients (*M1* and *M2*), the intensity correlation quotient (ICQ) value as suggested by Li,[49] and Costes' *p*-value are shown underneath.[47-48] Micrographs are representative of 3 independent experiments with ten acquisitions per sample. **(D)** TAG accumulation is partially blocked by the click-ready **HPOX$_{yne}$** and **CyC$_{31yne}$** (Ser/Cys)-based enzyme inhibitors. Following a 24 h-culture in MSM-NL, lipid rich mycobacteria were harvested, re-suspended in fresh MSM-NL at $OD_{600\ nm}$ of 20 and incubated with **HPOX$_{yne}$** or **CyC$_{31yne}$** for additional 24 h. Cells were collected and their lipids were extracted and analyzed by TLC. Each TLC plate is representative of three independent experiments. TAG levels from each *M. abscessus* S culture were analyzed by TLC with triolein as standard. Results from densitometry are expressed as mean values ± SD of three biologically independent experiments, and reported as relative values using the TAG levels of *M. abscessus* WT in the MSM-NL as 100%. Statistical significance was assessed with one-way ANOVA followed by Tukey's multiple comparisons post-hoc test using Prism 8.0 (GraphPad, Inc): ** *p*-value <0.01; *** *p*-value <0.001; *ns*, not significant (*p*-value >0.05).

OX and CyC click-ready probes allow identifying potential enzymes involved in TAG accumulation. As recently reported in the case of *M. tuberculosis*,[44] to gain access to putative enzymes involved in ILI metabolism, lipid-rich (*i.e.*, MSM-NL) and lipid-poor (*i.e.*, MSM) *M. abscessus* S cultures were subjected to the chemoproteomic CC-ABPP approach using the two alkyne-containing inhibitors (**Figure 2A**). After either 24 h or 48 h of culture in MSM or MSM-NL, the bacteria were centrifuged and the pellets resuspended in fresh medium in presence of **HPOX$_{yne}$**, **CyC$_{31yne}$**, or DMSO (control) for additional 24 h incubation at 37 °C. Following cell lysis, click-chemistry reaction between the obtained **HPOX$_{yne}$**- or **CyC$_{31yne}$**-enzyme complexes and the Desthiobiotin-N_3 *via* copper(I)-catalyzed Huisgen's 1,3-dipolar cycloaddition reaction afforded a stable triazole ring.[33] Enrichment on streptavidin agarose-beads followed by subsequent digestion with trypsin, the resulting peptides were analyzed by liquid chromatography-tandem mass spectrometry (LC-MS/MS), and quantified by label-free quantitative analysis (**Figure 2A**).

A first comparative proteomic analysis between each control sample (*i.e.*, DMSO-treated *M. abscessus* for non-specific binding to streptavidin agarose-beads) at the two time-points and the APB-treated samples led to a first set of target enzymes with **HPOX$_{yne}$** and **CyC$_{31yne}$**, respectively,

when applying *p*-value ≤0.01 and Fold change (Log_2) ≥1.0 thresholds on the proteomic analysis results (**Tables S1-S4**).

Each of these first data sets, *i.e*., the target proteins of **HPOX$_{yne}$** and **CyC$_{31yne}$** identified in MSM-NL culture of *M. abscessus* at 24 h and 48 h incubation, was further refined by means of a second comparative proteomic analysis using the data obtained from the same fishing experiments carried out in MSM (**Tables S1-S4**). The resulting mycobacterial targets of **HPOX$_{yne}$** and **CyC$_{31yne}$**, displayed as volcano plots (**Figure 2B**), highlight the proteins captured by the two ABPs that were significantly more abundant in MSM-NL *vs*. MSM (*p*-value ≤0.05 and Fold change (Log_2) ≥1.0), and thus involved in physiological processes directly related to nitrogen-deprived condition and ILI-rich phenotype. As shown in the Venn diagram (**Figure 2C, upper panel**), using **HPOX$_{yne}$** as a probe, 26 and 236 enzymes were found to be differentially expressed after 24 and 48 h of incubation in MSM-NL, respectively, with 14 proteins conserved over time. Most of the identified proteins belonged to the categories of conserved hypothetical proteins (4 / 26 and 35 / 236), cell wall/cell processes (2 / 26 and 14 / 236), intermediary metabolism/respiration (7 / 26 and 129 / 236), and global lipid metabolism (12 / 26 and 43 / 236). Interestingly, among the 14 conserved identified enzymes, 10 belonged to the global lipid metabolism functional category and 4 to the intermediary metabolism/respiration (**Table S5** and **Figure 2C, upper panel**).

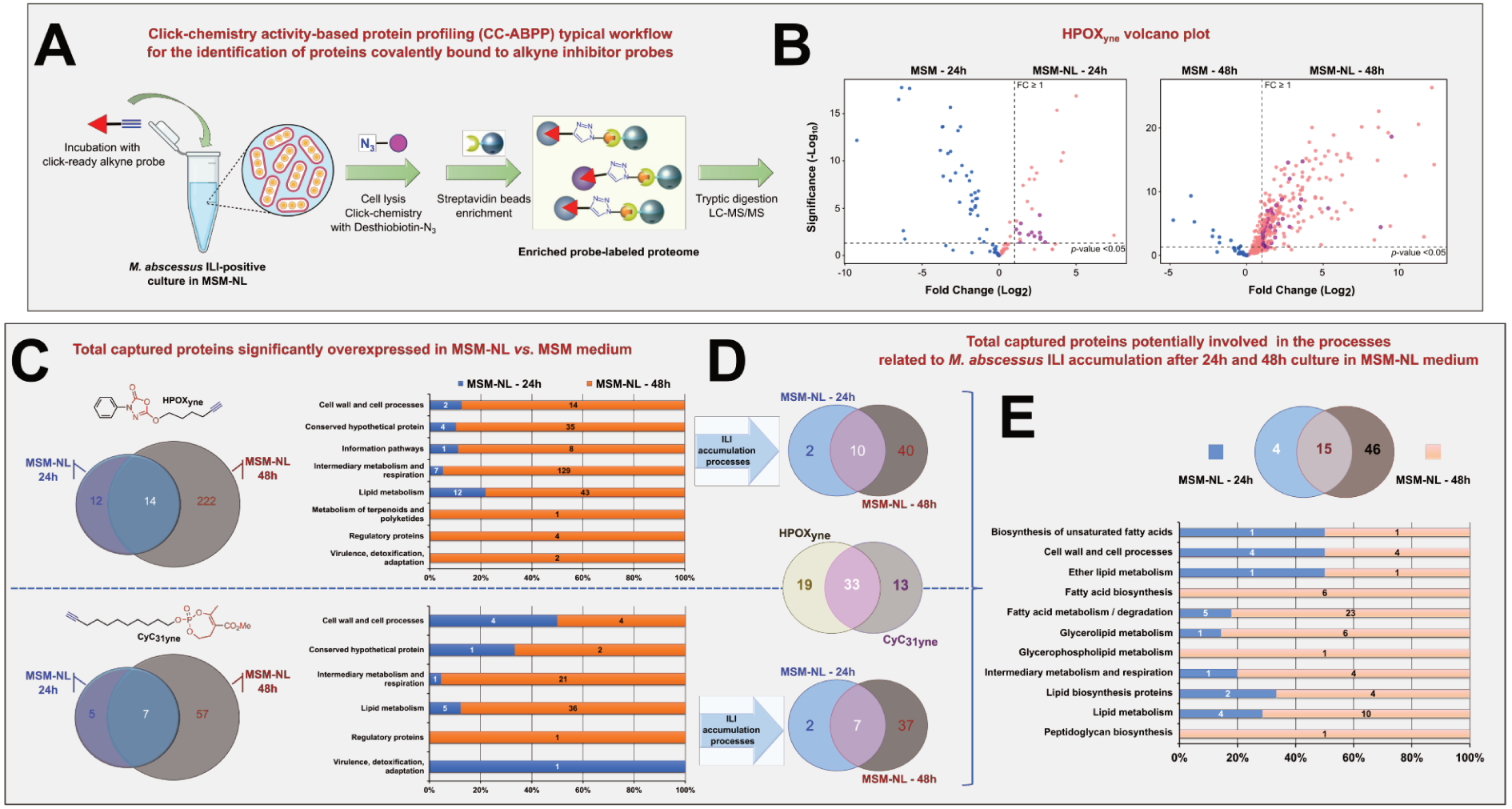

Figure 2. Click chemistry activity-based protein profiling in living *M. abscessus* in MSM-NL. (A) Click chemistry activity-based protein profiling (CC-ABPP) typical workflow for the identification of proteins covalently bound to the **HPOX$_{yne}$** or **CyC$_{31yne}$** inhibitors. A 24 h or 48 h growth phase culture of *M.*

abscessus S was pre-treated with either **HPOX$_{yne}$** or **CyC$_{31yne}$** prior to cell lysis and subsequent click-reaction with Azide-PEG$_3$-Desthiobiotin reporter. Samples were then treated with streptavidin-agarose beads for the capture and enrichment of labeled proteins, followed by tryptic digestion. Tandem mass spectrometry analyses and subsequent differential peptides analysis allowed the identification of the target enzymes captured by the two inhibitors. **(B)** Volcano plot of the differential proteomic analysis between MSM-NL and MSM captured enzymes by **HPOX$_{yne}$** and showing the significance of two sample *t*-test (-Log(*p*-value)) *versus* fold-change (Log$_2$(LFQ normalized intensity in NSN-NL *vs*. MSM condition)) on the *y* and *x* axes, respectively. The dashed lines indicate the threshold of *p-value* ≤ 0.05 and a fold-change ≥ 1.0. Purple dots represent proteins potentially involved in mycobacterial lipid metabolism. **(C)** Venn diagrams showing the total number of proteins that were differentially captured by **HPOX$_{yne}$** or **CyC$_{31yne}$**, respectively, from a 24 h or 48 h culture in MSM-NL; and corresponding Functional categories of *M. abscessus* proteins identified with the two probes, according to the functional classification system of the KEGG[56-57] and Mycobrowser[58] databases. The numbers correspond to the total number of identified proteins in each category. Proteins without functional annotation are denoted as uncharacterized proteins. **(D)** Venn diagrams showing the total number of proteins potentially involved in lipid metabolism that were differentially captured by **HPOX$_{yne}$** or **CyC$_{31yne}$** from a 24 h or 48 h culture in MSM-NL, and total merged captured enzymes from each probe (medium panel). **(E)** Venn diagram showing the total number of *M. abscessus* proteins potentially involved in lipid metabolism that were differentially captured from a 24 h or 48 h culture in MSM-NL and their corresponding Functional categories according to the functional classification system of the KEGG[56-57] and Mycobrowser[58] databases.

A comparable distribution profile of differentially expressed proteins at 24 h and 48 h incubation in MSM-NL was obtained using **CyC$_{31yne}$** as a probe (**Figure 2C, lower panel**), with 12 and 64 enzymes differentially expressed after 24 and 48 h of incubation in MSM-NL, respectively (**Table S6**). As observed above, these identified proteins mainly belonged to the functional categories of conserved hypothetical proteins (1 / 12 and 2 / 64), cell wall/cell processes (4 / 12 and 4 / 64), intermediary metabolism/respiration (1 / 12 and 21 / 64), and global lipid metabolism (5 / 12 and 36 / 64). Seven proteins were conserved over time, 4 of which belonging to the cell wall/cell processes and 3 to the global lipid metabolism functional categories (**Table S6**). Such distribution profiles agree with previous competitive ABPP experiments conducted with **OX** and **CyC** on *M. tuberculosis* and *M. abscessus* cultures.[35-38]

To further focus on enzymes potentially involved in ILI metabolism, and considering that orthologs usually perform equivalent functions in the respective organisms,[28, 59] the corresponding orthologs in the *M. tuberculosis* H37Rv genome of all identified proteins were reported using the KEGG database.[56-57] These data, cross-referenced with the Uniprot[60] and Mycobrowser[58] databases, provide reliable predictions of gene function in terms of essentiality, genomic location and activity.

The results of this differential pathway analysis led to the selection of 52 and 46 enzymes, captured by **HPOX$_{yne}$** and **CyC$_{31yne}$**, respectively, that may potentially be involved in the total lipid metabolism associated with ILI accumulation (**Figure 2D** and **Tables S7-S10**). In view of the similarity of their mechanisms of action,[29] a comparable distribution of the captured "lipolytic" enzymes was obtained at 24 h and 48 h in MSM-NL, as reported for each inhibitor probe in the Venn diagrams (**Figure 2D**). Interestingly, while both inhibitors share 33 common targets, 19 and 13 additional specific target enzymes were obtained with **HPOX$_{yne}$** (**Tables S7-S8**) and **CyC$_{31yne}$** (**Tables S9-S10**), respectively (**Figure 2D**).

The full list of these target enzymes is shown in **Table 1**, confirming the complementary selectivity of these two families of inhibitors with respect to the enzymes they capture. Of these 65 enzymes, 4 were captured only at 24 h, 46 only at 48 h, and 15 were fully conserved at both time points (**Figure 2E**), implying a dynamic process of ILI biosynthesis[3-4] with mostly different protein partners recruited over time.

Table 1. Target proteins potentially involved in ILI accumulation after 24/48 h culture of *M. abscessus* S in MSM-NL, through CC-ABPP by LC-ESI-MS/MS analysis [a]

$HPOX_{yne}$		CyC_{31yne}		Protein Ids	*M. tuberculosis* Ortholog	Essentiality	Protein names	Pathways
24h	48h	24h	48h					
	+		+	MAB_2891c	Rv2605c		Probable acyl-CoA thioesterase II TesB2	Biosynthesis of unsaturated fatty acids
		+		MAB_3588 *	Rv2500c		Putative acyl-CoA oxidase	Biosynthesis of unsaturated fatty acids
	+	+	+	MAB_3765 *	Rv3451 *		Probable Cutinase Cut3	Cell wall / cell processes
	+	+	+	MAB_3763 *	Rv2301 *		Probable Cutinase Cut2	Cell wall / cell processes
		+	+	MAB_3766 *	Rv3451/Rv3452 *		Probable Cutinase precursor Cut3/Cut4	Cell wall / cell processes
	+	+	+	MAB_3809c *	Rv3452 *	GA	Probable Cutinase Cut4	Cell wall / cell processes
+	+		+	MAB_3884 *	Rv2251		Possible flavoprotein	Ether lipid metabolism
	+		+	MAB_0952	Rv1928c		3-oxoacyl-[acyl-carrier protein] reductase	Fatty acid biosynthesis
			+	MAB_0949c	Rv2589		Hypothetical aminotransferase	Fatty acid biosynthesis
	+		+	MAB_1512	Rv2524c †	ES	Probable fatty acid synthase Fas-I	Fatty acid biosynthesis
	+		+	MAB_3592c	Rv3089		Putative medium-chain acyl-CoA ligase FadD13	Fatty acid biosynthesis
	+			MAB_0598 *	Rv3559c		Short-chain dehydrogenase/reductase	Fatty acid biosynthesis
	+			MAB_1978c *	Rv2187 †		Probable long-chain-fatty-acid--CoA ligase FadD15	Fatty acid biosynthesis
	+		+	MAB_0850 *	Rv0859		Probable acyl-CoA thiolase FadA	Fatty acid degradation
	+		+	MAB_1187c *	Rv1071c		Probable enoyl-CoA hydratase	Fatty acid degradation
+	+		+	MAB_0612c #	Rv3546		Probable acetyl-CoA acetyltransferase FadA5	Fatty acid degradation
	+		+	MAB_1192c *	Rv1074c		Probable acyl-CoA thiolase FadA3	Fatty acid degradation
	+		+	MAB_0981c *	Rv0860		Possible enoyl-CoA hydratase/isomerase	Fatty acid degradation
+	+		+	MAB_0983c *	Rv0162c		Probable alcohol dehydrogenase, zinc-containing	Fatty acid degradation
	+			MAB_1069c	Rv0971c		Probable enoyl-CoA hydratase EchA7	Fatty acid degradation
+	+			MAB_2085	Rv0975c	GA	Probable acyl CoA dehydrogenase	Fatty acid degradation
+	+			MAB_3636c	Rv2500c		Probable acyl-CoA dehydrogenase	Fatty acid degradation
	+			MAB_0900c	Rv0223c *		Bifunctional aldehyde dehydrogenase/enoyl-CoA hydratase	Fatty acid degradation
	+			MAB_3350 *	Rv3774		Putative enoyl-CoA hydratase/isomerase	Fatty acid degradation
	+			MAB_3649	Rv3293		Probable aldehyde dehydrogenase	Fatty acid degradation
	+			MAB_3481	Rv0231		Probable acyl-CoA dehydrogenase FadE4	Fatty acid degradation
	+			MAB_0851 *	Rv0860		3-hydroxyacyl-CoA dehydrogenase FadB	Fatty acid degradation
+	+		+	MAB_4437 #	Rv0244c		Probable acyl-CoA dehydrogenase FadE5	Fatty acid metabolism
			+	MAB_4780 *	Rv0636		MaoC-like dehydratase component of FasII	Fatty acid metabolism
			+	MAB_0902	Rv1074c *		Probable beta-ketoadipyl-CoA thiolase	Fatty acid metabolism/degradation
	+		+	MAB_4609c	Rv0400c †		Putative acyl-CoA dehydrogenase FadE7	Fatty acid metabolism/degradation
	+		+	MAB_3455c #	Rv3556c		Acetyl-CoA acetyltransferase FadA6	Fatty acid metabolism/degradation
	+		+	MAB_2042c *	Rv1867	GA	Acetyl-CoA C-acetyltransferase FadA	Fatty acid metabolism/degradation

	+		+	MAB_0255	Rv0154c †		Putative acyl-CoA dehydrogenase FadE2	Fatty acid metabolism/degradation
	+		+	MAB_1463 *	Rv1323	GA	Probable acetyl-CoA acetyltransferase FadA4	Fatty acid metabolism/degradation
	+			MAB_3040c *	Rv2724c		Probable acyl-CoA dehydrogenase FadE20	Fatty acid metabolism/degradation
	+		+	MAB_0328 *	Rv0154c		Putative acyl-CoA dehydrogenase	Fatty acid metabolism/degradation
+	+	+	+	MAB_0175 *	Rv0129c *		Antigen 85-C FbpC	Glycerolipid metabolism
			+	MAB_0177 *	Rv3804c *	GA	Antigen 85-A/B/C	Glycerolipid metabolism
			+	MAB_0176 *	Rv3804c *		Antigen 85-A	Glycerolipid metabolism
	+		+	MAB_3400 *	Rv3045 *		NADP-dependent alcohol dehydrogenase C	Glycerolipid metabolism
	+		+	MAB_0382 *	Rv3696c	GD	Glycerol kinase GlpK	Glycerolipid metabolism
			+	MAB_2357	Rv1692 *	GA	HAD superfamily hydrolase (Glycerol-1-phosphatase)	Glycerolipid metabolism
	+		+	MAB_3655c	Rv3302c	ES	Glycerol-3-phosphate dehydrogenase GlpD2	Glycerophospholipid metabolism
+	+		+	MAB_2814 *	Rv1399c		Probable lipase LipH	Intermediary metabolism and respiration
	+		+	MAB_3447c *	Rv0220		Putative lipase/esterase LipC	Intermediary metabolism and respiration
	+		+	MAB_2818c	Rv0480c		Putative hydrolase	Intermediary metabolism and respiration
	+		+	MAB_3810	Rv3569c *	GA	Putative hydrolase, alpha/beta fold	Intermediary metabolism and respiration
			+	MAB_2348	Rv1683 †		Possible long-chain acyl-CoA synthase	Lipid biosynthesis proteins
	+		+	MAB_0425c *	Rv3667		Acetyl-coenzyme A synthetase	Lipid biosynthesis proteins
			+	MAB_1141c *	Rv0533c *		3-oxoacyl-[acyl-carrier-protein] synthase 3 FabH	Lipid biosynthesis proteins
	+			MAB_2212	Rv1527c *		Probable polyketide synthase Pks5	Lipid biosynthesis proteins
+				MAB_0179	Rv3801c	ES	Probable fatty-acid-CoA ligase FadD32	Lipid biosynthesis proteins
+				MAB_1140	Rv1013		Putative polyketide synthase Pks16	Lipid biosynthesis proteins
		+	+	MAB_0178	Rv3802c *	ES	Probable Cutinase Cut6	Lipid metabolism
		+		MAB_4587c *	Rv3767c		Putative S-adenosyl-L-methionine-dependent methyltransferase	Lipid metabolism
+	+	+	+	MAB_4328c	Rv0281 *		Putative S-adenosyl-L-methionine-dependent methyltransferase	Lipid metabolism
	+		+	MAB_3860c	Rv0672 *		Probable acyl-CoA dehydrogenase FadE8	Lipid metabolism
+	+		+	MAB_4336 *	Rv0271c		Probable acyl-CoA dehydrogenase FadE6	Lipid metabolism
			+	MAB_2619	Rv1627c		Probable lipid-transfer protein Ltp1 (Thiolase?)	Lipid metabolism
	+			MAB_0310c *	Rv3720 †		Putative cyclopropane-fatty-acyl-phospholipid synthase	Lipid metabolism
	+			MAB_4055c #	Rv3561		Putative acyl-CoA synthetase/ligase FadD3	Lipid metabolism
	+			MAB_0065c *	Rv2724c	GA	Probable acyl-CoA dehydrogenase FadE20	Lipid metabolism
	+			MAB_1188c	Rv0752c		Probable acyl-CoA dehydrogenase FadE9	Lipid metabolism
	+			MAB_3234 *	Rv2911	GA	Probable D-alanyl-D-alanine carboxypeptidase DacB	Peptidoglycan biosynthesis

[a] *M. tuberculosis* orthologs were retrieved using the KEGG database[56-57] and then cross-referenced with the Uniprot[60] and Mycobrowser[58] databases for accurate **Protein names** and **Pathways**. The **Essentiality** of each *mab* gene was checked using the *Data Set S1B* (xls file) from Rifat *et al.*[61]: ES, essential gene; GA, causing growth advantage; GD, causing a growth defect. *, proteins previously identified from ABPP experiments on culture or total lysate of *M. abscessus*[35-36] or *M. tuberculosis*[37-38, 44] with the **OX** and **CyC**. † proteins involved in lipid metabolism and identified as part of *M. tuberculosis* ILIome.[28] #, genes predicted to encode enzymes necessary for the biochemical activation and β-oxidation of fatty acids that were up-regulated in both *M. abscessus*-infected amoebae and murine macrophages.[62]

All these identified proteins covered nearly all functional categories listed under the pathways related to *M. abscessus* total lipid metabolism, ranging from biosynthesis of unsaturated fatty acids (2 proteins), cell wall/cell processes (4 proteins), ether lipid metabolism (1 protein), fatty acid biosynthesis (6 proteins), fatty acid metabolism/degradation (23 proteins), glycerolipid metabolism (6 proteins), glycerophospholipid metabolism (1 protein), lipid biosynthesis proteins (6 proteins), and peptidoglycan biosynthesis (1 protein). An additional 10 proteins classified as being involved in lipid metabolism, and 4 proteins belonging to intermediary metabolism and respiration have also been added (**Table 1**).

In agreement with previous work, 41 / 65 (63%) proteins had already been identified *via* ABPP with **OX** and **CyC** molecules either on culture and/or total lysate of *M. abscessus*[35-36] and *M. tuberculosis*.[37-38, 44] These included five Cutinase-like proteins (MAB_3763 – Cut2; Mab_3765 – Cut3; MAB_3766 – Cut2/Cut3 precursor; MAB_3809c – Cut4; MAB_0178 – Cut6); two Lip-family members (MAB_2814 – LipH; MAB_3447c - LipC); a possible α/β-fold hydrolase (MAB_3810); two putative methyltransferases (MAB_4587c; MAB_4328c); the probable D-alanyl-D-alanine carboxypeptidase DacB (MAB_3234); the β-ketoacyl-ACP synthase III (MAB_1141c - FabH); and members of the antigen 85 complex (MAB_177 – Ag85A/B/C; MAB_0176 – Ag85A; MAB_0175 – Ag85C) (**Table 1**).

Given our *in vitro* model of ILI accumulation based on nitrogen starvation in presence of glycerol as the sole carbon source, glycerolipid and glycerophospholipid metabolism thus plays a central role in TAG production.[2-3] Accordingly, key enzymes in the regulation of glycerol uptake and metabolism were identified. This included the glycerol kinase (MAB_0382 - Glpk) and the HAD superfamily hydrolase (MAB_2357) which participated in the conversion of glycerol to glycerol-3-phosphate; and the glycerol-3-phosphate dehydrogenase GlpD2 (MAB_3655c) involved in the reduction of glycerol-3-phosphate to generate glycerone phosphate.

In addition to these proteins, 38 / 65 (58.5%) enzymes were found directly associated with fatty acid biosynthesis, metabolism and degradation. Among these, the essential fatty-acid synthase (MAB_1512 – Fas-I), four putative acyl-CoA synthetase/ligase (MAB_3592c – FadD13; MAB_1978c – FadD15; MAB_0179 – FadD32; MAB_4055c – FadD3), two probable acyl-CoA thiolase (MAB_0850 – FadA; MAB_1192c – FadA3), four probable acetyl-CoA acetyltransferase (MAB_0612c – FadA5; MAB_3455c – FadA6; MAB_2042c – FadA; MAB_1463 – FadA4), four probable enoyl-CoA hydratase/isomerase (MAB_1187c; MAB_0981c; MAB_1069c – AchA7; MAB_3350), twelve probable acyl-CoA dehydrogenase (MAB_2085; MAB_3636c; MAB_3481 – FadE4; MAB_4437 – FadE5; MAB_4609c – FadE7;MAB_0255 – FadE2; MAB_0328; MAB_3040c – FadE20; MAB_3860c – FadE8; MAB_4336 – FadE6; MAB_0065c – FadE; MAB_1188c – FadE9), and two dehydrogenases (MAB_0598; MAB_0983c) were identified (**Table 1**). Four additional proteins annotated as the acetyl-coenzyme A synthetase (MAB_0425c), two polyketide synthases (MAB_2212 - Pks5; MAB_1140 – Pks16), and the putative cyclopropane-fatty-acyl-phospholipid synthase (MAB_0310c) were also identified. Finally, our differential proteomic analysis has highlighted the presence of the putative long-chain acyl-CoA synthase MAB_2348. This protein is indeed homologous to the bifunctional long-chain acyl-CoA synthase/lipase BCG_1721 (65% sequence identity) which has been reported as an important regulator of TAG levels and so in ILI formation in *M. bovis* BCG.[7]

Recently, Dubois et al. reported the complete description and analysis of the *M. abscessus* transcriptome both in an amoebic environmental host and in infected murine macrophages.[62] Interestingly, the genes encoding the fatty acid-CoA synthase *fadD3*, the acyl-CoA dehydrogenase *fadE5*, and the two acetyl-CoA transferases *fadA5* and *fadA6* were among the 15 genes up-regulated in both *M. abscessus*-infected amoebae and murine macrophages, demonstrating their potential role in the biochemical activation and β-oxidation of fatty acids upon infection (**Table 1**). In addition, 6 of our captured proteins, namely MAB_1512 (Rv2524c - Fas-I), MAB_1978c (Rv2187 - FadD15), MAB_4609c (Rv0400c - FadE7), MAB_0255 (Rv0154c - FadE2), MAB_2348 (Rv1683) and

MAB_0310c (Rv3720), were also among the 28 proteins belonging to the lipid metabolism functional category recently reported as potential core components of the *M. tuberculosis* ILI-associated proteome.[28]

Overall, the diversity of proteins captured under these nitrogen-limiting conditions suggests that TAG accumulation in the form of ILI may not be limited to energy storage, but may also provide a source of lipids dedicated to maintaining overall cellular homeostasis of mycobacteria under stringent conditions.[3] Most importantly, these results underscore the power and combined value of using both **OX** and **CyC** probes to identify key mycobacterial enzymes involved in ILI accumulation through activity-based profiling approaches, enlightening our understanding of the metabolic pathways used by pathogenic mycobacteria to catabolize host-derived lipids for survival.

The long chain-fatty-acid--CoA ligase MAB_1978c (FadD15) is involved in TAG production and ILI accumulation. To further investigate the impact of these identified enzymes on TAG accumulation, the MAB_1978c (FadD15) was further selected to investigate its involvement in ILI accumulation.

FadD15 is a putative long-chain-fatty-acid--CoA ligase that is functionally categorized as being involved in lipid metabolism. Like its *M. tuberculosis* ortholog Rv2187,[63] FadD15 is predicted to act at the termination of the fatty acid biosynthesis pathway [KEGG PATH:mab00061] and to catalyze the activation of long-chain fatty acids as acyl-CoA, that would be further processed for elongation, glycerolipid and/or glycerophospholipid biosynthesis, as well as for their recycling *via* the β-oxidation pathway [KEGG PATH:mab00071]. In addition, Rv2187 is core component of the *M. tuberculosis* ILI-associated proteome,[28] thus reinforcing the potential involvement of this protein in ILI biosynthesis.

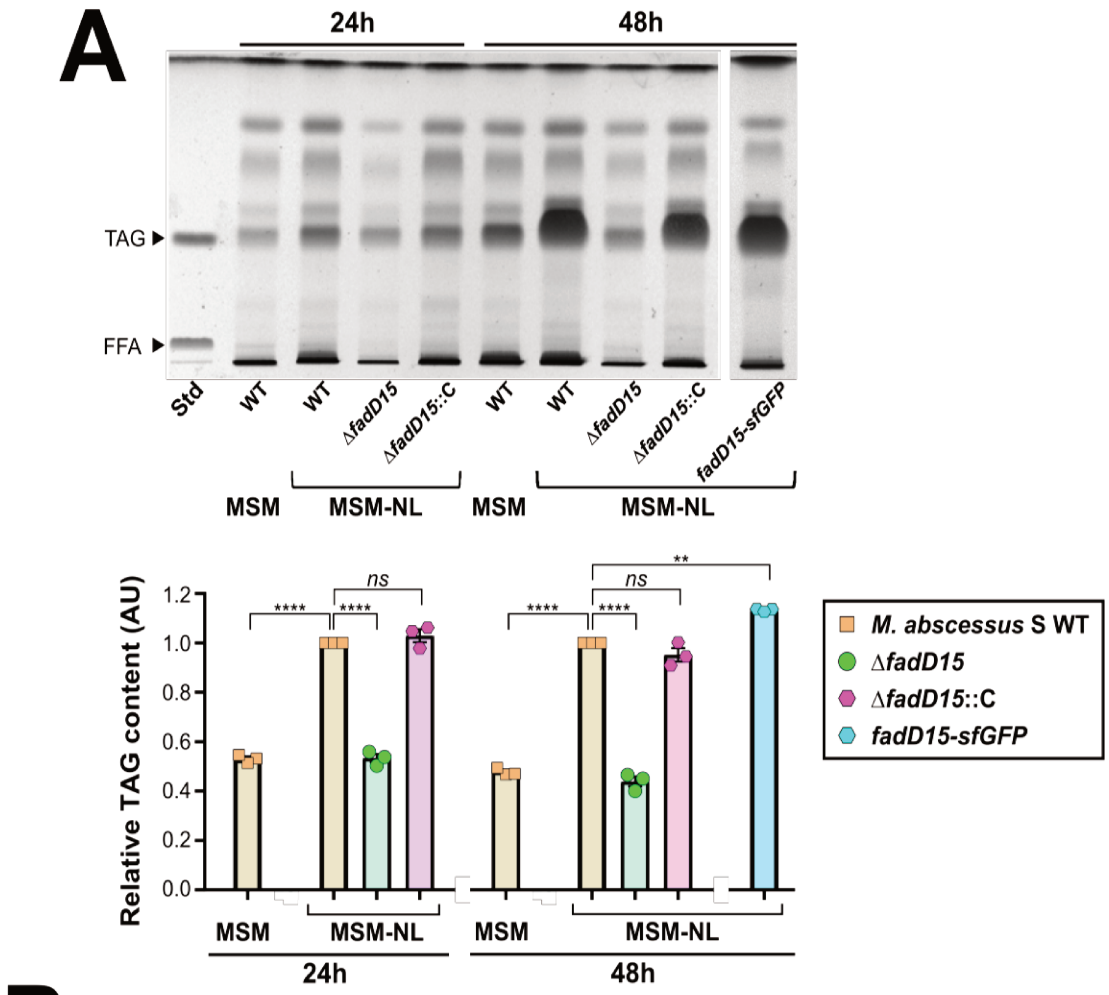

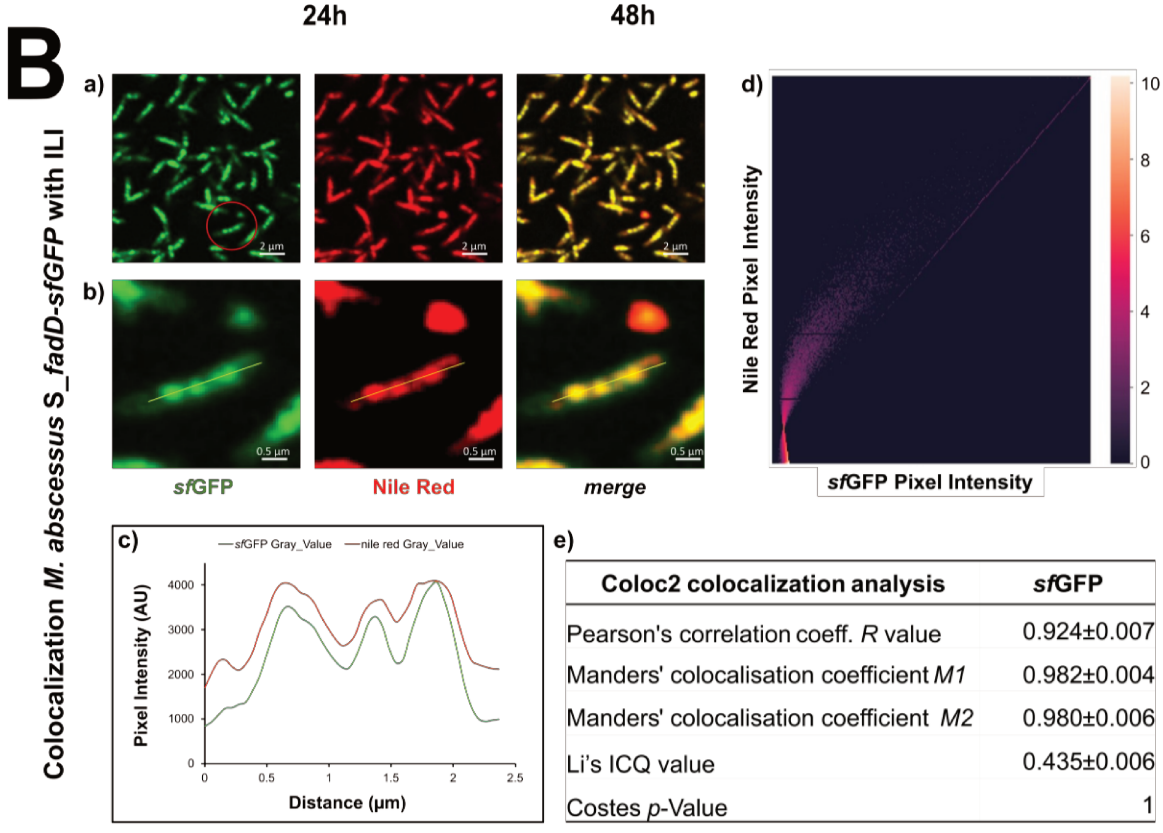

Coloc2 colocalization analysis	*sf*GFP
Pearson's correlation coeff. *R* value	0.924±0.007
Manders' colocalisation coefficient *M1*	0.982±0.004
Manders' colocalisation coefficient *M2*	0.980±0.006
Li's ICQ value	0.435±0.006
Costes *p*-Value	1

Figure 3. **MAB_1978c (FadD15) is essential for TAG production and accumulation in the form of ILI in *M. abscessus*. (A)** TAG levels from *M. abscessus* cultures in MSM-NL. Cultures were collected after a 24 h or 48 h incubation period, lyophilized and equal weights of dry cells were used for apolar lipid extraction. TAG levels from *M. abscessus* WT, Δ*fadD15*, and its complemented strain Δ*fadD15*::C as well as the *fadD15*-*sf*GFP overexpressing strain were analyzed by TLC with triolein as standard. TLC densitometry analysis of relative TAG levels in each strain, with cultures from *M. abscessus* WT used as a reference, are reported. Results from densitometry are expressed as mean values ± SD of three biologically independent experiments, and reported as relative values using the TAG levels of *M. abscessus* WT in the MSM-NL as 100%. Statistical significance was assessed with one-way ANOVA followed by Tukey's multiple comparisons post-hoc test using Prism 8.0 (GraphPad, Inc): ** *p*-value <0.01; **** *p*-value <0.0001; *ns*, not significant (*p*-value >0.05). **(B)** The FadD15-*sf*GFP protein specifically co-localized with ILI in *M. abscessus*. Following a 48 h-culture in MSM-NL to induce ILI accumulation, lipid-rich mycobacteria were harvested, chemically fixed, stained with Nile Red fluorescent dye, and processed for confocal fluorescence imaging. Fluorescence controls are given in **Figure S5**. **Panel (a)**: Large field image representative of the dataset acquired. **Panel (b)**: zoom on a single bacterium to demonstrate *sf*GFP fluorescent colocalization with ILI when cultured in MSM-NL. **Panel (c)**: plot of fluorescence intensity of *sf*GFP channel and Nile Red channel as a function of the distance of each pixel from the yellow line depicted in **panel (b)**. The Coloc2 plugin of ImageJ/Fiji was used to assess the colocalization between *sf*GFP fluorescent tag (*i.e.*, green channel) and the Nile Red (*i.e.*, red channel), the corresponding pixel intensity scatterplots being shown on the right **panel (d)**. Summary of the correlation coefficients, including Pearson's correlation coefficient, Manders' coefficients (*M1* and *M2*), the intensity correlation quotient (ICQ) value as suggested by Li, and Costes' *p*-value are shown underneath.[47-49] Micrographs are representative of 3 independent experiments with ten acquisitions per sample.

Thus, a deletion mutant, designated Δ*fadD15,* was generated by using a two-step homologous recombination procedure using the pUX1-*katG* vector.[64] Its complemented counterpart Δ*fadD15*::C was obtained using the integrative *pMV306*::*fadD15* vector that allows the constitutive production of MAB_1978c under its own promoter. In parallel, *mab_1978c* was cloned and overexpressed in *M. abscessus* using the *pVV16*::*fadD15-sfGFP* multicopy vector allowing the constitutive production of MAB_1978c fused to a *sf*GFP protein under the control of the *hsp60* promoter, for subsequent fluorescence microscopy experiments. First, when grown in 7H9TG^{OADC}, MSM or MSM-NL for 72 h at 37 °C, no significant differences in growth rate were observed between the *M. abscessus* wild-type and Δ*fadD15* (**Figure S3**), in agreement with the non-essentiality annotation of the *fadD15* gene in *M. abscessus*.[61]

Then, each strain was grown in MSM-NL for 24 h and 48 h, and then processed for apolar lipids TLC analysis (**Figure 3A**). At the two time points, quantitative densitometry revealed that TAG production was impaired by 46.7 ± 1.4% and 56.1 ± 2.5% (p-value < 0.0001) in Δ*fadD15* after 24 and 48 h of incubation in MSM-NL, respectively, as compared to the WT strain (**Figure 3A**). In contrast, complete restoration of TAG levels, *i.e.*, 102.9 ± 2.6% and 95.2 ± 2.7%, at 24 and 48 h, respectively, was achieved upon complementation in Δ*fadD15*::C. Moreover, the *fadD15-sfGFP* overexpressing strain induced a slight but significant increase in TAG levels by 1.13-fold (p-value < 0.01) as compared to the WT strain. Most importantly, comparable TAG levels were reached with Δ*fadD15* and a triacylglycerol synthase 1 deletion mutant (Δ*tgs1*) in *M. abscessus* using the MSM-NL [24]. Indeed, it has been clearly demonstrated that TAG accumulation in the form of ILI was *tgs1* dependent, in *M. tuberculosis* (*rv3130c*),[13, 65-67] *M. marinum* (*mmar_1519*),[20, 68] and in *M. abscessus* (*mab_3551c*).[24-25] Moreover, this major TAG synthase has also been identified on the surface of mature ILI in *M. bovis* BCG,[7] confirming its major contribution in ILI formation.

The *fadD15-sfGFP* overexpressing strain was grown in MSM-NL or MSM for 48 h, harvested, fixed with 4% paraformaldehyde, then stained with Nile Red and processed for fluorescent microscopy. As observed previously with the fluorescent inhibitor probes, in MSM a diffuse and mainly peripheral fluorescence signal was observed, suggesting a homogeneous distribution of the labelled FadD15-*sf*GFP protein in the lipid-poor bacteria (**Figure S4**). Conversely, *fadD15-sfGFP* cultured in MSM-NL displayed clear, intense and compact Nile Red ILI' positive regions, which co-localized with the *sf*GFP fluorescent signal (**Figure 3B**). Statistical analysis confirmed the overlap between green (*sf*GFP) and red pixel (Nile Red) with Pearson's correlation coefficients and Manders' co-localization coefficients[47] of 0.924 and 0.982, respectively; a Costes p-value[48] of 1 and Li's ICQ value[49] of 0.435.

All these results demonstrated the clear role of MAB_1978c/FadD15 in TAG production and subsequent ILI formation *in vitro*.

More globally, the fact that glycerol is the sole carbon source available in our MSM-NL model implies the use of well conserved pathways to synthesize TAG.[69] Consequently, from the set of the 65 captured proteins with both **HPOX$_{yne}$** and **CyC$_{31yne}$**, and literature data on *M. tuberculosis*[70-72] and *M. abscessus*[62] transcriptomic studies, it is possible to map some enzymes involved in *M. abscessus* lipid metabolism related to TAG formation and accumulation through ILI (**Figure 4**).

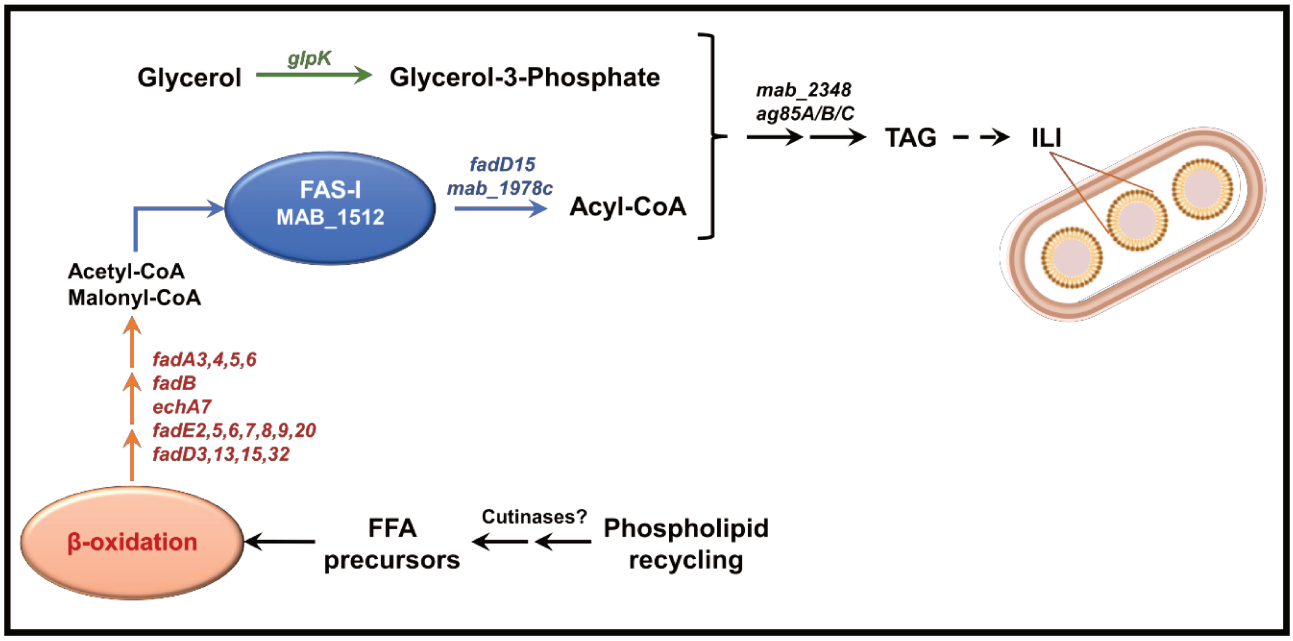

Figure 4. **Schematic diagram of the biosynthetic pathways involved in TAG accumulation in the form of ILI in in *M. abscessus*.** This pathway provides a brief overview of the main findings and illustrates the involvement of proteins belonging to the lipid metabolism's functional category in TAG formations and storage as ILI following *M. abscessus* growth in MSM-NL.

The initial step would consist in the *de novo* biosynthesis of fatty acyl-compounds in the form of acyl-CoA molecules through the action of the type I fatty acid synthase (Fas-I) as well as all enzymes necessary for the biochemical activation and β-oxidation of fatty acids: fatty acid-CoA synthase/ligase (FadD3,13,15,32), acyl-CoA dehydrogenase (FadE2,5,6,7,8,9,20), enoyl-CoA hydratase (EchA7), hydroxybutyryl-CoA dehydrogenase (FadB), and acetyl-CoA transferase (FadA3,4,5,6). However, given the energetic costs associated with such *de novo* fatty acid biosynthesis in MSM-NL, where glycerol is the sole carbon source, it is likely that other rearrangements of lipid metabolism, such as phospholipid recycling through the action of some

Cutinase-like proteins (*e.g.*, MAB_3809c/Cut4),[73-74] may led to fatty acid precursors that could be incorporated into biosynthetic pathways *via* the β-oxidation pathway. The second step is the formation of glycerol-3-phosphate (G3P) substrates generated by the action of the glycerol kinase (MAB_0382/GlpK). Finally, the sequential acylation of the G3P substrates with the latter fatty acyl-CoA residues is mediated by the enzymes from the Kennedy pathway. These may include the bifunctional long-chain acyl-CoA synthase/lipase (MAB_2348) which *M. bovis* BCG ortholog[7] has been demonstrated to be involved in long-chain TAG and ILI formation processes when assessed under non-replicating conditions; as well as the Ag85A/B/C complex proteins which were found to express diacylglycerol acyltransferase (DGAT) activity and to mediate the transesterification of diacylglycerol using long-chain acyl-CoA, making thus an important contribution in TAG synthesis.[42]

CONCLUSION

Using an *in vitro* model based on nitrogen deprivation to promote TAG accumulation and subsequent production of lipid-loaded *M. abscessus* cells, together with two selective multitarget inhibitors belonging to the **OX** and **CyC** distinct families, we identified a set of 65 enzymes that may directly or indirectly participate in these processes. We have validated this approach by demonstrating that the long-chain-fatty-acid-CoA ligase MAB_1978c/FadD15 co-localizes with ILI and acts as a major contributor in ILI formation. More work remains to be done to fully characterize and validate the other proteins identified *via* ABPP to generate a clear picture regarding their specific role(s) in ILI metabolism.

Overall, our data confirm the importance of fatty acid and lipid metabolism in *M. abscessus* under nutritional stress and highlight the importance of proteins involved in TAG mobilization as potential therapeutic targets. Nevertheless, it is true that the nutrients available *in vivo* differ from the *in vitro* conditions described here, as mycobacteria can be found in different cellular compartments (*e.g.* phagosome, macrophage, etc.) during infection. In particular, mycobacteria reside in different lipidic

environments, such as foamy macrophages, giving them access to host lipids to metabolize their own TAGs, which are subsequently stored into ILI.[4]

In summary, the multi-targeted **OX** & **CyC** inhibitors represent powerful probes for monitoring mycobacterial infection and identifying key specific targets within infected macrophages. In particular, their use as specific activity-based probes to identify the mycobacterial lipolytic enzymes involved in host lipid bodies degradation, lipid accumulation in ILI, as well as in the consumption of these intrabacterial lipids using the model of infected foamy and non-foamy macrophages,[11, 23, 31] will open exciting opportunities. By working on living infected cells, such knowledge will also provide crucial information on the life cycle of intracellular mycobacteria, inspiring new therapeutic strategies to counter latent/persistent bacilli in infected individuals. Such studies are currently under progress and will be reported in due course.

METHODS

Chemistry

Synthesis of OX and CyC activity-based probes. The Cyclipostins analogs **CyC$_{31}$**, **CyC$_{31yne}$** and **CyC$_{31\text{-}Dansyl}$**, as well as the Oxadiazolone derivative **HPOX**, were synthesized as described previously.[37, 40, 44] Stock solutions (10 mM) in which the **OX** & **CyC** molecules (purity of ≥95%) were found to be completely soluble in dimethyl sulfoxide (DMSO) were prepared and stored at 4 °C. See **Supporting Information** for NMR spectra of the new **OX** probes (**Figure S6**).

General Methods. All solvents were anhydrous reagents from commercial sources. Unless otherwise noted, all chemicals and reagents were obtained commercially and used without purification. The reactions were monitored using TLC on plates that were pre-coated with silica gel 60 (Merck, Kenilworth, New Jersey, USA). The reaction components were visualized using a 254 nm UV lamp, stained with phosphomolybdic acid solution followed by gentle heating. Purifications of the synthesized compounds were performed by column chromatography on silica gel 40–63 µm. Melting points (Mp) were determined on a Stuart capillary apparatus and are uncorrected. High resolution mass spectrometry (HRMS) was recorded using electrospray ionization (ESI) techniques on Q-TOF mass spectrometer. NMR spectra were recorded at 300 or 500 MHz (^{1}H) and 75 or 126 MHz (^{13}C) using Bruker spectrometers. Chemical shifts are reported in parts per million (ppm, δ) relative to residual deuterated solvent peaks. The NMR spectra were assigned with the help of 2D NMR analyses. The multiplicities reported are as follows: br = broad singlet, m = multiplet, s = singlet, d = doublet, t = triplet, q = quadruplet, quint = quintuplet, h = hexuplet, or combinations thereof.

5-(hex-5-ynyloxy)-3-phenyl-1,3,4-oxadiazol-2(3H)-one (HPOX$_{yne}$).

Commercial 5-hexyn-1-ol (**3**) (720 µL, 6.44 mmol, 2.5 equiv.) was dissolved in dry CH_2Cl_2 (25 mL) in presence of dry distilled Et_3N (1 mL, 7.50 mmol, 2.9 equiv.) and stirred at 0 °C. Then, a solution of triphosgene (760 mg, 2.60 mmol, 1 equiv.) in CH_2Cl_2 (10 mL) was added dropwise. The resulting

mixture was stirred at 0 °C for 30 min, then 1.5 h at room temperature. The mixture was then degassed with N_2 in order to evacuate remaining phosgene and poured into pentane (100 mL). The resulting suspension was filtered on celite and solvents evaporated cautiously to afford crude chloroformate directly engaged in the next step without further purification (Rf = 0.3 (cyclohexane/EtOAc 80:20)). The crude hex-5-yn-1 chloroformate (**2**) was dissolved in CH_2Cl_2 (12 mL), and slowly added dropwise over a period of 5 min at 0-5 °C to a solution of phenylhydrazine hydrochloride (**1**) (800 mg, 5.53 mmol, 1 equiv.) and 1-methyl pyrrolidone (480 µL, 4.98 mmol, 0.9 equiv.) in dry pyridine (11 mL). The reaction was stirred for 1 h at 0 °C and 1h at room temperature. The reaction mixture was diluted by addition of CH_2Cl_2 (50 mL) and dry pyridine (11 mL) and cooled at -10 °C using an ice-salt bath. A solution of diphosgene (1 mL, 8.3 mmol, 1.5 equiv.) in CH_2Cl_2 (5 mL) was added dropwise over a period of 10 min while maintaining -10 °C with an ice-salt bath. After the addition is complete, the reaction mixture was stirred 2 h at -10 °C, then 2 h at room temperature. The mixture was then degassed with N_2 to eliminate the remaining phosgene. The reaction mixture was diluted with water (100 mL) and extracted with diethyl ether (3×50 mL). The combined organic layers were washed with water (2×50 mL) and brine (3×50 mL), dried over $MgSO_4$, and filtered. Purification by column chromatography using cyclohexane/ethyl acetate (99:1 to 90:10, *v/v*) as eluent, followed by recrystallization with hexane gave the title compound as a white solid (680 mg, 47%).

Analytical data for **HPOX$_{yne}$**. Mp: 61.0-63.2° C. R*f* (AcOEt/Cyclohexane 1:3, *v/v*) 0.50. IR (neat) *v* 3283 (C≡C-H), 2974 (C-H), 1787 (C=O), 1661, 1646 (C=C) cm^{-1}. HRMS (ESI) *m/z* $[M+H]^+$ calcd. for $C_{14}H_{14}N_2O_3$: 259.1080 Da; found: 259.1083 Da. ^1H NMR (300 MHz, $CDCl_3$) δ 7.80-7.77 (m, 2H, H_{Ar}), 7.45-7.38 (m, 2H, H_{Ar}), 7.26-7.19 (m, 1H, H_{Ar}), 4.44 (t, $^3J_{H,H}$ = 6.3 Hz, 2H, CH_2-O), 2.29 (td, $^3J_{H,H}$ = 6.9, $^4J_{H,H}$ = 2.6 Hz, 2H, CH_2-C≡CH), 2.04-1.94 (m, 3H, CH_2-CH_2 + C≡C*H*), 1.76-1.66 (m, 2H, CH_2-CH_2). ^{13}C NMR (75 MHz, $CDCl_3$) δ 155.4, 148.4, 136.3, 129.2 (2C), 125.6, 118.0 (2C), 83.5, 71.2, 69.3, 27.5, 24.5, 18.0.

5-(hexyloxy)-3-(4-nitrophenyl)-1,3,4-oxadiazol-2(3H)-one (6)

A solution of *p*-nitrophenylhydrazine (**4**) (3 g, 15.82 mmol, 1 equiv.) in dry pyridine (28 mL) was stirred at room temperature. After 15 min, the mixture was cooled to 0 °C and a solution of hexylchloroformate (**5**) (2.59 mL, 15.82 mmol, 1 equiv.) in dry CH_2Cl_2 (12 mL) was slowly added dropwise over a period of 5 min at 0-5 °C. The mixture was stirred at 0 °C for 30 min followed by 2 h at room temperature. Additional hexylchloroformate (**5**) (1.30 mL, 7.94 mmol, 1 equiv.) in dry CH_2Cl_2 (6 mL) was slowly added to increase full conversion of starting material. After 40 min, the mixture was diluted with dry CH_2Cl_2 (45 mL), dry pyridine (12.5 mL) and cooled to 0 °C. A solution of diphosgene (1.91 mL, 15.82 mmol, 1 equiv.) in dry CH_2Cl_2 (12 mL) was added dropwise. The mixture was stirred at 0 °C for 30 min followed by 2 h at room temperature. The mixture was then degassed with N_2 to eliminate the remaining phosgene, treated with 1M HCl (50 mL) and extracted with Et_2O (2×100 mL). The organic layers were washed with brine (100 mL), dried over $MgSO_4$ and solvents were removed under reduced pressure. The crude product was then adsorbed on silica and purified through gel chromatography in isocratic pentane/Et_2O (90:10, *v/v*) to give the titled compound (**6**) (2.476 g, 8.05 mmol, 51% over 2 steps) as a yellow solid.

Analytical data for compound (**6**). Mp: 43.3-44.6° C. R*f* (AcOEt/Cyclohexane 20:80, *v/v*) 0.50. IR (neat) *v* 3125, 2920 (C-H), 1780 (C=O), 1660, 1596, 1521 (C=C), 1353 (NO_2), 734 (C-H aromatic) cm^{-1}. HRMS (ESI) *m/z* $[M+H]^+$ calcd. for $C_{14}H_{18}N_3O_5$: 308.1241 Da; found: 308.1243 Da. ^1H NMR (300 MHz, $CDCl_3$) δ 8.30 (d, $^3J_{H,H}$ = 9.3 Hz, 2H, H_{Ar}), 8.00 (d, $^3J_{H,H}$ = 9.3 Hz, 2H, H_{Ar}), 4.44 (t, $^3J_{H,H}$ = 6.7 Hz, 2H, CH_2-O), 1.86 (quint, $^3J_{H,H}$ = 7.0 Hz, 2H, CH_2-CH_3), 1.49-1.43 (m, 2H, CH_2), 1.38-1.33 (m, 4H, 2xCH_2), 0.92 (t, 3H, $^3J_{H,H}$ = 7 Hz, CH_2-CH_3). ^{13}C NMR (75 MHz, $CDCl_3$) δ 155.9, 148.0, 144.6, 141.2, 125.1 (2C), 117.6 (2C), 72.5, 31.3, 28.4, 25.2, 22.6, 14.0.

3-(4-aminophenyl)-5-(hexyloxy)-1,3,4-oxadiazol-2(3H)-one (7)

A solution of the nitro-oxadiazolone (**6**) (500 mg, 1.60 mmol, 1 equiv.) in EtOAc (7.5 mL) was prepared at room temperature. Then, Pd/C (10% *w/w*, 50 mg) was added. The resulting suspension was stirred for 1 h under H_2 atmosphere. After elimination of the remaining H_2, the mixture was

filtered on celite and the solvent was removed under reduced pressure. The crude compound was adsorbed on silica and purified through gel chromatography in isocratic pentane/EtOAc (70:30, *v/v*) to give the titled compound (**7**) (420 mg, 1.50 mmol, 95%) as a yellow solid.

Analytical data for compound (**7**). Mp: 69.1-71.1° C. R*f* (AcOEt/Hexane 30:70, *v/v*) 0.29. IR (neat) *v* 3470, 3373 (N-H), 2961, 2926 (C-H), 1772 (C=O), 1648 (δ N-H), 1630, 1516 (C=C), 718 (C-H aromatic) cm^{-1}. HRMS (ESI) *m/z* $[M+H]^+$ calcd. for $C_{14}H_{20}N_3O_3$: 278.1499 Da; found: 278.1503 Da. ^1H NMR (300 MHz, $CDCl_3$) δ 7.51 (d, $^3J_{H,H}$ = 8.9 Hz, 2H, H_{Ar}), 6.71 (d, $^3J_{H,H}$ = 8.9 Hz, 2H, H_{Ar}), 4.36 (t, $^3J_{H,H}$ = 6.6 Hz, 2H, CH_2-O), 3.69 (br, 2H, NH_2), 1.82 (quint, $^3J_{H,H}$ = 7.0 Hz, 2H, CH_2-CH_3), 1.48-1.41 (m, 2H, CH_2), 1.35-1.32 (m, 4H, 2xCH_2), 0.91 (t, $^3J_{H,H}$ = 7.0 Hz, 3H, CH_2-CH_3). ^{13}C NMR (75 MHz, $CDCl_3$) δ 155.3, 148.7, 144.6, 127.8, 120.4 (2*C*), 115.3 (2*C*), 71.7, 31.3, 28.5, 25.2, 22.6, 14.1.

5-(hexyloxy)-3-(4-((7-nitrobenzo[c][1,2,5]oxadiazol-4-yl)amino)phenyl)-1,3,4-oxadiazol-2(3H)-one (HP-NBD-OX)

A solution 4-chloro-7-nitro-2,1,3-benzoxadiazole (NBD-Cl, 296 mg, 1.35 mmol, 1.5 equiv.) in absolute EtOH (25 mL) was prepared. To this solution, the aniline-oxadiazolone (**7**) (250 mg, 0.90 mmol, 1 equiv.) was added. Then, NaOAc (4 mg, 0.05 mmol, 0.05 equiv.) was added and the mixture was stirred at reflux for 2 h. The resulting suspension was cooled to room temperature and diluted with Et_2O (50 mL). The precipitate was filtered and washed with Et_2O (10×10 mL) to afford a crude residue which was purified by recrystallization in CH_2Cl_2 to give the titled compound (106 mg, 0.24 mmol, 27%) as a red solid.

Analytical data for **HP-NBD-OX**. Mp: 225-226° C. R*f* (AcOEt/Hexane 20:80, *v/v*) 0.39. IR (neat) *v* 3345, 3110 (N-H), 2927 (C-H), 1768 (C=O), 1655 (δ N-H), 1597, 1567, 1503 (C=C), 897, 830 (C-H aromatic) cm^{-1}. HRMS (ESI) *m/z* $[M+H]^+$ calcd. for $C_{20}H_{21}N_6O_6$: 441.1517 Da; found: 441.1516 Da. ^1H NMR (300 MHz, $CDCl_3$) δ 11.08 (s, 1H, N*H*), 8.52 (d, $^3J_{H,H}$ = 8.8 Hz, 1H, H_{Ar}), 7.79 (d, $^3J_{H,H}$ = 8.8 Hz, 2H, H_{Ar}), 7.59 (d, $^3J_{H,H}$ = 8.75 Hz, 2H, H_{Ar}), 6.73 (d, $^3J_{H,H}$ = 8.82 Hz, 1H, H_{Ar}), 4.41 (t, $^3J_{H,H}$

= 6 Hz, 2H, CH_2-O), 1.79 (quint, $^3J_{H,H}$ = 6.0 Hz, 2H, CH_2-CH_3), 1.41-1.37 (m, 2H, CH_2), 1.32-1.31 (m, 4H, 2xCH_2), 0.89 (t, $^3J_{H,H}$ = 6.0 Hz, 3H, CH_2-CH_3). ^{13}C NMR (75 MHz, $CDCl_3$) δ 154.8, 147.9, 145.0, 144.1, 142.1, 137.5, 134.8, 133.8, 124.7 (2C), 123.2, 118.6 (2C), 101.8, 71.7, 30.7, 27.7, 24.6, 21.9, 13.8.

Biological evaluation

Bacterial strains and growth conditions. *M. abscessus* CIP104536^T with either a smooth (S) or a rough (R) morphotype, was classically grown in Middlebrook 7H9 liquid medium (BD Difco, Le Pont de Claix, France) supplemented with 0.05% Tween 80 (Sigma-Aldrich, Saint-Quentin Fallavier, France), 0.2% glycerol (Euromedex, France) and 10% oleic albumin dextrose catalase (OADC enrichment, BD Difco, France) (7H9-S^{OADC}) at 37 °C and 200 rpm.

Generation of lipid-loaded cells. ILI accumulation in *M. abscessus* S liquid culture was performed as previously reported.[24] Briefly, from a culture at the logarithmic growth stage (OD_{600} ~1-1.5), *M. abscessus* S cells were harvested by centrifugation at 5,000 rpm for 15 min. Pellets were washed once with sterile PBS buffer (pH 7.4) containing 0.05% (*v*/*v*) Tween-20, then once with PBS buffer, and finally re-suspended in PBS at a final theoretical OD_{600} of 10. This bacterial solution was used to inoculate at an initial OD_{600} of 0.1, either fresh Mineral Salt Medium (MSM) (2 g/L Na_2HPO_4, 1 g/L KH_2PO_4, 0.5 g/L NaCl, 0.2 g/L $MgSO_4$, 20 mg/L $CaCl_2$, 1 g/L NH_4Cl, and 5% glycerol) or Mineral Salt Medium Nitrogen Limiting (MSM-NL) containing only 0.15 g/L NH_4Cl. To avoid bacterial clumping, Tyloxapol (Sigma-Aldrich) was added at a final concentration of 0.02% (*v*/*v*). The MSM and MSM-NL culture media were next incubated for 24 and 48 h at 37 °C under agitation (200 rpm). Alternatively, after 24 h incubation period at 37 °C and 200 rpm, the latter cultures were centrifuged and the pellets resuspended in respective fresh MSM or MSM-NL at a final theoretical OD_{600} of 20. One mL sample of these homogeneous bacterial suspensions was further incubated with **CyC$_{31yne}$** (200 µM final concentration), **HPOX$_{yne}$** (500 µM final concentration) or DMSO (control), as well as

with the fluorescent **CyC$_{31\text{-Dansyl}}$** or **HP$_{\text{-NBD-}}$OX** probes (100 µM final concentration) for additional 24 h at 37 °C under shaking at 200 rpm.

Normalization, lipid extraction and thin layer chromatography (TLC) analysis – adapted from [24]. *M. abscessus* S cells were grown in MSM or MSM-NL in presence or absence of inhibitor as described above. At 24 and 48 h incubation period, cultures were centrifuged at 3,500 rpm for 10 min at 4 °C. Cells were washed three times with distilled water, heated at 95 °C for 15 min and removed. Pellets were next lyophilized overnight and weighed to obtain the exact dry weight of the mycobacterial residue. Apolar lipids were extracted as previously reported.[24] Briefly, 2 mL of MeOH-0.3% NaCl (10:1, *v/v*) was added per 10 mg dry extract. The saline-MeOH solution containing the bacterial dry extract was mixed for 15 min with 1 mL petroleum ether in Pyrex® tubes at room temperature using a tube rotator. After centrifugation at 3,000 rpm for 5 min, the upper organic layer was transferred to a fresh tube. This step was repeated two times. The combined organic layers containing apolar lipids were transferred to a fresh pre-weighed vial, and the solvent was evaporated to dryness under nitrogen stream. Finally, the obtained dry apolar lipid residue was re-suspended in 200 µL dichloromethane.

The obtained extracted lipids were analyzed using glass TLC plates (TLC Silica Gel 60 F_{254}, Merck). Petroleum ether (40-60 °C fraction)/diethyl ether (90:10, *v/v*) was used as eluent for the TLC analysis of TAG. Following eluent migration, the plates were dried at room temperature for 10 min, and then sprayed with a cupric acetate-orthophosphoric acid solution prepared by mixing a saturated aqueous solution of cupric acetate with 85% phosphoric acid in a 1-to-1 volume ratio, followed by heating at 140 °C in an oven for 5-10 min. Each resolved plate was scanned using a Chemidoc™ MP Imaging System (Bio-Rad), and densitometric analyses were performed using the open-source program ImageJ/Fiji 1.53f51 (NIH, USA) to determine relative TAG content per sample.

MIC determination. The antibacterial activity of the fluorescent **CyC$_{31\text{-Dansyl}}$** and **HP$_{\text{-NBD-}}$OX**, as well as the **CyC$_{31yne}$** and **HPOX$_{yne}$** probes as compared to the parent **CyC$_{31}$** and **HPOX** against *M. abscessus* S & R growth, was assessed by determining their MICs in 96-well flat-bottom Nunclon Delta Surface microplates with lid (Thermo-Fisher Scientific, Illkirch, France) using the REMA assay.[35-36, 40, 46] Briefly, a log-phase *M. abscessus* culture was diluted to a cell density of 5×10^6 cells/mL in 7H9-S^{OADC}. Then 100 µL of the above inoculum (*i.e.*, 5×10^5 cells per well) were added to 100 µL of a serial two-fold dilutions of each compound (or DMSO as control) in 7H9-S^{OADC} medium, to a final volume of 200 µL per well of the 96-well plate.[35-36, 40] Plates were incubated at 37 °C for 3-5 days. Then, 20 µL of a 0.025% (*w/v*) resazurin solution was added to each well, and the plates were incubated at 37 °C for color change from blue to pink or violet and for a reading of fluorescence units (FU). Fluorescence corresponding to the resazurin reduction to its metabolite resorufin ($\lambda_{ex}/\lambda_{em}$ = 530/590 nm) was quantified using a Tecan Spark 10M multimode microplate reader (Tecan Group Ltd, France). MIC values were determined by fitting the relative fluorescence unit (RFU%) sigmoidal dose-response curves in Kaleidagraph 4.2 software (Synergy Software). The lowest compound concentration leading to 50% and 90% growth inhibition was defined as the MIC_{50} and MIC_{90}, respectively. Amikacin (AMK) and Imipenem (IMP) were used as reference drugs.

Activity-based protein profiling (ABPP) experiments – adapted from [44].

Capture of M. abscessus S potential target enzymes from HPOX$_{yne}$ and CyC$_{31yne}$-treated MSM and MSM-NL culture. A pre-culture in 7H9-S^{OADC} was grown to the logarithmic growth stage (OD_{600} ~1-1.5), then *M. abscessus* S cells were harvested by centrifugation at 5,000 rpm for 15 min, washed with PBS-Tween 20 (0.05%, *v/v*) and PBS, resuspended in PBS at an $OD_{600\ nm}$ of 10, and inoculated to either fresh MSM or MSM-NL at an initial $OD_{600\ nm}$ of 0.1. After 24 h or 48 h incubation period at 37 °C and 200 rpm, the culture was centrifuged and the pellets were resuspended in fresh MSM or MSM-NL at a final theoretical $OD_{600\ nm}$ of 20. One mL sample of these homogeneous bacterial suspensions was incubated with **CyC$_{31yne}$** (200 µM final concentration), **HPOX$_{yne}$** (500 µM final

concentration) or DMSO (control) at 37 °C for additional 24 h under shaking at 200 rpm. Bacteria were harvested (13,000 rpm, 4 °C, 2 min) and washed with 3× 500 µL PBS. Pellets were resuspended in 750 µL PBS supplemented with EDTA-free protease inhibitors (cOmplete Mini, EDTA-free, Roche) at a 1:1 (*w/v*) ratio. The bacterial cells were then mixed with 200 µL of 0.1 mm diameter glass beads (BioSpec) in a 1.5-mL Eppendorf tube and disrupted during 2×4 min of violent shaking, with ice cooling between each run, using Mini-Beadbeater-96 (BioSpec). The lysate was cooled down in ice for 5 min and then centrifuged at 4 °C and at 1300 rpm for 10 min to remove the cell debris and unbroken cells. The concentration of total proteins in the supernatants was determined *via* the Bradford method, adjusted to a concentration of 1 mg/mL, snap frozen in liquid nitrogen and stored at –80 °C until further use.

Both **CyC31yne**- and **HPOXyne**-treated *M. abscessus* and DMSO-control lysate samples (500 µL – 0.5 mg total proteins) were subjected to click-chemistry reaction by successive addition of Desthiobiotin-PEG_3-N_3 (Jena Bioscience, CLK-AZ104P4-100), TBTA ligand and fresh TCEP solution (Sigma-Aldrich) to the cells (see table below for added volumes).

Reagents	**Stock solution**	**Volume of reagent (µL) depending on the probe concentration 200 µM / 500 µM**
Desthiobiotin-Peg_3-N_3	40 mM DMSO	3.2 / 8.0
TCEP	50 mM H_2O	6.3 / 16.0
TBTA	1.667 mM *t*BuOH/DMSO (80:20, *v/v*)	19.0 / 48.1
$CuSO_4$	50 mM H_2O	6.3 / 16.0

After gently vortexing of the samples, the cycloaddition reaction was initiated by addition of fresh $CuSO_4$ solution (50 mM in H_2O). The lysates were mixed by vortexing again and incubated for 2 h under gentle rotative agitation (15 rpm) at room temperature in the dark. The proteins were further precipitated overnight at -20 °C by adding 1.2 mL ice-cold acetone, and pelletized by centrifugation (13,000 rpm, 4 °C, 15 min). The supernatant was discarded and the proteins were washed with 2×500 µL cold MeOH (resuspension by sonication, 3×1 min, 10% max. intensity). After centrifugation (13,000 rpm, 4 °C, 10 min), the pellets were resuspended in 0.2% (*w/v*) SDS in PBS (250 µL) at room

temperature by mild sonication (4×1 min, 10% max. intensity). Affinity enrichment was performed with 25 µL Pierce™ High-Capacity Streptavidin Agarose Resin (Thermo Scientific ref. 20359; pre-washed 3×500 µL 0.4% (*w/v*) SDS in PBS, then 3×500 µL PBS, centrifugation was performed at 3,000 rpm for 2 min). Each *M. abscessus* S treated-lysate was enriched for labelled proteins by transfer to the previously washed beads (around 250 µg) and incubated under gentle rotative agitation (15 rpm) at room temperature for 3 h. Beads were stringently washed following pull-down (1 mL each time): 2× 0.4% (*w/v*) SDS in PBS, and 1× 10 M urea in PBS. All centrifugation steps were conducted at 3,000 rpm for 2 min at room temperature. The beads containing bound, biotinylated proteins were resuspended in 40 µL PBS buffer pH 7.4 containing 50 mM free D-biotin. The resulting solution was mixed with 5X Laemmli reducing sample buffer, and heated at 95°C for 5 min. This step allowed the recovery of the captured labelled proteins by exchanging the initially captured Desthiobiotin/streptavidin complex to the greater affinity biotin/streptavidin complex. Each sample was snap frozen in liquid nitrogen and stored at –80°C before mass spectrometry experiments. To check for unspecific binding, the DMSO-treated lysate sample was also incubated with the streptavidin-agarose beads, and processed as described above.

Mass spectrometry analysis. The protein isolates were loaded on NuPAGE™ 4-12% Bis–tris acrylamide gels according to the manufacturer's instructions (Invitrogen, Life Technologies). Running of samples was stopped as soon as proteins stacked as a single band. Protein containing bands were stained with Thermo Scientific Imperial Blue, cut from the gel, and following reduction and iodoacetamide alkylation, digested with high sequencing grade trypsin (Promega, Madison, WI, USA).[36, 44] Extracted peptides were concentrated before mass spectrometry analysis under speed-vacuum. Samples were reconstituted with 0.1% trifluoroacetic acid in 2% acetonitrile and analyzed by liquid chromatography (LC)-tandem MS (MS/MS) using a Q Exactive Plus Hybrid Quadrupole-Orbitrap online with a nanoLC Ultimate 3000 chromatography system (Thermo Fisher Scientific™, San Jose, CA). For each biological sample, 3 µL corresponding to 16.6% of digested sample were injected in duplicate on the system. After pre-concentration and washing of the sample on a Acclaim

PepMap 100 column (C18, 2 cm × 100 µm i.d. 100 Å pore size, 5 µm particle size), peptides were separated on a LC EASY-Spray column (C18, 50 cm × 75 µm i.d., 100 Å, 2 µm, 100 Å particle size) at a flow rate of 300 nL/min with a two-step linear gradient (2-22% acetonitrile/H_20; 0.1% formic acid for 100 min and 22-32% acetonitrile/H_20; 0.1% formic acid for 20 min). For peptides ionization in the EASY-Spray source, spray voltage was set at 1.9 kV and the capillary temperature at 250 °C. All samples were measured in a data dependent acquisition mode. Each run was preceded by a blank MS run in order to monitor system background. The peptide masses were measured in a survey full scan (scan range 375-1500 *m/z*, with 70 K FWHM resolution at *m/z*=400, target AGC value of 3.00×10^6 and maximum injection time of 100 ms). Following the high-resolution full scan in the Orbitrap, the 10 most intense data-dependent precursor ions were successively fragmented in HCD cell and measured in Orbitrap (normalized collision energy of 25%, activation time of 10 ms, target AGC value of 1.00×10^5, intensity threshold 1.00×10^4 maximum injection time 100 ms, isolation window 2 *m/z*, 17.5 K FWHM resolution, scan range 200 to 2000 *m/z*). Dynamic exclusion was implemented with a repeat count of 1 and exclusion duration of 20 s.

Protein identification and quantification. Relative intensity-based label-free quantification (LFQ) was processed using the MaxLFQ algorithm[75] from the freely available MaxQuant computational proteomics platform, version 1.6.3.4.[76] Analysis was done on three biological duplicates, each injected two times on mass spectrometers. The acquired raw LC Orbitrap MS data were first processed using the integrated Andromeda search engine.[77] Spectra were searched against the *Mycobacterium abscessus* (UP000007137) database extracted from UniProt (date 2021-03-10; 4,940 entries).[78] The false discovery rate (FDR) at the peptide and protein levels were set to 1% and determined by searching a reverse database. For protein grouping, all proteins that could not be distinguished based on their identified peptides were assembled into a single entry according to the MaxQuant rules. The statistical analysis was done with Perseus program (version 1.6.15) from the MaxQuant environment (www.maxquant.org). Quantifiable proteins were defined as those detected in above 70% of samples in one condition or more. Protein LFQ normalized intensities were base 2

logarithmized to obtain a normal distribution. Missing values were replaced using data imputation by randomly selecting from a normal distribution centered on the lower edge of the intensity values that simulates signals of low abundant proteins using default parameters (a downshift of 1.8 standard deviation and a width of 0.3 of the original distribution). To determine whether a given detected protein was specifically differential in **CyC$_{31yne}$** pulldown, a two-sample t-test was done using permutation-based FDR-controlled at 5 and employing 250 permutations. The *p*-value was adjusted using a scaling factor s0 with a value of 0.1. In case of **HPOX$_{yne}$**, the permutation-based FDR was controlled at 1 and the scaling factor s0 with a value of 1.[79]

The mass spectrometry proteomics data have been deposited to the ProteomeXchange Consortium (www.proteomexchange.org)[80] *via* the PRIDE partner repository[81] with the dataset identifier PXD048770 (Reviewer account details: **username**: reviewer_pxd048770@ebi.ac.uk / **password**: UTx078nj).

Fluorescence imaging of lipid-loaded *M. abscessus* cells

Nile Red staining. After 24 h and 48 h incubation period either in MSM or MSM-NL, and in presence/absence of inhibitors, *M. abscessus* S cultures were centrifuged at 3,500 rpm for 10 min, washed with 2× 1 mL of PBS, and then fixed with 4% paraformaldehyde in PBS for 20 min at room temperature. The pellets were washed three times with PBS-Tween 80 (0.05%, *v/v*) and resuspended in PBS at a theoretical OD_{600} of 10. The above fixed bacterial suspension (300 µL) was further incubated for 20-30 min at 37 °C in the dark with 15 µL (0.5 mg/mL in absolute ethanol) of Nile Red fluorescent dye (Interchim, Montluçon, France) for ILI staining as previously described.[24] Stained bacteria were harvested for 5 min at 5,000 rpm, then washed with 2× 500 µL of PBS-Tween 80 (0.05%, *v/v*), and re-suspended in 300 µL of PBS.

Fluorescent Microscopy. Fixed stained samples (5 µL bacterial suspension, *i.e.*, 7.5×10^6 cells, spotted between a coverslip of 170 µm thickness and a 1.5% agarose-PBS pad) were analyzed by snapshot fluorescence imaging at room temperature using an Olympus IX81 confocal microscope

equipped with a UPlanSApo 100× 1.40 NA objective and operated with the FV1000 software. Acquisitions were taken using a 2-line Kalman integration with sequential channels acquisition. Exposure time was 10 µs/pixel for both laser transmission and fluorescence images with conserved settings (HV, Gain and offset). The Dansyl was detected by excitation with a 405 nm laser with 39-50% intensity, and emission was collected using a semi-transparent mirror collecting all wavelength below 560 nm. The NBD was detected by excitation with a 405 nm laser with 40% intensity, and emission was collected using a semi-transparent mirror collecting all wavelength below 560 nm. The GFP signal was detected by excitation with a 443 nm laser with 33% intensity, and emission was collected using a semi-transparent mirror collecting all wavelength below 560 nm. The Nile Red was detected by excitation with a 543 nm laser with 39-50% intensity, and emission was collected using a semitransparent mirror collecting all wavelength over 640 nm.

Images recorded (126.98 µm × 126.98 µm; 512 × 512 pixels) were processed using the open-source program ImageJ/Fiji 1.53f51 (NIH, USA). In all cases, three biological replicates were made; and for each sample, 10 different images were taken per frame in order to get more than 200 bacteria in total. In addition, all corresponding control images were taken/checked prior to any fluorescence imaging and quantification.

Colocalization analysis between the Dansyl, NBD or GFP and Nile Red fluorescence using coloc2 plugin of ImageJ/Fiji (adapted from[82]). Colocalization between the Nile Red and Dansyl, NBD or GFP fluorescence intensity was assessed by evaluating the pixel intensity correlation over space using the Coloc2 plugin of ImageJ/Fiji, through the computed colocalization parameters: the Manders' correlation coefficients, the Pearson coefficient, and the intensity correlation quotient (ICQ) value as suggested by Li[49]. Manders' coefficients (*M1* and *M2*) estimate the co-occurrence fraction of a fluorescent signal on one channel (*i.e.*, red color) with a fluorescent signal of another channel (*i.e.*, green color). Pearson's coefficient (*R*) evaluate the correlation between two signals by measuring the relationship between the signal intensities in one image (*i.e.*, channel red) and the corresponding values in another (*i.e.*, channel green).[47] The statistical significance of these computed correlation

coefficients has been assessed by the Costes randomization test,[48] resulting in a Costes' *p*-value which should be ≥95%.

The Manders' coefficients vary from 0 to 1, the former corresponding to non-overlapping images and the latter reflecting 100% co-localization between two images. A calculated Pearson coefficient value ranges from 1 to -1, with 1 standing for complete positive correlation and -1 for a negative one, while a 0 value indicates no correlation. The ICQ value varies from 0.5 (co-localisation) to -0.5 (exclusion) while random staining and images impeded by noise will give a value close to 0. The table below depicts the values of the different colocalization coefficients and their meanings with respect to the colocalization results.

Colocalization coefficients, their values and meanings

Coefficients	Values	Meanings
Manders' coefficients *M1* & *M2*	0	Co-occurrence
	1	No co-occurrence
Pearson coefficient *R*	-1	Negative correlation
	0	No correlation
	1	Positive correlation
	±0.5-±1	Strong correlation
	±0.3-±0.49	Moderate correlation
	±0.1-±0.29	Weak correlation
ICQ value	-0.5	Exclusion
	0	Random
	0.5	Co-localization

First, 32-bit images were transformed into 8-bit single channels images, and a background noise was calculated by taking the mean fluorescence intensity of 10 different areas free of any cells for each channel (*i.e.*, Dansyl, NBD, GFP or Nile red frames, respectively), and was subtracted to each frame before running the Coloc2 analyses plugin.

Plasmid construction and cloning. All specific primers and plasmids used in this study are listed in **Supporting Information Tables S11-S12**. All cloned fragments were amplified using purified *M. abscessus* genomic DNA.

Construction of MAB_1978c mutant strains. Deletion mutant Δ*mab_1978c* (= Δ*fadD15*) was obtained by a simple and rapid gene disruption strategy in *M. abscessus* using the double homologous recombination unmarked strategy developed by Richard *et al.*[64] First, the *pUX1-katG::*Δ*fadD15_outer* and *pUX1-katG::*Δ*fadD15_inner* primers were PCR amplified using their respective forward and reverse oligonucleotides. These two amplicons were fused together through PCR with *pUX1-katG::*Δ*fadD15-inner_Fw* and *pUX1-katG::*Δ*fadD15-outer_Rev* primers thanks to their overlapping extension. The resulting product was gel purified (Macherey Nagel #740609) and cloned into pUX1-*katG* vector using NheI and HpaI restriction sites by classical cloning.[64, 83-84] All the constructs were further transformed in electrocompetent *M. abscessus* S wild-type strain. Red kanamycin-resistant colonies were selected for the first homologous recombination event, and further subjected to a second homologous recombination and removal of the kanamycin cassette providing nonfluorescent isoniazid-resistant colonies.[64, 83-84]

For complementation strain, the *fadD15* gene was amplified using the primer pairs *pMV306::fadD15-Fw* and *pMV306::fadD15-Rv*, then fused with *sfGfp* gene, and cloned into pMV306 plasmid[85] downstream of the *fadD15* own promoter also containing a kanamycin resistance cassette, using BamHI and NdeI restriction sites by classical cloning to generate *pMV306::fadD15-sfGFP*. Sequence integrity of each construct was confirmed by DNA sequencing (Eurofins Genomics). All the constructs were further transformed in electrocompetent *M. abscessus* S_Δ*fadD15* strains and selected on respective antibiotic agar plates as described previously.[64, 83-84] as well as on GFP fluorescence.

Alternatively, overexpressing mutant strain was built using the primer pairs *pVV16::fadD15-Fw* and *pVV16::fadD15-Rv*, then fused with *sfGfp* gene, and cloned into pVV16 plasmid downstream of the *hsp60* promoter also containing a kanamycin resistance cassette, using BamHI and NdeI restriction sites by classical cloning to generate *pVV16::fadD15-sfGFP*. Sequence integrity of each construct was confirmed by DNA sequencing (Eurofins Genomics). All the constructs were further transformed

in electrocompetent *M. abscessus* S wild-type strain and selected on respective antibiotic agar plates and GFP fluorescence as described previously.[83].

Identification of Δ*mab_1978c* mutant was first made based on red fluorescent colonies, then followed by PCR amplification using the primers pairs: *pUX1-katG::ΔfadD15-inner_Fw* and *pUX1-katG::ΔfadD15-outer_Rv* (**Table S11** & **Figure S5**),[64, 83-84] and by DNA sequencing of the genomic region surrounding the site of gene deletion. The *M. abscessus* S_Δ*fadD15*::C complementation strain as well as the overexpressing *M. abscessus* S_*fadD15-sfGFP* strain were checked by PCR amplification.

Functional validation of mab_1978c in ILI accumulation. The abovementioned transformed bacteria; *i.e.*, the *M. abscessus* S_Δ*fadD15* deletion strain and its complemented counterpart *M. abscessus* S_Δ*fadD15*::C, as well as the overexpressing *M. abscessus* S_*fadD15-sfGFP* strain were cultured in MSM and MSM-NL, supplemented with 250 µg/mL kanamycin when needed, for their ability to accumulate ILI. After 48 h incubation, all bacterial cultures were processed for TAG content analysis through TLC as described above.

Statistical analysis. GraphPad Prism 8 (GraphPad Inc.) was used to perform all statistical analyses, which details are given in each figure legend. Differences were considered significant when the calculated *p*-values were smaller than 0.05.

ASSOCIATED CONTENT

* Supporting Information

Supporting Information for this article is available online

Tables S1-S10. Target proteins identified after a 24 h or 48 h culture of *M. abscessus* S in MSM-NL, through CC-ABPP by LC-ESI-MS/MS analysis, using **HPOX$_{yne}$** or **CyC$_{31yne}$** probes (XLSX).

S1 Appendix. List of primers and plasmids used in this study (**Tables S11-S12**); **Figure S1**, the **HP-$_{NBD}$-OX** and **the CyC$_{31\text{-}Dansyl}$** colocalized with ILI on *M. abscessus* S cultured in MSM-NL; **Figure S2**, controls for fluorescent microscopy imaging related to the colocalization of the fluorescent probes with ILI on culture of *M. abscessus* S in MSM-NL medium; **Figure S3**, growth curves of *M. abscessus* S wild-type and Δ*fadD15* deletion mutant in 7H9TG^{OADC}, MSM and MSM-NL, respectively; **Figure S4**, *fadD15-sfGFP* overexpressing strain displays a diffuse fluorescence when grown in MSM; **Figure S5**, controls for fluorescent microscopy imaging related to the colocalization of FadD15-*sf*GFP with ILI on culture of *M. abscessus* S_*fadD15-sfGFP* overexpressing strain in MSM-NL medium; **Figure S6**, NMR spectra of the new **HPOX$_{yne}$** and **HP-$_{NBD}$-OX** compounds; **Figure S7**, unmarked deletion strategy for the deletion of *MAB_1978c* (= *fadD15*) in *M. abscessus*. (PDF).

AUTHOR INFORMATION

Corresponding Author

Jean-François Cavalier - Aix-Marseille Univ, CNRS, LISM, IMM FR3479, Marseille, France. https://orcid.org/0000-0003-0864-8314; Email: jfcavalier@imm.cnrs.fr.

Authors

Romain Avellan - Aix-Marseille Univ, CNRS, LISM, IMM FR3479, Marseille, France.

Jordan Lehoux - IBMM, Univ Montpellier, CNRS, ENSCM, Montpellier, France.

Tonia Dargham - Aix-Marseille Univ, CNRS, LISM, IMM FR3479, Marseille, France; and IHU Méditerranée Infection, Aix-Marseille Univ., Marseille, France

Thomas Francis - Aix-Marseille Univ, CNRS, LISM, IMM FR3479, Marseille, France.

Léa Celik - Aix-Marseille Univ, CNRS, LISM, IMM FR3479, Marseille, France.

Alexandre Guy - IBMM, Univ Montpellier, CNRS, ENSCM, Montpellier, France

Isabelle Poncin - Aix-Marseille Univ, CNRS, LISM, IMM FR3479, Marseille, France

Vanessa Point - Aix-Marseille Univ, CNRS, LISM, IMM FR3479, Marseille, France

Laurent Kremer - Centre National de la Recherche Scientifique UMR 9004, Institut de Recherche en Infectiologie de Montpellier (IRIM), Université de Montpellier, 1919 route de Mende, 34293, Montpellier, France; and INSERM, IRIM, 34293 Montpellier, France. https://orcid.org/0000-0002-6604-4458

Thierry Durand - IBMM, Univ Montpellier, CNRS, ENSCM, Montpellier, France. https://orcid.org/0000-0001-6086-7296

Stéphane Audebert - INSERM, CNRS, Institut Paoli-Calmettes, CRCM, Marseille Prot´eomique, Aix-Marseille University, France. https://orcid.org/0000-0002-9409-2588

Luc Camoin - INSERM, CNRS, Institut Paoli-Calmettes, CRCM, Marseille Prot´eomique, Aix-Marseille University, France. https://orcid.org/0000-0002-1230-4787

Christopher D. Spilling - Department of Chemistry and Biochemistry, University of Missouri-St. Louis, MO, USA

Pierre Santucci - Aix-Marseille Univ., CNRS, LISM UMR7255, IMM FR3479, Marseille, France. https://orcid.org/0000-0002-6291-3425

Céline Crauste - IBMM, Univ Montpellier, CNRS, ENSCM, Montpellier, France. https://orcid.org/0000-0002-5714-8749

Stéphane Canaan - Aix-Marseille Univ., CNRS, LISM UMR7255, IMM FR3479, Marseille, France. https://orcid.org/0000-0001-7478-300X

Author Contributions

Conceptualization: S.C. and J.-F.C. Data curation: S.A. and L.C. Resources: J.L., A.G., T.D., C.C. and C.D.S. Investigations: R.A., T.D., T.F., S.A., L.C., I.P. and V.P. Formal analysis: R.A., T.D., T.F., S.A., L.C., P.S., S.C. and J.-F.C. Visualization: R.A., T.D. and J.-F.C. Writing-original draft: J.-F.C. Writing-review & editing: R.A., T.D., L.K., T.D., S.A., L.C., C.D.S., P.S., C.C., S.C. and J.-F.C. Supervision: S.C. and J.-F.C. Funding acquisition: S.C. and J.-F.C. Validation: J.-F.C. Project administration: J.-F.C.

R.A., J.L. and T.D. contributed equally and should be considered as first coauthors. All authors have given approval to the final version of the manuscript.

Declaration of interests

The authors declare no competing interests.

ACKNOWLEDGEMENTS

This work was supported by the CNRS, Aix Marseille University, and the Agence Nationale de la Recherche (LipInTB project N°ANR-19-CE44-0011, and ILIome project N°ANR-20-CE44-0019). Proteomics analyses were done using the mass spectrometry facility of Marseille Proteomics (marseille-proteomique.univ-amu.fr) supported by IBISA, the Cancéropôle PACA, the Provence-Alpes-Côte d'Azur Region, the Institut Paoli-Calmettes, and Fonds Européen de Développement Regional (FEDER). R.A. was supported by a PhD fellowship from the Agence Nationale de la Recherche (LipInTB project N°ANR-19-CE44-0011). T.D. PhD fellowship was funded by the foundation IHU Méditerranée Infection. T.F. PhD fellowship is supported by the Ministère de l'Enseignement Supérieur et de la Recherche. J-F.C. is particularly grateful to Deezer and Carte Noire coffee for their invaluable help and support during the writing of this manuscript. The authors wish also to thank Dr Wassim Daher (IRIM, Montpellier, France) for his valuable input and discussions.

ABBREVIATIONS

ABP, activity-based probe; ABPP, activity-based protein profiling; au, arbitrary unit; AMK, amikacin; CC-ABPP, click-chemistry activity-based protein profiling; CC_{50}, compound concentration leading to 50% of cell cytotoxicity; CyC, Cyclipostins and Cyclophostin analogues; ILI, intrabacterial lipid inclusion; IMP, imipenem; MIC_{50}/MIC_{90}, minimal inhibitory concentration leading to 50% or 90% of growth inhibition; MSM, mineral salt medium; MSM-NL, mineral salt medium nitrogen limiting; NTM, nontuberculous mycobacterial; REMA, resazurin microtiter assay; OX, oxadiazolone derivatives; TAG, triacylglycerol; TB, tuberculosis; TLC, thin layer chromatography; VLDL, very low-density lipoproteins.

REFERENCES

(1) Brennan, P. J., Structure, function, and biogenesis of the cell wall of *Mycobacterium tuberculosis*. *Tuberculosis* **2003**, *83* (1), 91-97.

(2) Alvarez, H. M.; Steinbuchel, A., Triacylglycerols in prokaryotic microorganisms. *Appl Microbiol Biotechnol* **2002**, *60* (4), 367-76.

(3) Mallick, I.; Santucci, P.; Poncin, I.; Point, V.; Kremer, L.; Cavalier, J.-F.; Canaan, S., Intrabacterial lipid inclusions in mycobacteria: unexpected key players in survival and pathogenesis? *FEMS Microbiol Rev* **2021**, *45* (6), fuab029.

(4) Dargham, T.; Mallick, I.; Raze, D.; Kremer, L.; Canaan, S., Chapter 12 - Intrabacterial lipid inclusions: overview of an amazing organelle. In *Biology of Mycobacterial Lipids*, Fatima, Z.; Canaan, S., Eds. Academic Press: 2022; pp 253-269. DOI: https://doi.org/10.1016/B978-0-323-91948-7.00003-8.

(5) Fujimoto, T.; Ohsaki, Y., Cytoplasmic lipid droplets: rediscovery of an old structure as a unique platform. *Ann N Y Acad Sci* **2006**, *1086*, 104-15.

(6) Garton, N. J.; Barer, M. R., Mycobacterial Lipid Bodies and the Chemosensitivity and Transmission of Tuberculosis. In *Health Consequences of Microbial Interactions with Hydrocarbons, Oils, and Lipids*, 2020; pp 109-132. DOI: http://doi.org/10.1007/978-3-030-15147-8_6.

(7) Low, K. L.; Shui, G.; Natter, K.; Yeo, W. K.; Kohlwein, S. D.; Dick, T.; Rao, S. P.; Wenk, M. R., Lipid droplet-associated proteins are involved in the biosynthesis and hydrolysis of triacylglycerol in *Mycobacterium bovis* bacillus Calmette-Guerin. *J Biol Chem* **2010**, *285* (28), 21662-70.

(8) Walther, T. C.; Farese, R. V., Jr., Lipid droplets and cellular lipid metabolism. *Annu Rev Biochem* **2012**, *81*, 687-714.

(9) Wilfling, F.; Haas, J. T.; Walther, T. C.; Farese, R. V., Jr., Lipid droplet biogenesis. *Curr Opin Cell Biol* **2014**, *29*, 39-45.

(10) Daniel, J.; Maamar, H.; Deb, C.; Sirakova, T. D.; Kolattukudy, P. E., *Mycobacterium tuberculosis* Uses Host Triacylglycerol to Accumulate Lipid Droplets and Acquires a Dormancy-Like Phenotype in Lipid-Loaded Macrophages. *PLOS Pathogens* **2011**, *7* (6), e1002093.

(11) Caire-Brändli, I.; Papadopoulos, A.; Malaga, W.; Marais, D.; Canaan, S.; Thilo, L.; de Chastellier, C.; Flynn, J. L., Reversible Lipid Accumulation and Associated Division Arrest of *Mycobacterium avium* in Lipoprotein-Induced Foamy Macrophages May Resemble Key Events during Latency and Reactivation of Tuberculosis. *Infect Immun.* **2014**, *82* (2), 476-490.

(12) Neyrolles, O.; Hernández-Pando, R.; Pietri-Rouxel, F.; Fornès, P.; Tailleux, L.; Payán, J. A. B.; Pivert, E.; Bordat, Y.; Aguilar, D.; Prévost, M.-C.; Petit, C.; Gicquel, B., Is Adipose Tissue a Place for *Mycobacterium tuberculosis* Persistence? *PLoS ONE* **2006**, *1* (1), e43.

(13) Deb, C.; Lee, C.-M.; Dubey, V. S.; Daniel, J.; Abomoelak, B.; Sirakova, T. D.; Pawar, S.; Rogers, L.; Kolattukudy, P. E., A Novel In Vitro Multiple-Stress Dormancy Model for *Mycobacterium tuberculosis* Generates a Lipid-Loaded, Drug-Tolerant, Dormant Pathogen. *PLOS ONE* **2009**, *4* (6), e6077.

(14) Garton, N. J.; Waddell, S. J.; Sherratt, A. L.; Lee, S.-M.; Smith, R. J.; Senner, C.; Hinds, J.; Rajakumar, K.; Adegbola, R. A.; Besra, G. S.; Butcher, P. D.; Barer, M. R., Cytological and Transcript Analyses Reveal Fat and Lazy Persister-Like Bacilli in Tuberculous Sputum. *PLOS Medicine* **2008**, *5* (4), e75.

(15) Sloan, D. J.; Mwandumba, H. C.; Garton, N. J.; Khoo, S. H.; Butterworth, A. E.; Allain, T. J.; Heyderman, R. S.; Corbett, E. L.; Barer, M. R.; Davies, G. R., Pharmacodynamic Modeling of Bacillary Elimination Rates and Detection of Bacterial Lipid Bodies in Sputum to Predict and Understand Outcomes in Treatment of Pulmonary Tuberculosis. *Clin Infect Dis.* **2015**, *61* (1), 1-8.

(16) Hammond, R. J.; Baron, V. O.; Oravcova, K.; Lipworth, S.; Gillespie, S. H., Phenotypic resistance in mycobacteria: is it because I am old or fat that I resist you? *J Antimicrob Chemother* **2015**, *70* (10), 2823-7.

(17) Iona, E.; Giannoni, F.; Pardini, M.; Brunori, L.; Orefici, G.; Fattorini, L., Metronidazole plus rifampin sterilizes long-term dormant *Mycobacterium tuberculosis*. *Antimicrob Agents Chemother* **2007**, *51* (4), 1537-40.

(18) Bouzid, F.; Bregeon, F.; Poncin, I.; Weber, P.; Drancourt, M.; Canaan, S., *Mycobacterium canettii* Infection of Adipose Tissues. *Front Cell Infect Microbiol* **2017**, *7*, 189.

(19) Mattos, K. A.; Oliveira, V. G.; D'Avila, H.; Rodrigues, L. S.; Pinheiro, R. O.; Sarno, E. N.; Pessolani, M. C.; Bozza, P. T., TLR6-driven lipid droplets in *Mycobacterium leprae*-infected Schwann cells: immunoinflammatory platforms associated with bacterial persistence. *J Immunol* **2011**, *187* (5), 2548-58.

(20) Barisch, C.; Soldati, T., *Mycobacterium marinum* Degrades Both Triacylglycerols and Phospholipids from Its Dictyostelium Host to Synthesise Its Own Triacylglycerols and Generate Lipid Inclusions. *PLoS Pathog* **2017**, *13* (1), e1006095.

(21) Robbe-Saule, M.; Foulon, M.; Poncin, I.; Esnault, L.; Varet, H.; Legendre, R.; Besnard, A.; Grzegorzewicz, A. E.; Jackson, M.; Canaan, S.; Marsollier, L.; Marion, E., Transcriptional adaptation of *Mycobacterium ulcerans* in an original mouse model: New insights into the regulation of mycolactone. *Virulence* **2021**, *12* (1), 1438-1451.

(22) Garton, N. J.; Christensen, H.; Minnikin, D. E.; Adegbola, R. A.; Barer, M. R., Intracellular lipophilic inclusions of mycobacteria *in vitro* and *in sputum*. *Microbiology (Reading)* **2002**, *148* (Pt 10), 2951-8.

(23) Santucci, P.; Diomande, S.; Poncin, I.; Alibaud, L.; Viljoen, A.; Kremer, L.; de Chastellier, C.; Canaan, S., Delineating the Physiological Roles of the PE and Catalytic Domains of LipY in Lipid Consumption in Mycobacterium-Infected Foamy Macrophages. *Infect Immun* **2018**, *86* (9).

(24) Santucci, P.; Johansen, M. D.; Point, V.; Poncin, I.; Viljoen, A.; Cavalier, J. F.; Kremer, L.; Canaan, S., Nitrogen deprivation induces triacylglycerol accumulation, drug tolerance and hypervirulence in mycobacteria. *Sci Rep* **2019**, *9* (1), 8667.

(25) Viljoen, A.; Blaise, M.; de Chastellier, C.; Kremer, L., MAB_3551c encodes the primary triacylglycerol synthase involved in lipid accumulation in *Mycobacterium abscessus*. *Molecular microbiology* **2016**.

(26) Armstrong, R. M.; Carter, D. C.; Atkinson, S. N.; Terhune, S. S.; Zahrt, T. C., Association of Mycobacterium Proteins with Lipid Droplets. *J Bacteriol* **2018**, *200* (16).

(27) Dhouib, R.; Ducret, A.; Hubert, P.; Carriere, F.; Dukan, S.; Canaan, S., Watching intracellular lipolysis in mycobacteria using time lapse fluorescence microscopy. *Biochim Biophys Acta* **2011**, *1811* (4), 234-241.

(28) Dargham, T.; Mallick, I.; Kremer, L.; Santucci, P.; Canaan, S., Intrabacterial lipid inclusion-associated proteins: A core machinery conserved from saprophyte Actinobacteria to the human pathogen *Mycobacterium tuberculosis*. *FEBS Open Bio* **2023**.

(29) Cavalier, J. F.; Spilling, C. D.; Durand, T.; Camoin, L.; Canaan, S., Lipolytic enzymes inhibitors: A new way for antibacterial drugs discovery. *Eur J Med Chem* **2021**, *209*, 112908.

(30) Daniel, J.; Kapoor, N.; Sirakova, T.; Sinha, R.; Kolattukudy, P., The perilipin-like PPE15 protein in *Mycobacterium tuberculosis* is required for triacylglycerol accumulation under dormancy-inducing conditions. *Mol Microbiol* **2016**, *101* (5), 784-794.

(31) Santucci, P.; Bouzid, F.; Smichi, N.; Poncin, I.; Kremer, L.; De Chastellier, C.; Drancourt, M.; Canaan, S., Experimental Models of Foamy Macrophages and Approaches for Dissecting the Mechanisms of Lipid Accumulation and Consumption during Dormancy and Reactivation of Tuberculosis. *Front Cell Infect Microbiol* **2016**, *6*, 122.

(32) Johnson, G., The alpha/beta Hydrolase Fold Proteins of *Mycobacterium tuberculosis*, with Reference to their Contribution to Virulence. *Curr Protein Pept Sci* **2017**, *18* (3), 190-210.

(33) Avellan, R.; Sarrazin, M.; Spilling, C. D.; Crauste, C.; Canaan, S.; Cavalier, J.-F., Chapter 11 - Deciphering the physiological role of serine enzymes involved in mycobacterial lipid metabolism using activity-based protein profiling. In *Biology of Mycobacterial Lipids*, Fatima, Z.; Canaan, S.,

Eds. Academic Press: 2022; pp 235-251. DOI: https://doi.org/10.1016/B978-0-323-91948-7.00001-4.

(34) Lin, H.; Xing, J.; Wang, H.; Wang, S.; Fang, R.; Li, X.; Li, Z.; Song, N., Roles of Lipolytic enzymes in Mycobacterium tuberculosis pathogenesis. *Front Microbiol* **2024**, *15*, 1329715.

(35) Madani, A.; Mallick, I.; Guy, A.; Crauste, C.; Durand, T.; Fourquet, P.; Audebert, S.; Camoin, L.; Canaan, S.; Cavalier, J. F., Dissecting the antibacterial activity of oxadiazolone-core derivatives against *Mycobacterium abscessus*. *PLoS One* **2020**, *15* (9), e0238178.

(36) Madani, A.; Ridenour, J. N.; Martin, B. P.; Paudel, R. R.; Abdul Basir, A.; Le Moigne, V.; Herrmann, J. L.; Audebert, S.; Camoin, L.; Kremer, L.; Spilling, C. D.; Canaan, S.; Cavalier, J. F., Cyclipostins and Cyclophostin Analogues as Multitarget Inhibitors That Impair Growth of *Mycobacterium abscessus*. *ACS Infect Dis* **2019**, *5* (9), 1597-1608.

(37) Nguyen, P. C.; Delorme, V.; Benarouche, A.; Guy, A.; Landry, V.; Audebert, S.; Pophillat, M.; Camoin, L.; Crauste, C.; Galano, J. M.; Durand, T.; Brodin, P.; Canaan, S.; Cavalier, J. F., Oxadiazolone derivatives, new promising multi-target inhibitors against *M. tuberculosis*. *Bioorg Chem* **2018**, *81*, 414-424.

(38) Nguyen, P. C.; Delorme, V.; Bénarouche, A.; Martin, B. P.; Paudel, R.; Gnawali, G. R.; Madani, A.; Puppo, R.; Landry, V.; Kremer, L.; Brodin, P.; Spilling, C. D.; Cavalier, J.-F.; Canaan, S., Cyclipostins and Cyclophostin analogs as promising compounds in the fight against tuberculosis. *Sci Rep* **2017**, *7* (1), 11751.

(39) Nguyen, P. C.; Madani, A.; Santucci, P.; Martin, B. P.; Paudel, R. R.; Delattre, S.; Herrmann, J.-L.; Spilling, C. D.; Kremer, L.; Canaan, S.; Cavalier, J.-F., Cyclophostin and Cyclipostins analogs, new promising molecules to treat mycobacterial-related diseases. *Int J Antimicrob Agents* **2018**, *51*, 651-654.

(40) Sarrazin, M.; Martin, B. P.; Avellan, R.; Gnawali, G. R.; Poncin, I.; Le Guenno, H.; Spilling, C. D.; Cavalier, J. F.; Canaan, S., Synthesis and Biological Characterization of Fluorescent

Cyclipostins and Cyclophostin Analogues: New Insights for the Diagnosis of Mycobacterial-Related Diseases. *ACS Infect Dis* **2022**, *8* (12), 2564-2578.

(41) Santucci, P.; Point, V.; Poncin, I.; Guy, A.; Crauste, C.; Serveau-Avesque, C.; Galano, J. M.; Spilling, C. D.; Cavalier, J.-F.; Canaan, S., LipG a bifunctional phospholipase/thioesterase involved in mycobacterial envelope remodeling. *Bioscience Reports* **2018**, *38* (6), BSR20181953.

(42) Viljoen, A.; Richard, M.; Nguyen, P. C.; Fourquet, P.; Camoin, L.; Paudal, R. R.; Gnawali, G. R.; Spilling, C. D.; Cavalier, J.-F.; Canaan, S.; Blaise, M.; Kremer, L., Cyclipostins and Cyclophostin analogs inhibit the antigen 85C from *Mycobacterium tuberculosis* both *in vitro* and *in vivo*. *J. Biol. Chem.* **2018**, *293* (8), 2755–2769.

(43) Nguyen, P. C.; Nguyen, V. S.; Martin, B. P.; Fourquet, P.; Camoin, L.; Spilling, C. D.; Cavalier, J.-F.; Cambillau, C.; Canaan, S., Biochemical and structural characterization of TesA, a major thioesterase required for outer-envelope lipid biosynthesis in *M. tuberculosis*. *J Mol Biol.* **2018**, *430* (24), 5120-5136.

(44) Barelier, S.; Avellan, R.; Gnawali, G. R.; Fourquet, P.; Roig-Zamboni, V.; Poncin, I.; Point, V.; Bourne, Y.; Audebert, S.; Camoin, L.; Spilling, C. D.; Canaan, S.; Cavalier, J. F.; Sulzenbacher, G., Direct capture, inhibition and crystal structure of HsaD (Rv3569c) from *M. tuberculosis*. *FEBS J* **2023**, *290* (6), 1563-1582.

(45) Point, V.; Bénarouche, A.; Zarillo, J.; Guy, A.; Magnez, R.; Fonseca, L.; Raux, B.; Leclaire, J.; Buono, G.; Fotiadu, F.; Durand, T.; Carrière, F.; Vaysse, C.; Couëdelo, L.; Cavalier, J.-F., Slowing down fat digestion and absorption by an oxadiazolone inhibitor targeting selectively gastric lipolysis. *Eur J Med Chem.* **2016**, *123* (8), 834-848.

(46) Palomino, J. C.; Martin, A.; Camacho, M.; Guerra, H.; Swings, J.; Portaels, F., Resazurin microtiter assay plate: simple and inexpensive method for detection of drug resistance in *Mycobacterium tuberculosis*. *Antimicrob Agents Chemother* **2002**, *46* (8), 2720-2722.

(47) Bolte, S.; Cordelieres, F. P., A guided tour into subcellular colocalization analysis in light microscopy. *J Microsc* **2006**, *224* (Pt 3), 213-32.

(48) Costes, S. V.; Daelemans, D.; Cho, E. H.; Dobbin, Z.; Pavlakis, G.; Lockett, S., Automatic and quantitative measurement of protein-protein colocalization in live cells. *Biophys J* **2004**, *86* (6), 3993-4003.

(49) Li, Q.; Lau, A.; Morris, T. J.; Guo, L.; Fordyce, C. B.; Stanley, E. F., A syntaxin 1, Galpha(o), and N-type calcium channel complex at a presynaptic nerve terminal: analysis by quantitative immunocolocalization. *J Neurosci* **2004**, *24* (16), 4070-81.

(50) Delorme, V.; Diomandé, S. V.; Dedieu, L.; Cavalier, J.-F.; Carrière, F.; Kremer, L.; Leclaire, J.; Fotiadu, F.; Canaan, S., M*m*PPOX Inhibits *Mycobacterium tuberculosis* Lipolytic Enzymes Belonging to the Hormone-Sensitive Lipase Family and Alters Mycobacterial Growth. *PLoS ONE* **2012**, *7* (9), e46493.

(51) Goins, C. M.; Sudasinghe, T. D.; Liu, X.; Wang, Y.; O'Doherty, G. A.; Ronning, D. R., Characterization of Tetrahydrolipstatin and Stereoderivatives on the Inhibition of Essential *Mycobacterium tuberculosis* Lipid Esterases. *Biochemistry* **2018**, *57* (16), 2383-2393.

(52) Lehmann, J.; Cheng, T. Y.; Aggarwal, A.; Park, A. S.; Zeiler, E.; Raju, R. M.; Akopian, T.; Kandror, O.; Sacchettini, J. C.; Moody, D. B.; Rubin, E. J.; Sieber, S. A., An Antibacterial beta-Lactone Kills *Mycobacterium tuberculosis* by Disrupting Mycolic Acid Biosynthesis. *Angew Chem Int Ed Engl.* **2018**, *57* (1), 348-353.

(53) Lehmann, J.; Vomacka, J.; Esser, K.; Nodwell, M.; Kolbe, K.; Ramer, P.; Protzer, U.; Reiling, N.; Sieber, S. A., Human lysosomal acid lipase inhibitor lalistat impairs *Mycobacterium tuberculosis* growth by targeting bacterial hydrolases. *MedChemComm* **2016**, *7*, 1797-1801.

(54) Ravindran, M. S.; Rao, S. P.; Cheng, X.; Shukla, A.; Cazenave-Gassiot, A.; Yao, S. Q.; Wenk, M. R., Targeting lipid esterases in mycobacteria grown under different physiological conditions using activity-based profiling with tetrahydrolipstatin (THL). *Mol Cell Proteomics* **2014**, *13* (2), 435-48.

(55) Rens, C.; Laval, F.; Daffe, M.; Denis, O.; Frita, R.; Baulard, A.; Wattiez, R.; Lefevre, P.; Fontaine, V., Effects of lipid-lowering drugs on vancomycin susceptibility of mycobacteria. *Antimicrob Agents Chemother.* **2016**, *60* (10), 6193-6199.

(56) Ogata, H.; Goto, S.; Sato, K.; Fujibuchi, W.; Bono, H.; Kanehisa, M., KEGG: Kyoto Encyclopedia of Genes and Genomes. *Nucleic Acids Res* **1999**, *27* (1), 29-34.

(57) Kanehisa, M.; Sato, Y.; Kawashima, M.; Furumichi, M.; Tanabe, M., KEGG as a reference resource for gene and protein annotation. *Nucleic Acids Res* **2016**, *44* (D1), D457-62.

(58) Kapopoulou, A.; Lew, J. M.; Cole, S. T., The MycoBrowser portal: a comprehensive and manually annotated resource for mycobacterial genomes. *Tuberculosis (Edinb)* **2011**, *91* (1), 8-13.

(59) Koonin, E. V., Orthologs, paralogs, and evolutionary genomics. *Annu Rev Genet* **2005**, *39*, 309-38.

(60) UniProt, C., UniProt: the Universal Protein Knowledgebase in 2023. *Nucleic Acids Res* **2023**, *51* (D1), D523-D531.

(61) Rifat, D.; Chen, L.; Kreiswirth, B. N.; Nuermberger, E. L., Genome-Wide Essentiality Analysis of Mycobacterium abscessus by Saturated Transposon Mutagenesis and Deep Sequencing. *mBio* **2021**, *12* (3), e0104921.

(62) Dubois, V.; Pawlik, A.; Bories, A.; Le Moigne, V.; Sismeiro, O.; Legendre, R.; Varet, H.; Rodriguez-Ordonez, M. D. P.; Gaillard, J. L.; Coppee, J. Y.; Brosch, R.; Herrmann, J. L.; Girard-Misguich, F., *Mycobacterium abscessus* virulence traits unraveled by transcriptomic profiling in amoeba and macrophages. *PLoS Pathog* **2019**, *15* (11), e1008069.

(63) Trivedi, O. A.; Arora, P.; Sridharan, V.; Tickoo, R.; Mohanty, D.; Gokhale, R. S., Enzymic activation and transfer of fatty acids as acyl-adenylates in mycobacteria. *Nature* **2004**, *428* (6981), 441-5.

(64) Richard, M.; Gutierrez, A. V.; Viljoen, A.; Rodriguez-Rincon, D.; Roquet-Baneres, F.; Blaise, M.; Everall, I.; Parkhill, J.; Floto, R. A.; Kremer, L., Mutations in the MAB_2299c TetR Regulator Confer Cross-Resistance to Clofazimine and Bedaquiline in Mycobacterium abscessus. *Antimicrob Agents Chemother* **2019**, *63* (1).

(65) Daniel, J.; Deb, C.; Dubey, V. S.; Sirakova, T. D.; Abomoelak, B.; Morbidoni, H. R.; Kolattukudy, P. E., Induction of a novel class of diacylglycerol acyltransferases and triacylglycerol

accumulation in *Mycobacterium tuberculosis* as it goes into a dormancy-like state in culture. *J Bacteriol* **2004**, *186* (15), 5017-30.

(66) Kapoor, N.; Pawar, S.; Sirakova, T. D.; Deb, C.; Warren, W. L.; Kolattukudy, P. E., Human granuloma in vitro model, for TB dormancy and resuscitation. *PLoS One* **2013**, *8* (1), e53657.

(67) Sirakova, T. D.; Dubey, V. S.; Deb, C.; Daniel, J.; Korotkova, T. A.; Abomoelak, B.; Kolattukudy, P. E., Identification of a diacylglycerol acyltransferase gene involved in accumulation of triacylglycerol in *Mycobacterium tuberculosis* under stress. *Microbiology (Reading)* **2006**, *152* (Pt 9), 2717-2725.

(68) Barisch, C.; Soldati, T., Breaking fat! How mycobacteria and other intracellular pathogens manipulate host lipid droplets. *Biochimie* **2017**, *141*, 54-61.

(69) Gago, G.; Arabolaza, A.; Diacovich, L.; Gramajo, H., Components and Key Regulatory Steps of Lipid Biosynthesis in Actinomycetes. In *Biogenesis of Fatty Acids, Lipids and Membranes*, Geiger, O., Ed. Springer International Publishing: Cham, 2019; pp 409-433. DOI: https://doi.org/10.1007/978-3-319-50430-8_65.

(70) Aguilar-Ayala, D. A.; Tilleman, L.; Van Nieuwerburgh, F.; Deforce, D.; Palomino, J. C.; Vandamme, P.; Gonzalez, Y. M. J. A.; Martin, A., The transcriptome of *Mycobacterium tuberculosis* in a lipid-rich dormancy model through RNAseq analysis. *Sci Rep* **2017**, *7* (1), 17665.

(71) Mekonnen, D.; Derbie, A.; Mihret, A.; Yimer, S. A.; Tonjum, T.; Gelaw, B.; Nibret, E.; Munshae, A.; Waddell, S. J.; Aseffa, A., Lipid droplets and the transcriptome of *Mycobacterium tuberculosis* from direct sputa: a literature review. *Lipids Health Dis* **2021**, *20* (1), 129.

(72) Schnappinger, D.; Ehrt, S.; Voskuil, M. I.; Liu, Y.; Mangan, J. A.; Monahan, I. M.; Dolganov, G.; Efron, B.; Butcher, P. D.; Nathan, C.; Schoolnik, G. K., Transcriptional Adaptation of *Mycobacterium tuberculosis* within Macrophages: Insights into the Phagosomal Environment. *J Exp Med* **2003**, *198* (5), 693-704.

(73) Larrouy-Maumus, G.; Biswas, T.; Hunt, D. M.; Kelly, G.; Tsodikov, O. V.; de Carvalho, L. P., Discovery of a glycerol 3-phosphate phosphatase reveals glycerophospholipid polar head recycling in *Mycobacterium tuberculosis*. *Proc Natl Acad Sci U S A* **2013**, *110* (28), 11320-5.

(74) Crotta Asis, A.; Savoretti, F.; Cabruja, M.; Gramajo, H.; Gago, G., Characterization of key enzymes involved in triacylglycerol biosynthesis in mycobacteria. *Sci Rep* **2021**, *11* (1), 13257.

(75) Cox, J.; Hein, M. Y.; Luber, C. A.; Paron, I.; Nagaraj, N.; Mann, M., Accurate proteome-wide label-free quantification by delayed normalization and maximal peptide ratio extraction, termed MaxLFQ. *Mol Cell Proteomics* **2014**, *13* (9), 2513-2526.

(76) Cox, J.; Mann, M., MaxQuant enables high peptide identification rates, individualized p.p.b.-range mass accuracies and proteome-wide protein quantification. *Nat Biotechnol.* **2008**, *26* (12), 1367-1372.

(77) Cox, J.; Neuhauser, N.; Michalski, A.; Scheltema, R. A.; Olsen, J. V.; Mann, M., Andromeda: a peptide search engine integrated into the MaxQuant environment. *J Proteome Res.* **2011**, *10* (4), 1794-1805.

(78) The UniProt, C., UniProt: the universal protein knowledgebase. *Nucleic Acids Res* **2017**, *45* (D1), D158-D169.

(79) Tusher, V. G.; Tibshirani, R.; Chu, G., Significance analysis of microarrays applied to the ionizing radiation response. *Proc Natl Acad Sci U S A* **2001**, *98* (9), 5116-21.

(80) Deutsch, E. W.; Bandeira, N.; Sharma, V.; Perez-Riverol, Y.; Carver, J. J.; Kundu, D. J.; Garcia-Seisdedos, D.; Jarnuczak, A. F.; Hewapathirana, S.; Pullman, B. S.; Wertz, J.; Sun, Z.; Kawano, S.; Okuda, S.; Watanabe, Y.; Hermjakob, H.; MacLean, B.; MacCoss, M. J.; Zhu, Y.; Ishihama, Y.; Vizcaino, J. A., The ProteomeXchange consortium in 2020: enabling 'big data' approaches in proteomics. *Nucleic Acids Res* **2020**, *48* (D1), D1145-D1152.

(81) Perez-Riverol, Y.; Bai, J.; Bandla, C.; Garcia-Seisdedos, D.; Hewapathirana, S.; Kamatchinathan, S.; Kundu, D. J.; Prakash, A.; Frericks-Zipper, A.; Eisenacher, M.; Walzer, M.;

Wang, S.; Brazma, A.; Vizcaino, J. A., The PRIDE database resources in 2022: a hub for mass spectrometry-based proteomics evidences. *Nucleic Acids Res* **2022**, *50* (D1), D543-D552.

(82) Woglar, A.; Yamaya, K.; Roelens, B.; Boettiger, A.; Kohler, S.; Villeneuve, A. M., Quantitative cytogenetics reveals molecular stoichiometry and longitudinal organization of meiotic chromosome axes and loops. *PLoS Biol* **2020**, *18* (8), e3000817.

(83) Viljoen, A.; Gutierrez, A. V.; Dupont, C.; Ghigo, E.; Kremer, L., A Simple and Rapid Gene Disruption Strategy in *Mycobacterium abscessus*: On the Design and Application of Glycopeptidolipid Mutants. *Front Cell Infect Microbiol* **2018**, *8*, 69.

(84) Ung, K. L.; Kremer, L.; Blaise, M., Structural analysis of the N-acetyltransferase Eis1 from Mycobacterium abscessus reveals the molecular determinants of its incapacity to modify aminoglycosides. *Proteins* **2021**, *89* (1), 94-106.

(85) Cortes, M.; Singh, A. K.; Reyrat, J. M.; Gaillard, J. L.; Nassif, X.; Herrmann, J. L., Conditional gene expression in Mycobacterium abscessus. *PLoS One* **2011**, *6* (12), e29306.

SUPPORTING INFORMATION

Mapping of mycobacterial lipolytic enzymes involved in triacylglycerol accumulation as intrabacterial lipid inclusions using activity-based multi-target inhibitor probes

Romain Avellan[1,#], Jordan Lehoux[2,#], Tonia Dargham[1,3,#], Thomas Francis[1], Léa Celik[1], Alexandre Guy[2], Isabelle Poncin[1], Vanessa Point[1], Laurent Kremer[4,5], Thierry Durand[2], Stéphane Audebert[6], Luc Camoin[6], Christopher D. Spilling[7], Céline Crauste[2], Stéphane Canaan[1], Jean-François Cavalier[1]*

[1] Aix-Marseille Univ., CNRS, LISM UMR7255, IMM FR3479, Marseille, France

[2] IBMM, Univ Montpellier, CNRS, ENSCM, Montpellier, France

[3] IHU Méditerranée Infection, Aix-Marseille Univ., Marseille, France

[4] Centre National de la Recherche Scientifique UMR 9004, Institut de Recherche en Infectiologie de Montpellier (IRIM), Université de Montpellier, 1919 route de Mende, 34293, Montpellier, France

[5] INSERM, IRIM, 34293 Montpellier, France

[6] INSERM, CNRS, Institut Paoli-Calmettes, CRCM, Marseille Protéomique, Aix-Marseille Univ., France

[7] Department of Chemistry and Biochemistry, University of Missouri-St. Louis, MO, USA

Contents

Supplementary **Tables S11-S12**: primers and plasmids used in this study S2

Supplementary **Figures S1-S5** S3

Supplementary **Figure S6**: ^{1}H, ^{13}C NMR spectra of new synthesized compounds S8

Supplementary **Figure S7** S12

References S13

Table S11: Primers used in this study.

pUX1-katG::ΔfadD15	
pUX1-katG::ΔfadD15-inner_Fw (NheI)	5'-CAACTTGTCTGGTGTGCTAGCgatcgccccgtccaggg-3'
pUX1-katG::ΔfadD15-inner_Rv	3'-CGAGGTCGACGGTATCGACTAacgcccttggcgataagac-5'
pUX1-katG::ΔfadD15-outer_Fw	5'-TCGATACCGTCGACCTCGTCGcggagatcggaaccg-3'
pUX1-katG::ΔfadD15-outer_Rv (HpaI)	3'-AGTCGATCGTACGCTAGTTAACgcgcccgggggttgg-5'
pMV306::fadD15-sfGFP	
pMV306::fadD15-sfGFP_Fw (KpnI)	5'-GAGAGGTACCGCCGGCCACACGACGGG-3'
pMV306::fadD15-sfGFP_Rv (EcoRI)	3'-GAGAGAATTCCTGGGGTGCTCCCGCGT-5'
pVV16::fadD15-sfGFP	
pVV16::fadD15-sfGFP_Fw (NdeI)	5'-GAGACATATGGTGCGAGAGTTCAGCGTTC-3'
pVV16::fadD15-sfGFP_Rv (BamHI)	3'-GAGAGGTCCACTGGGGTGCTCCCGCGT-5'
PCR identification (see **Figure S5**)	
ΔfadD15::C_Fw (=*pUX1-katG::ΔfadD15-inner_Fw*)	5'-CAACTTGTCTGGTGTGCTAGCgatcgccccgtccaggg-3'
ΔfadD15::C_Rv (= *pUX1-katG::ΔfadD15-outer_Rv*)	3'-AGTCGATCGTACGCTAGTTAACgcgcccgggggttgg-5'

Fw and *Rv* stand for forward and reverse, respectively. Restriction sites are underlined and specified inside brackets.

Table S12: Plasmids used in this study.

Name	Description	Reference
pUX1-*katG*	Variant of pUX1 vector[1] containing the *katG* gene of *M. tuberculosis* H37Rv as a counter-selectable marker in the presence of isoniazid and used for the generation of unmarked chromosomal alterations.	[2]
pMV306	Integrative *E. coli* - mycobacterium shuttle vector, kanamycin cassette	[3-4]
pVV16	Multicopy *E. coli* - mycobacterium shuttle vector, kanamycin cassette, *hsp60* constitutive promoter	[5]

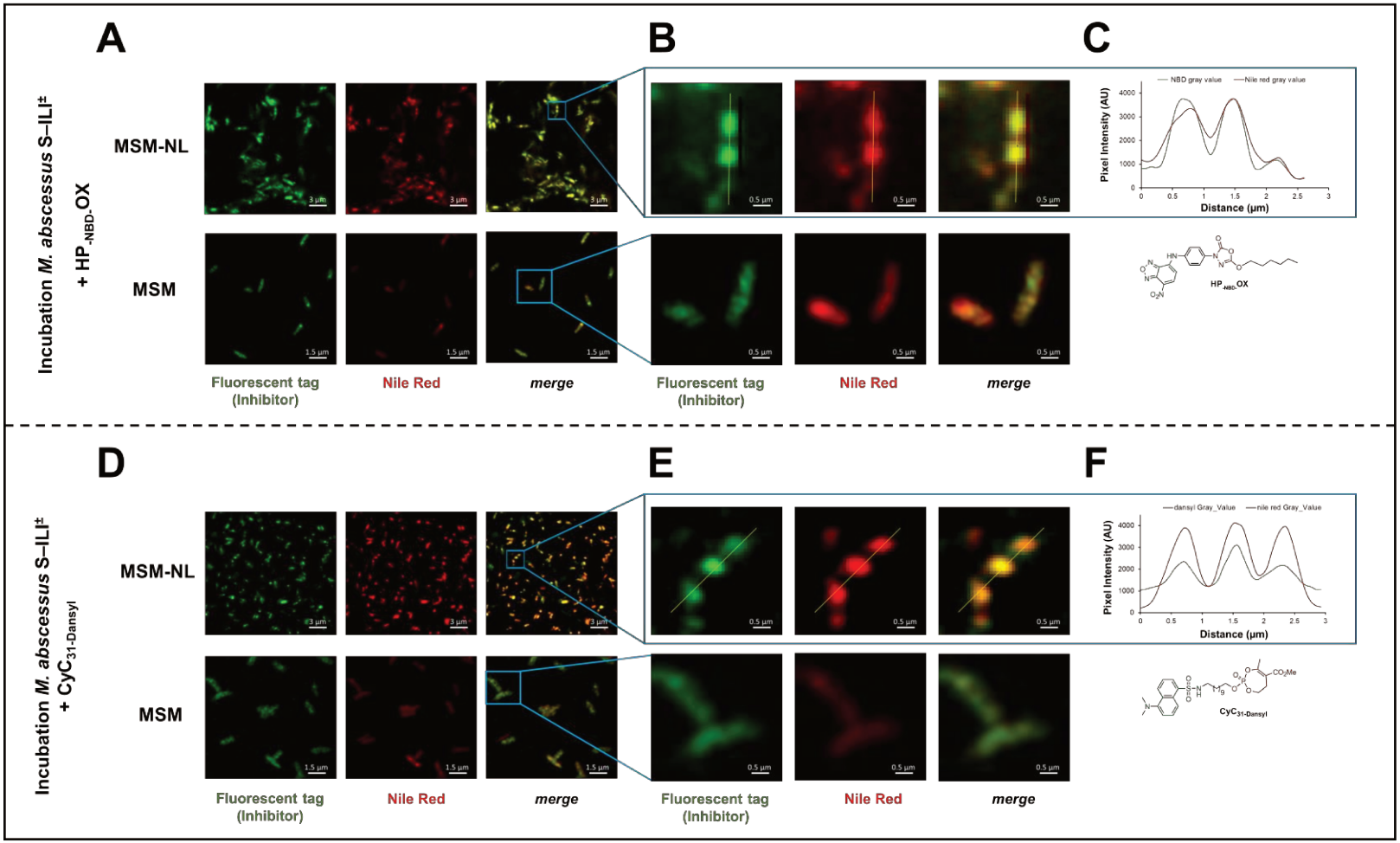

Figure S1. The HP-NBD-OX and the CyC31-Dansyl colocalized with ILI on *M. abscessus* S cultured in MSM-NL medium. Following a 24h-culture of *M. abscessus* S in MSM-NL medium to induce ILI accumulation, or MSM medium as ILI-negative control, mycobacteria were harvested, re-suspended in fresh medium in presence of **(A-C) HP-NBD-OX** or **(D-F) CyC31-Dansyl** fluorescent probe for additional 24 h before chemical fixation, neutral lipids staining with Nile Red fluorescent dye, and confocal fluorescence imaging. Fluorescence controls are given in **Figure S2**. The Coloc2 plugin of ImageJ/Fiji was used to assess the colocalization between NBD or Dansyl fluorescent tag (*i.e.*, green channel) and Nile Red (*i.e.*, red channel). Micrographs are representative of 3 independent experiments with ten acquisitions per sample. **(A, D)** Large filed image representative of the dataset acquired. **(B, E)** Zoom on a single bacterium to demonstrate a single fluorescent tag colocalization with ILI when cultured in MSM-NL medium, or a diffuse fluorescence with no ILI when cultured in MSM medium. **(C, F)** Plot of fluorescence intensity of NBD or Dansyl channel and Nile Red channel as a function of the distance of each pixel from the yellow line depicted in panels **C & F**.

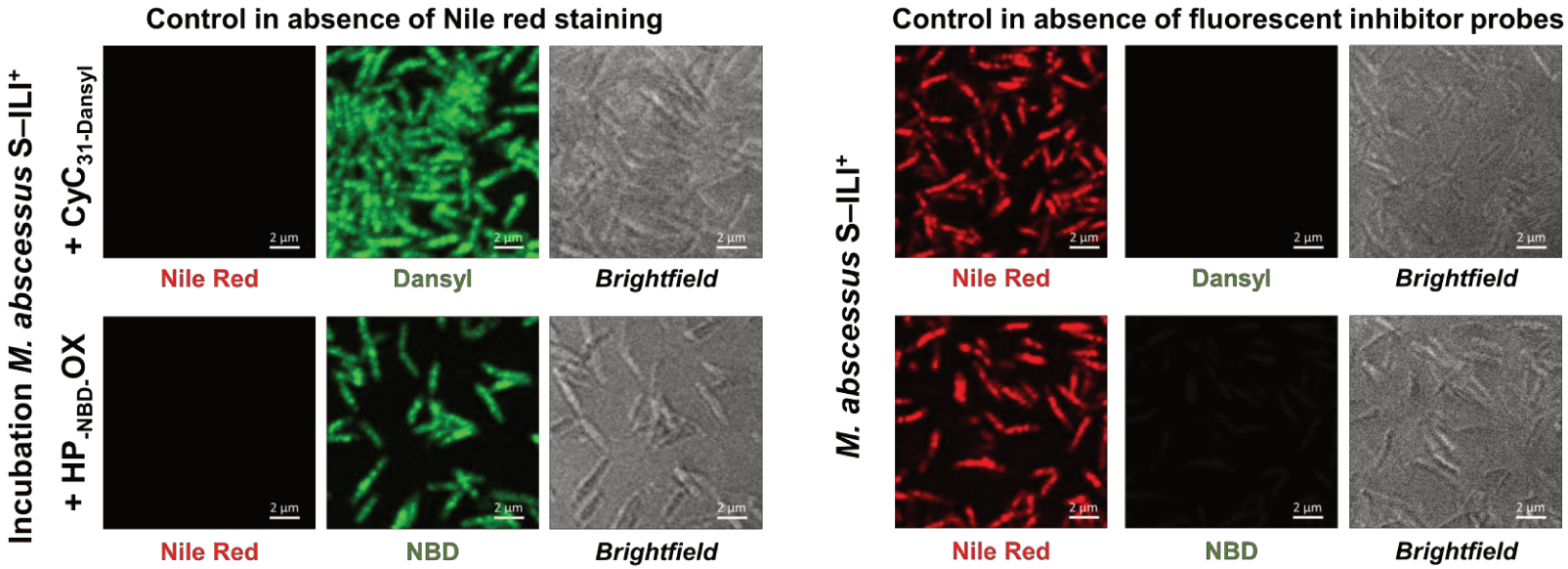

Figure S2. Controls for fluorescent microscopy imaging related to the colocalization of the fluorescent probes with ILI on culture of *M. abscessus* S in MSM-NL medium. *M. abscessus* S ILI positive bacteria were harvested, re-suspended in fresh medium in presence or absence of **CyC$_{31\text{-Dansyl}}$** or **HP$_{\text{-NBD}}$-OX** fluorescent probes, and incubated for additional 24 h before chemical fixation. Neutral lipids staining with Nile Red fluorescent dye was done only in absence of inhibitor fluorescent probes, and confocal fluorescence imaging was done to confirm the absence of overlap between the Nile Red (*i.e.*, red channel) and the NBD or Dansyl fluorescent tag (*i.e.*, green channel) signals.

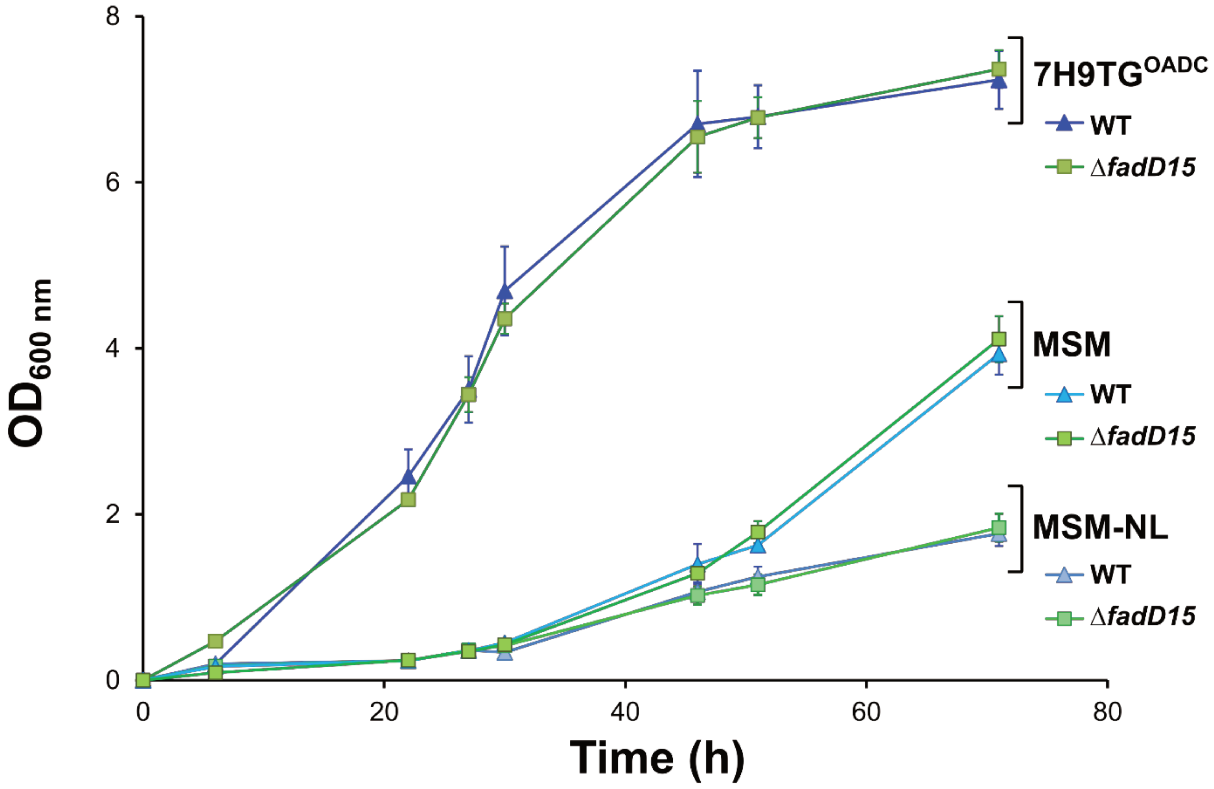

Figure S3. Growth curves of *M. abscessus* S wild-type and Δ*fadD15* deletion mutant in 7H9TG^{OADC}, MSM and MSM-NL medium, respectively. Media were inoculated at initial OD_{600nm} = 0.05, and growth was followed over a 72h period. Each data point is the mean ± SD of three independent assays.

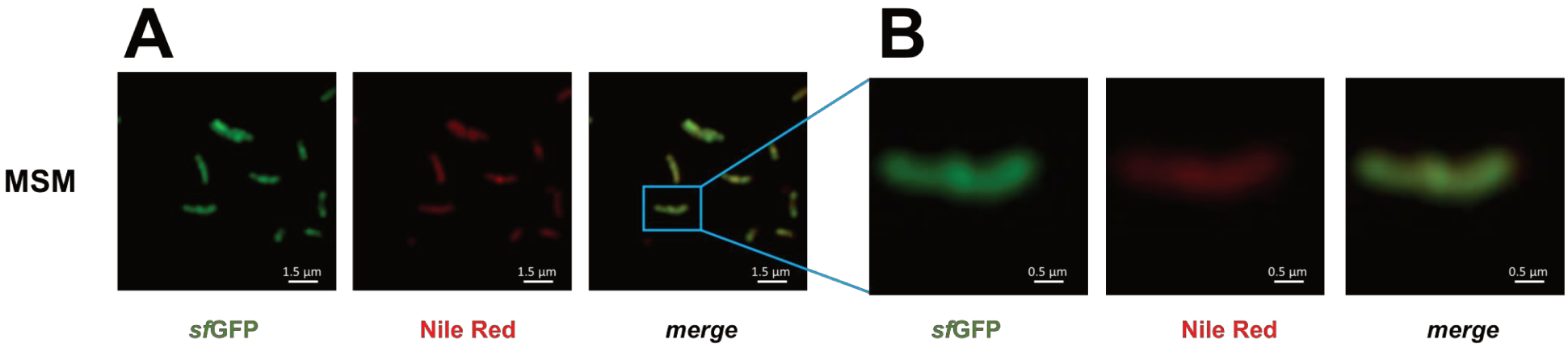

Figure S4. ***M. abscessus*** **S*_fadD15-sfGFP* overexpressing strain displays a diffuse fluorescence when grown in MSM medium.** Following a 48h-culture of *M. abscessus* S*_fadD15-sfGFP* in MSM medium as ILI-negative control, mycobacteria were harvested, fixed with 4% paraformaldehyde, stained for neutral lipids with Nile Red fluorescent dye, and processed for confocal fluorescence imaging. Micrographs are representative of 3 independent experiments with ten acquisitions per sample. **(A)** Large filed image representative of the dataset acquired. **(B)** Zoom on a single bacterium showing a diffuse *sf*GFP fluorescence with no ILI when cultured in MSM medium.

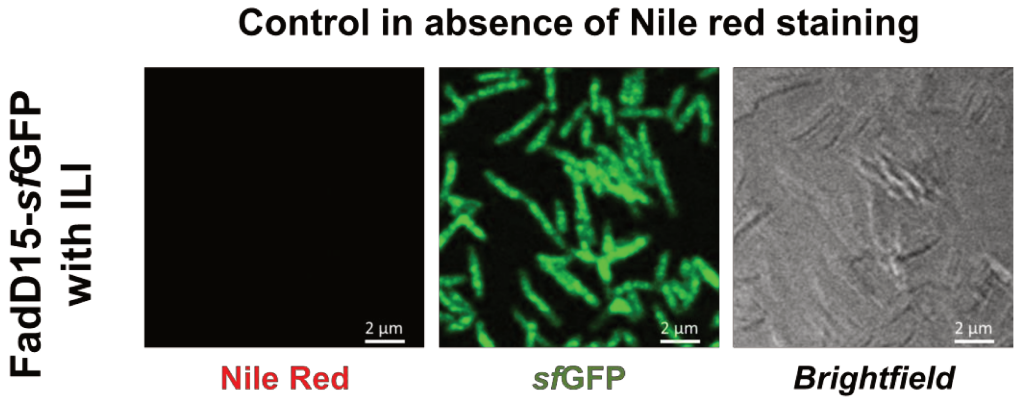

Figure S5. Controls for fluorescent microscopy imaging related to the colocalization of FadD15-*sf*GFP with ILI on culture of *M. abscessus* S_*fadD15-sfGFP* overexpressing strain in MSM-NL medium. Following a 48h-culture of *M. abscessus* S_*fadD15-sfGFP* in MSM-NL medium, mycobacteria were harvested, and fixed with 4% paraformaldehyde. Confocal fluorescence imaging was done in absence of neutral lipids staining with Nile Red fluorescent dye to confirm the absence of overlap between the Nile Red (*i.e.*, red channel) and the *sf*GFP (*i.e.*, green channel) fluorescent signals.

Figure S6. ^{1}H and ^{13}C NMR spectra

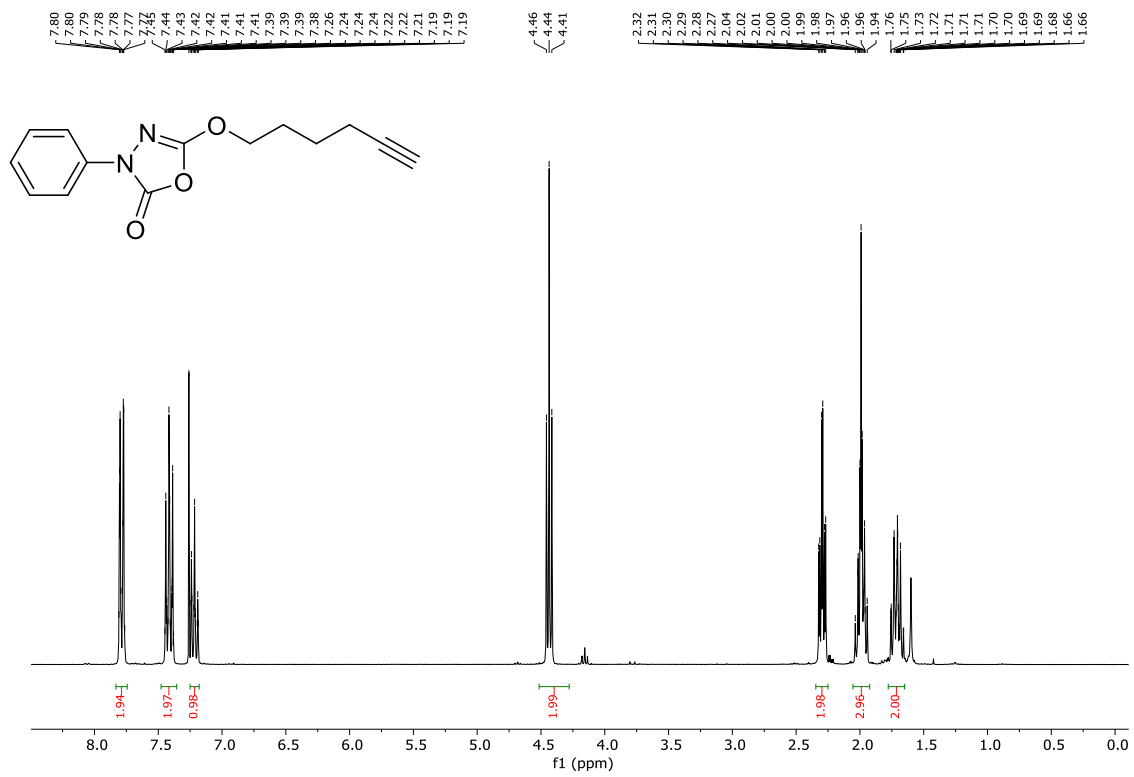

^{1}H NMR Spectrum (300 MHz, $CDCl_3$)

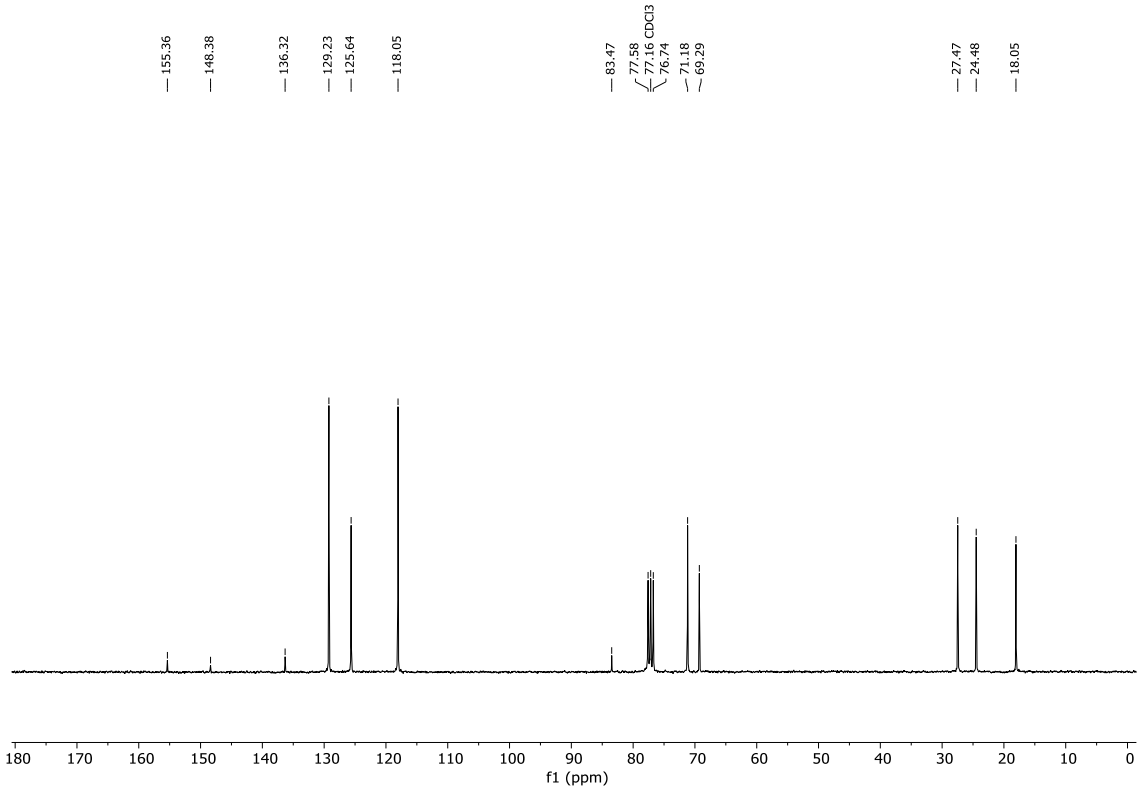

^{13}C NMR Spectrum (75 MHz, $CDCl_3$)

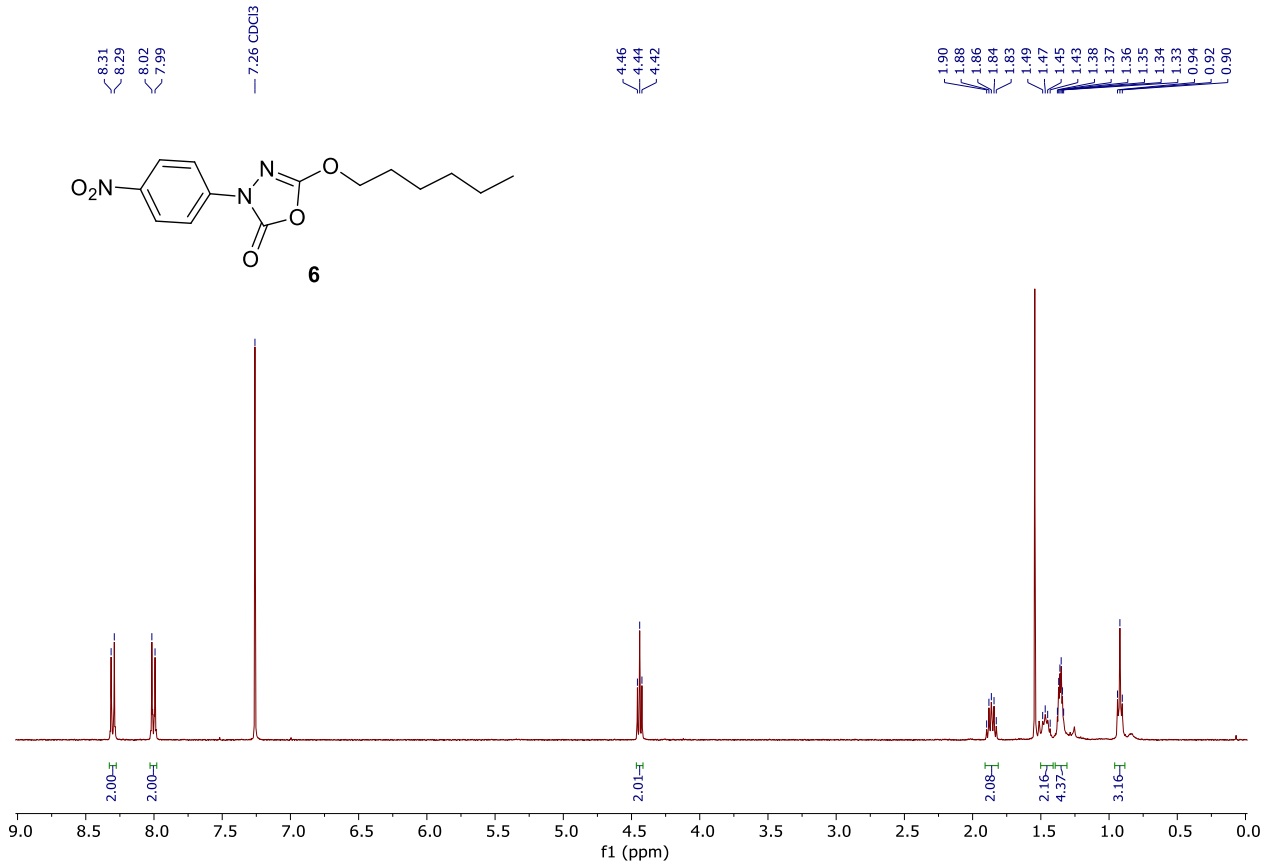

^{1}H NMR Spectrum (400 MHz, $CDCl_3$)

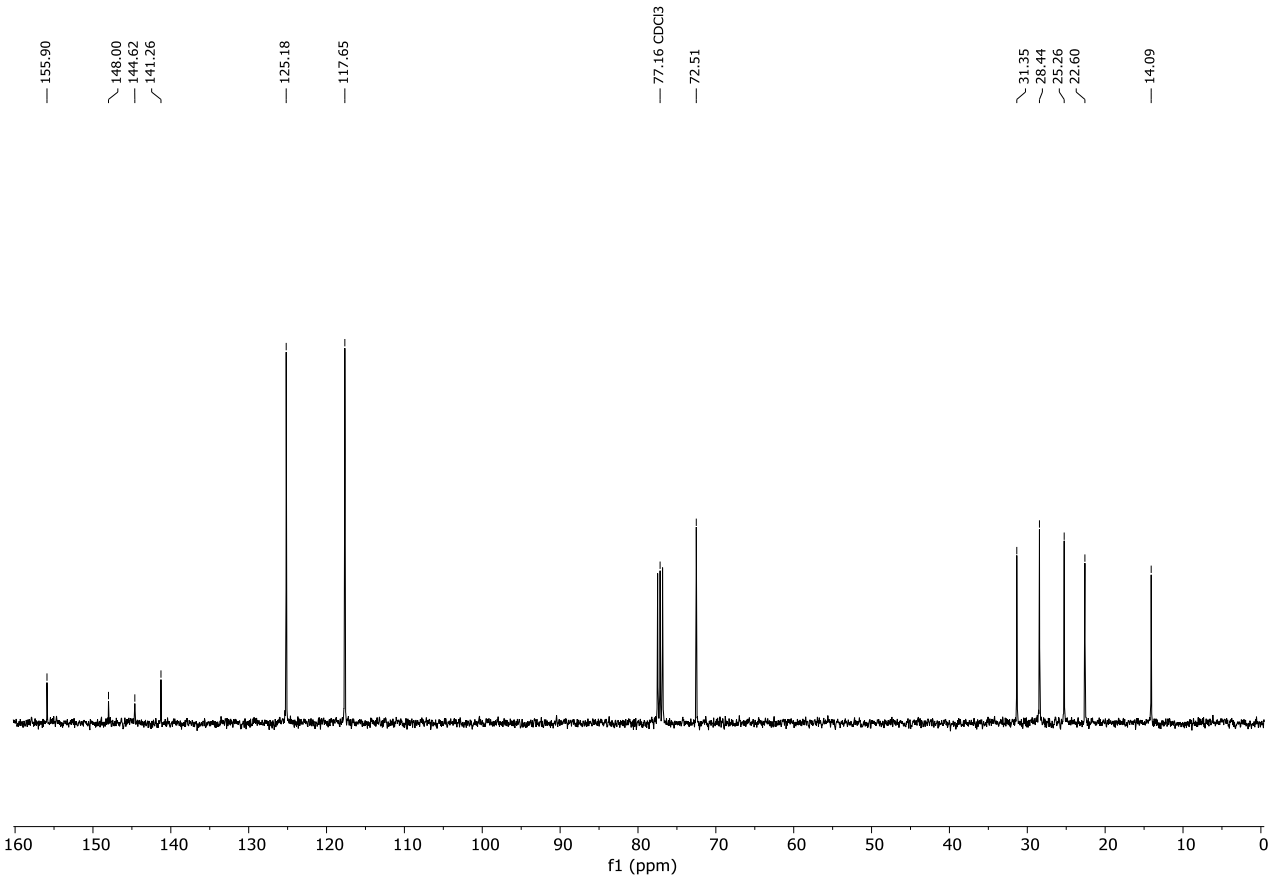

^{13}C NMR Spectrum (100 MHz, $CDCl_3$)

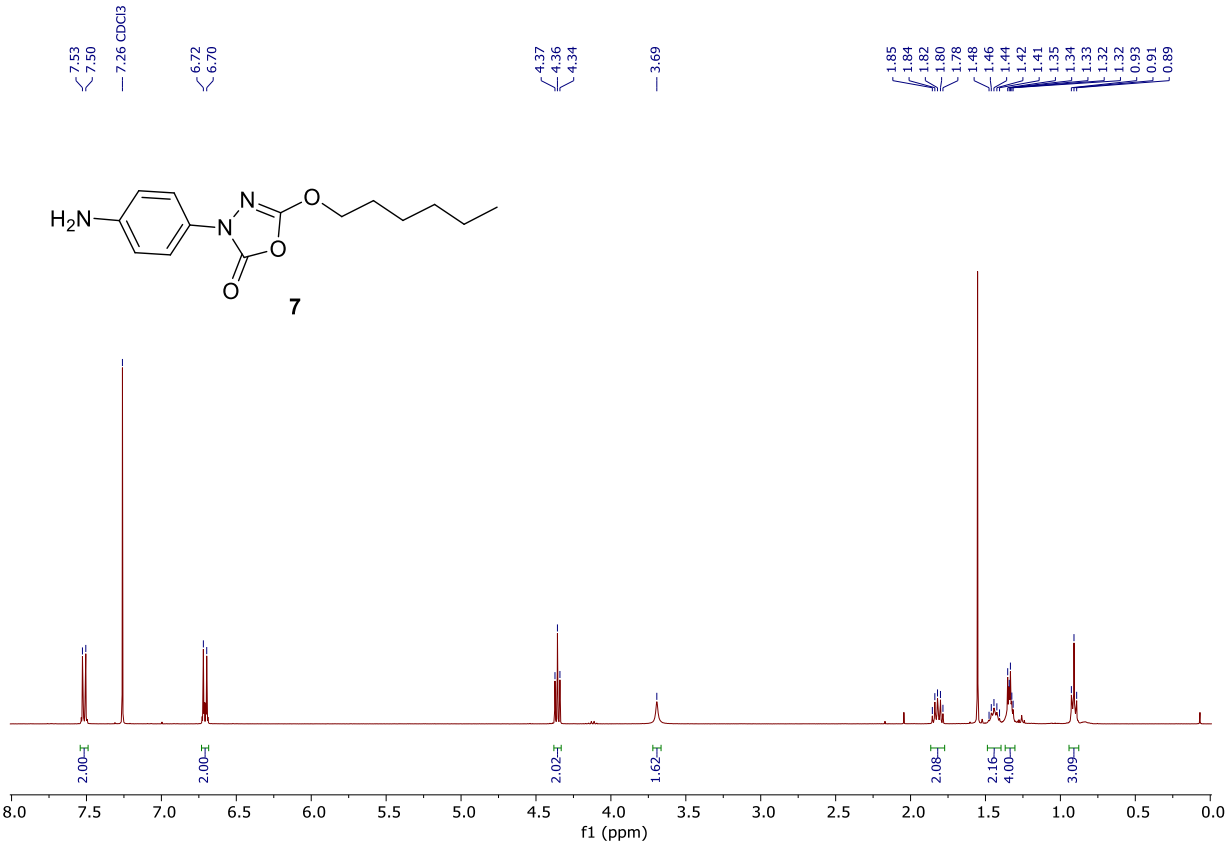

^{1}H NMR Spectrum (400 MHz, $CDCl_3$)

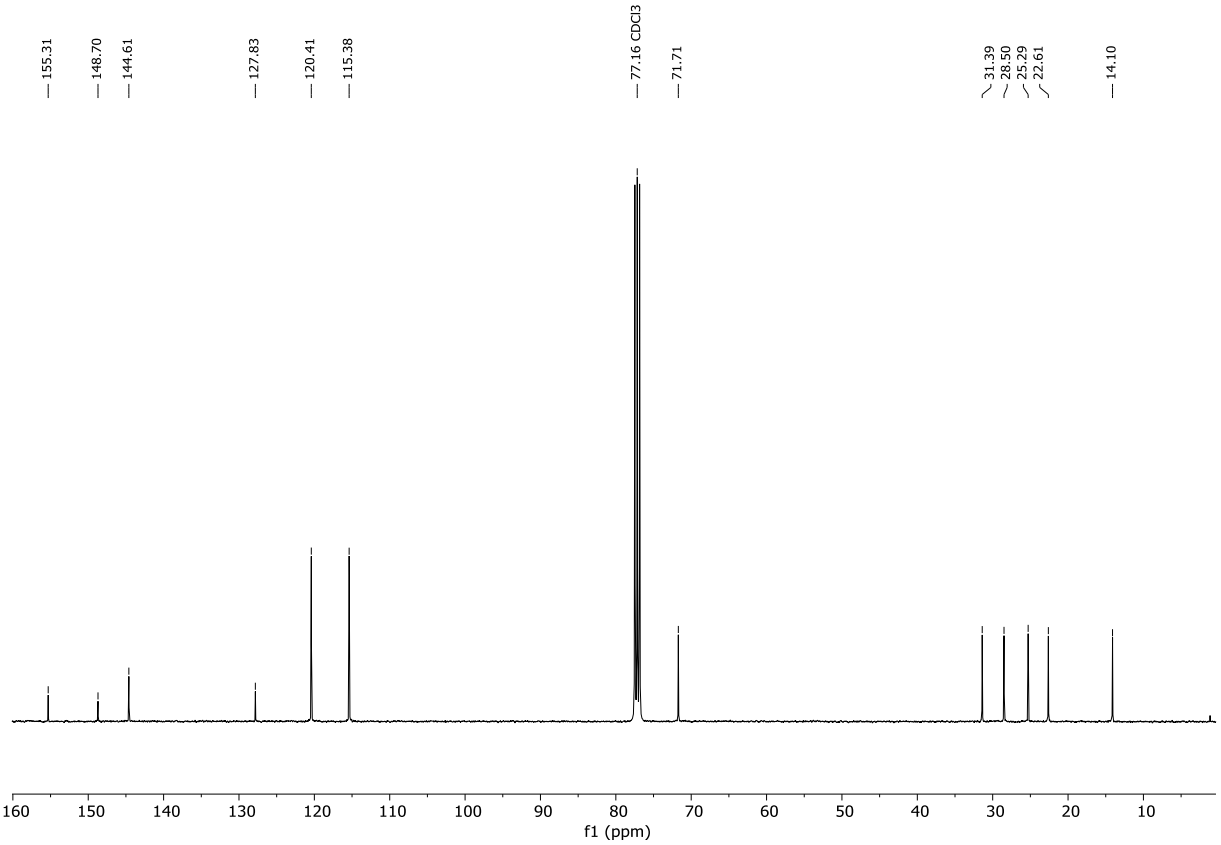

^{13}C NMR Spectrum (100 MHz, $CDCl_3$)

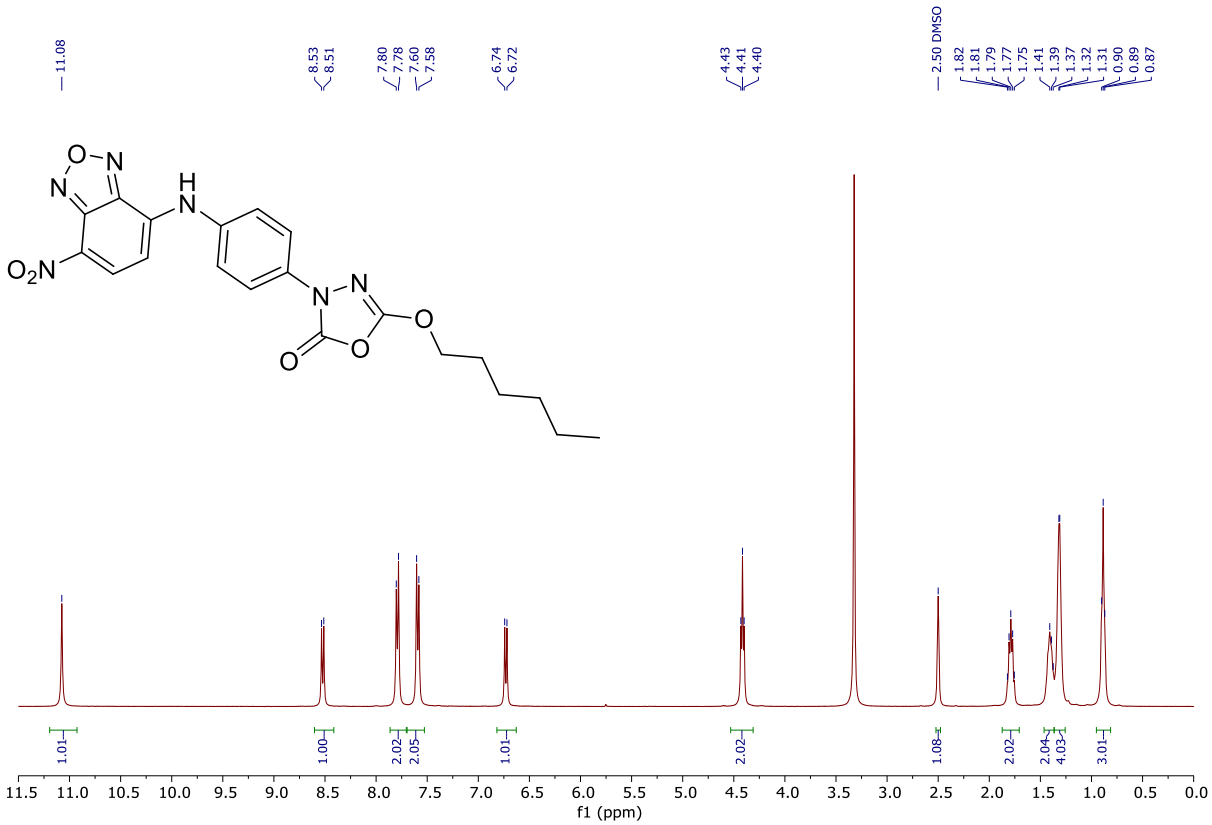

^{1}H NMR Spectrum (400 MHz, $(CD_3)_2SO$)

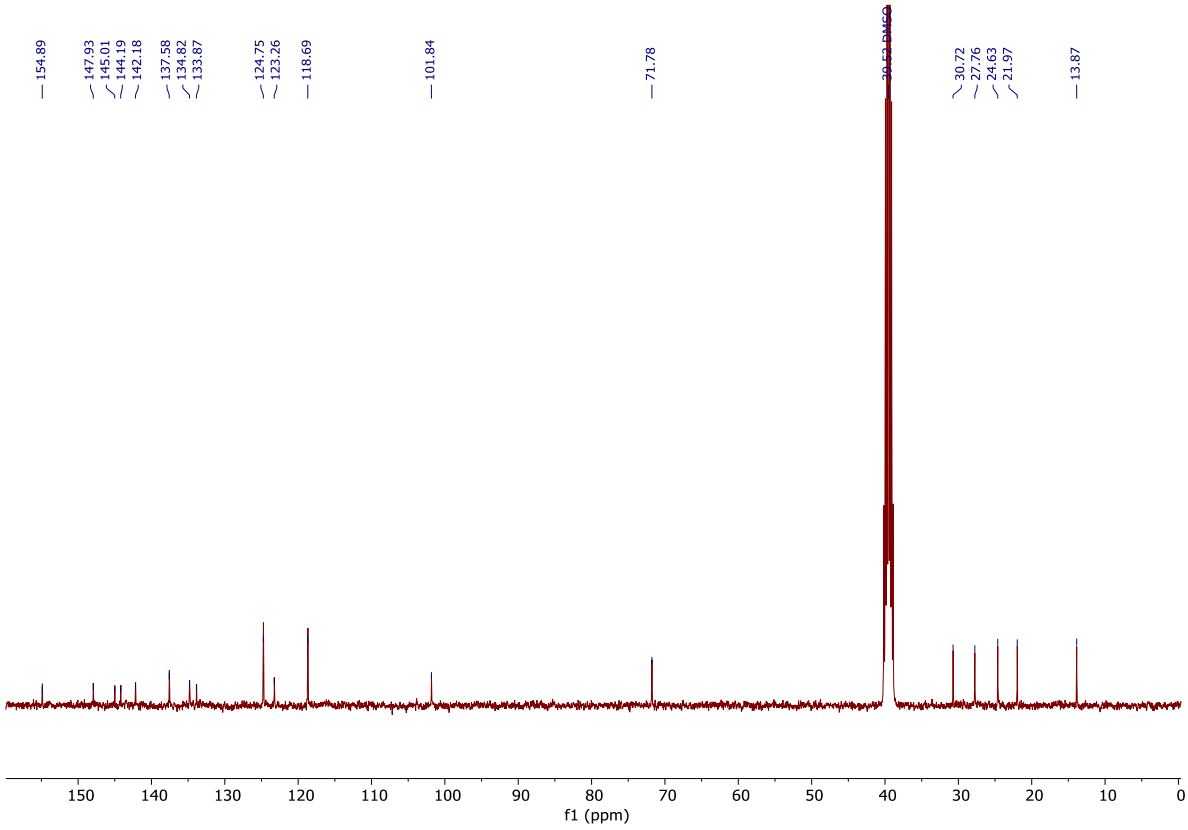

^{13}C NMR Spectrum (100 MHz, $(CD_3)_2SO$)

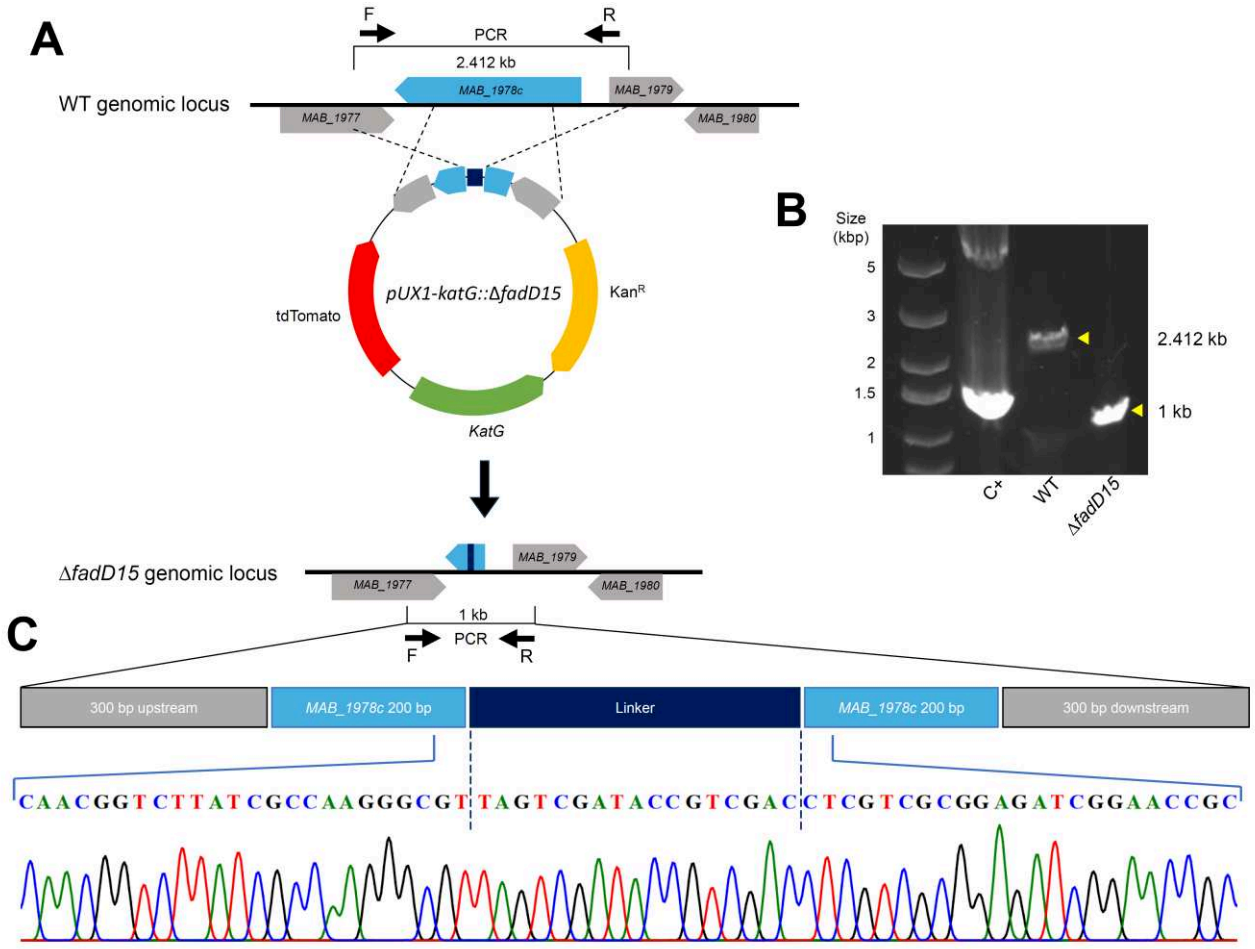

Figure S7. **Unmarked deletion strategy for the deletion of *MAB_1978c* (= *fadD15*) in *M. abscessus*. (A)** Schematic representation of the *fadD15* genetic locus in the parental *M. abscessus* WT strain, and construction of the Δ*fadD15* mutant strain by double homologous recombination using the *pUX1-katG::*Δ*fadD15* plasmid.[2] The size of the expected PCR products in *M. abscessus* WT (2.412 kb) and Δ*fadD15* mutant (1 kb) strain are displayed. **(B)** Genetic locus of both *M. abscessus* WT and Δ*fadD15* mutant strains analyzed by PCR profiling using the Δ*fadD15*::C_*Fw* and Δ*fadD15*::C_*Rv* primers. C+ corresponds to control amplification from the *pUX1-katG::*Δ*fadD15* plasmid using the same primers. **(C)** Sequencing result of the 1 kb band excised from the Δ*fadD15* PCR gel. Only part of the *fadD15* gene including the linker is represented to validate the deletion.

References

(1) Viljoen, A.; Gutierrez, A. V.; Dupont, C.; Ghigo, E.; Kremer, L., A Simple and Rapid Gene Disruption Strategy in *Mycobacterium abscessus*: On the Design and Application of Glycopeptidolipid Mutants. *Front Cell Infect Microbiol* **2018**, *8*, 69.

(2) Richard, M.; Gutierrez, A. V.; Viljoen, A.; Rodriguez-Rincon, D.; Roquet-Baneres, F.; Blaise, M.; Everall, I.; Parkhill, J.; Floto, R. A.; Kremer, L., Mutations in the MAB_2299c TetR Regulator Confer Cross-Resistance to Clofazimine and Bedaquiline in Mycobacterium abscessus. *Antimicrob Agents Chemother* **2019**, *63* (1).

(3) Cortes, M.; Singh, A. K.; Reyrat, J. M.; Gaillard, J. L.; Nassif, X.; Herrmann, J. L., Conditional gene expression in Mycobacterium abscessus. *PLoS One* **2011**, *6* (12), e29306.

(4) Stover, C. K.; de la Cruz, V. F.; Fuerst, T. R.; Burlein, J. E.; Benson, L. A.; Bennett, L. T.; Bansal, G. P.; Young, J. F.; Lee, M. H.; Hatfull, G. F.; et al., New use of BCG for recombinant vaccines. *Nature* **1991**, *351* (6326), 456-60.

(5) Santucci, P.; Point, V.; Poncin, I.; Guy, A.; Crauste, C.; Serveau-Avesque, C.; Galano, J. M.; Spilling, C. D.; Cavalier, J.-F.; Canaan, S., LipG a bifunctional phospholipase/thioesterase involved in mycobacterial envelope remodeling. *Bioscience Reports* **2018**, *38* (6), BSR20181953.

Article V

A proteomic and functional view of intrabacterial lipid inclusion biogenesis in mycobacteria

---

T. Dargham*, J. Aguilera-Correa*, **R. Avellan***, I. Mallick, L. Celik, G. Brasseur, I. Poncin, V. Point, S. Audebert, L. Camoin, W. Daher, J.-F. Cavalier, L. Kremer, S. Canaan

Manuscrit soumis

* Contribution égale

L'ensemble des bactéries de la famille des actinomycètes sont capable d'accumuler des lipides dans leur cytoplasme sous forme d'inclusions lipidiques intracytoplasmiques ou ILI. Ces structures sont généralement produites en réponse à des conditions de stress environnemental spécifiques et servent de source d'énergie ou de précurseur métabolique pour répondre à ces stress. Cette spécificité des actinomycètes les différencie de la plupart des autres microorganismes qui accumulent plutôt du glycogène, des polyphosphates ou encore des polyhydroxyalcanoates pour répondre à ces besoins [212].

Les mycobactéries, comme les autres actinomycètes, sont donc capables de stocker des TAG dans leur cytoplasme sous forme d'ILI en réponse à divers stress environnementaux [293, 425, 426].

En effet, l'accumulation des ILI joue un rôle dans la pathogénie de diverses mycobactéries infectant l'homme. Ainsi lors des infections pulmonaires à *M. tb*, certains macrophages au sein du granulome se différentient en macrophages spumeux en accumulant des lipides neutres au sein de vésicules lipidiques appelés « *lipid body* » (LB). *M. tb* est capable de survivre et de se développer au sein de ces macrophages et de détourner les lipides de l'hôte pour accumuler des ILI. Cette accumulation d'ILI est corrélée avec l'entrée en dormance du bacille qui va rentrer dans un état de non réplication, présenter une activité métabolique plus lente et une résistance accrue aux antibiotiques. On parle alors de tuberculose latente et les lipides accumulés vont servir de source de carbone durant la dormance et lors de la réactivation de l'infection.

D'autre part, il a également été établi que les ILI jouent un rôle important dans la pathogénie de *M. abs*. En effet, des études ont montré que lors des infection de poisson-zèbres par *M. abs*, l'accumulation d'ILI par le bacille pré-infection entraine une surmortalité et accroit la virulence des infections [220, 426]. Il a été montré que lors des infections à *M. ulcerans*, le bacille adapte son métabolisme dans les tissus en guérison en réduisant son métabolisme secondaire ce qui conduit à une formation conséquente d'ILI [427].

Etant donnée l'importance des ILI, plusieurs études se sont penchées sur leur composition et ont montré qu'elle se constituent d'un cœur de lipides neutres principalement composé de TAG, entouré d'une monocouche de phospholipides au sein de laquelle de nombreuses protéines sont ancrées.

Cependant, ces protéines associées aux ILI restent assez peu connues, notamment leur nombre et leur fonction dans la synthèse, le maintien et la dégradation des ILI. Des études de protéomique ont été réalisé sur les ILI de *R. opacus* [428] et *R. jostii* [429] qui ont conduit à l'identification de 200 protéines associées aux ILI.

Chez les mycobactéries, une étude sur *M. bovis* a conduit à l'identification de sept de ces protéines [205] et une étude chez *M. smegmatis* en a identifié 400 [430]. Dans ces deux études, les ILI ont été purifié après lyse des bactéries ce qui peut conduire à des artéfacts co-purifié avec les ILI.

Parmi ces protéines, on retrouve la triglycéride synthase Tgs1 qui a été identifiée comme impliquée dans l'accumulation des TAG chez *M. bovis* [205], *M. tuberculosis* [431] et *M. abscessus* [220]. En effet, sa mutation entraine une diminution drastique de la synthèse des TAG. De plus, *tgs1* est surexprimée lors de l'accumulation d'ILI dans le modèle de dormance de Wayne [432]. Ces différents résultats confirment ainsi que l'accumulation d'ILI est médiée par Tgs1 et est liée à l'entré en dormance des mycobactéries.

Le but de cette étude est d'établir plus précisément le protéome associé aux ILI durant les différentes étapes de leur synthèse [19], de façon à mieux comprendre la dynamique de ce processus et son impact sur la pathogénie des infections mycobactériennes. Pour cela, une approche différente des études précédentes a été appliquée en utilisant une technique de marquage de proximité sur cellules entières afin d'obtenir le proxysome des ILI et ainsi éviter tous faux positifs dus à la purification des ILI. Ainsi, nous avons utilisé l'ascorbate peroxydase APEX2, qui est une protéine monomérique de 27 kDa dérivé des graine de soja, et qui est capable d'oxyder de la biotine phénol en présence de peroxyde d'hydrogène pour générer un radical phénoxylique. Ce radical ainsi formé va pouvoir biotinyler toutes les protéines présentes dans un rayon de 20 nm. Il est ainsi possible de construire une protéine de fusion entre APEX2 et une protéine dont la localisation sur un compartiment cellulaire est connue afin d'obtenir le proxysome de ce compartiment en purifiant les protéines biotinylées avec des billes de streptavidine.

Cette démarche a déjà été appliquée sur des cellules eucaryotes pour étudier le proxysome des gouttelettes lipidiques de cellules cancéreuses humaines, de hamster et d'autres

organismes [433-436], mais n'a jamais été appliquée sur le proxysome des ILI procaryotes [437, 438].

Dans cette étude, une protéine de fusion entre APEX2 et le domaine C-terminal de Tgs1 (MAB_3551) a été exprimée chez *M. abs* de façon à identifier le proxysome des ILI à différents moments de leur synthèse. Pour ce faire, le modèle expérimental d'induction de cette synthèse par carence en azote (MSM-NL) a été utilisé, et le biotin-phénol ainsi que le peroxyde d'hydrogène ont été ajoutés à 24 ou à 48h d'accumulation des ILI. Les protéines biotinylées ont ensuite été purifiées avec des billes de streptavidine et analysées par LC-MS/MS.

Cette méthode a permis d'identifier 228 protéines : 84 ont été enrichies à 24h, 105 à 48h, et 37 protéines sont présentes aux deux temps testés. Ces résultats soulignent la nature dynamique du proxysome des ILI au cours de leur synthèse et met en avant la nécessité d'utiliser une approche cinétique pour ce type d'étude.

Afin de valider l'implication de ces cibles potentielles dans la physiologie des ILI, 10 protéines ont été sélectionnées sur la base de leurs annotations fonctionnelles en lien avec le métabolisme des lipides mycobactériens.

Les 10 gènes codant ces protéines ont tout d'abord été fusionnés au gène de la GFP, et les souches correspondantes ont été cultivées en milieu MSM-NL afin d'induire l'accumulation des ILI. L'observation par microscopie de fluorescence de ces souches a permis de confirmer leurs colocalisations sur les ILI, et donc leur implication dans le processus de synthèse de ces organelles. Des mutant de délétion ont ensuite été construits par double recombinaison homologue avec le vecteur PUX1-KatG [439]. La capacité de ces souches de délétion à accumuler des ILI a été évaluée par quantification des TAGs par chromatographie sur couches minces. Nous avons ainsi pu démontrer que les protéines MAB_1463 et MAB_3486 étaient directement impliquées dans la synthèse des ILI, leur délétion induisant une diminution significative de la quantité de TAG dans le modèle MSM-NL.

En résumé, ces données représentent le premier proxysome des ILI chez les mycobactéries et fournissent ainsi de précieuses informations sur la dynamique de ces organelles, ouvrant la voie à la découverte de nouvelles cibles thérapeutiques potentielles pour traiter les infections mycobactériennes.

A proteomic and functional view of intrabacterial lipid inclusion biogenesis in mycobacteria

Tonia Dargham[1,2,*], John Jairo Aguilera-Correa[3,*], Romain Avellan[1,*], Ivy Mallick[1], Léa Celik[1], Gael Brasseur[4], Isabelle Poncin[1], Vanessa Point[1], Stéphane Audebert[5], Luc Camoin[5], Wassim Daher[3,6], Jean-François Cavalier[1], Laurent Kremer[3,6] & Stéphane Canaan[1§]

[1]Aix-Marseille Univ., CNRS, LISM-UMR 7255, IMM FR3479, IM2B, Marseille, France

[2]IHU Méditerranée Infection, Aix-Marseille Univ., Marseille, France

[3]CNRS UMR 9004, IRIM, Université de Montpellier, Montpellier, France

[4]Aix-Marseille Univ., CNRS, LCB-UMR 7283, IMM FR3479, IM2B, Marseille, France

[5]Aix-Marseille Univ., INSERM, CNRS, Institut Paoli-Calmettes, CRCM, Marseille, Marseille Protéomique, France

[6]INSERM, IRIM, Montpellier, France

*Authors contributed equally to this work, and should be considered as first co-authors

[§]Correspondence address to Stéphane Canaan, canaan@imm.cnrs.fr.

Keywords: Intracellular lipid inclusion, lipid metabolism, persistence, *Mycobacterium abscessus*, ILI-associated proteins, proteomic, proximity labelling, APEX2.

Abstract

During infection and granuloma formation, pathogenic mycobacteria store triacylglycerol as Intrabacterial Lipid Inclusions (ILI). These organelles help bacteria evade the immune system and provide a carbon source for bacterial persistence. *Mycobacterium abscessus* (*Mab*), a rapidly-growing non-tuberculous actinobactirium, produces similar structures throughout its infection cycle. Herein, *Mab* was used as a model organism to identify proteins associated with ILI accumulation on a global scale. Using the APEX2 proximity labeling method in an *in vitro* model for ILI accumulation, 228 proteins potentially implicated in ILI biosynthesis were identified. Fluorescence microscopy of strains overexpressing eight ILI-associated proteins (IAP) candidates fused to GFP showed co-localization with ILI. Genetic inactivation of these potential IAP-encoding genes and subsequent lipid analysis emphasized the importance of MAB_3486 and MAB_4532c as key enzymes influencing triacylglycerol accumulation. This study underscores the dynamic process of ILI biogenesis involving different proteins and advances our understanding of lipid metabolism in pathogenic mycobacteria. Identifying the major players in lipid accumulation may lead to better control of pathogenic bacterial growth and persistence during infection. Moreover, further research into these IAP could uncover new therapeutic targets for future medical applications.

Importance: This study sheds light on the complex process of ILI formation and its key role in the survival and persistence of pathogenic mycobacteria, with is of clinical importance. By identifying the proteins involved in ILI biosynthesis and revealing their impact on lipid metabolism, the research provides crucial insights into how these bacteria evade the immune system and maintain chronic infections. This knowledge could lead to the development of new therapeutic strategies to target and control pathogenic mycobacteria, potentially improving outcomes for patients with mycobacterial infections.

Introduction

Actinobacteria accumulate neutral lipids as intrabacterial lipid inclusions (ILI) under certain environmental conditions. Unlike many microorganisms that store glycogen, polyphosphates, and polyhydroxyalkanoates, mycobacteria store triacylglycerol (TAG) in their cytoplasm during particular stress conditions (1-4). During granuloma formation in *Mycobacterium tuberculosis* (*Mtb*) infected hosts, foamy macrophages (FM) accumulate large lipid bodies, which the bacilli use to synthesize ILI, enabling the pathogen to persist in a non-replicating dormant state for extended periods (5). ILI play a crucial role in the virulence and induction of dormancy of Mtb (3, 6) and are associated with antibiotic tolerance (6, 7). All mycobacterial species can accumulate ILI in their cytoplasm, including *Mycobacterium abscessus* (*Mab*) (8), *M. ulcerans* (9), *M. avium* (10), *M. bovis BCG* (*Mbv BCG*) (11, 12) and *M. leprae* (13). ILI serve as an energy reservoir and play a role in mycobacterial virulence, as shown by higher mortality rates in zebrafish infected with lipid-rich *Mab* (3, 8). Similarly, during tissue repair following *M. ulcerans* infection, bacilli adapt by modifying their metabolic activity and nutrient sources for survival in healing tissues (9). Cells infected with *M. leprae* also highlight the importance of ILI in pathogenesis, using host lipids for survival and inducing an inflammatory response conducive to bacterial proliferation (13). ILI have also been reported in saprophytic *Mycobacterium smegmatis* (*Msmeg*) since the 1970s (14, 15), and more recently in *M. brumae,* suggesting that these organelles confer significant advantages to the mycobacterial life cycle.

The role of proteins in ILI formation, function, and degradation remains poorly understood. Proteomic experiments on lipid droplets from *Rhodococcus opacus* (16) and *Rhodococcus jostii* (17) identified approximately 200 distinct proteins. In mycobacteria, only two studies have been conducted previously. The first, using *Mbv* BCG (12), identified five proteins exclusively associated with ILI, while a second study using *Msmeg* (14) acknowledged around 400 potential IAP. A major difference between these studies lies in the ILI accumulation and purification methods used, leading to variations in ILI size and the number of IAP. Among the IAP identified, a bifunctional enzyme with a synthase domain (ACSL) in its C-terminal and a lipase domain in its N-terminal was isolated among the 50 most abundant proteins in *Msmeg* (MSMEG_3637) or *Mbv* BCG (BCG1721), resulting in increased TAG production and degradation when overexpressed (12). Other IAP include triglyceride

synthase 1 (Tgs1), involved in TAG biosynthesis in *Mbv* BCG (12), *Mtb* (18), and *Mab* (8), while deletion of its gene drastically decreased TAG production. These two studies suggest a link between ILI accumulation/degradation and the action of both Tgs1 and the bifunctional enzyme long-chain-fatty-acid—CoA ligase (ACSL).

To gain insights into ILI-protein interactions and the significance of this organelle in bacteria, an *in silico* analysis was conducted to identify a conserved ILIome core in Actinobacteria, using three independent ILI-associated proteomes (19). These bioinformatic findings revealed a conserved amphipathic helix in both Tgs1 and ACSL structure, potentially interacting with ILI (19). From these observations, it was inferred that Tgs1 and ACSL are highly conserved across all mycobacterial species and could serve as probes to elucidate neighboring partners involved in ILI synthesis and degradation.

This study aimed to detail the ILI proteome (ILIome) involved in ILI formation and reveal the dynamics of this process. Unlike prior studies on *Mbv* BCG (12) and *Msmeg* (14), our approach employed a non-invasive method applied on living mycobacteria based on the APEX2-proximity labeling technique to identify the ILIome, thus minimizing false-positive hits. Ascorbate peroxidase (APEX2) catalyzes the oxidation of biotin-phenol substrate to a short-lived biotinphenoxyl radical within a radius of less than 20 nm in the presence of hydrogen peroxide. The biotinylated proteins can be enriched by streptavidin beads and identified by mass spectrometry (MS). Moreover, APEX2 has already been successfully used in mycobacteria to identify bacterial proteins specifically located in the cytoplasm or specific substrates of the type VII secretion system (20-22). Compared to conventional methods like the two-hybrid system or co-immunoprecipitation coupled with mass spectrometry analysis, proximity labeling offers a robust approach for proteomic mapping (23-25), aiding in deciphering the kinetics of the ILIome in live cells by reducing artefacts.

Herein, APEX2 (20, 24, 26) was fused to Tgs1, and the resulting strain was used to monitor the ILIome kinetics, leading to the identification of 228 potential IAP, of which 100 are potentially involved in lipid biosynthetic pathways. Although additional studies are warranted to confirm the function and contribution of each IAP during ILI biogenesis, we validated our approach by focusing on 10 selected targets. This study reports the first ILI proxisome and provides new insight into the dynamics of ILI

formation, paving the way for the discovery of potential therapeutic targets with translational value.

Results & Discussion

Whole proteome analysis alone is insufficient to fully depict the ILIome content

To identify proteins involved in ILI biosynthesis, we used an established *in vitro* model employing a nitrogen-limiting minimal salt medium (MSM NL) (**Fig. 1A**) (3). Initially, we assessed population homogeneity over time within this medium. Flow cytometry analysis with Nile Red staining quantified and distinguished between ILI-positive and ILI-negative bacteria (**Fig. 1A**). To ensure homogeneity of lipid-rich bacilli, flow cytometry analyzed bacterial populations at 24 and 48h under two media conditions: MSM and MSM NL. MSM NL yielded a homogeneous population with a unimodal Gaussian distribution at both time points, indicating lipid-rich ILI-positive bacteria. Conversely, control MSM consistently displayed a bimodal Gaussian distribution, reflecting a diverse population of lipid-poor and lipid-rich bacteria (**Fig. 1B**). After confirming population homogeneity in MSM NL, we adapted the same culture workflow to isolate bacteria at 24 and 48h for subsequent proteomic analyses, depicting the proteomic landscape during various ILI formation stages (**Fig. 1C**).

Given the significant lipid accumulation at 24 and 48h in MSM NL, we initially conducted a full proteome analysis, anticipating an abundance of proteins associated with lipid metabolism. At 24h, label-free proteomic analysis revealed 21 differentially expressed proteins in MSM NL compared to MSM (p-value ≤0.05 and a fold change (Log_2)≥1) (**Fig. 1C**, **Table S1**). Among these proteins, five (MAB_1066, MAB_1774, MAB_1262, MAB_4558c, and MAB_1704c) lack orthologs in *Mtb*, while only three proteins (MAB_4455c, MAB_2258, and MAB_2035) belong to the lipid metabolism functional category.

The remaining proteins are associated with cell wall processes (MAB_2448, MAB_1432, MAB_4615, MAB_1262, MAB_0356c), intermediary metabolism (MAB_1273, MAB_0451c, MAB_0459c), virulence and detoxification processes (MAB_3904), information pathways (MAB_3100), or regulatory proteins (MAB_3099c).

At 48h, a greater number of proteins were overproduced in both media compared to the 24h time point (**Fig. 1C**, **Table S2**). Fifty-five proteins were more abundant in MSM NL, while 22 were over-produced in MSM. The most abundantly produced protein at 48h was MAB_3100, an L-alanine dehydrogenase (Ald) involved in amino-acid metabolism, also detected at 24h. During *Mtb's* non-replicating state, the alanine dehydrogenase Rv2780, sharing 77.8% sequence identity with MAB_3100, is upregulated, likely maintaining the optimal NADH/NAD ratio during anaerobiosis (27). Hence, the observed increase in MAB_3100 expression may suggest that lipid-rich bacteria may have entered a persistence-like physiological state, characterized by adaptations to environmental stresses, metabolic pathway alterations, and upregulation of specific genes such as *Ald* (27). Highly abundant proteins in MSM NL, including ABC transporter MAB_2262c, hypothetical protein MAB_0131c, siderophore-interacting protein MAB_2235, and putative polyketide synthase MAB_2119c involved in mycobactin synthesis (28), suggest a response to iron limitation. The presence of iron-related enzymes may be due to bacterial modulation of iron-related protein expression in response to the absence of iron from the medium. Upregulation of these proteins may optimize iron acquisition under nitrogen-limiting conditions. Five proteins (MAB_3100, MAB_1704, MAB_3099, MAB_0459 and KdpB MAB_3256c), involved in secondary metabolism or classified as regulatory proteins, were present at both time points. Interestingly, the proteins identified by Low *et al.* (12) were present in our model at 48h (coinciding with complete ILI formation) but not at 24h, though not exhibiting significant differential expression. In contrast, among the 50 highly abundant proteins identified by Armstrong *et al*. in *Msmeg* (14), two proteins lack an ortholog in *Mab* (MSMEG_6291, MSMEG_6049), while 12 proteins were undetected at 24 and 48h (MSMEG_1030, MSMEG_1442, MSMEG_0098, MSMEG_4936, MSMEG_1445, MSMEG_2776, MSMEG_0023, MSMEG_1399, MSMEG_5430, MSMEG_1401, MSMEG_1368, MSMEG_4938). These latter proteins are mainly involved in genetic information processing, including elongation factors or ribosomal subunits, or related to cofactor metabolism and ATP synthesis. The remaining proteins were detected in our model at both time points.

The identification of 8 ribosomal proteins (rplP,rplO, rpsL, rpsK, rpsN, rspR, rpmG1) in MSM suggests an increased demand for protein translation, possibly indicating an

adaptive response. The 11 remaining proteins are mainly conserved hypotheticals with unknown function.

Proteins involved in TAG biosynthesis pathways and lipid synthesis based on *Mtb* annotation were found in our data, with a fold change (Log_2) between -0.5 and 0.5 and a $-Log_{10}$ (*p*-value) less than 2 (**Fig. 1C**). We could only identify mycobactin and polyketide synthases. Furthermore, the near absence of TAG biosynthesis enzymes suggests that these pathways might not be the primary metabolic pathway occurring under these experimental conditions. It would be plausible that other metabolic pathways are prioritized to persist in the nitrogen-limiting environment, emphasizing the complexity of bacterial metabolic responses and their adaptability to environmental cues.

These results support the view that ILI have roles beyond energy storage. The identification of diverse protein families in our experimental design implies underrepresentation of enzymes associated with lipid metabolism in our model. We suppose that each non-physiological model can induce proteome bias, motivating the development of a more sensitive and specific technique. This procedure focuses on the proximity labeling of the ILI core-structure using APEX2 technology (21). Enriching proteins in the vicinity of the ILI is expected to offer a more accurate view of the ILIome, revealing specific key players associated with lipid metabolism during the formation of these organelles. Moreover, this approach could enhance our understanding of lipid metabolism dynamics and intricacies within mycobacterial cells *in vivo* and provide a more accurate depiction of the metabolic landscape during ILI synthesis.

<u>Validation of APEX2 proximity labeling for identifying ILI-associated proteins.</u>

To specifically identify IAP, we adapted the APEX2 approach in an *in vitro* lipid accumulation model (3, 20). However, it was crucial to have a bait at the ILI surface contributing to TAG synthesis, given APEX2's cytoplasmic localization (26). To confirm Tgs1 as a genuine IAP in *Mab*, as suggested in *Mbv* BCG (12), the protein was fused with a superfolder Green Fluorescent Protein (sfGFP)-tag to study ILI colocalization (**Fig. 2A**). Western blot confirmed Tgs1 expression at both 24 and 48h during the synthesis phase (**Fig. S1**). Therefore, APEX2 was directed to ILI *via* an integrative plasmid containing *tgs1* gene with its own promoter fused with *apex2*

coding sequence *via* a linker domain (**Fig. 2B**). Nile Red signal quantification by flow cytometry revealed higher fluorescence levels in MSM NL at 48h (700 a.u) compared to 24h (150 a.u) or MSM at 48h (270 a.u). No significant fluorescence intensity variation was observed between WT *Mab* and *Mab* containing pMV306-*tgs1-apex2*, indicating no alteration in ILI accumulation (**Fig S2**).

In the presence of biotin phenol, APEX2 biotinylates proteins within a 20-nm radius by generating short-lived phenoxyl radicals (1 ms) **(Fig. 2C**) (29). To avoid contamination with endogenous biotinylated proteins, these latter, identified in the control group (MSM NL without biotin phenol), were removed from the analysis. Silver staining was performed after streptavidin enrichment for all lysates, both with and without BP, to confirm that ILI-targeted APEX2 biotinylates proteins exclusively under conditions of biotin phenol addition.

Recombinant *Mab* strain producing Tgs1-APEX2 was grown in MSM NL and pulsed with biotin phenol and hydrogen peroxide. From the bacterial lysates, biotinylated products were enriched using streptavidin-coated beads, followed by protein stripping, trypsin digestion, and LC-MS/MS analysis. This assay identified 228 highly enriched proteins, with 85 present at 24h, 105 at 48h, and 38 at both time points, establishing APEX2-mediated protein tagging as an accurate method for localizing proteins to the ILI surface. However, some limitations can be associated with this technique. Firstly, target proteins should possess tyrosine, cysteine, histidine, or tryptophan residues on their surface for efficient biotinylation by biotin phenol. Secondly, *Mab* possesses endogenous biotinylated proteins, such as pyruvate carboxylase MAB_3267c and acetyl-CoA/propionyl-CoA carboxylase MAB_1876c (30), excluded from our analysis but that could be involved in ILI synthesis. Overall, the use of APEX2 seems appropriate for probing cytoplasmic protein-protein interactions, consistent with established methodologies for examining eukaryotic lipid droplet proteomes (23, 25).

Deciphering the ILIome using the Tgs1-APEX2 strategy

The enriched biotinylated proteins derived from the *Mab* strain producing Tgs1-APEX2 were analyzed by MS. Proteins identified at 24 and 48h are listed in **Table S3** and **S4**.

Due to the sensitivity of the method, at 24h in MSM NL, 463 proteins were identified. However, by applying a *p*-value ≤0.05 (*i.e.*, -Log (*p*-value) >1.3) and a fold change

(Log$_2$) ≥1, this set was reduced to 123 proteins significantly more abundant in MSM NL compared to MSM. At 48h, 624 proteins were identified, with 143 meeting the cut-off criteria. Notably, 38 were present at both time points, resulting in a set of 228 distinct proteins enriched at both time points compared to the un-induced control, highlighting the dynamic nature of ILI synthesis (31, 32). Differences in ILI characteristics such as size, composition, hydrophobicity, and surface tension between the 24 and 48h time points suggest that certain proteins may have varying affinities for distinct lipid molecules or, as already proposed (33, 34), require specific structures like anchors, beta hairpins, or amphipathic helices to efficiently interact with ILI (**Fig. 3A**). It has been suggested that in prokaryotes, these amphipathic helices are commonly involved in interactions, considering that these structural motifs as essential for understanding how proteins grasp with lipid droplets, particularly in prokaryotic systems (14, 19).

Most proteins (7/85 at 24h, 28/105 at 48h, and 4/38 at both 24 and 48h) had unknown predicted functions (**Fig. 3B**). Proteins associated with lipid metabolism were equally represented in abundance at 24h (22/85) and 48h (16/105), while those engaged in amino-acid and carbohydrate metabolism represented 24/85, 17/105, and 10/38 respectively, of the 228 distinct proteins (**Fig. 3B, Table S5**). These findings align with previous *in silico* analyses (19), where only 17% of identified proteins were classified in the lipid metabolism functional category. These data support the emerging understanding of the physiological function of ILI, primarily designed for lipid storage but also crucial for cellular homeostasis under challenging conditions (6, 35).

From the pool of 228 protein candidates, 10 were chosen for subsequent validation as IAP. These proteins are encoded by non-essential genes, sharing orthologs in *Mtb* with a sequence identity of ≥25% and annotated in the lipid metabolism category (**Table 1**). Genes encoding transcription factors were excluded from selection.

Among the selected protein candidates, four acyl-CoA dehydrogenases (MAB_4437, MAB_3040, MAB_3481, and MAB_3486) were identified at 24h and 48h, along with Tgs2 (MAB_1917) (detected at 48h) and an acyl-CoA acetyltransferase (MAB_1463). A probable enoyl-CoA hydratase (MAB_1187c) was also identified at 24h. Two proteins with diverse functions (MAB_4532c, and MAB_2737c) were common at both time points. The lipoprotein LprG (MAB_2806) was identified at 48h based on its role

in TAG transport throughout the membrane (36). LprG is located in the inner membrane (36), and its identification with APEX2 was expected. However, at 48h, when ILI size is optimal, APEX2 may biotinylate LprG due to close contact between the mature ILI and the inner membrane (**Fig. 3A**) (36).

To assess the potential presence of amphipathic helices in our selected candidate targets (14, 19), we employed Heliquest software (http://heliquest.ipmc.cnrs.fr). Remarkably, 7 out of 10 candidates exhibited at least one amphipathic helix, utilizing the same cut-off criteria as in our previous studies (**Fig S3**) (14, 19). MAB_4532c, MAB_2806, and MAB_1917 did not show apparent amphipathic helix structures. Therefore, alternative structural patterns may play a role in the interaction between these proteins and ILI.

What are the impacts of these selected targets on ILI synthesis?

The 10 chosen IAP candidates were overexpressed in *Mab* fused with sfGFP under each gene's native promoter (**Fig. 4A, Fig S1 and S4**) to confirm their intracellular localization. In MSM, a diffuse fluorescence signal was observed, suggesting a lipid-poor bacterium with a homogenous protein distribution in the cytoplasm (**Fig. 4B**). Conversely, in MSM NL, well-defined regions marked by Nile Red indicated ILI-positive bacteria with clear colocalization with the sfGFP signal (**Fig. 4B, Fig S4**). Eight fusion proteins successfully colocalized with Nile Red (MAB_3481, MAB_3486, MAB_1917, MAB_4437, MAB_1187, MAB_2737c, MAB_4532c, and MAB_3040), validating the effectiveness and selectivity of APEX2 technology to identify IAP. Western blot analysis using anti-GFP or anti-HA antibodies showed equal protein production in MSM and MSM NL. Thus, the co-localization of the proteins with ILI is not related to increased expression levels in MSM NL but relies on protein redistribution to the ILI surface. Unfortunately, MAB_2806 and MAB_1463 were not produced at detectable levels, limiting localization analysis, and were not further studied.

To assess the impact of each designated IAP on ILI formation, double homologous recombination was employed to delete the 8 corresponding genes (*MAB_2737c, MAB_1917, MAB_1187c, MAB_4532c, MAB_3040c, MAB_4437, MAB_3486,* and *MAB_3481*) (**Fig S5**) in *Mab* as described previously (37).

After verifying proper gene deletion by PCR fragment sequencing, and bacterial growth in all mutants (**Fig S6 and S7**), TAG accumulation was subsequently examined by TLC (**Fig S8A**). We reasoned that a defect in TAG accumulation at 24h would affect final TAG quantity at 48h. TAG production was quantified at 48h only, avoiding difficulty in obtaining enough bacteria at 24h for lipid analysis. Three phenotypes were observed at 48h (**Fig S8A**). Two genes (*tgs2* (*MAB_1917*) and acyl-CoA dehydrogenase (*MAB_4437*)) showed no impact on lipid accumulation, as their deletion did not result in TAG changes compared to the WT strain. These data are not surprising since *tgs2* gene has been found to have a low impact on ILI synthesis in *Mab* (8), and *Mab* genome contained a large number of other genes exhibiting similar activity, suggesting that other redundant proteins might compensate for their absence. The deletion of other genes showing the second kind of phenotype (two acyl-CoA dehydrogenases *MAB_3040* and *MAB_3481*, and two enoyl-CoA hydratases *MAB_1187* and *MAB_2737c*) resulted in a modest (25 to 40%) reduction in TAG levels (**Fig S8**), suggesting an indirect or secondary role in TAG accumulation. The *Mtb* orthologue of MAB_2737c (Rv1472/EchA12), involved in fatty acid oxidation, may play a role in phosphatidyl-*myo*-inositol mannoside elongation (38). We propose that these IAP may have an impact on membrane lipids as well as TAG accumulation. However, further studies and biochemical characterization are needed to better understand their roles and localization on the ILI. Finally, the third observed phenotype includes *MAB*_3486 (corresponding protein identified at 48h, Table 1) and *MAB_4532c* (corresponding protein identified at 24 and 48h) genes, whose deletion mutants displayed significant reductions (57% and 49%) in TAG levels, respectively (**Fig. 4C**). Complementation with an integrative vector restored TAG levels (**Fig. 4C, Fig S9**), confirming the primary role of MAB_3486 and MAB_4532c in TAG biosynthesis, despite not being in the core ILIome previously described (19). Analyzing the acylglycerol content in Δ*MAB_3486* and Δ*MAB_4532*c revealed higher amounts of free fatty acid accumulation compared to the wild-type (WT) strain, which disappeared after complementation (**Fig S10**). This strengthens the idea that while both mutants fail to synthesize TAG, they accumulate an important quantity of fatty acids, which are intermediates in TAG synthesis and used by the WT and complemented strains to generate TAG.

The orthologue of MAB_3486 in *Mtb* is FadE24 (Rv3139), belonging to the FadE23-FadE24 complex, repressed by cholesterol and involved in fatty acid recycling, particularly in β-oxidation (39, 40). This may explain the important reduction of TAG formation in Δ*MAB_3486* following β-oxidation inhibition. However, the complex has a different catalytic activity than dehydrogenating the acyl-CoA and is upregulated in the presence of isoniazid (41). Indeed, FadE23-FadE24 is controlled by *SigE*, which helps manage environmental stresses. Therefore, its presence in our biological model, inducing nutrient stress, aligns with previous findings.

The structure of MAB_4532c, also known as Eis2 in *Mab*, belongs to the GNAT (GCN5-related N-acetyltransferase) family (42). Knocking-out this gene in *Mab* reduces bacterial survival within murine macrophages (43). Notably, Eis2 is known to confer resistance to aminoglycoside antibiotics, and numerous inhibitors targeting this protein have been developed, emphasizing its potential significance as a therapeutic target against mycobacteria (44). Although Eis2 acetylates the primary amine of aminoglycosides (42), the endogenous substrate of this enzyme in mycobacteria remains to be established. Thus, the specific mechanism by which Eis2 interacts with ILI remains elusive and has yet to be determined.

At 48h, two major acyltransferases, PlsB (MAB_1984) and PlsM (MAB_0165), were identified, as highlighted by Angala *et al.* (45). These two enzymes, one of which is essential, are involved in phosphatidic acid biosynthesis leading to TAG accumulation. However, they were excluded from our study because they did not meet the initial selection criteria for further characterization (MAB_1984 FC 1.24, Log_{10}(*p*-value)=2.04, and MAB_0165 FC 1.25, Log_{10}(*p*-value)=1.81), but their presence underscores their potential importance, warranting future investigation to elucidate their specific roles in ILI formation.

Conclusion

Lipid droplet-associated proteins encompass various families such as structural proteins, signaling proteins, membrane trafficking components, metabolism enzymes, and proteins implicated in protein degradation and DNA-binding (46-48). Although IAP have not been extensively investigated, their significance is progressively gaining elucidation. Increasing evidence points to the pivotal role of mycobacterial ILI in

virulence. Though studies on *Msmeg* and *Mbv* BCG have explored ILI-associated proteins (12, 14), direct identification and validation of IAP remain largely incomplete. Identifying and characterizing these interacting enzymes could pave the way for understanding ILI metabolism in pathogenic mycobacteria, offering new approaches for managing mycobacterial-related diseases.

This study demonstrated the use of APEX2 for the first time on prokaryotic lipid droplets and validated the technology for identifying new IAP. Through proximity labelling in a nutrient/nitrogen-starved model, we identified 228 proteins potentially involved in a direct or indirect role in ILI biogenesis. This process is highly dynamic and complex, involving numerous protein families with overlapping activities. Based on TAG quantification, MAB_3486 and MAB_4532c were found to be the most important proteins among the 10 selected candidates. Overall, this is the first comprehensive study on mycobacterial ILI, providing a detailed proteomic view of ILI formation. APEX2 paves the way for a complete ILIome and may map proteins involved in ILI degradation. Combining APEX2 with TurboID (49), known as TransitID, could help track a specific proteome from the beginning of biogenesis to ILI maturation.

Although more work is needed to validate additional IAP, this study enhances our understanding of mycobacterial lipid metabolism. In the long term, it may help discover new therapeutic targets for future treatments against *Mab*.

Material and Methods

Bacterial strains and growth conditions

Escherichia coli DH10B cells used for cloning were cultured on Luria-Bertani agar plates at 37°C, supplemented with 50 µg/mL kanamycin when necessary.

The smooth (S) variant of *Mab* CIP104536^T was cultivated in Middlebrook 7H9 liquid medium (BD Difco, Le Pont de Claix, France) supplemented with 0.05% Tween 80 (Sigma-Aldrich, Saint-Quentin Fallavier, France), 0.2% glycerol (Euromedex, France), and 10% oleic albumin dextrose catalase (OADC enrichment, BD Difco, France) (7H9-S^{OADC}) at 37°C with shaking at 200 rpm. ILI accumulation in *Mab* liquid culture was performed as previously described (3) (refer to supplementary data for details).

Plasmid construction and cloning

Primers used in this study are detailed in (**Table S6**) and were synthetized by IDT (Integrated DNA Technologies). The *MAB_3551c* (*tgs1*) gene was PCR amplified using Phusion High-Fidelity Enzyme (ThermoFisher Scientific, Waltham, MA), fused with *apex* or *gfp* gene, and cloned using the SLIC method (50) into the pMV306 containing a kanamycin resistance cassette under the endogenous *tgs1* promoter. The sequence of each clone was validated by GATC Eurofins (Germany).

The deletion of each selected gene from the *Mab* genome was performed as previously described (37) (**Fig S5**). Briefly, electrocompetent cells were transformed with pUX1-*katG-target.* Red kanamycin-resistant colonies underwent a second selection based on isoniazid resistance and loss of red fluorescence. Screening by PCR and sequencing validated each deletion mutant strain (**Fig S6, Table S6**) (51).

Bacterial fixation and Nile Red staining

Bacterial cells cultured in MSM or MSM NL were harvested by centrifugation at 3,500*g* for 10 min at 20°C, fixed with 2% paraformaldehyde in PBS for 1h at room temperature, washed twice with PBS-Tween 80 (0.05%, v/v), re-suspended in PBS to a theoretical OD_{600nm} of 10, and incubated with Nile Red fluorescent dye (Interchim, Montluçon, France) for ILI staining, as described (3). The bacterial suspension was visualized using an Olympus IX81 confocal microscope equipped with an UPlanSApo 100 ×1.40 NA objective and operated with the FV1000 software.

Flow cytometry

Bacterial populations studied by flow cytometry were at OD_{600nm} = 0.1. Fixed cells were stained with Nile Red. Scatter plots obtained (forward scattering FSC versus side scattering SSC signals) were gated on the population of interest, filtered to remove multiple events, and then analyzed for fluorescence intensity (FL3 615/25 nm) using both 488 and 561 nm lasers excitation. For each biological sample, 300,000 events were measured. Data were acquired with a S3E cells sorter (Bio-Rad) and analyzed and plotted using FlowJo v10.8. Data represent at least 3 biological replicates, and statistical analyses were performed with Prism v8.2 software using two-way ANOVA.

Whole cell protein extract

Bacteria were centrifuged, washed twice in PBS, and re-suspended in PBS-urea 8 M (Euromedex) at pH 8, then sonicated for complete lysis. The lysate was recovered after centrifugation at 4°C for 5 min at 1,300*g*, and protein concentration in the supernatant was determined using the Bradford method (Bio-Rad). SDS-PAGE was performed after loading 100 µg of lysate, while 50 µg were used for mass spectrometry.

Biotinylation reaction

Mab harboring the pMV306-*tgs1-apex2* was grown in MSM and MSM NL at 37°C under agitation at 200 rpm (3). Cells were harvested by centrifugation for 10 min at 3,500*g* at 20°C, washed twice with PBS, and re-suspended in PBS to an OD_{600nm} of 40. Biotin phenol (100 mM, Iris Biotech) was added, followed by incubation at 37°C, 200 rpm, in the dark for 30 min. Hydrogen peroxide (100 mM) was then added under the same conditions for exactly 2 min. The reaction was stopped by adding 1 mL of 2× quenching solution composed of PBS, 1 M sodium ascorbate (Sigma), and 1 M sodium azide (Sigma). After centrifugation at 3,500*g* for 10 min at 20°C, pellets were washed twice with 1 mL of 1× quenching solution and 1 mL of PBS-Tween 80 (0.05%, *v/v*) each, resuspended in 2 mL ice-cold PBS-protease inhibitor cocktail (c*O*mplete Mini, EDTA-free, Sigma-Aldrich) (21) and lysed using a Mini-Beadbeater-96 (BioSpec) for 3×4 min with 250 µL of glass beads (0.1 mm-diameter glass beads, BioSpec). The lysates were centrifuged for 5 min at 1,300*g* at 4°C, and the supernatant was collected to determine the protein concentration.

Streptavidin enrichment

Twenty µL of 10 mg/mL Streptavidin agarose resin (ThermoFisher Scientific, Waltham, MA) were washed twice with 500 µL of PBS and centrifuged for 5 min at 5,000*g*. In parallel, 1 µg of each lysate was heated at 95°C for 5 min. Streptavidin was then mixed with the heated lysates and incubated under gentle rotation (15 rpm) for 3h. Beads were washed with 200 µL PBS-20% SDS and incubated for 20 min on the orbital shaker (15 rpm/min) at room temperature. After two PBS washes and centrifugation at 5,000*g* for 5 min, SDS loading dye 1× was added, and the sample was boiled for 10 min at 95°C.

Mass spectrometry

1-The whole proteome analysis is detailed in the supplementary data. Briefly, proteins were first stacked as a single band using an acrylamide gel. After in-gel digestion, extracted peptides were analyzed by LC-MS/MS using an Orbitrap Fusion Lumos Tribrid Mass Spectrometer (ThermoFisher Scientific, San Jose, CA). Label-free quantification (LFQ) was processed using the DIA-NN 1.8 algorithm using the *Mab* database (UP000007137) extracted from UniProt on March 10, 2021, which contains 4940 entries. The DIA-NN primary output file was filtered at 1% FDR, and LFQ intensity was recalculated using the DIAgui package at 1% q-value (52). Statistical analysis was performed using the Perseus program (version 1.6.15.0) from the MaxQuant environment (http://www.maxquant.org). To determine whether a given detected protein was specifically differential, a two-sample t-test was performed using permutation-based FDR control at 0.05.

2-For the biotinylated proteome, protein samples were prepared similarly, and analysis was conducted using a Q Exactive Plus Hybrid Quadrupole-Orbitrap (ThermoFisher Scientific™, San Jose, CA) in data-dependent acquisition mode. Relative intensity-based label-free quantification (LFQ) was processed using the MaxLFQ algorithm available on the MaxQuant computational proteomics platform, version 1.6.3.4. Statistical analysis was performed similarly to the whole proteome analysis.

The mass spectrometry proteomics data have been deposited to the ProteomeXchange Consortium (www.proteomexchange.org) (53) *via* the PRIDE partner repository (54) with datasets identifiers PXD052312 (Reviewer account details: username: reviewer_pxd052312@ebi.ac.uk password: QbTFUBeniAp1) and

PXD052310 (Reviewer account details: username: reviewer_pxd052310@ebi.ac.uk password: wmd2IwZGGO98).

Lipid extraction and TLC analysis

Mycobacteria grown in MSM NL until reaching an OD_{600nm} of 1 were collected after 24 or 48h and processed for apolar lipids extraction and quantification by thin layer chromatography (TLC) (3) (See Supplementary data for details).

Legends

Figure 1

Whole proteome analysis. (A) Illustration depicting the whole proteome analysis workflow, including mass spectrometry and flow cytometry. **(B**) Nile red fluorescence in *Mab* measured by flow cytometry: bacterial cells were harvested at 24, 48h from MSM and MSM NL, fixed and stained by Nile red, washed, and diluted in PBS. A total of 300,000 events were measured for each biological sample, and Nile Red fluorescence was collected at 615/25 nm. **(C)** Volcano map illustrating differentially expressed proteins. Blue dots represent up-regulated proteins in MSM, red dots indicate up-regulated proteins in MSM NL, and grey dots represent proteins with no significant difference, at 24 and 48h of incubation. Red circles highlight lipid metabolism proteins. Generated using the VolcaNoseR web app (55).

Figure 2

Setting up the APEX2 system. (A) Diagram of the construct encoding *tgs1* fused with *sfGFP* under the endogenous promoter. *Mab* cells were grown in MM NL, and fixed in paraformaldehyde. Fluorescence microscopy images showing Nile red (559/635 nm), *sf*GFP (488/510 nm), and merge channels of cells containing ILI colocalizing with Tgs1. **(B)** Diagram illustrating the construct encoding the native promoter and full genomic sequence of *tgs1* fused with *APEX2 via* a linker domain. Data represent the mean of Nile Red fluorescence accumulation in three biological replicates measured by flow cytometry. Statistical analyses were carried using a two way ANOVA with a Šidák test. * *p-value* <0.05, ** *p-value* <0.01, *** *p-value* <0.001, **** *p-value* <0.0001. **(C)** Representative workflow depicting APEX2 action with the chosen bait (Tgs1) in green and APEX2 molecule in purple. The main amino acids interacting with biotin-phenol (BP) are shown by their chemical formula. Silver staining of SDS-PAGE gel: a representative silver-stained SDS-PAGE gel of treated (+BP) and untreated (-BP) lysate following streptavidin enrichment, at 24 and 48h respectively. 35 ng of BSA was loaded as a control. Images were taken using the Chemidoc™ MP Imaging System (Bio-Rad). Color information was preserved to display the different hues produced by the stain. No other digital manipulation was performed.

Figure 3

Targets selection by APEX2. (A) ILI biosynthesis kinetics adapted from Dargham *et al* (32), followed by a Venn diagram representing selected targets at 24h and 48h based on a -Log(*p*-value) threshold of 1.3 and a fold change (Log_2) of 1. Thin sections of *in vitro* cultures of *Mab* in MSM NL at 24 and 48h, respectively. **(B)** Distribution of the selected ILI-associated protein candidates based on their respective KEGG pathways (https://www.genome.jp/kegg/) at each time point. Yellow bars represent 24h, blue bars represent 48h, and grey bars represent 24-48h.

Figure 4

Validation of IAP mutants in *M. abscessus*. (A) *Mab* strains were transformed with plasmids allowing overexpression of the genes of interest fused with *sf*GFP for colocalization studies. The Western blot shows the fusion between the selected proteins and GFP (28kDa). Ag85 was included as a loading control. **(B)** Bacteria were grown in MSM and MSM NL for 48h, fixed with 2% paraformaldehyde, stained with Nile Red, and visualized by fluorescence microscopy. Scale bars, 2 µm. **(C)**. Deletion mutants and complemented *Mab* strains were grown in MSM NL, and cultures were collected at 24h and 48h. After lyophilization, equal amounts of dry cells were used for apolar lipid extraction. TAG levels from each culture were analyzed by TLC. Each TLC plate is representative of experiments performed in triplicate. Densitometry results for 48h are expressed as mean values ± SD of three biologically independent experiments and reported as the percentage of TAG levels relative to those in *Mab* WT grown in MSM-NL (set at 100%). Statistical significance was assessed with one-way ANOVA followed by Tukey's multiple comparisons post-hoc test using Prism 8.0 (GraphPad, Inc): ** *p*-value <0.01; *** *p*-value <0.001; *ns*, not significant (*p*-value >0.05). C: Cholesterol; CE: Cholesterol Ester; FA: Fatty Acid; FAME: Fatty Acid Methyl Esters; MQ: Mena Quinone; TAG: Triacylglycerol.

Table 1. Selected ILI-associated proteins after 24h and 48h culture of *M. abscessus* in MSM NL using Tgs1-APEX2 as bait, and identified by LC-ESI-MS/MS analysis by applying *p*-value < 0.05 and Fold change (Log2) >1 threshold values[a]

24h	48h	Genes	Protein names	*M. tuberculosis* orthologs			
				Rv number	Sequence identity%	Essentiality	Functional category
+		*MAB_3040c*	Probable acyl-CoA dehydrogenase	Rv2724c	77.3	Non-Essential	Lipid metabolism
+		*MAB_1187c*	Probable enoyl-CoA hydratase	Rv1071c	70.5	Non-Essential	Lipid metabolism
+		*MAB_4437*	Probable acyl-CoA dehydrogenase FadE5	Rv0244c	79.1	Non-Essential	Lipid metabolism
+	+	*MAB_2737c*	Probable enoyl-CoA hydratase/isomerase	Rv1472	75.7	Non-Essential	Lipid metabolism
+	+	*MAB_4532c*	Uncharacterized N-acetyltransferase	Rv2416c	28.7	Non-Essential	Virulence, detoxification, adaptation
	+	*MAB_1463*	Probable acetyl-CoA acetyltransferase FadA4	Rv1323	76.5	Non-Essential	Lipid metabolism
	+	*MAB_3481*	Probable acyl-CoA dehydrogenase FadE4	Rv0231	52.9	Growth-Advantage	Lipid metabolism
	+	*MAB_3486*	Probable acyl-CoA dehydrogenase	Rv3139	69.4	Non-Essential	Lipid metabolism
	+	*MAB_1917*	Diacylglycerol O-acyltransferase	Rv1760	56.2	Non-Essential	Lipid metabolism
	+	*MAB_2806*	Lipoprotein LprG	Rv1411c	42.2	Non-Essential	Cell wall and cell processes

[a]*M. tuberculosis* orthologs were retrieved using the KEGG database (56, 57) and then cross-referenced with the Mycobrowser (58) database for accurate **Protein names**, **Rv numbers** and **sequence identity (%)**. The **Essentiality** and the **Functional category** related to *M. tuberculosis* orthologs were from Dejesus *et al.* and Camus *et al.*, respectively (59, 60).

Acknowledgements

This work was supported by the CNRS, Aix Marseille University, and the Agence Nationale de la Recherche (ILIome project N°ANR-20-CE44-0019 and LipInTB project N°ANR-19-CE44-0011). Proteomics analyses were done using the mass spectrometry facility of Marseille Proteomics (marseille-proteomique.univ-amu.fr) supported by IBISA, the Cancéropôle PACA, the Provence-Alpes-Côte d'Azur Region, the Institut Paoli-Calmettes, and Fonds Européen de Développement Regional (FEDER). T.D. PhD fellowship was funded by the foundation IHU Méditerranée Infection. JJ.A-C. post doctorate fellowship was supported by the Agence Nationale de la Recherche (ILIome project N°ANR-20-CE44-0019). R.A. was supported by a PhD fellowship from the Agence Nationale de la Recherche (LipInTB project N°ANR-19-CE44-0011).

Authors' contribution

S.C. secured funding and supervised the study. T.D and I.M performed most of the analysis with the help of JJ.A-C, L.C, I.P, W.D and R.A. V.P. helps in lipidomic analysis. G.B performed all the flow cytometry analysis. L.C[2] and S.A performed all proteomic analysis with the help of J.-F.C for the data analysis. JJ.A-C and W.D performed most of deletion mutants' construction. T.D and S.C edited the figures. All authors provided intellectual input by analyzing and/or discussing data. T.D, L.K and S.C wrote the initial version of the manuscript with input from all authors. All authors read the manuscript and provided critical feedback before submission.

Declaration of interests

The authors declare no competing interests.

References

1. Murphy DJ. 2001. The biogenesis and functions of lipid bodies in animals, plants and microorganisms. Prog Lipid Res 40:325-438.
2. Wayne LG, Hayes LG. 1996. An in vitro model for sequential study of shiftdown of Mycobacterium tuberculosis through two stages of nonreplicating persistence. Infect Immun 64:2062-9.
3. Santucci P, Johansen MD, Point V, Poncin I, Viljoen A, Cavalier JF, Kremer L, Canaan S. 2019. Nitrogen deprivation induces triacylglycerol accumulation, drug tolerance and hypervirulence in mycobacteria. Sci Rep 9:019-45164.
4. Rodriguez GM, Voskuil MI, Gold B, Schoolnik GK, Smith I. 2002. ideR, An essential gene in mycobacterium tuberculosis: role of IdeR in iron-dependent gene expression, iron metabolism, and oxidative stress response. Infect Immun 70:3371-81.
5. Mallick I, Santucci P, Poncin I, Point V, Kremer L, Cavalier JF, Canaan S. 2021. Intrabacterial lipid inclusions in mycobacteria: unexpected key players in survival and pathogenesis? FEMS Microbiol Rev 45.
6. Deb C, Lee CM, Dubey VS, Daniel J, Abomoelak B, Sirakova TD, Pawar S, Rogers L, Kolattukudy PE. 2009. A novel in vitro multiple-stress dormancy model for Mycobacterium tuberculosis generates a lipid-loaded, drug-tolerant, dormant pathogen. PLoS One 4:0006077.
7. Hammond RJ, Baron VO, Oravcova K, Lipworth S, Gillespie SH. 2015. Phenotypic resistance in mycobacteria: is it because I am old or fat that I resist you? J Antimicrob Chemother 70:2823-7.
8. Viljoen A, Blaise M, de Chastellier C, Kremer L. 2016. MAB_3551c encodes the primary triacylglycerol synthase involved in lipid accumulation in Mycobacterium abscessus. Mol Microbiol 102:611-627.
9. Robbe-Saule M, Foulon M, Poncin I, Esnault L, Varet H, Legendre R, Besnard A, Grzegorzewicz AE, Jackson M, Canaan S, Marsollier L, Marion E. 2021. Transcriptional adaptation of Mycobacterium ulcerans in an original mouse model: New insights into the regulation of mycolactone. Virulence 12:1438-1451.
10. Caire-Brandli I, Papadopoulos A, Malaga W, Marais D, Canaan S, Thilo L, de Chastellier C. 2014. Reversible lipid accumulation and associated division arrest of Mycobacterium avium in lipoprotein-induced foamy macrophages may resemble key events during latency and reactivation of tuberculosis. Infect Immun 82:476-90.
11. Santucci P, Diomande S, Poncin I, Alibaud L, Viljoen A, Kremer L, de Chastellier C, Canaan S. 2018. Delineating the Physiological Roles of the PE and Catalytic Domains of LipY in Lipid Consumption in Mycobacterium-Infected Foamy Macrophages. Infect Immun 86.
12. Low KL, Shui G, Natter K, Yeo WK, Kohlwein SD, Dick T, Rao SP, Wenk MR. 2010. Lipid droplet-associated proteins are involved in the biosynthesis and hydrolysis of triacylglycerol in Mycobacterium bovis bacillus Calmette-Guerin. J Biol Chem 285:21662-70.
13. Mattos KA, Oliveira VG, D'Avila H, Rodrigues LS, Pinheiro RO, Sarno EN, Pessolani MC, Bozza PT. 2011. TLR6-driven lipid droplets in Mycobacterium leprae-infected Schwann cells: immunoinflammatory platforms associated with bacterial persistence. J Immunol 187:2548-58.
14. Armstrong RM, Carter DC, Atkinson SN, Terhune SS, Zahrt TC. 2018. Association of Mycobacterium Proteins with Lipid Droplets. J Bacteriol 200:00240-18.
15. Barksdale L, Kim KS. 1977. Mycobacterium. Bacteriol Rev 41:217-372.
16. Chen Y, Ding Y, Yang L, Yu J, Liu G, Wang X, Zhang S, Yu D, Song L, Zhang H, Zhang C, Huo L, Huo C, Wang Y, Du Y, Zhang P, Na H, Xu S, Zhu Y, Xie Z, He T, Zhang Y, Wang G, Fan Z, Yang F, Liu H, Zhang X, Zhang MQ, Li Y, Steinbüchel A, Fujimoto T, Cichello S, Liu P. 2014. Integrated omics study delineates the dynamics of lipid droplets in Rhodococcus opacus PD630. Nucleic Acids Res 42:1052-64.

17. Ding Y, Yang L, Zhang S, Wang Y, Du Y, Pu J, Peng G, Chen Y, Zhang H, Yu J, Hang H, Wu P, Yang F, Yang H, Steinbüchel A, Liu P. 2012. Identification of the major functional proteins of prokaryotic lipid droplets. J Lipid Res 53:399-411.
18. Sirakova TD, Dubey VS, Deb C, Daniel J, Korotkova TA, Abomoelak B, Kolattukudy PE. 2006. Identification of a diacylglycerol acyltransferase gene involved in accumulation of triacylglycerol in Mycobacterium tuberculosis under stress. Microbiology 152:2717-2725.
19. Dargham T, Mallick I, Kremer L, Santucci P, Canaan S. 2023. Intrabacterial lipid inclusion-associated proteins: a core machinery conserved from saprophyte Actinobacteria to the human pathogen Mycobacterium tuberculosis. FEBS Open Bio 23:2211-5463.
20. Ahamed M, Jaisinghani N, Li M, Winkeler I, Silva S, Previti ML, Seeliger JC. 2022. Optimized APEX2 peroxidase-mediated proximity labeling in fast- and slow-growing mycobacteria. Methods Enzymol 664:267-289.
21. Ganapathy US, Bai L, Wei L, Eckartt KA, Lett CM, Previti ML, Carrico IS, Seeliger JC. 2018. Correction to Compartment-Specific Labeling of Bacterial Periplasmic Proteins by Peroxidase-Mediated Biotinylation. ACS Infect Dis 4:25.
22. Jaisinghani N, Previti ML, Andrade J, Askenazi M, Ueberheide B, Seeliger JC. Cell wall proteomics in live Mycobacterium tuberculosis uncovers exposure of ESX substrates to the periplasm. bioRxiv. 2023 Mar 29:2023.03.29.534792. doi: 10.1101/2023.03.29.534792. Preprint.
23. Bersuker K, Peterson CWH, To M, Sahl SJ, Savikhin V, Grossman EA, Nomura DK, Olzmann JA. 2018. A Proximity Labeling Strategy Provides Insights into the Composition and Dynamics of Lipid Droplet Proteomes. Dev Cell 44:97-112.
24. Lam SS, Martell JD, Kamer KJ, Deerinck TJ, Ellisman MH, Mootha VK, Ting AY. 2015. Directed evolution of APEX2 for electron microscopy and proximity labeling. Nat Methods 12:51-4.
25. Peterson CWH, Deol KK, To M, Olzmann JA. 2021. Optimized protocol for the identification of lipid droplet proteomes using proximity labeling proteomics in cultured human cells. STAR Protoc 2:18.
26. Becker JT, Auerbach AA, Harris RS. 2023. APEX3 - An Optimized Tool for Rapid and Unbiased Proximity Labeling. J Mol Biol 435:13.
27. Giffin MM, Shi L, Gennaro ML, Sohaskey CD. 2016. Role of Alanine Dehydrogenase of Mycobacterium tuberculosis during Recovery from Hypoxic Nonreplicating Persistence. PLoS One 11.
28. Etienne G, Malaga W, Laval F, Lemassu A, Guilhot C, Daffé M. 2009. Identification of the polyketide synthase involved in the biosynthesis of the surface-exposed lipooligosaccharides in mycobacteria. J Bacteriol 191:2613-21.
29. Rhee HW, Zou P, Udeshi ND, Martell JD, Mootha VK, Carr SA, Ting AY. 2013. Proteomic mapping of mitochondria in living cells via spatially restricted enzymatic tagging. Science 339:1328-1331.
30. Sullivan MR, McGowen K, Liu Q, Akusobi C, Young DC, Mayfield JA, Raman S, Wolf ID, Moody DB, Aldrich CC, Muir A, Rubin EJ. 2023. Biotin-dependent cell envelope remodelling is required for Mycobacterium abscessus survival in lung infection. Nat Microbiol 8:481-497.
31. Wältermann M, Hinz A, Robenek H, Troyer D, Reichelt R, Malkus U, Galla HJ, Kalscheuer R, Stöveken T, von Landenberg P, Steinbüchel A. 2005. Mechanism of lipid-body formation in prokaryotes: how bacteria fatten up. Mol Microbiol 55:750-63.
32. Dargham T, Mallick I, Raze D, Kremer L, Canaan S. 2022. Chapter 12 - Intrabacterial lipid inclusions: overview of an amazing organelle, p 253-269. *In* Fatima Z, Canaan S (ed), Biology of Mycobacterial Lipids doi:https://doi.org/10.1016/B978-0-323-91948-7.00003-8. Academic Press.
33. Skinner JR, Shew TM, Schwartz DM, Tzekov A, Lepus CM, Abumrad NA, Wolins NE. 2009. Diacylglycerol enrichment of endoplasmic reticulum or lipid droplets recruits perilipin 3/TIP47 during lipid storage and mobilization. J Biol Chem 284:30941-8.

34. Zhang C, Liu P. 2019. The New Face of the Lipid Droplet: Lipid Droplet Proteins. Proteomics 19:8.
35. Cabruja M, Mondino S, Tsai YT, Lara J, Gramajo H, Gago G. 2017. A conditional mutant of the fatty acid synthase unveils unexpected cross talks in mycobacterial lipid metabolism. Open Biol 7.
36. Drage MG, Tsai HC, Pecora ND, Cheng TY, Arida AR, Shukla S, Rojas RE, Seshadri C, Moody DB, Boom WH, Sacchettini JC, Harding CV. 2010. Mycobacterium tuberculosis lipoprotein LprG (Rv1411c) binds triacylated glycolipid agonists of Toll-like receptor 2. Nat Struct Mol Biol 17:1088-95.
37. Richard M, Gutiérrez AV, Viljoen A, Rodriguez-Rincon D, Roquet-Baneres F, Blaise M, Everall I, Parkhill J, Floto RA, Kremer L. 2018. Mutations in the MAB_2299c TetR Regulator Confer Cross-Resistance to Clofazimine and Bedaquiline in Mycobacterium abscessus. Antimicrob Agents Chemother 63:01316-18.
38. Srivastava S, Chaudhary S, Thukral L, Shi C, Gupta RD, Gupta R, Priyadarshan K, Vats A, Haque AS, Sankaranarayanan R, Natarajan VT, Sharma R, Aldrich CC, Gokhale RS. 2015. Unsaturated Lipid Assimilation by Mycobacteria Requires Auxiliary cis-trans Enoyl CoA Isomerase. Chem Biol 22:1577-87.
39. Voskuil MI. 2013. Mycobacterium tuberculosis cholesterol catabolism requires a new class of acyl coenzyme A dehydrogenase. J Bacteriol 195:4319-21.
40. Wipperman MF, Yang M, Thomas ST, Sampson NS. 2013. Shrinking the FadE proteome of Mycobacterium tuberculosis: insights into cholesterol metabolism through identification of an alpha2beta2 heterotetrameric acyl coenzyme A dehydrogenase family. J Bacteriol 195:4331-41.
41. Ansong C, Ortega C, Payne SH, Haft DH, Chauvigne-Hines LM, Lewis MP, Ollodart AR, Purvine SO, Shukla AK, Fortuin S, Smith RD, Adkins JN, Grundner C, Wright AT. 2013. Identification of widespread adenosine nucleotide binding in Mycobacterium tuberculosis. Chem Biol 20:123-33.
42. Ung KL, Alsarraf H, Olieric V, Kremer L, Blaise M. 2019. Crystal structure of the aminoglycosides N-acetyltransferase Eis2 from Mycobacterium abscessus. Febs J 286:4342-4355.
43. Dubois V, Pawlik A, Bories A, Le Moigne V, Sismeiro O, Legendre R, Varet H, Rodríguez-Ordóñez MDP, Gaillard JL, Coppée JY, Brosch R, Herrmann JL, Girard-Misguich F. 2019. Mycobacterium abscessus virulence traits unraveled by transcriptomic profiling in amoeba and macrophages. PLoS Pathog 15.
44. Willby MJ, Green KD, Gajadeera CS, Hou C, Tsodikov OV, Posey JE, Garneau-Tsodikova S. 2016. Potent Inhibitors of Acetyltransferase Eis Overcome Kanamycin Resistance in Mycobacterium tuberculosis. ACS Chem Biol 11:1639-46.
45. Angala SK, Carreras-Gonzalez A, Huc-Claustre E, Anso I, Kaur D, Jones V, Palčeková Z, Belardinelli JM, de Sousa-d'Auria C, Shi L, Slama N, Houssin C, Quémard A, McNeil M, Guerin ME, Jackson M. 2023. Acylation of glycerolipids in mycobacteria. Nat Commun 14:023-42478.
46. Kimmel AR, Sztalryd C. 2016. The Perilipins: Major Cytosolic Lipid Droplet-Associated Proteins and Their Roles in Cellular Lipid Storage, Mobilization, and Systemic Homeostasis. Annu Rev Nutr 36:471-509.
47. Greenberg AS, Egan JJ, Wek SA, Garty NB, Blanchette-Mackie EJ, Londos C. 1991. Perilipin, a major hormonally regulated adipocyte-specific phosphoprotein associated with the periphery of lipid storage droplets. J Biol Chem 266:11341-6.
48. Bickel PE, Tansey JT, Welte MA. 2009. PAT proteins, an ancient family of lipid droplet proteins that regulate cellular lipid stores. Biochim Biophys Acta 6:419-40.
49. Qin W, Cheah JS, Xu C, Messing J, Freibaum BD, Boeynaems S, Taylor JP, Udeshi ND, Carr SA, Ting AY. 2023. Dynamic mapping of proteome trafficking within and between living cells by TransitID. Cell 186:3307-3324 e30.

50. Li MZ, Elledge SJ. 2012. SLIC: a method for sequence- and ligation-independent cloning. Methods Mol Biol 852:51-9.
51. Ung KL, Kremer L, Blaise M. 2021. Structural analysis of the N-acetyltransferase Eis1 from Mycobacterium abscessus reveals the molecular determinants of its incapacity to modify aminoglycosides. Proteins 89:94-106.
52. Gerault MA, Camoin L, Granjeaud S. 2024. DIAgui: a Shiny application to process the output from DIA-NN. Bioinform Adv 4:vbae001.
53. Deutsch EW, Bandeira N, Perez-Riverol Y, Sharma V, Carver JJ, Mendoza L, Kundu DJ, Wang S, Bandla C, Kamatchinathan S, Hewapathirana S, Pullman BS, Wertz J, Sun Z, Kawano S, Okuda S, Watanabe Y, MacLean B, MacCoss MJ, Zhu Y, Ishihama Y, Vizcaino JA. 2023. The ProteomeXchange consortium at 10 years: 2023 update. Nucleic Acids Res 51:D1539-D1548.
54. Perez-Riverol Y, Bai J, Bandla C, Garcia-Seisdedos D, Hewapathirana S, Kamatchinathan S, Kundu DJ, Prakash A, Frericks-Zipper A, Eisenacher M, Walzer M, Wang S, Brazma A, Vizcaino JA. 2022. The PRIDE database resources in 2022: a hub for mass spectrometry-based proteomics evidences. Nucleic Acids Res 50:D543-D552.
55. Goedhart J, Luijsterburg MS. 2020. VolcaNoseR is a web app for creating, exploring, labeling and sharing volcano plots. Sci Rep 10:20560.
56. Ogata H, Goto S, Sato K, Fujibuchi W, Bono H, Kanehisa M. 1999. KEGG: Kyoto Encyclopedia of Genes and Genomes. Nucleic Acids Res 27:29-34.
57. Kanehisa M, Sato Y, Kawashima M, Furumichi M, Tanabe M. 2016. KEGG as a reference resource for gene and protein annotation. Nucleic Acids Res 44:D457-62.
58. Kapopoulou A, Lew JM, Cole ST. 2011. The MycoBrowser portal: a comprehensive and manually annotated resource for mycobacterial genomes. Tuberculosis (Edinb) 91:8-13.
59. DeJesus MA, Gerrick ER, Xu W, Park SW, Long JE, Boutte CC, Rubin EJ, Schnappinger D, Ehrt S, Fortune SM, Sassetti CM, Ioerger TR. 2017. Comprehensive Essentiality Analysis of the Mycobacterium tuberculosis Genome via Saturating Transposon Mutagenesis. mBio 8:02133-16.
60. Camus JC, Pryor MJ, Médigue C, Cole ST. 2002. Re-annotation of the genome sequence of Mycobacterium tuberculosis H37Rv. Microbiology 148:2967-2973.

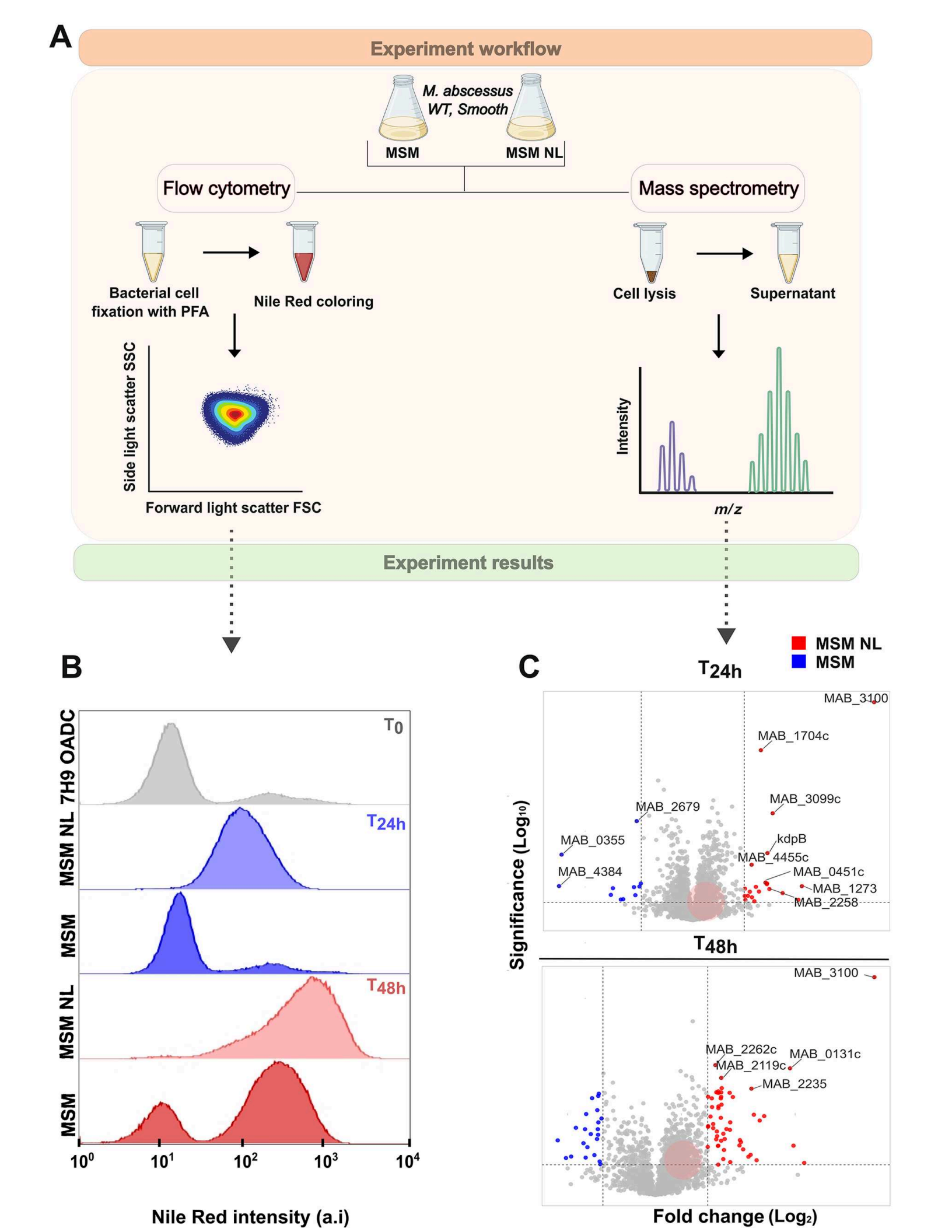
A
Experiment workflow
M. abscessus
WT, Smooth
MSM
MSM NL
Flow cytometry
Mass spectrometry
Bacterial cell
fixation with PFA
Nile Red coloring
Cell lysis
Supernatant
Side light scatter SSC
Forward light scatter FSC
Intensity
m/z
Experiment results
B
MSM NL 7H9 OADC
MSM
MSM NL
MSM
T0
T24h
T48h
10^0
10^1
10^2
10^3
10^4
Nile Red intensity (a.i)
C
MSM NL
MSM
T24h
MAB_3100
MAB_1704c
MAB_3099c
MAB_2679
MAB_0355
kdpB
MAB_4455c
MAB_4384
MAB_0451c
MAB_1273
MAB_2258
T48h
MAB_3100
MAB_2262c
MAB_0131c
MAB_2119c
MAB_2235
Significance (Log10)
Fold change (Log2)


A
native promotor
TGS 1
sfGFP


B
native promotor
TGS 1
APEX2

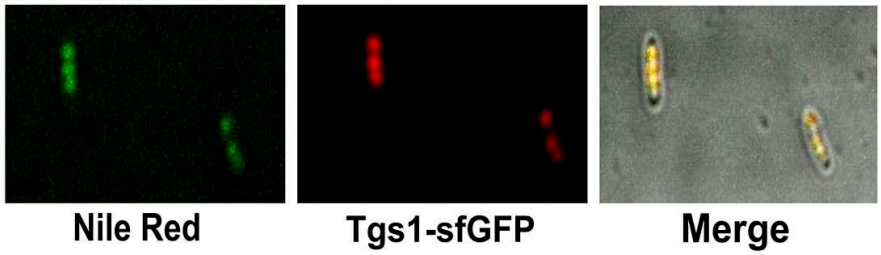
Nile Red
Tgs1-sfGFP
Merge

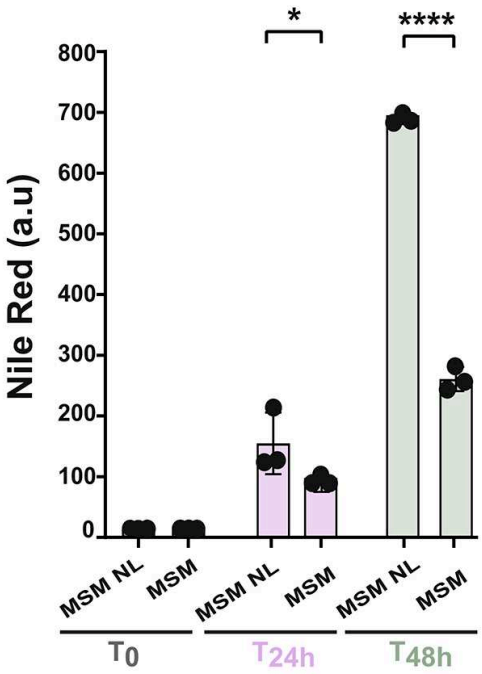
*
****
800
700
600
500
400
300
200
100
0
Nile Red (a.u)
MSM NL
MSM
MSM NL
MSM
MSM NL
MSM
T0
T24h
T48h

C

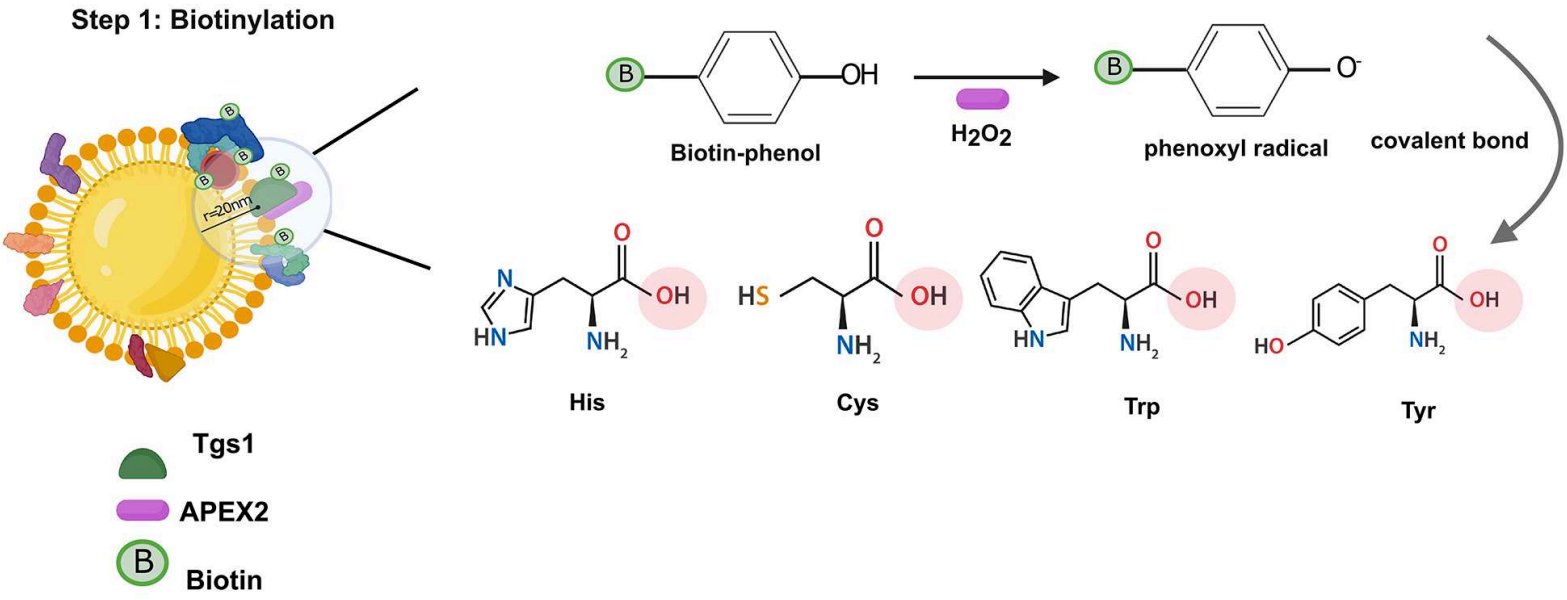
Step 1: Biotinylation
r=20nm
Tgs1
APEX2
Biotin
Biotin-phenol
H2O2
phenoxyl radical
covalent bond
His
Cys
Trp
Tyr

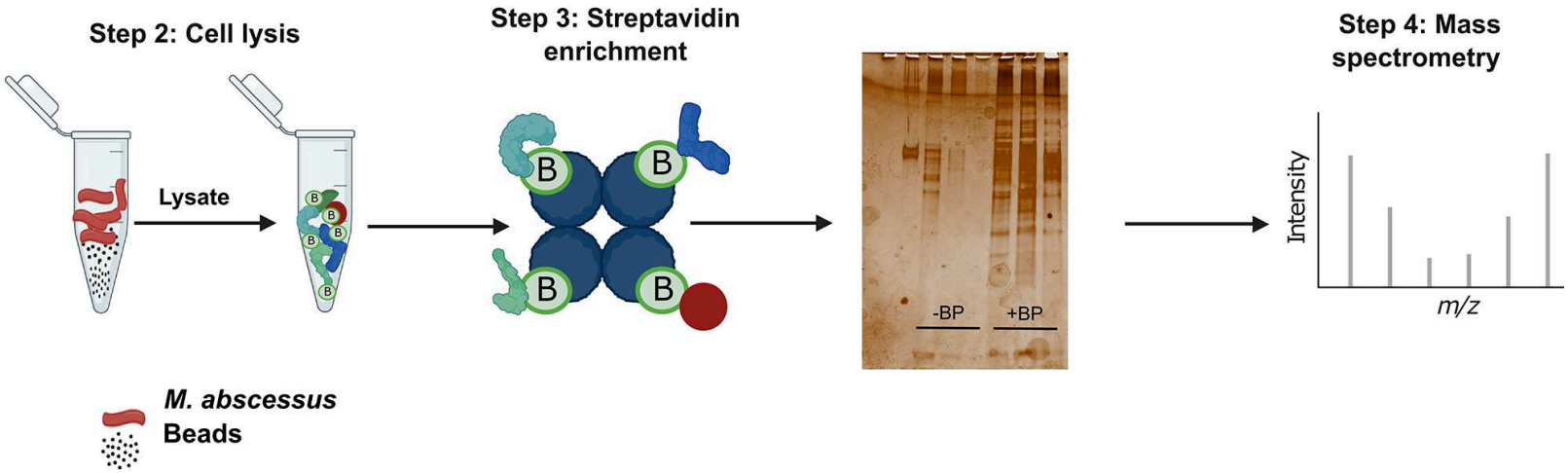
Step 2: Cell lysis
Lysate
Step 3: Streptavidin enrichment
Step 4: Mass spectrometry
-BP
+BP
Intensity
m/z
M. abscessus
Beads

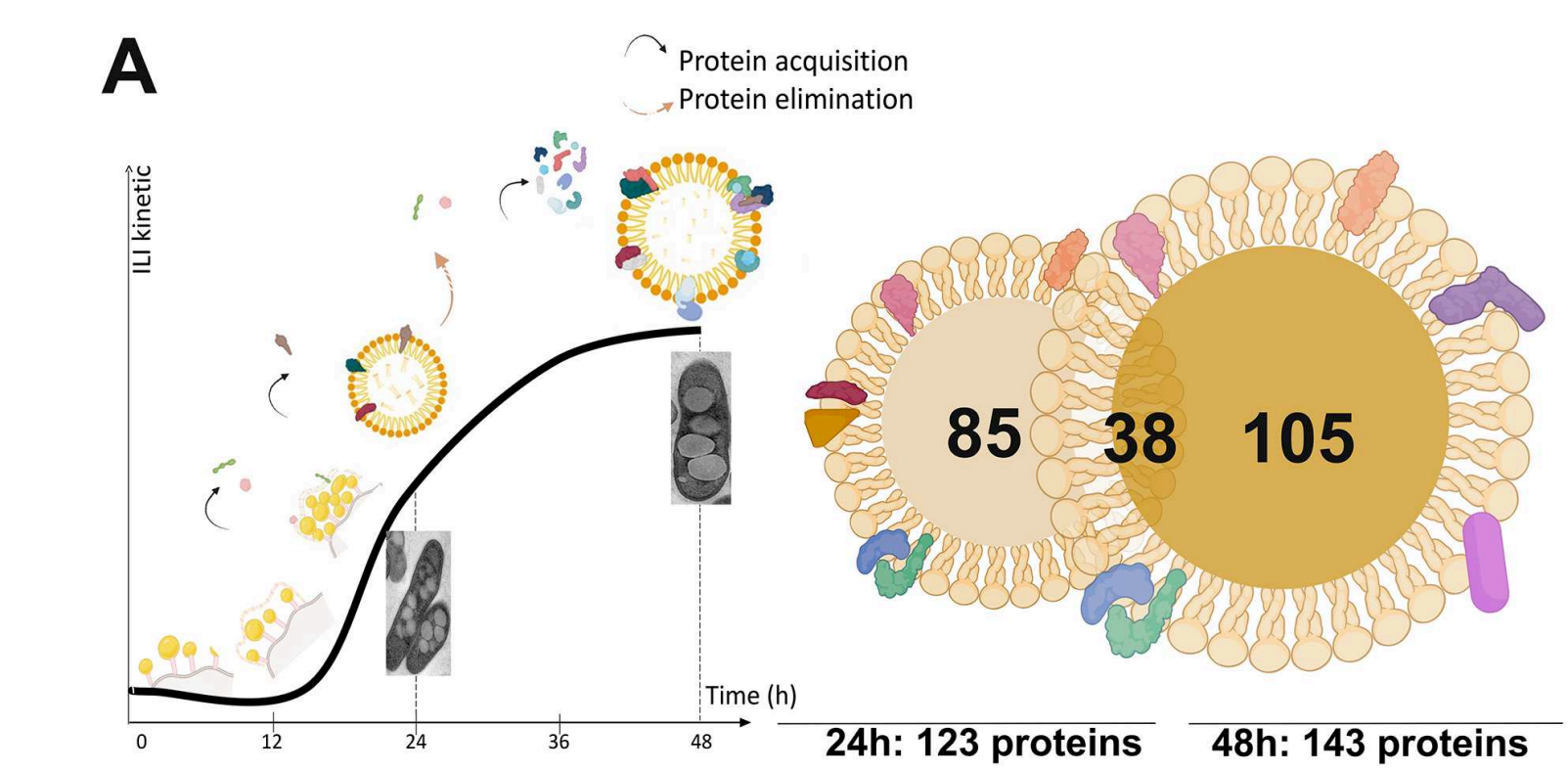
A
Protein acquisition
Protein elimination
ILI kinetic
Time (h)
0
12
24
36
48
85
38
105
24h: 123 proteins
48h: 143 proteins

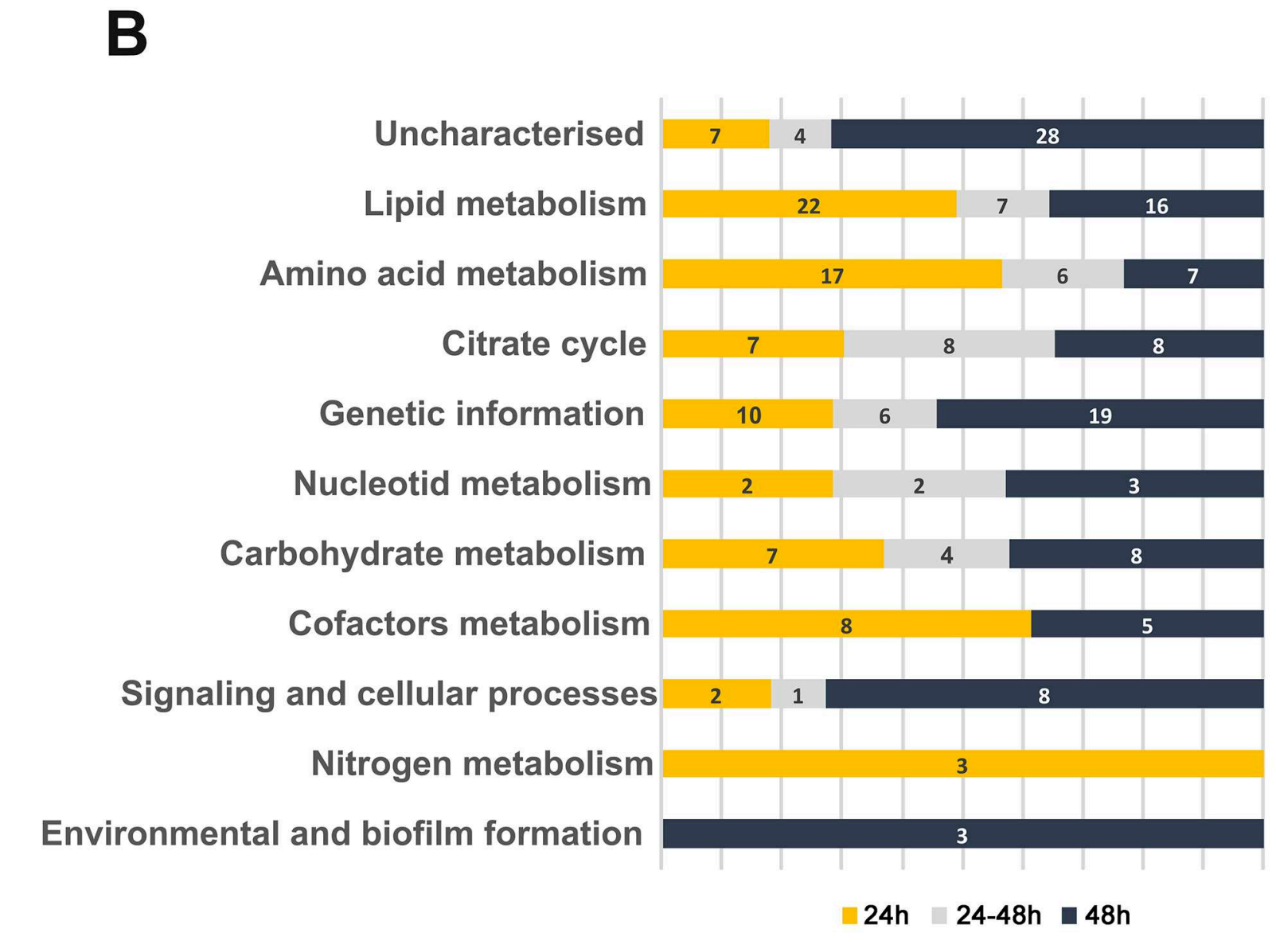
B
Uncharacterised
7
4
28
Lipid metabolism
22
7
16
Amino acid metabolism
17
6
7
Citrate cycle
7
8
8
Genetic information
10
6
19
Nucleotid metabolism
2
2
3
Carbohydrate metabolism
7
4
8
Cofactors metabolism
8
5
Signaling and cellular processes
2
1
8
Nitrogen metabolism
3
Environmental and biofilm formation
3
24h
24-48h
48h

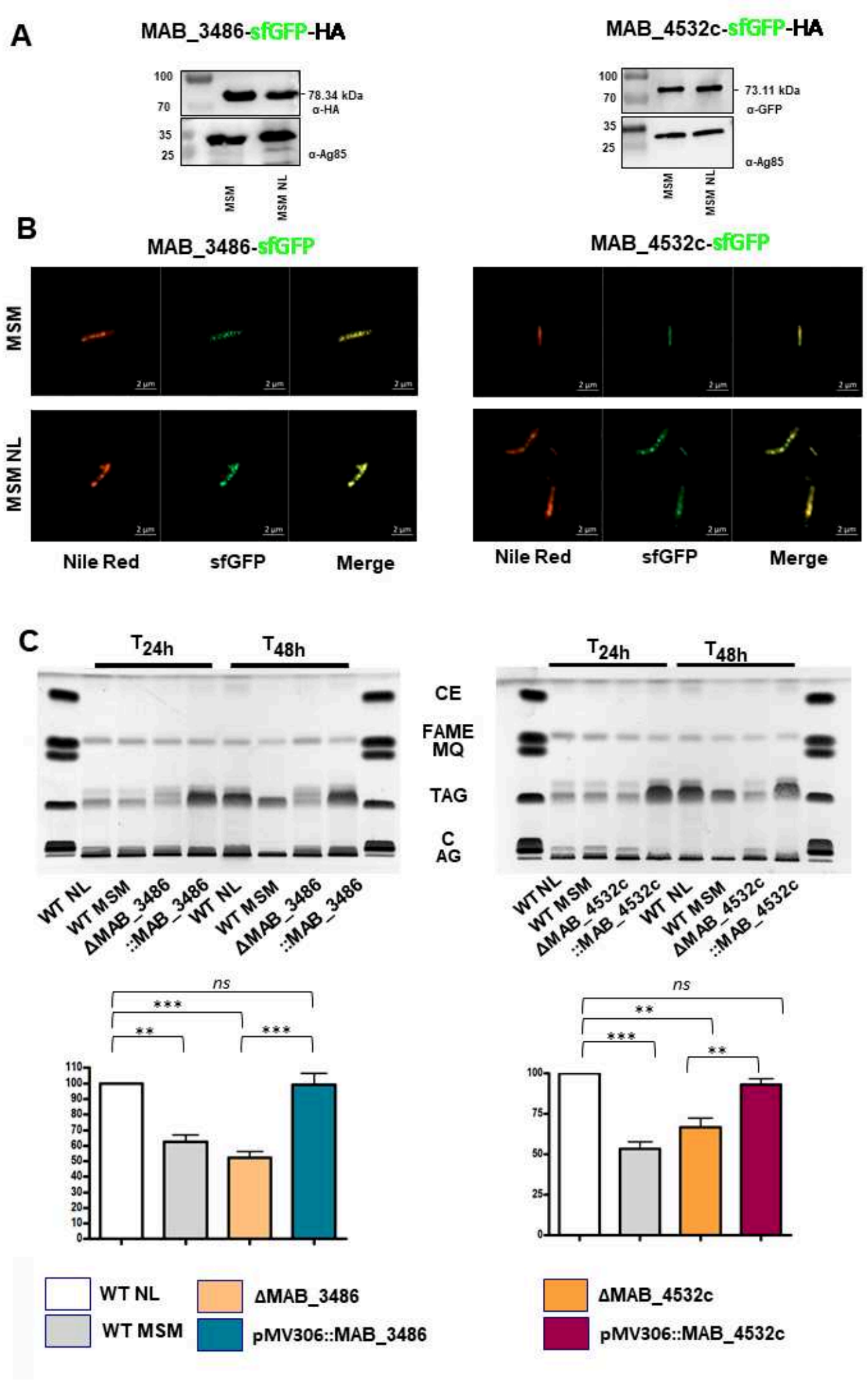
A
MAB_3486-sfGFP-HA
100
70
35
25
78.34 kDa
α-HA
α-Ag85
MSM
MSM NL
MAB_4532c-sfGFP-HA
100
70
35
25
73.11 kDa
α-GFP
α-Ag85
MSM
MSM NL
B
MAB_3486-sfGFP
MAB_4532c-sfGFP
MSM
MSM NL
2 µm
Nile Red
sfGFP
Merge
Nile Red
sfGFP
Merge
C
T24h
T48h
CE
FAME MQ
TAG
C AG
WT NL
WT MSM
ΔMAB_3486
::MAB_3486
WT NL
WT MSM
ΔMAB_3486
::MAB_3486
T24h
T48h
WT NL
WT MSM
ΔMAB_4532c
::MAB_4532c
WT NL
WT MSM
ΔMAB_4532c
::MAB_4532c
ns
***
**
***
110
100
90
80
70
60
50
40
30
20
10
0
ns
**
***
**
100
75
50
25
0
WT NL
WT MSM
ΔMAB_3486
pMV306::MAB_3486
ΔMAB_4532c
pMV306::MAB_4532c

SUPPLEMENTARY DATA

A proteomic and functional view of intrabacterial lipid inclusion biogenesis in mycobacteria

Tonia Dargham[1,2,*], John Jairo Aguilera-Correa[3,*], Romain Avellan[1,*], Ivy Mallick[1], Léa Celik[1], Gael Brasseur[4], Isabelle Poncin[1], Vanessa Point[1], Stéphane Audebert[5], Luc Camoin[5], Wassim Daher[3,6], Jean-François Cavalier[1], Laurent Kremer[3,6] & Stéphane Canaan[1§]

[1] Aix-Marseille Univ., CNRS, LISM UMR 7255, IMM FR3479, IM2B, Marseille, France

[2] IHU Méditerranée Infection, Aix-Marseille Univ., Marseille, France

[3]Centre National de la Recherche Scientifique UMR 9004, Institut de Recherche en Infectiologie de Montpellier (IRIM), Université de Montpellier, 1919 route de Mende, 34293, Montpellier, France.

[4] Aix-Marseille Univ., CNRS, LCB UMR 7283, IMM FR3479, IM2B, Marseille, France

[5] Aix-Marseille Univ., INSERM, CNRS, Institut Paoli-Calmettes, CRCM, Marseille, France

[6]INSERM, IRIM, 34293 Montpellier, France.

* Authors contributed equally to this work, and should be considered as first co-authors

§ Correspondence address to Stéphane Canaan, canaan@imm.cnrs.fr.

Content

Supplementary methods

Supplementary figures

Figure S1: Validation of the sfGFP fusion to each selected protein.

Figure S2: Comparison of Nile Red intensity staining in *M. abscessus* carrying pMV306-*tgs1-apex2* and WT strains.

Figure S3: Detection of an amphipathic helix in each selected protein.

Figure S4: Colocalization of each selected IAP with ILI.

Figure S5: Unlabeled deletion strategy for the deletion of MAB_3486 in *M. abscessus*.

Figure S6: Genetic validation of each *M. abscessus* deletion mutant.

Figure S7: Growth curves for the deletion mutants.

Figure S8: Apolar lipid profile in IAP deletion genes.

Figure S9: Validation of the sfGFP-tagged complementation of each *M. abscessus* mutant.

Figure S10: Acylglycerol migration profile in IAP deleted mutants.

Supplementary methods

ILI accumulation in *M. abscessus*

Briefly, from a logarithmic growth phase culture (OD_{600} ~1-1.5), *M abscessus* cells were harvested by centrifugation at 3,500 *g* for 10 min. Pellets were washed twice with sterile phosphate-buffered saline (PBS) (pH 7.4) containing 0.05% (*v/v*) Tween-20, then once with PBS, and finally re-suspended in PBS at a final theoretical OD_{600} of 10. This bacterial suspension was used to inoculate at an initial OD_{600} of 0.1, either fresh Mineral Salt Medium (MSM) (2 g/L Na_2HPO_4, 1 g/L KH_2PO_4, 0.5 g/L NaCl, 0.2 g/L $MgSO_4$, 20 mg/L $CaCl_2$, 1 g/L NH_4Cl, and 5% glycerol) or Mineral Salt Medium Nitrogen Limited (MSM NL) containing only 0.15 g/L NH_4Cl. To prevent bacterial clumping, Tyloxapol (Sigma-Aldrich) was added at a final concentration of 0.02% (*v/v*). The MSM and MSM NL culture media were then incubated for 24 and 48h at 37°C under shaking (200 rpm).

SDS PAGE and Western blotting

After 24h or 48h of culture in MSM or MSM NL, bacterial pellets were recovered, and total lysates were denatured by incubating with 1×SDS loading dye for 10 min at 95 °C and subjected to SDS-PAGE. Proteins were transferred onto 0.2 µm polyvinylidene difluoride (PVDF) using the Trans-Blot Turbo transfer system at 25 V, 1 A for 7 min (Bio-Rad, Hercules, CA). The membrane was then blocked in TBS-T (0.3% BSA) and incubated with a primary antibody anti-APEX2 (1 µg/ml, Thermo Fisher Scientific, Waltham, MA) overnight at 4 °C. After three quick washes with TBST for 10 min each, the membrane was incubated for 1 h with the secondary anti-llama antibody. Detection was achieved using the Pierce ECL Western blotting substrate solution (Thermo Fisher Scientific, Waltham, MA) and visualized using the ChemiDoc MP imaging system (Bio-Rad).

Bacteria were harvested, resuspended in PBS, and disrupted by bead beating using 1 mm diameter glass beads. Protein concentration was assessed using the BCA Protein Assay Reagent kit, according to the manufacturer's instructions. Equal amounts of proteins (50 mg) were separated by SDS-PAGE and transferred to a nitrocellulose membrane. For GFP detection, nitrocellulose membranes were probed for 1h with mouse anti-GFP antibodies (dilution 1:2,000). Anti-GFP antibodies were diluted in 5% non-fat milk powder in TNT buffer (50 mM Tris pH 8; 150 mM NaCl; and 0.05% Tween

20). After washing, membranes were incubated for 45 min with goat anti-mouse antibodies conjugated to HRP (dilution 1:5,000). The GFP signal was revealed using a ChemiDoc MP system for imaging and analyzing gels.

1-Whole proteome analysis:

For relative proteomic analysis, 15 µg of proteins were solubilized in LDS sample buffer (2× concentrated) (Invitrogen, Life Technologies), before loading on NuPAGE™ 4–12% Bis–tris acrylamide gels according to the manufacturer's instructions (Invitrogen, Life Technologies). Running of samples was stopped as soon as proteins stacked as a single band, and following imperial blue staining (Life Technologies), the upper part of the gel containing the proteins was cut and processed for classical in-gel digestion (washes, thiols reduction with 10 mM DTT, and cysteine alkylation with 55 mM iodoacetamide). Extracted peptides were concentrated under speed-vacuum. Samples were reconstituted with 0.1% trifluoroacetic acid in 2% acetonitrile and analyzed by liquid chromatography (LC)-tandem MS (MS/MS) using an Orbitrap Fusion Lumos Tribrid Mass Spectrometer (ThermoFisher Scientific, San Jose, CA) online with a nanoRSLC Ultimate 3000 chromatography system (ThermoFisher Scientific, Sunnyvale, CA). First, peptides were concentrated and purified on a pre-column PepMap100 C18, 2 cm × 100 µm I.D, 100 Å pore size, 5-µm particle size in solvent A (0.1% formic acid in 2% acetonitrile). In the second step, peptides were separated on a reverse phase LC EASY-Spray C18 column PepMap RSLC C18, 50cm × 75 µm I.D, 100 Å pore size, 2-µm particle size (ThermoFisher) at 300 nL/min flow rate and 40°C. After column equilibration using 4% of solvent B (20% water - 80% acetonitrile - 0.1% formic acid), peptides were eluted from the analytical column by a two-step linear gradient (2-20% acetonitrile/H_2O; 0.1% formic acid for 90 min and 20-45% acetonitrile/H_2O; 0.1% formic acid for 20 min). For peptide ionization in the EASY-Spray nanosource in front of mass spectrometer, spray voltage was set at 2.2 kV and the capillary temperature at 275°C. The Orbitrap Lumos was used in data-independent mode with the following parameters. First, MS spectra were acquired in the Orbitrap in the range of m/z 375-1,500 at a FWHM resolution of 120,000 measured at 400 m/z. AGC target was set at standard parameters with an automatic Maximum Injection Time. MS2 spectra were acquired in the Orbitrap with a resolution of 30,000, in the mass range of 200-1,800 m/z after isolation of parent ion in the quadrupole and fragmentation in the HCD cell under collision Energy of 30%. DIA parent ion range was

from 400 to 1,000 m/z divided into 40 windows 16 Da wide and from 1,000 to 1,500 m/z divided into 10 windows 50 Da wide.

Relative intensity-based label-free quantification (LFQ) was processed using the DIA-NN 1.8 algorithm. Spectra were searched against the *M. abcessus* database (UP000007137) extracted from UniProt on March 10, 2021, containing 4940 entries, with the addition of a protein contaminant bank (1). The search parameters included: *(i)* trypsin allowing cleavage before proline; *(ii)* one missed cleavages were allowed; *(iii)* cysteine carbamidomethylation (+57.02146) as a fixed modification, and methionine oxidation (+15.99491) and N-terminal acetylation (+42.0106) as variable modifications; *(iv)* a maximum of 1 variable modification per peptide was allowed; and *(v)* a minimum peptide length was 7 amino acids and a maximum of 30 amino acids. The match between runs option was enabled to transfer identifications across different LC-MS/MS replicates based on their masses and retention time. The precursor false discovery rate was set to 1%. DIA-NN parameters were configured on Single-pass mode for Neural Network classifier, Robust LC High precision for quantification strategy, and RT-dependent mode for Cross-run normalization. A library was generated using Smart profiling set up. The primary output file from DIA-NN was further filtered at 1% FDR, and LFQ intensity was calculated using the DIAgui package at 1% q-value (2).

Statistical analysis was conducted using the Perseus program (version 1.6.15.0) from the MaxQuant environment (http://www.maxquant.org). Quantifiable proteins were defined as those detected in above 70% of samples in one condition or more. Missing values were replaced using data imputation by randomly selecting from a normal distribution centered on the lower edge of the intensity values that simulates signals of low abundant proteins using default parameters (a downshift of 1.8 standard deviation and a width of 0.3 of the original distribution). To determine whether a given detected protein was specifically differential, a two-sample t-test was performed using permutation-based FDR control at 0.05 and employing 250 permutations. The *p*-value was adjusted using a scaling factor s0 with a value of 1. Analysis was performed on biological triplicates, each injected twice on mass spectrometers.

2-Biotinylated proteome: Protein samples were prepared in a similar way to the whole proteome analysis. The final digest was analyzed by liquid chromatography (LC)-

tandem MS (MS/MS) using a Q Exactive Plus Hybrid Quadrupole-Orbitrap online with a nanoLC Ultimate 3,000 chromatography system (ThermoFisher Scientific™, San Jose, CA). Peptides were ionized in the EASYSpray source, with a spray voltage set at 1.9 kV and the capillary temperature at 250°C. All samples were measured in a data-dependent acquisition mode. Peptide masses were measured in a survey full scan (scan range 375-1,500 m/z, with 70 K FWHM resolution at m/z=400, target AGC value of 3.00×10^6 and maximum injection time of 100 ms), and the 10 most intense data-dependent precursor ions were successively fragmented in the HCD cell and measured in Orbitrap (normalized collision energy of 25%, activation time of 10 ms, target AGC value of 1.00×10^5, intensity threshold 1.00×10^4 maximum injection time 100 ms, isolation window 2 *m/z*, 17.5 K FWHM resolution, scan range 200 to 2000 *m/z*). Dynamic exclusion was implemented with a repeat count of 1 and exclusion duration of 20 s.

Relative intensity-based label-free quantification (LFQ) was processed using the MaxLFQ algorithm available on the MaxQuant computational proteomics platform, version 1.6.3.4. Analysis was performed on three biological replicates, each injected twice into mass spectrometers. The acquired raw LC Orbitrap MS data underwent initial processing using the integrated Andromeda search engine. Spectra were searched against the *M. abcessus* database (UP000007137) extracted from UniProt on March 10, 2021, containing 4,940 entries. The false discovery rate (FDR) at the peptide and protein levels was set to 1% and determined by searching a reverse database. For protein grouping, all proteins that could not be distinguished based on their identified peptides were assembled into a single entry according to the MaxQuant rules. Statistical analysis was carried out in a similar way to the whole proteome analysis.

Lipid extraction and TLC analysis.

Cultures underwent centrifugation for 15 min at 4,000 *g* and were washed twice with water. Pellets were boiled at 95 °C for 10 min, lyophilized overnight, and weighted to determine the exact dry weight of mycobacterial cells. Apolar lipids were extracted according to a previously described method (3). Briefly, 2 mL of MeOH-0.3% NaCl (10:1, *v/v*) was added per 10 mg of dry extract. This saline-MeOH solution containing the bacterial dry extract was mixed for 15 min with 1 mL petroleum ether in Pyrex®

tubes at room temperature using a tube rotator. After centrifugation at 3,000 *g* for 5 min, the upper organic layer was transferred to a fresh tube. This step was repeated twice. The combined organic layers containing apolar lipids were transferred to a pre-weighed vial, and the solvent was evaporated to dryness under a nitrogen stream. Finally, the resulting dry apolar lipid residue was re-suspended in dichloromethane.

The extracted lipids were analyzed by thin-layer chromatography (TLC) using glass TLC plates (TLC Silica Gel 60 F_{254}, Merck). Following eluent migration (*i.e.*, petroleum ether (40-60 °C fraction) / diethyl ether 90:10 (*v/v)* for non-polar lipid and Heptane/ diethyl ether/ formic acid 55:45:1 (v/v/v) for acylglycerols), the plates were dried at room temperature for 10 min, and then sprayed with a cupric acetate-orthophosphoric acid solution. This solution was prepared by mixing a saturated aqueous solution of cupric acetate with 85% phosphoric acid in a 1-to-1 volume ratio, followed by heating at 140 °C in an oven for 5-10 min.

References

1. Frankenfield AM, Ni J, Ahmed M, Hao L. 2022. Protein Contaminants Matter: Building Universal Protein Contaminant Libraries for DDA and DIA Proteomics. J Proteome Res 21:2104-2113.
2. Gerault MA, Camoin L, Granjeaud S. 2024. DIAgui: a Shiny application to process the output from DIA-NN. Bioinform Adv 4:vbae001.
3. Santucci P, Johansen MD, Point V, Poncin I, Viljoen A, Cavalier JF, Kremer L, Canaan S. 2019. Nitrogen deprivation induces triacylglycerol accumulation, drug tolerance and hypervirulence in mycobacteria. Sci Rep 9:019-45164.

Supplementary figures

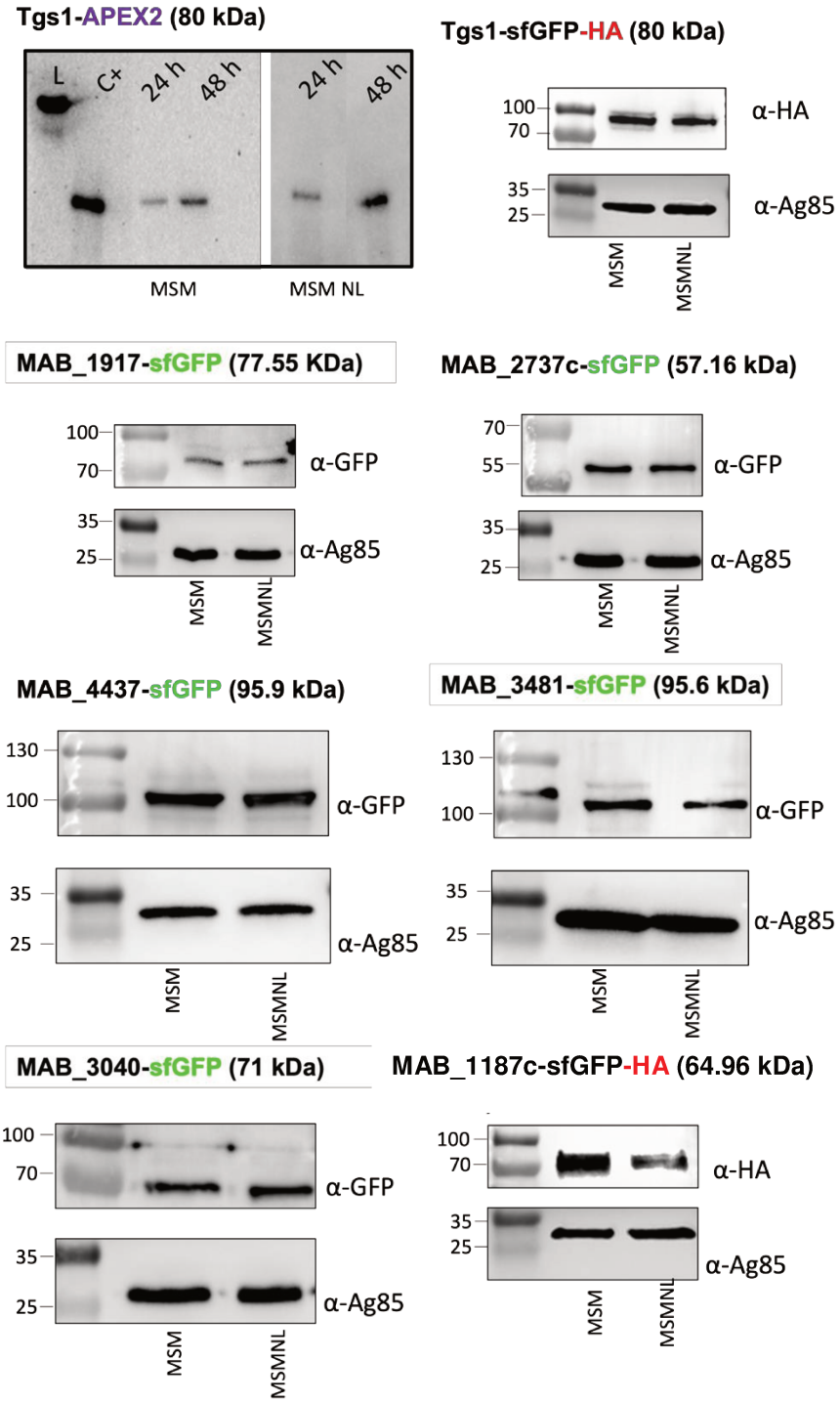

Figure S1: Validation of the sfGFP fusion to each selected protein. Protein expression pattern of each fusion in (WT) in MSM NL and MSM at the specific identification time. Western blotting using anti-APEX2-tag, anti-HA-tag, anti-GFP-tag primary antibodies attest for the expression of APEX2-, HA-, sfGFP-tagged protein in the strains transformed with pMV306. Note: Some proteins (Tgs1 and MAB_1187c) were weakly expressed, so that they were double tagged with GFP and HA since the HA detection is more sensitive than sfGFP detection by Western blotting. Twenty micrograms of proteins were deposited per each well.

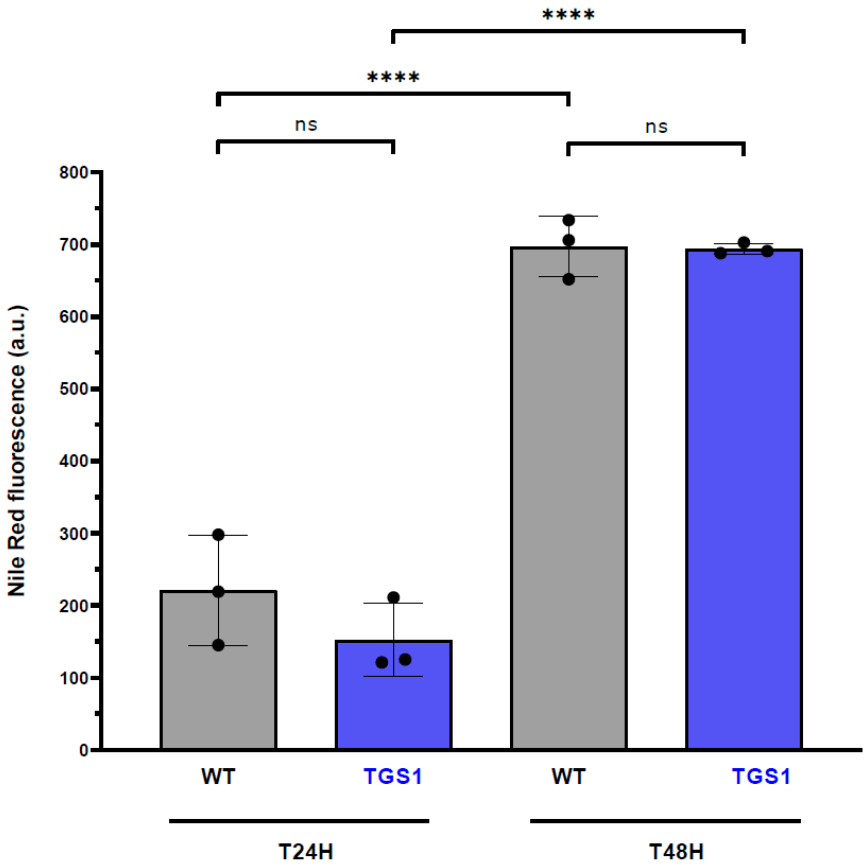

Figure S2: Comparison of Nile Red intensity staining in *M. abscessus* carrying pMV306-*tgs1-apex2* and WT strains. Diagram of the construct encoding the native promoter and full genomic sequence of *tgs1* fused to *apex2* compared to a WT *M. abscessus* strain. Data represent the mean of Nile Red fluorescence accumulation from three biological replicates measured by flow cytometry. Statistical analyses were carried using a two ways ANOVA using a Šidák test. **** *p*-value <0.0001.

MAB_4437
1 Seq QIFYNIATDEQKKWAEFVA Pos 139 157

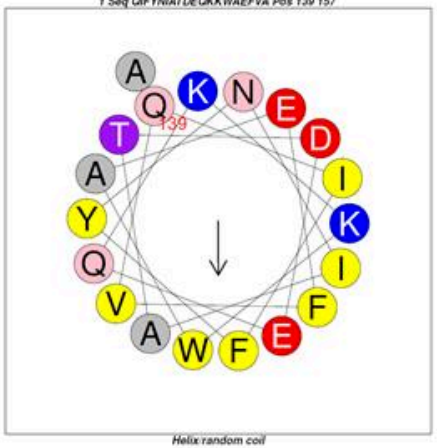

Helix random coil

MAB_4437
2 Seq LVGEVHNGIAQMFDVIEQA Pos 285 303

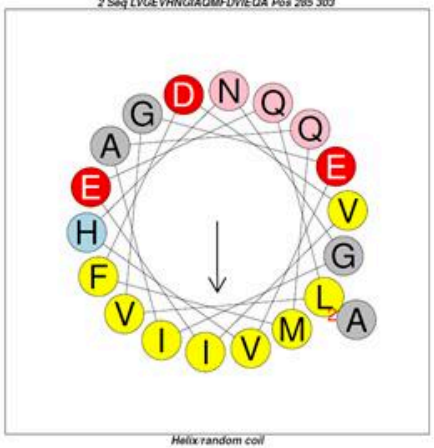

Helix random coil

MAB_4437
3 Seq DFFFRKIVKDGGKSLAFIS Pos 459 477

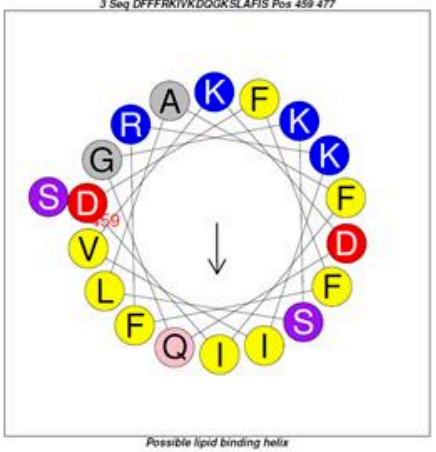

Possible lipid binding helix

MAB_3481
4 Seq DDILHVGADAFSAALNTVN Pos 245 263

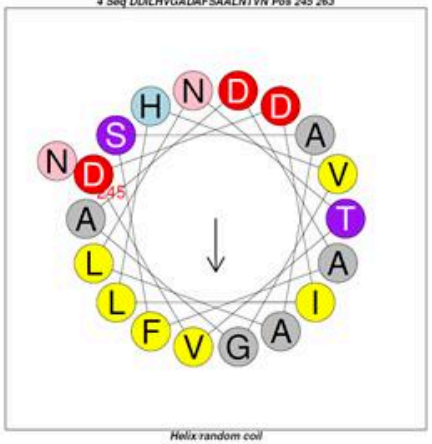

Helix random coil

MAB_3481
5 Seq FDHVRREFVDAYARLLAM Pos 301 318

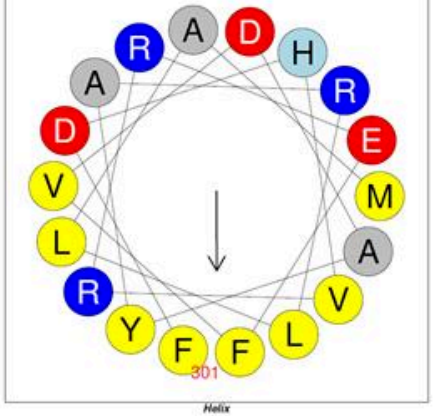

Helix

MAB_3481
6 Seq AQLRGTDSALIDQIFEFLNRDFSVYAVDL Pos 508 536

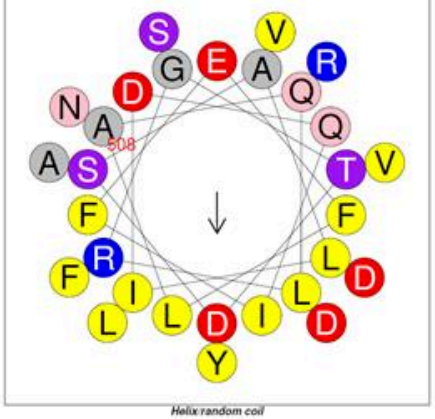

Helix random coil

MAB_3040
7 Seq ANLLGEEGQGFIYLMKNL Pos 229 246

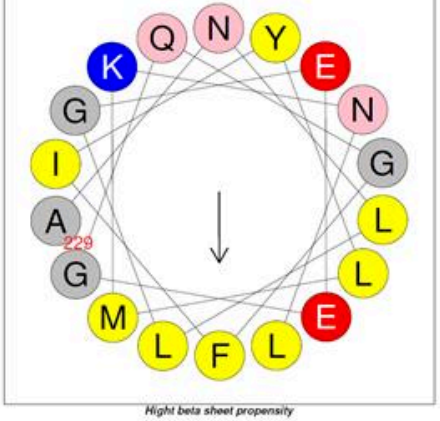

Hight beta sheet propensity

MAB_3040
8 Seq DATVIRVMVDEFISLLNKEE Pos 298 317

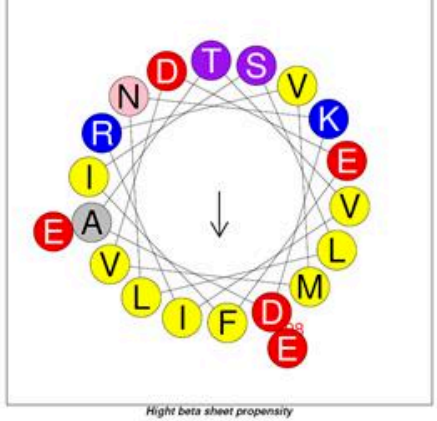

Hight beta sheet propensity

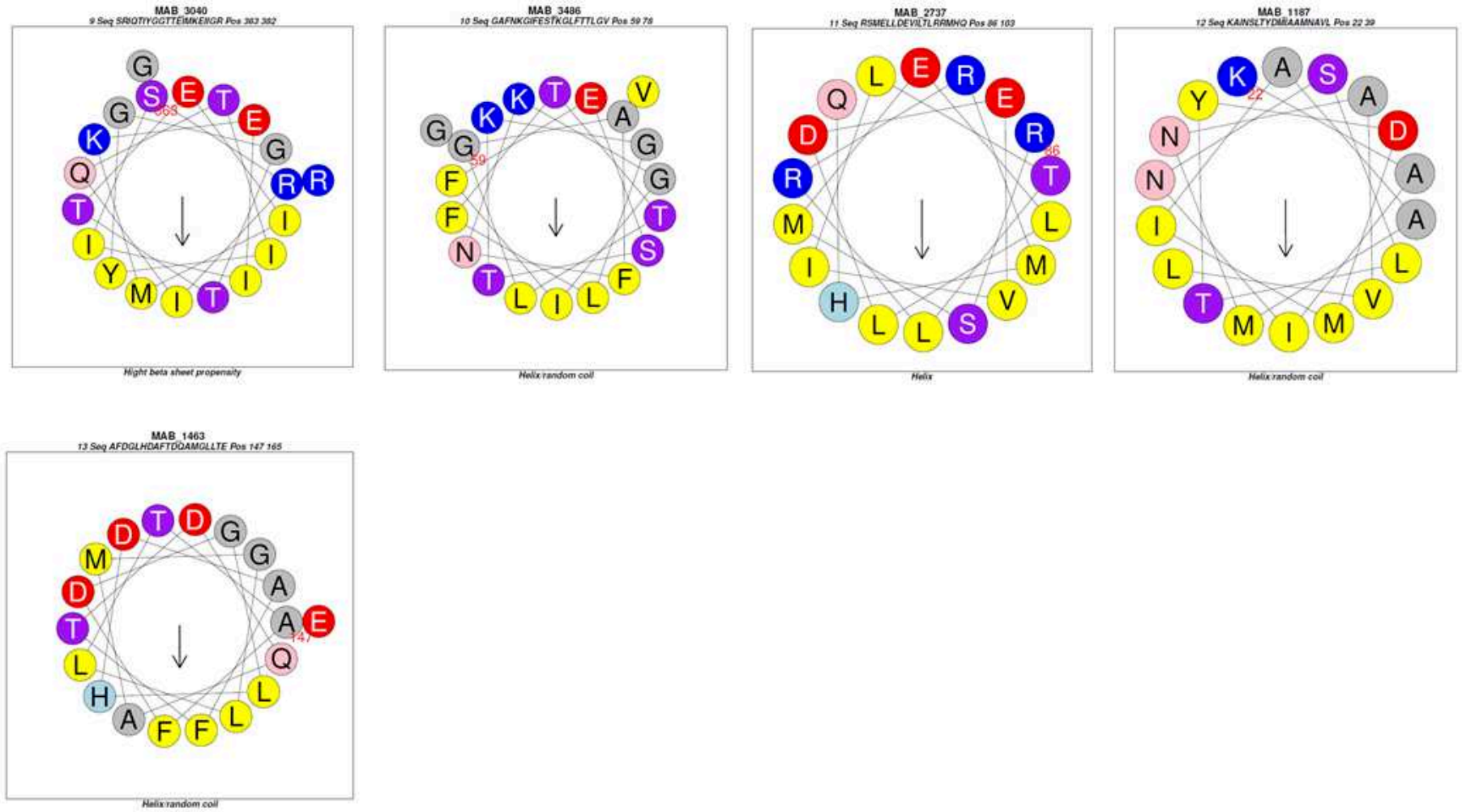

Figure S3: Detection of an amphipathic helix in each selected protein. Representation of amphipathic helices as helical wheel diagrams from multiple selected proteins in *M. abscessus*. The arrow indicates the angle of the mean hydrophobic moment toward the hydrophobic face of the amphipathic helix

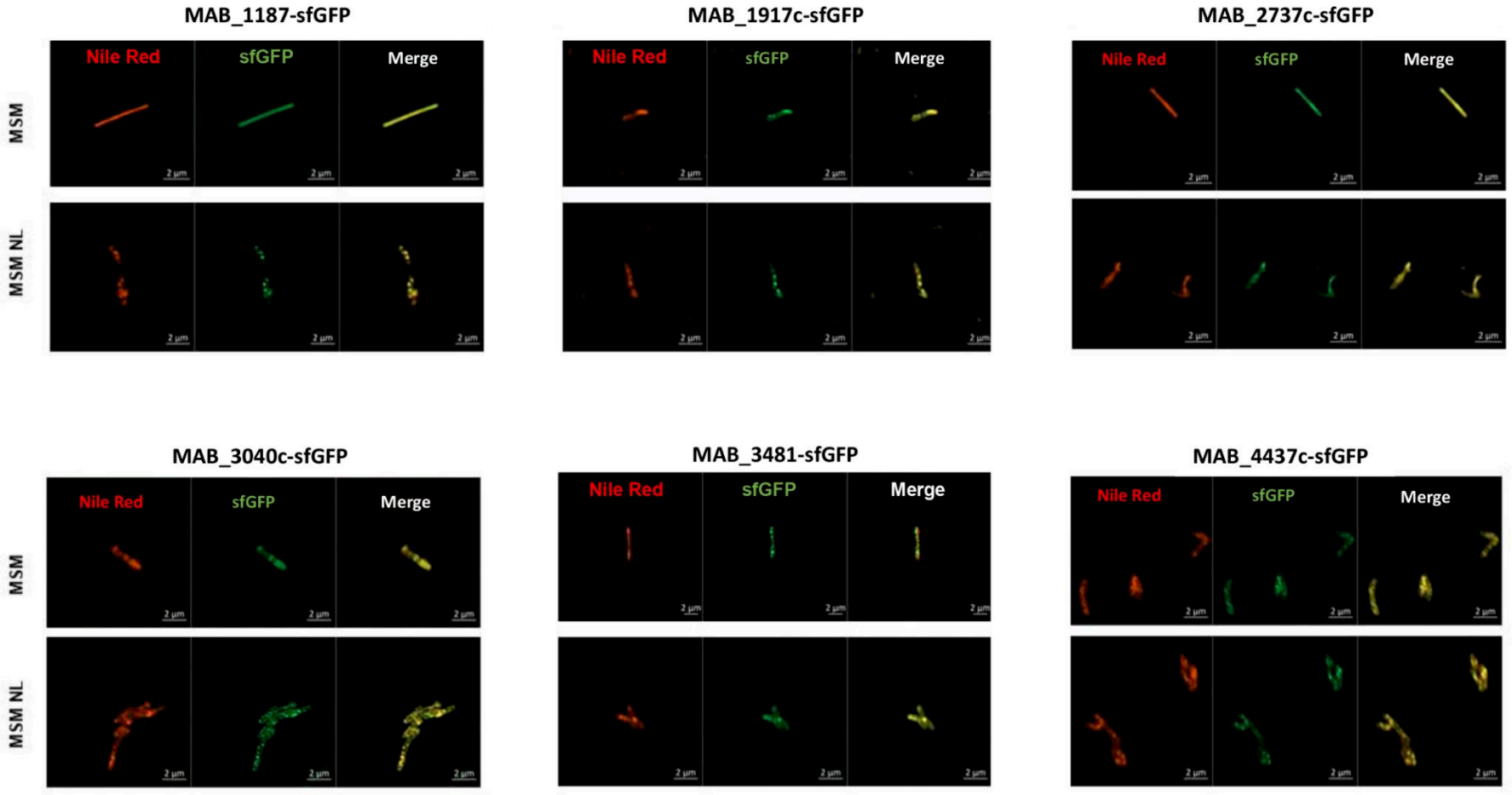

Figure S4: Colocalization of each selected IAP with ILI. WT strains are transformed with pMV306-*gene-sfGFP* and grown in both MSM and MSM NL. Bacteria were fixed with 2% PFA, stained with Nile Red and observed by fluorescence microscopy. All the strains expressing each sfGFP-tagged protein strains were grown for 24h except for MAB_3481-GFP which was grown for 48h.

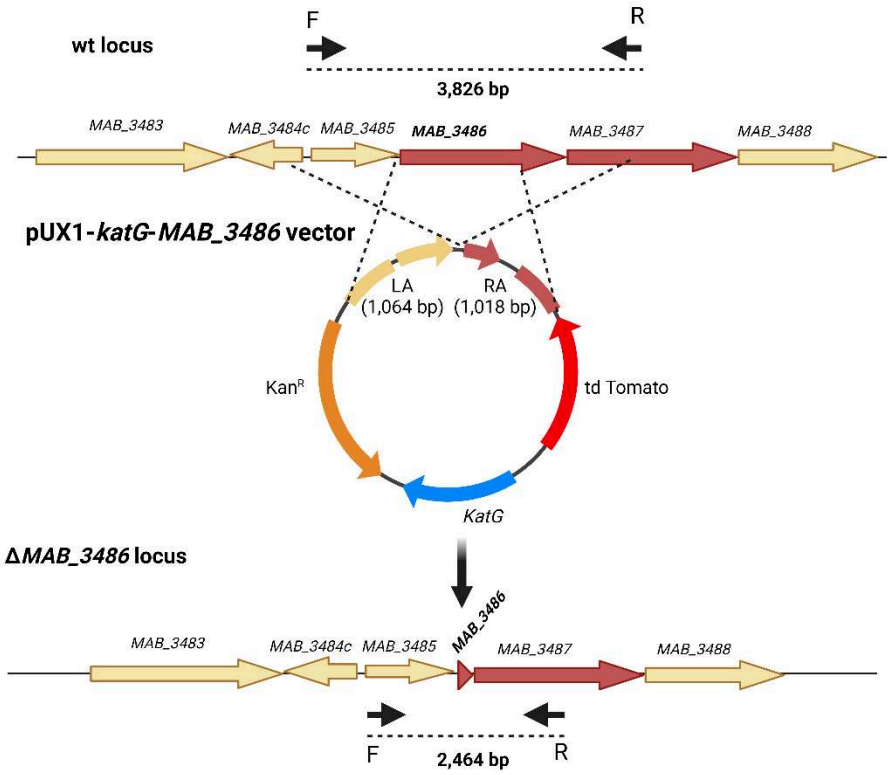

Figure S5: Unlabeled deletion strategy for the deletion of MAB_3486 in *M. abscessus*. *MAB_3486* is located between *MAB_3485* and *MAB_3487*. The pUX1-*katG-MAB_3486* plasmid was generated to remove *MAB_3486* by double homologous recombination. The DNA sequence of the left arm (LA) of *MAB_3486* (1,064 bp) was amplified by PCR and cloned into the PacI and MfeI sites of pUX1-*katG*. The DNA sequence of the right arm (RA) of *MAB_3486* (1,018 bp) was amplified by PCR and subcloned into the EcoRI and NheI sites of pUX1-*katG*. The resulting suicide plasmid (lacking motifs for episomal replication or mobile elements promoting chromosomal integration) was used to transform *M. abscessus*, replicating only by homologous recombination between the cloned sequences and their chromosomal homologous sequences. The first recombination events were selected in the presence of kanamycin. Single red fluorescent tdTomato-expressing clones were subjected to the second round of recombination selected with isoniazid and analyzed for double crossover phenotypes, *i.e.* loss of red fluorescence, sensitivity to kanamycin and resistance to isoniazid. The dashed lines represent the size of the expected PCR products in *M. abscessus* wild-type and Δ*MAB_3486*. Black arrows represent the forward (F) and reverse (R) primers used for PCR analysis.

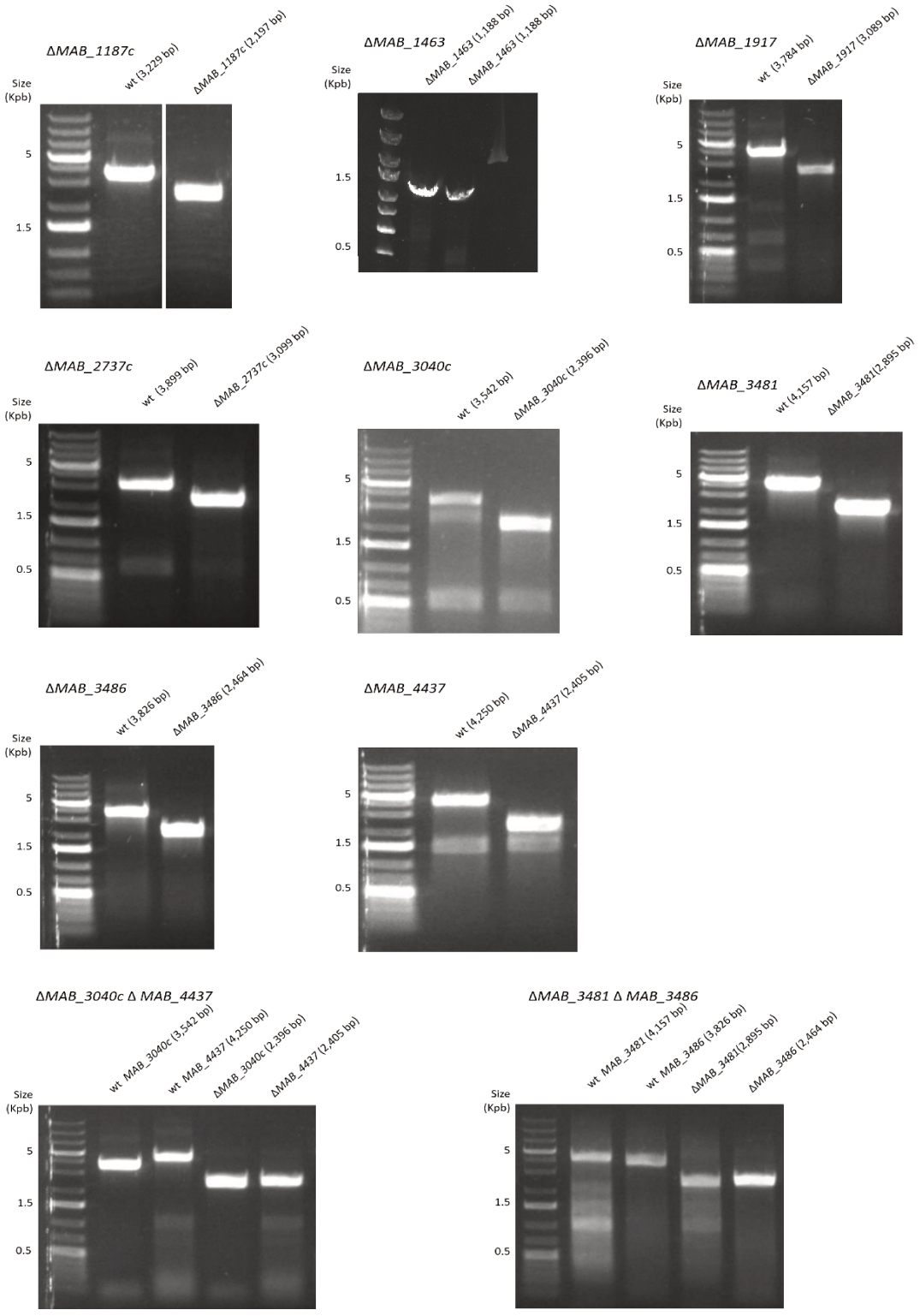

Figure S6: Genetic validation of each *M. abscessus* deletion mutant. PCR profile confirming the proper gene deletion of the 10 selected targets. PCR products were amplified from each mutant genomic DNA compared to the WT genome.

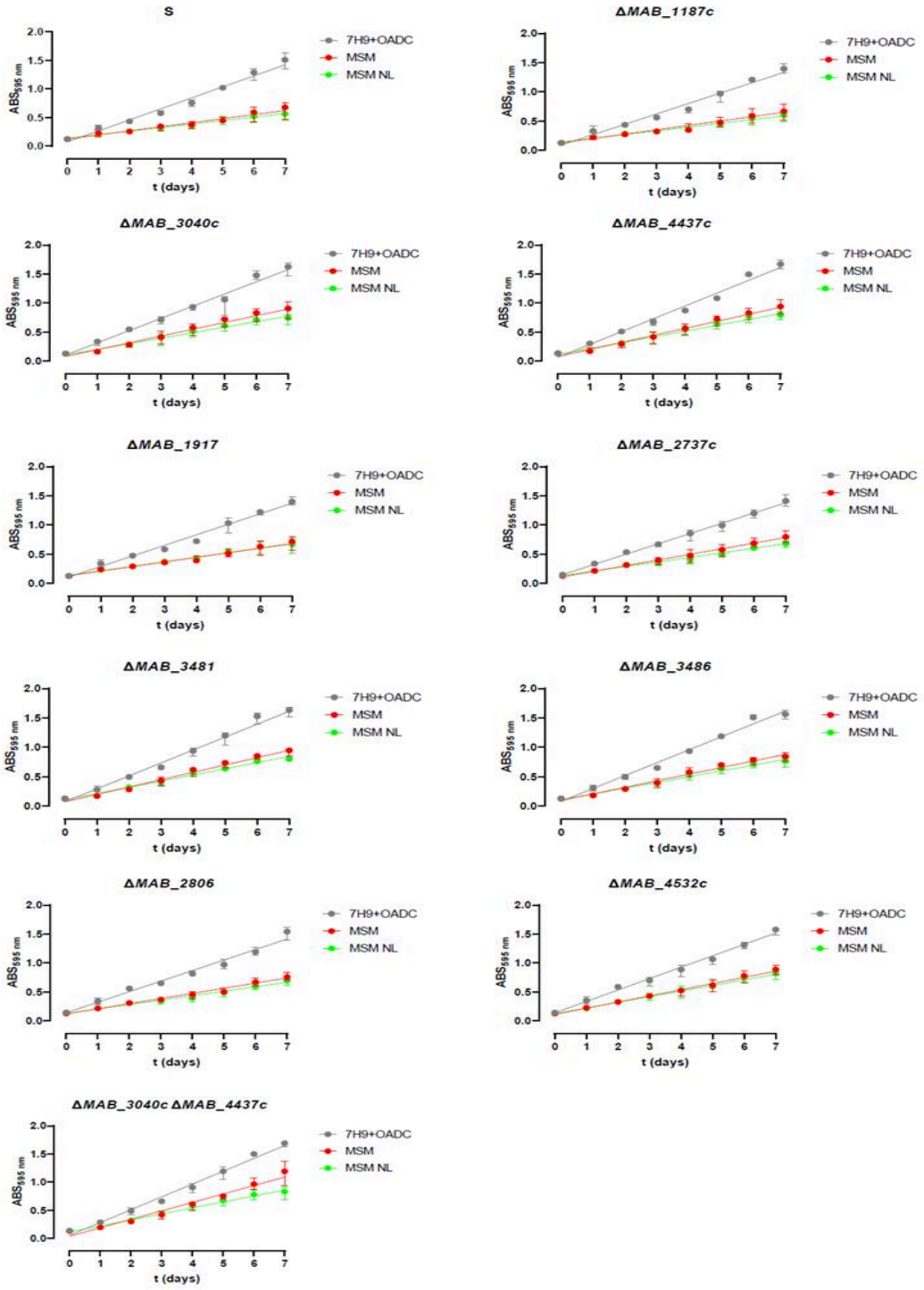

Figure S7: Growth curves for the deletion mutants. Each deleted strain was grown in 7H9 OADC supplemented with 0.025% tyloxapol (grey), MSM (red), and MSM NL (green) in flat-bottom 96-wells plate for 7 days. Absorbance was measured at 595nm every 24h. Error bars represent standard deviation from three biological replicates. S: smooth morphotype.

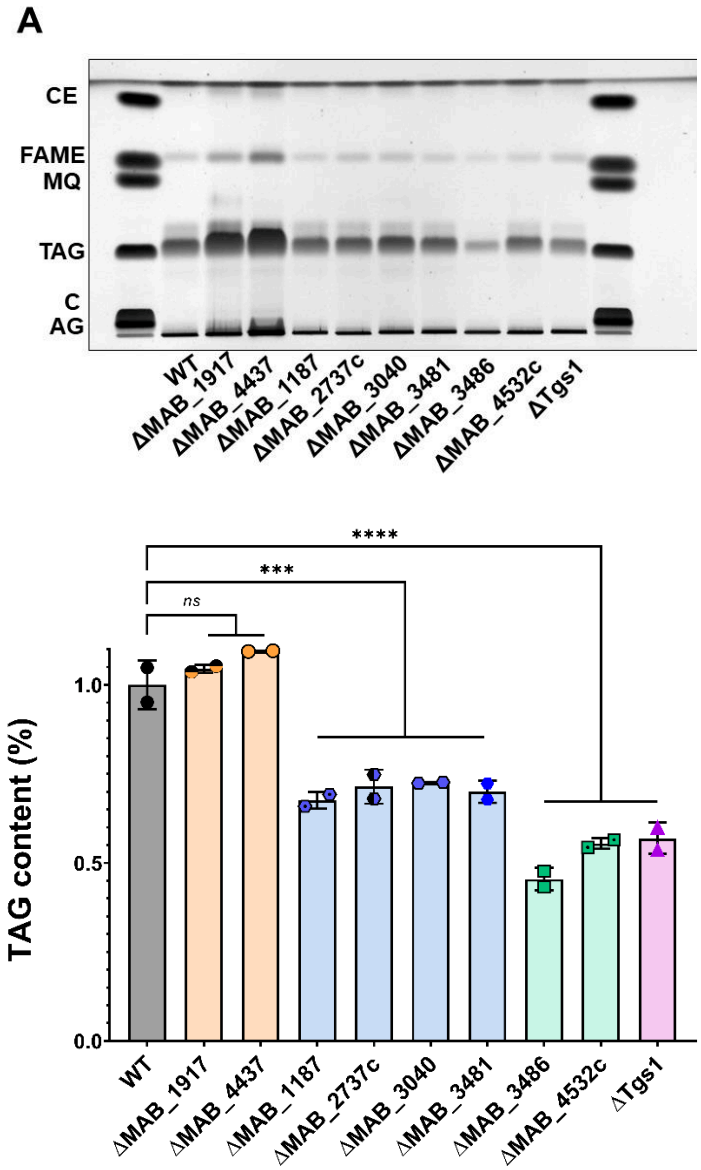

Figure S8: Apolar lipid profile in IAP deletion genes. *M. abscessus* deletion mutants were grown in MSM NL. Cultures were collected after a 48h incubation period, lyophilized, and equal amount of dry cells used for apolar lipid extraction. **A**) TAG level from each culture were analyzed by TLC. **B**) Results from densitometry are expressed as mean values ± SD of at least two biologically independent experiments, and reported as relative values using the TAG levels of *M. abscessus* WT in the MSM-NL as 100%. Statistical significance was assessed with one-way ANOVA followed by Tukey's multiple comparisons post-hoc test using Prism 8.0 (GraphPad, Inc): *** *p*-value <0.001; **** *p*-value <0.0001; *ns*, not significant (*p*-value >0.05). C: Cholesterol; CE: Cholesterol Ester; FA: Fatty Acid; FAME: Fatty Acid Methyl Esters; MQ: Mena Quinone; TAG: Triacylglycerol.

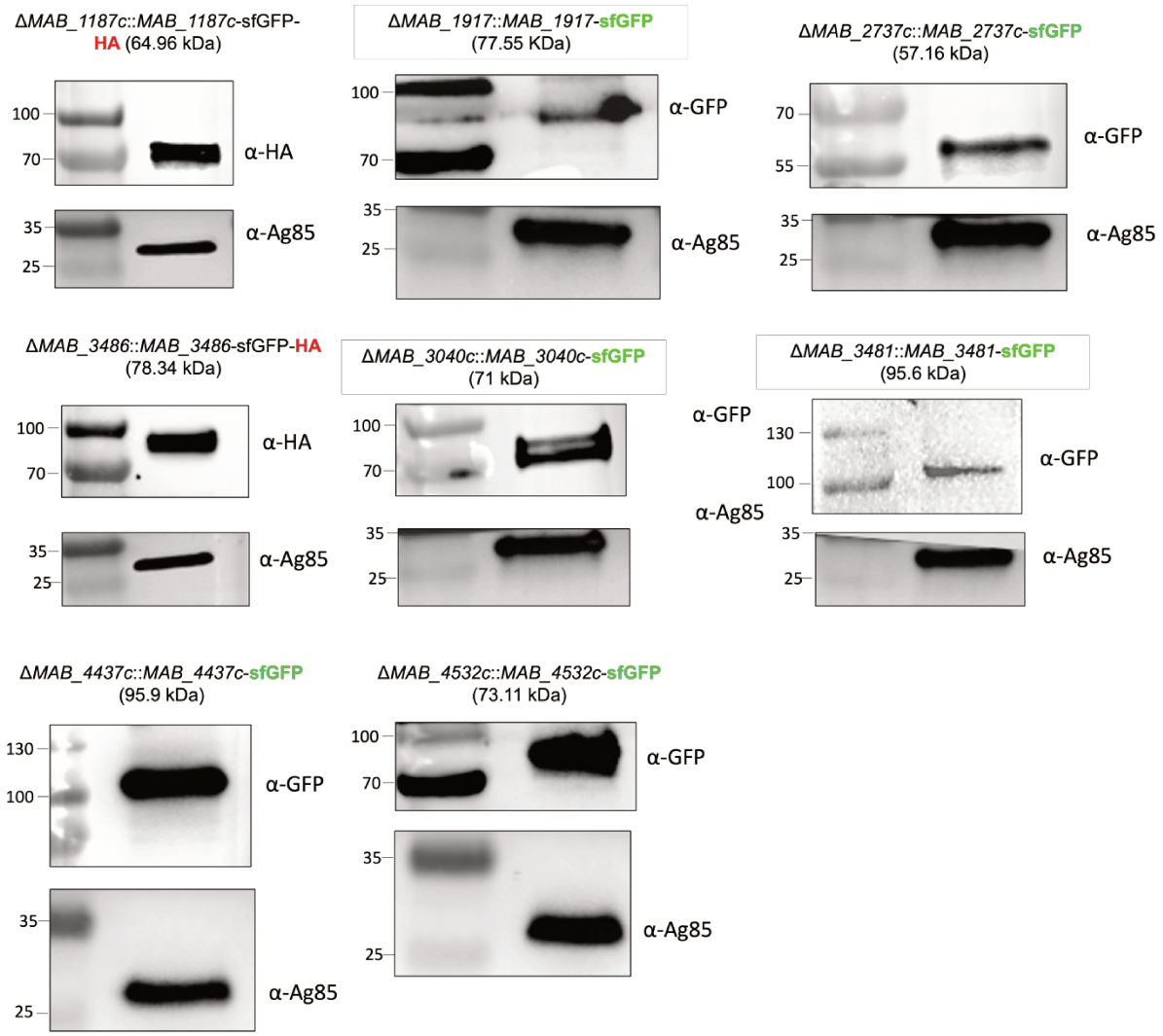

Figure S9: Validation of the sfGFP-tagged complementation of each *M. abscessus* mutant. The expression of the sfGFP or HA-tagged protein in each mutant was evaluated in MSM at their corresponding time point. Twenty micrograms of proteins were loaded in each well.

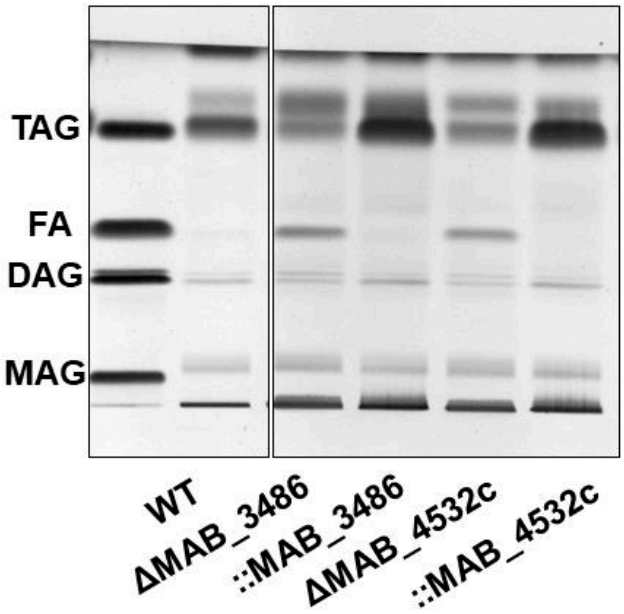

Figure S10: Acylglycerol migration profile in IAP deleted mutants. *M. abscessus* deletion mutants were grown in MSM NL. Cultures were collected after a 48h incubation period, lyophilized, and equal amount of dry cells used for apolar lipid extraction. FA level from each culture were analyzed by TLC. TAG: Triacylglycerol; FA: Fatty Acid; DAG: diacylglycerol; MAG: monoacylglycerol.

Conclusion et perspectives

Conclusion

En plus de *M. tb*, l'agent étiologique de la tuberculose, les mycobactéries non tuberculeuses (MNT) sont des agents pathogènes opportunistes responsables d'un large éventail de syndromes cliniques. Parmi les MNT, *M. abs* provoque des infections pulmonaires pseudo-granulomateuses, similaires à la tuberculose, en particulier chez les patients atteints de mucoviscidose. En outre, l'infection pulmonaire des patients atteints de mucoviscidose est généralement polybactérienne avec des combinaisons de bactéries à Gram-négatif, à Gram-positif et de MNT ; *M. abscessus* représentant jusqu'à 68% de toutes les MNT isolées. Étant l'une des espèces mycobactériennes les plus résistantes aux antibiotiques, sa présence peut conduire à des impasses thérapeutiques, à des refus de greffe et au décès du patient. Il y a donc une recherche constante de nouvelles molécules pour traiter les infections à *M. abs* et pour détecter sa présence afin de mettre en place des thérapies efficaces et spécifiques.

L'infection par *M. tb* ou *M. abs* peut entraîner la formation de granulomes dans les poumons, où certains macrophages infectés accumulent des lipides dans des corps lipidiques (LB) donnant aux cellules un aspect spumeux. Dans ces macrophages spumeux, les bactéries peuvent accumuler les lipides de l'hôte dans leur propre cytoplasme sous la forme d'inclusions lipidiques intrabactériennes (ILI), et persister dans un état non-réplicatif de dormance ou de persistance. Lors de la réactivation, ces ILI sont hydrolysées par les bacilles et utilisées comme source de carbone pour la propagation des mycobactéries et provoquer une infection aiguë.

Tous ces résultats impliquent la présence d'enzymes lipolytiques mycobactériennes capables de dégrader les LB et/ou les ILI, et qui jouent donc un rôle majeur dans le cycle de vie infectieux des mycobactéries. Dans ce contexte, l'utilisation d'inhibiteurs d'enzymes lipolytiques capables de bloquer ces activités représente un outil chimique intéressant pour identifier et étudier les enzymes impliquées dans le métabolisme des lipides afin de mieux comprendre comment les bacilles peuvent persister/se réactiver à l'intérieur des macrophages riches en lipides.

Dans ce contexte, notre équipe a développé deux familles d'antimycobactériens prometteurs, les dérivés d'oxadiazolone (**OX**) et les analogues de Cyclophostines et de Cyclipostins (**CyC**). Les **OX** et **CyC** sont ainsi capables de bloquer la croissance de *M. tb* ou *M. abs in vitro* et/ou *ex vivo* dans des macrophages infectés, en inhibant un grand nombre d'enzymes à sérine ou

cystéine mycobactériennes majoritairement impliquées dans le métabolisme des lipides mycobactériens. Ces **OX**/**CyC** sont également non toxiques pour les cellules hôtes ou chez la souris.

Les études effectuées pendant ce projet ont donc eu pour objectifs l'exploitation des inhibiteurs **OX**/**CyC** en tant que sondes pour le développement de nouveaux outils de diagnostic et pour l'identification de nouvelles cibles thérapeutiques contre les infections liées aux mycobactéries.

Etude de la pénétration des CyC *in vitro* et *ex vivo* dans des macrophages murins

Dans un premier temps, l'utilisation de **CyC$_{\text{-Dansyl}}$** fluorescents nous a permis de mettre en évidence la pénétration spécifique de ces molécules chez les mycobactéries, et par conséquence de comprendre pourquoi les **CyC** sont totalement inactifs sur les bactéries à Gram-positif et Gram-négatif comme *S. aureus* et *P. aeruginosa*, car incapables de traverser leur membrane respective. Cette propriété nous a poussé à tester leur usage comme outil de diagnostic rapide pour les infections mycobactériennes en démontrant leur capacité à marquer spécifiquement *M. abs* au sein d'une polyculture bactérienne complexe.

Le devenir des **CyC$_{\text{-Dansyl}}$** fluorescents au sein de macrophages murins nous a également permis de mettre en évidence un tropisme clair de nos composés pour les mycobactéries intra-macrophagiques. De plus, de nos résultats il est possible de classer les **CyC** testés en deux ensembles phénotypiques distincts :

- Les **CyC$_{31/32}$** qui présentent des activités antibactériennes *in vitro*, sont totalement inactifs à l'intérieur des macrophages et présentent une répartition homogène au sein de ces derniers.
- Les **CyC$_{7\alpha/\beta}$** qui ne présentent aucune activité antibactérienne *in vitro* mais qui sont actifs sur la croissance intracellulaire de *M. abs*, qui se retrouvent localisés dans des compartiments subcellulaires acides au sein des macrophages.

Nous avons également montré que l'inhibition de la pompe à protons vacuolaire eucaryote, grâce à l'usage de Concanamycin A, abolit cette colocalisation des **CyC$_{7\alpha/\beta}$** au sein de compartiments acides des macrophages au profit d'un phénotype de répartition homogène et diffus dans les cellules. Enfin, l'utilisation de Concanamycin A abolit également la

colocalisation des **CyC$_{7\alpha/\beta}$** avec les mycobactéries intracellulaires dans des macrophages infectés, avec pour conséquence une perte de l'activité *in cellulo* de ces composés. Ces résultats montrent ainsi le rôle prépondérant de ces compartiments acides dans le mécanisme d'action des **CyC$_{7\alpha/\beta}$**. Ce travail a donc fait l'objet d'une publication présentée dans ce manuscrit (**Article II**).

Mise en place de la CC-ABPP pour la capture directe des cibles des CyC

Par la suite, nous avons utilisé les analogues alcynes de **CyC** et d'**OX** afin de déterminer leur spectre de cibles sur *M. tb*. Ceci nous a permis de fournir la preuve du concept d'utilisation des **OX**/**CyC** comme sondes de « *click-chemistry activity-based protein profiling* », ou CC-ABPP, tout en mettant en évidence de nombreuses cibles thérapeutiques parmi les enzymes à sérine et cystéine identifiées.

Parmi ces cibles, on retrouve l'hydrolase HsaD (Rv3569c) impliquée dans le métabolisme du cholestérol chez *M. tb*. Le fait que HsaD soit essentielle pour la survie intracellulaire de *M. tb* et que sa surexpression ait été associée à des niveaux de résistance accrus vis-à-vis du **CyC$_{17}$**, nous a incité à étudier plus en détail ses interactions biochimiques et structurelles avec les **CyC**.

Ainsi, après incubation de la protéine purifiée avec différents **CyC**, une inhibition dose-dépendante a été observée, et la nature covalente de l'inhibition a été confirmée par spectrométrie de masse MALDI-TOF, digestion trypsique et analyse MS/MS des peptides obtenus. En particulier, les spectres MS/MS du peptide modifié ont confirmé la formation d'une liaison covalente entre chaque **CyC** et la sérine catalytique Ser^{114} de HsaD. Enfin, l'étude structurale des complexes entre HsaD et quatre **CyC** testés (**CyC$_{7\beta}$**, **CyC$_{8\beta}$**, **CyC$_{17}$** et **CyC$_{31}$**) a conduit à l'obtention de structures bien définies pour ces complexes avec une résolution variant de 1.62 à 2.20 Å, permettant d'identifier les interactions des composés au sein du site actif.

Cette étude, qui a donné lieu à une publication (**Article III**), a donc permis ***1)*** de valider l'approche par chimie click avec les sondes **CyC$_{yne}$** pour réaliser la capture directe d'enzymes jouant un rôle crucial dans le métabolisme des lipides ou des stéroïdes dans le cycle de vie de *M. tb*, et ***2)*** de confirmer HsaD comme cible effective de nos composés.

Expériences de capture en phase d'accumulation d'ILI – modèle *in vitro*

Une fois la démarche de capture directe de cibles par CC-ABPP validée, nous l'avons appliquée avec le **CyC_{31yne}** et l'**$HPOX_{yne}$** sur une culture de *M. abs* en conditions d'accumulation et de consommation d'ILI en utilisant le modèle d'étude *in vitro* développé au laboratoire, à savoir un milieu carencé en azote (MSM-NL) pour l'accumulation des TAG sous la forme d'ILI, et un milieu dépourvu de source de carbone (MSM Gly^-) pour la consommation de ces ILI.

Dans les deux cas, les enzymes capturées et identifiées par analyse protéomique ont ensuite été comparées aux jeux de données de ces mêmes inhibiteurs dans des conditions standards de culture. L'analyse différentielle de ces jeux de données de protéomiques a ainsi permis d'identifier 65 enzymes potentiellement impliquées dans l'accumulation des ILI.

Afin de confirmer l'implication des enzymes ainsi identifiées dans le processus de synthèse des ILI, des mutants de répression inductibles de chacune de ces cibles ont été construits avec le système CRISPR interférence. La capacité de ces souches à accumuler des ILI a ensuite été testée avec le modèle d'accumulation *in vitro* MSM-NL et les TAG accumulés ont été quantifiés par CCM quantitative. Ainsi, la répression de l'expression du gène *mab_1978c*, une probable long-chain-fatty-acyl-CoA ligase (= FadD15) a entrainé une diminution de 50% de l'accumulation des TAG par rapport à une souche sauvage ou au mutant CRISPR non induit, ce qui vient corroborer son implication dans la synthèse des ILI. Par la suite un mutant de délétion du gène *mab_1978c* a été réalisé par double recombinaison homologue avec le système *pUX1*, puis complémenté. La souche de délétion a confirmé un phénotype similaire de 50% de réduction des TAG par rapport à la souche sauvage, avec une restauration du phénotype d'accumulation pour la souche de complémentation. Enfin, la construction d'une souche reportrice de fusion *mab_1978c-sf*GFP nous a permis de confirmer la colocalisation de cette enzyme sur les ILI. L'ensemble de ces résultats confirme l'implication de MAB_1978c dans le métabolisme de synthèse des ILI.

Ainsi, l'ensemble de ces travaux concernant l'analyse des données protéomiques de capture des cibles lors de l'accumulation d'ILI ainsi que l'étude du rôle et de la localisation de MAB_1978c dans ce processus viennent valider la pertinence de la démarche de CC-ABPP appliquée. Cette étude fait l'objet d'un article en préparation qui sera soumis pour publication, et qui se trouve dans ce manuscrit (**Article IV**).

Détermination du proxysome des ILI en phase d'accumulation – modèle *in vitro*

En parallèle, afin d'établir plus précisément le protéome associé aux ILI durant les différentes étapes de leur synthèse [19], une approche de marquage de proximité avec l'ascorbate peroxydase APEX2 a été utilisée.

Dans cette étude, une protéine de fusion entre APEX2 et le domaine C-terminal de Tgs1 (MAB_3551) a été exprimée chez *M. abs* de façon à déterminer le proxysome des ILI à différents moments de leur synthèse. Pour ce faire, le modèle expérimental d'accumulation des TAG sous la forme d'ILI par carence en azote (MSM-NL) a été utilisé, et le biotine-phénol ainsi que le peroxyde d'hydrogène ont été ajoutés à 24 ou à 48h d'accumulation des ILI. Les protéines biotinylées ont ensuite été purifiées avec des billes de streptavidine et analysées par LC-MS/MS.

Cette méthode a permis d'identifier 228 protéines distinctes dont 85 ont été enrichies à 24h, 106 à 48h, et 37 sont présentes aux deux temps. Ces résultats soulignent la nature dynamique du proxysome des ILI au cours de leur synthèse et mettent en avant la nécessité d'employer une approche cinétique pour ce type d'étude.

Nous avons par la suite sélectionné 10 protéines sur ces 228 et construit des fusion GFP avec ces cibles pour vérifier leur co-localisation sur les ILI, afin de confirmer leur implication potentielle dans le processus de synthèse de ces ILI. Des mutant de délétions ont été construits par double recombinaison homologue avec un vecteur *pUX1-katG* [439]. Nous avons ainsi pu valider que les protéines MAB_1463 et MAB_3486 étaient directement impliquées dans la synthèse des ILI, leur délétion induisant une diminution significative de la quantité de TAG dans le modèle MSM-NL. A noter que 10 protéines identifiées par cette méthode APEX2 ont également été identifiées par capture avec nos inhibiteurs.

Ces données représentent le premier proxysome des ILI chez les mycobactéries et fournissent ainsi de précieuses informations sur la dynamique de ces organelles, ouvrant ainsi la voie pour la découverte de nouvelles cibles thérapeutiques pour traiter les infections mycobactériennes.

Cette étude fait l'objet d'un article qui a été soumis pour publication, et qui se trouve dans ce manuscrit (**Article V**).

Perspectives

La seconde étude actuellement en cours de finalisation, concerne l'étude du métabolisme de consommation des ILI par CC-ABPP avec les **CyC$_{yne}$** et les **OX$_{yne}$**. En effet le modèle d'accumulation des ILI par carence en azote (MSM-NL) est réversible. Une fois que les bactéries ont accumulé des ILI dans le milieu MSM-NL, le transfert de ces bactéries riches en ILI dans un milieu MSM Gly$^-$ exempt de source de carbone (= glycérol) permet d'induire la consommation des ILI. En effet, le glycérol étant la seule source de carbone du milieu MSM, son absence va forcer les bactéries à utiliser les TAG contenus dans leurs ILI pour leur propre survie.

A

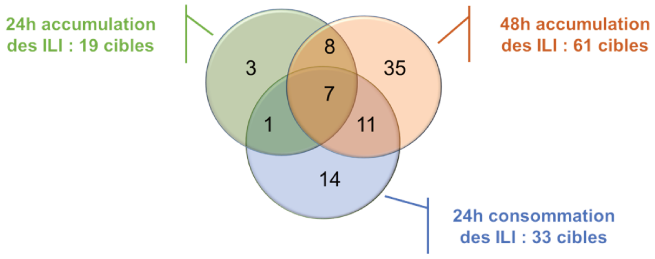

B

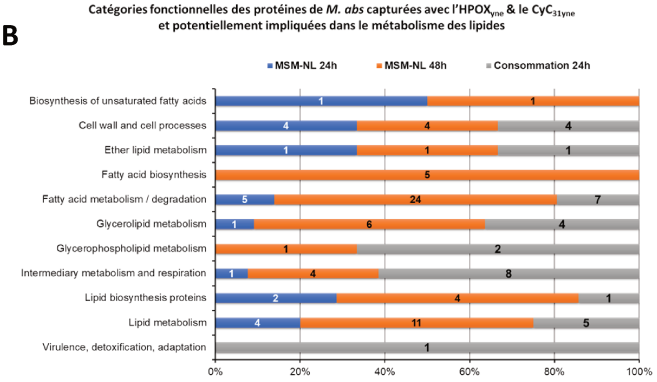

C

CyC31yne			HPOXyne									
MSM-NL 24h	MSM-NL 48h	Conso 24h	MSM-NL 24h	MSM-NL 48h	Conso 24h	Pathways	Protein IDs	Gene	*Mtb* ortholog	Sequence identity	Essentiality	Protein names
+	+	+		+		Cell wall and cell processes	B1MG94	MAB_3765	Rv3451	0.44	Non essential	Probable Cutinase Cut3
+	+	+		+		Cell wall and cell processes	B1MG92	MAB_3763	Rv2301	0.459	Non essential	Probable Cutinase Cut2
+	+	+		+		Cell wall and cell processes	B1MGD9	MAB_3809c	Rv3452	0.445	Non essential	Probable cutinase Cut4
		+				Cell wall and cell processes	B1MDM9	MAB_3272c	Rv1758	0.533	Non-Essential	Probable cutinase Cut1
	+		+	+	+	Ether lipid metabolism	B1MH77	MAB_3884	Rv2251	0.609	Non-Essential	Possible flavoprotein
				+	+	Fatty acid degradation	B1MP09	MAB_1978c	Rv2187	0.706	Non-Essential	Probable long-chain-fatty-acid--CoA ligase FadD15
	+	+		+	+	Fatty acid degradation	B1MKI3	MAB_1187c	Rv1071c	0.705	Non-Essential	Probable enoyl-CoA hydratase
	+	+		+	+	Fatty acid degradation	B1MKI8	MAB_1192c	Rv1074c	0.832	Growth-Advantage	Probable acyl-CoA thiolase FadA3
					+	Fatty acid degradation	B1MP78	MAB_2047c	Rv1869c	0.377	Non-Essential	Probable ferredoxin reductase
	+	+				Fatty acid metabolism	B1MM63	MAB_4780	Rv0636	0.54	Essential	MaoC-like dehydratase component of FasII
		+				Fatty acid metabolism	B1MDN8	MAB_3281	Rv1070c	0.341	Non-Essential	Putative enoyl-CoA hydratase/isomerase
	+	+		+	+	Fatty acid metabolism / degradation	B1MES5	MAB_3455c	Rv3556c	0.491	Non-Essential	Acetyl-CoA acetyltransferase FadA6
+	+	+	+	+	+	Glycerolipid metabolism	B1MEL1	MAB_0175	Rv0129c	0.599	Non essential	Secreted antigen 85-C FbpC
	+	+		+		Glycerolipid metabolism	B1ME07	MAB_3400	Rv3045	0.731	Non-Essential	NADP-dependent alcohol dehydrogenase C
	+	+				Glycerolipid metabolism	B1MEL2	MAB_0176	Rv3804c	0.636	Non-Essential	Antigen 85-A
	+	+				Glycerolipid metabolism	B1MEL3	MAB_0177	Rv3804c	0.604	Non-Essential	Antigen 85-A/B/C
		+				Glycerophospholipid metabolism	B1MEF9	MAB_0123	Rv3842c	0.774	Growth-Advantage	Putative glycerophosphoryl diester phosphodiesterase GlpQ1
		+			+	Glycerophospholipid metabolism	B1MGY7	MAB_0573	Rv2277c	0.304	Non-Essential	Putative glycerophosphoryl diester phosphodiesterase (GlpQ)
		+				Intermediary metabolism and respiration	B1MDM7	MAB_3270c	Rv2970c	0.559	Non-Essential	Probable lipase/esterase LipN
	+	+	+	+	+	Intermediary metabolism and respiration	B1MCC2	MAB_2814	Rv1399c	0.552	Non essential	Probable lipase LipH
	+	+		+		Intermediary metabolism and respiration	B1MER7	MAB_3447c	Rv0220	0.343	Non-Essential	Putative lipase/esterase LipC
		+				Intermediary metabolism and respiration	B1MGD3	MAB_3803c	Rv2045c	0.326	Non-Essential	Carboxylic ester hydrolase LipT
		+				Intermediary metabolism and respiration	B1MLM0	MAB_1361c	Rv1220c	0.722	Non-Essential	Putative O-methyltransferase
		+				Intermediary metabolism and respiration	B1MH22	MAB_0608	Rv3548c	0.776	Non-Essential	Probable short-chain dehydrogenase/reductase
		+				Intermediary metabolism and respiration	B1MP76	MAB_2045	Rv3473c	0.442	Non-Essential	Putative hydrolase (Alpha/beta fold)
					+	Intermediary metabolism and respiration	B1MJ05	MAB_0867c	Rv1377c	0.438	Non-Essential	Putative transferase
	+			+	+	Lipid biosynthesis proteins	B1MFX4	MAB_0425c	Rv3667	0.732	Non-Essential	Acetyl-coenzyme A synthetase (AcCoA synthetase) (Acs)
+	+	+				Lipid metabolism	B1MEL4	MAB_0178	Rv3802c	0.641	Essential	Hypothetical cutinase Cut6
+		+				Lipid metabolism	B1ML11	MAB_4587c	Rv3767c	0.46	Non essential	Putative S-adenosyl-L-methionine-dependent methyltransferase
	+			+	+	Lipid metabolism	B1MGI9	MAB_3860c	Rv0672	0.804	Non essential	Probable acyl-CoA dehydrogenase FadE8
		+				Lipid metabolism	B1ML08	MAB_4584c	Rv0145	0.469	Non-Essential	Putative S-adenosyl-L-methionine-dependent methyltransferase
					+	Lipid metabolism	B1MGQ0	MAB_0485	Rv1175c	0.274	Non-Essential	Putative oxidoreductase
		+				Virulence, detoxification, adaptation	B1MHC7	MAB_3934c	Rv0554	0.611	Non-Essential	Possible hydrolase, alpha/beta fold BpoC

Figure 43 : **(A)** Diagramme de Venn des cibles capturées avec le **CyC$_{31yne}$** et l'**HPOX$_{yne}$** lors des différentes expériences de CC-ABPP en phase d'accumulation des ILI à 24 et 48h, et en phase de consommation des ILI. **(B)** Histogramme des catégories fonctionnelles des différentes expériences de captures réalisé. **(C)** Tableau des cibles identifié comme prenant part au métabolisme des ILI.

En utilisant la même méthodologie que précédemment pour l'accumulation des ILI, des expériences de capture directe ont été effectuées avec le **CyC$_{31yne}$** et l'**HPOX$_{yne}$** 24h après la mise en consommation des ILI dans le milieu MSM Gly$^-$. Ces expériences ont conduit à

l'identification de 33 cibles statistiquement plus abondantes lors de la consommation des ILI ; parmi lesquelles, 19 ont déjà été identifiées à 24 et 48h d'accumulation dans le modèle MSM-NL (**Figure 43 A,C**).

L' étude fonctionnelle des annotations des voies métaboliques auxquelles elles prennent part en utilisant la **KEGG PATHWAY Database** (https://www.genome.jp/kegg/pathway.html) indique que ces enzymes prennent principalement part aux voies métaboliques liées à la dégradation des acide gras, suivie par le métabolisme des lipides et le métabolisme intermédiaire et la respiration (**Figure 43 B**).

MAB_1978c (FadD15) a également été identifiée lors de cette phase de consommation (**Figure 43 C**). Un mutant de répression a été construit avec le système CRISPR interférence nous permettant de réprimer le gène MAB_1978c de façon inductible. Nous avons ensuite fait accumuler des ILI à ce mutant sans induire la répression, puis la répression du gène a été induite et la culture transférée dans le milieu MSM-NL sans glycérol de façon à forcer la consommation des ILI tout en réprimant l'expression de MAB_1978c. Nous avons testé par CCM la capacité de consommation des TAG du mutant de répression, ce qui nous a permis de valider l'implication de FadD15 dans la consommation des ILI. En effet, après 48h d'accumulation dans le milieu MSM-NL et transfert dans un milieu exempt de source de carbone en induisant la répression du gène, le mutant a présenté une consommation en TAG très réduite par rapport à la souche sauvage, avec plus de 70% des TAG initialement non consommés après 24 h, soit près de 3× plus que la souche sauvage (**Figure 44**).

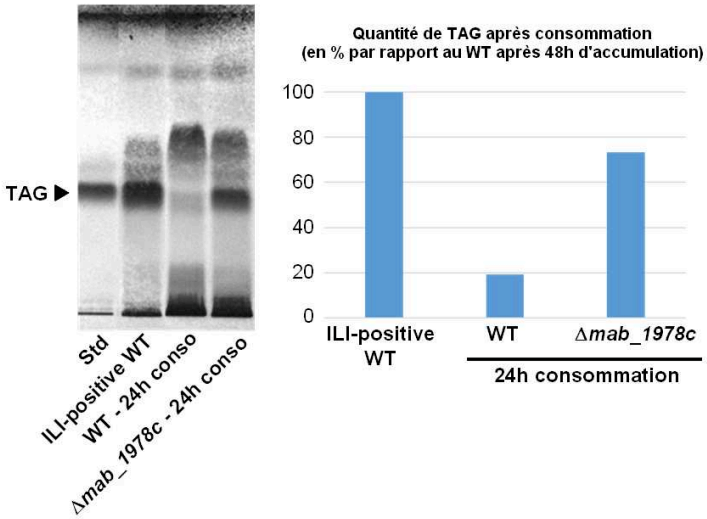

Figure 44 : Quantification des TAG chez le mutant CRISPRi Δ*mab_1978c* après 24h de mise en consommation des ILI.

L'analyse des données de protéomique de consommation des ILI a conduit à la sélection de 20 enzymes supplémentaires dont l'implication dans le processus de consommation des ILI est en cours de vérification. Pour cela, des souches de CRISPR interférence ont été construites pour chacune de ces 20 cibles et la caractérisation de leur capacité à consommer des ILI est en cours d'évaluation. L'obtention d'un phénotype clair lors de cette étude pourrait conduire par la suite à une étude similaire à celle décrite précédemment comprenant une délétion, complémentation et fusion GFP.

Un financement de thèse a été obtenu dans notre équipe, ce qui permettra d'utiliser les données protéomiques en phase de consommation des ILI chez *M. abs* ainsi que les différentes souches construites pour étudier ces protéines.

D'autre part, ce projet de thèse s'inscrit dans une continuité de méthodes et de thématiques par rapport aux travaux réalisés au cours de mon projet. En effet, de façon similaire, les sondes **CyC** et **OX** cliquables seront utilisées pour investiguer le métabolisme des ILI par CC-ABPP. Cependant, une approche similaire sera appliquée sur un système biologique différent. Un modèle d'accumulation et de consommation des ILI à l'intérieur des macrophages sera utilisé pour identifier les enzymes impliquées dans l'accumulation et la consommation des ILI en intracellulaire. Une fois ces protéines identifiées, une approche génétique de construction de mutant de répression ou de délétion sera utilisée pour valider l'implication de ces cibles dans le métabolisme des ILI intracellulaire. Des approches biochimiques et structurales pourront également être employées par la production de protéines recombinantes, afin d'étudier leur activité et leurs interactions avec nos inhibiteurs.

Références bibliographiques

[1] G.A. Hansen, Bacillus leprae, J Archiv für pathologische Anatomie und Physiologie und für klinische Medicin, 79 (1880) 32-42.

[2] W. Zopf, Die spaltpilze, Eduard Trewendt, 1885.

[3] K.B. Lehmann, Atlas und Grundriss der Bakteriologie und Lehrbuch der speziellen bakteriologischen Diagnostik, Lehmann, 1920.

[4] V.B.D. Skerman, V. McGowan, P.H.A. Sneath, Approved lists of bacterial names, International journal of systematic bacteriology, 30 (1980) 225-230.

[5] P. Chen, M. Shi, G.D. Feng, J.Y. Liu, B.J. Wang, X.D. Shi, L. Ma, X.D. Liu, Y.N. Yang, W. Dai, T.T. Liu, Y. He, J.G. Li, X.K. Hao, G. Zhao, A highly efficient Ziehl-Neelsen stain: identifying de novo intracellular Mycobacterium tuberculosis and improving detection of extracellular M. tuberculosis in cerebrospinal fluid, J Clin Microbiol, 50 (2012) 1166-1170.

[6] T.M. Shinnick, R.C. Good, Mycobacterial taxonomy, Eur J Clin Microbiol Infect Dis, 13 (1994) 884-901.

[7] R.S. Gupta, B. Lo, J. Son, Phylogenomics and comparative genomic studies robustly support division of the genus Mycobacterium into an emended genus Mycobacterium and four novel genera, Frontiers in microbiology, 9 (2018) 67.

[8] N. Rastogi, E. Legrand, C. Sola, The mycobacteria: an introduction to nomenclature and pathogenesis, Rev Sci Tech, 20 (2001) 21-54.

[9] L. Chiaradia, C. Lefebvre, J. Parra, J. Marcoux, O. Burlet-Schiltz, G. Etienne, M. Tropis, M. Daffe, Dissecting the mycobacterial cell envelope and defining the composition of the native mycomembrane, Sci Rep, 7 (2017) 12807.

[10] M. Jackson, The mycobacterial cell envelope—lipids, Cold Spring Harbor perspectives in medicine, 4 (2014).

[11] E.C. Hett, E.J. Rubin, Bacterial growth and cell division: a mycobacterial perspective, Microbiol Mol Biol Rev, 72 (2008) 126-156, table of contents.

[12] M. Daffé, P. Draper, The envelope layers of mycobacteria with reference to their pathogenicity, Advances in microbial physiology, 39 (1997) 131-203.

[13] M. Daffe, G. Etienne, The capsule of Mycobacterium tuberculosis and its implications for pathogenicity, Tuber Lung Dis, 79 (1999) 153-169.

[14] N.N. Driessen, R. Ummels, J.J. Maaskant, S.S. Gurcha, G.S. Besra, G.D. Ainge, D.S. Larsen, G.F. Painter, C.M. Vandenbroucke-Grauls, J. Geurtsen, B.J. Appelmelk, Role of phosphatidylinositol mannosides in the interaction between mycobacteria and DC-SIGN, Infect Immun, 77 (2009) 4538-4547.

[15] G. Wang, L.F. Lo, L.S. Forsberg, R.J. Maier, Helicobacter pylori peptidoglycan modifications confer lysozyme resistance and contribute to survival in the host, mBio, 3 (2012) e00409-00412.

[16] Y.M. Boudehen, L. Kremer, *Mycobacterium abscessus*, Trends Microbiol, 29 (2021) 951-952.

[17] M. Sani, E.N. Houben, J. Geurtsen, J. Pierson, K. de Punder, M. van Zon, B. Wever, S.R. Piersma, C.R. Jimenez, M. Daffe, B.J. Appelmelk, W. Bitter, N. van der Wel, P.J. Peters, Direct visualization by cryo-EM of the mycobacterial capsular layer: a labile structure containing ESX-1-secreted proteins, PLoS Pathog, 6 (2010) e1000794.

[18] M. Daffe, H. Marrakchi, Unraveling the Structure of the Mycobacterial Envelope, Microbiology spectrum, 7 (2019).

[19] WHO, Global tuberculosis report, (2021) https://www.who.int/teams/global-tuberculosis-programme/data.

[20] WHO, Global tuberculosis report, in, 2022.

[21] G. Gunther, F. van Leth, N. Altet, M. Dedicoat, R. Duarte, G. Gualano, H. Kunst, I. Muylle, V. Spinu, S. Tiberi, P. Viiklepp, C. Lange, Tbnet, Beyond multidrug-resistant tuberculosis in Europe: a TBNET study, Int J Tuberc Lung Dis, 19 (2015) 1524-1527.

[22] WHO, Global Tuberculosis Report, (2023).

[23] F. Daher Ede, G.B. da Silva, Jr., E.J. Barros, Renal tuberculosis in the modern era, The American journal of tropical medicine and hygiene, 88 (2013) 54-64.

[24] J.Y. Lee, Diagnosis and treatment of extrapulmonary tuberculosis, Tuberc Respir Dis (Seoul), 78 (2015) 47-55.

[25] R.O. Onyango, State of the globe: tracking tuberculosis is the test of time, Journal of global infectious diseases, 3 (2011) 1.

[26] D.G. Russell, Who puts the tubercle in tuberculosis?, Nat Rev Microbiol, 5 (2007) 39-47.

[27] P. Narasimhan, J. Wood, C.R. Macintyre, D. Mathai, Risk factors for tuberculosis, Pulm Med, 2013 (2013) 828939.

[28] B.R. Edlin, J.I. Tokars, M.H. Grieco, J.T. Crawford, J. Williams, E.M. Sordillo, K.R. Ong, J.O. Kilburn, S.W. Dooley, K.G. Castro, An outbreak of multidrug-resistant tuberculosis among hospitalized patients with the acquired immunodeficiency syndrome, New England Journal of Medicine, 326 (1992) 1514-1521.

[29] G. Günther, Multidrug-resistant and extensively drug-resistant tuberculosis: a review of current concepts and future challenges, Clinical medicine, 14 (2014) 279.

[30] P. Chandra, S.J. Grigsby, J.A. Philips, Immune evasion and provocation by Mycobacterium tuberculosis, Nat Rev Microbiol, 20 (2022) 750-766.

[31] D.G. Russell, C.E. Barry, 3rd, J.L. Flynn, Tuberculosis: what we don't know can, and does, hurt us, Science, 328 (2010) 852-856.

[32] S. Ahmad, Pathogenesis, immunology, and diagnosis of latent Mycobacterium tuberculosis infection, Clin Dev Immunol, 2011 (2011) 814943.

[33] S.J. Sasindran, J.B. Torrelles, Mycobacterium tuberculosis infection and inflammation: what is beneficial for the host and for the bacterium?, Frontiers in microbiology, 2 (2011) 2.

[34] J.R. Andrews, F. Noubary, R.P. Walensky, R. Cerda, E. Losina, C.R. Horsburgh, Risk of progression to active tuberculosis following reinfection with Mycobacterium tuberculosis, Clin Infect Dis, 54 (2012) 784-791.

[35] P.R. Donald, B.J. Marais, C.E. Barry, 3rd, Age and the epidemiology and pathogenesis of tuberculosis, Lancet, 375 (2010) 1852-1854.

[36] M. Pai, C. Rodrigues, Management of latent tuberculosis infection: An evidence-based approach, Lung India, 32 (2015) 205-207.

[37] J.L. Flynn, J. Chan, Tuberculosis: latency and reactivation, Infect Immun, 69 (2001) 4195-4201.

[38] P.L. Lin, J.L. Flynn, Understanding latent tuberculosis: a moving target, J Immunol, 185 (2010) 15-22.

[39] I. Caire-Brandli, A. Papadopoulos, W. Malaga, D. Marais, S. Canaan, L. Thilo, C. de Chastellier, Reversible lipid accumulation and associated division arrest of Mycobacterium

avium in lipoprotein-induced foamy macrophages may resemble key events during latency and reactivation of tuberculosis, Infect Immun, 82 (2014) 476-490.

[40] I. Mallick, P. Santucci, I. Poncin, V. Point, L. Kremer, J.F. Cavalier, S. Canaan, Intrabacterial lipid inclusions in mycobacteria: unexpected key players in survival and pathogenesis?, FEMS microbiology reviews, 45 (2021).

[41] Y.J. Ryu, Diagnosis of pulmonary tuberculosis: recent advances and diagnostic algorithms, Tuberc Respir Dis (Seoul), 78 (2015) 64-71.

[42] M.T. Rahman, A.J. Codlin, M.M. Rahman, A. Nahar, M. Reja, T. Islam, Z.Z. Qin, M.A.S. Khan, S. Banu, J. Creswell, An evaluation of automated chest radiography reading software for tuberculosis screening among public-and private-sector patients, European Respiratory Journal, 49 (2017).

[43] C.C. Boehme, P. Nabeta, D. Hillemann, M.P. Nicol, S. Shenai, F. Krapp, J. Allen, R. Tahirli, R. Blakemore, R. Rustomjee, A. Milovic, M. Jones, S.M. O'Brien, D.H. Persing, S. Ruesch-Gerdes, E. Gotuzzo, C. Rodrigues, D. Alland, M.D. Perkins, Rapid molecular detection of tuberculosis and rifampin resistance, N Engl J Med, 363 (2010) 1005-1015.

[44] D. Hillemann, C. Haasis, S. Andres, T. Behn, K. Kranzer, Validation of the FluoroType MTBDR Assay for Detection of Rifampin and Isoniazid Resistance in Mycobacterium tuberculosis Complex Isolates, J Clin Microbiol, 56 (2018) 10.1128/jcm. 00072-00018.

[45] A.N. Zeka, S. Tasbakan, C. Cavusoglu, Evaluation of the GeneXpert MTB/RIF assay for rapid diagnosis of tuberculosis and detection of rifampin resistance in pulmonary and extrapulmonary specimens, J Clin Microbiol, 49 (2011) 4138-4141.

[46] A. Zumla, A. George, V. Sharma, R.H.N. Herbert, A. Oxley, M. Oliver, The WHO 2014 global tuberculosis report—further to go, The Lancet Global Health, 3 (2015) e10-e12.

[47] J. Bernstein, W.A. Lott, B.A. Steinberg, H.L. Yale, Chemotherapy of experimental tuberculosis. V. Isonicotinic acid hydrazide (nydrazid) and related compounds, Am Rev Tuberc, 65 (1952) 357-364.

[48] Y.J. Zhang, T.R. Ioerger, C. Huttenhower, J.E. Long, C.M. Sassetti, J.C. Sacchettini, E.J. Rubin, Global assessment of genomic regions required for growth in Mycobacterium tuberculosis, PLoS Pathog, 8 (2012) e1002946.

[49] L. Fattorini, G. Piccaro, A. Mustazzolu, F. Giannoni, Targeting dormant bacilli to fight tuberculosis, Mediterr J Hematol Infect Dis, 5 (2013) e2013072.

[50] D. Damtie, D. Woldeyohannes, B. Mathewos, Review on molecular mechanism of first line antibiotic resistance in Mycobacterium tuberculosis, Mycobact Dis, 4 (2014) 174.

[51] X. Carpena, S. Loprasert, S. Mongkolsuk, J. Switala, P.C. Loewen, I. Fita, Catalase-peroxidase KatG of Burkholderia pseudomallei at 1.7A resolution, J Mol Biol, 327 (2003) 475-489.

[52] M.V. Dias, I.B. Vasconcelos, A.M. Prado, V. Fadel, L.A. Basso, W.F. de Azevedo, Jr., D.S. Santos, Crystallographic studies on the binding of isonicotinyl-NAD adduct to wild-type and isoniazid resistant 2-trans-enoyl-ACP (CoA) reductase from Mycobacterium tuberculosis, J Struct Biol, 159 (2007) 369-380.

[53] P. Sensi, History of the development of rifampin, Rev Infect Dis, 5 Suppl 3 (1983) S402-406.

[54] Y. Zhang, The magic bullets and tuberculosis drug targets, Annu Rev Pharmacol Toxicol, 45 (2005) 529-564.

[55] D. Mitchison, G. Davies, The chemotherapy of tuberculosis: past, present and future [State of the art], The international journal of tuberculosis lung disease, 16 (2012) 724-732.

[56] S.C. Vedithi, S. Malhotra, M. Das, S. Daniel, N. Kishore, A. George, S. Arumugam, L. Rajan, M. Ebenezer, D.B. Ascher, E. Arnold, T.L. Blundell, Structural Implications of Mutations Conferring Rifampin Resistance in Mycobacterium leprae, Sci Rep, 8 (2018) 5016.

[57] K. Takayama, E.L. Armstrong, K.A. Kunugi, J.O. Kilburn, Inhibition by ethambutol of mycolic acid transfer into the cell wall of Mycobacterium smegmatis, Antimicrobial agents chemotherapy, 16 (1979) 240-242.

[58] L. Zhang, Y. Zhao, Y. Gao, L. Wu, R. Gao, Q. Zhang, Y. Wang, C. Wu, F. Wu, S.S. Gurcha, N. Veerapen, S.M. Batt, W. Zhao, L. Qin, X. Yang, M. Wang, Y. Zhu, B. Zhang, L. Bi, X. Zhang, H. Yang, L.W. Guddat, W. Xu, Q. Wang, J. Li, G.S. Besra, Z. Rao, Structures of cell wall arabinosyltransferases with the anti-tuberculosis drug ethambutol, Science, 368 (2020) 1211-1219.

[59] R. Goude, A. Amin, D. Chatterjee, T.J.A.a. Parish, chemotherapy, The arabinosyltransferase EmbC is inhibited by ethambutol in Mycobacterium tuberculosis, 53 (2009) 4138-4146.

[60] M. Bassam H, S. Seemin Afshan, H. Amna, M. Arif Noor, I. Muzaffar, V. Mayank, A.R. Jamal, S. Bassel, A.Z. Ashraf, A.S. Mohamad, Respiratory diseases burden in the United Arab Emirates, (2013).

[61] M.A. Steele, R.M. Des Prez, The role of pyrazinamide in tuberculosis chemotherapy, Chest, 94 (1988) 845-850.

[62] W. Shi, X. Zhang, X. Jiang, H. Yuan, J.S. Lee, C.E. Barry, 3rd, H. Wang, W. Zhang, Y. Zhang, Pyrazinamide inhibits trans-translation in Mycobacterium tuberculosis, Science, 333 (2011) 1630-1632.

[63] Q. Sun, X. Li, L.M. Perez, W. Shi, Y. Zhang, J.C. Sacchettini, The molecular basis of pyrazinamide activity on Mycobacterium tuberculosis PanD, Nat Commun, 11 (2020) 339.

[64] E.A. Lamont, N.A. Dillon, A.D. Baughn, The Bewildering Antitubercular Action of Pyrazinamide, Microbiol Mol Biol Rev, 84 (2020) 10.1128/mmbr.00070-00019.

[65] P. Santucci, D.J. Greenwood, A. Fearns, K. Chen, H. Jiang, M.G. Gutierrez, Intracellular localisation of Mycobacterium tuberculosis affects efficacy of the antibiotic pyrazinamide, Nat Commun, 12 (2021) 3816.

[66] Y. Zhang, A. Scorpio, H. Nikaido, Z. Sun, Role of acid pH and deficient efflux of pyrazinoic acid in unique susceptibility of Mycobacterium tuberculosis to pyrazinamide, J Bacteriol, 181 (1999) 2044-2049.

[67] H.J. Corper, M.L. Cohn, The probable mechanism of streptomycin action in tuberculosis, Yale J Biol Med, 21 (1949) 181-200.

[68] P.E. Almeida Da Silva, J.C. Palomino, Molecular basis and mechanisms of drug resistance in Mycobacterium tuberculosis: classical and new drugs, J Antimicrob Chemother, 66 (2011) 1417-1430.

[69] H.C. Hinshaw, M.M. Pyle, W.H. Feldman, Streptomycin in tuberculosis, The American journal of medicine, 2 (1947) 429-435.

[70] H. Demirci, F.t. Murphy, E. Murphy, S.T. Gregory, A.E. Dahlberg, G. Jogl, A structural basis for streptomycin-induced misreading of the genetic code, Nat Commun, 4 (2013) 1355.

[71] T.A. Black, U.K. Buchwald, The pipeline of new molecules and regimens against drug-resistant tuberculosis, J Clin Tuberc Other Mycobact Dis, 25 (2021) 100285.

[72] C. Lienhardt, P. Nahid, Advances in clinical trial design for development of new TB treatments: A call for innovation, PLoS Med, 16 (2019) e1002769.

[73] T.J. Hwang, S. Dotsenko, A. Jafarov, K. Weyer, D. Falzon, K. Lunte, P. Nunn, E. Jaramillo, S. Keshavjee, D.F. Wares, Safety and availability of clofazimine in the treatment of multidrug and extensively drug-resistant tuberculosis: analysis of published guidance and meta-analysis of cohort studies, BMJ Open, 4 (2014) e004143.

[74] M. Ibrahim, K. Andries, N. Lounis, A. Chauffour, C. Truffot-Pernot, V. Jarlier, N. Veziris, Synergistic activity of R207910 combined with pyrazinamide against murine tuberculosis, Antimicrob Agents Chemother, 51 (2007) 1011-1015.

[75] N. Lounis, N. Veziris, A. Chauffour, C. Truffot-Pernot, K. Andries, V. Jarlier, Combinations of R207910 with drugs used to treat multidrug-resistant tuberculosis have the potential to shorten treatment duration, Antimicrobial agents chemotherapy, 50 (2006) 3543-3547.

[76] T.V.A. Nguyen, R.M. Anthony, A.L. Banuls, T.V.A. Nguyen, D.H. Vu, J.C. Alffenaar, Bedaquiline Resistance: Its Emergence, Mechanism, and Prevention, Clin Infect Dis, 66 (2018) 1625-1630.

[77] I.V. Peretokina, L.Y. Krylova, O.V. Antonova, M.S. Kholina, E.V. Kulagina, E.Y. Nosova, S.G. Safonova, S.E. Borisov, D.V. Zimenkov, Reduced susceptibility and resistance to bedaquiline in clinical M. tuberculosis isolates, J Infect, 80 (2020) 527-535.

[78] D. Almeida, P.J. Converse, S.Y. Li, A.M. Upton, N. Fotouhi, E.L. Nuermberger, Comparative Efficacy of the Novel Diarylquinoline TBAJ-876 and Bedaquiline against a Resistant Rv0678 Mutant in a Mouse Model of Tuberculosis, Antimicrob Agents Chemother, 65 (2021) e0141221.

[79] S.E. Cellitti, J. Shaffer, D.H. Jones, T. Mukherjee, M. Gurumurthy, B. Bursulaya, H.I. Boshoff, I. Choi, A. Nayyar, Y.S. Lee, J. Cherian, P. Niyomrattanakit, T. Dick, U.H. Manjunatha, C.E. Barry, 3rd, G. Spraggon, B.H. Geierstanger, Structure of Ddn, the deazaflavin-dependent nitroreductase from Mycobacterium tuberculosis involved in bioreductive activation of PA-824, Structure, 20 (2012) 101-112.

[80] M. Matsumoto, H. Hashizume, T. Tomishige, M. Kawasaki, H. Tsubouchi, H. Sasaki, Y. Shimokawa, M. Komatsu, OPC-67683, a nitro-dihydro-imidazooxazole derivative with promising action against tuberculosis in vitro and in mice, PLoS Med, 3 (2006) e466.

[81] X. Chen, H. Hashizume, T. Tomishige, I. Nakamura, M. Matsuba, M. Fujiwara, R. Kitamoto, E. Hanaki, Y. Ohba, M. Matsumoto, Delamanid Kills Dormant Mycobacteria In Vitro and in a Guinea Pig Model of Tuberculosis, Antimicrob Agents Chemother, 61 (2017) 10.1128/aac. 02402-02416.

[82] M. Fujiwara, M. Kawasaki, N. Hariguchi, Y. Liu, M. Matsumoto, Mechanisms of resistance to delamanid, a drug for Mycobacterium tuberculosis, Tuberculosis, 108 (2018) 186-194.

[83] D. Rifat, S.-Y. Li, T. Ioerger, K. Shah, J.-P. Lanoix, J. Lee, G. Bashiri, J. Sacchettini, E. Nuermberger, Mutations in fbiD (Rv2983) as a novel determinant of resistance to pretomanid and delamanid in Mycobacterium tuberculosis, Antimicrobial agents chemotherapy, 65 (2020) 10.1128/aac. 01948-01920.

[84] E. Nuermberger, S. Tyagi, R. Tasneen, K.N. Williams, D. Almeida, I. Rosenthal, J.H. Grosset, Powerful bactericidal and sterilizing activity of a regimen containing PA-824, moxifloxacin, and pyrazinamide in a murine model of tuberculosis, Antimicrob Agents Chemother, 52 (2008) 1522-1524.

[85] J. Xu, S.-Y. Li, D.V. Almeida, R. Tasneen, K. Barnes-Boyle, P.J. Converse, A.M. Upton, K. Mdluli, N. Fotouhi, E.L. Nuermberger, Contribution of pretomanid to novel regimens containing bedaquiline with either linezolid or moxifloxacin and pyrazinamide in murine models of tuberculosis, Antimicrobial agents chemotherapy, 63 (2019) 10.1128/aac. 00021-00019.

[86] J. Rock, Tuberculosis drug discovery in the CRISPR era, PLoS Pathog, 15 (2019) e1007975.

[87] N. Bourgeois-Nicolaos, O. Piriou, M. Butel, F. Doucet-Populaire, Le linézolide: activité antibactérienne, intérêts cliniques et résistance, in: Annales de Biologie Clinique, 2006, pp. 549-564.

[88] T. Zhu, S.O. Friedrich, A. Diacon, R.S. Wallis, Population pharmacokinetic/pharmacodynamic analysis of the bactericidal activities of sutezolid (PNU-100480) and its major metabolite against intracellular Mycobacterium tuberculosis in ex vivo whole-blood cultures of patients with pulmonary tuberculosis, Antimicrob Agents Chemother, 58 (2014) 3306-3311.

[89] K. Williams, C. Stover, T. Zhu, R. Tasneen, S. Tyagi, J. Grosset, E. Nuermberger, Promising antituberculosis activity of the oxazolidinone PNU-100480 relative to that of linezolid in a murine model, Antimicrobial agents chemotherapy, 53 (2009) 1314-1319.

[90] R. Tasneen, F. Betoudji, S. Tyagi, S.Y. Li, K. Williams, P.J. Converse, V. Dartois, T. Yang, C.M. Mendel, K.E. Mdluli, E.L. Nuermberger, Contribution of Oxazolidinones to the Efficacy of Novel Regimens Containing Bedaquiline and Pretomanid in a Mouse Model of Tuberculosis, Antimicrob Agents Chemother, 60 (2016) 270-277.

[91] R.S. Wallis, W. Jakubiec, V. Kumar, G. Bedarida, A. Silvia, D. Paige, T. Zhu, M. Mitton-Fry, L. Ladutko, S. Campbell, P.F. Miller, Biomarker-assisted dose selection for safety and efficacy in early development of PNU-100480 for tuberculosis, Antimicrob Agents Chemother, 55 (2011) 567-574.

[92] R.S. Wallis, R. Dawson, S.O. Friedrich, A. Venter, D. Paige, T. Zhu, A. Silvia, J. Gobey, C. Ellery, Y. Zhang, K. Eisenach, P. Miller, A.H. Diacon, Mycobactericidal activity of sutezolid (PNU-100480) in sputum (EBA) and blood (WBA) of patients with pulmonary tuberculosis, PLoS One, 9 (2014) e94462.

[93] Y. Choi, S.W. Lee, A. Kim, K. Jang, H. Nam, Y.L. Cho, K.S. Yu, I.J. Jang, J.Y. Chung, Safety, tolerability and pharmacokinetics of 21 day multiple oral administration of a new oxazolidinone antibiotic, LCB01-0371, in healthy male subjects, J Antimicrob Chemother, 73 (2018) 183-190.

[94] J. Mencarini, M. Spinicci, L. Zammarchi, A. Bartoloni, Tuberculosis in the European Region, Curr Trop Med Rep, (2023) 1-6.

[95] T. Christophe, M. Jackson, H.K. Jeon, D. Fenistein, M. Contreras-Dominguez, J. Kim, A. Genovesio, J.-P. Carralot, F. Ewann, E.H. Kim, High content screening identifies decaprenyl-phosphoribose 2' epimerase as a target for intracellular antimycobacterial inhibitors, PLoS pathogens, 5 (2009) e1000645.

[96] V. Makarov, G. Manina, K. Mikusova, U. Mollmann, O. Ryabova, B. Saint-Joanis, N. Dhar, M.R. Pasca, S. Buroni, A.P. Lucarelli, A. Milano, E. De Rossi, M. Belanova, A. Bobovska, P. Dianiskova, J. Kordulakova, C. Sala, E. Fullam, P. Schneider, J.D. McKinney, P. Brodin, T. Christophe, S. Waddell, P. Butcher, J. Albrethsen, I. Rosenkrands, R. Brosch, V. Nandi, S. Bharath, S. Gaonkar, R.K. Shandil, V. Balasubramanian, T. Balganesh, S. Tyagi, J. Grosset, G.

Riccardi, S.T. Cole, Benzothiazinones kill Mycobacterium tuberculosis by blocking arabinan synthesis, Science, 324 (2009) 801-804.

[97] M.E. Ramey, F. Kaya, A.A. Bauman, L.M. Massoudi, J.P. Sarathy, M.D. Zimmerman, D.W.L. Scott, A.M. Job, J.A. Miller-Dawson, B.K. Podell, M.A. Lyons, V. Dartois, A.J. Lenaerts, G.T. Robertson, Drug distribution and efficacy of the DprE1 inhibitor BTZ-043 in the C3HeB/FeJ mouse tuberculosis model, Antimicrob Agents Chemother, 67 (2023) e0059723.

[98] M. Imran, S.A. Khan, S.M.B. Asdaq, M. Almehmadi, O. Abdulaziz, M. Kamal, M.K. Alshammari, L.I. Alsubaihi, K.H. Hussain, A.S. Alharbi, An insight into the discovery, clinical studies, compositions, and patents of macozinone: A drug targeting the DprE1 enzyme of Mycobacterium tuberculosis, Journal of Infection Public Health, (2022).

[99] M. Moore, J.B. Frerichs, An unusual acid-fast infection of the knee with subcutaneous, abscess-like lesions of the gluteal region; report of a case with a study of the organism, Mycobacterium abscessus, n. sp, J Invest Dermatol, 20 (1953) 133-169.

[100] I.K. Park, K.N. Olivier, Nontuberculous mycobacteria in cystic fibrosis and non-cystic fibrosis bronchiectasis, Seminars in respiratory and critical care medicine, 36 (2015) 217-224.

[101] D.E. Griffith, T. Aksamit, B.A. Brown-Elliott, A. Catanzaro, C. Daley, F. Gordin, S.M. Holland, R. Horsburgh, G. Huitt, M.F. Iademarco, M. Iseman, K. Olivier, S. Ruoss, C.F. von Reyn, R.J. Wallace, Jr., K. Winthrop, A.T.S.M.D. Subcommittee, S. American Thoracic, A. Infectious Disease Society of, An official ATS/IDSA statement: diagnosis, treatment, and prevention of nontuberculous mycobacterial diseases, American journal of respiratory and critical care medicine, 175 (2007) 367-416.

[102] T.d. Adékambi, M. Reynaud-Gaubert, G. Greub, M.-J. Gevaudan, B. La Scola, D. Raoult, M. Drancourt, Amoebal coculture of “Mycobacterium massiliense” sp. nov. from the sputum of a patient with hemoptoic pneumonia, Journal of clinical microbiology, 42 (2004) 5493-5501.

[103] T. Adékambi, P. Berger, D. Raoult, M. Drancourt, rpoB gene sequence-based characterization of emerging non-tuberculous mycobacteria with descriptions of Mycobacterium bolletii sp. nov., Mycobacterium phocaicum sp. nov. and Mycobacterium aubagnense sp. nov, International journal of systematic evolutionary microbiology, 56 (2006) 133-143.

[104] T. Adekambi, M. Sassi, J. Van Ingen, M. Drancourt, Reinstating Mycobacterium massiliense and Mycobacterium bolletii as species of the Mycobacterium abscessus complex, International journal of systematic evolutionary microbiology, 67 (2017) 2726-2730.

[105] M.D. Johansen, J.L. Herrmann, L. Kremer, Non-tuberculous mycobacteria and the rise of Mycobacterium abscessus, Nat Rev Microbiol, 18 (2020) 392-407.

[106] A. Bernut, J.L. Herrmann, K. Kissa, J.F. Dubremetz, J.L. Gaillard, G. Lutfalla, L. Kremer, Mycobacterium abscessus cording prevents phagocytosis and promotes abscess formation, Proceedings of the National Academy of Sciences of the United States of America, 111 (2014) E943-952.

[107] A.L. Roux, A. Viljoen, A. Bah, R. Simeone, A. Bernut, L. Laencina, T. Deramaudt, M. Rottman, J.L. Gaillard, L. Majlessi, R. Brosch, F. Girard-Misguich, I. Vergne, C. de Chastellier, L. Kremer, J.L. Herrmann, The distinct fate of smooth and rough Mycobacterium abscessus variants inside macrophages, Open biology, 6 (2016).

[108] E. Catherinot, J. Clarissou, G. Etienne, F. Ripoll, J.F. Emile, M. Daffe, C. Perronne, C. Soudais, J.L. Gaillard, M. Rottman, Hypervirulence of a rough variant of the Mycobacterium abscessus type strain, Infect Immun, 75 (2007) 1055-1058.

[109] B.E. Jönsson, M. Gilljam, A. Lindblad, M. Ridell, A.E. Wold, C. Welinder-Olsson, Molecular epidemiology of Mycobacterium abscessus, with focus on cystic fibrosis, Journal of clinical microbiology, 45 (2007) 1497-1504.

[110] A. Pawlik, G. Garnier, M. Orgeur, P. Tong, A. Lohan, F. Le Chevalier, G. Sapriel, A.L. Roux, K. Conlon, N. Honoré, Identification and characterization of the genetic changes responsible for the characteristic smooth-to-rough morphotype alterations of clinically persistent M ycobacterium abscessus, Molecular microbiology, 90 (2013) 612-629.

[111] R. Nessar, E. Cambau, J.M. Reyrat, A. Murray, B. Gicquel, Mycobacterium abscessus: a new antibiotic nightmare, J Antimicrob Chemother, 67 (2012) 810-818.

[112] H. Medjahed, J.L. Gaillard, J.M. Reyrat, Mycobacterium abscessus: a new player in the mycobacterial field, Trends Microbiol, 18 (2010) 117-123.

[113] K.N. Olivier, D.J. Weber, R.J. Wallace, Jr., A.R. Faiz, J.H. Lee, Y. Zhang, B.A. Brown-Elliot, A. Handler, R.W. Wilson, M.S. Schechter, L.J. Edwards, S. Chakraborti, M.R. Knowles, G. Nontuberculous Mycobacteria in Cystic Fibrosis Study, Nontuberculous mycobacteria. I:

multicenter prevalence study in cystic fibrosis, American journal of respiratory and critical care medicine, 167 (2003) 828-834.

[114] A.-L. Roux, J.-L. Herrmann, J.-L. Gaillard, M. Rottman, Mycobacterium abscessus, pathogène émergent dans la mucoviscidose, Immuno-analyse Biologie Spécialisée, 25 (2010) 26-33.

[115] M.R. Holt, S. Kasperbauer, Management of extrapulmonary nontuberculous mycobacterial infections, in: Seminars in respiratory and critical care medicine, Thieme Medical Publishers, 2018, pp. 399-410.

[116] M.R. Lee, W.H. Sheng, C.C. Hung, C.J. Yu, L.N. Lee, P.R. Hsueh, Mycobacterium abscessus Complex Infections in Humans, Emerg Infect Dis, 21 (2015) 1638-1646.

[117] S.A. Leon-Icaza, S. Bagayoko, R. Verge, N. Iakobachvili, C. Ferrand, T. Aydogan, C. Bernard, A. Sanchez Dafun, M. Murris-Espin, J. Mazieres, P.J. Bordignon, S. Mazeres, P. Bernes-Lasserre, V. Rame, J.M. Lagarde, J. Marcoux, M.P. Bousquet, C. Chalut, C. Guilhot, H. Clevers, P.J. Peters, V. Molle, G. Lugo-Villarino, K. Cam, L. Berry, E. Meunier, C. Cougoule, Druggable redox pathways against Mycobacterium abscessus in cystic fibrosis patient-derived airway organoids, PLoS Pathog, 19 (2023) e1011559.

[118] A. Bernut, J.L. Herrmann, D. Ordway, L. Kremer, The Diverse Cellular and Animal Models to Decipher the Physiopathological Traits of Mycobacterium abscessus Infection, Front Cell Infect Microbiol, 7 (2017) 100.

[119] F. Mougari, L. Guglielmetti, L. Raskine, I. Sermet-Gaudelus, N. Veziris, E. Cambau, Infections caused by Mycobacterium abscessus: epidemiology, diagnostic tools and treatment, Expert Rev Anti Infect Ther, 14 (2016) 1139-1154.

[120] J.F. Tomashefski, Jr., R.C. Stern, C.A. Demko, C.F. Doershuk, Nontuberculous mycobacteria in cystic fibrosis. An autopsy study, American journal of respiratory and critical care medicine, 154 (1996) 523-528.

[121] D.E. Griffith, T.R. Aksamit, Understanding nontuberculous mycobacterial lung disease: it's been a long time coming, FResearch, 5 (2016).

[122] A.R. Cullen, C.L. Cannon, E.J. Mark, A.A. Colin, Mycobacterium abscessus infection in cystic fibrosis. Colonization or infection?, American journal of respiratory and critical care medicine, 161 (2000) 641-645.

[123] R. Wallace Jr, Diagnosis and treatment of disease caused by nontuberculous mycobacteria, American journal of respiratory and critical care medicine, 156 (1997) s1-s25.

[124] H. Sohn, H.J. Kim, J.M. Kim, O. Jung Kwon, W.J. Koh, S.J. Shin, High virulent clinical isolates of Mycobacterium abscessus from patients with the upper lobe fibrocavitary form of pulmonary disease, Microb Pathog, 47 (2009) 321-328.

[125] E.R. Rhoades, A.S. Archambault, R. Greendyke, F.F. Hsu, C. Streeter, T.F. Byrd, Mycobacterium abscessus Glycopeptidolipids mask underlying cell wall phosphatidyl-myo-inositol mannosides blocking induction of human macrophage TNF-alpha by preventing interaction with TLR2, J Immunol, 183 (2009) 1997-2007.

[126] I.K. Park, A.P. Hsu, H. Tettelin, S.J. Shallom, S.K. Drake, L. Ding, U.I. Wu, N. Adamo, D.R. Prevots, K.N. Olivier, S.M. Holland, E.P. Sampaio, A.M. Zelazny, Clonal Diversification and Changes in Lipid Traits and Colony Morphology in Mycobacterium abscessus Clinical Isolates, J Clin Microbiol, 53 (2015) 3438-3447.

[127] L.J. Caverly, S.M. Caceres, C. Fratelli, C. Happoldt, K.M. Kidwell, K.C. Malcolm, J.A. Nick, D.P. Nichols, Mycobacterium abscessus morphotype comparison in a murine model, PLoS One, 10 (2015) e0117657.

[128] S.T. Howard, E. Rhoades, J. Recht, X. Pang, A. Alsup, R. Kolter, C.R. Lyons, T.F. Byrd, Spontaneous reversion of Mycobacterium abscessus from a smooth to a rough morphotype is associated with reduced expression of glycopeptidolipid and reacquisition of an invasive phenotype, Microbiology, 152 (2006) 1581-1590.

[129] A. Viljoen, F. Viela, L. Kremer, Y.F. Dufrêne, Fast chemical force microscopy demonstrates that glycopeptidolipids define nanodomains of varying hydrophobicity on mycobacteria, Nanoscale Horizons, 5 (2020) 944-953.

[130] B. Jönsson, M. Ridell, A.E. Wold, Phagocytosis and cytokine response to rough and smooth colony variants of M ycobacterium abscessus by human peripheral blood mononuclear cells, Apmis, 121 (2013) 45-55.

[131] T.F. Byrd, C.R. Lyons, Preliminary characterization of a Mycobacterium abscessus mutant in human and murine models of infection, Infect Immun, 67 (1999) 4700-4707.

[132] J.B. Lyczak, C.L. Cannon, G.B. Pier, Lung infections associated with cystic fibrosis, Clin Microbiol Rev, 15 (2002) 194-222.

[133] D.C. Gadsby, P. Vergani, L. Csanady, The ABC protein turned chloride channel whose failure causes cystic fibrosis, Nature, 440 (2006) 477-483.

[134] T.C. Hwang, K.L. Kirk, The CFTR ion channel: gating, regulation, and anion permeation, Cold Spring Harb Perspect Med, 3 (2013) a009498.

[135] K. Fujita, Y. Ito, T. Hirai, K. Maekawa, S. Imai, S. Tatsumi, A. Niimi, Y. Iinuma, S. Ichiyama, M. Mishima, Genetic relatedness of mycobacterium avium-intracellulare complex isolates from patients with pulmonary mac disease and their residential soils, Clinical Microbiology Infection, 19 (2013) 537-541.

[136] C. Dupont, Étude fonctionnelle et intérêt thérapeutique des MmpL chez Mycobacterium abscessus, in, Université Paris-Saclay (ComUE), 2016.

[137] H. Heijerman, Infection and inflammation in cystic fibrosis: a short review, J Cyst Fibros, 4 Suppl 2 (2005) 3-5.

[138] G. John, A.O. Yildirim, B.K. Rubin, D.C. Gruenert, M.O. Henke, TLR-4–mediated innate immunity is reduced in cystic fibrosis airway cells, American journal of respiratory cell molecular biology, 42 (2010) 424-431.

[139] R.A. Floto, K.N. Olivier, L. Saiman, C.L. Daley, J.-L. Herrmann, J.A. Nick, P.G. Noone, D. Bilton, P. Corris, R.L. Gibson, US Cystic Fibrosis Foundation and European Cystic Fibrosis Society consensus recommendations for the management of non-tuberculous mycobacteria in individuals with cystic fibrosis, Thorax, 71 (2016) i1-i22.

[140] J.B. Orens, M. Estenne, S. Arcasoy, J.V. Conte, P. Corris, J.J. Egan, T. Egan, S. Keshavjee, C. Knoop, R. Kotloff, International guidelines for the selection of lung transplant candidates: 2006 update—a consensus report from the Pulmonary Scientific Council of the International Society for Heart and Lung Transplantation, The Journal of heart lung transplantation, 25 (2006) 745-755.

[141] A.L. Roux, E. Catherinot, F. Ripoll, N. Soismier, E. Macheras, S. Ravilly, G. Bellis, M.A. Vibet, E. Le Roux, L. Lemonnier, C. Gutierrez, V. Vincent, B. Fauroux, M. Rottman, D. Guillemot, J.L. Gaillard, O.M.A.G. Jean-Louis Herrmann for the, Multicenter study of prevalence of nontuberculous mycobacteria in patients with cystic fibrosis in france, J Clin Microbiol, 47 (2009) 4124-4128.

[142] R.C. Lopeman, J. Harrison, M. Desai, J.A.G. Cox, Mycobacterium abscessus: Environmental Bacterium Turned Clinical Nightmare, Microorganisms, 7 (2019) 90.

[143] J. van Ingen, M.J. Boeree, D. van Soolingen, J.W. Mouton, Resistance mechanisms and drug susceptibility testing of nontuberculous mycobacteria, Drug Resist Updat, 15 (2012) 149-161.

[144] S.H. Lee, H.K. Yoo, S.H. Kim, W.J. Koh, C.K. Kim, Y.K. Park, H.J. Kim, The drug resistance profile of Mycobacterium abscessus group strains from Korea, Ann Lab Med, 34 (2014) 31-37.

[145] G.M. Eliopoulos, P. Huovinen, Resistance to Trimethoprim-Sulfamethoxazole, Clinical Infectious Diseases, 32 (2001) 1608-1614.

[146] C.S. Haworth, J. Banks, T. Capstick, A.J. Fisher, T. Gorsuch, I.F. Laurenson, A. Leitch, M.R. Loebinger, H.J. Milburn, M. Nightingale, P. Ormerod, D. Shingadia, D. Smith, N. Whitehead, R. Wilson, R.A. Floto, British Thoracic Society guidelines for the management of non-tuberculous mycobacterial pulmonary disease (NTM-PD), Thorax, 72 (2017) ii1-ii64.

[147] R.N. Jones, Review of the in vitro spectrum of activity of imipenem, Am J Med, 78 (1985) 22-32.

[148] W.C. Hellinger, N.S. Brewer, Imipenem, Mayo Clin Proc, 66 (1991) 1074-1081.

[149] M.S. Ramirez, M.E. Tolmasky, Amikacin: Uses, Resistance, and Prospects for Inhibition, Molecules, 22 (2017) 2267.

[150] T. Prammananan, P. Sander, B.A. Brown, K. Frischkorn, G.O. Onyi, Y. Zhang, E.C. Böttger, R.J. Wallace Jr, A single 16S ribosomal RNA substitution is responsible for resistance to amikacin and other 2-deoxystreptamine aminoglycosides in Mycobacterium abscessus and Mycobacterium chelonae, Journal of Infectious diseases, 177 (1998) 1573-1581.

[151] G.E. Stein, T. Babinchak, Tigecycline: an update, Diagn Microbiol Infect Dis, 75 (2013) 331-336.

[152] Y. Cai, N. Bai, X. Liu, B. Liang, J. Wang, R. Wang, Tigecycline: Alone or in combination?, Infect Dis (Lond), 48 (2016) 491-502.

[153] Q. Kaewpoowat, L. Ostrosky-Zeichner, Tigecycline : a critical safety review, Expert Opin Drug Saf, 14 (2015) 335-342.

[154] S. Yaghoubi, A.O. Zekiy, M. Krutova, M. Gholami, E. Kouhsari, M. Sholeh, Z. Ghafouri, F. Maleki, Tigecycline antibacterial activity, clinical effectiveness, and mechanisms and

epidemiology of resistance: narrative review, Eur J Clin Microbiol Infect Dis, 41 (2022) 1003-1022.

[155] S. Luthra, A. Rominski, P. Sander, The Role of Antibiotic-Target-Modifying and Antibiotic-Modifying Enzymes in Mycobacterium abscessus Drug Resistance, Front Microbiol, 9 (2018) 2179.

[156] J.V. Philley, R.J. Wallace Jr, J.L. Benwill, V. Taskar, B.A. Brown-Elliott, F. Thakkar, T.R. Aksamit, D.E. Griffith, Preliminary results of bedaquiline as salvage therapy for patients with nontuberculous mycobacterial lung disease, Chest, 148 (2015) 499-506.

[157] M.L. Wu, D.B. Aziz, V. Dartois, T. Dick, NTM drug discovery: status, gaps and the way forward, Drug Discov Today, 23 (2018) 1502-1519.

[158] J.L. Low, M.L. Wu, D.B. Aziz, B. Laleu, T. Dick, Screening of TB Actives for Activity against Nontuberculous Mycobacteria Delivers High Hit Rates, Front Microbiol, 8 (2017) 1539.

[159] D.M. Livermore, Linezolid in vitro: mechanism and antibacterial spectrum, J Antimicrob Chemother, 51 Suppl 2 (2003) ii9-16.

[160] T.S. Kim, J.H. Choe, Y.J. Kim, C.S. Yang, H.J. Kwon, J. Jeong, G. Kim, D.E. Park, E.K. Jo, Y.L. Cho, J. Jang, Activity of LCB01-0371, a Novel Oxazolidinone, against Mycobacterium abscessus, Antimicrob Agents Chemother, 61 (2017) 10.1128/aac. 02752-02716.

[161] D.B. Aziz, J.L. Low, M.-L. Wu, M. Gengenbacher, J.W. Teo, V. Dartois, T. Dick, Rifabutin is active against Mycobacterium abscessus complex, Antimicrobial agents chemotherapy, 61 (2017) 10.1128/aac. 00155-00117.

[162] A. Viljoen, C. Raynaud, M.D. Johansen, F. Roquet-Baneres, J.L. Herrmann, W. Daher, L. Kremer, Verapamil Improves the Activity of Bedaquiline against Mycobacterium abscessus In Vitro and in Macrophages, Antimicrob Agents Chemother, 63 (2019) 10.1128/aac. 00705-00719.

[163] C. Dupont, A. Viljoen, S. Thomas, F. Roquet-Banères, J.-L. Herrmann, K. Pethe, L. Kremer, Bedaquiline inhibits the ATP synthase in Mycobacterium abscessus and is effective in infected zebrafish, Antimicrobial agents chemotherapy, 61 (2017) 10.1128/aac. 01225-01217.

[164] W.Y.-K. Chan, P.-L. Ho, K.K.-W. To, A.Y.-L. Lam, K.W.-Y. Ho, T.-W. Lau, N.L.-W. So, S.-Y. Ha, A child with acute myeloid leukemia complicated by calcaneal osteomyelitis due to

Mycobacterium abscessus infection after induction chemotherapy successfully salvaged with bedaquiline and clofazimine, International Journal of Infectious Diseases, 103 (2021) 9-12.

[165] J. Lee, N. Ammerman, A. Agarwal, M. Naji, S.Y. Li, E. Nuermberger, Differential In Vitro Activities of Individual Drugs and Bedaquiline-Rifabutin Combinations against Actively Multiplying and Nutrient-Starved Mycobacterium abscessus, Antimicrob Agents Chemother, 65 (2021) 10.1128/aac. 02179-02120.

[166] T. Gao, C. Yao, Y. Shang, R. Su, X. Zhang, W. Ren, S. Li, W. Shu, Y. Pang, Q. Li, Antimicrobial Effect of Oxazolidinones and Its Synergistic Effect with Bedaquiline Against Mycobacterium abscessus Complex, Infect Drug Resist, 16 (2023) 279-287.

[167] M.M. Ruth, J.J. Sangen, K. Remmers, L.J. Pennings, E. Svensson, R.E. Aarnoutse, S.M. Zweijpfenning, W. Hoefsloot, S. Kuipers, C. Magis-Escurra, A bedaquiline/clofazimine combination regimen might add activity to the treatment of clinically relevant non-tuberculous mycobacteria, Journal of Antimicrobial Chemotherapy, 74 (2019) 935-943.

[168] V.C. Barry, J.G. Belton, M.L. Conalty, J.M. Denneny, D.W. Edward, J.F. O'Sullivan, D. Twomey, F. Winder, A new series of phenazines (rimino-compounds) with high antituberculosis activity, Nature, 179 (1957) 1013-1015.

[169] R. Mirnejad, A. Asadi, S. Khoshnood, H. Mirzaei, M. Heidary, L. Fattorini, A. Ghodousi, D. Darban-Sarokhalil, Clofazimine: A useful antibiotic for drug-resistant tuberculosis, Biomed Pharmacother, 105 (2018) 1353-1359.

[170] A. Van Deun, A.K. Maug, M.A. Salim, P.K. Das, M.R. Sarker, P. Daru, H.L. Rieder, Short, highly effective, and inexpensive standardized treatment of multidrug-resistant tuberculosis, American journal of respiratory and critical care medicine, 182 (2010) 684-692.

[171] C.L. Daley, J.M. Iaccarino, C. Lange, E. Cambau, R.J. Wallace Jr, C. Andrejak, E.C. Böttger, J. Brozek, D.E. Griffith, L. Guglielmetti, Treatment of nontuberculous mycobacterial pulmonary disease: an official ATS/ERS/ESCMID/IDSA clinical practice guideline, Clinical Infectious Diseases, 71 (2020) e1-e36.

[172] B. Schulthess, F.N. Akdogan Kittana, R. Homke, P. Sander, In Vitro Bedaquiline and Clofazimine Susceptibility Testing in Mycobacterium abscessus, Antimicrob Agents Chemother, 66 (2022) e0234621.

[173] F.C. Adler-Shohet, J. Singh, D. Nieves, N. Ashouri, M.T. Tran, M.C. Flores, A. Arrieta, Safety and Tolerability of Clofazimine in a Cohort of Children With Odontogenic Mycobacterium abscessus Infection, J Pediatric Infect Dis Soc, 9 (2020) 483-485.

[174] A. Pinapala, L.J. Koh, K.H. Ng, P.A. Tambyah, H.K. Yap, Clofazimine in Mycobacterium abscessus peritonitis: A pediatric case report, Perit Dial Int, 41 (2021) 104-109.

[175] B. Yang, B.W. Jhun, S.M. Moon, H. Lee, H.Y. Park, K. Jeon, D.H. Kim, S.Y. Kim, S.J. Shin, C.L. Daley, W.J. Koh, Clofazimine-Containing Regimen for the Treatment of Mycobacterium abscessus Lung Disease, Antimicrob Agents Chemother, 61 (2017) 10.1128/aac. 02052-02016.

[176] T. Yano, S. Kassovska-Bratinova, J.S. Teh, J. Winkler, K. Sullivan, A. Isaacs, N.M. Schechter, H. Rubin, Reduction of clofazimine by mycobacterial type 2 NADH:quinone oxidoreductase: a pathway for the generation of bactericidal levels of reactive oxygen species, J Biol Chem, 286 (2011) 10276-10287.

[177] A. Heikal, K. Hards, C.Y. Cheung, A. Menorca, M.S. Timmer, B.L. Stocker, G.M. Cook, Activation of type II NADH dehydrogenase by quinolinequinones mediates antitubercular cell death, J Antimicrob Chemother, 71 (2016) 2840-2847.

[178] K.L. Leach, S.J. Brickner, M.C. Noe, P.F. Miller, Linezolid, the first oxazolidinone antibacterial agent, Ann N Y Acad Sci, 1222 (2011) 49-54.

[179] S.J. Brickner, D.K. Hutchinson, M.R. Barbachyn, P.R. Manninen, D.A. Ulanowicz, S.A. Garmon, K.C. Grega, S.K. Hendges, D.S. Toops, C.W. Ford, G.E. Zurenko, Synthesis and antibacterial activity of U-100592 and U-100766, two oxazolidinone antibacterial agents for the potential treatment of multidrug-resistant gram-positive bacterial infections, J Med Chem, 39 (1996) 673-679.

[180] J.A. Ippolito, Z.F. Kanyo, D. Wang, F.J. Franceschi, P.B. Moore, T.A. Steitz, E.M. Duffy, Crystal structure of the oxazolidinone antibiotic linezolid bound to the 50S ribosomal subunit, J Med Chem, 51 (2008) 3353-3356.

[181] K. Tsai, V. Stojkovic, D.J. Lee, I.D. Young, T. Szal, D. Klepacki, N. Vazquez-Laslop, A.S. Mankin, J.S. Fraser, D.G. Fujimori, Structural basis for context-specific inhibition of translation by oxazolidinone antibiotics, Nat Struct Mol Biol, 29 (2022) 162-171.

[182] D.N. Wilson, F. Schluenzen, J.M. Harms, A.L. Starosta, S.R. Connell, P. Fucini, The oxazolidinone antibiotics perturb the ribosomal peptidyl-transferase center and effect tRNA

positioning, Proceedings of the National Academy of Sciences of the United States of America, 105 (2008) 13339-13344.

[183] D.A. Negatu, W.W. Aragaw, V. Dartois, T. Dick, Characterization of In Vitro Resistance to Linezolid in Mycobacterium abscessus, Microbiology spectrum, 11 (2023) e0219923.

[184] E.H. Cho, H.J. Huh, D.J. Song, S.H. Lee, C.K. Kim, S.Y. Shin, C.S. Ki, B.W. Jhun, S.M. Moon, O.J. Kwon, W.J. Koh, N.Y. Lee, Drug susceptibility patterns of Mycobacterium abscessus and Mycobacterium massiliense isolated from respiratory specimens, Diagn Microbiol Infect Dis, 93 (2019) 107-111.

[185] A.W. Baker, E.K. Maziarz, S.S. Lewis, J.E. Stout, D.J. Anderson, P.K. Smith, J.N. Schroder, M.A. Daneshmand, B.D. Alexander, R.J. Wallace, D.J. Sexton, C.R. Wolfe, Invasive Mycobacterium abscessus Complex Infection After Cardiac Surgery: Epidemiology, Management, and Clinical Outcomes, Clin Infect Dis, 72 (2021) 1232-1240.

[186] J. Chen, L. Zhao, Y. Mao, M. Ye, Q. Guo, Y. Zhang, L. Xu, Z. Zhang, B. Li, H. Chu, Clinical Efficacy and Adverse Effects of Antibiotics Used to Treat Mycobacterium abscessus Pulmonary Disease, Front Microbiol, 10 (2019) 1977.

[187] Z. Zhang, J. Lu, Y. Song, Y. Pang, In vitro activity between linezolid and other antimicrobial agents against Mycobacterium abscessus complex, Diagnostic Microbiology Infectious Disease, 90 (2018) 31-34.

[188] R. Cremades, A. Santos, J.C. Rodriguez, E. Garcia-Pachon, M. Ruiz, G. Royo, Mycobacterium abscessus from respiratory isolates: activities of drug combinations, J Infect Chemother, 15 (2009) 46-48.

[189] J. Chen, H. Zhang, Q. Guo, S. He, L. Xu, Z. Zhang, J. Ma, H. Chu, In vitro activity of rifabutin against Mycobacterium abscessus, clinical isolates, Clin Exp Pharmacol Physiol, 49 (2022) 767-775.

[190] T. Dick, S.J. Shin, W.-J. Koh, V. Dartois, M. Gengenbacher, Rifabutin is active against Mycobacterium abscessus in mice, Antimicrobial agents chemotherapy, 64 (2020) 10.1128/aac. 01943-01919.

[191] E. Le Run, M. Arthur, J.L. Mainardi, In Vitro and Intracellular Activity of Imipenem Combined with Tedizolid, Rifabutin, and Avibactam against Mycobacterium abscessus, Antimicrob Agents Chemother, 63 (2019) 10.1128/aac. 01915-01918.

[192] E. Story-Roller, E.C. Maggioncalda, G. Lamichhane, Select beta-Lactam Combinations Exhibit Synergy against Mycobacterium abscessus In Vitro, Antimicrob Agents Chemother, 63 (2019) 10.1128/aac. 02613-02618.

[193] A. Cheng, Y.T. Tsai, S.Y. Chang, H.Y. Sun, U.I. Wu, W.H. Sheng, Y.C. Chen, S.C. Chang, In Vitro Synergism of Rifabutin with Clarithromycin, Imipenem, and Tigecycline against the Mycobacterium abscessus Complex, Antimicrob Agents Chemother, 63 (2019) 10.1128/aac. 02234-02218.

[194] T. Lan, U.S. Ganapathy, S. Sharma, Y.M. Ahn, M. Zimmerman, V. Molodtsov, P. Hegde, M. Gengenbacher, R.H. Ebright, V. Dartois, J.S. Freundlich, T. Dick, C.C. Aldrich, Redesign of Rifamycin Antibiotics to Overcome ADP-Ribosylation-Mediated Resistance, Angew Chem Int Ed Engl, 61 (2022) e202211498.

[195] L. Paulowski, K.S.H. Beckham, M.D. Johansen, L. Berneking, N. Van, Y. Degefu, S. Staack, F.V. Sotomayor, L. Asar, H. Rohde, B.B. Aldridge, M. Aepfelbacher, A. Parret, M. Wilmanns, L. Kremer, K. Combrink, F.P. Maurer, C25-modified rifamycin derivatives with improved activity against Mycobacterium abscessus, PNAS Nexus, 1 (2022) pgac130.

[196] J.C. Camus, M.J. Pryor, C. Medigue, S.T. Cole, Re-annotation of the genome sequence of Mycobacterium tuberculosis H37Rv, Microbiology (Reading), 148 (2002) 2967-2973.

[197] B. Brust, M. Lecoufle, E. Tuaillon, L. Dedieu, S. Canaan, V. Valverde, L. Kremer, Mycobacterium tuberculosis lipolytic enzymes as potential biomarkers for the diagnosis of active tuberculosis, PloS one, 6 (2011) e25078.

[198] G. Johnson, The α/β Hydrolase Fold Proteins of Mycobacterium tuberculosis, with Reference to their Contribution to Virulence, Current Protein Peptide Science, 18 (2017) 190-210.

[199] R. Dhouib, A. Ducret, P. Hubert, F. Carriere, S. Dukan, S. Canaan, Watching intracellular lipolysis in mycobacteria using time lapse fluorescence microscopy, Biochim Biophys Acta, 1811 (2011) 234-241.

[200] K. Côtes, R. Dhouib, I. Douchet, H. Chahinian, A. De Caro, F. Carrière, S. Canaan, Characterization of an exported monoglyceride lipase from Mycobacterium tuberculosis possibly involved in the metabolism of host cell membrane lipids, Biochemical Journal, 408 (2007) 417-427.

[201] K.C. Mishra, C. de Chastellier, Y. Narayana, P. Bifani, A.K. Brown, G.S. Besra, V.M. Katoch, B. Joshi, K.N. Balaji, L. Kremer, Functional role of the PE domain and immunogenicity of the Mycobacterium tuberculosis triacylglycerol hydrolase LipY, Infect Immun, 76 (2008) 127-140.

[202] J. Daniel, H. Maamar, C. Deb, T.D. Sirakova, P.E. Kolattukudy, Mycobacterium tuberculosis uses host triacylglycerol to accumulate lipid droplets and acquires a dormancy-like phenotype in lipid-loaded macrophages, PLoS Pathog, 7 (2011) e1002093.

[203] K.L. Low, P.S. Rao, G. Shui, A.K. Bendt, K. Pethe, T. Dick, M.R. Wenk, Triacylglycerol utilization is required for regrowth of in vitro hypoxic nonreplicating Mycobacterium bovis bacillus Calmette-Guerin, Journal of bacteriology, 191 (2009) 5037-5043.

[204] C. Deb, J. Daniel, T.D. Sirakova, B. Abomoelak, V.S. Dubey, P.E. Kolattukudy, A novel lipase belonging to the hormone-sensitive lipase family induced under starvation to utilize stored triacylglycerol in Mycobacterium tuberculosis, J Biol Chem, 281 (2006) 3866-3875.

[205] K.L. Low, G. Shui, K. Natter, W.K. Yeo, S.D. Kohlwein, T. Dick, S.P. Rao, M.R. Wenk, Lipid droplet-associated proteins are involved in the biosynthesis and hydrolysis of triacylglycerol in Mycobacterium bovis bacillus Calmette-Guerin, J Biol Chem, 285 (2010) 21662-21670.

[206] G. Xu, H. Jia, Y. Li, X. Liu, M. Li, Y. Wang, Hemolytic phospholipase Rv0183 of Mycobacterium tuberculosis induces inflammatory response and apoptosis in alveolar macrophage RAW264.7 cells, Can J Microbiol, 56 (2010) 916-924.

[207] M. Schué, D. Maurin, R. Dhouib, J.C.B. N'Goma, V. Delorme, G. Lambeau, F. Carrière, S. Canaan, Two cutinase-like proteins secreted by Mycobacterium tuberculosis show very different lipolytic activities reflecting their physiological function, The FASEB Journal, 24 (2010) 1893-1903.

[208] P. Santucci, F. Bouzid, N. Smichi, I. Poncin, L. Kremer, C. De Chastellier, M. Drancourt, S. Canaan, Experimental Models of Foamy Macrophages and Approaches for Dissecting the Mechanisms of Lipid Accumulation and Consumption during Dormancy and Reactivation of Tuberculosis, Front Cell Infect Microbiol, 6 (2016) 122.

[209] P. Santucci, S. Diomande, I. Poncin, L. Alibaud, A. Viljoen, L. Kremer, C. de Chastellier, S. Canaan, Delineating the Physiological Roles of the PE and Catalytic Domains of LipY in Lipid Consumption in Mycobacterium-Infected Foamy Macrophages, Infect Immun, 86 (2018).

[210] D.J. Murphy, J. Vance, Mechanisms of lipid-body formation, Trends Biochem Sci, 24 (1999) 109-115.

[211] P.K. Lundquist, K.K. Shivaiah, R. Espinoza-Corral, Lipid droplets throughout the evolutionary tree, Prog Lipid Res, 78 (2020) 101029.

[212] D.J. Murphy, The biogenesis and functions of lipid bodies in animals, plants and microorganisms, Prog Lipid Res, 40 (2001) 325-438.

[213] H.M. Alvarez, H. Luftmann, R.A. Silva, A.C. Cesari, A. Viale, M. Wältermann, A. Steinbüchel, Identification of phenyldecanoic acid as a constituent of triacylglycerols and wax ester produced by Rhodococcus opacus PD630, Microbiology, 148 (2002) 1407-1412.

[214] H.M. Alvarez, Triacylglycerol and wax ester-accumulating machinery in prokaryotes, Biochimie, 120 (2016) 28-39.

[215] M. Wältermann, A. Steinbüchel, Neutral lipid bodies in prokaryotes: recent insights into structure, formation, and relationship to eukaryotic lipid depots, Journal of bacteriology, 187 (2005) 3607-3619.

[216] T. Dargham, I. Mallick, D. Raze, L. Kremer, S. Canaan, Intrabacterial lipid inclusions: overview of an amazing organelle, Biology of Mycobacterial Lipids, (2022) 253-269.

[217] N.J. Garton, H. Christensen, D.E. Minnikin, R.A. Adegbola, M.R. Barer, Intracellular lipophilic inclusions of mycobacteria in vitro and in sputum, Microbiology (Reading), 148 (2002) 2951-2958.

[218] P. Santucci, M.D. Johansen, V. Point, I. Poncin, A. Viljoen, J.F. Cavalier, L. Kremer, S. Canaan, Nitrogen deprivation induces triacylglycerol accumulation, drug tolerance and hypervirulence in mycobacteria, Sci Rep, 9 (2019) 8667.

[219] R.M. Armstrong, D.C. Carter, S.N. Atkinson, S.S. Terhune, T.C. Zahrt, Association of Mycobacterium Proteins with Lipid Droplets, J Bacteriol, 200 (2018) 10.1128/jb. 00240-00218.

[220] A. Viljoen, M. Blaise, C. de Chastellier, L. Kremer, MAB_3551c encodes the primary triacylglycerol synthase involved in lipid accumulation in Mycobacterium abscessus, Mol Microbiol, 102 (2016) 611-627.

[221] C. Barisch, T. Soldati, Mycobacterium marinum degrades both triacylglycerols and phospholipids from its Dictyostelium host to synthesise its own triacylglycerols and generate lipid inclusions, PLoS pathogens, 13 (2017) e1006095.

[222] M. Robbe-Saule, M. Foulon, I. Poncin, L. Esnault, H. Varet, R. Legendre, A. Besnard, A.E. Grzegorzewicz, M. Jackson, S. Canaan, Transcriptional adaptation of Mycobacterium ulcerans in an original mouse model: New insights into the regulation of mycolactone, Virulence, 12 (2021) 1438-1451.

[223] K.A. Mattos, V.G. Oliveira, H. D'Avila, L.S. Rodrigues, R.O. Pinheiro, E.N. Sarno, M.C. Pessolani, P.T. Bozza, TLR6-driven lipid droplets in Mycobacterium leprae-infected Schwann cells: immunoinflammatory platforms associated with bacterial persistence, J Immunol, 187 (2011) 2548-2558.

[224] N.J. Garton, S.J. Waddell, A.L. Sherratt, S.M. Lee, R.J. Smith, C. Senner, J. Hinds, K. Rajakumar, R.A. Adegbola, G.S. Besra, P.D. Butcher, M.R. Barer, Cytological and transcript analyses reveal fat and lazy persister-like bacilli in tuberculous sputum, PLoS Med, 5 (2008) e75.

[225] F. Bouzid, F. Bregeon, I. Poncin, P. Weber, M. Drancourt, S. Canaan, Mycobacterium canettii Infection of Adipose Tissues, Front Cell Infect Microbiol, 7 (2017) 189.

[226] H.L. Sheehan, F. Whitwell, The staining of tubercle bacilli with Sudan black B, J Pathol Bacteriol, 61 (1949) 269-271, pl.

[227] R. Kalscheuer, A. Steinbuchel, A novel bifunctional wax ester synthase/acyl-CoA: diacylglycerol acyltransferase mediates wax ester and triacylglycerol biosynthesis inAcinetobacter calcoaceticus ADP1, Journal of Biological Chemistry, 278 (2003) 8075-8082.

[228] J. Daniel, C. Deb, V.S. Dubey, T.D. Sirakova, B. Abomoelak, H.R. Morbidoni, P.E. Kolattukudy, Induction of a novel class of diacylglycerol acyltransferases and triacylglycerol accumulation in Mycobacterium tuberculosis as it goes into a dormancy-like state in culture, Journal of bacteriology, 186 (2004) 5017-5030.

[229] T.D. Sirakova, V.S. Dubey, C. Deb, J. Daniel, T.A. Korotkova, B. Abomoelak, P.E. Kolattukudy, Identification of a diacylglycerol acyltransferase gene involved in accumulation of triacylglycerol in Mycobacterium tuberculosis under stress, Microbiology (Reading), 152 (2006) 2717-2725.

[230] A.A. Elamin, M. Stehr, R. Spallek, M. Rohde, M. Singh, The Mycobacterium tuberculosis Ag85A is a novel diacylglycerol acyltransferase involved in lipid body formation, Molecular microbiology, 81 (2011) 1577-1592.

[231] J.M. Hayashi, C.Y. Luo, J.A. Mayfield, T. Hsu, T. Fukuda, A.L. Walfield, S.R. Giffen, J.D. Leszyk, C.E. Baer, O.T. Bennion, A. Madduri, S.A. Shaffer, B.B. Aldridge, C.M. Sassetti, S.J. Sandler, T. Kinoshita, D.B. Moody, Y.S. Morita, Spatially distinct and metabolically active membrane domain in mycobacteria, Proceedings of the National Academy of Sciences of the United States of America, 113 (2016) 5400-5405.

[232] M. Wältermann, A. Hinz, H. Robenek, D. Troyer, R. Reichelt, U. Malkus, H.J. Galla, R. Kalscheuer, T. Stöveken, P. Von Landenberg, Mechanism of lipid-body formation in prokaryotes: how bacteria fatten up, Molecular microbiology, 55 (2005) 750-763.

[233] M. Stehr, A. A, M. Singh, Lipid Inclusions in Mycobacterial Infections, in: Tuberculosis - Current Issues in Diagnosis and Management, 2013.

[234] E.K. Schroeder, N. de Souza, D.S. Santos, J.S. Blanchard, L.A. Basso, Drugs that inhibit mycolic acid biosynthesis in Mycobacterium tuberculosis, Curr Pharm Biotechnol, 3 (2002) 197-225.

[235] E. Schweizer, J. Hofmann, Microbial type I fatty acid synthases (FAS): major players in a network of cellular FAS systems, Microbiol Mol Biol Rev, 68 (2004) 501-517, table of contents.

[236] S. Smith, A. Witkowski, A.K. Joshi, Structural and functional organization of the animal fatty acid synthase, Prog Lipid Res, 42 (2003) 289-317.

[237] O. Zimhony, C. Vilcheze, W.R. Jacobs, Jr., Characterization of Mycobacterium smegmatis expressing the Mycobacterium tuberculosis fatty acid synthase I (fas1) gene, J Bacteriol, 186 (2004) 4051-4055.

[238] G. Lamichhane, M. Zignol, N.J. Blades, D.E. Geiman, A. Dougherty, J. Grosset, K.W. Broman, W.R. Bishai, A postgenomic method for predicting essential genes at subsaturation levels of mutagenesis: application to Mycobacterium tuberculosis, Proceedings of the National Academy of Sciences of the United States of America, 100 (2003) 7213-7218.

[239] N. Elad, S. Baron, Y. Peleg, S. Albeck, J. Grunwald, G. Raviv, Z. Shakked, O. Zimhony, R. Diskin, Structure of Type-I Mycobacterium tuberculosis fatty acid synthase at 3.3 A resolution, Nat Commun, 9 (2018) 3886.

[240] N.D. Fernandes, P.E. Kolattukudy, Cloning, sequencing and characterization of a fatty acid synthase-encoding gene from Mycobacterium tuberculosis var. bovis BCG, Gene, 170 (1996) 95-99.

[241] J. Pawełczyk, L. Kremer, The Molecular Genetics of Mycolic Acid Biosynthesis, in: Molecular Genetics of Mycobacteria, 2015, pp. 611-631.

[242] K. Bloch, Control Mechanisms for Fatty Acid Synthesis in Mycobacterium Smegmatis, in: Advances in Enzymology and Related Areas of Molecular Biology, 1977, pp. 1-84.

[243] S. Kikuchi, D.L. Rainwater, P.E. Kolattukudy, Purification and characterization of an unusually large fatty acid synthase from Mycobacterium tuberculosis var. bovis BCG, Arch Biochem Biophys, 295 (1992) 318-326.

[244] M.L. Schaeffer, G. Agnihotri, H. Kallender, P.J. Brennan, J.T. Lonsdale, Expression, purification, and characterization of the Mycobacterium tuberculosis acyl carrier protein, AcpM, Biochim Biophys Acta, 1532 (2001) 67-78.

[245] D.I. Chan, H.J. Vogel, Current understanding of fatty acid biosynthesis and the acyl carrier protein, Biochem J, 430 (2010) 1-19.

[246] H. Marrakchi, S. Ducasse, G. Labesse, H. Montrozier, E. Margeat, L. Emorine, X. Charpentier, M. Daffe, A.K. Quemard, MabA (FabG1), a Mycobacterium tuberculosis protein involved in the long-chain fatty acid elongation system FAS-II, Microbiology (Reading), 148 (2002) 951-960.

[247] M. Cohen-Gonsaud, S. Ducasse, F. Hoh, D. Zerbib, G. Labesse, A. Quemard, Crystal structure of MabA from Mycobacterium tuberculosis, a reductase involved in long-chain fatty acid biosynthesis, J Mol Biol, 320 (2002) 249-261.

[248] T. Kussau, M. Flipo, N. Van Wyk, A. Viljoen, V. Olieric, L. Kremer, M. Blaise, Structural rearrangements occurring upon cofactor binding in the Mycobacterium smegmatis beta-ketoacyl-acyl carrier protein reductase MabA, Acta Crystallogr D Struct Biol, 74 (2018) 383-393.

[249] E. Sacco, A.S. Covarrubias, H.M. O'Hare, P. Carroll, N. Eynard, T.A. Jones, T. Parish, M. Daffe, K. Backbro, A. Quemard, The missing piece of the type II fatty acid synthase system from Mycobacterium tuberculosis, Proceedings of the National Academy of Sciences of the United States of America, 104 (2007) 14628-14633.

[250] B. Vogeli, R.G. Rosenthal, G.M.M. Stoffel, T. Wagner, P. Kiefer, N.S. Cortina, S. Shima, T.J. Erb, InhA, the enoyl-thioester reductase from Mycobacterium tuberculosis forms a covalent adduct during catalysis, J Biol Chem, 293 (2018) 17200-17207.

[251] L. Kremer, L.G. Dover, S. Carrere, K.M. Nampoothiri, S. Lesjean, A.K. Brown, P.J. Brennan, D.E. Minnikin, C. Locht, G.S. Besra, Mycolic acid biosynthesis and enzymic characterization of the beta-ketoacyl-ACP synthase A-condensing enzyme from Mycobacterium tuberculosis, Biochem J, 364 (2002) 423-430.

[252] M.L. Schaeffer, G. Agnihotri, C. Volker, H. Kallender, P.J. Brennan, J.T. Lonsdale, Purification and biochemical characterization of the Mycobacterium tuberculosis beta-ketoacyl-acyl carrier protein synthases KasA and KasB, J Biol Chem, 276 (2001) 47029-47037.

[253] R.A. Slayden, C.E. Barry, 3rd, The role of KasA and KasB in the biosynthesis of meromycolic acids and isoniazid resistance in Mycobacterium tuberculosis, Tuberculosis (Edinb), 82 (2002) 149-160.

[254] R.R. Lovewell, C.M. Sassetti, B.C. VanderVen, Chewing the fat: lipid metabolism and homeostasis during M. tuberculosis infection, Curr Opin Microbiol, 29 (2016) 30-36.

[255] D. Hirsch, A. Stahl, H.F. Lodish, A family of fatty acid transporters conserved from mycobacterium to man, Proceedings of the National Academy of Sciences of the United States of America, 95 (1998) 8625-8629.

[256] J. Daniel, T. Sirakova, P. Kolattukudy, An acyl-CoA synthetase in Mycobacterium tuberculosis involved in triacylglycerol accumulation during dormancy, PLoS One, 9 (2014) e114877.

[257] A.K. Pandey, C.M. Sassetti, Mycobacterial persistence requires the utilization of host cholesterol, Proceedings of the National Academy of Sciences of the United States of America, 105 (2008) 4376-4380.

[258] S.T. Cole, R. Brosch, J. Parkhill, T. Garnier, C. Churcher, D. Harris, S.V. Gordon, K. Eiglmeier, S. Gas, C.E. Barry, 3rd, F. Tekaia, K. Badcock, D. Basham, D. Brown, T. Chillingworth, R. Connor, R. Davies, K. Devlin, T. Feltwell, S. Gentles, N. Hamlin, S. Holroyd, T. Hornsby, K. Jagels, A. Krogh, J. McLean, S. Moule, L. Murphy, K. Oliver, J. Osborne, M.A. Quail, M.A. Rajandream, J. Rogers, S. Rutter, K. Seeger, J. Skelton, R. Squares, S. Squares, J.E. Sulston, K. Taylor, S. Whitehead, B.G. Barrell, Deciphering the biology of Mycobacterium tuberculosis from the complete genome sequence, Nature, 393 (1998) 537-544.

[259] D.C. Ekiert, G. Bhabha, G.L. Isom, G. Greenan, S. Ovchinnikov, I.R. Henderson, J.S. Cox, R.D. Vale, Architectures of Lipid Transport Systems for the Bacterial Outer Membrane, Cell, 169 (2017) 273-285 e217.

[260] E.V. Nazarova, C.R. Montague, T. La, K.M. Wilburn, N. Sukumar, W. Lee, S. Caldwell, D.G. Russell, B.C. VanderVen, Rv3723/LucA coordinates fatty acid and cholesterol uptake in Mycobacterium tuberculosis, Elife, 6 (2017) e26969.

[261] C. Deb, C.M. Lee, V.S. Dubey, J. Daniel, B. Abomoelak, T.D. Sirakova, S. Pawar, L. Rogers, P.E. Kolattukudy, A novel in vitro multiple-stress dormancy model for Mycobacterium tuberculosis generates a lipid-loaded, drug-tolerant, dormant pathogen, PLoS One, 4 (2009) e6077.

[262] A.J. Martinot, M. Farrow, L. Bai, E. Layre, T.Y. Cheng, J.H. Tsai, J. Iqbal, J.W. Annand, Z.A. Sullivan, M.M. Hussain, J. Sacchettini, D.B. Moody, J.C. Seeliger, E.J. Rubin, Mycobacterial Metabolic Syndrome: LprG and Rv1410 Regulate Triacylglyceride Levels, Growth Rate and Virulence in Mycobacterium tuberculosis, PLoS Pathog, 12 (2016) e1005351.

[263] M. Cabruja, S. Mondino, Y.T. Tsai, J. Lara, H. Gramajo, G. Gago, A conditional mutant of the fatty acid synthase unveils unexpected cross talks in mycobacterial lipid metabolism, Open biology, 7 (2017) 160277.

[264] P. Peyron, J. Vaubourgeix, Y. Poquet, F. Levillain, C. Botanch, F. Bardou, M. Daffe, J.F. Emile, B. Marchou, P.J. Cardona, C. de Chastellier, F. Altare, Foamy macrophages from tuberculous patients' granulomas constitute a nutrient-rich reservoir for M. tuberculosis persistence, PLoS Pathog, 4 (2008) e1000204.

[265] J.G. Rodríguez, A.C. Hernández, C. Helguera-Repetto, D. Aguilar Ayala, R. Guadarrama-Medina, J.M. Anzóla, J.R. Bustos, M.M. Zambrano, J. González-y-Merchand, M.J. García, Global adaptation to a lipid environment triggers the dormancy-related phenotype of Mycobacterium tuberculosis, MBio, 5 (2014) 10.1128/mbio. 01125-01114.

[266] W. Lee, B.C. VanderVen, R.J. Fahey, D.G. Russell, Intracellular Mycobacterium tuberculosis exploits host-derived fatty acids to limit metabolic stress, J Biol Chem, 288 (2013) 6788-6800.

[267] L.L. Listenberger, X. Han, S.E. Lewis, S. Cases, R.V. Farese, Jr., D.S. Ory, J.E. Schaffer, Triglyceride accumulation protects against fatty acid-induced lipotoxicity, Proceedings of the National Academy of Sciences of the United States of America, 100 (2003) 3077-3082.

[268] J. Garbarino, S.L. Sturley, Saturated with fat: new perspectives on lipotoxicity, Curr Opin Clin Nutr Metab Care, 12 (2009) 110-116.

[269] J. Garbarino, M. Padamsee, L. Wilcox, P.M. Oelkers, D. D'Ambrosio, K.V. Ruggles, N. Ramsey, O. Jabado, A. Turkish, S.L. Sturley, Sterol and diacylglycerol acyltransferase deficiency triggers fatty acid-mediated cell death, J Biol Chem, 284 (2009) 30994-31005.

[270] J. Petschnigg, H. Wolinski, D. Kolb, G. Zellnig, C.F. Kurat, K. Natter, S.D. Kohlwein, Good fat, essential cellular requirements for triacylglycerol synthesis to maintain membrane homeostasis in yeast, J Biol Chem, 284 (2009) 30981-30993.

[271] H.M. Alvarez, R.A. Silva, A.C. Cesari, A.L. Zamit, S.R. Peressutti, R. Reichelt, U. Keller, U. Malkus, C. Rasch, T. Maskow, F. Mayer, A. Steinbuchel, Physiological and morphological responses of the soil bacterium Rhodococcus opacus strain PD630 to water stress, FEMS Microbiol Ecol, 50 (2004) 75-86.

[272] C. Zhang, L. Yang, Y. Ding, Y. Wang, L. Lan, Q. Ma, X. Chi, P. Wei, Y. Zhao, A. Steinbüchel, Bacterial lipid droplets bind to DNA via an intermediary protein that enhances survival under stress, Nature communications, 8 (2017) 15979.

[273] D. Raze, C. Verwaerde, G. Deloison, E. Werkmeister, B. Coupin, M. Loyens, P. Brodin, C. Rouanet, C. Locht, Heparin-binding hemagglutinin adhesin (HBHA) is involved in intracytosolic lipid inclusions formation in mycobacteria, Frontiers in microbiology, 9 (2018) 2258.

[274] J.D. McKinney, K. Honer zu Bentrup, E.J. Munoz-Elias, A. Miczak, B. Chen, W.T. Chan, D. Swenson, J.C. Sacchettini, W.R. Jacobs, Jr., D.G. Russell, Persistence of Mycobacterium tuberculosis in macrophages and mice requires the glyoxylate shunt enzyme isocitrate lyase, Nature, 406 (2000) 735-738.

[275] D. Schnappinger, S. Ehrt, M.I. Voskuil, Y. Liu, J.A. Mangan, I.M. Monahan, G. Dolganov, B. Efron, P.D. Butcher, C. Nathan, Transcriptional adaptation of Mycobacterium tuberculosis within macrophages: insights into the phagosomal environment, The Journal of experimental medicine, 198 (2003) 693-704.

[276] J. Timm, F.A. Post, L.G. Bekker, G.B. Walther, H.C. Wainwright, R. Manganelli, W.T. Chan, L. Tsenova, B. Gold, I. Smith, G. Kaplan, J.D. McKinney, Differential expression of iron-, carbon-, and oxygen-responsive mycobacterial genes in the lungs of chronically infected mice and tuberculosis patients, Proceedings of the National Academy of Sciences of the United States of America, 100 (2003) 14321-14326.

[277] W. Segal, H. Bloch, Biochemical differentiation of Mycobacterium tuberculosis grown in vivo and in vitro, Journal of bacteriology, 72 (1956) 132-141.

[278] D.J. Sloan, H.C. Mwandumba, N.J. Garton, S.H. Khoo, A.E. Butterworth, T.J. Allain, R.S. Heyderman, E.L. Corbett, M.R. Barer, G.R. Davies, Pharmacodynamic Modeling of Bacillary Elimination Rates and Detection of Bacterial Lipid Bodies in Sputum to Predict and Understand Outcomes in Treatment of Pulmonary Tuberculosis, Clin Infect Dis, 61 (2015) 1-8.

[279] D. Mekonnen, A. Derbie, A. Mihret, S.A. Yimer, T. Tonjum, B. Gelaw, E. Nibret, A. Munshae, S.J. Waddell, A. Aseffa, Lipid droplets and the transcriptome of Mycobacterium tuberculosis from direct sputa: a literature review, Lipids Health Dis, 20 (2021) 129.

[280] J. Dietrich, S. Roy, I. Rosenkrands, T. Lindenstrom, J. Filskov, E.M. Rasmussen, J. Cassidy, P. Andersen, Differential influence of nutrient-starved Mycobacterium tuberculosis on adaptive immunity results in progressive tuberculosis disease and pathology, Infect Immun, 83 (2015) 4731-4739.

[281] J. Dietrich, S. Roy, I. Rosenkrands, T. Lindenstrom, J. Filskov, E.M. Rasmussen, J. Cassidy, P. Andersen, Correction for Dietrich et al., Differential Influence of Nutrient-Starved Mycobacterium tuberculosis on Adaptive Immunity Results in Progressive Tuberculosis Disease and Pathology, Infect Immun, 84 (2016) 608.

[282] M.J. Kim, H.C. Wainwright, M. Locketz, L.G. Bekker, G.B. Walther, C. Dittrich, A. Visser, W. Wang, F.F. Hsu, U. Wiehart, L. Tsenova, G. Kaplan, D.G. Russell, Caseation of human tuberculosis granulomas correlates with elevated host lipid metabolism, EMBO Mol Med, 2 (2010) 258-274.

[283] N. Jaisinghani, S. Dawa, K. Singh, A. Nandy, D. Menon, P.D. Bhandari, G. Khare, A. Tyagi, S. Gandotra, Necrosis Driven Triglyceride Synthesis Primes Macrophages for Inflammation During Mycobacterium tuberculosis Infection, Front Immunol, 9 (2018) 1490.

[284] A. Queiroz, L.W. Riley, Bacterial immunostat: Mycobacterium tuberculosis lipids and their role in the host immune response, Revista da Sociedade Brasileira de Medicina Tropical, 50 (2017) 09-18.

[285] A. Singh, D.K. Crossman, D. Mai, L. Guidry, M.I. Voskuil, M.B. Renfrow, A.J. Steyn, Mycobacterium tuberculosis WhiB3 maintains redox homeostasis by regulating virulence lipid anabolism to modulate macrophage response, PLoS Pathog, 5 (2009) e1000545.

[286] S.H. Baek, A.H. Li, C.M. Sassetti, Metabolic regulation of mycobacterial growth and antibiotic sensitivity, PLoS Biol, 9 (2011) e1001065.

[287] N. Kapoor, S. Pawar, T.D. Sirakova, C. Deb, W.L. Warren, P.E. Kolattukudy, Human granuloma in vitro model, for TB dormancy and resuscitation, PLoS One, 8 (2013) e53657.

[288] R.J. Hammond, V.O. Baron, K. Oravcova, S. Lipworth, S.H. Gillespie, Phenotypic resistance in mycobacteria: is it because I am old or fat that I resist you?, Journal of Antimicrobial Chemotherapy, 70 (2015) 2823-2827.

[289] L.G. Wayne, L.G. Hayes, An in vitro model for sequential study of shiftdown of Mycobacterium tuberculosis through two stages of nonreplicating persistence, Infection immunity, 64 (1996) 2062-2069.

[290] M.P. Weir, W. Langridge III, R. Walker, Relationships between oleic acid uptake and lipid metabolism in Mycobacterium smegmatis, American Review of Respiratory Disease, 106 (1972) 450-457.

[291] H. Nakagawa, Y. Kashiwabara, G. Matsuki, Metabolism of triacylglycerol in Mycobacterium smegmatis, J Biochem, 80 (1976) 923-928.

[292] J. Bacon, L.G. Dover, K.A. Hatch, Y. Zhang, J.M. Gomes, S. Kendall, L. Wernisch, N.G. Stoker, P.D. Butcher, G.S. Besra, P.D. Marsh, Lipid composition and transcriptional response of Mycobacterium tuberculosis grown under iron-limitation in continuous culture: identification of a novel wax ester, Microbiology (Reading), 153 (2007) 1435-1444.

[293] G.M. Rodriguez, M.I. Voskuil, B. Gold, G.K. Schoolnik, I. Smith, ideR, An essential gene in mycobacterium tuberculosis: role of IdeR in iron-dependent gene expression, iron metabolism, and oxidative stress response, Infect Immun, 70 (2002) 3371-3381.

[294] R. Pal, S. Hameed, P. Kumar, S. Singh, Z. Fatima, Understanding lipidomic basis of iron limitation induced chemosensitization of drug-resistant Mycobacterium tuberculosis, 3 Biotech, 9 (2019) 122.

[295] S. Vijay, H.T. Hai, D.D.A. Thu, E. Johnson, A. Pielach, N.H. Phu, G.E. Thwaites, N.T.T. Thuong, Ultrastructural Analysis of Cell Envelope and Accumulation of Lipid Inclusions in Clinical Mycobacterium tuberculosis Isolates from Sputum, Oxidative Stress, and Iron Deficiency, Front Microbiol, 8 (2017) 2681.

[296] H.M. Alvarez, F. Mayer, D. Fabritius, A. Steinbuchel, Formation of intracytoplasmic lipid inclusions by Rhodococcus opacus strain PD630, Arch Microbiol, 165 (1996) 377-386.

[297] H.M. Alvarez, R. Kalscheuer, A. Steinbuchel, Accumulation and mobilization of storage lipids by Rhodococcus opacus PD630 and Rhodococcus ruber NCIMB 40126, Appl Microbiol Biotechnol, 54 (2000) 218-223.

[298] T. Dargham, I. Mallick, D. Raze, L. Kremer, S. Canaan, Intrabacterial lipid inclusions, in: Z. Fatima, S. Canaan (Eds.) Biology of Mycobacterial Lipids, Academic Press, 2022, pp. 253-269.

[299] J. Amon, T. Brau, A. Grimrath, E. Hanssler, K. Hasselt, M. Holler, N. Jessberger, L. Ott, J. Szokol, F. Titgemeyer, A. Burkovski, Nitrogen control in Mycobacterium smegmatis: nitrogen-dependent expression of ammonium transport and assimilation proteins depends on the OmpR-type regulator GlnR, J Bacteriol, 190 (2008) 7108-7116.

[300] N. Jeßberger, Y. Lu, J. Amon, F. Titgemeyer, S. Sonnewald, S. Reid, A. Burkovski, Nitrogen starvation-induced transcriptome alterations and influence of transcription regulator mutants in Mycobacterium smegmatis, BMC Research Notes, 6 (2013) 1-19.

[301] K.J. Williams, V.A. Jenkins, G.R. Barton, W.A. Bryant, N. Krishnan, B.D. Robertson, Deciphering the metabolic response of M ycobacterium tuberculosis to nitrogen stress, Molecular microbiology, 97 (2015) 1142-1157.

[302] J.S. Davila Costa, R.A. Silva, L. Leichert, H.M. Alvarez, Proteome analysis reveals differential expression of proteins involved in triacylglycerol accumulation by Rhodococcus jostii RHA1 after addition of methyl viologen, Microbiology (Reading), 163 (2017) 343-354.

[303] M.A. Hernández, J. Lara, G. Gago, H. Gramajo, H.M.J.M.m. Alvarez, The pleiotropic transcriptional regulator N lp R contributes to the modulation of nitrogen metabolism, lipogenesis and triacylglycerol accumulation in oleaginous rhodococci, 103 (2017) 366-385.

[304] V.A. Jenkins, G.R. Barton, B.D. Robertson, K.J. Williams, Genome wide analysis of the complete GlnR nitrogen-response regulon in Mycobacterium smegmatis, BMC Genomics, 14 (2013) 301.

[305] J.D. Maarsingh, S.E. Haydel, Mycobacterium smegmatis PrrAB two-component system influences triacylglycerol accumulation during ammonium stress, Microbiology (Reading), 164 (2018) 1276-1288.

[306] J. Desmoras, D. Ambrosi, R. Boesch, ETUDES AU LABORATOIRE ET EN SERRE DU 23465 RP NOUVEL HERBICIDE DE LA FAMILLE DES UREIDOPHENYLOXADIAZOLONES, (1974).

[307] C.H. Tieman, Pesticidal 3-(2, 3-dihydrobenzofuran-7-yl)-5-methoxy-1, 3, 4-oxadiazol-2 (3H)-one, in, Google Patents, 1981.

[308] S. Petry, K.H. Baringhaus, K. Schoenafinger, C. Jung, H. Kleine, G. Müller, High-throughput Screening of Hormone-sensitive Lipase and Subsequent Computer-assisted Compound Optimization, Lipases Phospholipases in Drug Development: From Biochemistry to Molecular Pharmacology, (2004) 121-137.

[309] K. Schoenafinger, S. Petry, G. Mueller, K. Baringhaus, Substituted 3-Phenyl-5-Alkoxi-1, 3, 4-Oxadiazol-2-one and use thereof for Inhibiting Hormone-Sensitive Lipase, WO0166531, Sept, 13 (2001).

[310] Y. Ben Ali, H. Chahinian, S. Petry, G. Muller, R. Lebrun, R. Verger, F. Carriere, L. Mandrich, M. Rossi, G. Manco, L. Sarda, A. Abousalham, Use of an inhibitor to identify members of the hormone-sensitive lipase family, Biochemistry, 45 (2006) 14183-14191.

[311] V. Point, R.K. Malla, S. Diomande, B.P. Martin, V. Delorme, F. Carriere, S. Canaan, N.P. Rath, C.D. Spilling, J.F. Cavalier, Synthesis and kinetic evaluation of cyclophostin and cyclipostins phosphonate analogs as selective and potent inhibitors of microbial lipases, J Med Chem, 55 (2012) 10204-10219.

[312] V. Point, A. Benarouche, J. Zarrillo, A. Guy, R. Magnez, L. Fonseca, B. Raux, J. Leclaire, G. Buono, F. Fotiadu, T. Durand, F. Carriere, C. Vaysse, L. Couedelo, J.F. Cavalier, Slowing down fat digestion and absorption by an oxadiazolone inhibitor targeting selectively gastric lipolysis, Eur J Med Chem, 123 (2016) 834-848.

[313] Y.B. Ali, R. Verger, F. Carriere, S. Petry, G. Muller, A. Abousalham, The molecular mechanism of human hormone-sensitive lipase inhibition by substituted 3-phenyl-5-alkoxy-1,3,4-oxadiazol-2-ones, Biochimie, 94 (2012) 137-145.

[314] G.G. Muccioli, G. Labar, D.M. Lambert, CAY10499, a novel monoglyceride lipase inhibitor evidenced by an expeditious MGL assay, Chembiochem, 9 (2008) 2704-2710.

[315] A. Minkkilä, J.R. Savinainen, H. Käsnänen, H. Xhaard, T. Nevalainen, J.T. Laitinen, A. Poso, J. Leppänen, S.M.J.C. Saario, Screening of various hormone-sensitive lipase inhibitors as endocannabinoid-hydrolyzing enzyme inhibitors, 4 (2009) 1253-1259.

[316] D.M. Lambert, C.J. Fowler, The endocannabinoid system: drug targets, lead compounds, and potential therapeutic applications, J Med Chem, 48 (2005) 5059-5087.

[317] A.J. Alfred, S. Arthur, Heterocyclic antituberculous compounds, in, Google Patents, 1954.

[318] A. Wilder Smith, The action of phosgene on acid hydrazides to give 1, 3, 4-oxdiazolones of interest in the treatment of tuberculosis, Science, 119 (1954) 427.

[319] A. Wilder Smith, H. BRODHAGE, Biological spectrum of some new tuberculostatic 1, 3, 4-oxadiazolones with special reference to cross-resistance and rates of emergence of resistance, Nature, 192 (1961) 1195-1195.

[320] A.W. Smith, H. Brodhage, G. Haukenes, Some tuberculostatic 1, 3, 4-oxadiazolones (-5) and 1, 3, 4-oxadiazolthiones (-5). II: biological spectrum in vitro and activity in vivo in relation to resistance emergence, Arzneimittel-Forschung, 12 (1962) 275-280.

[321] A.W. Smith, Some recently synthesised tuberculostatic 4-substituted oxadiazolones and oxadiazol-thiones. VI, Arzneimittel-Forschung, 16 (1966) 1034-1038.

[322] M.G. Mamolo, D. Zampieri, L. Vio, M. Fermeglia, M. Ferrone, S. Pricl, G. Scialino, E. Banfi, Antimycobacterial activity of new 3-substituted 5-(pyridin-4-yl)-3H-1, 3, 4-oxadiazol-2-one and 2-thione derivatives. Preliminary molecular modeling investigations, Bioorganic medicinal chemistry, 13 (2005) 3797-3809.

[323] D. Zampieri, M.G. Mamolo, E. Laurini, M. Fermeglia, P. Posocco, S. Pricl, E. Banfi, G. Scialino, L. Vio, Antimycobacterial activity of new 3, 5-disubstituted 1, 3, 4-oxadiazol-2 (3H)-one derivatives. Molecular modeling investigations, Bioorganic medicinal chemistry, 17 (2009) 4693-4707.

[324] A. Bellamine, A.T. Mangla, W.D. Nes, M.R. Waterman, Characterization and catalytic properties of the sterol 14α-demethylase from Mycobacterium tuberculosis, Proceedings of the National Academy of Sciences, 96 (1999) 8937-8942.

[325] K.J. McLean, A.J. Dunford, R. Neeli, M.D. Driscoll, A.W. Munro, Structure, function and drug targeting in Mycobacterium tuberculosis cytochrome P450 systems, Arch Biochem Biophys, 464 (2007) 228-240.

[326] V. Delorme, S.V. Diomandé, L. Dedieu, J.-F. Cavalier, F. Carrière, L. Kremer, J. Leclaire, F. Fotiadu, S. Canaan, M m PPOX Inhibits Mycobacterium tuberculosis lipolytic enzymes belonging to the hormone-sensitive lipase family and alters mycobacterial growth, (2012).

[327] P. Santucci, S. Diomande, I. Poncin, L. Alibaud, A. Viljoen, L. Kremer, C. de Chastellier, S. Canaan, Delineating the Physiological Roles of the PE and Catalytic Domains of LipY in Lipid

Consumption in Mycobacterium-Infected Foamy Macrophages, Infect Immun, 86 (2018) e00394-00318.

[328] M.S. Ravindran, S.P. Rao, X. Cheng, A. Shukla, A. Cazenave-Gassiot, S.Q. Yao, M.R. Wenk, Targeting lipid esterases in mycobacteria grown under different physiological conditions using activity-based profiling with tetrahydrolipstatin (THL), Mol Cell Proteomics, 13 (2014) 435-448.

[329] S. Ülker, C. Placidi, V. Point, B. Gadenne, C. Serveau-Avesque, S. Canaan, F. Carrière, J.-F. Cavalier, New lipase assay using Pomegranate oil coating in microtiter plates, Biochimie, 120 (2016) 110-118.

[330] J.F. Cavalier, C.D. Spilling, T. Durand, L. Camoin, S. Canaan, Lipolytic enzymes inhibitors: A new way for antibacterial drugs discovery, Eur J Med Chem, 209 (2021) 112908.

[331] T. Kurokawa, K. Suzuki, T. Hayaoka, T. Nakagawa, T. Izawa, M. Kobayashi, N. Harada, Cyclophostin, acetylcholinesterase inhibitor from Streptomyces lavendulae, J Antibiot (Tokyo), 46 (1993) 1315-1318.

[332] L. Vertesy, B. Beck, M. Bronstrup, K. Ehrlich, M. Kurz, G. Muller, D. Schummer, G. Seibert, Cyclipostins, novel hormone-sensitive lipase inhibitors from Streptomyces sp. DSM 13381. II. Isolation, structure elucidation and biological properties, J Antibiot (Tokyo), 55 (2002) 480-494.

[333] J. Wink, F.R. Schmidt, G. Seibert, W. Aretz, Cyclipostins: novel hormone-sensitive lipase inhibitors from Streptomyces sp. DSM 13381. I. Taxonomic studies of the producer microorganism and fermentation results, J Antibiot (Tokyo), 55 (2002) 472-479.

[334] G. Seibert, L. Toti, J. Wink, Treating mycobacterial infections with cyclipostins, Sanofi-Aventis Deutschland GmbH patent WO//025449, (2008).

[335] V. Point, R.K. Malla, F. Carriere, S. Canaan, C.D. Spilling, J.F. Cavalier, Enantioselective inhibition of microbial lipolytic enzymes by nonracemic monocyclic enolphosphonate analogues of cyclophostin, J Med Chem, 56 (2013) 4393-4401.

[336] P.C. Nguyen, V. Delorme, A. Benarouche, B.P. Martin, R. Paudel, G.R. Gnawali, A. Madani, R. Puppo, V. Landry, L. Kremer, P. Brodin, C.D. Spilling, J.F. Cavalier, S. Canaan, Cyclipostins and Cyclophostin analogs as promising compounds in the fight against tuberculosis, Sci Rep, 7 (2017) 11751.

[337] J.F. Cavalier, G. Buono, R. Verger, Covalent inhibition of digestive lipases by chiral phosphonates, Acc Chem Res, 33 (2000) 579-589.

[338] C.D. Spilling, The Chemistry and Biology of Cyclophostin, the Cyclipostins and Related Compounds, Molecules, 24 (2019) 2579.

[339] S. Dutta, R.K. Malla, S. Bandyopadhyay, C.D. Spilling, C.M.J.B. Dupureur, m. chemistry, Synthesis and kinetic analysis of some phosphonate analogs of cyclophostin as inhibitors of human acetylcholinesterase, 18 (2010) 2265-2274.

[340] E. Vasilieva, S. Dutta, R.K. Malla, B.P. Martin, C.D. Spilling, C.M.J.B. Dupureur, m. chemistry, Rat hormone sensitive lipase inhibition by cyclipostins and their analogs, 23 (2015) 944-952.

[341] B.P. Martin, E. Vasilieva, C.M. Dupureur, C.D. Spilling, Synthesis and comparison of the biological activity of monocyclic phosphonate, difluorophosphonate and phosphate analogs of the natural AChE inhibitor cyclophostin, Bioorg Med Chem, 23 (2015) 7529-7534.

[342] S. Bandyopadhyay, S. Dutta, C.D. Spilling, C.M. Dupureur, N.P. Rath, Synthesis and biological evaluation of a phosphonate analog of the natural acetyl cholinesterase inhibitor cyclophostin, J Org Chem, 73 (2008) 8386-8391.

[343] R.K. Malla, S. Bandyopadhyay, C.D. Spilling, S. Dutta, C.M.J.O.l. Dupureur, The first total synthesis of (±)-cyclophostin and (±)-cyclipostin P: inhibitors of the serine hydrolases acetyl cholinesterase and hormone sensitive lipase, 13 (2011) 3094-3097.

[344] A. Madani, J.N. Ridenour, B.P. Martin, R.R. Paudel, A. Abdul Basir, V. Le Moigne, J.L. Herrmann, S. Audebert, L. Camoin, L. Kremer, C.D. Spilling, S. Canaan, J.F. Cavalier, Cyclipostins and Cyclophostin Analogues as Multitarget Inhibitors That Impair Growth of Mycobacterium abscessus, ACS Infect Dis, 5 (2019) 1597-1608.

[345] V. Point, R.K. Malla, S. Diomande, B.P. Martin, V. Delorme, F. Carriere, S. Canaan, N.P. Rath, C.D. Spilling, J.F.o.J.J.o.m.c. Cavalier, Synthesis and kinetic evaluation of cyclophostin and cyclipostins phosphonate analogs as selective and potent inhibitors of microbial lipases, 55 (2012) 10204-10219.

[346] P. Aschauer, R. Zimmermann, R. Breinbauer, T. Pavkov-Keller, M. Oberer, The crystal structure of monoacylglycerol lipase from M. tuberculosis reveals the basis for specific inhibition, Sci Rep, 8 (2018) 8948.

[347] N. Lenfant, T. Hotelier, Y. Bourne, P. Marchot, A.J.C.-b.i. Chatonnet, Proteins with an alpha/beta hydrolase fold: Relationships between subfamilies in an ever-growing superfamily, 203 (2013) 266-268.

[348] P.C. Nguyen, V. Delorme, A. Benarouche, A. Guy, V. Landry, S. Audebert, M. Pophillat, L. Camoin, C. Crauste, J.M. Galano, T. Durand, P. Brodin, S. Canaan, J.F. Cavalier, Oxadiazolone derivatives, new promising multi-target inhibitors against M. tuberculosis, Bioorganic Chemistry, 81 (2018) 414-424.

[349] T. Christophe, M. Jackson, H.K. Jeon, D. Fenistein, M. Contreras-Dominguez, J. Kim, A. Genovesio, J.P. Carralot, F. Ewann, E.H. Kim, S.Y. Lee, S. Kang, M.J. Seo, E.J. Park, H. Skovierova, H. Pham, G. Riccardi, J.Y. Nam, L. Marsollier, M. Kempf, M.L. Joly-Guillou, T. Oh, W.K. Shin, Z. No, U. Nehrbass, R. Brosch, S.T. Cole, P. Brodin, High content screening identifies decaprenyl-phosphoribose 2' epimerase as a target for intracellular antimycobacterial inhibitors, PLoS Pathog, 5 (2009) e1000645.

[350] M. Flipo, M. Desroses, N. Lecat-Guillet, B. Dirie, X. Carette, F. Leroux, C. Piveteau, F. Demirkaya, Z. Lens, P. Rucktooa, V. Villeret, T. Christophe, H.K. Jeon, C. Locht, P. Brodin, B. Deprez, A.R. Baulard, N. Willand, Ethionamide boosters: synthesis, biological activity, and structure-activity relationships of a series of 1,2,4-oxadiazole EthR inhibitors, J Med Chem, 54 (2011) 2994-3010.

[351] P.C. Nguyen, A. Madani, P. Santucci, B.P. Martin, R.R. Paudel, S. Delattre, J.L. Herrmann, C.D. Spilling, L. Kremer, S. Canaan, J.F. Cavalier, Cyclophostin and Cyclipostins analogues, new promising molecules to treat mycobacterial-related diseases, International Journal of Antimicrobial Agents, 51 (2018) 651-654.

[352] C.J. Schulze, G. Navarro, D. Ebert, J. DeRisi, R.G. Linington, Salinipostins A-K, long-chain bicyclic phosphotriesters as a potent and selective antimalarial chemotype, J Org Chem, 80 (2015) 1312-1320.

[353] E. Yoo, C.J. Schulze, B.H. Stokes, O. Onguka, T. Yeo, S. Mok, N.F. Gnadig, Y. Zhou, K. Kurita, I.T. Foe, S.M. Terrell, M.J. Boucher, P. Cieplak, K. Kumpornsin, M.C.S. Lee, R.G. Linington, J.Z. Long, A.C. Uhlemann, E. Weerapana, D.A. Fidock, M. Bogyo, The Antimalarial Natural Product Salinipostin A Identifies Essential alpha/beta Serine Hydrolases Involved in Lipid Metabolism in P. falciparum Parasites, Cell Chem Biol, 27 (2020) 143-157 e145.

[354] A. Madani, I. Mallick, A. Guy, C. Crauste, T. Durand, P. Fourquet, S. Audebert, L. Camoin, S. Canaan, J.F. Cavalier, Dissecting the antibacterial activity of oxadiazolone-core derivatives against Mycobacterium abscessus, PLoS One, 15 (2020) e0238178.

[355] L. Laencina, V. Dubois, V. Le Moigne, A. Viljoen, L. Majlessi, J. Pritchard, A. Bernut, L. Piel, A.L. Roux, J.L. Gaillard, B. Lombard, D. Loew, E.J. Rubin, R. Brosch, L. Kremer, J.L. Herrmann, F. Girard-Misguich, Identification of genes required for Mycobacterium abscessus growth in vivo with a prominent role of the ESX-4 locus, Proceedings of the National Academy of Sciences of the United States of America, 115 (2018) E1002-E1011.

[356] J.J. Lu, W. Pan, Y.J. Hu, Y.T. Wang, Multi-target drugs: the trend of drug research and development, PLoS One, 7 (2012) e40262.

[357] J.L. Medina-Franco, M.A. Giulianotti, G.S. Welmaker, R.A. Houghten, Shifting from the single to the multitarget paradigm in drug discovery, Drug Discov Today, 18 (2013) 495-501.

[358] C.M. Sassetti, D.H. Boyd, E.J. Rubin, Genes required for mycobacterial growth defined by high density mutagenesis, Mol Microbiol, 48 (2003) 77-84.

[359] J.E. Griffin, J.D. Gawronski, M.A. Dejesus, T.R. Ioerger, B.J. Akerley, C.M. Sassetti, High-resolution phenotypic profiling defines genes essential for mycobacterial growth and cholesterol catabolism, PLoS Pathog, 7 (2011) e1002251.

[360] B.F. Cravatt, A.T. Wright, J.W. Kozarich, Activity-based protein profiling: from enzyme chemistry to proteomic chemistry, Annual review of biochemistry, 77 (2008) 383-414.

[361] G.M. Simon, B.F. Cravatt, Activity-based proteomics of enzyme superfamilies: serine hydrolases as a case study, J Biol Chem, 285 (2010) 11051-11055.

[362] C. Ortega, L.N. Anderson, A. Frando, N.C. Sadler, R.W. Brown, R.D. Smith, A.T. Wright, C. Grundner, Systematic Survey of Serine Hydrolase Activity in Mycobacterium tuberculosis Defines Changes Associated with Persistence, Cell Chem Biol, 23 (2016) 290-298.

[363] D.A. Bachovchin, S.J. Brown, H. Rosen, B.F. Cravatt, Identification of selective inhibitors of uncharacterized enzymes by high-throughput screening with fluorescent activity-based probes, Nat Biotechnol, 27 (2009) 387-394.

[364] J.T. Belisle, V.D. Vissa, T. Sievert, K. Takayama, P.J. Brennan, G.S. Besra, Role of the major antigen of Mycobacterium tuberculosis in cell wall biogenesis, Science, 276 (1997) 1420-1422.

[365] L. Alibaud, Y. Rombouts, X. Trivelli, A. Burguiere, S.L. Cirillo, J.D. Cirillo, J.F. Dubremetz, Y. Guerardel, G. Lutfalla, L. Kremer, A Mycobacterium marinum TesA mutant defective for major cell wall-associated lipids is highly attenuated in Dictyostelium discoideum and zebrafish embryos, Mol Microbiol, 80 (2011) 919-934.

[366] J. Rengarajan, B.R. Bloom, E.J. Rubin, Genome-wide requirements for Mycobacterium tuberculosis adaptation and survival in macrophages, Proceedings of the National Academy of Sciences of the United States of America, 102 (2005) 8327-8332.

[367] N.A. Lack, K.C. Yam, E.D. Lowe, G.P. Horsman, R.L. Owen, E. Sim, L.D. Eltis, Characterization of a carbon-carbon hydrolase from Mycobacterium tuberculosis involved in cholesterol metabolism, J Biol Chem, 285 (2010) 434-443.

[368] A. Ryan, E. Polycarpou, N.A. Lack, D. Evangelopoulos, C. Sieg, A. Halman, S. Bhakta, O. Eleftheriadou, T.D. McHugh, S. Keany, E.D. Lowe, R. Ballet, A. Abuhammad, W.R. Jacobs, Jr., A. Ciulli, E. Sim, Investigation of the mycobacterial enzyme HsaD as a potential novel target for anti-tubercular agents using a fragment-based drug design approach, Br J Pharmacol, 174 (2017) 2209-2224.

[369] A. Viljoen, M. Richard, P.C. Nguyen, P. Fourquet, L. Camoin, R.R. Paudal, G.R. Gnawali, C.D. Spilling, J.F. Cavalier, S. Canaan, M. Blaise, L. Kremer, Cyclipostins and cyclophostin analogs inhibit the antigen 85C from Mycobacterium tuberculosis both in vitro and in vivo, J Biol Chem, 293 (2018) 2755-2769.

[370] P.C. Nguyen, V.S. Nguyen, B.P. Martin, P. Fourquet, L. Camoin, C.D. Spilling, J.F. Cavalier, C. Cambillau, S. Canaan, Biochemical and Structural Characterization of TesA, a Major Thioesterase Required for Outer-Envelope Lipid Biosynthesis in Mycobacterium tuberculosis, J Mol Biol, 430 (2018) 5120-5136.

[371] P. Santucci, V. Point, I. Poncin, A. Guy, C. Crauste, C. Serveau-Avesque, J.M. Galano, C.D. Spilling, J.F. Cavalier, S. Canaan, LipG a bifunctional phospholipase/thioesterase involved in mycobacterial envelope remodeling, Biosci Rep, 38 (2018) BSR20181953.

[372] M. Jackson, C. Raynaud, M.A. Laneelle, C. Guilhot, C. Laurent-Winter, D. Ensergueix, B. Gicquel, M. Daffe, Inactivation of the antigen 85C gene profoundly affects the mycolate content and alters the permeability of the Mycobacterium tuberculosis cell envelope, Mol Microbiol, 31 (1999) 1573-1587.

[373] T. Warrier, M. Tropis, J. Werngren, A. Diehl, M. Gengenbacher, B. Schlegel, M. Schade, H. Oschkinat, M. Daffe, S. Hoffner, A.N. Eddine, S.H. Kaufmann, Antigen 85C inhibition restricts Mycobacterium tuberculosis growth through disruption of cord factor biosynthesis, Antimicrob Agents Chemother, 56 (2012) 1735-1743.

[374] P.K. Crellin, J.P. Vivian, J. Scoble, F.M. Chow, N.P. West, R. Brammananth, N.I. Proellocks, A. Shahine, J. Le Nours, M.C. Wilce, W.J. Britton, R.L. Coppel, J. Rossjohn, T. Beddoe, Tetrahydrolipstatin inhibition, functional analyses, and three-dimensional structure of a lipase essential for mycobacterial viability, J Biol Chem, 285 (2010) 30050-30060.

[375] C.M. Goins, S. Dajnowicz, M.D. Smith, J.M. Parks, D.R. Ronning, Mycolyltransferase from Mycobacterium tuberculosis in covalent complex with tetrahydrolipstatin provides insights into antigen 85 catalysis, J Biol Chem, 293 (2018) 3651-3662.

[376] J. Lehmann, T.Y. Cheng, A. Aggarwal, A.S. Park, E. Zeiler, R.M. Raju, T. Akopian, O. Kandror, J.C. Sacchettini, D.B. Moody, E.J. Rubin, S.A. Sieber, An Antibacterial beta-Lactone Kills Mycobacterium tuberculosis by Disrupting Mycolic Acid Biosynthesis, Angew Chem Int Ed Engl, 57 (2018) 348-353.

[377] L.J. Keller, B.M. Babin, M. Lakemeyer, M. Bogyo, Activity-based protein profiling in bacteria: Applications for identification of therapeutic targets and characterization of microbial communities, Curr Opin Chem Biol, 54 (2020) 45-53.

[378] F. Faucher, J.M. Bennett, M. Bogyo, S. Lovell, Strategies for Tuning the Selectivity of Chemical Probes that Target Serine Hydrolases, Cell Chem Biol, 27 (2020) 937-952.

[379] M.J. Niphakis, B.F. Cravatt, Enzyme inhibitor discovery by activity-based protein profiling, Annual review of biochemistry, 83 (2014) 341-377.

[380] K.R. Tallman, S.R. Levine, K.E. Beatty, Small-Molecule Probes Reveal Esterases with Persistent Activity in Dormant and Reactivating Mycobacterium tuberculosis, ACS Infect Dis, 2 (2016) 936-944.

[381] A. Adibekian, B.R. Martin, C. Wang, K.L. Hsu, D.A. Bachovchin, S. Niessen, H. Hoover, B.F. Cravatt, Click-generated triazole ureas as ultrapotent in vivo-active serine hydrolase inhibitors, Nature chemical biology, 7 (2011) 469-478.

[382] M. Li, H.V. Patel, A.B. Cognetta, T.C. Smith, I. Mallick, J.-F. Cavalier, S. Canaan, B.B. Aldridge, B.F. Cravatt, J.C. Seeliger, A competitive activity-based protein profiling platform

yields cell wall synthesis inhibitors active against replicating and non-replicating <em>Mycobacterium tuberculosis</em&gt, bioRxiv, (2021) 2021.2004.2016.440156.

[383] M.S. Ravindran, M.R.J.A.-B.P.M. Wenk, Protocols, Activity-Based Lipid Esterase Profiling of M. bovis BCG at Different Metabolic States Using Tetrahydrolipstatin (THL) as Bait, (2017) 75-85.

[384] J. Lehmann, J. Vomacka, K. Esser, M. Nodwell, K. Kolbe, P. Rämer, U. Protzer, N. Reiling, S.A. Sieber, Human lysosomal acid lipase inhibitor lalistat impairs Mycobacterium tuberculosis growth by targeting bacterial hydrolases, MedChemComm, 7 (2016) 1797-1801.

[385] J. Hou, X. Liu, J. Shen, G. Zhao, P.G. Wang, The impact of click chemistry in medicinal chemistry, Expert Opinion on Drug Discovery, 7 (2012) 489-501.

[386] C. Spiteri, J.E. Moses, Copper-catalyzed azide-alkyne cycloaddition: regioselective synthesis of 1,4,5-trisubstituted 1,2,3-triazoles, Angew Chem Int Ed Engl, 49 (2010) 31-33.

[387] J.E. Stout, W.-J. Koh, W.W. Yew, Update on pulmonary disease due to non-tuberculous mycobacteria, International Journal of Infectious Diseases, 45 (2016) 123-134.

[388] A. Aubry, F. Mougari, F. Reibel, E. Cambau, Mycobacterium marinum, Microbiology spectrum, 5 (2017).

[389] E. Tortoli, T. Fedrizzi, C.J. Meehan, A. Trovato, A. Grottola, E. Giacobazzi, G.F. Serpini, S. Tagliazucchi, A. Fabio, C. Bettua, R. Bertorelli, F. Frascaro, V. De Sanctis, M. Pecorari, O. Jousson, N. Segata, D.M. Cirillo, The new phylogeny of the genus Mycobacterium: The old and the news, Infect Genet Evol, 56 (2017) 19-25.

[390] J. van Ingen, D. Wagner, J. Gallagher, K. Morimoto, C. Lange, C.S. Haworth, R.A. Floto, J. Adjemian, D.R. Prevots, D.E. Griffith, N.E.T. Ntm, Poor adherence to management guidelines in nontuberculous mycobacterial pulmonary diseases, Eur Respir J, 49 (2017).

[391] H.F. Schiff, S. Jones, A. Achaiah, A. Pereira, G. Stait, B. Green, Clinical relevance of non-tuberculous mycobacteria isolated from respiratory specimens: seven year experience in a UK hospital, Sci Rep, 9 (2019) 1730.

[392] N. Wetzstein, A. Geil, G. Kann, A. Lehn, G. Schüttfort, J. Kessel, T.M. Bingold, C.P. Küpper-Tetzel, A. Haberl, C.J.P.o. Graf, Disseminated disease due to non-tuberculous mycobacteria in HIV positive patients: A retrospective case control study, 16 (2021) e0254607.

[393] J.M. Leung, K.N. Olivier, Nontuberculous mycobacteria in patients with cystic fibrosis, in: Seminars in respiratory and critical care medicine, Thieme Medical Publishers, 2013, pp. 124-134.

[394] M. Osmani, D. Sotello, S. Alvarez, J.A. Odell, M. Thomas, Mycobacterium abscessus infections in lung transplant recipients: 15-year experience from a single institution, Transpl Infect Dis, 20 (2018) e12835.

[395] S.K. Cribbs, J.M. Beck, Microbiome in the pathogenesis of cystic fibrosis and lung transplant-related disease, Transl Res, 179 (2017) 84-96.

[396] M.R. Kiedrowski, J.M. Bomberger, Viral-Bacterial Co-infections in the Cystic Fibrosis Respiratory Tract, Front Immunol, 9 (2018) 3067.

[397] A.Y.H. Lim, S.H. Chotirmall, E.T.K. Fok, A. Verma, P.P. De, S.K. Goh, S.H. Puah, D.E.L. Goh, J.A. Abisheganaden, Profiling non-tuberculous mycobacteria in an Asian setting: characteristics and clinical outcomes of hospitalized patients in Singapore, BMC Pulm Med, 18 (2018) 85.

[398] C. Pierre-Audigier, A. Ferroni, I. Sermet-Gaudelus, M. Le Bourgeois, C. Offredo, H. Vu-Thien, B. Fauroux, P. Mariani, A. Munck, E.J.J.o.C.M. Bingen, Age-related prevalence and distribution of nontuberculous mycobacterial species among patients with cystic fibrosis, 43 (2005) 3467-3470.

[399] C.D. Spilling, B.P. MARTIN, S. CANAAN, J.-F. Cavalier, Fluorescent labeled inhibitors, in, Google Patents, 2015.

[400] H. Susani-Etzerodt, H. Schmidinger, G. Riesenhuber, R. Birner-Gruenberger, A. Hermetter, A versatile library of activity-based probes for fluorescence detection and/or affinity isolation of lipolytic enzymes, Chem Phys Lipids, 144 (2006) 60-68.

[401] H. Ouellet, J.B. Johnston, P.R.O.J.T.i.m. de Montellano, Cholesterol catabolism as a therapeutic target in Mycobacterium tuberculosis, 19 (2011) 530-539.

[402] R. Van der Geize, K. Yam, T. Heuser, M.H. Wilbrink, H. Hara, M.C. Anderton, E. Sim, L. Dijkhuizen, J.E. Davies, W.W. Mohn, L.D. Eltis, A gene cluster encoding cholesterol catabolism in a soil actinomycete provides insight into Mycobacterium tuberculosis survival in macrophages, Proceedings of the National Academy of Sciences of the United States of America, 104 (2007) 1947-1952.

[403] G. Singh, G. Singh, D. Jadeja, J.J.C.r.i.m. Kaur, Lipid hydrolizing enzymes in virulence: Mycobacterium tuberculosis as a model system, 36 (2010) 259-269.

[404] L. Dedieu, C. Serveau-Avesque, L. Kremer, S. Canaan, Mycobacterial lipolytic enzymes: a gold mine for tuberculosis research, Biochimie, 95 (2013) 66-73.

[405] J. Krysiak, S.A. Sieber, Activity-Based Protein Profiling in Bacteria, Methods Mol Biol, 1491 (2017) 57-74.

[406] M. Li, H.V. Patel, A.B. Cognetta, 3rd, T.C. Smith, 2nd, I. Mallick, J.F. Cavalier, M.L. Previti, S. Canaan, B.B. Aldridge, B.F. Cravatt, J.C. Seeliger, Identification of cell wall synthesis inhibitors active against Mycobacterium tuberculosis by competitive activity-based protein profiling, Cell Chem Biol, 29 (2022) 883-896 e885.

[407] P.J. Brennan, Structure, function, and biogenesis of the cell wall of Mycobacterium tuberculosis, Tuberculosis (Edinb), 83 (2003) 91-97.

[408] H.M. Alvarez, A. Steinbuchel, Triacylglycerols in prokaryotic microorganisms, Appl Microbiol Biotechnol, 60 (2002) 367-376.

[409] I. Mallick, P. Santucci, I. Poncin, V. Point, L. Kremer, J.F. Cavalier, S. Canaan, Intrabacterial lipid inclusions in mycobacteria: unexpected key players in survival and pathogenesis?, FEMS microbiology reviews, 45 (2021) fuab029.

[410] T. Fujimoto, Y. Ohsaki, Cytoplasmic lipid droplets: rediscovery of an old structure as a unique platform, Ann N Y Acad Sci, 1086 (2006) 104-115.

[411] N.J. Garton, M.R. Barer, Mycobacterial Lipid Bodies and the Chemosensitivity and Transmission of Tuberculosis, in: Health Consequences of Microbial Interactions with Hydrocarbons, Oils, and Lipids, 2020, pp. 109-132.

[412] T.C. Walther, R.V. Farese, Jr., Lipid droplets and cellular lipid metabolism, Annual review of biochemistry, 81 (2012) 687-714.

[413] F. Wilfling, J.T. Haas, T.C. Walther, R.V. Farese, Jr., Lipid droplet biogenesis, Curr Opin Cell Biol, 29 (2014) 39-45.

[414] J. Daniel, H. Maamar, C. Deb, T.D. Sirakova, P.E. Kolattukudy, Mycobacterium tuberculosis Uses Host Triacylglycerol to Accumulate Lipid Droplets and Acquires a Dormancy-Like Phenotype in Lipid-Loaded Macrophages, PLOS Pathogens, 7 (2011) e1002093.

[415] O. Neyrolles, R. Hernandez-Pando, F. Pietri-Rouxel, P. Fornes, L. Tailleux, J.A. Barrios Payan, E. Pivert, Y. Bordat, D. Aguilar, M.C. Prevost, C. Petit, B. Gicquel, Is adipose tissue a place for Mycobacterium tuberculosis persistence?, PLoS One, 1 (2006) e43.

[416] D.J. Sloan, H.C. Mwandumba, N.J. Garton, S.H. Khoo, A.E. Butterworth, T.J. Allain, R.S. Heyderman, E.L. Corbett, M.R. Barer, G.R. Davies, Pharmacodynamic Modeling of Bacillary Elimination Rates and Detection of Bacterial Lipid Bodies in Sputum to Predict and Understand Outcomes in Treatment of Pulmonary Tuberculosis, Clin Infect Dis., 61 (2015) 1-8.

[417] R.J. Hammond, V.O. Baron, K. Oravcova, S. Lipworth, S.H. Gillespie, Phenotypic resistance in mycobacteria: is it because I am old or fat that I resist you?, J Antimicrob Chemother, 70 (2015) 2823-2827.

[418] E. Iona, F. Giannoni, M. Pardini, L. Brunori, G. Orefici, L. Fattorini, Metronidazole plus rifampin sterilizes long-term dormant Mycobacterium tuberculosis, Antimicrob Agents Chemother, 51 (2007) 1537-1540.

[419] A. Viljoen, M. Blaise, C. de Chastellier, L. Kremer, MAB_3551c encodes the primary triacylglycerol synthase involved in lipid accumulation in Mycobacterium abscessus, Molecular microbiology, (2016).

[420] J. Daniel, N. Kapoor, T. Sirakova, R. Sinha, P. Kolattukudy, The perilipin-like PPE15 protein in Mycobacterium tuberculosis is required for triacylglycerol accumulation under dormancy-inducing conditions, Mol Microbiol, 101 (2016) 784-794.

[421] G. Johnson, The alpha/beta Hydrolase Fold Proteins of Mycobacterium tuberculosis, with Reference to their Contribution to Virulence, Current protein & peptide science, 18 (2017) 190-210.

[422] R. Avellan, M. Sarrazin, C.D. Spilling, C. Crauste, S. Canaan, J.-F. Cavalier, Deciphering the physiological role of serine enzymes involved in mycobacterial lipid metabolism using activity-based protein profiling, in: Z. Fatima, S. Canaan (Eds.) Biology of Mycobacterial Lipids, Academic Press, 2022, pp. 235-251.

[423] M. Sarrazin, B.P. Martin, R. Avellan, G.R. Gnawali, I. Poncin, H. Le Guenno, C.D. Spilling, J.F. Cavalier, S. Canaan, Synthesis and Biological Characterization of Fluorescent Cyclipostins and Cyclophostin Analogues: New Insights for the Diagnosis of Mycobacterial-Related Diseases, ACS Infect Dis, 8 (2022) 2564-2578.

[424] S. Barelier, R. Avellan, G.R. Gnawali, P. Fourquet, V. Roig-Zamboni, I. Poncin, V. Point, Y. Bourne, S. Audebert, L. Camoin, C.D. Spilling, S. Canaan, J.F. Cavalier, G. Sulzenbacher, Direct capture, inhibition and crystal structure of HsaD (Rv3569c) from M. tuberculosis, FEBS J, 290 (2023) 1563-1582.

[425] L.G. Wayne, L.G. Hayes, An in vitro model for sequential study of shiftdown of Mycobacterium tuberculosis through two stages of nonreplicating persistence, Infect Immun, 64 (1996) 2062-2069.

[426] P. Santucci, M.D. Johansen, V. Point, I. Poncin, A. Viljoen, J.F. Cavalier, L. Kremer, S. Canaan, Nitrogen deprivation induces triacylglycerol accumulation, drug tolerance and hypervirulence in mycobacteria, Sci Rep, 9 (2019) 019-45164.

[427] M. Robbe-Saule, M. Foulon, I. Poncin, L. Esnault, H. Varet, R. Legendre, A. Besnard, A.E. Grzegorzewicz, M. Jackson, S. Canaan, L. Marsollier, E. Marion, Transcriptional adaptation of Mycobacterium ulcerans in an original mouse model: New insights into the regulation of mycolactone, Virulence, 12 (2021) 1438-1451.

[428] Y. Chen, Y. Ding, L. Yang, J. Yu, G. Liu, X. Wang, S. Zhang, D. Yu, L. Song, H. Zhang, C. Zhang, L. Huo, C. Huo, Y. Wang, Y. Du, P. Zhang, H. Na, S. Xu, Y. Zhu, Z. Xie, T. He, Y. Zhang, G. Wang, Z. Fan, F. Yang, H. Liu, X. Zhang, M.Q. Zhang, Y. Li, A. Steinbüchel, T. Fujimoto, S. Cichello, P. Liu, Integrated omics study delineates the dynamics of lipid droplets in Rhodococcus opacus PD630, Nucleic Acids Res, 42 (2014) 1052-1064.

[429] Y. Ding, L. Yang, S. Zhang, Y. Wang, Y. Du, J. Pu, G. Peng, Y. Chen, H. Zhang, J. Yu, H. Hang, P. Wu, F. Yang, H. Yang, A. Steinbüchel, P. Liu, Identification of the major functional proteins of prokaryotic lipid droplets, J Lipid Res, 53 (2012) 399-411.

[430] R.M. Armstrong, D.C. Carter, S.N. Atkinson, S.S. Terhune, T.C. Zahrt, Association of Mycobacterium Proteins with Lipid Droplets, J Bacteriol, 200 (2018) 00240-00218.

[431] T.D. Sirakova, V.S. Dubey, C. Deb, J. Daniel, T.A. Korotkova, B. Abomoelak, P.E. Kolattukudy, Identification of a diacylglycerol acyltransferase gene involved in accumulation of triacylglycerol in Mycobacterium tuberculosis under stress, Microbiology, 152 (2006) 2717-2725.

[432] C. Deb, C.M. Lee, V.S. Dubey, J. Daniel, B. Abomoelak, T.D. Sirakova, S. Pawar, L. Rogers, P.E. Kolattukudy, A novel in vitro multiple-stress dormancy model for Mycobacterium

tuberculosis generates a lipid-loaded, drug-tolerant, dormant pathogen, PLoS One, 4 (2009) 0006077.

[433] K. Bersuker, C.W.H. Peterson, M. To, S.J. Sahl, V. Savikhin, E.A. Grossman, D.K. Nomura, J.A. Olzmann, A Proximity Labeling Strategy Provides Insights into the Composition and Dynamics of Lipid Droplet Proteomes, Dev Cell, 44 (2018) 97-112.

[434] P. Liu, Y. Ying, Y. Zhao, D.I. Mundy, M. Zhu, R.G. Anderson, Chinese hamster ovary K2 cell lipid droplets appear to be metabolic organelles involved in membrane traffic, J Biol Chem, 279 (2004) 3787-3792.

[435] S. Cermelli, Y. Guo, S.P. Gross, M.A. Welte, The lipid-droplet proteome reveals that droplets are a protein-storage depot, Curr Biol, 16 (2006) 1783-1795.

[436] A.S. Zembroski, C. Andolino, K.K. Buhman, D. Teegarden, Proteomic Characterization of Cytoplasmic Lipid Droplets in Human Metastatic Breast Cancer Cells, Front Oncol, 11 (2021).

[437] U.S. Ganapathy, L. Bai, L. Wei, K.A. Eckartt, C.M. Lett, M.L. Previti, I.S. Carrico, J.C. Seeliger, Correction to Compartment-Specific Labeling of Bacterial Periplasmic Proteins by Peroxidase-Mediated Biotinylation, ACS Infect Dis, 4 (2018) 25.

[438] N. Jaisinghani, M.L. Previti, J. Andrade, M. Askenazi, B. Ueberheide, J.C. Seeliger, Cell wall proteomics in live Mycobacterium tuberculosis uncovers exposure of ESX substrates to the periplasm, bioRxiv. 2023 Mar 29:2023.03.29.534792. doi: 10.1101/2023.03.29.534792. Preprint.

[439] M. Richard, A.V. Gutiérrez, A. Viljoen, D. Rodriguez-Rincon, F. Roquet-Baneres, M. Blaise, I. Everall, J. Parkhill, R.A. Floto, L. Kremer, Mutations in the MAB_2299c TetR Regulator Confer Cross-Resistance to Clofazimine and Bedaquiline in Mycobacterium abscessus, Antimicrob Agents Chemother, 63 (2018) 01316-01318.